# Cardiff University
# School of Physics and Astronomy



# Silicon-Based Quantum Optics and Quantum Computing

A thesis submitted in partial fulfilment

of the requirement for the degree of Doctor of

Philosophy

# Ryan Henry Stock

# May 30, 2018

# Dedication

To everyone before me who built, lived, and learnt, so that we could get here.

# Acknowledgements

I would like begin by thanking Cardiff University as a whole, for the 8 years of learning so far; first as an overconfident undergraduate, and then later as a confused graduate student.

I express my sincerest gratitude to Stephen Lynch, the guidance and motivation provided have been crucial to getting here. Without the motivation, encouragement, analysis, laboratory direction, and critical comments on writing style, this thesis would never have been begun, let alone completed.

I would like to thank Sean Giblin, for pointing out the overlooked, and demonstrating a frenetic combination of physics and phrasing.

I also thank Annabel Cartwright, for being available to discuss the PhD process when I was most lost in it.

I am grateful to the review and progress panel, Giampaulo Pisano, David Jesson and Joe Wilkes; without oversight where might I have wandered?

I thank Chris Hodges for invaluable assistance in lab, and his encyclopaedic optical components knowledge.

# Oral and Poster Presentations

During the work for this thesis the author has given talks and presented research posters at several conferences, these are listed below.

R. H. Stock. *FTIR and time resolved fluorescence.* Cardiff School of Physics and Astronomy Postgraduate Conference. Talk on 24/09/2014

R. H. Stock, W. S. Royle, C. Hodges, M. J. Graf, B. Z. Malkin, S. R. Giblin and S. A. Lynch. *Time-resolved FT-IR spectroscopy of rare earth ions in fluoride crystals.* PHOTONICA 2015, V International School and Conference on Photonics, Belgrade, Serbia. Poster presented on 25/08/2015.

R. H. Stock, William S. Royle, Chris Hodges, Yuri A. Astrov, Valentina B. Shuman, Leonid M. Portsel, Anatoly N. Lodygin, and Stephen A. Lynch. *Transient FT-IR Spectroscopy of Dilute Rare Earth Ions; the Dynamic Quantum System of* $Ho^{3+} : LiY F_4$. Semiconductor and Integrated Optoelectronics, SIOE 16. Cardiff University. Poster presented on 05/04/2016.

Ryan H. Stock, William S. Royle, Chris Hodges, Yuri A. Astrovy, Valentina B. Shumany, Leonid M. Portsely, Anatoly N. Lodyginy, and Stephen A. Lynch. *Mid-infrared Spectroscopy of Sulphur and Selenium Donors in Silicon for Quantum Optics.* IRMMW-THZ 2016, 41st International Conference on Infrared, Millimeter and

Terahertz Waves, Copenhagen Denmark. Talk given on 29/09/2016.

# Work to be Published

Ryan H. Stock, William S. Royle, Chris Hodges, Yuri A. Astrov, Valentina B. Shuman, Leonid M. Portsel, Anatoly N. Lodygin, and Stephen A. Lynch. *Long-lived Infrared Donor Centres in Silicon for Quantum Information Technologies.* Manuscript yet to be submitted.

# Abstract

In this thesis is presented a brief review of quantum computing, the DiVincenzo criteria, and the possibility of using a solid state system for building a quantum computing architecture. Donor electron systems in silicon are discussed, before chalcogen, "deep", double donors are suggested as a good candidate for fulfilment of the criteria; the optically driven Stoneham proposal, where the spin-spin interaction between two donor electron spin qbits is mediated by the optically controlled, excited, state of a third donor electron, forms the basis of this [1]. Coherence lifetimes are established as a vital requirement of a quantum bit, but radiative lifetimes must also be long. If the spin-spin interaction between qbits is decreased, or turned off, by the de-excitation of the mediating donor electron then the coherence of the qbit is rendered irrelevant; de-excitation will ruin quantum computations that depend upon an interaction that only happens when the mediating electron is in an excited state.

Effective mass theory is used to estimate excited state donor, $2P$, wavefunctions for selenium doped silicon, and recent Mott semiconductor to metal transition doping data [2] is used to scale the spatial extent of the $1S(A_1)$ ground state wavefunction. Using these wavefunctions, the expected radiative lifetimes are then calculated, via Fermi's golden rule, to be between 9 ns and 17 ns for the $2P_0$ state, and 12 ns to 20 ns for the $2P_{\pm 1}$ state. Fourier Transform InfraRed (FTIR) absorbance spectroscopy is used to determine the optical transitions for selenium donors in silicon, this has

allowed agreement between literature, measured, and effective mass theory energy values for the particular samples measured. FTIR time resolved spectroscopy has then been used to measure the radiative emission spectrum of selenium doped silicon samples at 10-300K, following a 1220 nm laser pulse. Fitting to the exponentially decaying emission data, selenium radiative lifetimes as long as 80 ns are found; for the $2P_0$ to $1S(A_1)$ transition in an atomic selenium donor complex at 10K. A factor of between 4 and 8 agreement is found between calculated and measured radiative lifetimes. This offers the possibility of nanosecond scale donor electron coherence times for chalcogen dopants in silicon.

# Contents

Contents

# Contents

# Contents

All non photograph images, graphs, and plots in this thesis, unless specified ot-

herwise, are generated with the use of either: The matplotlib [3], numpy [4], and scipy [5] libraries of the python 2.7[6] programming language, or the Inkscape vector drawing software.

# List of Acronyms Used

**AC** Alternating Current

**ADC** Analogue to Digital Converter

**BS** Beam Splitter

**DC** Direct Current

**DFT** Discrete Fourier Transform

**DS** Dispersive Spectroscopy

**EM** ElectroMagnetic

**EMT** Effective Mass Theory

**FFT** Fast Fourier Transform

**FS** Fourier Series

**FT** Fourier Transform

**FTIR** Fourier Transform InfraRed

**FTS** Fourier Transform Spectroscopy

**FWHM** Full Width Half Maximum

**IR** InfraRed

# Contents

**NIR** Near InfraRed

**MIR** Mid InfraRed

**OPD** Optical Path Difference

**Qbit** Quantum bit - Sometimes written as qbit / qubit / Qubit

**qbit** Quantum bit

**qbits** Quantum bits

**RSFTS** Rapid Scan Fourier Transform Spectroscopy

**STM** Scanning Tunnelling Microscope

**SNR** Signal to Noise Ratio

**SSFTS** Step Scan Fourier Transform Spectroscopy

**RSA** Rivest-Shamir-Adleman

# Thesis Overview

A brief overview of this thesis is given here, along with a schematic diagram in figure 0.1. The document should be read starting with chapters 1 and 2. A thorough background of Fourier transform spectroscopy is given in appendixes C and D, these provide context and detail for the experimental methods in chapter 4. Similarly, a review of the basic quantum mechanics used and necessary derivations are shown in appendixes A and B respectively; these then provide support to chapter 3 which is an introduction to, and application of, effective mass theory for estimating radiative transition rates. Chapter 5 then contains experimental results and their comparison to the calculations from chapter 3. The conclusions and future directions are summarised in chapter 6.

Contents
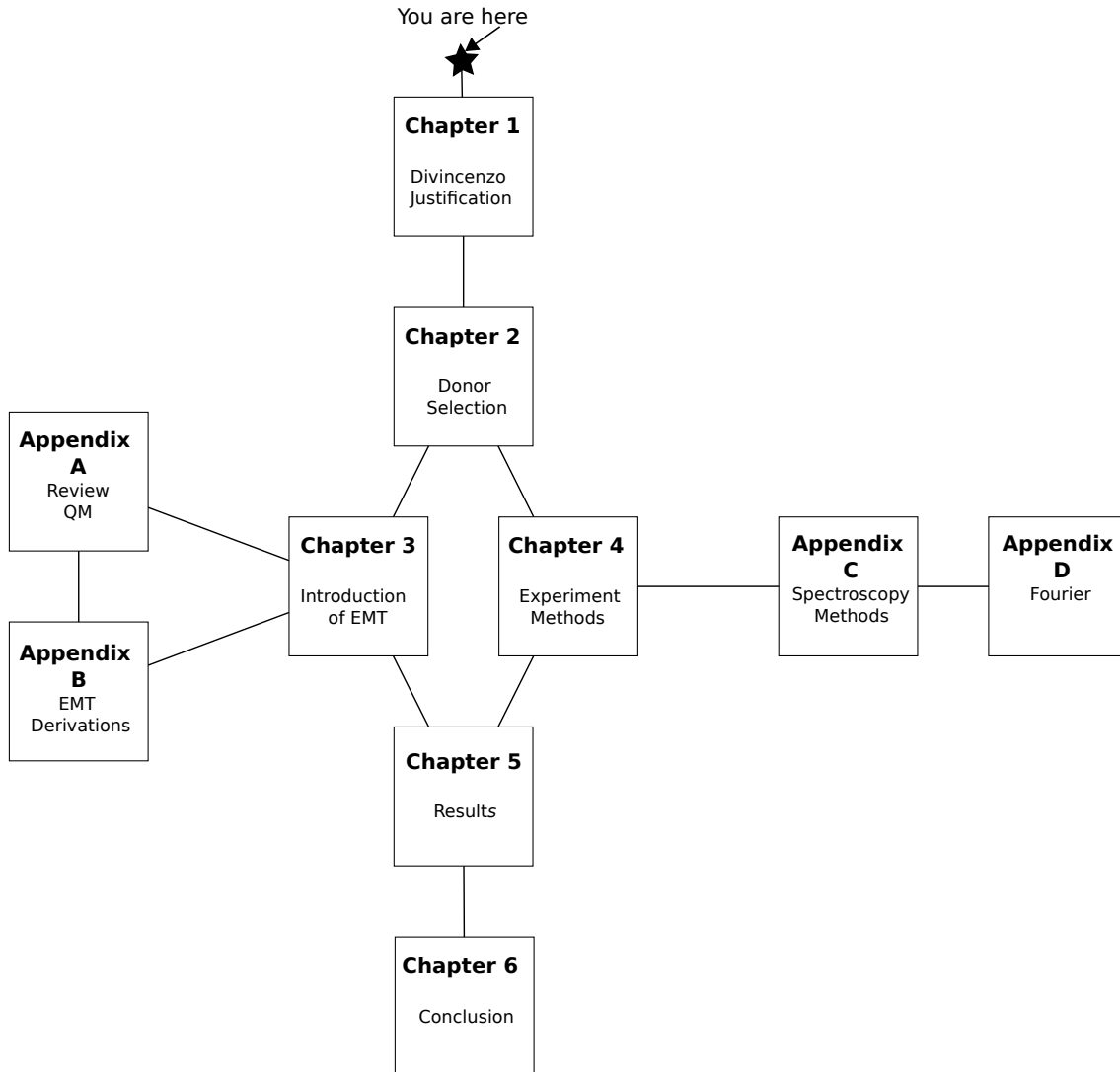


Figure 0.1.: Sketch of the thesis layout. Read from chapter 1 to chapter 6. Chapters 3 and 4 may be read in either order. Appendixes A and B may be omitted if familiar with EMT, while the same is true of C and D for Fourier transform spectroscopy.

**Chapter 1**    The thesis begins with a chapter justifying and providing a goal for the work carried out. This consists of a brief explanation of the need for quantum computing and what it is, followed by a review of the DiVincenzo criteria. The use of donor electron system in silicon as part of both the Kane [7] and Stoneham[1] quantum computing proposals is described. The long decoherence lifetime DiVincenzo criteria is singled out as a target to move towards. However, firstly the radiative lifetimes must be confirmed and this must be done via a comparison of measurement

and calculated prediction.

**Chapter 2** This is a review of some of the relevant properties of silicon, along with the reasons for its choice as a host material and chalcogens as donors. The reasons for the choice of dopants, such as manufacturing ability and possible doping concentrations, are discussed along with donor energy levels and vulnerability to thermal perturbation.

**Chapter 3** Here an attempt is made to calculate radiative transition lifetimes, this is to compare them with measured values. This is done using an effective mass degenerate scaled hydrogenic basis to obtain dipole transition elements for donor electrons in silicon. It begins with a reproduction of the EMT wavefunction calculations by Kohn[8]. The published literature only provides a framework and calculated energy levels, no wavefunction parameters, thus the energy functions must be re-obtained and parameters recalculated. The central cell problem, which is a breakdown in applicability of the EMT approximations for the ground donor state, is then overcome by the use of recent Mott semiconductor to metal transition data[2]. Transition rates are then estimated using Fermi's golden rule.

**Chapter 4** Chapter four then contains the experimental methods, and a brief description of the equipment used. FTS is introduced, along with absorbance and step scan time resolved spectroscopy. The measurement of the time evolution of the emission from a selenium doped silicon sample, following 5 ns 1220 nm optical pumping with 7.5 mJ pulses, is fully explained; this experiment allows an estimate of the radiative lifetime to be extracted from a fit to the data.

**Chapter 5** Absorbance spectroscopy used to identify the optimal sample available is shown. This is followed by the results of the time resolved emission experiment, explained in chapter 4. Fits to emission data are compared to the calculations from

chapter 3.

**Chapter 6**   Finally a conclusion is given where the results, the usefulness of EMT in predicting them, and the implications are summarised. Possible avenues of future work are briefly discussed.

# 1. A Brief Review of Quantum Computing in Silicon

This chapter begins by explaining the question that this thesis attempts to answer, and justifying why this is important. Firstly, an introduction to quantum computing and its purpose is given. Secondly, the criteria for a potential system to be used for quantum computing are detailed, these are the DiVincenzo criteria [9][10]. Finally, the satisfaction of these criteria is reviewed for silicon based quantum computing architecture, the Kane[11][7] and Stoneham[1] proposals, and a gap in our knowledge is thus identified. Can chalcogen group dopants in silicon provide a system that fulfils the criteria for long decoherence times?

This question is narrowed down by considering that a quantum computing architecture must have a 2 level system, to be used as a Quantum bit (qbit), and these must remain coherent over any computation time; it has been suggested that the qbit information can be encoded on deep donor electron spins[1], or shallow donor nuclear spins [7]. Sets of these qbits must be able to interact, and must remain coherent over the interaction time. Chalcogen group donors in silicon are a possible donor system because of their deep binding energy, giving the expectation that they will be more resistant to thermal excitation, and have a smaller ground state than shallow donors. Such a donor's excited electron states could provide the interaction between qbits of a different donor element, as for Stoneham[1], or the small ground

state could use its spin as a qbit. To expand on this, Stoneham proposes an architecture where there are two spatially separated donor electrons whose spin states form qbits, with a third and different donor in-between them. Excited states of the middling donor electron overlap both the others, far more so than the ground state, thus increasing their spin to spin interaction strength.

Either way, the optically excited state must have a long decoherence time and a long radiative lifetime. The question prompted is then: what are the radiative lifetimes of chalcogen donor electrons in silicon? This thesis attempts to begin answering that for the chalcogen selenium.

## 1.1. Introduction to Quantum Computing

A quantum computer is simply a computer that uses the principles of quantum, rather than classical, mechanics. The justification for why we as a civilisation should, and arguably must, work towards building such a computer are outlined here. Following this an introduction, albeit brief, of the basic principles and terminology is given.

### 1.1.1. Justifying the Importance of Quantum Computing

As computing architecture tends to smaller and smaller scales, it is in one sense inevitable that quantum effects must be considered at some point. But this doesn't justify, it merely indicates that quantum effects must be considered; perhaps a classical computer could be built in such a manner as to bypass or overcome quantum effects. The fundamental motivation comes from the practical need to be able to simulate, or calculate, the behaviour of reality. However, reality depends on quantum behaviour, that is, to simulate reality exactly requires a computer based upon the principles of quantum mechanics; this line of reasoning was outlined by Feynman in

1982 [12].

This is the quantum simulation justification. To numerically calculate the behaviour of any quantum system, described by the Schrodinger equation, various approximations must be applied, this is true for both a classical or a quantum computer. However, as the size of the system increases linearly the computational complexity increases exponentially. For a classical computer this means the cost in time (or in size and clock speed) is exponential, but for a quantum computer this cost scales polynomially; for example, molecular systems are notoriously complex to simulate using classical computers resulting primarily in simple diatomic and triatomic molecular systems being studied [13]. This has severe implications for novel drug development, etc, being that many organic molecules are far more complex than triatomic systems. In addition, the potential technological applications for precisely engineered atomic scale electronic, and optical, devices cannot be easily realised unless their behaviour can be simulated.

The potential of a quantum computer beyond simulating physics systems then became apparent in 1994 with the Shor algorithm[14]. The factorisation of large numbers into their prime factors is a task that can only be accomplished by a classical computer in approximately exponential time, while Shor showed that a quantum algorithm could solve this in polynomial time.[15] This is a concern because the well known Rivest-Shamir-Adleman (RSA) public key encryption algorithm, the basis of secure online communication and commerce, this is a public key encryption scheme that relies on the computational difficulty of finding the prime factors of very large numbers. The factorisation of primes using Shor's algorithm has been demonstrated for the number 15 [16][17][18][19].

Other quantum algorithms that solve a problem faster than is possible with a classi-

cal system do exist, for example Grover's search[20]; Grover's search finds an object in a list of size $N$ in at least $\sqrt{N}$ steps, compared to the classical $N$ steps. Thus quantum computing is justified because it allows the simulation of things a classical computer cannot simulate, and algorithms exist for specific tasks that are faster than the classical alternative. The source of this improvement is that the quantum system can use interference, this causes the most probable measured outcome to be the answer to the computation.

## 1.1.2. Quantum Computer Basics

A quantum computer relies on the fundamental properties of interference and superposition[21][22]. To build a computing architecture exploiting these properties thus requires a quantum bit and a quantum logic gate to replace the classical analogues. While not complete, these quantum bits and gates are the basics necessary for an understanding of what a quantum computing architecture would be like.

### 1.1.2.1. A Quantum Bit

A classical bit is a two state switch, with the two state 0 and 1. Correspondingly a qbit is a two state system, the simplest possible quantum system; the qbits state is then a unit vector in a two dimension vector space [21][22], shown in figure1.1. The two states of the system are then orthogonal and are represented by the state vectors $|0\rangle$ and $|1\rangle$, these are then the quantum analogues of the classical bit states of 0 and 1. This qbit is in general in a superposition of the form $\psi = a\,|0\rangle + b\,|1\rangle$, where $a$ and $b$ are complex constants subject to the normalisation $|a|^2 + |b|^2 = 1$; when measured the probability of the qbit to be found in a particular state is then $|a|^2$ or $|b|^2$ for the states $|0\rangle$ and $|1\rangle$ respectively.

The probability coefficients $a$ and $b$ are complex numbers because of being quantum objects, it is their defined fundamental property[23]. Being complex vectors they

can be represented as a phasor $ae^{i\theta}$, however, only the phase difference $\phi$ is relevant, thus the state of the qbit can be written as in equation 1.1[24, p15], or in column vector form in equation 1.2. This can be represented as a vector on a sphere, the Bloch sphere shown in figure 1.1.

$$|\psi\rangle = \cos\left(\frac{\theta}{2}\right)|0\rangle + e^{i\phi}\sin\left(\frac{\theta}{2}\right)|1\rangle \tag{1.1}$$

$$\psi = \begin{bmatrix} \cos\left(\frac{\theta}{2}\right) \\ e^{i\phi}\sin\left(\frac{\theta}{2}\right) \end{bmatrix} \tag{1.2}$$
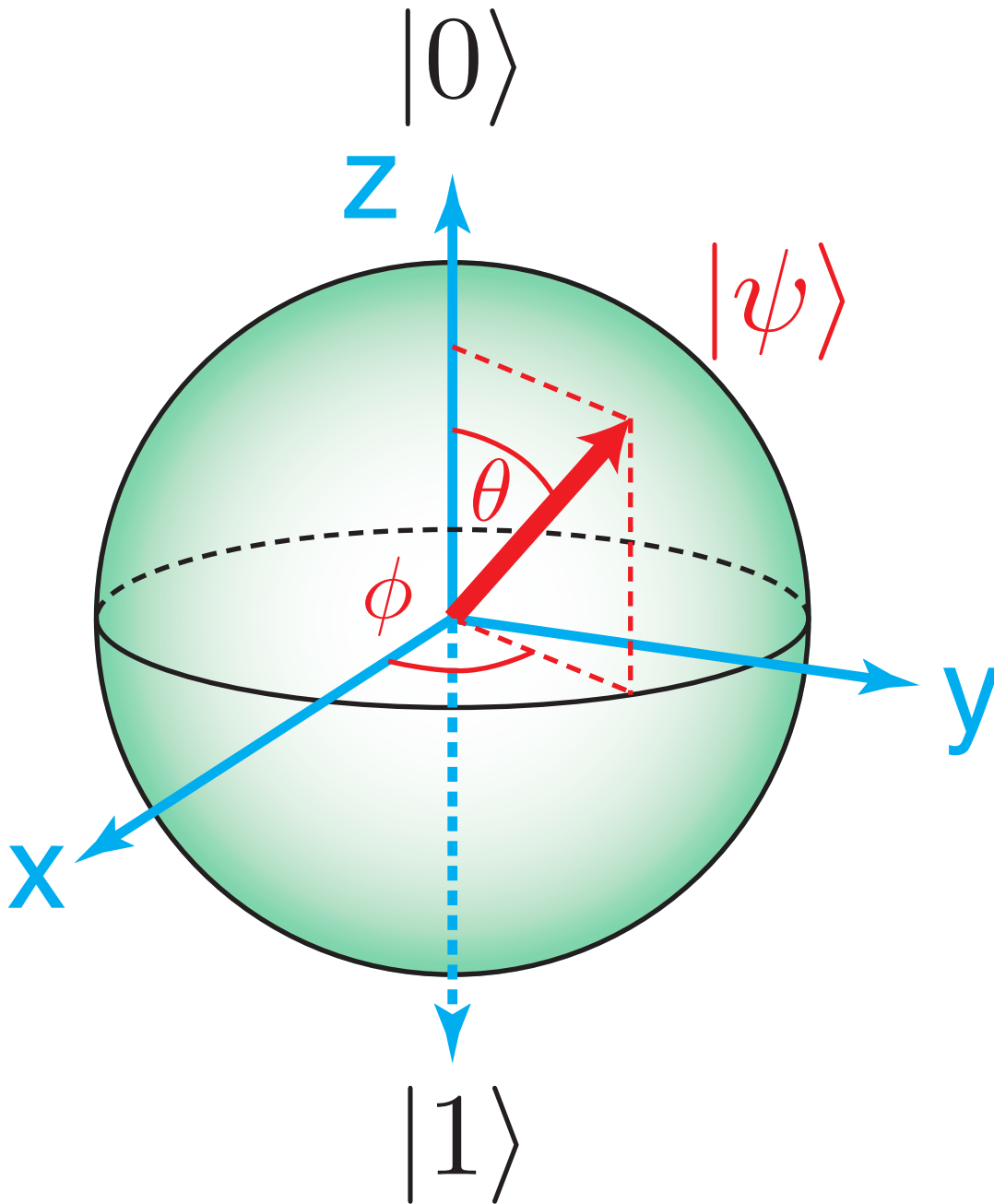
Figure 1.1.: Bloch sphere representing a qbit. The direction of a vector on the surface of the sphere shows the state of the qbit, directly up is the $|0\rangle$ state while down is $|1\rangle$. Superposition of the states is then represented by any vector not directly up or down, i.e the $\theta$ angle. The phase of the state is represented by the x,y direction, i.e the $\phi$ angle.

## 1.1.2.2. The Gate Model

In order to carry out any simulation or algorithm the qbit state must be acted upon. Classical computing uses various logic gates, for example the AND, OR, NOT, etc and the quantum equivalent is correspondingly an operator which can be written as a matrix; the gate matrix then acts on the column vector representation of the qbit. This operator can be written in terms of the interaction Hamiltonian $H'$ of the system, this could be caused optically, via magnetic field, or some other method; this is shown in equation 1.3. This is an arbitrary quantum gate, the form and time evolution of the Hamiltonian dictating the operation performed; however, it must be unitary to preserve the norm of the system, $U^\dagger U = I$ where $I$ is the unit matrix [24, p206].

$$U = e^{-\frac{i}{\hbar} \int_{t_0}^{t} H'(t')dt'}$$ (1.3)

In general, in a matrix representation that acts on the column vector qbit, a quantum gate has the form of equation 1.4[24, 1.17]. Here $\beta$ and $\delta$ are phase angles corresponding to rotation around the x,y plane of the Bloch sphere, and $\gamma$ is a rotation angle corresponding to a rotation between the $|0\rangle$ and $|1\rangle$ states, $\alpha$ is then just a phase term for the whole gate and is practically irrelevant.

$$U = e^{i\alpha} \begin{bmatrix} e^{-i\frac{\beta}{2}} & 0 \\ 0 & e^{i\frac{\beta}{2}} \end{bmatrix} \begin{bmatrix} \cos(\frac{\gamma}{2}) & -\sin(\frac{\gamma}{2}) \\ \sin(\frac{\gamma}{2}) & -\cos(\frac{\gamma}{2}) \end{bmatrix} \begin{bmatrix} e^{-i\frac{\delta}{2}} & 0 \\ 0 & e^{i\frac{\delta}{2}} \end{bmatrix}$$ (1.4)

## 1.2. DiVincenzo Criteria

The qbit and quantum gates are the basic building blocks, but there are conditions necessary for a quantum computing architecture. DiVincenzo outlines the "five" conditions for the realization of a physical quantum computer [10] :

1. *"A scalable physical system with well characterized qubits"*

2. *"The ability to initialize the state of the qubits to a simple fiducial state"*

3. *"Long relevant decoherence times, much longer than the gate operation time "*

4. *"A 'universal' set of quantum gates"*

5. *"A qubit specific measurement capability"*

The requirements form a check list for a quantum computer, but there are two bonus criteria for exchanging quantum information [10] :

1. *"The ability to interconvert stationary and flying qubits"*

2. *"The ability faithfully to transmit flying qubits between specified locations"*

The initial five criteria are those directly applicable to a quantum computer, which can be achieved by fulfilling these directly. However, a larger number of qbits, or a geographically wider quantum information network, requires the final two criteria to be met; these will not be focused on in this thesis in any further detail.

### 1.2.1. Fulfilment of the Criteria

There are several systems that could fulfil the DiVincenzo criteria, such as trapped ions[25], superconductors[26], but they are not the focus of this thesis. Instead silicon is the target, specifically dopant atoms in silicon so as to form a solid state

quantum architecture. A brief explanation of how each criterion can be met by donor dopants in silicon, along with any specific advantages, is given here.

### 1.2.1.1. Scalable System

The first requirement is that there is a "scalable physical system with well characterised qubits". As the computation revolution of the 20th century has shown, doped silicon is indeed a scalable physical system; the computer this was written on is evidence for this. While the requirement for a qbit could be met by the two distinct spin states of donor nuclei or electrons, it is even conceivable that the ground state and an excited state of a donor electron in silicon could correspond to the two states of a qbit. Indeed all that is required is a two level system that is scalable, and doped silicon is full of them. For the system to be well characterised, DiVincenzo states that the Hamiltonian of the system must be known [10]; the Hamiltonian of spin states in Si is known [27, eq1], and that of an electromagnetic interaction with a donor electron system is well known [28, eq 7.1]. Thus doped silicon meets the first criteria.

### 1.2.1.2. A Universal set of Quantum Gates And Initialisable qbits

The second and third requirements are grouped together here, because while explicitly separate requirements, they are both "solved" by the same properties of resonant optical interaction with the two level atomic system that a donor electron can form.

### Initialization

The second requirement is "The ability to initialize the state of the qubits to a simple fiducial state..." . This requirement is relatively simple, in that it only requires that qbits are initialised into a known state in reproducible manner before any computation begins. This has been demonstrated in phosphorus doped silicon,

with hyperpolarization of nuclear spins [29], and effectively for an optical interaction by the coherent control of the electron state [30].

**Universal Quantum Gates**

The third requirement is then "A 'Universal' set of quantum gates". Every quantum gate must then be a unitary transformation that can be applied to a qbit; if it is not unitary then the normalisation of the qbit wavefunction no longer holds, the consequences of this are non-physical. Any scheme for quantum computation requires an implementation of the quantum gates that is good enough that quantum error correction can function [10]; quantum error correction is beyond the scope of this thesis and will not be discussed in any more detail.

As shown above in equations 1.2 and 1.4, a quantum gate can be built out of the application of some perturbing Hamiltonian to a system. A resonant interaction between a perturbing electromagnetic field and a donor electron system can then be represented as equation 1.5; where $\omega$ is the angular frequency corresponding the energy difference between the $|0\rangle$ and $|1\rangle$ states, $T$ is the total time of the gate operation and the optical pulse is assumed to be zero outside of this time window, while $\Omega$ is the pulse area defined in equation 1.6[31, 13.23][22]; for a constant field amplitude this gives the Rabi frequency multiplied by $T$.

$$U = e^{i\alpha} \begin{bmatrix} e^{-i\frac{\omega T}{2}} & 0 \\ 0 & e^{i\frac{\omega T}{2}} \end{bmatrix} \begin{bmatrix} \cos(\frac{\Omega}{2}) & -\sin(\frac{\Omega}{2}) \\ \sin(\frac{\Omega}{2}) & -\cos(\frac{\Omega}{2}) \end{bmatrix} \tag{1.5}$$

$$\Omega = |\frac{\vec{d_{i,j}}}{\hbar} \cdot \int_0^T \vec{E}(t')dt'| \tag{1.6}$$

Thus a resonant optical pulse can form any arbitrary quantum gate by tuning the pulse area to obtain rotation between $|0\rangle$ and $|1\rangle$; tuning refers to both the optical field strength and the duration of the pulse. The phase is then determined only by the timing of the pulse. If such a pulse can arbitrarily set the state of a qbit and apply arbitrary gate operations to it, both criteria are satisfied.

### 1.2.1.3. Qbit Specific Measurement

The fourth condition is "A qubit specific measurement capability". This requirement is arguably the most immediately obvious of the five, one must be able to read the quantum state of output qbits for any computation to have been or be of any practical use. This is required to happen without influencing any other qbits.

A simple comparison with classical computing shows just why this appears to be necessary and is, in common physics terminology, a "non trivial" task. For a set of classical bits, for example chained together in a shift register, the state of any bit can be found by merely shifting that state along the register until it reaches the end and outputting that bit; it is key to point out that in this case each bit has no effect upon the state of those in front of or behind it. However, because of the quantum no cloning theorem [32] a quantum shift register cannot exist. This is because the state of one qbit cannot be copied to another; the information in one qbit can be transferred, but this is no more than entangling multiple qbits and would directly violate the qbit specific measurement criteria. Thus any measurement must occur for each specific qbit, as the criterion states, and there is no universal solution to this problem for silicon dopant atoms.

The specific readout method will depend upon the exact scheme implemented. An example proposed method [1] uses essentially what is a blockade effect along with a separate control qbit system; blockade effects have been experimentally demon-

strated for e.g. rubidium [33] and so are plausibly potential for silicon. The control qbit must be close enough to interact with the other, so that when one is in an excited state the other cannot be excited to the same state because of their mutual interaction. If a resonant laser is directed at only the control qbit and it absorbs a photon then the other qbit must be in its ground or $|0\rangle$ state, otherwise if photons are scattered then the qbit must be in a $|1\rangle$ state. This is only a proposed scheme and it is highly likely to be extremely challenging to realise in practice, especially only targeting the control atom; it is possible that a blockade occurs between two different atoms and thus the laser is only resonant with the control atom, removing the chance for catastrophic readout caused changes of the qbit.

### 1.2.1.4. Long Decoherence Times

The fifth condition for quantum computation is "Long relevant decoherence times, much longer than the gate operation time". While the gate operation time is dependent on the implementation of the gate, using qbits with the longest possible decoherence times is ideal; this reduces the constraints on possible gate implementations. Decoherence time is one of the key issues which the use of doped silicon can address. The decoherence time is a measure of the qbits interaction with their environment, and depending on the implementation, the dephasing manifests differently e.g. at a different speed.

For a single two level system (e.g. electron or nucleus spin) acting as a qbit, the dephasing can manifest as the evolution of the relative phase between the $|0\rangle$ and $|1\rangle$ states. If the state is written as $|\psi\rangle = a|0\rangle + e^{i\phi}b|1\rangle$, then the dephasing is essentially the changing of the $a$ and $e^{i\phi}b$ complex coefficients by interaction with the environment; $\phi$ is then the phase angle between the two states that changes in an unknown manner due to the dephasing. For an ensemble of spins acting as the qbit, not only does each particle dephase as a single particle qbit, but due to

inhomogeneity of their environment each particle may, and probably will, dephase at a different rate. In a solid state doped silicon approach, for example, this inhomogeneity can arise due to thermal gradients, doping gradients, or different isotopes being present, etc.

This leads on to one of the main advantages to using silicon, that it is one of the most isotopically pure materials that can be created [34], thus reducing any isotopically caused decoherence; although environmentally caused decoherence will always occur to some extent. However, it has been shown that this problem could partially be overcome by using coherent $\pi$ laser pulses, demonstrated by the optical analogue of the "Hann echo", where an ensemble of phosphorus donor spins have been shown to be brought back into phase with each other. While it has been demonstrated for an ensemble[30], in principle it should work for single spins as well, albeit with a much smaller and harder to detect signal because of the lack of in phase emission amplification, i.e. super-radiant emission as in the Dicke model [35]. This means that by applying $\pi$ pulses , which do not change the $|0\rangle$ or $|1\rangle$ magnitudes, the state is rotated by $\pi$ around the Bloch sphere and the dephasing then operates backwards relative to before.

### 1.2.1.5. Stationary and Moving Qbit Conversion

In brief this requirement is that a qbit must be able to be transferred to an object that can move; for example from a spin state to a photon polarisation.

### 1.2.1.6. Transmittable

Once converted to a qbit form that can move, such as a photon polarisation, this must then be able to travel to another piece of quantum computing architecture without losing its state or phase coherence; lasers are particularly good at this.

## 1.2.2. Decoherence and State Lifetimes

With the conditions for quantum computation now reviewed, the condition that is most relevant to doped Si is the fifth condition, long decoherence lifetimes. However, as long as the decoherence is invariant over the gate operation time, it is possible that this decoherence can be corrected or ignored by the use of ensembles of qbits; this relies on applying a $\pi$ pulse to the set of qbits and allowing the phase decoherence to work in reverse, putting the elements of the ensemble back into phase with each other at their original phase point [30]. Quantum error correction also exists, where errors caused by the decoherence can be corrected [36], and have been demonstrated [37]. However, decoherence is by its very nature not known to be time invariant, and cannot by definition be predicted quantifiably.

The problem of state lifetimes must then be considered. That is, any qbit requires a two level system, where one state must be of higher energy than the other; otherwise there is only the single level, or there are two systems. Intrinsically the qbit can then transition from one of the states to the other, emitting a quanta of energy (probably radiation) as it does so, and will do so with an average lifetime following an exponential decay pattern. If that radiative lifetime is less than the average time for the state to decohere, then the long decoherence time is useless. Thus there are two lifetime parameters that are of vital importance, the radiative and decoherence lifetimes. These are often referred to as the $T_1$ and $T_2$ lifetimes or transverse and longitudinal; the reason for this can be seen on the Bloch sphere, where dephasing is transverse to the state axis and decaying from one state to the other is longitudinal.

### 1.2.2.1. $T_1$ Radiative Lifetime

The radiative lifetime only becomes relevant in specific implementations of the qbit. If Kane's scheme [11] were to be used, then the radiative lifetime would be relevant as a donor electron is used to mediate interaction between two nuclear spins. The

electron needs to be able to be shifted between the two nuclei, in order to transfer spin states from one to the other. The ground state S wavefunctions of the electron are localised upon the nucleus, and thus less susceptible to being moved than the larger P like states. However, the P like states are excited states and as such they have a characteristic lifetime before they decay back to the ground state. The Stoneham scheme [1] also calls for excited electron states to control spin based qbits, and this has a similar decay problem. Decays between spin states is one additional possibility. The natural decay lifetime can also be decreased by the local environment of the electron via inhomogenous processes.

Whatever the radiative lifetime is, it is certain that for a quantum computation to be successful it must be completed before any electron involved decays back to its ground state by itself. This radiative lifetime then sets the upper bound on the realisable decoherence lifetime.

## 1.2.2.2. $T_2$ Coherence Lifetime

The mechanics of quantum computation rely upon exploiting quantum interference effects between qbits. These qbits evolve in time in a unitary manner, that is they do not lose or gain information. When interacting with the environment, qbits are said to become decoherent if their evolution is non unitary; it must be noted that the system as a whole including the environment will still have unitary evolution even if parts of it do not do so in isolation.

A physical example of this is an electron spin state; if it interacts with a nuclear spin state of a nearby atom unintentionally, then while the combined evolution will be unitary, the state of a given electron may be non unitary. What this means is that the electron spin state may appear to be forced into one state or another, i.e. the appearance of wave function "collapse". Another way of looking at it is that by

interacting with the nuclear spin, the relative phase of the electron's state becomes dependent on that of the nuclear spin. If the nuclear spin state is unknown, then the phase of the electron is unknown, so that when the electron's wavefunction interferes with that of another (during a quantum computing operation), the result is then altered by the phase difference between them. Thus it is called decoherence, the phase is no longer coherent. [22] [38] [39] [40]

The decoherence lifetime is then the average time before the phase of a qbit is changed significantly, or the average time before its evolution is no longer unitary. It is the $T_2$ decoherence times that are of ultimate utility, as they are in effect the lifetime of the quantum information in the system, and are typically shorter than the $T_1$ state relaxation times. However, the measured $T_2$ are bounded by the $T_1$ relaxation times, that is $T_2 \leq T_1$. Thus it can be seen that the first step in investigating any new system is to establish $T_1$, and then if this is sufficient to measure $T_2$.

### 1.2.2.3. Minimum Practical Lifetimes for Donor Qbit Systems

As lifetime measurements have been carried out on a variety of systems, establishing lifetime targets is vital for assessing whether a particular system is suitable or not for quantum computing. These lifetime targets are then the time necessary for the operation of some quantum gate operation. The precise times necessary will of course depend on the exact implementation, but comparisons are still possible.

Chalcogen donors were first suggested as qbits in 2001[41]. The scheme proposed involved the use of magnetic force microscopy to address the spins of the qbits. Their conclusion was that a coherence time $\leq 2.5\text{ms}$ would be needed for quantum computation [41]. Different methods will, of course, require different coherence times. For example, optical read out of the state of chalcogen donors would also

require the coherence lifetime to be longer than the Rabi time period; although this is an ultimate lower bound on the coherence time. This then depends upon the specific donor states used for the qbit, via the dipole moment, along with the strength of the exciting field.

The selection of the specific dopant in silicon then sets the lifetime constraints.

## 1.3. Proposalsfor Silicon Based Quantum Computing in the Literature

There has been interest in using doped silicon as the containing medium for quantum bits, i.e silicon would be the substrate of the quantum computing architecture. Kane's proposal [11], is one of the first attempts to outline a quantum computing architecture in silicon, while that of Stoneham [1] proposes using donor impurity electron states as a key part of a, different, silicon quantum computing architecture. These, along with several other proposed competing quantum computing schemes in silicon, their key advantages, and relative pros and cons are briefly discussed below.

### 1.3.1. Kane's Proposal: Electrical

Several others had previously proposed using spins half particles as qbits, with nuclear spins[42], nuclear or electron spin [22]. The first detailed proposal using silicon is attributed to Kane [11], and is expanded in [7]. Following this, Kane proposed using the nuclear spin of a donor atom in Si as the qbit, as the nuclear spin state is a typical two level system.

The Kane proposal calls for phosphorus donors to be located in silicon, beneath arrays of of metal gates; these are used to apply magnetic fields to the donor electron and nucleus to act as the quantum gates and for state readout. This state readout

then occurs via the electrical contacts, as the donor charge can move only if in a specific state. This can then be measured by its effect on the capacitance of the gate to gate system; giving in effect an electrical readout of the state. Electric fields can be applied to shift the spatial distribution of donor wavefunctions, turning on qbit to qbit interactions by making them overlap. The qbit is the nuclear spin of the phosphorus donor. In silicon the nuclear spin of the donor atom can be used to advantage, as silicon has (excluding for the moment isotopes) 28 protons and neutrons which give it a total nuclear spin of 0; this lack of nuclear spin offers the advantage that spin interaction is minimised, thus reducing decoherence; especially for any proposal using the spin state to form the qbit.

Kane proposes that the electron spin could then be used to control and readout the state of the nuclear spin, mediated by the electron-nucleus hyperfine coupling. This has been experimentally achieved [43]. Here a radio frequency $\pi$ pulse changes the nuclear spin state, while a microwave frequency $\pi$ does the same for the donor electron spin. The combination state is then written $|ab\rangle$, where $a$ is the nuclear spin state and $b$ the electron; $|0\rangle$ and $|1\rangle$ represents spin down and up respectively. States $|00\rangle$ and $|01\rangle$ then form the electron spin qbit, where the electron spin is in a superposition of spin up and down; the nuclear spin is here only in the down state. The states $|11\rangle$ and $|01\rangle$ then form the nuclear spin qbit, where the nuclear spin is in a superposition of spin up and down; the electron spin is here only in the up state. Beginning in the $X|00\rangle + e^{i\phi}Y|01\rangle$, or electron qbit state, an application of a radio $\pi$ pulse brings the system to the state $X|00\rangle + e^{i\phi}Y|11\rangle$; coherence is maintained, as the $X, Y$ coefficients and $\phi$ angle are unaffected by the pulse. Following this a microwave $\pi$ pulse is applied, bringing the state to $X|01\rangle + e^{i\phi}Y|11\rangle$. Thus the state of the qbit has been transferred from the nuclear spin to that of the electron.

The nuclear spin is thus chosen to be the qbit over the electron spin, as the electron

is less isolated from its environment, and thus more likely to become decoherent, or entangled with its environment, leading to error in any quantum computation. Nuclear spin coherence times are then measured to be in the second time-scale, but only for donor nuclear spins as this is two orders of magnitude greater than bulk silicon [44].

## 1.3.2. The Stoneham Proposal: Optical

The Stoneham [1] proposal bypasses the need for metal gates as in Kane's scheme. Nearby metal contacts give a risk of thermally ionised donor electrons wandering off, and would be a manufacturing challenge due to the atomic scale required; this would present difficulties when attaching electrodes to these metal gates. Stoneham instead introduces the idea of using deep donor states, which have binding energies of 100's of meV compared to 30 meV for phosphorus; this can prevent the accidental thermal ionisation risk. The proposal then proceeds by using one type of donor element as the qbit, with the spin states acting as the two level system. Another donor element of a different type would then act as a control and qbit interaction mediator, where an excited state of the control electron would need to have a large enough spatial extent that it overlaps two qbits. These are then controlled optically, with no need for electrodes; a similar scheme to that used to move nuclear and electron spin states in the Kane proposal could be used for this, albeit with optical $\pi$ pulses.

This proposal is less well experimentally realised than Kane's, but by focusing on measuring the radiative, and eventually the coherence, lifetimes of chalcogen donors in silicon it is hoped that this may soon not be the case. The reasons for the choice of chalcogen donors are outlined in chapter 2.

**Quantum computing remarks**

A silicon deep donor system has great potential to become the foundation of a quantum computing architecture. The first three DiVincenzo criteria are fulfilled already in principle, and qbit specific measurement is then an engineering challenge along with the plus two. Only the decoherence, and thus radiative, lifetimes remain entirely dependent upon experiment. In the system outlined here optical pulses provide arbitrary quantum gates, these then act upon donor electron state qbits which interact with each other via higher excited states; the nuclear spin could then form longer lived qbits and quantum memory. The excited states which provide qbit interaction must then have long radiative lifetimes, this thesis attempts to move towards a greater understanding of these lifetimes. In conclusion, the promised potential of silicon donor systems is matched only by the amount of work necessary to implement it; step one is to check whether chalcogen donor states have longer lifetimes than the current best donor, phosphorus, with 200ps lifetimes [45].

There is one immediate potential problem to using chalcogen donors in silicon as part of the Stoneham proposal, that is, because they are double donors the net spin of the ground state system is zero spin. Therefore, the ground state cannot be used for any quantum computation, as any interaction, and subsequent measurement, would not be able to distinguish which electron was which, giving a 50/50 probability of any resulting qbit being 1 or 0.

However, the Stoneham proposal involves using a donor excited state to act as an interaction mechanism between two other, different, donors. In this case the lack of precision regarding the spin of the excited electron need not be a problem, as there are several possible solutions. Firstly, the Hadamard quantum gate operation could be applied to the excited chalcogen donor electron, this puts a qbit into an equal superposition of 0 and 1 states irrespective of its prior state. Secondly, a

magnetic field could be applied at the site of the donor impurity, Zeeman splitting the two donor electron ground states, and allowing a specific spin state to be selected, perhaps optically. Thirdly, donors may be singly ionised and the resulting single donor impurity centres may be used. It is clear that further work needs to be done to specifically incorporate any chalcogen donor into the Stoneham proposal.

## 1.3.3. Silicon Quantum Dots

Quantum dots provide an alternative method of creating a silicon based quantum computing architecture. A quantum dot is a small region, typically on the nanometre scale, that has different electrical and optical properties to the material that surrounds it. Because the quantum dot confines electrons, or holes, in all three spatial dimensions they are often referred to as zero dimensional. This acts much like an artificially created atom, making the similarities to donor impurities in silicon clear. One of the key advantages of qunatum dots is that their coupling to theElectroMagnetic (EM) spectrum, size, and location are all dependant on their physical dimensions, which are themselves precisely controllable via conventional semiconductor compound growth techniques.[46]

One of the earliest quantum dot for computing proposals[47] made the case that such quantum dots may be strongly coupled together, allowing qbit to qbit interactions and therefore the implementation of two qbit quantum gates. The essential function of this scheme is as many others in silicon, to treat the spin state of an electron, confined in the quantum dot, as the qbit. The tunnelling between nearby quantum dots can then be controlled via applied voltages, and the interaction, or not, of multiple qbits can be measured by charge readout methods[47]. In addition, it has been shown that the spin state of such a quantum dot may be read out using electrical methods, i.e. the applicaiton of a voltage to the quantum dot .[48] Furthermore, spin lifetimes in silicon quantum dots, when the conduction band valley degeneracy

is lifted by an applied electric field, can exhibit spin relaxation lifetimes "exceeding 2 s"[49]. An alternative method uses a double well quantum dot, allowing electron confinement in two locations within the quantum dot, which may also be coupled to a single electron transistor quantum dot allowing measurement of the position of the electron, therefore showing that charge based Quantum bit (Qbit)states are possible.[50]

Double well quantum dots coupled to single electron transitors have been shown to operate like a "single electron memory latch"[51], that is, they form a quantum system capable of storing information that can be accessed, or made to interact with part of a larger quantum system, by the controlled application of a voltage. Electron tunnelling between quantum dots can also be controlled by GHZ radiation, and detected by electrical charge measurements.[52] It has also been demonstrated that error proof, high fidelity, quantum dot qbits are possible, i.e. that the application of quantum gate operations to such structures is possible, along with the readout of the resulting state, that is, the combination of silicon spin quantum information storage and electrical control.[46]

What this means is that purely electrically quantum dot qbits are possible, via the application of controllable voltages and single electronic charge measurement techniques, and that they remain coherent long enough for gate operations to be carried out. In addition, combining such electrical readout and control methods with optical, GHZ, radiation is possible. Therefore silicon based quantum dots allow for the exploitation of the precision of semiconductor growth, a combination of electrical and optical control and readout techniques, electrically and optically controllable qbit to qbit coupling, and the long intrinsic spin lifetimes possible in isotope free silicon.

## 1.3.4. Morse Proposal for a Chalcogen Qbit

A proposal for a chalcogen impurity in silicon based qbit exists in the literature, this is the proposal by K. J. Morse. [53] This is an elegant proposal, where singly ionised selenium donors in silicon form the qbit system. In isotopically pure silicon, discussed in chapter 2, different spin states are spectroscopically resolvable. It is proposed that the $1s(A_1)$ ground state spin operates as a qbit while the EMT forbidden, but reality allowed due to the failure of EMT assumptions to be fully applicable to the ground state (discussed in chapter 3 ), transition to the symmetry split $1S(A_1)$ ground state from the $1S(T_1)\Gamma_7$ spin state is then optically measurable. This would allow, in conjunction with careful use of photonic crystal structures, optical measurement of donor qbit states. The ground state of the system is mentioned as being only weakly affected by "fields, strain, and phonons"[53] making a long coherence lifetime likely, as the only large interaction of the ground state spin is with magnetic dipole, of which there are few in isotopically enriched silicon. The optical transition in question has a long lifetime of $\approx 39\mu s$.

It is suggested that by implanting the donor centre into an optical cavity, the resonance of specific $1S(T_1)\Gamma_7$ states with modes of that cavity can be tuned by the application of electric and magnetic fields, allowing a single spin state to be coupled, or uncoupled, strongly with the cavity - "the cavity will preferentially transmit any light matching the bare cavity frequency (or reflect, depending on how light is coupled to the cavity)" [53]. This would allow for the readout of the spin state, without exciting any transitions and affecting the qbit. This is a similar readout method to that of the Stoneham proposal. This scheme may be applicable to the $2P_0$ to $1S(A_1)$, rather than the $1S(T_1)\Gamma_7$ to $1S(A_1)$, transitions, although excited state lifetimes may be shorter due to the likely stronger dipole matrix element due to the $2P$ state being not just p like as the $1S(T_1)$ states.

## 1.3.5. Specific advantage of Silicon - Donor Placement Via Hydrogen Lithography

There are several advantages to using silicon donor impurities for a quantum computing architecture, discussed above. An additional advantage to donor impurities is the potential for precision positioning, such as with a Scanning Tunnelling Microscope (STM) hydrogen lithography method.

It has been possible to use a STM tip to precisely position atoms on a metal surface for some time [54], however, the strong covalent bonding typical of semiconductors prevents this from being applied as is to position donor atoms on a silicon substrate, instead hydrogen lithography can be used [55].

Firstly, "a clean, defect free silicon surface"[55] is prepared, this can be done via heating to 1200°C in a high vacuum chamber, and then slowly bringing the temperature down while maintaining the vacuum.[55] Then atomic hydrogen can be deposited upon the surface via a heated filament source. There are several different ways in which the hydrogen can be adsorbed by the silicon, depending upon the surface temperature, and these include single or double hydrogen complexes upon the surface, or triplet groups these complexes.[55] It has been shown that the type of hydrogen complexes formed on the silcon surface are experimentally measurable[56], and theoretically understood. [57]

A STM tip then removes, or desorbs, specific hydrogen atoms from the silicon surface by the application of a controlled voltage[55]; precise dangling bond configurations, where surface hydrogen atoms are removed with a STM tip and electrons trapped in the dangling silicon bond, have been investigated and it was found that "atomically precise quantum states can be fabricated on silicon"[58]. It has been found that, counter intuitively, STM tips that facilitate accurate, single atom,

measurement are the least likely to desorb a hydrogen atom, while those unable to resolve single atoms are most likely to remove single atoms. [59]. In addition some rapid patterning techniques developed for e-beam lithography have been investigated as potentially applicable to STM hydrogen lithography, specifically the removeal of hydrogen atoms from the silicon surface in line shaped, and grid like, patterns. [60] Phosphene gas can then be used to adbsord phosphorus atoms into the spaces where the hydrogen layer has been removed[55], it is possible that a similar corresponding gas compound may be used for different donor atoms. The remaining hydrogen layer can then be removed by heating, "without disturbing the lithographically defined structure".[61]

Using this technique single atom transistors have been built[62] , along with the measurement of anti correlated spins in nearby single donors [63] - a quantification of the donor separations necessary for donor wavefunctions to have measurable overlap.

The result of this is that donor impurity atoms can be reliably positioned, using hydrogen lithography, in arbitrary patterns, with measurable wavefunction overlaps, to create arbitrary quantum systems and potentially form the basis of a universal quantum computing architecture.

## 1.3.6. Alternative Quantum Computing Schemes

There are several alternative, non silicon based, proposals being worked towards to build a quantum computer. Some of the prominent and promising ones are, briefly, discussed here along with their relative pros and cons to silicon based approaches.

### 1.3.6.1. Superconducting Resonators

One of the alternative proposals for quantum computing is to use superconducting resonators. These exploit the properties of superconductivity, where when cooled

past some critical temperature a material exhibits zero resistance due to cooper pairs of electrons forming, which condensing into the same, now macroscopic, quantum state. The macroscopic quantum state, like any other, is subject to interference, quantised eigenstates, etc that are manipulatable and measurable on a macroscopic scale. There are two primary attributes of this that are exploitable for quantum engineering: flux quantisation, and Josephson tunnelling through a Josephson junction. For the former, when subject to a magnetic field (during the cooling past the critical temperature) which is then turned off, the magnetic field per unit area (flux) remains constant due to an induced superconducting current which is then quantised. For the latter, a Josephson junction is an insulting barrier between two parts of a superconducting material, which cooper pairs of electrons, as they are in a coherent quantum state, can tunnel through allowing a constant electric current to flow through the insulating region (depending upon its thickness); it is possible to engineer the two superconducting regions of a Josephson junction to have differing energy levels for the electrons. This readily gives the basis for a qbit, a pair of discrete quantum states. [64]

There are three main proposals for superconducting qbits : *flux*, where the two states correspond to an electric current flowing clockwise or anticlockwise to maintain the magntic flux present during the superconducting transition[65][66]; *charge*, where a pair of Josephson junctions form a superconducting region with quantised energy states, i.e. a potential well, that can be higher than those outside of it, called a "Cooper pair box"[64] thus forming the two states: charged, and uncharged[67][68][69][70]; *flow*, where an electric current is applied across a pair of Josephson junctions close to the maximum current that can flow before the superconducting region is no longer superconducting, in this state there is a large energy gap between the quantised levels of the superconducting potential well region allowing the two lowest lying to be used as qbit states.[71][72]

Like donors in silicon, superconductor based  qbits  are scalable, being built of of Josephson junctions, which relies on conventional lithography techniques, although each superconducting qbit  is slightly different and the coupling between different qbits cannot easily reconfigured.[73] Their properties can also be more easily tuned than that of a donor impurity atom, i.e a donor atom has predefined electronic energy levels, while that of the resonator can be adjusted by external parameters, such as the application of a controllable electric field across a Josephson junction. However, this tunability is also a source of weakness, providing strong coupling to external fields.  In addition, the coherence times are poor, compared to that of silicon donors, with 1.2s, 2.0s, and 0.3 for flux, charge, and phase qbits  respcetively. [64][74]

### 1.3.6.2.  Cold Ion Vacuum Traps

Vacuum ion traps are similar to donors in silicon in many ways.  They take atoms and confine then spatially using EM field traps, and are laser cooled to bring the atoms to the bottom of the potential wells formed by the EM  traps. This is done in an ultra high vacuum to minimise interference, decohering collisions, stray coulomb fields from contaminant atoms etc, with collisions typically occuring "roughly once per hour per ion"[73].[75] These confined atoms are then ionised, and typically arranged in lattice like grids which form due to the coloumbic repulsion of the ions balancing against the  EM  field trap force. The  qbit  can be formed in one of two ways: from two electronic energy levels of the trapped ions, or sing the spin of the ground orbital state. Both can be interacted with optically or with EM pulses of the appropriate frequency.

Trapped ion  qbits are identical, as the ions are all the same.  They can be coupled to other  qbits  via optical interactions, which also allow state initialisation, quantum

gate application, and initialised with almost 100% fidelity.[76] A problem with the coherence times of trapped ion systems, is that they are limited by the average rate of collision with contaminant atoms in the vacuum chambers. However, the greatest difficulty faced by trapped ions is that of scaling to the large number of qbits needed for a practically useful quantum computer, with 14 reported in 2011[77] . Recently, scalable methods[78] have been proposed allowing up to $10^6$ qbits but this is far from being experimentally achieved yet.

# 2. Dopants in Silicon: Which Atoms to Choose?

## 2.1. Introduction

With the ultimate goal being to work, in some small part, towards a solid state system that could eventually be used for quantum computing, the group iv material silicon appears to be the most convenient to use; it has been proposed as the substratum of both an electrically [11] and optically [1] mediated quantum computing.

However, before discussing the relevant details of deep and shallow donor doping in silicon, first it must be established, albeit briefly, why the semiconductor discussed should be silicon at all. Or in a more succinct question: "what are the advantages of using silicon as opposed to any other semiconductor material with potential scalable fabrication and controllable doping?"

In order to place this thesis into the correct context, next it is necessary to summarise several topics. Firstly, the relevant properties of silicon, a brief mention of how to manufacture silicon of the necessary purity, and the effects of doping silicon with the group iii to vi elements; group vi are known as the chalcogens. This is essentially highlighting the important manufacture and material properties.

Secondly and finally, what the current "state-of-the-art" is with regard to, or working towards, fulfilling the necessary conditions for quantum computing using donor atom electrons in a silicon host lattice as the quantum bit, with ideally optical as opposed to electrical, quantum interactions.

As a caveat, while pure optical control of the qbits is ideal, electronic control of some aspects of a donor qbit in silicon may or may not need to be integrated, as schemes such as that proposed by Kane [11] differ from those of Stoneham [1] substantially. Ultimately elements from both will probably need to be used, as after all it is presumed that any optics are still electronically controlled, and silicon is an ideal material in which to integrate optical and electrical components. Briefly, optical control is ideal because control and readout must be coherent, and a laser is in general easier to produce (for now) than a coherent electrical current. However, coherent readout of spin states has been demonstrated experimentally for phosphorus in silicon [79]. Optically induced Rabi oscillation, corresponding to quantum gate operation, is also possible at much higher speeds than electrical. Optical switching frequencies are THz, while electrical are GHz for a factor of $10^3$ difference.

## 2.2. Properties of Silicon

Here some of the basic properties of silicon are summarised. These include the structure and size of the unit cell, the phonon spectrum, and the Debye temperature.

### 2.2.1. Structure

Silicon has a tetrahedral bonding structure, with a face centre cubic lattice. The basic face centre cubic crystal has a lattice point at each vertex and the centre of each face of a cube. As this lattice structure is periodic, only 4 of the 14 total points are in each unit cell. For silicon the lattice then has a basis of two atoms, the first at

the (0, 0, 0) and the second at the $(\frac{1}{4}, \frac{1}{4}, \frac{1}{4})$ coordinates with respect to the lattice points; there are then 8 total silicon atoms per unit cell. The cubic lattice has side length of 0.565nm.[80][81] The silicon unit cell is shown in figure 2.1.
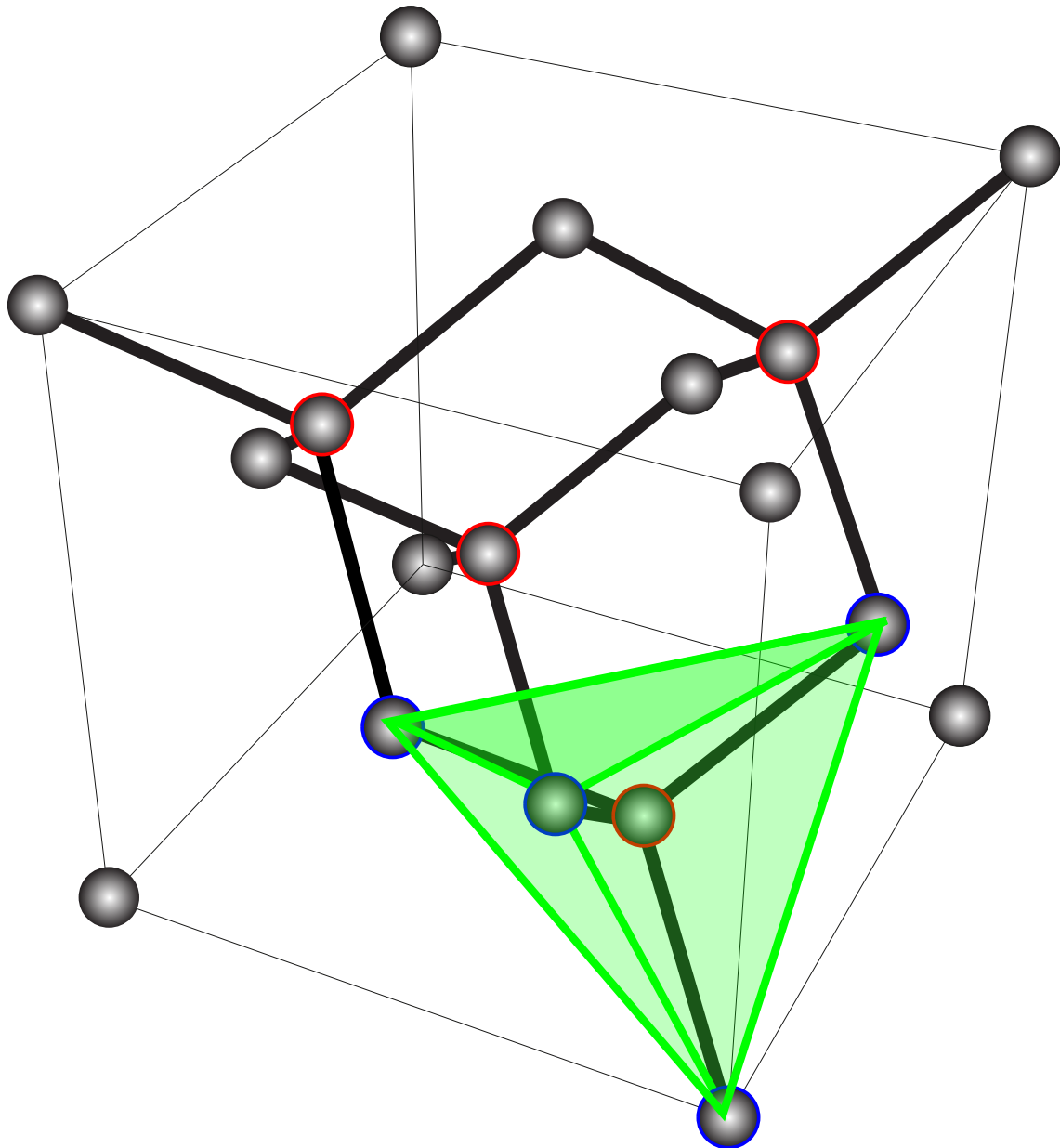


Figure 2.1.: Silicon unit cell, grey circles represent silicon atoms. The tetrahedral primitive basis is shown highlighted in **green**. The **blue** atoms are the primitive lattice points. Those in **red** are the $(\frac{1}{4}, \frac{1}{4}, \frac{1}{4})$ offset additional atoms for the two atom silicon basis. Each silicon atom has 4 covalent bonds with its nearest neighbouring atoms. $a_{si} = 0.545$nm.

The elemental properties of silicon are: an atomic mass of 28, with 14 protons, and an electronic configuration of $1s^2 2s^2 2p^6 3s^2 3p^2$.[82] Each silicon atom must have 4 covalent bonds to form the tetrahedral structure that it has, one bond to each of its nearest neighbouring atoms. The four valence electrons, filling the $3s$ band and two possible $3p$ states, then form the bonds between silicon atoms.

## 2.2.2. Phonon Spectrum

The reciprocal lattice of a face center cubic lattice is shown in figure 2.2. This is necessary to match to the various wavevector positions in the phonon spectrum shown in figure 2.3
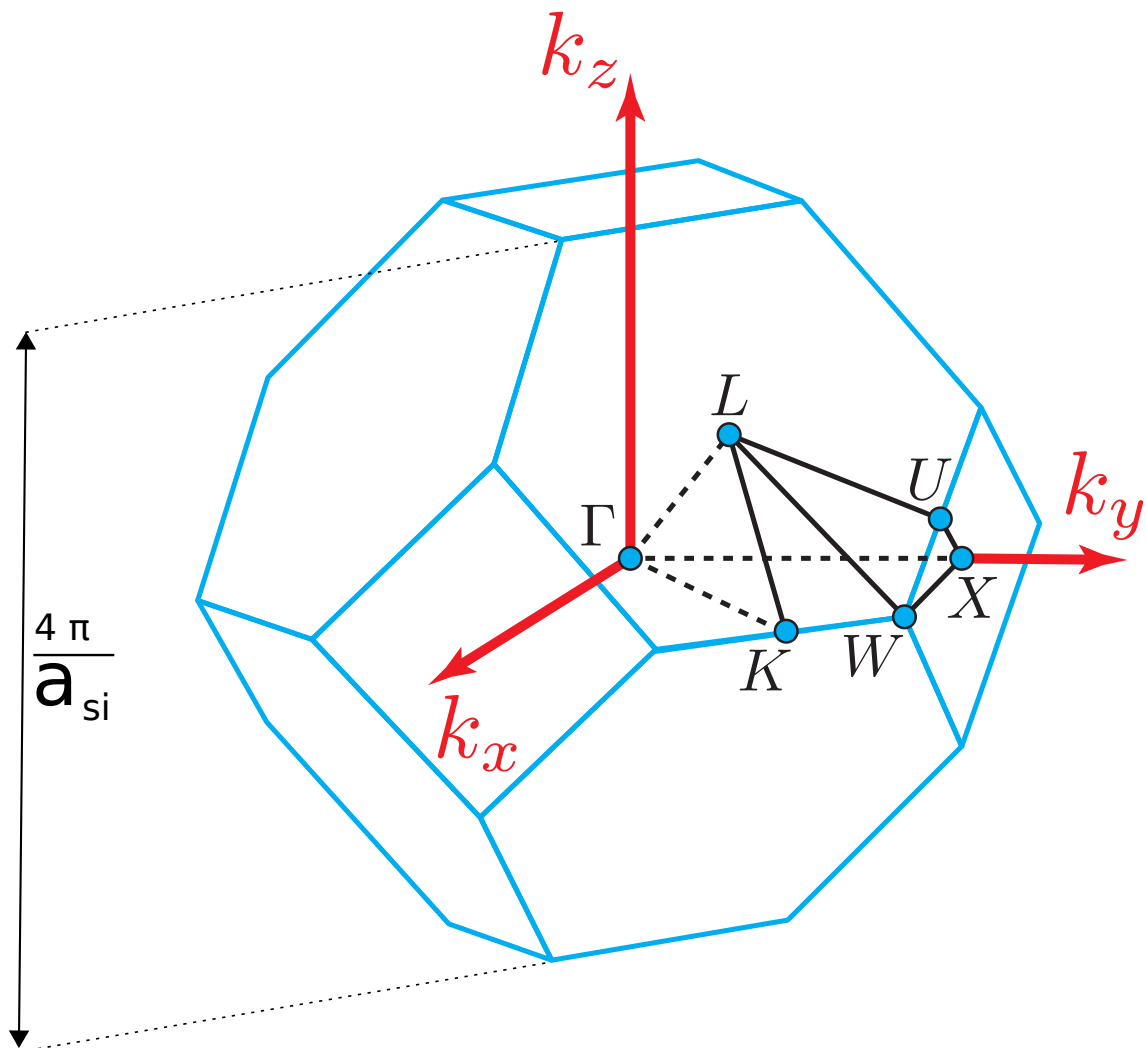


Figure 2.2.: The reciprocal lattice of silicon.
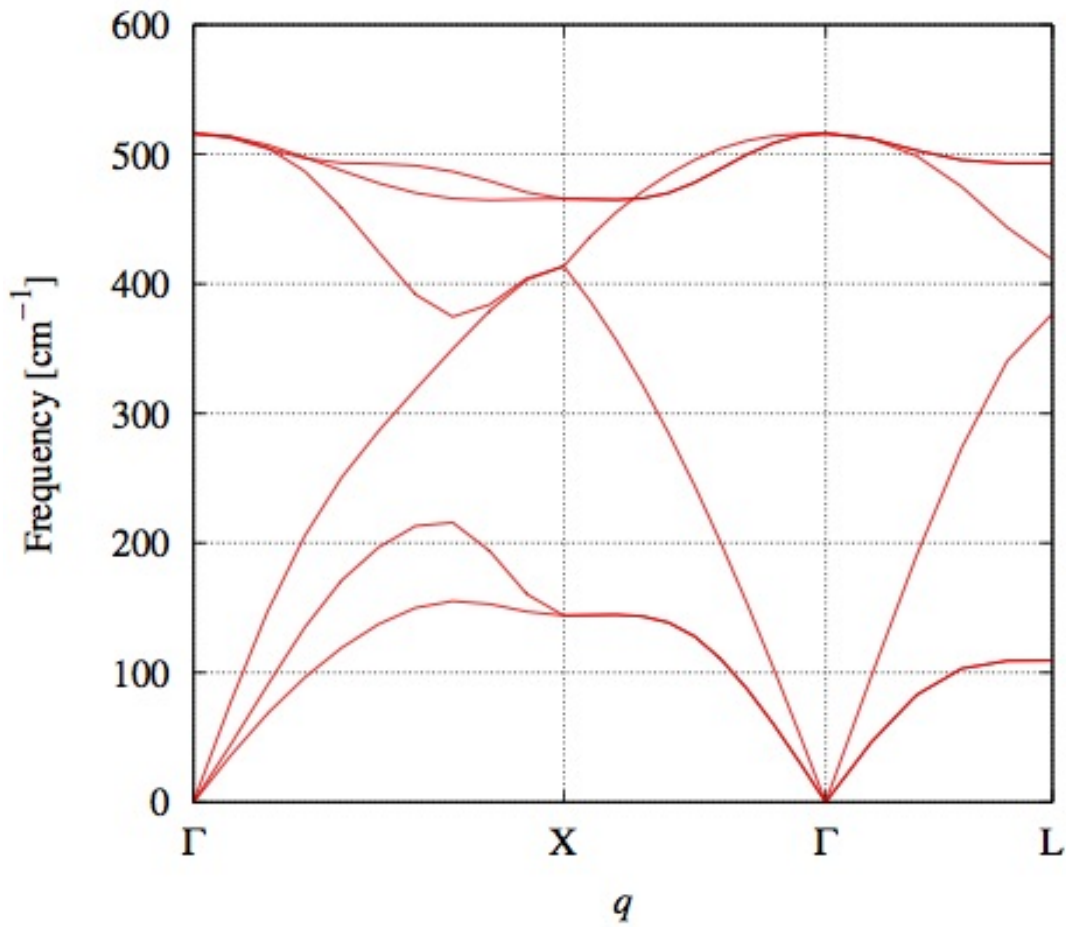
Figure 2.3.: Phonon dispersion bands of silicon, along with density of states. Modified reproduction of [83, fig 1 and fig 2].

The density of states of the phonon modes in silicon are then shown in more detailed form in figure 2.4.
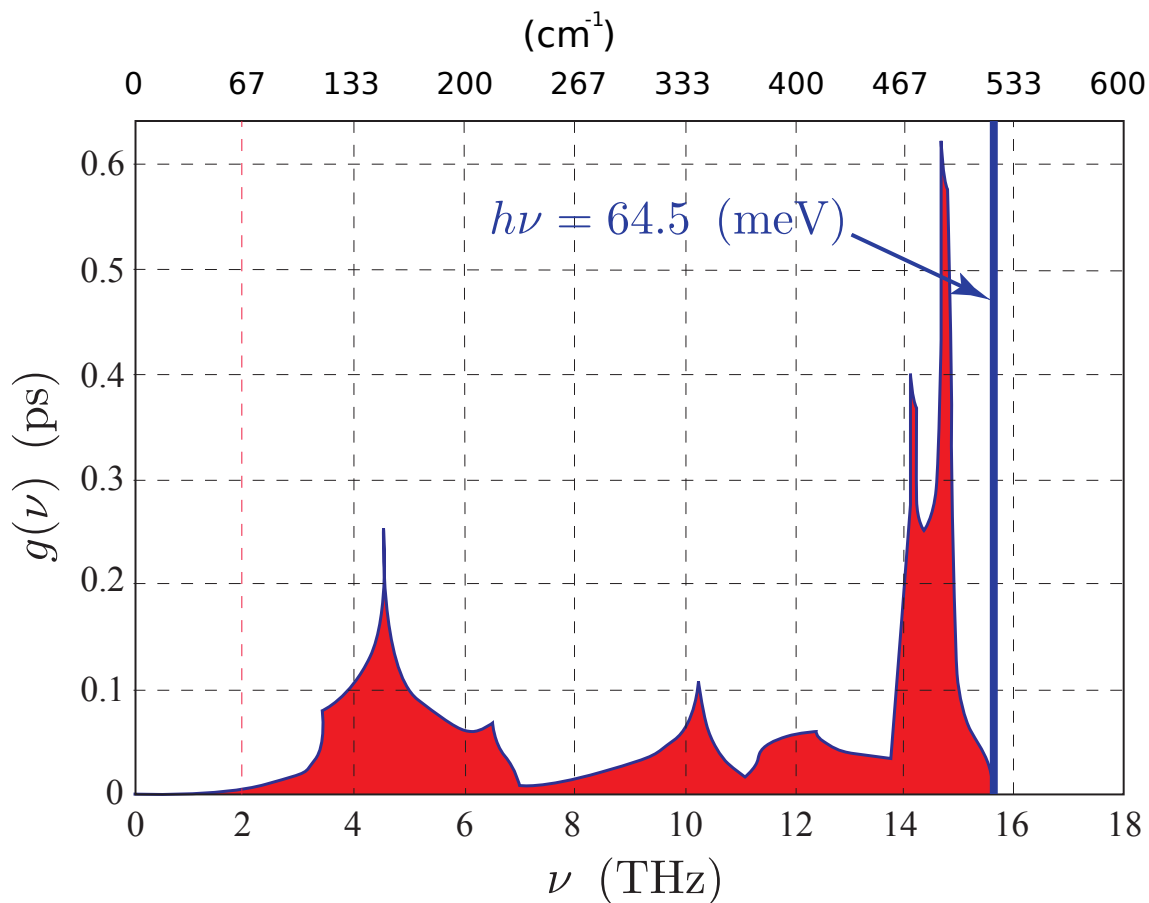
Figure 2.4.: Density of states of silicon phonon modes. Modified reproduction of [83, fig 2], maximum phonon energy value of 64.5meV taken from [84, table 1].

A key point from the phonon dispersion bands and density of states is the maximum frequency, and thus energy, of phonon possible. The highest phonon energy in silicon is 520.2 $cm^{-1}$ (64.5meV or 15.6THz) [84, table 1] which agrees with the phonon dispersion bands from source [83, fig 1]; the Debye temperature corresponding to this is 748.5K.

## 2.3. Manufacture and Growth

The decoherence of any prospective qbit is maximised by high levels of impurities, defects, and asymmetries, this can be expressed succinctly as a non uniform local environment; where local means the limits of what can be interacted with before

coherence is, on average, lost. This is vital to the idea, and more importantly any future physical implementation, of a silicon based quantum computer. A non-uniform environment is also intrinsically tied to the scalability of the material, but it must be confirmed that silicon of high uniformity or purity can be manufactured, so that the decoherence and scalability DiVincenzo criteria can be met. Thus, following is a brief review of the state of silicon manufacture, and recent developments in high isotopic purity silicon which should allow for longer coherence times.

## 2.3.1. Mass Production

Commercially mass produced silicon can be broadly split into two categories, metallurgical and electronic.

### 2.3.1.1. Metallurgical Grade

Metallurgical grade silicon has impurity concentrations sometimes as high as 1 part in a thousand to 1 part in 250 for aluminium, with the difference compared to electrical grade silicon being explained by the lack of an intermediate chemical purification stage; the purity of metallurgical grade silicon is then 98 to 99%.[85, p116]

### 2.3.1.2. Electronic Grade

Due to the needs of the semiconductor based microprocessor industry, silicon elemental purity has been a historically pursued goal. However, the bulk nature of classical computing architecture means that the concentration of unwanted impurities must be less than the concentration of wanted $n^-$ or $p^+$ type dopants. As can be discovered from a consideration of the number of donors and acceptors, their binding energies, and Fermi-Dirac statistics, the charge carrier density of a doped semiconductor is approximately linear with respect to the dominant dopant concentration. Because of this, if the unwanted impurity concentration is very small then it can be concluded that the bulk electrical characteristics are unduly affected.

Electrical grade single crystal silicon has a typical purity of 99.9999% as claimed by chipmaker Intel [86, p3], which corresponds to 1 part in a million. This is largely carbon and oxygen, at 1 part in two million and between 5 to 20 parts per million respectively, with other impurities such as iron being present at 1 part in a trillion. This corresponds to a concentration of $10^{10}$cm$^{-3}$ to $10^{16}$cm$^{-3}$ for oxygen, carbon and iron, compared to those ranging from $10^{12}$cm$^{-3}$ to $10^{20}$cm$^{-3}$ for specifically introduced impurities. [87, table 3.2 p58] Much lower concentrations are required for the group iii, v, and metallic impurities, of less than 0.3, 1.5, and 0.1 parts per billion respectively.[85, p115] This is often referred to as "eleven nines"[85], for it is 99.999999999% pure silicon.

For the above impurity concentrations it can be noted that 1 part per billion corresponds to a concentration of $4.99 \times 10^{13}$cm$^{-3}$; this is based upon a typical silicon atom number density of $4.99 \times 10^{22}$cm$^{-3}$, calculated from the volume of a unit cell cube, of side length $5.43 \times 10^{-8}$ cm, containing 8 silicon atoms in total.

## 2.3.2. Isotopically Pure: Bespoke for Now

Electronic grade silicon, sufficient for bulk scale electrical effects such as the mass charge movement of millions and billions of electrons through transistors, whether FET or BJT, still presents decoherence problems for a quantum computer; the classical computer experiences no ill effect from isotopic impurities such as $^{29}$Si, whereas this is not true for any application sensitive to the phase evolution of the system, i.e. a quantum computer.

However, isotopic and elemental impurities in silicon do present a problem to the realisation of a donor electron based qbit. For example, if a donor electron is intended to contain quantum information in the wavefunction of its spin, then additional

spin moments around it will increase perturbations to that wavefunction. This will both lessen the coherence of the electron spins and lead to increased scattering interactions, decreasing the $T_2$ coherence lifetime and $T_1$ state lifetimes respectively.

Elemental impurities provide a differing set of problems, as the most common elemental impurities in silicon are carbon and oxygen[88], which have many fewer nuclei and electrons than silicon and thus do not increase the spin to spin interactions over a silicon atom. However, a differing set of spins in the local environment, from the elemental and isotopic impurities, will affect the phase evolution of the donor electron spin, leading to differences in the phase evolution that depend on the specific qbit implementation. Thus qbits are not responding in the same way to each other.

Coulombic interactions, due to elemental impurities having differing charge structures to the host silicon atoms, can also be found to cause two main problems. The first being additional poles which provide a scattering mechanism, e.g. changing the state of donor electrons and rendering any quantum operation void; this is seen in a reduction of the relevant $T_1$ lifetime of the excited donor spin states. A donor electron could also be elevated into a excited, higher energy, spin state via interactions with electronic poles and spin moments.

The difference in the coulombic potential, due to the local donor environment, also changes the Hamiltonian for the system, thus altering the energies of the donor electron states. It is clear that if the state of the donor electron is to be inferred via optical scattering, such as in the Stoneham proposal[1], or indeed any method that uses a specific wavelength of light and its interaction with the donor electron, then a change in the energy of the states will reduce the reliability of the interaction.

Schemes for quantum computing require that two qbits can interact in a coherent

manner, for example the use of donor electron excited states and its coupling (entanglement) with other donor atoms of a differing type [1]. To remain coherent this interaction must not be perturbed by any impurities in the qbits' local environment. However, the interaction between two systems is proportional to the integrated over all space of their respective wavefunctions. Thus because as an excited state has a wavefunction typically with a greater spatial extent, the probability of interaction with any single impurity is small. If the number of impurities in the qbits' local environment is too high, then the total interaction probability increases. As the impurities are not perfectly uniformly distributed, the interactions they have with any qbit will be different, the time evolution of each qbit will then be different; if the evolution of qbits is different then each quantum gate and readout operation must be qbit specific, making scalability questionable. Thus the impurity concentration must be low enough that a qbit impurity interaction is probably not going to happen over the time scale of any calculation.

The effect of the silicon purity on the state and coherence lifetimes of donor states can be described by a"catch-all" name, familiar to any physicist, inhomogeneous broadening. This makes more sense when viewed in the opposite Fourier domain to time, frequency, where any optical transition between donor electron states will be some form of Gaussian curve. The Fourier relations between the two domains is the same as the Heisenberg uncertainty principle, shown in equation 2.1. Because of the differing local environments, each donor atom in a region of silicon will have slightly different energy states. This gives a Lorentzian spectral lineshape of the donor electron transitions, thus due to the Fourier domain inverse relationship these transitions have a width inversely proportional to the lifetime of the upper state. The different local environments cause different wavefunctions, the higher energy wavefunctions then have different overlaps with the lower, causing different transition probabilities. This is the cause of the inhomogeneous broadening name.

Reducing the inhomogeneity of the environment will reduce this.

$$\Delta E \Delta t \leq \frac{\hbar}{2} \tag{2.1}$$

### 2.3.2.1. The Avogadro Project

With decoherence in mind, the Avogadro project is fortuitous. The Avogadro project is "aimed at determining the Avogadro constant by counting the atoms in an isotopically enriched silicon crystal" [89]. This has led to the creation highly isotopically pure $^{28}$Si silicon.

The Avogadro project aims to define the Avogadro constant, in order to provide a method of defining the kilogram. This can be done, for example, via the relation defining the Rydberg constant $R_\infty = \frac{\alpha M_e c}{2 N_A h}$ [89]. Here $R_\infty$ is the Rydberg constant, $\alpha$ the fine structure constant, $M_e$ the rest mass of an electron, $h$ Planck constant, and finally $N_A$ the Avogadro constant apart from which each is a fundamental constant.

The Avogadro constant itself is then determined by applying the equation $N_A = \frac{nM}{\rho a^3}$ to a sphere of purified silicon; $n$ is the number of atoms per unit cell, $a$ the lattice constant, $a^3$ the volume per unit cell, $\rho$ the density, and $M$ the molar mass of silicon. The average molar mass can be determined by the fundamental masses of the different isotopes of silicon,$^{28}$Si ,$^{29}$Si, and $^{30}$Si, along with their ratio which itself is determined by mass spectroscopy. This is a reason why the Avogadro project requires high isotopic purity silicon, without highly pure silicon, errors in determining the ratio of isotopes would, in all likelihood, be larger in absolute terms, leading to an absolutely larger error in any quantities calculated downstream.

Next is the number of atoms per unit cell, determined by the crystal structure;

for silicon this is face centre cubic. This is determined experimentally by X-ray and, along with the volume of the sphere of silicon and the lattice constant, optical interferometric measurements [89].

The final variable left is the density, $\rho$, which requires that the mass and volume of a fixed portion of silicon be known. Turning to the definition of the molar mass, $M_m = N_A M_a$, the mass of an atom $M_a$ can be defined in atomic mass units, and the molar mass $M_m$ is, again by definition, the number of grams that there are atomic mass units in the mass of the atom. The volume is then known from the interferometric measurement of the silicon lattice constant, $a$. This is then another part of the origin of the Avogadros projects need for isotopically pure silicon. For if the atomic mass varies, then so does the mass and thus the density, creating greater uncertainty or errors in the determination of Avogadros constant . [90].

The question is then, why is isotopically pure silicon of any value to quantum information processing?

There are two reasons for this. Fistly, there is the nuclear spin of $^{29}Si$, and secondly, the different mass of the $^{29}Si$ and $^{30}Si$ atoms.

The additional neutron in $^{29}Si$ causes it to possess a net nuclear spin of $\pm\frac{1}{2}$. Thus a silicon bulk with some of the atoms being $^{29}Si$ will be, in effect, a bath of nuclear spin moments. The precise state of these nuclear spin moments will be, in general, unknown; they will be susceptible to fluctuation, from, for example, thermally caused agitation via phonon interactions, or stray, unaccounted for, magnetic fields from the outside environment. This bath of nuclear spins can then, via the hyperfine interaction, couple with the spin of a donor electron. The nuclear spins can also couple to each other and cause each other to flip; this changes the magnetic field

environment of the silicon, thus changing the energy of donor electron states, via the Zeeman effect.

This not only causes incoherence of the donor electron state, as the phase evolution has changed via the unknown and unpredictable interaction with the spin bath, but inhomogeneous broadening. This broadening occurs, because a change of the state of the spin bath changes the energy of the donor states, via affecting the surrounding magnetic fields, thus effecting each donors spin energy levels in an unpredictable manner, creating a broadened spectrum of energies.

In addition to the spin bath, the different masses of the silicon isotopes, $^{29}Si$ and $^{30}Si$, contribute to the homogeneous broadening. This occurs because the different isotopes have different masses than that of normal, $^{28}Si$, silicon. This different mass alters the interactions of the valence electrons, particularly when forming the bonds of the lattice. Thus the ground states of the valence electrons are changed by their host atom being, itself, or bonded to, a non-standard isotope of silicon. The presence of the isotopes in the surrounding environment also changes the interaction of the excess donor electrons with the lattice; due to the nucleus mass being coupled to the electromagnetic field.

All of these isotope mass interaction differences cause the donor electron states, via the mass coupled electromagnetic interactions, to have different energies that they otherwise would have had. As this depends upon the local environment which, due the random distribution of isotopes in the lattice, is inhomogeneous, inhomogeneous broadening is a result.

According to the Avogadro project, the isotopic purity needed for a highly accurate measurement would only be 99.99% [91], giving a ratio of not $^{28}$ Si to $^{28}$ Si as only

more than 1 in $10^4$. The Avogadro project has yielded samples with $^{28}$Si isotopic purities of at least 99.9957 [92, p362, t1], giving only 43 in a million non $^{28}Si$ isotopes.

## 2.4. Doping

The advantage of silicon in doping is largely due to the ease with which silicon can be doped with extrinsic materials, typically those in groups iii to v for $p^+$ and $n^-$ doping respectively. This is key for the integration advantage of the solid state and silicon, the well developed control of the electrical characteristics of any silicon adjoining the part to be used in any quantum operation. Doping is also intrinsically part of the two primary (Kane and Stoneham; electrical, and optical) silicon quantum computing proposals, as the donor electrons of dopants are intended to form the basis from which the two level system that is the qbit, is formed.

Dopant types are then reviewed in brief, along with some of the relevant problems associated with them. The specific doping element groups, and the possible doping concentrations are then discussed, leading to the conclusion of which grouping of donor elements is believed to be most suitable as the basis for a qbit in silicon.

### 2.4.1. Types of Dopant

The first issue to be considered is the location of the dopant. There are two main possible locations of a dopant atom, substitutional or interstitial; these replace the position of a silicon atom or are somewhere else in the lattice, in between silicon atoms. If a dopant is substitutional then assumptions about bonding are correct, that is, there is a donor electron or electrons or there is a similar number of hole states.

Secondly, and despite the great range of possible dopants in silicon, dopants can

all be reduced to two broad categories: acceptors and donors. Acceptors are atoms that typically have one fewer valence electron than the host silicon, that is, 3 valence electrons. Using the periodic table excerpt shown in figure 2.5, silicon can be seen to be in group iv the typical acceptor atoms are then from group iii; double acceptors are known to be possible in silicon [93], triple acceptors would be very weakly bound, and a quadruple acceptor would be no more than a wandering atom diffusing randomly through the silicon bulk. The corresponding elements from groups v, or higher, then form the donors; a factor limiting the amount of possible donor electrons is then the size of the atom, eventually a potential donor will become too large to fit inside the silicon lattice, double donors are experimentally known [94].

The lack of valence electrons, relative to the surrounding silicon atoms, causes acceptor atoms to form electron hole states. These are states of the system that behave as particles to complement the electron; they are states of the acceptor system, holes are fully described by the Schrödinger equation, etc. Donor atoms then have extra electrons than the surrounding silicon, these remain bound to the dopant nucleus.[95]

Acceptors and donors have been commonly used to control the electrical characteristics of silicon, such as the conductivity, by creating regions with an excess of electrons or holes. This allows the creation of modern electronics, e.g. the bipolar junction transistor. Both acceptors and donors also have defined energy states in between the conduction and valence bands of the host silicon.[95] Donor electrons can then behave very similarly to simpler hydrogenic, or helium like and so on, atomic systems; holes also have corresponding states. Quantum computing schemes for acceptors do exist, e.g. for boron acceptors in silicon [96], but these are not examined here, only donor states are focused on in this thesis. This is a necessary narrowing of the possible avenues of investigation, partly because of a lack of time, partly because the Kane and Stoneham proposals utilise donor atoms and these are

the quantum computing schemes focused on.

## 2.5. Donor Atoms Suitable as Qbits

Considering donor atom systems, the properties are then largely governed by a combination of the charge carrier wavefunction overlapping, the density of states of the material, and the availability of energy, e.g. as temperature or applied magnetic or electric field. When selecting a possible donor to build the quantum system outlined in chapter 1, the periodic table is the ideal construct to visualise the possibilities.

Figure 2.5.: Part of the periodic Table, information taken from [82]. Data for Groups iii to v and the adjacent pnictogen and chalcogen groups are labelled, along with the elements, atomic numbers, masses, and electron configuration.

If intending to use a donor atom's outermost electrons as as qbit, it must be conside-

red why that atom and in what environment it must be. Many of the advantages of silicon rely upon the use of the periodic table, or the basic properties of the elements, to succinctly explain; once the unsuitable elements are removed from the periodic table you are left with the group iii to v elements.

The assumption is taken that electrons in a solid state material are used to form a qbit, or qbit interaction method. The two primary reasons for using the solid state are that this is highly scalable, and allows easier integration with classical electronic components. It can be seen by considering a target of a solid state quantum computer, such as the Kane or Stoneham proposals discussed in chapter 1, a section of silicon doped with material that forms at least 2 qbits with controllable interaction. As Stoneham proposes[1], it can be imagined to be 2 donor atoms substitutionally replacing silicon atoms, these are the qbits, and then with some third atom, different to the first 2 and not silicon, substitutionally replacing another silicon atom at some position in between them.

Via optical pumping, the middle atom's donor electron could then mediate interaction between the other two donor electrons; this would allow the interaction of multiple qbits. It could then be imagined that some optical waveguides are present, embedded in the surrounding silicon, to channel optical pulses of the appropriate wavelength, intensity, and duration, to implement quantum gate operations. If this model could be repeated, it could be possible to construct a quantum computer of arbitrary size. This is so far no different to having qbits in any other medium, ion traps, superconducting wires, etc, however, as silicon fabrication is inherently scalable, and the quantum system required is only on order of a few unit cells of silicon at most, a large number of qbit building blocks can be assembled in a small piece of silicon; the only space hungry requirement then being the waveguides and source of the light necessary for interaction with the qbits.

## 2. Dopants in Silicon: Which Atoms to Choose?

The second advantage, of easy integration, can then be seen. it is imagined that classically controlled diode lasers are embedded into the silicon material, and then used to pump and control the qbit systems, this is one possible integration with classical electronics. It does not take much more to see how the results of a quantum computation could be then converted, of course now no longer quantum information, into classical transistor states and read out on a classical computer screen. While any other method of quantum computing can do all this, separate structures are required to do so.

As the use of a dopant atom in silicon has been shown to possess some benefits, then it must be determined which atom. Some possible choices are immediately removed for practical reasons. The noble gases, firstly for the obvious reason that, being renowned for their lack of reactivity, they have filled outer electron (sp) shells, and are thus inert; this hinders the formation of shared electron bonds with the surrounding silicon lattice. As a result the gas atom is often found in an interstitial position, allowing unwanted variance in the local environment from dopant atom to atom; it should also be noted that such interstitial gas atoms are thought to diffuse through the host material [97], rendering a precisely constructed quantum system, as a qbit most surely must be, from being maintained. The atoms are also thought to form complexes [97], groups of multiple dopant atoms interstitially positioned and interacting in a non-trivial manner; this again adds decoherence mechanisms that ruin the noble gases for use in the solid state as a qbit. Finally, it should be noted that noble gases do have one redeeming feature, they form mid bandgap states in silicon, which is vital for the qbit to remain localised [98, p66].

Nor are the alkali or alkaline earth metals suitable, for they are too reactive outside the bulk. Because of their singular unpaired outer electrons, alkali metals are then

only able to form single covalent bonds with the bulk silicon. This makes it seem problematic for them to be interstitially located, as a substitutional donor requires the capacity for 4 bonds; the single bond is assumed to be a weaker than more, making the atom weakly bound to its location, i.e. highly mobile. Metals are also unsuitable, for similar reasons to the noble gases in regard to bonding with the silicon. Metals also form band structures that, due to significant wavefunction overlap, delocalise electrons; this makes localised coherent states much more difficult to achieve. The periodic table can then be used to guide guesses that the elements further from silicon will have greater problems as substitutional dopants in silicon, due to greater differences in outer electron shells (for silicon the 3s and 3p levels). The relevant remaining section is the semiconductors, shown in the periodic table excerpt in figure 2.5.

The periodic table excerpt in figure 2.5 shows the semiconductor elements, such as Si, Ge, and the elements used to form composite semiconductor compounds from groups iii to v such as InP, AlGaAs, etc. With the ultimate aim of using a donor atom as a qbit in an optically addressed quantum computer, one can remove the compound semiconductors from contention. This is because of their fundamental structure, being comprised of more than one atom each with a differing number of outermost electrons, a substitutional donor atom may replace either of the intrinsic material atoms, thus being either an n or p type donor.

Once it has been decided to use a semiconductor dopant atom as a quantum system, in general, dopant atoms in silicon, or indeed in any semiconductor material, can be categorized in one of two ways, as a "shallow" or a "deep" donor. These donors are referred to as such because of the binding energy of their donor electrons. Different energy levels will then require different wavelengths for optical interactaction and will have wavefunctions of different spatial extents. This will change the donor

spacing, and thus concentration, needed for qbit to qbit interactions; such qbit to qbit interactions are vital because of the universality of two bit quantum gates [99], that is, a set of pairs of qbits where each qbit can interact with one other and the result can be read out, is capable of being a universal quantum computer and carrying out any arbitrary quantum computation given sufficient time and or number of qbits. Such multiple qbit interactions, probably mediated by a donor electron in a higher and thus spatially larger energy state or even an electron from a different donor element entirely, are of course vital for the implementation of the various operations necessary for a quantum computer; these operations will be analogues to the classical computing operations AND, OR, and NOT. Thus is it vital for there to be donor states with both a large spatial extent, and with the small.

The following topics are discussed below: the "shallow" and "deep" donors in silicon and their uses, along with the causes of the respective shallow or deepness of their energy levels, the links between the "deepness" of the energy level and the likely wavefunction extent, and the currently existing measured and inferred lifetimes. The body of knowledge about lifetimes, in different systems for different dopants, are then added to by the results later in this thesis.

## 2.5.1. "Shallow" Donors: The Pnictogens

The first group of donors in silicon to receive attention were the "shallow" or group 15/group v donors. Shallow donors are the ideologically simpler donor type, ideally with the dopant atom substitutionally replacing a silicon atom. This substitutional replacement is ideal because it is repeatable, and the dopant atom is less susceptible to diffusion throughout the host material than if it were interstitial. To clarify this point, if the interstitial atom displaces one of silicon and then does not occupy the silicon atom's former position, then the silicon structure is broken and this is not the most stable configuration of the lattice; if the interstitial atom does not displace

a silicon atom, then it must only have weak bonds with the silicon lattice due to the lack of spare valence electrons in silicon to form additional bonds. Either way, the interstitial atom can be expected to be more susceptible to thermally agitated positional drift, than a substitutional atom. Continuing on, if multiple dopants replace multiple silicon atoms it can be assured that their local environments are at least broadly similar, they will each be bonded to 4 surrounding silicon atoms and sit somewhere in the tetrahedral structure, and thus experience similar if not identical phase evolution with respect to time and other dopants, compared to e.g. interstitial dopants which may have a much more variable interaction with the surrounding silicon.

For the dopant to be of use, part of itself must have at least 2 nondegenerate states to form the $|0\rangle$ and $|1\rangle$ quantum states necessary for representation of quantum information. To be valid in silicon, it must have a greater or fewer number of outer shell electrons than silicon ($...3s^23p^2$, henceforth referred to as 3sp), and will thus allow a pair of donor electron states, or acceptor hole states, to act as the qbit. This need for extra or fewer electrons is made clear by recalling that conduction (electrons), or valence (holes), band states are not spatially confined in a single material; thus any qbit cannot have controllable interactions and be in the conduction or valence bands. As acceptors are not considered in this thesis, the shallow donors that fulfil these conditions are the pnictogens: nitrogen, phosphorus, arsenic, antimony, and bismuth.

If a donor dopant has a different number of 3sp electrons than the surrounding silicon, the additional electron will posses energy states that are not part of the host materials conduction band. The donor electrons states are in between the conduction and valence bands, and these are referred to as mid band-gap states.

## 2. Dopants in Silicon: Which Atoms to Choose?

If the doping concentration is high enough, then the donor electron wavefunctions may overlap significantly enough that a new dopant band is formed. An example of this, in the case of pnictogens who have one additional electron over the silicon host, is found once the doping concentration is high enough that the ground state wavefunctions overlap. Here the conduction of the silicon can increase rapidly as the doping concentration increases past some threshold point. This is known as the Mott semiconductor transition, and is discussed in further detail in section 3.7.2. For "shallow" dopants, these mid-bandgap states are, as may expected, quite shallow binding energies typically a few tens of meV; some examples of pnictogen binding energies are shown in table 2.1.

The "shallow" dopants are often referred to as "Hydrogenic Impurities"[95] because of their single donor electron being similar, in some ways (wavefunction, Hamiltonian, etc), to a hydrogen atom. Because of coulombic attraction affecting binding energies, "shallow" donor electron states are found for single donor dopants, i.e. for silicon, the pnictogens. The hydrogenic label then comes from the single donor atom having one additional valence electron compared with the surrounding silicon, and assuming substitutional doping, this leaves one electron. This remaining electron will be subject to a coulombic attraction to the donor core, although this will be reduced both by the inner electron structure of the donor, and by the electrons in the surrounding silicon lattice. As a gross approximation, the donor electron is then like or analogous to a scaled hydrogen atom. If, as for the "shallow" donor case, the binding energies are small and thus the donor electron wavefunction is likely to be large in spatial extent, then the donor electron can be treated exactly as a hydrogen atom but by accounting for the different dielectric constant (electric permittivity) of the bulk silicon lattice, which is approximately $\epsilon_r = 11.7$[80]. This implicitly assumes that the average distance of the donor electron is so great as to allow the averaging of the electric field from the surrounding silicon over multiple unit cells.

This "shallow" hydrogenic approximation can be readily seen in equation 2.2, describing the energy behaviour of the pnictogen donor electron; where m* is the effective mass, n an integer, and $\epsilon_0$ the dielectric constant in vacuum. This then leads into the effective mass approximation, originally derived by Kohn and Luttinger [8], and discussed in much more detail in chapter 3. However, only the excited states are accurately described by this equation, due to the approximations inherent in EMT theory, that the donor electron has a large wavefunction with respect to the host crystal unit cell, the ground state requires alternative description as described in more detail in chapter 3. [100]

$$E_n = \frac{m*}{2(n\hbar)^2} \left( \frac{q^2}{4\pi\epsilon_0\epsilon_r} \right)^2 \tag{2.2}$$

Equation 2.2 then makes clear the phrase "shallow" donors when referring to group v semiconductors. Using equation 2.2 to estimate the binding energy of the ground state gives $\tilde{5}0$meV, whereas the room temperature ($\tilde{3}00$K) bandgap of silicon is 1.11eV [100]. The ground state is much closer to the conduction band than the valence band, hence the name "shallow".

The common examples of single donor or acceptor dopants are phosphorus and boron, as donor and acceptor respectively. Boron is more commonly used than aluminium due to issues of solubility in silicon, as the achievable concentration of aluminium is lower; although the concept of using aluminium as the simplest acceptor is still perfectly valid. However, due to differences in the conduction and valence bands of silicon, and the extra difficulty in calculating the properties of acceptor hole states [95, p174], only pnictogen donors are discussed.

There is much material on donor lifetimes in the literature, primarily on the phos-

phorus substitutional donor. The $T_1$ of some dopant levels are collated and shown in table 2.1; it should be noted that most values are not direct lifetime measurements, they are inferred lifetimes from spectral linewidths, which may be converted into a lifetime using the uncertainty principle and the differential of the energy,

$$\Delta E = \left(\frac{\partial E}{\partial \nu}\right)\Delta \nu = \left(\frac{\partial hc\nu}{\partial \nu}\right)\Delta \nu = hc\Delta \nu.$$

Only $T_1$ lifetimes are shown in table 2.1, because the single $T_2$ lifetime, at least known to the present author, has been measured as $160 \pm 20 ps$ [101]; this is for a $2P_0$ state of a phosphorus donor.

| Donor Element | Transition | Energy (meV) | $T_1$ (ps) |
|---|---|---|---|
| P | $2p_{\pm 1} \rightarrow 1S(A_1)$ | 34 | 118 [5] |
| P | $2p_0 \rightarrow 1S(A_1)$ | 34.1 | 205 [3] |
| P | $2p_{\pm 1} \rightarrow 1S(A_1)$ | 34.1 | 160 [3] |
| P | $2p_0 \rightarrow 1S(A_1)$ | 34.1 | 235 |
| P | $2p_0 \rightarrow 1S(A_1)$ | 34.1 | 71.0 * [1] |
| Li | $2p_{\pm 1} \rightarrow 1S(A_1)$ | 26.6 | 18.5 * [1] |
| P | $2p_0 \rightarrow 1S(A_1)$ | 34.1 | 73.1 * [2] |
| P | $2p_{\pm 1} \rightarrow 1S(A_1)$ | 39.2 | 39.6 * [2] |
| P | $3p_0 \rightarrow 1S(A_1)$ | 40.1 | 17.9 * [2] |
| P | $4p_0 \rightarrow 1S(A_1)$ | 42.3 | 30.9 * [2] |
| P | $3p_{\pm 1} \rightarrow 1S(A_1)$ | 42.5 | 47.3 * [2] |
| P | $4p_{\pm 1} \rightarrow 1S(A_1)$ | 43.4 | 83.2 * [2] |
| P | $4f_{\pm 1} \rightarrow 1S(A_1)$ | 43.7 | 92.8 * [2] |
| P | $5p_{\pm 1} \rightarrow 1S(A_1)$ | 44.1 | 109.7 * [2] |
| P | $6p_{\pm 1} \rightarrow 1S(A_1)$ | 44.5 | 104.9 * [2] |
| B | (w) | 44.6 | 56.1 * [4] |
| B | (ao) | 44.5 | 201 * [4] |

Table 2.1.: Energy levels with respect to the conduction band, state or phase lifetimes, for pnictogen donors in Silicon. *:Lifetime inferred from linewidth. [1]: [102]. [2]:isotopically enriched $^{28}Si$ [103]. [3]:These direct measurement values are for 10K[45]. [4]: Boron transitions are unidentified, hence the letter label which is the same as used in the source [103, table III]; only the widest and narrowest boron transitions are given, as they are unlabelled and cannot be compared in full to phosphorus. [5]: This is a phosphorus donor in $Si_{0.991}Ge_{0.009}$ at 6K:[104]. [6]: isotopically enriched $^{28}Si$[105].

Once the lifetimes have been considered, the next limiting factor for the shallow

donors is their utility at room temperature. The shallow nature of the dopant donor atom states requires low temperatures; at room temperature the donor atom is typically completely disassociated from the donor nucleus. According to the equipartition theorem, from basic statistical mechanics, the average energy of a particle in a system at thermal equilibrium is approximately $k_b T$(per degree of freedom); energy is linear with respect to temperature; here $k_b$ is the Boltzmann constant. For a room temperature of 300K the average energy is then 25 meV, which is comparable to the binding energies of the donors in table 2.1. Any pnictogen donor is then susceptible to unwanted thermal ionisation at room temperature, delocalising the electron and disrupting if not utterly ruining, via decoherence, any quantum operation that involves said donor. This is a factor motivating the investigation of "deep" donor states.

The shallow donor levels are not just susceptible to thermal effects, but the inherent phonon spectrum of silicon works against them. As discussed above in section 2.2.2, the Debye energy of silicon is 64.5meV, there is also a plethora of possible phonon frequencies up to this energy. It can then be seen that the $T_1$ lifetime of any pnictogen donor states is not just limited by the radiative, but by the phonon lifetimes as well. There is also the possibility of the donor electron not only decaying and emitting phonons, but of being excited from the ground state; both of these interactions will render the phase evolution of a quantum state incoherent.

## 2.5.2. "Deep" Donors: The Chalcogens

When considering the donor atom of choice in the silicon lattice, by inspection of the periodic table (figure 2.5) it is noticed that the next column from the pnictogens is the chalcogen group. This group has an electron state structure that is similar to the pnictogens and the group iv elements, with one and two additional electrons respectively, in the outermost $np$ states, where $n$ is 2 for the uppermost row and

proceeds incrementally downwards. From the periodic table it would be expected that sulphur would make an ideal substitutional donor in the silicon lattice, due to the same electron structure, allowing the formation of similar, if not identical, bonds to the surrounding silicon atoms (as would be found for the donor atom if it were also silicon). The outer electron configurations of the other chalcogen elements are p states, where the p states all have similar wavefunctions and a large spatial extent, and it could also be expected that some form of similar bond could form with the surrounding silicon atoms, irrespective of the particular chalcogen; the chalcogens have similar s states that also contribute to their bond structure. As the chalcogens have two additional electrons than those of silicon, in the same manner that the pnictogens form hydrogen like systems, the chalcogens can form helium like or hydrogen like exciton systems, for un-ionised and singly ionised donor atoms.

Calculations based on the EMT model have been used to confirm that isolated sulphur and selenium donors occupy substitutional sites in silicon. This is based on using the difference in EMT[106][107] calculated and measured spectra, of both donor transitions and silicon conduction band; calculated energies, based on the assumption of being a substitutional donor, that match to those measured validate, at least partially, the assumptions used in the calculation. The small difference, in calculated excited state measured and calculated energy, is then attributed to the donor atom causing expansion of the silicon lattice, due to the different local volume of the donor and silicon atoms. The conclusion is that single, un-ionised, chalcogen group donors are highly likely to be substitutional in nature[108].

Of course, it is to be expected that a doubly ionised donor atom will differ, if only minimally, from a silicon atom. Silicon in its most common form is $^{28}Si$, as discussed in section 2.3.2, and thus has zero nuclear spin, if the donor atom has an odd atomic number and thus a nuclear spin which will affect the electron energy states, affecting

the bonds between donor and silicon atoms. The greater mass, with the exclusion of oxygen impurities, will also have an effect upon the atom to atom spacing, or lattice constant; as this has been measured for isotopic mass differences in silicon [109], it can be concluded that mass differences due to elemental differences will also affect the lattice spacing and thus the nature of the bonds or vice versa. Finally while the p states are similar they do differ, most notably in extent, which will again affect the bond structure and thus affect the lattice spacing.

Thus the key difference between the chalcogens and the pnictogens is then the energy of the donor electron states, with the pnictogens referred to as "shallow" donors, and the chalcogens as "deep" donors. While for an ionised chalcogen donor it may be expected that the energy levels are deeper, simply due to the greater coulombic attraction from an additional positive charge on the nucleus, it is not immediately clear that the un-ionised double donor states would also be.

This greater binding energy leads to the possible advantages of the "deep" donor states over those of more "shallow" states, of course this is with respect to use as a qbit. Thus not only is there is a lesser chance of a donor electron being excited out of a low energy state, but it may remain in that low energy state, on average, at greater temperatures.

Consider the phonon spectrum, discussed in section 2.2.2, where the Debye energy of silicon is 64.5meV at room temperature. This Debye energy is much less than the several hundred meV binding energies that the ground states for "deep" donors have. Therefore multiple phonon interactions are required with a"deep" donor simultaneously for it to be excited out of a low energy ground state. It is also less likely for multiple phonons to be emitted simultaneously, thus reducing the likelihood of an excited state decaying to a lower or ground state, if the energy gap is

greater than the Debye frequency; the probability then decreases as the energy gap increases.

This highlights one key advantage that deep donors have in regard to fulfilling the DiVincenzo criteria[10] for quantum bits to have long lifetimes. A lower probability of interacting with phonons will increase the radiative lifetime of the excited donor states. Although the interaction of a phonon, without emission of absorption of said phonon, with a donor electron is possible by simply changing the local environment that the electron is in, altering the phase evolution and thus possibly reducing the phase lifetime of the donor electron states.

Just as the energy levels of pnictogen donor electrons can be described well by an EMT hydrogen model, deep donors in silicon could be described by a helium analogue [100]. The binding energies of sulphur and selenium agree well with effective mass model calculations, while the bound states of telurium donor electrons are deeper than effective mass models suggest [110] [94]. However, as discussed in chapter 3, due to the smaller wavefunction or greater attractive potential of the "deep" donors, the lowest lying energy levels are increasingly poorly described by EMT. This is known as the central cell problem, essentially the small ground state wavefunctions are not large enough to average over the dielectric permittivity of the silicon crystal; the ground state wavefunctions being on order of the silicon unit while the next smallest is 36 times area. The ground state energies of even the pnictogen donors are included in this, but the discrepancy is less due to the ground state being bigger.

Energy measurements are collected in table 2.2; these show that the ground state energy levels of chalcogen group donors in silicon are much greater than those of the Pnictogens; however, the singlet ($E$) and triplet ($T_2$) 1S and p like states are then comparable to those of the pnictogens. The energies can then be compared to the

Debye energy of 64.5 meV and the average thermal energy of 25 meV to evaluate their prospective utility.

| Donor Element | State | Energy (mev) |
|---|---|---|
| $S^0$ | $1S(A_1)$ | $318.32^1$ |
| $S^0$ | $1S(T_2)$ | $34.62^1$ |
| $S^0$ | $1S(E)$ | $31.6$ [1] |
| $S^0$ | $2S(A_1)$ | $18.4$ [1] |
| $S^0$ | $2p_0$ | $11.48$ [1] |
| $S^0$ | $2S(T_2)$ | $9.22$ [1] |
| $S^0$ | $2p_{\pm 1}$ | $6.39$ [1] |
| $S^+$ | $1S(T_2)[\Gamma_7]$ | $429.3^2$ |
| $S^+$ | $1S(T_2)[\Gamma_8]$ | $429.6^2$ |
| $Se^0$ | $1S(A1)$ | $306.63^1$ |
| $Se^0$ | $1S(T_2)$ | $34.44^1$ |
| $Se^0$ | $1S(E)$ | $26.46$ [1] |
| $Se^0$ | $2S(A_1)$ | $18.0$ [1] |
| $Se^0$ | $2p_0$ | $11.49$ [1] |
| $Se^0$ | $2S(T_2)$ | $9.27$ [1] |
| $Se^0$ | $2p_{\pm 1}$ | $6.39$ [1] |
| $Te^0$ | $1S(A_1)$ | $199$ [3] |
| $Te^0$ | $1S(T_2)$ | $39$ [3] |
| $Te^0$ | $2p_0$ | $12$ [3] |
| $Te^0$ | $2p_{\pm 1}$ | $7$ [3] |
| $Te^+$ | $1S(A_1)$ | $411$ [3] |
| $Te^+$ | $1S(T_2)$ | $177$ [3] |
| $Te^+$ | $2p_0$ | $47$ [3] |
| $Te^+$ | $2p_{\pm 1}$ | $26$ [3] |

Table 2.2.: Energy levels of chalcogen group donors in silicon with respect to the conduction band. Binding energies are taken with respect to the conduction band. [1]:[94, table 2, p29] [2]:[111, fig 2] [3]:[110, table 4, page 4583]

It can be seen that the chalcogen group donors in silicon have the sufficient binding energies to be less susceptible to either phonon decay, or unwanted excitation from the ground state.

Once it has been shown that the chalcogen group donors have the advantage of greater, or deeper, binding energies, the next step is the verification that they might also fulfil some of the other necessary criteria for use as a qbit. The key criterion

that this thesis is concerned with is lifetime. Evidence is found in the literature to support the further investigation of chalcogen donors in silicon, however direct measurement of $T_2$ or even $T_1$ lifetimes of suitable donor states are somewhat lacking, and thus are largely limited to a few linewidth inferred possible $T_1$ lifetimes; hence the absence of any comprehensive tabulation of the lifetime values. There are no direct $T_2$ decoherence times measurements for chalcogen dopants that the present author is aware of in the literature.

Absorbance spectroscopy, of sulphur donors in silicon, shows at a temperature of 1.5K that the Full Width Half Maximum (FWHM) absorbance linewidth for the $1S(A_1)$ to $1S(T_2)(\Gamma_7)$ and $1S(T_2)(\Gamma_8)$ (the 1S states are split due to the symmetry of the silicon lattice) for singly ionised sulphur states to be 0.008 $cm^{-1}$ and 0.022 cm$^{-1}$[111][112]; this is assumed to be the transition to the silicon conduction band minimum. The difference between the two transition linewidths can be understood by the following argument. As sulphur has an outer electron configuration with two extra electrons over the host silicon lattice, there are both singly ionised and un-ionsed donor electron states; due to the much smaller FWHM of the ionised state it is the only one considered here. A singly ionised donor atom will have a stronger coulombic potential, due to the absence of the negatively charged electron, which should cause a greater binding energy and a wavefunction extent that is lesser; the smaller wavefunction will then have a smaller overlap with any inhomogeneity in the silicon and thus be less likely to be perturbed by such deviations and thus would have a narrow FWHM and a longer lifetime. These absorbance lines also have the Lorentzian shape which is a characteristic signature of an exponential population decay; the connection may be made that the intrinsic state decays are of an exponential form and thus this Lorenzian shape is highly likely to be due to this, however, a direct measurement of the state decay is needed for proof. The linewidths of 0.008cm$^{-1}$ and 0.022cm$^{-1}$ then equate to lifetimes of 301ps and 109ps

respectively.

Further evidence for the chalcogen donors can be found for the donor selenium. For this chalcogen double donor, the narrowest linewidth measured was again $0.008 cm^{-1}$, as for the sulphur[112]. In addition to this narrow linediwdth, hyperfine splitting "due to a hyperfine coupling with the $I = 1/2$ nuclear spin was shown for $^{77}Se^{+}$"[113]. The hyperfine splitting for the ionised $^{77}Se$ donor $1S(A_1)$ to $1S(T_2)(\Gamma_7)$ transistion at 1.5k was found to be 0.056 $cm^{-1}$, or 0.00694 meV [113]. This raises the possibility of a potential donor for the Stoneham quantum computing proposal [1], as the resolvable nuclear hyperfine splitting could be used to form between the $|1\rangle$ and $|0\rangle$ qbit states.

These Chalcogen $T_1$ lifetimes are then collated into table 2.3.

| Donor Element | Transition | $T_1$ (ps) |
|---|---|---|
| $S^+$ | $1S(T_2)[\Gamma_7] \rightarrow$ Cond. | 301* [1] |
| $S^+$ | $1S(T_2)[\Gamma_8] \rightarrow$ Cond. | 109 ns* [1] |

Table 2.3.: Phase and state lifetimes for chalcogen donors in Silicon. *: Inferred from linewidth. [1]: [111, fig 2]. **Cond.:** Conduction Band.

One possible factor limiting future measurements of the chalcogens, is their solid solubility; this is how much of the element can be mixed into silicon by thermal diffusion processes. It is important, because the measurement of lifetimes is not going to be done using single donor atoms, but with large ensembles. This makes measurement easier, simply because of the greater possible signal from many donors as opposed to one. The maximum solid solubility of sulphur in silicon is $3 \times 10^{16} cm^{-3}$[114] ; this is not as high as the $10^{20}$ factor that is common for electrical dopants in silicon, but may be sufficient.

## 2.5.2.1. Conclusion

Thus it is found that, for at least the sulphur and selenium donors, long radiative lifetimes are likely. This encourages further investigation, firstly to prove for certain that there are in fact long radiative lifetimes, via direct measurement. Secondly, the phase coherence lifetimes of the electron donor states must be measured, so that their ultimate utility as qbits may be known.

# 3. Introduction to Effective Mass Theory in Silicon

## 3.1. Introduction

It is necessary to give a brief description of EMT before introducing each part in the following sections. The detailed working through of the mathematics, including required derivations, are left to the more detailed appendix B. This chapter outlines the EMT framework and its application to the calculation of donor state transition rates.

The EMT single donor approach is that followed in this chapter, which would seem to be naively inappropriate for application to double donors. It is, however, able to provide extremely good agreement with all non-ground state energies, and more importantly as I will show, order of magnitude agreement for radiative lifetimes are obtained. These indicate that there is some truth in the model.

While this chapter is an introduction to EMT in silicon, the formalism is the same in all materials with the same degree of electron effective mass anisotropy, i.e. the same in the x, y plane but different along the z axis. The material must also have a set of conduction band energy minimums equidistant in each momentium direction, and, of course, the explicitly stated assumptions of the effective mass model must

hold, as will be discussed further below. In addition, the different electron effective mass, and also the average dielectric constant must be changed from material to material.

EMT was originally developed by Kohn and Luttinger to describe donor impurity states in semiconductors [106][8] with conduction band minima that are prolate spheres. The rest of this chapter follows their and Faulkner's [107] work. It does this by estimating the wavefunctions and energies of hydrogen like systems with x, y and z, axis nondegenerate effective masses; this is achieved by the solving of the Schrödinger equation with the EMT Hamiltonian. Also the dielectric permittivity is not restricted to that of vacuum, being scaled to that of the macroscopic average dielectric permittivity of the environment surrounding the modelled hydrogenic system.

Because the true wavefunctions of the Hamiltonian are not analytically known, and because of the naive similarities of the system to that of scaled hydrogen (and helium) atoms, a trial basis of scaled hydrogen wavefunctions is used. Variational parameters are used to scale the hydrogen wavefunctions, in the x, y and z axis directions, until the calculated energy meets some criteria. Single hydrogen basis states, or multiple basis states of the same parity and magnetic quantum number, can be used, with appropriate weighting, to construct an estimate of the wavefunction. This is in effect using a scaled $1S$ wavefunction or 1S and 2S,3S,4S....,3D,4D...,5G..etc. states out of which to build the estimated wavefunction.

For the ground state of the system the variational criterion can be the minimum possible energy, within the bounds imposed by constraints upon the variational parameters, or the minimum difference between the calculated and experimentally measured energies. The former condition can be shown (see section A.2.2.2) to be

an upper bound on the true ground state energy of the Hamiltonian used; this is not necessarily the same as the real physical system, due to the simplifications and neglections implicit in any model.

For the higher energy states the same minimisation of the calculated energy criteria can be used, but there is then no guarantee that the calculated energy is an upper bound of the Hamiltonian's energy; despite this it should be noted that this still gives good agreement with experimental results for the higher energy excited states of selenium in silicon.

The calculated $2p_0$ state has deviations, with respect to the measured [94, table 2] energies of substitutional atomic selenium donors in silicon, of $-2.44\%$, $+0.174\%$ and $+0.0174\%$ , while those of the 1S state energy are much greater at $-90.2\%$, $-89.8\%$ and $-89.8\%$ for 1, 18, and 90 basis states respectively. The 1S inaccuracy is, however, due to the degeneracy of the 1S state being broken by the symmetry of the crystal field of the surrounding silicon, also called the central cell correction; higher energy states are more widely spatially distributed, often over multiple silicon unit cells, and thus are less susceptible as a fraction of the energy to asymmetries in the crystal field.

Thus the 1S state results, while inaccurate, are still in agreement with being an upper bound on the true energy of the Hamiltonian, and that Hamiltonian being an approximately correct description of the measured system. The energies for the 18 and 90 basis state energies are also taken from [94, table 2], with the 1 basis state energies taken from my own calculations described in detail; shown in results section 3.7.1.

Once the wavefunction parameters have been variationally found, such that the

energy eigenvalues are in approximate agreement with measured values, it can then be assumed that the wavefunction is approximately correct. This is discussed in more detail in the following sections.

## 3.2. Assumptions of the Effective Mass Theory Model

The effective mass model of donor states is often said to be based upon two key assumptions [106][115][8] [116].

1. The perturbation to the host, due to the donor, is slowly varying over the scale of the host's lattice constant.

2. The donor wavefunctions extend over such large distances that they can be represented by the Bloch states at only the conduction band minima, or only from states within a very narrow range of momentium values.

However, it is clear that each of the assumptions implies the other. For the donor wavefunctions to be made up of basis states within a very narrow range of momentium values, they must be slowly varying with respect to real space. If the wavefunctions are slowly varying then the potential, of which they are eigenfunctions of, must also be slowly varying, and vice versa.

## 3.3. The EMT Schrödinger Equation

Following Kohn[8][106], to find the wavefunction $\Psi(r)$ of an impurity donor state in a semiconductor the Schrödinger equation, shown below, must be solved

$$\left(H_0 + U(r)\right)\Psi(r) = E\Psi(r) \tag{3.1}$$

Where, in the Schrödinger equation 3.1, $r$ is the 3D radial distance coordinate, the centre of the donor atom nucleus is the origin, $U(r)$ is the additional potential from the donor atom, and $H_0$ is the Hamiltonian of the system without the donor impurity.

The Hamiltonian $H_0$, where $V(r)$ is the periodic potential of the crystal lattice, is then of the familiar form shown:

$$H_0 = -\frac{\hbar^2}{2m}\nabla^2 + V(r) \tag{3.2}$$

Because of the first assumption of the effective mass model the donor atom potential $U(r)$ can be assumed to be of the form:

$$U(r) = -\frac{e^2}{4\pi\epsilon_0\epsilon_r r} \tag{3.3}$$

Equation 3.3 is for a single donor, $\epsilon_r$ and $\epsilon_0$ are then the relative and vacuum dielectric constants.

The donor atom potential is, of course, not in reality of this form. It is only approximated by this if the expected positions of the donor states are at distances such that the donor atoms core electrons can be assumed to be a single point. This is the first of two key assumptions in the EMT, the donor atom electrons are far away from the donor nucleus. It should be noted that while this is explicitly only true for a single donor, the calculated energy values for the non-ground states, using a potential of

this form, are reasonably accurate for double donors, and this is discussed in more detail in chapter 4.

It is assumed that the, perturbing, "fractional change of U over a unit cell is small"[106]. To see explicitly why this is the case , and increasingly so as the distance from the donor atom increases, consider the fractional strength of the potential $U(r)$ at some distance from the donor, $r_1$, compared to one lattice constant further away, $r_2$. Here $r_1 = aN$, and $r_2 = a(N+1)$, where $a$ is the lattice constant, and $N$ is some number of lattice constants. As shown in equation 3.4 (via L'Hospitals's rule [117]), as the distance from the donor atom increases the fractional potential change over one unit cell tends towards 0; the ratio of the potentials, in the limit of N tending towards infinity, is 1.

That is, the further away the donor electron from the donor nuclei, the greater the accuracy of the statement; the potential is only valid at large distances. This assumption amounts to taking the FT of the "true" physical potential and neglecting all but the lowest spatial frequency, or momentium, components; it is directly equivalent to the second assumption of EMT.

$$
\begin{aligned}
\frac{U(r_1)}{U(r_2)} &= \frac{-\frac{e^2}{\epsilon r_1}}{-\frac{e^2}{\epsilon r_2}} = \frac{r_2}{r_1} \\
&= \frac{(N+1)a}{Na} = \frac{(N+1)}{N} \\
\lim_{N\to\infty}\left(\frac{(N+1)}{N}\right) &= \lim_{N\to\infty}\left(\frac{\frac{\partial(N+1)}{\partial N}}{\frac{\partial(N)}{\partial N}}\right) \\
&= \frac{1}{1} = 1
\end{aligned}
\tag{3.4}
$$

## 3.3.1. Bloch Function Basis

Now that the Hamiltonian of the system is described, complete with slowly varying donor potential, the wavefunction of the donor states must be considered. This can be accomplished by writing it as a basis element in a complete, orthonormal, basis of the $H_0 + U(r)$ operator. However, the basis of this operator is not known, and therefore the wavefunction must be expanded as a vector in another complete basis; the vector in this new basis is then a basis element in eigenbasis of $H_0 + U(r)$.

To find the basis with which to describe donor states, begin by following Kohn [106], consider the basis of conduction band electrons in silicon. It is possible to describe the wavefunction of any electron in the conduction band of the silicon by using the complete set of eigenfunctions of $H_0$, the Bloch functions $\Phi_{n,k}(r)$. The Bloch functions, being a complete set of eigenfunctions, describe all states in all bands, not just the conduction band. The Bloch functions are then the set of solutions of the Schrödinger equation, 3.5, where the energy $E_n(k)$ is the energy of the $n$th state with momentium $k$, this then describes the band structure of the silicon.

$$H_0\Phi_{n,k}(r) = E_n(k)\Phi_{n,k}(r) \tag{3.5}$$

The Bloch functions can be written as in equation 3.6, where $u_{n,k}(r)$ is a function with the periodicity of the silicon lattice.[81]

$$\Phi_{n,k}(r) = e^{ik.r}u_{n,k}(r) \tag{3.6}$$

## 3. Introduction to Effective Mass Theory in Silicon

The second assumption of EMT then becomes relevant, and is tied to the first. Because of the assumption that the donor electron states are far away from the donor atom, such that the donor potential can be assumed to be slowly varying and of the form in equation 3.3, the donor state comprises only a narrow range of momentium space states; because the spatial extent of any function, such as the wavefunction, has an inverse relation with the momentium space extent. Thus Kohn [106, eq II.4] is able to assert, and then prove [106, equations ii.4 to ii.12 ]) that the set of Bloch functions at the silicon conduction band minimum forms a complete basis set with which to describe the donor states.

The conduction band minima can be found at the positions shown in equation 3.7[116]; where $a_{si} = 5.431 \times 10^{-10}$m [80] is the silicon real space lattice parameter.

$$k_{\pm x} = 0.85 \frac{2\pi}{a_{si}} (\pm 1, 0, 0) \tag{3.7}$$

The new basis built out of the Bloch functions at the minima is described in equation 3.8; where $i$ indexes the conduction band minima, of which there are 6 for silicon, the minima at the $(+k_x, -k_x, +k_y, -k_y, +k_z, -k_z)$ positions for $i$ equals (1, 2, 3, 4, 5, 6) respectively.

$$\Phi_{k^{(i)}}(r) = e^{ik^{(i)} \cdot r} u_{n,k^{(i)}}(r) \tag{3.8}$$

Silicon has 6 degenerate conduction band minima, thus it may be concluded that each calculated EMT donor state is also at least 6 fold degenerate; this does not take into account any spin degeneracy, as the hyperfine interaction is neglected in the

73

EMT Hamiltonian. As the set of Bloch functions at the conduction band minima are a complete basis, any wavefunction should be a linear combination of these basis states. This then gives a total wavefunction.[106, equation ii.40] [8, equation 3.3]

$$\Psi(r) = \sum_i F_{k^{(i)}} \Phi_{k^{(i)}}(r) \tag{3.9}$$

Where in equation 3.9 each Bloch function is weighted by an envelope function $F_{k^{(i)}}$, which will vary depending on each specific state. Each individual effective mass basis state is then given by: [106, equation ii.40] [8, equation 3.3]

$$\Psi_{k^{(i)}}(r) = F_{k^{(i)}} \Phi_{k^{(i)}}(r) \tag{3.10}$$

## 3.3.2. The Effective Mass Equation

The envelope functions, $F^{(i)}$, are then the solutions to the effective mass equation.

$$\left[ -\frac{\hbar^2}{2m_\perp}\left(\frac{\partial^2}{\partial x_i^2} + \frac{\partial^2}{\partial y_i^2}\right) - \frac{\hbar^2}{2m_\parallel}\frac{\partial^2}{\partial z_i^2} - \frac{e^2}{4\pi\epsilon_0\epsilon_r r} \right] F^{(i)}(r) = E_c F^{(i)}(r) \tag{3.11}$$

In the effective mass equation, 3.11, $m_\perp$ and $m_\parallel$ are the effective masses in the perpendicular and parallel directions respectively, $m_e$ is the rest mass of an electron, and $E_c$ is then the energy of the state with respect to the conduction band minimum; see [106, equations ii.13 to ii.38 or A.1 to A.15] for a derivation of the effective mass equation. As the effective mass equation applies to the envelope wavefunctions of silicon donors, $i$ indexes the six degenerate conduction band minima. The values for the effective masses in silicon are:

$$m_\perp = 0.19 m_e$$
$$m_\parallel = 0.98 m_e$$

$$(3.12)$$

There are then 6 effective mass equations, one for each conduction band minimum in silicon indexed by $i$, where each of the 6 $F^{(i)}(r)$ states is the solution of the $i$th effective mass equation. Kohn [106] states that $z_i$ is along the direction of the $i$th $k$ (momentium) vector, which points in the direction of the $i$th conduction band minimum in momentium space. This can be seen by considering that the $k^{(0)}$ vector is in the direction of the $k_x$ axis minimum in k space, which is then perpendicular to the x axis in real space, and allowing it to be in the direction of $z_1$.

It is possible to write the effective mass equation in one set of coordinates, rather than the 6 $i$ coordinates systems. To do so the coordinates used must be switched around, with $(+x, -x, +y, -y, +z, -z)$ being the possible directions in laboratory coordinates of the $z_i$ coordinate. Because of the second order dependence upon the spatial coordinates, the replacement of $x$ with $-x$ results in the same $F^{(i)}(r)$ solution. Thus the $k_{+x}$ and $k_{-x}$ effective mass equations have the same solutions, just like the $k_{+y}$ and $k_{-y}$, and the $k_{+z}$ and $k_{-z}$. To obtain each of the respective effective mass equations, simply switch $z_i$ with $x$ for $k_{+y}$ and $k_{-y}$ ($k_3$ and $k_4$), or $y$ for $k_{+z}$ and $k_{-z}$ ($k_5$ and $k_6$).

The envelope function solutions, $F^{(i)}(r)$ can thus be seen to have the same solutions, except with the coordinates similarly switched. This is because they must have the same energy eigenvalues, and thus if the effective mass equation has altered its coordinates, by what is in effect a label switching, for the energy to remain the same the eigenfunctions must also switch coordinate labels in the same way. As an

example, rewriting $F^{(1)}(r)$ as $F^{(1)}(x, y, z)$, the function is of the same form for the 3rd or 4th conduction band index but with the coordinates changed to $F^{(3,4)}(z, y, x)$; the other states will then have solutions $F^{(5,6)}(x, z, y)$.

This is the single valley description of donor states. For this effective mass description of the donor states each state will then have a degeneracy of six, corresponding to the six conduction band minima and their respective effective mass equations and envelope function solutions.

Now in the rescaled cartesian coordinates the final transform is applied, that to spherical coordinates. The advantage here is that it makes the analytical maths easier. In particular, the wavefunction basis states become easier to integrate, making the analytical calculation of the Hamiltonian matrix elements simpler. For example, for the ground state the form changes from $e^{-(x^2+y^2+g^2)^{\frac{1}{2}}}$, to $e^{-r_g}$.

### 3.3.2.1. The Unitless Effective Mass Equation

The effective mass equation, 3.11, can in effect be treated as a Schrödinger equation with Hamiltonian $H_1$. To make the analytical calculation of the Hamiltonian matrix elements easier a series of coordinate transformations are then carried out. The first of these is to change to unitless coordinates. This converts the EMT Hamiltonian into a slightly simpler form and removes Bohr radii factors from the hydrogenic donor electron wavefunction basis. Not only does this make analytically dealing with the EMT Hamiltonian and wavefunctions easier, it makes numerical calculations ( such as the later variational minimising of the Hamiltonian matrix) less susceptible to rounding errors and instability from the physical constant values at, sometimes, differing scales.

To obtain the unitless effective mass equation, the units of length and energy are

defined as :

$$a_B = \frac{4\pi\hbar^2\epsilon_r\epsilon_0}{m_\perp e^2}$$
$$E_0 = \frac{m_\perp e^4}{2\hbar^2(4\pi\epsilon_r\epsilon_0)^2}$$

(3.13)

Then the ratio of effective masses $\gamma$ is defined as:

$$\gamma = \frac{m_\perp}{m_\parallel}$$

(3.14)

Finally the $i$ superscript is dropped for convenience, and taking the unit and $\gamma$ definitions from equations 3.13 and 3.14 respectively the effective mass equation 3.11 becomes:

$$H_1 = -\left(\frac{\partial^2}{\partial x^2} + \frac{\partial^2}{\partial y^2}\right) - \gamma\frac{\partial^2}{\partial z^2} - \frac{2}{r}$$
$$H_1 F(r) = E_c F(r)$$

(3.15)

In equation 3.15 $H_1$ is the effective mass hamiltonian; for a more detailed derivation of the unitless effective mass equation see appendix B.1.

To obtain the unitless effective mass Hamiltonian for the different $i$ states, equation 3.15, the coordinates can simply be altered as for the non unitless effective mass equation.

### 3.3.2.2. Converting to Spherical Coordinates

It is then possible to perform a coordinate transformation to change the effective mass Hamiltonian, and the donor envelope functions, into radial coordinates. However, the coordinate system must first be transformed in a scaled Cartesian coordinate system. This is the second coordinate transformation applied to the EMT Hamiltonian and wavefunctions, after that to unitless form. In the EMT Hamiltonian, because of the non-degenerate electron effective masses along the xy and z directions in silicon, the z axis terms have a factor of $\gamma = \frac{m_\perp}{m_\parallel}$; for the same reason, the z axis terms of the hydrogenic wavefunction states have a factor of $\frac{\beta}{\gamma})^{\frac{1}{2}}$, where $\beta$ is a scaling parameter. To make this easier to deal with analytically, the $z$ coordinate is rescaled to $g = (\frac{\beta}{\gamma})^{\frac{1}{2}} z$.

Once in the rescaled Cartesian coordinates the final, third, transform is applied, that to spherical coordinates. This is done, like all the other transformations, to make the analytical maths easier. In particular, the wavefunction basis states become easier to integrate, making the analytical calculation of the Hamiltonian matrix elements simpler. For example, for the ground state the form changes from $e^{-(x^2+y^2+g^2)^{\frac{1}{2}}}$, to $e^{-r_g}$. The transformations to shifted Cartesian and then spherical coordinates are shown in appendix B.2.

The laboratory coordinates are $(x, y, z)$. Then the effective mass equations are $(x_i, y_i, z_i)$ for $i = 1, 2, 3, 4, 5, 6$. Let the $i = 1$ system coincide with the laboratory coordinates for simplicity. Thus the coordinates are defined as in table 3.1.

Then the scaled Cartesian system rescales the $z_i$ to become $g_i$, as in equation 3.16; where $\beta$ is now a variational parameter that is the same for all $i$ due to the imposed degeneracy of the states in the effective mass model.

| $i$ | $x_i$ | $y_i$ | $z_i$ | $(k_x,k_y,k_z)$ |
|---|---|---|---|---|
| 1 | x | y | z | (1, 0, 0) |
| 2 | x | y | -z | (-1, 0, 0) |
| 3 | z | y | x | (0, 1, 0) |
| 4 | z | y | -x | (0, -1, 0) |
| 5 | x | z | y | (0, 0, 1) |
| 6 | x | z | -y | (0, 0, -1) |

Table 3.1.: Relations of the $i$ Cartesian coordinate systems.

$$g_i = (\frac{\beta}{\gamma})^{\frac{1}{2}} z_i \tag{3.16}$$

Then the spherical coordinates, and their relation to the $i$th set of Cartesian coordinates, where the subscript$_{gi}$ indicates the $i$th scaled set of $g$ coordinates. is given below:

$$x_i = r_{gi} \sin(\theta_{gi}) \cos(\phi_{gi})$$

$$y_i = r_{gi} \sin(\theta_{gi}) \sin(\phi_{gi})$$

$$g_i = r_{gi} \cos(\theta_{gi})$$

$$r_{gi} = (x_i^2 + y_i^2 + g_i^2)^{\frac{1}{2}}$$

$$r_i = (x_i^2 + y_i^2 + z_i^2)^{\frac{1}{2}}$$

$$= (x_i^2 + y_i^2 + (\frac{\gamma}{\beta}) g_i^2)^{\frac{1}{2}} \qquad (3.17)$$

$$= r_{gi} \left( 1 - (1 - \frac{\gamma}{\beta}) \cos^2(\theta_{gi}) \right)^{\frac{1}{2}}$$

$$\phi_{gi} = \arccos(\frac{g_i}{r_{gi}})$$

$$\phi_i = \arccos(\frac{z_i}{r_i})$$

$$\theta_{gi} = \theta = \arctan(\frac{y_i}{x_i})$$

The Laplacian operator is taken to be:

$$\nabla_{g_i}^2 = \frac{1}{r_{g_i}^2} \frac{\partial}{\partial r_{gi}} (r_{g_i}^2 \frac{\partial}{\partial r_{gi}}) + \frac{1}{r_{g_i}^2 \sin(\theta_{gi})} \frac{\partial}{\partial \theta_{gi}} (\sin(\theta_{gi}) \frac{\partial}{\partial \theta_{gi}}) + \frac{1}{r_{g_i}^2 \sin^2(\theta_{gi})} \frac{\partial^2}{\partial \phi_{gi}^2} \qquad (3.18)$$

Rearranging, and changing the differential operator with respect to $z_i$ to the relevant spherical coordinates, the Hamiltonian $H_1$ then becomes:

$$H_{1i} = -\nabla_{gi}^2 + \left(1 - \beta\right) \left[ \left( \frac{\cos(\theta_{gi})\sin(\theta_{gi})}{r_{gi}^3} \left(2 - \frac{1}{\tan^2(\theta_{gi})}\right) + \frac{1}{\tan(\theta_{gi})r_{gi}} \right) \frac{\partial}{\partial\theta_{gi}} \right.$$
$$+ \frac{\sin^2(\theta_{gi})}{r_{gi}} \frac{\partial}{\partial r_{gi}} + \frac{\sin^2(\theta_{gi})}{r_{gi}^2} \frac{\partial^2}{\partial\theta_{gi}^2} + \cos^2(\theta_{gi}) \frac{\partial^2}{\partial r_{gi}^2}$$
$$\left. - 2\frac{\sin(\theta_{gi})}{r_{gi}} \cos(\theta_{gi}) \frac{\partial}{\partial r_{gi}} \frac{\partial}{\partial\theta_{gi}} \right]$$
$$- \frac{2}{r_{gi}\left(1 - (1 - \frac{\gamma}{\beta})\cos^2(\theta_{gi})\right)^{\frac{1}{2}}}$$

$$(3.19)$$

## 3.4. The Scaled Hydrogenic Basis for $F_{k^{(i)}}(r)$

The effective mass equation, equation 3.11, cannot be directly solved analytically. Thus a scaled hydrogen basis is used as solutions for the $F(r)$. If the scaled hydrogen basis includes variational parameters, then an upper bound on the energy for the ground state, and a surprisingly good agreement with experimentally measured energy for higher excited states, can be found. This is discussed in detail in appendix A.2.2. The variational parameters are then the same for each of the 6 $i$ states, because otherwise the states would not be degenerate in energy $E_c$.

Following Faulkner [107, eq 2.5 and 2.6] a scaled set of hydrogen wavefunctions can be used as the donor envelop wavefunctions $F_i(r)$.

$$F_{n,\ell,m}(r) = \frac{\beta^{\frac{1}{4}}}{\gamma} R_{n,\ell,m}(r) Y_{\ell,m}(\theta, \phi) \tag{3.20}$$

In equation 3.20 $\alpha_{\ell,m}$ is a variational parameter that depends upon the angular momentium and magnetic quantum numbers. The radial parts of the hydrogenic

basis is given by:

$$R_{n,\ell,m}(r) = \frac{2\alpha_{\ell,m}^{\frac{3}{2}}}{n^2}\left(\frac{(n-\ell-1)!}{[(n+\ell)!]^3}\right)^{\frac{1}{2}}\left(\frac{2\alpha_{\ell,m}r}{n}\right)^{\ell}e^{\left[-\frac{\alpha_{\ell,m}r}{n}\right]}L_{n-\ell-1}^{2\ell+1}(\frac{2\alpha_{\ell,m}r}{n}) \qquad (3.21)$$

The angular by:

$$Y_{\ell',m}(\theta,\phi) = \sqrt{\frac{2\ell+1}{4\pi}\frac{(\ell-m)!}{(\ell+m)!}}P_l^m\big(\cos(\theta)\big)e^{im\phi} \qquad (3.22)$$

For both angular and radial hydrogenic state functions, equations 3.21 and 3.22, the coordinates are the radial $g_i$ coordinates described in section 3.3.2.2, however, the $i$ and $g$ subscripts have been dropped for clarity. In all future cases it should be assumed that the coordinates are in a $g_i$ spherical system, unless specified otherwise.

For equation 3.21 $L_{n-\ell-1}^{2\ell+1}(\frac{2\alpha(\ell)r}{n})$ is the associated Laguerre polynomial [118], and is then defined below:

$$L_{n-\ell-1}^{2\ell+1}(\frac{2\alpha_{\ell,m}r}{n}) = \sum_{s=0}^{n-\ell-1}(-1)^s\frac{[(n+\ell)!]^2}{(n-\ell-1-s)!(2\ell+1+s)!s!}\left(\frac{2\alpha_{\ell,m}r}{n}\right)^s \qquad (3.23)$$

For equation 3.22 $P_\ell^m\big(\cos(\theta)\big)$ is then the associated Legendre polynomial [119], shown below:

$$P_\ell^m\big(\cos(\theta)\big) = \frac{(-1)^m}{2^\ell\ell!}\big(1-\cos(\theta)^2\big)^{\frac{m}{2}}\frac{d^{\ell+m}}{d\cos(\theta)^{\ell+m}}\big(\cos(\theta)^2-1\big)^\ell \qquad (3.24)$$

## 3.4.1. Multiple Hydrogenic States as a Basis State

Following Faulkner[107], a more accurate donor envelope function can be constructed from a linear combination of the hydrogenic states. That is, the set of hydrogenic states is used as a basis out of which to construct the basis of the donor envelope wavefunctions.

The effective mass Hamiltonian $H_1$ is invariant with respect to coordinate inversion, i.e. is of even parity. Because of this, states of differing parity will not contribute to the calculated energy expectation value; they are not part of wavefunctions of the $H_1$ operator. It can be seen that by considering the energy expectation value integral, $\langle F|H_1|F\rangle = E$, if the inside of the integral is a purely odd function with no even component then $E$ must be zero.

The Hamiltonian $H_1$ is also invariant with respect to any rotation about the $z_i$ axis. This can be seen by consideration of the spherical coordinate form of the Hamiltonian, where the components involving the $z_i$ axis are then dependent upon the azimuthal angle coordinate $\phi_{gi}$. The form of the hydrogenic basis states spherical harmonics, equation 3.22, then has an exponent $im\phi_{gi}$, this will force the overall energy expectation value integral to have odd parity and thus be zero. Thus it can be concluded that states of differing angular momentum projection, defined by the magnetic quantum number $m$, are not mixed in the energy overlap integral.

Thus the envelope functions become of the form in equation 3.25; where $a_{n,\ell}$ is simply a weighting coefficient, and depends upon only $n$ and $\ell$ because of the non-mixing of states of different $m$ by the Hamiltonian $H_1$, and the $P_{n,\ell,m}(r)$ are hydrogenic basis states. The envelope function is no longer indexed by the same hydrogenic quantum numbers as the hydrogenic basis states, because of the dependence upon states of multiple quantum numbers, although all of its basis states will have the

same azimuthal angular momentium projection $m$ and thus $m' = m$ for all.

$$F_{n',\ell',m'}(r) = \sum_{n,\ell} a_{n,\ell}^{n',\ell',m'} P_{n,\ell,m}(r)$$

$$P_{n,\ell,m}(r) = \frac{\beta^{\frac{1}{4}}}{\gamma} R_{n,\ell,m}(r) Y_{\ell,m}(\theta, \phi)$$

(3.25)

## 3.4.2. How to Find the Correct Variational Parameters of the Donor Envelope Wavefunctions

To match the correct weighting of each hydrogenic basis state in any representation of the donor envelope function, the variational parameters $\alpha_{\ell,m}$ and $\beta$ must be scaled. There are then several possible procedures that can be followed, depending upon whether the donor envelope function is constructed out of a single or multiple hydrogenic basis states. For both situations the $\beta$ parameter is universal for all the donor envelope functions, $F(r)$, and the $\alpha_{\ell,m}$ parameters are then different for all separate $(\ell, m)$ pairs.

The process for either situation is then, in general, to multiply the Schrödinger equation from the left by the complex conjugate of that state. Evaluating this over all space, and making use of the normalisation and orthogonality of the hydrogenic basis, then yields a function of the variational parameters that described the energy expectation value of the state in question. This is discussed in much more detail in appendix A.2.

As discussed in appendix A.2.2.2, the ground state upper bound can be found by minimising the energy as a function of the variational parameters. For non-ground states this is not true; however a comparison to experimentally measured [100] energies and absorbance spectra in section 5.3, shows that minimisation does yield accurate results. Thus either minimisation, or a minimisation of the difference to a

measured energy for each state, can be used to variationally find the best parameter values.

For this function to be at a minimum, its derivative can be taken and set to zero, because of the nature of the hydrogenic basis states the second order differential will always then be positive; there are no maxima as the energy as the parameters tend to infinity is infinity. This then allows the two parameters to be related to each other, allowing only one to be varied. Then one parameter, with the other calculated from the minima condition, can be varied until the minimum energy or energy difference is found.

Alternatively for higher excited states, because the minimum upper bound condition is not provably true, both parameters can be varied independently. However, this yields results that are almost identical to those obtained by assuming the parameters are connected by the minimisation criterion.

**Note on number of variational parameters**

The requirement of minimisation of the energy expectation value allows the $\alpha$ parameters to be linked to the $\beta$ value. If the minimisation condition is extended to all other states, which appears to be the best fit to experimental data, then the number of variational parameters is greatly reduced. The final number of variational parameters then depends upon the choice of single or multiple basis states for the donor envelope function. For the single hydrogenic states, this means that the $\alpha$ parameters are all directly linked to $\beta$, resulting in $\beta$ being the only variational parameter; there is a one to one, or isomorphic, mapping of each $\alpha_{\ell,m}$ to the $\beta$.

However, if there are multiple hydrogenic states that form the basis, this results in a Hamiltonian matrix (see section 3.4.2.2) that must be diagonalised to obtain the

energy expectation values. In this situation the individual $\alpha$ parameters are not linked to $\beta$ in an isomorphic manner, but where $\beta$ is now equal to a sum of different $\alpha$s including multiple different power terms. Thus the wavefunctions are described by the eigenvectors of the Hamiltonian matrix, where this then implicitly causes a set of new parameters, the eigenvectors themselves. Therefore it is possible that different sets of $\alpha$ values, in combination with different eigenvectors, will yield the same energy expectation values.

### 3.4.2.1. Single Basis State per Donor Envelope

Considering the first situation, where we only have a single basis state, the energy equations are of the form shown in equation 3.26; where the $F_{n,\ell,m}$ states are then the states from equation 3.20.

$$\langle F_{n,l,m}|H_1|F_{n,l,m}\rangle = E_{n,l,m}(\beta, \alpha_{\ell,m}) \tag{3.26}$$

### 3.4.2.2. Multiple Basis State per Donor Envelope

For the second situation, that of multiple hydrogenic basis states, each donor wavefunction is of the form in equation 3.25. To evaluate equation 3.26 it can be written as the matrix equation 3.27; where the set of weighting coefficients, $a_{n,\ell}^{n,\ell,m}$, is then written as a column vector with individual elements now indexed by $j, k$ corresponding to $n, \ell$ of the basis states and $n, \ell, m$ labels of the donor envelope function respectively. This multiple basis state representation of the envelope functions is also sometimes known as the Rayleigh-Ritz method, as it was used to construct the modes of church organs out of a set of trial basis functions.[120][121]

It should be noted that because of the different basis states having only the same $m$, the $n, \ell$ of the donor envelope states are not explicit, they are merely labels; they can

be expected to indicate the hydrogenic basis state with the greatest contribution, or $a_{n,\ell}^{n,\ell,m}$ coefficient.

This is then for a single donor envelope function. For all states involved in the decomposition see appendix A.39 for the form of the equation, in essence $a_{n,\ell}^{n,\ell,m}$ are no longer a column vector but a square matrix with columns indexed by $n, \ell, m$. The Hamiltonian matrix elements are then defined as $h_{j,k} = \langle P_k(r)|H_1|P_j(r)\rangle$, where $P_j(r)$ are hydrogenic basis states which are then indexed as $n, \ell$ pairs with the $m$ dependence dropped because of the lack of mixing between states of different $m$. The $j$ and $k$ indexes refer to the initial and final states, as used else where in this thesis. The number $N$ is then the number of basis states used in any particular calculation, as $N$ tends to $\infty$ the accuracy of the calculated energy and the wavefunctions themselves will tend to 100%, but only for states which satisfy the initial assumptions of the effective mass model.

This Hamiltonian matrix can then be diagonalised with standard linear algebra techniques, producing a diagonal matrix where the diagonal elements are the energy expectation values of the donor envelope wavefunctions. The eigenvectors of this diagonalised Hamiltonian matrix are then the $a_{n,\ell}^{n,\ell,m}$ coefficients written as column vectors.

The $1S$ donor state then has hydrogenic $1S$, $2S$,.., $3P$,... basis states; of course states with even parity are only constructed out of states of even parity and thus it will always be so. The converse is true for states of odd parity. Thus the $S$ states are constructed out of basis states of $\ell = $ even numbers (0, 2, 4, 6, etc.....), because the $1S$ is confined to $m = 0$ they all are. The $P$ donor state is constructed out of basis states of $\ell = $ odd numbers (1, 3, 5, 7, etc.....), with $m$ now allowed to vary, but all different values of $m$ will have entirely separate Hamiltonian matrixes;

although including states of different $m$ will not affect the outcome, because they do not mix, it will increase the size of the matrix and thus the computational effort in diagonalising it, thus wasting time for no gain at all.

$$
\begin{bmatrix}
h_{1,1} & h_{1,2} & ... & h_{1,N} \\
h_{2,1} & h_{2,2} & ... & ... \\
... & ... & h_{3,3} & ... \\
h_{N,1} & ... & ... & h_{N,N}
\end{bmatrix}
\begin{bmatrix}
a_j^1 \\
a_j^2 \\
... \\
a_j^N
\end{bmatrix}
= E_j
\begin{bmatrix}
a_j^1 \\
a_j^2 \\
... \\
a_j^N
\end{bmatrix}
\tag{3.27}
$$

The same minimisation conditions as for single basis states then exist. That is, a link can be made between the $\alpha_{\ell,m}$ and $\beta$ parameters via the first order differential of the energy function. Thus the parameters that minimise the energy, or the energy difference with respect to a measured energy, can be found variationally. This results in both the energy, which can be easily verified via comparison with peaks from optical absorbance measurements, and the estimated donor envelope wavefunction.

## 3.4.3. Ground State Splitting Due to the Symmetry of the Silicon Lattice

The symmetry of the silicon lattice surrounding the donor atom, the tetrahedral group $T_d$, further complicates the effective mass theory. The effect of the symmetry upon the effective mass donor states is commonly called "valley orbit coupling"[95, p161]. This name arises from each individual donor state no longer being comprised of a single Bloch function from a single conduction band minimum, or valley, but rather being a combination of all or some of them; the combination and weighting is then determined by the symmetry of the donor's surroundings.

Due to the effect of the symmetry of the silicon lattice, the effective mass states

have their degeneracy split into smaller groupings or manifolds. These groupings are determined by the symmetry of the silicon lattice, whereby the effective mass states must then be a basis to construct representations of the Silicon lattice symmetry group. Or rather that each effective mass state is then split into components corresponding to the irreducible representations of the silicon symmetry.

The result is a set of donor states that are weighted linear combinations of the prior effective mass states, but now become representations of the symmetry group of the silicon lattice. Thus the states become, in general, of the form shown in equation 3.28; where $\Xi^j(r)$ is then the state that corresponds to an irreducible representation of the symmetry of the silicon lattice, $C_i^j$ is a weighting coefficient for each of the 6 non-degenerate $j$ states, $\Psi_{k^{(i)}}(r)$ are the 6 effective mass basis states indexed by $i$, $F_{k^{(i)}}(r)$ is the donor envelope function, and the $\Phi_{k^{(i)}}(r)$ are the Bloch functions at the conduction band minimum.

$$
\begin{aligned}
\Xi^j(r) &= \sum_{i=1}^{6} C_i^j \Psi_{k^{(i)}}(r) \\
&= \sum_{i=1}^{6} C_i^j F_{k^{(i)}}(r) \Phi_{k^{(i)}}(r)
\end{aligned}
\tag{3.28}
$$

The effective mass states corresponding to the irreducible representations of the $T_d$ tetrahedral symmetry group can then be nondegenerate. The raw silicon lattice has the symmetry of the cubic or octahedral $O_h$ group [122], which by adding a donor atom at the centre of the coordinate system breaks any translational symmetry. The silicon lattice around the donor then has the symmetry of the tetragonal $T_d$ group[8]. The point here being that the presence of the donor itself removes the translational symmetry.

*3. Introduction to Effective Mass Theory in Silicon*

There are then two singlet ($A_1$, $A_2$), one doublet ($E$) and two triplet ($T_1$,$T_2$) representations[122], so that any state will be comprised out of a combination of these; not all states will include all the representations. Each representation of each state will then be a separate manifold of states, with one, two or three degenerate states for singlet, doublet and triplet representations respectively; these will then will be further split by any hyperfine interaction with atomic nuclei.

However, in a most convenient manner, the symmetry caused splitting of effective mass states is largely inconsequential. The measured energies of excited donor states in silicon are largely degenerate, and they will have similar wavefunctions but with the coordinates exchanged in the respective parts of the linear combination of effective mass basis states, equation 3.10. Only the $1S$ like effective mass state appears to be significantly split by symmetry, becoming the $1S(A_1)$, $1S(E)$, and $1S(T_1)$ states.

The higher excited states in general, according to Kohn[8], all have a large spatial extent and thus the effective mass potential of equation 3.3, and the other assumptions, hold true. This then gives all the symmetry split states the same calculated energy. The $1S$ states are different due to the lowest lying symmetry spit state being very close to the donor atom, and as a result, the assumptions of the effective mass model no longer hold true.

The $1S$ wavefunctions can then be symmetrised, or made to obey the required symmetry conditions, by following [8, eq 4.30]. Thus the 6 degenerate effective mass $1S$ states become as in equation 3.28, with the $C_i^j$ coefficients for the $1S$ state given by equation 3.29; where the $1S(A_1)$, $E$, and $T_1$, then correspond to the $C^1$, $C^{2,3}$, and $C^{4,5,6}$ coefficients. It must be noted that equation 3.29 only gives the coefficients for the $1S$ state, although all other possible states will have a set of 6 weighting

vectors. There is a direct link to the vectors being in a 6 dimensional space and the 6 conduction band minima, or valleys; a semiconductor with $N$ valleys can have donor state wavefunctions expanded in a set of $N$, with symmetry then dictating a set of $N$ weighting vectors with $N$ elements.

$$
\begin{aligned}
A_1 &= \left\{ C^1 \quad = \tfrac{1}{\sqrt{6}}(1,1,1,1,1,1) \right. \\[1em]
E &= \left\{ \begin{aligned} C^2 \quad &= \tfrac{1}{2}(1,1,-1,-1,0,0) \\[0.5em] C^3 \quad &= \tfrac{1}{2}(1,1,0,0,-1,-1) \end{aligned} \right. \\[1em]
T_1 &= \left\{ \begin{aligned} C^4 \quad &= \tfrac{1}{\sqrt{2}}(1,-1,0,0,0,0) \\[0.5em] C^5 \quad &= \tfrac{1}{\sqrt{2}}(0,0,1,-1,0,0) \\[0.5em] C^6 \quad &= \tfrac{1}{\sqrt{2}}(0,0,0,0,1,-1) \end{aligned} \right.
\end{aligned}
\tag{3.29}
$$

To further explain why the $1S(A_1)$ state is the ground state, again paraphrasing Kohn[8], the $\Psi_{k^{(i)}}(r)$ basis states are all equal at the $r = 0$ point; this is due to periodicity, i.e. the donor atom is assumed to be equidistant from the conduction band minima. Thus it can be seen, from equation 3.29, that the $A_1$ representation will have a much greater wavefunction amplitude at the donor atom site $(r = 0)$. A direct consequence of this is that the assumed donor potential, equation 3.3, is no longer accurate, as the wavefunction is of large magnitude exactly upon the donor. Not only does this render the assumptions of the effective mass formalism not applicable, but it can easily be seen that due to coulombic interactions, such states must have a high binding energy to be so densely located. Thus to be correctly identified, the $1S$ state must always be referred to with an additional symmetry label.

The other two $1S$ states, $E$ and $T_1$, are described relatively well by the effective mass

formalism in the same way that higher excited states are. As a result of fulfilling the effective mass assumptions, the $1S(E)$ and $1S(T_1)$ are degenerate, giving an effective $1S(\text{not} A_1)$ state with a degeneracy of 5.

### 3.4.3.1. Higher Excited States

Kohn[106] is able to show that the higher excited states can be made to obey the symmetry of the surrounding silicon lattice. The result of this is that the states will split into the decomposition shown below, taken from [106, eq 5.11].

$$|m| = 0 : A_1 + E + T_1$$
$$|m|even(\neq 0) : A_1 + A_2 + 2E + T_1 + T_2 \tag{3.30}$$
$$|m|odd : 2T_1 + 2T_2$$

As will be seen later, the two excited states of principle interest are $2P_0$ and $2P_{\pm 1}$. Thus Kohn has given the decompositions necessary to construct the $2P_0$ state, as it has $|m| = 0$ and thus only has the $A_1 + E + T_1$ representations which are given by the coefficients in equation 3.29.

**Symmetry weighting vectors**

The symmetry weighting coefficients of equation 3.29 can be formed into vectors. These then describe the symmetrised effective mass states. Using the combinations of irreducible representations from equation 3.30, and with the ultimate intention of using them for calculating transition rates, the total symmetry weighting vectors for the $2P_0$ and $1S(A_1)$ states are given below:

$$C^{1\vec{S}(A_1)} = \frac{1}{\sqrt{6}}\big(1,1,1,1,1,1\big)$$

$$C^{\vec{2P_0}} = \frac{1}{\sqrt{6}}\big(1,1,1,1,1,1\big) + \frac{1}{2}\big(2,2,-1,-1,-1,-1\big) + \frac{1}{\sqrt{2}}\big(1,-1,1,-1,1,-1\big)$$

$$(3.31)$$

The $T_2$ irreducible representation of the $T_d$ symmetry group is not given by Kohn, and so far it has not been possible to calculate it. Because of this the weighting coefficients for the $2P_{\pm 1}$ state cannot be determined. However, as is outlined in detail at the end of section 3.6.1, it is possible to show that the dot product of the weighting coefficients of the $2P_{\pm 1}$ state with those of the $1S(A_1)$ are 1, as for the known $2P_0$ to $1S(A_1)$ product.

## 3.5. Applying the Effective Mass Hamiltonian to Single Hydrogenic Basis States

Evaluating the unitless effective mass Hamiltonian, equation 3.19, for single hydrogenic basis states gives energy functions with the $\beta$ and $\alpha_{\ell,m}$ as the functional parameters. The parameters can then be iteratively varied until the minimum, or minimum difference with respect to measured energy, can be found.

### 3.5.1. Simple Scaled Hydrogen Model

For comparison to the EMT states a far simpler model of the donor wavefunctions can be constructed by using a spherically symmetric scaled hydrogen model. The key difference is then between the ellipsoid EMT model and that of simply scaling a hydrogen wavefunction to the energy, i.e. the scaling is uniform not axially dependent. This is shown in detail in appendix B.4, and consists of adding in the effective

mass, relative dielectric permittivity, and a scaling factor to the well known energy and Bohr radius expressions for hydrogen.

Because this completely ignores the lack of full spherical symmetry in silicon, there is no variational routine to use; a direct solution for the scaling parameter is found from inputting the relevant energy, electron mass etc. It is obtained by rearranging equation B.128 to find $\alpha_{0,0}$, given in equation 3.32; where $E$ is the state energy. This uses the vector average value of the effective masses in silicon, $0.453m_e = m^*$, and the relative dielectric permittivity of 11.7.

It must then be noted that this simple hydrogenic model is the same as the EMT model with $\beta$ and $\gamma$ set to 1, while the effective masses are replaced with the vector average of the effective masses, $m^* = 0.453m_0$.

$$\alpha_{\ell,m} = \frac{4\pi\hbar\epsilon_0\epsilon_r n}{e^2}\sqrt{\frac{2E}{m^*}} \tag{3.32}$$

## 3.5.2. Donor Envelope Wavefunctions and Energy

The donor envelope wavefunctions for the $1S$, $2p_0$ and $2p_{\pm 1}$ states and their energy functions are listed here. All wavefunctions and energies are for the $i$th conduction band minimum and are in the $g_i$ spherical coordinate system; this is equivalent to the top left, or first, Hamiltonian matrix element for the multiple hydrogenic basis state expansion approach.

Application of the unitless Hamiltonian operator, multiplication from the left by the complex conjugate of the wavefunction, and integration over all space, yields the energy functions for the respective donor envelope wavefunctions. This is shown in equation 3.33; in appendix B.3 is shown the derivations of the individual energy

functions and the energy minimisation relationship between the $\alpha$ and $\beta$ parameters for each state.

$$
\begin{aligned}
E_j &= \langle F_j^i(r_{gi}, \theta_{gi}, \phi_{gi}) | H_1 | F_j^i(r_{gi}) \rangle \\
&= \left(\frac{\gamma}{\beta}\right)^{\frac{1}{2}} \int_0^\infty \int_0^\pi \int_0^{2\pi} r_g^2 \sin(\theta_g) F_j^*(r_g, \theta_g, \phi_g) H_1 F_j(r_g, \theta_g, \phi_g) dr_g d\theta_g d\phi_g
\end{aligned}
\tag{3.33}
$$

**3.5.2.1.** $1S$

The unitless $1S$ donor envelope basis function is:

$$
F_{1s(A_1)}^i(r_{gi}) = \left(\frac{\beta}{\gamma}\right)^{\frac{1}{4}} \frac{\alpha^{\frac{3}{2}}(0,0)}{\sqrt{\pi}} e^{-\alpha_{0,0} r_{gi}}
\tag{3.34}
$$

The energy function is:

$$
E_{1S}(\alpha_{0,0}, \beta, \gamma) = \frac{1}{3}\alpha_{0,0}^2 \left(\beta + 2\right) - \frac{2\alpha_{0,0}}{\left(1 - \frac{\gamma}{\beta}\right)^{\frac{1}{2}}} \arcsin\left(\left(1 - \frac{\gamma}{\beta}\right)^{\frac{1}{2}}\right)
\tag{3.35}
$$

For the derivation of the energy function see B.3.1.

For the reasons discussed previously, the calculated energy is only applicable for the $1S(E)$ and $1S(T_1)$ states due to the breakdown of the effective mass assumptions.

**Verifying the $1S$ Energy in the Free Space Hydrogen Limit**

When the $\gamma$, $\beta$, and $\alpha_{0,0}$ of equation 3.35 are all equal to, or tending towards, 1 the state becomes that of a hydrogen atom in free space. This can be easily checked by taking the limit of the $E_{1S}(\alpha_{0,0}, \beta, \gamma)$ as all of the parameters tend towards 1, shown in appendix B.3.5.1.

The final result for the $\alpha_{0,0}, \beta, \gamma \to 1$ case gives an energy of $-1$. As this is the unitless expression it can then be multiplied by $a_B$, equation 3.13 where $m_\perp$ is now the free space mass of an electron, which indeed gives the $1S$ state energy of a hydrogen atom in free space ($\approx$13.6eV).

**Relating $\alpha_{0,0}$ and $\beta$ at the Energy Minima**

For variational minimisation purposes the $\alpha_{0,0}$ and $\beta$ parameters can be related by taking the first order differential of the $1S$ energy function with respect to $\alpha_{0,0}$ and rearranging. This can then be written as:

$$\alpha_{0,0} = \frac{3\arcsin([1-\frac{\gamma}{\beta}]^{\frac{1}{2}})}{[1-\frac{\gamma}{\beta}]^{\frac{1}{2}}(2+\beta)} \tag{3.36}$$

### 3.5.2.2. $2p_0$

The unitless $2p_0$ donor envelope basis function is:

$$F_{2p_0}^i(r_{gi}) = \left(\frac{\beta}{\gamma}\right)^{\frac{1}{4}} \frac{\alpha^{\frac{5}{2}}(1,0)}{4\sqrt{2\pi}} r_{gi}\cos(\theta_{gi})e^{-\frac{\alpha_{1,0}r_{gi}}{2}} \tag{3.37}$$

The energy function is:

$$E_{2p_0} = \frac{1}{20}(2+3\beta)\alpha_{1,0}^2 - \frac{3}{8[1-\frac{\gamma}{\beta}]^{\frac{3}{2}}}\alpha_{1,0}\left(2\arcsin([1-\frac{\gamma}{\beta}]^{\frac{1}{2}}) - \sin(2\arcsin([1-\frac{\gamma}{\beta}]^{\frac{1}{2}}))\right)$$

$$= \frac{1}{20}(2+3\beta)\alpha_{1,0}^2 - \frac{3}{4[1-\frac{\gamma}{\beta}]^{\frac{3}{2}}}\alpha_{1,0}\left(\arcsin([1-\frac{\gamma}{\beta}]^{\frac{1}{2}}) - [1-\frac{\gamma}{\beta}]^{\frac{1}{2}}(\frac{\gamma}{\beta})^{\frac{1}{2}}\right)$$

$$\tag{3.38}$$

Equation 3.38 is derived in equation B.3.2.

**Verifying the $2P_0$ Energy in the Free Space Hydrogen Limit**

When the $\gamma$, $\beta$, and $\alpha_{1,0}$ of equation 3.38 are all equal to, or tending towards, 1, the state becomes that of a hydrogen atom in free space. Thus equation 3.38 can easily be checked by taking the limit as all of the parameters tend towards 1. This is shown in detail in appendix B.3.5.2.

The final result of this is that in the limit that the $\alpha_{1,0}, \beta, \gamma$ parameters all tend towards 1, the energy tends towards the unitless value of $\frac{-1}{4}$. As the energy of hydrogen states follows a $\frac{E_{1S}}{n^2}$ pattern, to obtain the energy requires multiplication by that of the ground state $E_{1S}$, and for the $2P_0$ state $n = 2$, the limiting energy value is correct ($\approx 3.4$eV ).

**Relating $\alpha_{1,0}$ and $\beta$ at the Energy Minima**

As for the $1S$ state, $\alpha_{1,0}$, corresponding to the $2p_0$ state, can be related to $\beta$, this is then written as:

$$\alpha_{1,0} = \frac{15}{2} \left( \frac{\arcsin([1 - \frac{\gamma}{\beta}]^{\frac{1}{2}}) - [1 - \frac{\gamma}{\beta}]^{\frac{1}{2}} (\frac{\gamma}{\beta})^{\frac{1}{2}}}{[1 - \frac{\gamma}{\beta}]^{\frac{1}{2}} (2 + 3\beta)} \right) \tag{3.39}$$

**3.5.2.3. $2p_{\pm 1}$**

The unitless $2p_{\pm 1}$ donor envelope basis function is:

$$F^i_{2p_{\pm 1}}(r_{gi}) = \mp (\frac{\beta}{\gamma})^{\frac{1}{4}} \frac{\alpha^{\frac{5}{2}}(1,1)}{8\sqrt{\pi}} r_{gi} \sin(\theta_{gi}) e^{\pm i\phi_{gi}} e^{-\frac{\alpha_{1,1} r_{gi}}{2}} \tag{3.40}$$

The energy function, derived in equation 3.41, is:

$$E_{2p_{\pm 1}} = \frac{1}{20}(4+\beta)\alpha_{1,1}^2 - \frac{3\alpha_{1,1}}{8[1-\frac{\gamma}{\beta}]^{\frac{1}{2}}} \left( 2\arcsin([1-\frac{\gamma}{\beta}]^{\frac{1}{2}})(1 - \frac{1}{2(1-\frac{\gamma}{\beta})}) + \frac{(\frac{\gamma}{\beta})^{\frac{1}{2}}}{[1-\frac{\gamma}{\beta}]^{\frac{1}{2}}} \right)$$

$$(3.41)$$

**Verifying the $2P_{\pm 1}$ Energy in the Free Space Hydrogen Limit**

When the $\gamma$, $\beta$, and $\alpha_{1,1}$ of equation 3.41 are all equal to, or tending towards, 1, the state becomes that of a hydrogen atom in free space. Thus equation 3.41 can easily be checked by taking the limit as all of the parameters tend towards 1. This is shown in detail in appendix B.3.5.3.

As for the $2P_0$ state, the final result of this is that in the limit that the $\alpha_{1,1}, \beta, \gamma$ parameters all tend towards 1, the energy tends towards the correct unitless value of $\frac{-1}{4}$ ($\approx 3.4$eV ); the energy of hydrogen states follows a $\frac{E_{1S}}{n^2}$ pattern and for the $2P_{\pm 1}$ state $n = 2$.

**Relating $\alpha_{1,1}$ and $\beta$ at the Energy Minima**

As for the other states, $\alpha_{1,1}$, corresponding to the $2p_{\pm 1}$ state, can be related to $\beta$.

$$\alpha_{1,1} = \frac{5\left( \frac{3}{4[1-\frac{\gamma}{\beta}]^{\frac{1}{2}}} \left( 2\arcsin([1-\frac{\gamma}{\beta}]^{\frac{1}{2}})(1 - \frac{1}{2(1-\frac{\gamma}{\beta})}) + \frac{(\frac{\gamma}{\beta})^{\frac{1}{2}}}{[1-\frac{\gamma}{\beta}]^{\frac{1}{2}}} \right) \right)}{4+\beta} \qquad (3.42)$$

# 3.6. Fermi's Golden Rule Transition Rates

It has been established that scaled hydrogenic functions are an approximate description of donor envelope wavefunctions in silicon. The likely transition rate between two of the effective mass donor states can be estimated by using Fermi's golden rule. Equation 3.43 shows this, and is of the form where the interaction of atomic states

with the electromagnetic field is assumed to be that of a dipole interacting with atomic state wavefunctions, and the density of states of the transition is that of the vacuum electromagnetic field. This is shown to be the case in appendix A.3; in this, $j$ and $k$ indexed the initial and final atomic states, $\omega_{j,k}$ is the angular frequency of the transition, $c$ the speed of light in a vacuum, $g_{j,k}$ the respective degeneracies of the atomic states, $\epsilon_0$ the permittivity of free space, and $e$ the charge of an electron.

$$\Gamma_{j,k} = \left( |\langle \phi_k^0| \, x \, |\phi_j^0 \rangle|^2 + |\langle \phi_k^0| \, y \, |\phi_j^0 \rangle|^2 + |\langle \phi_k^0| \, z \, |\phi_j^0 \rangle|^2 \right) \frac{e^2 \omega_{j,k}^3 g_k}{3\epsilon_0 \hbar c^3 \pi g_j} \qquad (3.43)$$

The donor medium, silicon, has a cubic structure, with six degenerate conduction band minima. There are identical odd-parity excited states in each of the $\pm$ x, y, z conduction band valleys, out of which the overall donor state is assembled. For an arbitrary perturbation it can be shown that the total transition rate, summed over all valleys, is equal to the maximum transition rate for a single valley (see section 5.4 for a related discussion). For example, the $2P_0$ state in the z valley has a maximum transition rate for z polarized light, and this single valley z polarized rate is the same as the total multi-valley rate for an arbitrary polarization. In this work the transition rate has been calculated for a fixed electric field amplitude and polarization of $E_0(1, 1, 1)$ (equations 3.50 and A.114), and in future work the calculations should be generalised to be applicable to an arbitrary polarisation.

### 3.6.1. Transitions with Effective Mass States

In the EMT framework outlined above, the total donor electron wavefunction $\Xi^j$ can be approximated as a linear combination of the 6 conduction band minima states $\Psi_{k(i)}$, with appropriate symmetry determined weighting factors $C_i^j$, as in equation 3.28; $j$ indexes the donor state, $i$ the conduction band minima (valley) in

the $+k_x, -k_x, +k_y, -k_y, +k_z, -k_z$ order, and $\Psi_{k^{(i)}}$ is the total wavefunction where $F_{k^{(i)}}$ is the EMT slowly varying envelope, and $\Phi_{k^{(i)}}$ the Bloch function at the $i$th valley.

With the wavefunction now known the dipole matrix element can be found If $\vec{E} = (a, b, c)$ is the perturbing electric field vector, $\vec{r} = (x, y, z)$ is the radial coordinate vector, $e$ the unit of electric charge, and $ex$ and $fi$ index the initial excited and final ground state respectively, the matrix element is:

$$
\begin{aligned}
\langle \Xi^{fi}| \, e\vec{r}.\vec{E} \, |\Xi^{ex}\rangle &= \langle \sum_{i=1}^{6} C_i^{fi} F_i^{fi} \Phi_i | e\vec{r}.\vec{E}| \sum_{j=1}^{6} C_j^{ex} F_j^{ex} \Phi_j \rangle \\
&= \sum_{i=1}^{6} C_i^{fi*} \sum_{j=1}^{6} C_j^{ex} \langle F_i^{fi} \Phi_i | e\vec{r}.\vec{E}| F_j^{ex} \Phi_j \rangle
\end{aligned}
\tag{3.44}
$$

Equation 3.44 can be significantly simplified by considering the orthogonality of the Bloch states $\Phi$.

$$
\langle \Phi_i | \Phi_j \rangle = \delta_{i,j}
\tag{3.45}
$$

It can be assumed that because the Bloch states are orthogonal, equation 3.45, the dipole matrix elements of two functions containing different Bloch states (at different conduction band minima) is zero. This is equivalent to saying that it can be assumed that there are no dipole transitions between different Bloch states.

It must be noted that, in general, the integral over all space of two orthogonal functions multiplied by two other arbitrary functions (in this case the EMTenvelope

functions) is not zero. The arbitrary functions change the weighting of the integral, for example, sin and cos are orthogonal but if the integral from 0 to $\frac{\pi}{2}$ is weighted as 1 and the rest of the integral to $2\pi$ at 0.1 then the result is not zero.

However, this assumption of wider orthogonality can be justified for the effective mass theory. The donor states are explicitly assumed to extend over a large area, many thousands of silicon unit cells, and the Bloch functions are periodic every unit cell. Thus the change in the weighting envelope function, over those many thousands of unit cells, may be assumed to be slow and consequentially relatively constant, at least compared to the Bloch functions, allowing the approximation that the donor envelopes are constant. This can be extended to apply to the dipole matrix element. If $i$ and $j$ index conduction band minima (valleys), while $ex$ and $fi$ label donor envelope wavefunctions, this can be shown as:

$$\langle F_i^{fi}\Phi_i|F_j^{ex}\Phi_j\rangle \approx \langle F_i^{fi}|F_j^{ex}\rangle \langle\Phi_i|\Phi_j\rangle$$

$$\approx \langle F_i^{fi}|F_j^{ex}\rangle \delta_{i,j}$$

$$(3.46)$$

$$\langle F_i^{fi}\Phi_i|e\vec{r}.\vec{E}|F_j^{ex}\Phi_j\rangle \approx \langle F_i^{fi}|e\vec{r}.\vec{E}|F_j^{ex}\rangle \delta_{i,j}$$

Additionally, the Bloch function states are, by definition, at different momentium positions. Because of this, a transition is only likely to occur if phonon emission (or absorption) occurs simultaneously, which is highly unlikely. Thus, even if the Bloch functions were not orthogonal, transitions that do not also involve extremely unlikely coincidental phonons can be considered to be unlikely.

By applying the conditions of equations 3.45 and 3.46, the dipole matrix element from equation 3.44 can be simplified. The form of this matrix element is then the

same as that obtained by Kohn [115, equation 5.56].

$$\sum_{i=1}^{6} C_i^{fi*} \sum_{j=1}^{6} C_j^{ex} \langle F_i^{fi} \Phi_i | e\vec{r}.\vec{E} | F_j^{ex} \Phi_j \rangle \approx \sum_{i=1}^{6} C_i^{fi*} \sum_{j=1}^{6} C_j^{ex} \langle F_i^{fi} | e\vec{r}.\vec{E} | F_j^{ex} \rangle \delta_{i,j}$$
$$\approx \sum_{i=1}^{6} C_i^{fi*} C_i^{ex} \langle F_i^{fi} | e\vec{r}.\vec{E} | F_i^{ex} \rangle$$

(3.47)

The effect of the different wavefunctions for the 6 different EMT states and the electric field polarisation within the dipole interaction term must then be considered; the final result is that, *in the case of spontaneous emission* where the perturbing electric field vector is (1,1,1), the net effect is as the total states were single basis states in free space. Recall that the upper and lower donor state wavefunctions are comprised out of a linear combination of the 6 effective mass basis states arising from the 6 conduction band minima in silicon. Each of the 6 effective mass valley states corresponds to one of the conduction band minima, with labels $\pm k_x$, $\pm k_y$, $\pm k_z$ corresponding to the energy degenerate minimum energy positions in momentium space.

To explain this, as discussed above in sections 3.4.3 and 3.3.2.2, in the EMT framework each of the 6 valley basis states has the same wavefunction as the others, but, and this is the key point, with x, y, z coordinates changed (where x,y,z refers to a fixed, laboratory, set of coordinates). The laboratory coordinates are taken to coincide with those of the conduction band minima at $+k_x$, with differences in coordinates between states given by table 3.1.

Hydrogenic wavefunctions cause a negligible, or entirely absent, effect upon the dipole matrix element squared for this coordinate change. For example, for the $1S$ state the coordinate terms all appear squared and added together in the radial

exponent and therefore a change results in an identical function. For each of the $2P_0$ or $2P_{\pm 1}$ wavefunctions, the coordinate change is an effective rotation, along with a change in the overall sign which when squared has no effect.

The dipole interaction must then be taken into account. To do this the electric field is taken to be of amplitude a,b,c in the x, y, z directions and to have a randomly varying due to being the vacuum field for spontaneous emission, appendix A.3.1.1 ) phase factor $e^{i\phi_{x,y,z}(t)}$.

$$\vec{E} = (ae^{i\phi_x(t)}, be^{i\phi_y(t)}, ce^{i\phi_z(t)}) \tag{3.48}$$

Therefore the dipole matrix element, taking into account the 6 conduction band valleys, from equation 3.47 , and taking the radial coordinate vector to be $r = (x, y, z)$, becomes:

$$\sum_{i=1}^{6} C_i^{fi*} C_i^{ex} \langle F_i^{fi}|e\vec{r}.\vec{E}|F_i^{ex}\rangle = \sum_{i=1}^{6} C_i^{fi*} C_i^{ex} \langle F_i^{fi}|e(xae^{i\phi_x(t)} + ybe^{i\phi_y(t)} + zce^{i\phi_z(t)})|F_i^{ex}\rangle$$

$$\tag{3.49}$$

Therefore the specific dipole matrix element for each polarisation must be considered. However, in the spontaneous emission case the electric field vector from equation 3.48 is equal in each direction, therefore the polarisation is:

$$\begin{aligned} \vec{E} &= (E_0 e^{i\phi_x(t)}, E_0 e^{i\phi_y(t)}, E_0 e^{i\phi_z(t)}) e^{i\omega_{j,k}t} \\ &= E_0 (e^{i\phi_x(t)}, e^{i\phi_y(t)}, e^{i\phi_z(t)}) e^{i\omega_{j,k}t} \end{aligned} \tag{3.50}$$

Therefore the dipole matrix element becomes:

$$E_0 \sum_{i=1}^{6} C_i^{fi*} C_i^{ex} \langle F_i^{fi}|e(xe^{i\phi_x(t)} + ye^{i\phi_y(t)} + ze^{i\phi_z(t)})e^{i\omega_{j,k}t}|F_i^{ex}\rangle \qquad (3.51)$$

This is the same result, albeit with the electric field vector chosen, as is shown in [115, p282, eq 5.56]

For the $2P_0$ to $1S$ transition it is well known that the dipole matrix element is only non zero for the z axis polarisation (see appendix B.5.0.1). Therefore, due to the coordinate changes between the 6 difference effective mass valley states, the $\pm k_x$ states will have non zero matrix elements for the z polarisation of the electric field, the $\pm k_y$ for x polarised, and $\pm k_z$ for y polarised. A similar point is true for the $2P_{\pm 1}$ to $1S$ transition, however, now it is the x and y polarisations that are non zero for the $\pm k_x$, y and z for $\pm k_y$, and z and x for $\pm k_z$.

Therefore, for the spontaneous emission case where the polarisation strength is isotropic, the total contribution to the dipole element of each conduction band valley state is the same. Each contributes the same transition amplitude for what is, from the perspective of each valley state, the polarisations that are non-zero. The dipole matrix element is then given by its symmetry determined weighting factor $C_i$ and the dipole matrix element of the non EMT state (as if the donor were in free space and not in silicon with its 6 conduction band minima). These are then summed in amplitude, as they are part of the same state linear superposition and cannot be incoherent relative to each other (otherwise they could not be parts of the same state as a linear combination to begin with). The envelope functions are now taken

to be the same as in free space which is the same as the laboratory coordinates and the $+k_x$ valley, the total matrix element squared is given by:

$$|E_0|^2 e^2 \left( |\sum_{i=1}^{6} C_i^{fi*} C_i^{ex} \langle F_i^{fi}|x|F_i^{ex}\rangle |^2 + |\sum_{i=1}^{6} C_i^{fi*} C_i^{ex} \langle F_i^{fi}|y|F_i^{ex}\rangle |^2 \right.$$
$$\left. + |\sum_{i=1}^{6} C_i^{fi*} C_i^{ex} \langle F_i^{fi}|z|F_i^{ex}\rangle |^2 \right) \tag{3.52}$$

The penultimate form of Fermi's golden rule for effective mass transitions, where $fi$ is the final and $ex$ the excited state, is then:

$$\Gamma_{fi,ex} = \frac{e^2 \omega_{fi,ex}^3 g_{fi}}{3\epsilon_0 \hbar c^3 \pi g_{ex}} \left( |\sum_{i=1}^{6} C_i^{fi*} C_i^{ex} \langle F_i^{fi}|x|F_i^{ex}\rangle |^2 + |\sum_{i=1}^{6} C_i^{fi*} C_i^{ex} \langle F_i^{fi}|y|F_i^{ex}\rangle |^2 \right.$$
$$\left. + |\sum_{i=1}^{6} C_i^{fi*} C_i^{ex} \langle F_i^{fi}|z|F_i^{ex}\rangle |^2 \right) \tag{3.53}$$

**3.6.1.1. Effect of Multiple Valleys on the $2P_0$ to $1S(A_1)$ transition**

The effect that the multiple conduction band valleys, and the symmetry of the silicon crystal, has upon the $2P_0$ to $1S(A_1)$ transition can be found by considering the dipole matrix element, from equation 3.52 , for each of the symmetry determined $2P_0$ states.

The $1S(A_1)$ state is a linear combination of all 6 valley states weighted equally, while the $2P_0$ state is a more complex combination of the 6 states; the combinations of the valley states are determined by the symmetry of the surrounding silicon crystal, however, the $2P_0$ weightings cannot be taken directly from equation 3.31. The $2P_0$ state is comprised of one $A_1$, two $E$, and three $T_1$ components. Of these, the $1S(A_1)$

to $2P0(A_1)$ is forbidden by parity, as is the $1S(E)$ to $2P0(A_1)$, i.e. the matrix element is zero due to valley orbit interference. As a proxy for the sum of the allowed transitions to the triply degenerate set of $2P_0(T_1)$ excited states, the rate for $1S(A_1)$ to the $2P0(A_1)$ shall be used and valley interference will be ignored. In future work the rate calculation should be made to include a general polarization, the valley orbit interference, and the degeneracy.

Only the z polarisation has a non zero matrix element for a $2P_0$ to $1S$ transition. Therefore the $\pm k_x$ components have a non zero matrix element for the z polarisation, and then because of the coordinate change in the different conduction band valley states the $\pm k_y$ and $\pm k_z$ components have non zero matrix elements for x and y polarised light respectively. As the electric field is assumed to be equal in all directions this has no overall effect.

The $2P_0(A_1)$ to $1S(A_1)$ transition, where the $C$ coefficients are all $\frac{1}{\sqrt{6}}$ for both states. The matrix elements are then:

$$|(\frac{1}{\sqrt{6}}\frac{1}{\sqrt{6}} + \frac{1}{\sqrt{6}}\frac{1}{\sqrt{6}}) \langle F^{fi}_{\pm kx}|z|F^{ex}_{\pm kx} \rangle|^2$$

$$+ |(\frac{1}{\sqrt{6}}\frac{1}{\sqrt{6}} + \frac{1}{\sqrt{6}}\frac{1}{\sqrt{6}}) \langle F^{fi}_{\pm ky}|x|F^{ex}_{\pm ky} \rangle|^2$$

$$+ |(\frac{1}{\sqrt{6}}\frac{1}{\sqrt{6}} + \frac{1}{\sqrt{6}}\frac{1}{\sqrt{6}}) \langle F^{fi}_{\pm kz}|y|F^{ex}_{\pm kz} \rangle|^2$$

$$= |\frac{2}{6} \langle F^{fi}_{\pm kx}|z|F^{ex}_{\pm kx} \rangle|^2 + |\frac{2}{6} \langle F^{fi}_{\pm ky}|x|F^{ex}_{\pm ky} \rangle|^2 + |\frac{2}{6} \langle F^{fi}_{\pm kz}|y|F^{ex}_{\pm kz} \rangle|^2 \tag{3.54}$$

$$= \frac{4}{36} \left( |\langle F^{fi}_{\pm kx}|z|F^{ex}_{\pm kx} \rangle|^2 + |\langle F^{fi}_{\pm ky}|x|F^{ex}_{\pm ky} \rangle|^2 + |\langle F^{fi}_{\pm kz}|y|F^{ex}_{\pm kz} \rangle|^2 \right)$$

$$= \frac{12}{36}|\langle F^{fi}_{\pm kx}|z|F^{ex}_{\pm kx} \rangle|^2$$
$$= \frac{1}{3}|\langle F^{fi}_{\pm kx}|z|F^{ex}_{\pm kx} \rangle|^2$$

As there are three total degenerate $2P_0(T_1)$ the total transition rate of equation 3.54 is multiplied by three. Therefore, the total transition rate is multiplied by a factor of 1 relative to that of a single valley transition rate without any consideration of the symmetry.

### 3.6.1.2. Effect of Multiple Valleys on the $2P_{\pm1}$ to $1S(A_1)$ transition

The $2P_{\pm1}$ state is comprised of $2T_1$ and $2T_2$ components. The present author has been unable to determine the $T_2$ coefficients. However, because only the perpendicular components of the matrix element are non zero for $2P_{\pm1}$ to $1S$, i.e x and y for $\pm k_x$, y and z for $\pm k_z$, and x and y for $\pm k_y$, which can be seen from inspection of equation 3.29 to only have $C$ coefficients of 0. Despite this, it is assumed that the net effect of the $T_2$ coefficients is to give an overall multiplication of 1 as for the $2P_0$ case; as absorption spectra show that $2P_{\pm1}$ transitions do occur, it can be inferred

that the $T_2$ group does have a non zero matrix element.

### 3.6.1.3. Accounting for Not Being in Free Space

There is then one final factor to be included in the form of Fermi's golden rule. The effective mass states are by definition not in a vacuum, thus the speed of light and dielectric permittivity must be altered. These factors, where $n$ is now the refractive index of the surrounding silicon, and $\mu_r$ is the relative magnetic susceptibility, assumed to be $\approx 1$ for silicon, are shown below:

$$c \to \frac{c}{n}$$

$$n = \sqrt{\epsilon_r \mu_r} \approx \sqrt{\epsilon_r}$$

$$\epsilon_0 \to \epsilon_0 \epsilon_r \tag{3.55}$$

$$\frac{1}{\epsilon_0 c^3} \to \frac{\epsilon_r^{\frac{3}{2}}}{\epsilon_0 \epsilon_r c^3}$$

$$= \frac{\epsilon_r^{\frac{1}{2}}}{\epsilon_0 c^3}$$

The final form of Fermi's golden rule for effective mass states is then:

$$\Gamma_{i,j} = \frac{e^2 \epsilon_r^{\frac{1}{2}}}{3\epsilon_0 \hbar c^3 \pi} \omega_{i,j}^3 \frac{g_j}{g_i} \left( \vec{C^{j*}} \cdot \vec{C^i} \right)^2 \left( |\langle F_0^j | x | F_0^i \rangle|^2 + |\langle F_0^j | y | F_0^i \rangle|^2 + |\langle F_0^j | z | F_0^i \rangle|^2 \right) \tag{3.56}$$

## 3.6.2. Dipole Elements for Specific Transitions

In order to estimate the transition rate for different donor envelope states, their dipole matrix elements are written here. This is done in terms of the effective mass variational parameters, $\alpha_{\ell,m}$ and $\beta$, so that the transition rate for differently scaled states can easily be obtained. This is done using scaled hydrogenic wavefunctions

of the form from equation 3.20.

There is one point that must be considered when estimating the transition rates using wavefunctions scaled with these variational parameters, the link between the $\beta$ and the $\alpha_{\ell,m}$. To be explicit, the $\alpha_{\ell,m}$ are different for each $(\ell, m)$, while the $\beta$ are not. For single basis states this partly subverts the need to minimise each state, as minimising merely the ground state then gives all the parameter information. For multiple basis states, the Hamiltonian matrix of even party states including the ground state must be minimised; the other parameters can then be input in the Hamiltonian matrixes that describe them, and then be diagonalised to find the final states.

### 3.6.2.1. $2p_0$ to $1S(A_1)$ **Dipole Element**

The $2p_0$ to $1S$ dipole matrix element squared, derived in appendix B.5.0.1, can be written as:

$$| \langle F_0^{1S}|x|F_0^{2P_0} \rangle |^2 + | \langle F_0^{1S}|y|F_0^{2P_0} \rangle |^2 + | \langle F_0^{1S}|y|F_0^{2P_0} \rangle |^2 = 2^{15} a_B^2 \left( \frac{\beta}{\gamma} \right) \frac{\alpha_{0,0}^3 \alpha_{1,0}^5}{\left[ 2\alpha_{0,0} + \alpha_{1,0} \right]^{10}}$$

$$(3.57)$$

### 3.6.2.2. $2p_{\pm 1}$ to $1S(A_1)$ **Dipole Element**

The $2p_{\pm 1}$ to $1S$ dipole matrix element, derived in appendix B.5.1, can be written as:

$$| \langle F_0^{1S}|x|F_0^{2P_{\pm 1}} \rangle |^2 + | \langle F_0^{1S}|y|F_0^{2P_{\pm 1}} \rangle |^2 + | \langle F_0^{1S}|z|F_0^{2P_{\pm 1}} \rangle |^2 = 2^{15} a_B^2 \frac{\alpha_{0,0}^3 \alpha_{1,1}^5}{\left[ 2\alpha_{0,0} + \alpha_{1,1} \right]^{10}}$$

$$(3.58)$$

### 3.6.2.3. Confirming the Dipole Elements in the Isotropic Hydrogen Limit

As a confirmation check the EMT dipole elements can be compared to those of a hydrogen electron in isotropic free space, as the various effective mass parameters tend towards those in such conditions. The EMT wavefunction scaling parameters $\alpha_{0,0}$, $\alpha_{1,0}$, $\alpha_{1,1}$, the hamiltonian $z$ axis scaling factor $\beta$, the ratio of the perpendicular and parallel (to the $z$ axis) effective masses $\gamma$, and the relative dielectric permittivity $\epsilon_r$ all tend towards their isotropic free space values of 1; the effective mass of the electron $m_\perp$ tends towards the mass of an electron in free space $m_e$.

The simple derivation of dipole elements for the $2P_0$ / $2P_{pm1} \rightarrow 1S$ transitions of a hydrogen atom in isotropic, free space, environment are shown in appendix section B.5.3 ; the EMT transition rates in the same limit are taken in appendix section B.5.2.

$2P_0 \rightarrow 1S$

The free space hydrogen $2P_0 \rightarrow 1S$ transition dipole element squared, duplicated here from equation B.162 , is then given by:

$$| \langle \psi_{hydrogen}^{1S} | x | \psi_{hydrogen}^{2P_0} \rangle |^2 + | \langle \psi_{hydrogen}^{1S} | y | \psi_{hydrogen}^{2P_0} \rangle |^2 + | \langle \psi_{hydrogen}^{1S} | z | \psi_{hydrogen}^{2P_0} \rangle |^2 = \frac{2^{15}}{3^{10}} a_0^2$$

$$(3.59)$$

The corresponding free space isotropic limit of the EMT $2P_0 \rightarrow 1S$ transition rate, equation 3.57 , is taken in appendix section B.5.2.1 , with the result shown below:

$$\lim_{\substack{\alpha_{0,0},\alpha_{1,0},\beta,\gamma,\epsilon_r \to 1 \\ m_\perp \to m_e}} \left( |\langle F_{EMT}^{1S}|x|F_{EMT}^{2P_0}\rangle|^2 + |\langle F_{EMT}^{1S}|y|F_{EMT}^{2P_0}\rangle|^2 + |\langle F_{EMT}^{1S}|z|F_{EMT}^{2P_0}\rangle|^2 \right)$$

$$= \frac{2^{15}}{3^{10}}a_0^2$$

$$(3.60)$$

A comparison of the EMT in the free space isotopic limit, equation 3.60, and isotropic hydrogen, equation 3.59 , transition rates shows that they are the same.

$2P_{\pm 1} \to 1S$

The corresponding $2P_{pm1} \to 1S$ isotropic free space hydrogen transition rate, duplicated from equation B.169 is:

$$|\langle \psi_{hydrogen}^{1S}|x|\psi_{hydrogen}^{2P_{\pm 1}}\rangle|^2 + |\langle \psi_{hydrogen}^{1S}|y|\psi_{hydrogen}^{2P_{\pm 1}}\rangle|^2 + |\langle \psi_{hydrogen}^{1S}|z|\psi_{hydrogen}^{2P_{\pm 1}}\rangle|^2 = \frac{2^{15}}{3^{10}}a_0^2$$

$$(3.61)$$

The corresponding free space isotropic limit of the EMT $2P_1 \to 1S$ transition rate, from equation 3.58 , is taken in appendix section B.5.2.2 , with the result shown below:

$$\lim_{\substack{\alpha_{0,0},\alpha_{1,1},\beta,\gamma,\epsilon_r \to 1 \\ m_\perp \to m_e}} \left( |\langle F_{EMT}^{1S}|x|F_{EMT}^{2P_{\pm 1}}\rangle|^2 + |\langle F_{EMT}^{1S}|y|F_{EMT}^{2P_{\pm 1}}\rangle|^2 + |\langle F_{EMT}^{1S}|z|F_{EMT}^{2P_{\pm 1}}\rangle|^2 \right) = \frac{2^{15}}{3^{10}}a_0^2$$

$$(3.62)$$

Again, a comparison of the EMT , equation 3.62, and isotropic hydrogen, equation 3.61 , transition rates shows that they are the same; that is, in the isotropic free space limit.

Therefore it can be concluded that the EMT obtained transition rates lead to the correct transition rate in the isotopic free space limit, and therefore they are less likely to be incorrect than if this was not the case.

## 3.7. Calculations

In the following section the results of the EMT calculations are shown. This is in three subsections. Firstly, the results of variational calculations are shown; these find the state energy, $\alpha_{\ell,m}$, and $\beta$ parameters. Secondly, due to the failure of EMT for the ground state, the Mott semiconductor-metal transition is briefly discussed and applied; thus allowing the $1S$ ground state to be correctly scaled. Thirdly, Fermi's golden rule is used to calculate transition rates based upon the variationally and Mott transition scaled parameters.

### 3.7.1. EMT Energies

The overall goal of this thesis is to check the agreement of EMT theory with the measured lifetimes of donor electron states in silicon. A simple consideration of Fermi's golden rule and the atomic state wavefunctions allows the calculation of transition rates for dipole interactions. Assuming that the calculated transitions are the dominant decay pathways, the average expected lifetime of upper atomic states is then obtained. In order to calculate the wavefunctions, EMT was used in section 3.5.

The eigenfunctions used in the nondegenerate effective mass environment of silicon are scaled hydrogenic wavefunctions, dependent upon the parameters $\alpha$ and $\beta$ scaling in all directions and along the silicon z axis (the unique effective mass axis) respectively. These parameters can be and are linked by the imposition of the

energy being at a minimum. Imposing such a condition then leads to the variationally minimised energy being an upper bound on the actual value, which can itself only be found by the selection of a perfectly true eigenbasis for the system, which is not possible as closed form analytical solutions for non-hydrogen systems are not known; this is explained in detail in appendix A.2.2.2. Minimisation of the energy (or difference with respect to a measured energy) by the variation of parameters, with appropriate choice of function dependent upon those parameters, allows an estimate of the wavefunction of the corresponding state.

Variationally minimising the energy of hydrogenic wavefunctions in silicon has been performed before by others in the literature, namely for single basis states by Kohn and Luttinger [8] and then for multiple basis states, albeit only those of the same parity and projection of angular momentium, by Faulkner [107]. Janzen [94] extended the work of Faulkner to chalcogen donors, and found a small improvement in accuracy of a few significant figures. Equation A.43 shows that if there is only a small change in calculated energy from increasing the number of basis states, then the single basis state is still the dominant part of the resulting wavefunction. This means that the multiple basis state method will yield only small improvements in accuracy to any lifetime calculation.

As an example of the small size of this correction, a calculation showing the energy correction for the $2p_0$ state, the lowest lying calculated with any accuracy, was performed by both Faulkner [107] and Janzen [94]. This was done with ellipsoidal hydrogenic basis states with quantum numbers $\ell=1$,n=$\{2,..7\}$, $\ell=3$, n=$\{4...9\}$ and $\ell=5$,n=$\{6,...11\}$, forming a total of 18 basis states for Faulkner, and 6 $\ell$ values with 15 n values for 90 basis states in a similar fashion by Janzen; $\ell$ is the angular momentium quantum number.

For an un-ionised atomic selenium complex in silicon the measured energy is 11.49meV [94], the single basis state energy is 11.21meV (from calculations shown below), the 18 basis state is 11.51meV [94, table 2], while that of the 90 basis state is 11.49meV [94, table 2]. This shows that a single basis state gives only $-2.43\%$ inaccuracy, 18 basis states a $+0.17\%$, and 90 basis states cannot be distinguished from the experimental measurement at the resolution at which it was taken at.

In general good agreement to measured energies for all but the $1S$ ground state of various donors is found. This lack of accuracy for the $1S$ state naively makes any lifetime calculation involving it inaccurate, however, is it possible to scale this state by the use of the Mott semiconductor-metal transition; this is discussed in detail in section 3.7.2. While the good agreement of non-ground states to the measured values has been long known (Kohn published in 1955), the present author is unaware of any published variational parameter values except for Kohn's $1S$ state [115]; only the energies have in general been published.

Because of the lack of variational parameters in the literature, it is necessary to fully reproduce the work of Kohn to obtain them, as the only given parameter is that for the $1S$ state, which is inaccurate. Unfortunately due to time constraints the approach of Faulklner[107], which is in essence the Rayleigh-Ritz method discussed in greater detail in appendix A.2.2.1, has not been completed; the multiple basis state approach, as mentioned above, can only be expected to yield small improvements in lifetime calculations.

The reproduction of Kohn's work for the $1S$, $2P_0$, and $2P_{\pm 1}$ states is then shown in section 3.5, with the results of calculations shown below. The longitudinal and perpendicular effective masses used in the calculations are those of silicon, i.e. 0.98 and 0.19 electron rest masses respectively[80]. The relative dielectric constant of

silicon is also used, this is 11.7.[80] The EMT $\gamma$ parameter, that is perpendicular over longitudinal effective masses, is $0.1939 \approx 0.19$ in silicon.

For the wavefunctions to be used to calculate the dipole matrix elements, using the functions shown in section 3.5, the different states must share a common $\beta$ parameter. While it is conceivable that the dipole elements based upon different $\beta$ parameters could be calculated, although the integral over all space would be awkward, this would not fit with the EMT Hamiltonian; the Hamiltonian is $\beta$ dependent, thus the different excited states are explicitly being modelled as in different environments if they have differing $\beta$ parameters. There are then several variations of the EMT calculations.

Firstly, the $\alpha$ and $\beta$ parameters can be linked by imposing minimisation conditions upon the state energy functions. In this regime the state energies can be variationally minimised, or the difference with measured energies can be minimised. However there is no difference, the obtained parameters should be identical, therefore only the values minimised absolutely are given. Secondly the $\alpha$ and $\beta$ parameters can be varied separately, this should give the same result as when they are linked by the minimisation condition; it is left in to show that the minimisation condition is correct by showing the same obtained parameters.

**3.7.1.1.** $1S$

The wavefunction, energy function, and $\alpha_{0,0}$ and $\beta$ parameter link from section 3.5.2.1 are used here. The results of variational calculations are then presented in table 3.2.

From table 3.2 it can clearly be seen that there is only minor difference in any of the calculated parameters. The different parameters calculated all agree to within

| Mode of Calculation | Calculated Energy (meV) | $\alpha_{0,0}$ | $\beta$ |
|:---:|:---:|:---:|:---:|
| Linked | $-30.0541016592$ | $1.35078313467$ | $0.616683622982$ |
| Separate | $-30.0541008846$ | $1.3511159818$ | $0.616488350005$ |
| Simple Hydrogenic | Na | $2.60965895981$ | $1$ |

Table 3.2.: Collection of variational calculation results for the $1S$ scaled hydrogenic state. The energy and $\alpha_{0,0}$ and $\beta$ parameters are shown for the parameters being linked by minimisation conditions, and for them being treated as independent variables. Both show similar energy results, that differ only because of the effect of finite step sizes for the parameters in the variational minimisation. In both the energy is minimised absolutely. **Linked:**$\alpha_{0,0}$ and $\beta$ related by equation 3.36. **Separated:** $\alpha_{0,0}$ and $\beta$ treated as independent variables. **Simple Hydrogenic:** The calculated parameter using the simple model from section 3.5.1, where the experimentally measured energy of $-306.63$ meV[94] is used to scale the $\alpha_{0,0}$ parameter. This shows the difference between the spherically symmetric hydrogen, and the EMT, wavefunctions. *Note:* the hydrogenic energy is not given in the table because it is not calculated, the hydrogenic wavefunction parameter is calculated from the measured energy, the opposite way around to the EMT states.

3 significant figures for $\alpha_{0,0} = 1.35$, and 2 s.f for $\beta = 0.61$. Taking the same precision as the measured energy, 5 significant figures, gives a value of $-30.054$meV. By comparison to the measured value of $-306mev$ it can be seen that the resulting EMT calculated energies of $-30mev$ is highly inaccurate. This is attributed to the breakdown in the effective mass assumptions, especially the donor potential accuracy, for the $1S(A_1)$ state. However, this is also just an upper bound on the possible "true" value, and in these terms it is still valid.

It is illustrative to compare the EMT wavefunction with its unscaled basis, that of hydrogen. Taking the $1S$ wavefunction from equation 3.34 and converting it back into Cartesian coordinates, with distance units included, and substituting in the variational parameters gives equation 3.63; where $a_b$ is the Bohr radius for hydrogen. The raw hydrogen wavefunction is obtained by replacing all the numerical values with 1.

$$F_{1S(A_1)}(x, y, z) = \left(\frac{\beta}{\gamma}\right)^{\frac{1}{4}} \left(\frac{\alpha_{0,0}}{a_b \epsilon_r}\right)^{\frac{3}{2}} \frac{1}{\sqrt{\pi}} e^{-\frac{\alpha_{0,0}}{a_b \epsilon_r}\left(x^2 + y^2 + \frac{\beta}{\gamma} z^2\right)^{\frac{1}{2}}}$$

$$\approx \frac{0.0525}{a_b^{\frac{3}{2}}} \frac{1}{\sqrt{\pi}} e^{-\frac{0.115}{a_b}\left(\left[x^2 + y^2\right] + 3.21 z^2\right)^{\frac{1}{2}}} \tag{3.63}$$

While the energy value may be incorrect, the form or equation of the resulting EMT wavefunction does appear to be consistent with the EMT model; however, this is not proof of it being correct. The relative dielectric permittivity of the silicon environment smears out the wavefunction over a large distance, that is, it has no preferred direction and thus could account for the $\approx 0.0525$ factor for the whole. The x, y plane and the z axis are then additionally stretched by the exponential term, and in differing amounts, $e^{0.115} = e^{0.115}$ and $e^{0.115\sqrt{0.321}} = e^{0.206}$ respectively; presumably this is due to the differing effective masses in those directions (0.98 and 0.19 electron rest masses respectively).

It should be noted that the square root in the scaling factors above comes from the square root in the exponent of the wavefunction, and that due to the nature of the square root the exponent cannot be removed in this fashion, hence the $\approx$ sign; it is not possible to quantify the x,y plane scaling without specifying the z coordinate, so in this case the scaling factor can be taken to be accurate for the $z = 0$ line. In a similar fashion the z axis scaling factor can be taken to be along the $x = y = 0$ line.

### Energy as a function of $\gamma^{\frac{1}{3}}$ compared to Faulkner and Kohn

For further confidence that the $1S$ energy function gives the same or similar results as Kohn [8] and Faukner[107], the energy as a function of $\gamma^{\frac{1}{3}}$ is calculated. This is plotted in figure 3.1, with select values shown in table 3.3; the values shown are the same as those given by Faulkner in [107, table I].

# 3. Introduction to Effective Mass Theory in Silicon

| $\gamma^{\frac{1}{3}}$ | Own | Faulkner | Kohn |
|---|---|---|---|
| 0.0 | 3.7010 | na | 3.701 |
| 0.1 | 3.1232 | 3.17 | 3.123 |
| 0.2 | 2.6666 | 2.69 | 2.667 |
| 0.3 | 2.3001 | 2.31 | 2.300 |
| 0.4 | 2.0017 | 2.01 | 2.002 |
| 0.5 | 1.7558 | 1.759 | 1.756 |
| 0.6 | 1.5510 | 1.553 | 1.551 |
| 0.7 | 1.3787 | 1.380 | 1.379 |
| 0.8 | 1.2326 | 1.233 | 1.233 |
| 0.9 | 1.1076 | 1.108 | 1.108 |
| 1.0 | 1.0000 | 1.000 | 1.000 |

Table 3.3.: Here are shown the calculated binding energies for the $1S$ state, relative to the conduction band minima, for a donor electron. The values for Kohn and Faulkner are taken from [107, table I], except the Kohn value for $\gamma^{\frac{1}{3}}$ which is from source [8, equation 4.26]. The energy values are in unitless energy form, see equation 3.13. Own refers to the values the present author has calculated using equation 3.35.
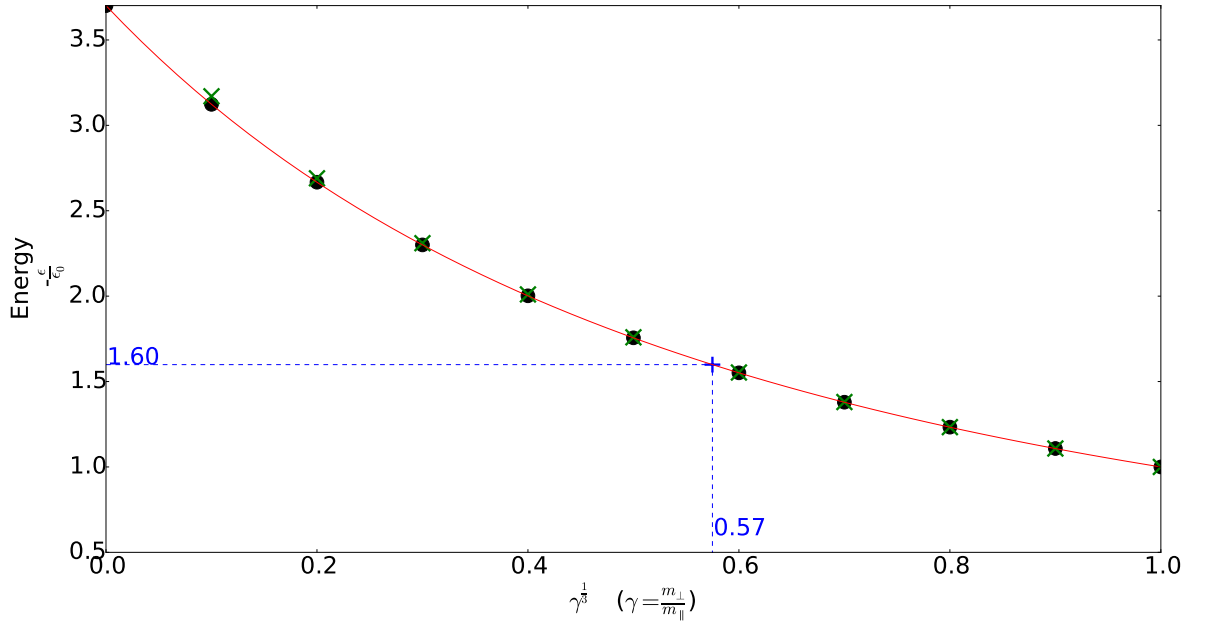


Figure 3.1.: Kohn and Faulkners energy values for the $1S$ state plotted against the author's own calculations. Kohn's values are the circular black dots, Faulkner's the diagonal green crosses, and the authors own are plotted as a line. The values for $\gamma^{\frac{1}{3}}$ and energy in silicon are highlighted by an upright blue cross with dashed blue lines to the two axis; here $\gamma = 0.19$ for silicon. The y axis is the energy in unitless form, while the x axis is the $\gamma$ ratio of the effective masses to the third root.

As table 3.3 and figure 3.1 show, the values the present author has calculated agree extremely well with those in the literature for the $1S$ state. Therefore the wavefunction parameters obtained can be assumed to accurate within the EMT framework for the $1S$ state.

**3.7.1.2.** $2P_0$

The wavefunction, energy function, and $\alpha_{1,0}$ and $\beta$ parameter link from section 3.5.2.2 are used here. The results of variational calculations are then, as for the $1S$ state, presented in table form, table 3.4. The same modes of obtaining the variational parameters as for the $1S$ state are used, but with an additional mode where the value of the $\beta$ variational parameter of the $1S$ state is used to obtain the $\alpha_{1,0}$ and energy values for the $2P_0$ state.

| Mode of Calculation | Calculated Energy (meV) | $\alpha_{1,0}$ | $\beta$ |
|---|---|---|---|
| Linked | $-11.2134095625$ | 1.80008053667 | 0.555020531689 |
| Separate | $-11.2134049187$ | 1.79897877598 | 0.55645981983 |
| 1S $\beta$ | $-11.1945871728$ | 1.7594153917 | 0.61 |
| Simple Hydrogenic | Na | 1.01033743392 | 1 |

Table 3.4.: Collection of variational calculation results for the $2P_0$ scaled hydrogenic state. The energy and $\alpha_{1,0}$ and $\beta$ parameters are shown for the parameters being linked by minimisation conditions, and for them being treated as independent variables. Both show similar energy results, that differ only because of the effect of finite step sizes for the parameters in the variational minimisation. In both the energy is minimised absolutely. **1S** $\beta$ : Energy and $\alpha_{1,0}$ calculated using $1S$ derived $\beta$ = 0.61, the energy here is minimised absolutely. **Linked** : $\alpha_{1,0}$ and $\beta$ related by equation 3.39. **Separated:** $\alpha_{1,0}$ and $\beta$ treated as independent variables. **Simple Hydrogenic:** The calculated parameter using the simple model from section 3.5.1,where the experimentally measured energy of $-11.49$meV[94] is used to scale the $\alpha_{1,0}$ parameter, the $\beta$ is arbitrarily set to 1. This shows the difference between the spherically symmetric hydrogen, and the EMT, wavefunctions. *Note:* the hydrogenic energy is not given in the table because it is not calculated, the hydrogenic wavefunction parameter is calculated from the measured energy, the opposite way around to the EMT states.

From table 3.4 it can be clearly seen that all the different methods of calculation yield extremely similar values. The energy values for the variational methods are now only 2.43% inaccurate with respect to experimental measurement. The different parameters calculated all agree to within 2 significant figures for $\alpha_{0,0} = 1.8$, and 2 s.f for $\beta = 0.55$. The $1S$ $\beta$ calculated energy is found to be extremely close to the variationally found energy, with an inaccuracy of only 2.61%.

Again the scaling of the wavefunction is shown by taking the $2P_0$ state wavefunction from equation 3.37, reintroducing units of distance, and writing it in Cartesian form yields:

$$
\begin{aligned}
F_{2p_0}(x,y,z) &= \left(\frac{\beta}{\gamma}\right)^{\frac{1}{4}} \left(\frac{\alpha_{1,0}}{a_b \epsilon_r}\right)^{\frac{5}{2}} \frac{1}{4\sqrt{2\pi}} \left(\frac{\beta}{\gamma}\right)^{\frac{1}{2}} z e^{-\frac{\alpha_{1,0}}{2a_b \epsilon_r}\left(\left[x^2+y^2\right]+\frac{\beta}{\gamma}z^2\right)^{\frac{1}{2}}} \\
&\approx 0.0210 \left(\frac{1}{a_b}\right)^{\frac{5}{2}} \frac{z}{4\sqrt{2\pi}} e^{-\frac{0.150}{2a_b}\left(\left[x^2+y^2\right]+3.21z^2\right)^{\frac{1}{2}}}
\end{aligned}
$$

(3.64)

In a similar manner as for the $1S$ state, the $2P_0$ state is found to be stretched out in all directions by a factor of 0.0210. There is then an additional scaling, or smearing, in the x,y axis by a factor of $e^{0.150} = e^{0.150}$ and in z axial direction by $e^{0.150\sqrt{3.21}} = e^{0.269}$. As before, these scaling factors are only applicable directly along the $z = 0$ line for the x,y plane, and the $x = y = 0$ line for the z axis.

For the state parameters to be consistent with EMT one must take the $\alpha_{1,0}$ with the same $\beta$ value as the $1S$ state. Thus one finds the $2P_0$ $\alpha_{1,0}$ and $\beta$ to be 1.76 to 3 s.f and 0.61 to 2 s.f respectively.

**Energy as a function of $\gamma^{\frac{1}{3}}$ compared to Faulkner and Kohn**

For further confidence that the $2P_0$ energy function gives the same or similar results

as Kohn [8] and Faukner[107], the energy as a function of $\gamma^{\frac{1}{3}}$ is again calculated. This is plotted in figure 3.2, with select values shown in table 3.5; the values shown are the same as those given by Faulkner in [107, table II]

| $\gamma^{\frac{1}{3}}$ | Own | Faulkner | Kohn |
|---|---|---|---|
| 0.0 | 3.4698 | na | 3.47 |
| 0.1 | 2.3710 | 2.41 | 2.371 |
| 0.2 | 1.6852 | 1.70 | 1.685 |
| 0.3 | 1.2368 | 1.24 | 1.237 |
| 0.4 | 0.9323 | 0.933 | 0.9323 |
| 0.5 | 0.7188 | 0.719 | 0.7188 |
| 0.6 | 0.5650 | 0.565 | 0.5650 |
| 0.7 | 0.4516 | 0.452 | 0.4516 |
| 0.8 | 0.3663 | 0.3663 | 0.3663 |
| 0.9 | 0.3009 | 0.3009 | 0.3009 |
| 1.0 | 0.2500 | 0.2500 | 0.2500 |

Table 3.5.: Here are shown the calculated binding energies for the $2P_0$ state, relative to the conduction band minima, for a donor electron. The values for Kohn and Faulkner are taken from [107, table II], except the Kohn value for $\gamma^{\frac{1}{3}}$ which is from source [8, table iv]. The energy values are in unitless energy form, see equation 3.13. Own refers to the values the present author has calculated using equation 3.35.
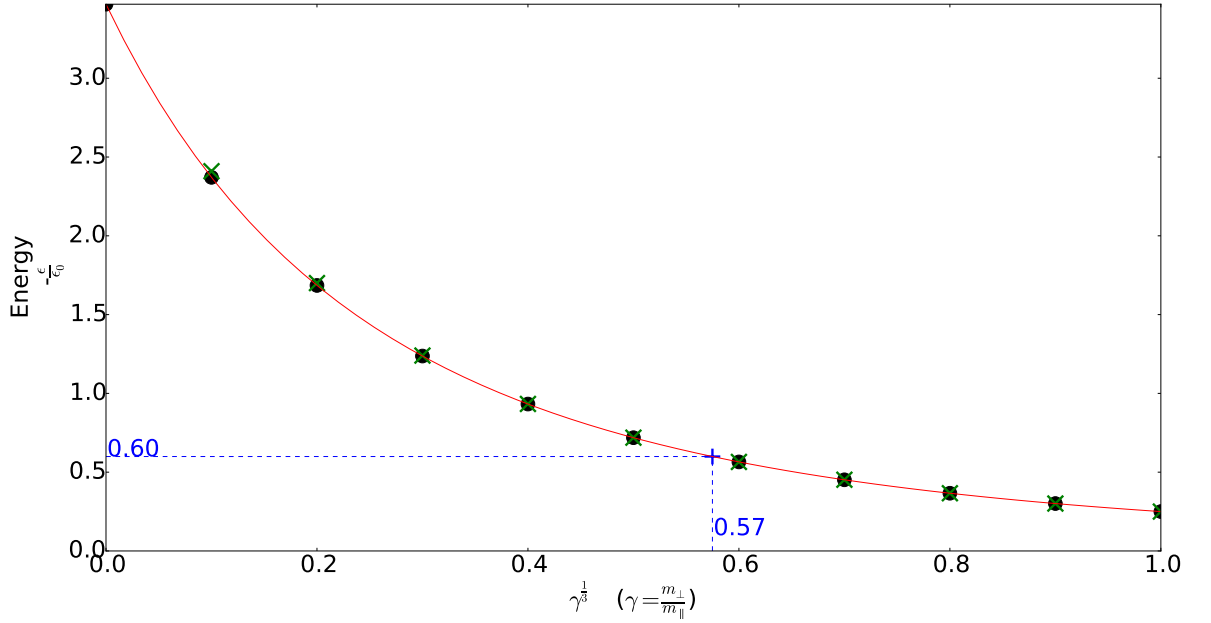
Figure 3.2.: Kohn and Faulkners energy values for the $2P_0$ state plotted against the author's own calculations. Kohn's values are the circular black dots, Faulkner's the diagonal green crosses, and the author's own are plotted as a line. The values for $\gamma^{\frac{1}{3}}$ and energy in silicon are highlighted by an upright blue cross with dashed blue lines to the two axis; here $\gamma = 0.19$ for silicon. The y axis is the energy in unitless form, while the x axis is the $\gamma$ ratio of the effective masses to the third root.

Table 3.5 and figure 3.2 show that the values the present author has calculated agree extremely well with those in the literature for the $2P_0$ state. The wavefunction parameters obtained can be assumed to then also be accurate within the EMT framework. EMT can now be used to estimate the radiative lifetime for the $2P_0 \rightarrow 1S$ transition, extending the application of EMT to not only energy values but to radiative lifetimes as well.

### 3.7.1.3. $2P_{\pm 1}$

The wavefunction, energy function, and $\alpha_{1,1}$ and $\beta$ parameter link from section 3.5.2.3 are used here. The results of variational calculations are shown in table 3.6. The possible modes of calculation are the same as for the $2P_0$ state calculations: the

variational parameters linked by differential minimisation conditions, the $\beta$ parameter taken from the $1S$ EMT calculations and obtaining the $\alpha_{1,0}$ via the differential minimisation condition, and for both parameters treated as independent variables.

| Mode of Calculation | Calculated Energy (meV) | $\alpha_{1,1}$ | $\beta$ |
|---|---|---|---|
| Linked | $-6.10552309506$ | 1.19390537711 | 0.5363914925 |
| Separate | $-6.10552131944$ | 1.19324869329 | 0.536206343773 |
| 1S $\beta$ | $-6.09659876777$ | 1.18346951914 | 0.61 |
| Simple Hydrogenic | Na | 0.753454201571 | 1 |

Table 3.6.: Collection of variational calculation results for the $2P_{\pm 1}$ scaled hydrogenic state. The energy and $\alpha_{1,1}$ and $\beta$ parameters are shown for the parameters being linked by minimisation conditions, and for them being treated as independent variables. Both show similar energy results, that differ only because of the effect of finite step sizes for the parameters in the variational minimisation. In both the energy is minimised absolutely. **1S** $\beta$:Energy and $\alpha_{1,1}$ calculated using $1S$ derived $\beta$ = 0.61, the energy here is minimised absolutely. **Linked** :$\alpha_{1,1}$ and $\beta$ related by equation 3.42. **Separated:** $\alpha_{1,1}$ and $\beta$ treated as independent variables. **Simple Hydrogenic:** The calculated parameter using the simple model from section 3.5.1,where the experimentally measured energy of $-6.39$ meV[94] is used to scale the $\alpha_{1,1}$ parameter, the $\beta$ is arbitrarily set to 1. This shows the difference between the spherically symmetric hydrogen, and the EMT, wavefunctions.

Again it can be seen that the different variational modes of calculation yield near, or perfectly identical values. All of the calculated energies have, to 3 s.f, an inaccuracy with respect to the measured energy of 4.54%.

To show the relative scaling with respect to a pure hydrogenic state one takes the $2P_{\pm 1}$ state wavefunction from equation 3.40, reintroducing units of distance and using Cartesian form to give:

$$F_{2p_{\pm 1}}(x,y,z) = \mp \left(\frac{\beta}{\gamma}\right)^{\frac{1}{4}} \left(\frac{\alpha_{1,1}}{a_b \epsilon_r}\right)^{\frac{5}{2}} \frac{1}{8\sqrt{\pi}} \left([x^2 + y^2] + \frac{\beta}{\gamma} z^2\right)^{\frac{1}{2}} \sqrt{1 - \left(\frac{\left(\frac{\beta}{\gamma}\right)^{\frac{1}{2}} z}{\left([x^2+y^2] + \frac{\beta}{\gamma} z^2\right)^{\frac{1}{2}}}\right)^2}$$

$$\times\, e^{\pm i \arctan\left(\frac{y}{x}\right)} e^{-\frac{\alpha_{1,1}}{2 a_b \epsilon_r}\left([x^2+y^2]+\frac{\beta}{\gamma}z^2\right)^{\frac{1}{2}}}$$

$$\approx \mp 0.00432 \left(\frac{1}{a_b}\right)^{\frac{5}{2}} \frac{1}{8\sqrt{\pi}} \left([x^2 + y^2] + 3.21 z^2\right)^{\frac{1}{2}} \sqrt{1 - \left(\frac{1.79 z}{\left([x^2+y^2]+3.21 z^2\right)^{\frac{1}{2}}}\right)^2}$$

$$\times\, e^{\pm i \arctan\left(\frac{y}{x}\right)} e^{-\frac{0.101}{2 a_b}\left([x^2+y^2]+3.21 z^2\right)^{\frac{1}{2}}}$$

$$(3.65)$$

The $2P_1$ state is found to be smeared out in all directions by a factor of 0.00432. The x, y plane and z axis are additionally scaled by, in this case, rather complex factors that are not easily stated as for the other states.

The final $1S$ $\beta = 0.61$ calculated $\alpha_{1,1}$ parameter is 1.18 to 3s.f.

## Energy as a function of $\gamma^{\frac{1}{3}}$ compared to Faulkner and Kohn

For further confidence that the $2P_{\pm 1}$ energy function gives the same or similar results as Kohn [8] and Faukner[107], the energy as a function of $\gamma^{\frac{1}{3}}$ is again calculated as for the $aS$ and $2P_0$ states. Figure 3.3 shows the energy as a function of $\gamma^{\frac{1}{3}}$, with select values shown in table 3.7; the values shown are the same as those given by Faulkner in [107, table III]

| $\gamma^{\frac{1}{3}}$ | Own | Faulkner | Kohn |
|---|---|---|---|
| 0.0 | 0.4337 | na | 0.434 |
| 0.1 | 0.4216 | 0.4265 | 0.4216 |
| 0.2 | 4.026 | 0.4057 | 0.4026 |
| 0.3 | 0.3816 | 0.3835 | 0.3816 |
| 0.4 | 0.3602 | 0.3612 | 0.3602 |
| 0.5 | 0.3392 | 0.3400 | 0.3392 |
| 0.6 | 0.3191 | 0.3195 | 0.3191 |
| 0.7 | 0.3001 | 0.3002 | 0.3001 |
| 0.8 | 0.2822 | 0.2823 | 0.2822 |
| 0.9 | 0.2656 | 0.2656 | 0.2656 |
| 1.0 | 0.2500 | 0.2500 | 0.2500 |

Table 3.7.: Here are shown the calculated binding energies for the $2P_{\pm1}$ state, relative to the conduction band minima, for a donor electron. The values for Kohn and Faulkner are taken from [107, table III], except the Kohn value for $\gamma^{\frac{1}{3}}$ which is from source [8, table iv]. The energy values are in unitless energy form, see equation 3.13. Own refers to the values the present author has calculated using equation 3.35.
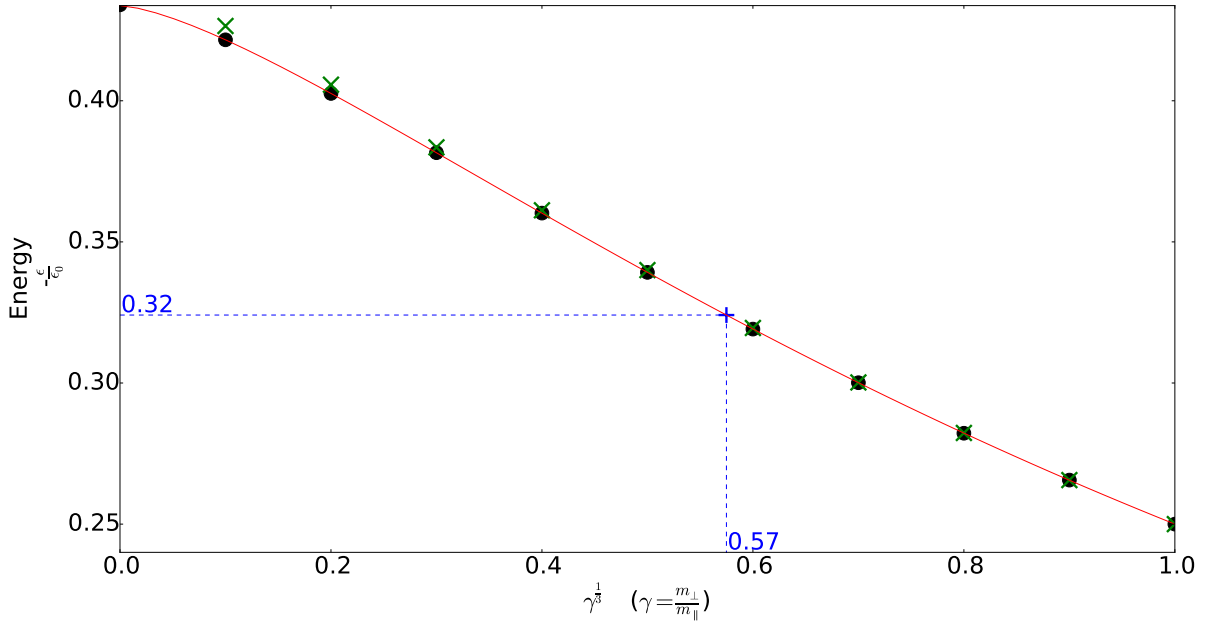


Figure 3.3.: Kohn and Faulkners energy values for the $2P_{\pm1}$ state plotted against the author's own calculations. Kohn's values are the circular black dots, Faulkner's the diagonal green crosses, and the author's own are plotted as a line. The values for $\gamma^{\frac{1}{3}}$ and energy in silicon are highlighted by an upright blue cross with dashed blue lines to the two axis; here $\gamma = 0.19$ for silicon. The y axis is the energy in unitless form, while the x axis is the $\gamma$ ratio of the effective masses to the third root.

Table 3.7 and figure 3.3 show that the values the present author has calculated agree extremely well with those in the literature for the $2P_{\pm 1}$ state; the wavefunction parameters are then assumed to be accurate within the EMT framework. Radiative lifetime calculations for the $2P_{\pm 1} \rightarrow 1S$ transition can now proceed.

## 3.7.2. Using the Mott Transition to Approximate the Ground State

The $1S(A_1)$ ground state cannot be correctly scaled in the effective mass framework; this is due to the state being too close to the donor nucleus for the relevant EMT assumptions to hold. For the dipole matrix elements to be as in section 3.6.2 the ground state wavefunction must be assumed to have a scaled hydrogenic wavefunction envelope, as is true for all other donor states. Because of the failure of the EMT to correctly scale this ground state, the Mott insulator-metal transition can be used.

### Mott Insulator-Metal Transition

The Mott transition is, as the name implies, where an insulator, or semiconductor material, undergoes a transition to exhibiting metal like conductivity.[123] This transition is caused by doping with donor or acceptor atoms. As the doping concentration, $n_d$ cm$^{-3}$, passes above some critical value, there is a rapid change in the conductivity, and number of charge carriers, in the material; this is characteristic of a metal.[124]

There are then three main features, or stages, of the simple Mott model of the phenomenon, corresponding to three characteristic doping concentrations, and shown in the list below, paraphrased from [124, p816].

1. At a critical donor concentration, $n_c$ cm$^{-3}$, donor electrons become delocalized;

as the ground state wavefunctions overlap significantly they begin to form a band, this is shown in explanatory cartoon form in figure 3.4. Below this the donor electrons are all bound to individual atoms. This concentration marks the Mott transition.

2. Above another generally separate concentration, $n_f$ cm$^{-3}$, the Fermi level of the system is within the conduction band of the host material. This is not necessary for the material to exhibit metallic behaviour, but must occur once the number of donor atom donated electrons is high enough. At this point the host material is most definitely metal like, due to having charge carriers in the conduction band; vice versa for acceptors and the valance band.

3. In between the Mott and Fermi doping concentrations lies what has been referred to as an "impurity band"[124]. In this state the donor atoms are sufficiently close together that donor electrons are delocalized and yet, except for thermal excitation, are not in the conduction band. In this case the doping concentration $n_d$ is $n_c < n_d < n_f$.

In order to explain and clarify the change in the Fermi level, it must be recalled that this is not the same as the Fermi energy. The Fermi level is the energy at which, if a state at this energy existed, there would be a 50% probability of it being occupied; the Fermi energy is the energy of the highest occupied state at 0K. In the silicon system, as the donor concentration increases, at any temperature other than absolute zero, the Fermi level will increase; assuming substitutional doping and thermal equilibrium.

Both the donor and intrinsic electrons follow a Fermi-Dirac distribution which, assuming the extra doping concentrating has a negligible effect upon the extra binding energy of each electron (eg. due to extra or lesser coulombic attraction from nearby

dopant atoms), for a given energy is only temperature dependent. This means that at any given temperature,when considered individually, the donor and host electrons will have the same energy difference between their ground state and the energy at which they have a 50% probability of being (this is the Fermi level). Because the donor electron has a ground energy state higher than the valence band of the host material silicon, the donor electron has a higher energy at which there is a 50% probability of such a state being occupied.

Replacing host atoms with dopants then adds in more donor electrons with a higher Fermi level, raising the total average Fermi level for the whole composite system. At a fixed temperature, if the Fermi level of a donor electron considered by itself is at an energy in the host materials conduction band, then increasing the doping concentration will eventually raise the Fermi level of the whole material into the conduction band. Increasing the doping concentrating brings the composite materials average Fermi level closer and closer to that of a single donor electron; at a doping concentration such that all host material atoms are replaced then the composite Fermi level is then, of course, that of the donors. If the temperature is low, such that the donor electron has a less than 50% probability of being in the lowest lying state in the host materials conduction band, then no increase in doping concentration will raise the Fermi level into the conduction band.
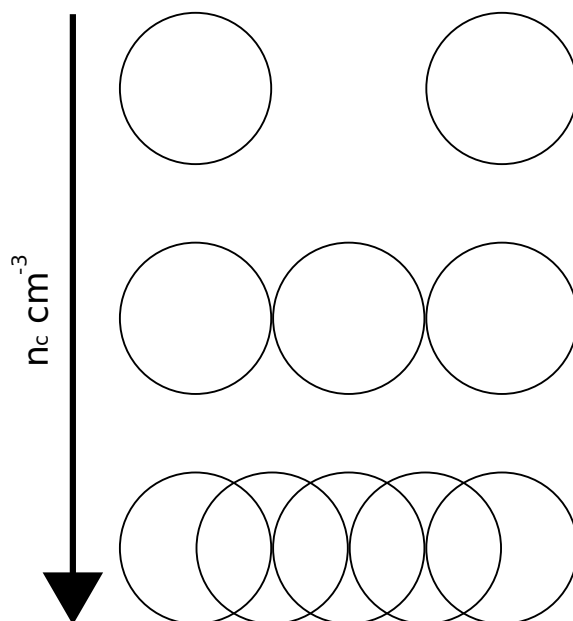
Figure 3.4.: Two dimension cartoon representation of the donor ground states. The three stages of dopant concentration $n_c$cm$^{-3}$ are shown. Edges of the circles represent the 1/e point in wavefunction magnitude. Firstly, the donor ground states do not significantly overlap. Secondly, they are on the threshold of doing so. Finally, they do overlap, forming a band like structure.

A single donor electron will be bound in a single set of mid-bandgap donor states, at a single location. The qualitative explanation of why metal like behaviour results from the crossing of a doping concentration threshold, is that as the concentration of donors is increased, they are closer together. If one assumes that the donor atoms' spatial locations are randomly distributed, but susceptible to change, perhaps via thermally energized wandering, then the system will eventually find an equilibrium state. This will be where the donors are, on average, equidistant and uniformly distributed; there will then probably be some form of Poissonian distribution of donor separation about the equilibrium separation distance. As the donor concentration reaches the $n_c$ mark, the ground state wavefunctions of the donor electrons begin to significantly overlap. As this overlap increases, the energy required to move an electron from adjacent state to state decreases, thus raising the conductivity. At a critical concentration the ground state electrons become fully delocalized and are

able to form a band like structure throughout, and are thus now exhibiting metallic behaviour. Once the host material is fully filled with a web of delocalized donor electrons, any extra donor electrons are able to add linearly to the number of charge carriers. See figure 1 and figure 2 of [124] for an example of the rapid then linear rise in charge carriers and the rapid increase in conductivity, with respect to doping concentration, respectively.

Mott was able to devise a relation between the Bohr radii of the donor ground state and the donor doping concentration, shown in equation 3.66; where $n_c$ is the critcal donor doping concentration, $C$ is a scalar constant, and $a_b$ is the ground state Bohr radius.[123] The constant $C$ can be shown to be $0.26 \pm 0.05$ for a wide range of physical systems and situations.[125]

$$n_c \cong \left(\frac{C}{a_b}\right)^3 \tag{3.66}$$

### 3.7.2.1. Application of the Mott Criteria to Chalcogens

The prior statements about the Mott criteria are all true for single donors, such as the pnictogens, however chalcogens double donors cause two problems.

Firstly, it is difficult to dope silicon with a high concentration of chalcogen atoms. Normal methods of doping can involve thermal diffusion of dopants throughout the silicon, and higher concentrations require higher temperatures. This, of course, puts a limit on the possible dopant concentrations, as at some point the silicon will simply melt.

In [2], Winkler et al were able to exceed the thermally diffusing equilibrium doping

concentration by the use of ion implantation, followed by melting with an excimer laser pulse, then finally ending with cooling and resolidification; they determined that this resulted in a host crystal with approximately 1% sulphur content. The ion implantation allowed for the greater number of dopant atoms to be implanted into a localised region of the silicon. The melting by the excimer laser allowed for the dopant to be distributed approximately homogeneously in the melted region. While rapid cooling, and resolidification afterwards, prevented the dopant concentration from reaching a lower concentration in equilibrium with the whole silicon crystal; the dopants are mixed to an equilibrium distribution in the melted region, but the rapid cooling prevents much diffusion of dopants outside from this region.

Secondly, the ground state of chalcogen donor electrons has a degeneracy of two. This is because of symmetry induced splitting of the $1S$ state, the $1S(A_1)$ state is then the ground state. As there are two donor electrons any impurity band, from overlapping ground state wavefunctions, cannot conduct at absolute zero; one of the donor electrons must be spin up, one spin down, there are then no empty states for electrons to move to as needed for conduction.

However, for the highest doping concentrations Winkler et al show that the conductivity remains approximately constant between 1.7K and 300K. For the less heavily doped samples the conductivity is thermally activated, with the thermal effect being stronger for the least doped of all their samples. [2, fig 1, and table 1] Winklers data shows that, for heavily sulphur doped silicon, there is only a weak temperature effect on conductivity such that the samples behave as if they were metals.[2, fig 2] It could be that the conductivity doesn't decrease with temperature like a metal because of the lack of phonons at the appropriate energy for single phonons to interact with the donor ground state, however this is speculation. There is also no mention of the assumed paucity of free states in any of the literature on the Mott transition

in chalcogen doped silicon, and I cannot explain why conduction does not seem to increase with temperature, due to an increase in empty ground states.

Regardless, the conductivity does not disappear at low temperature, and the findings of Winkler et all are assumed to be true for the purposes of estimating the Mott transition donor concentration.

Winkler et all were then able to use conductivity measurements to determine the Mott transition concentration to be between 1.8 and $4.3 \times 10^{20} \mathrm{cm}^{-3}$.[2]

The $1S(A_1)$ ground state binding energies, with respect to the conduction band minima, of sulphur and selenium dopants in silicon are 318.32 meV and 306.63 meV respectively.[94] The binding energy is related to the distance of the donor electron from the donor atom, or Bohr radii. Thus the closeness of the two binding energies suggests that selenium may have a similar Bohr radius to that of sulphur.

Referring back to the EMT energy expression for the $1S$ state, equation 3.35, one can see that there is both a linear and quadratic relation between energy and the variational $\alpha_{0,0}$ parameter. And $\alpha$ itself is then related to the Mott scaled Bohr radii as in equation 3.67, where one must highlight the distinction between $a_B$ the native or raw Bohr radii used as a unit of length in EMT (equation 3.13), and $a_b$ the Mott transition estimated Bohr radii (the actual ground state radius distance).

$$a_b = \frac{a_B}{\alpha_{0,0}} = \frac{4\pi\hbar^2\epsilon_r\epsilon_0}{\alpha_{0,0}m_\perp e^2} \tag{3.67}$$

**Mott Estimated Bohr Radii and $\alpha_{0,0}$**

The relation between $n_c$ and $\alpha_{0,0}$ is:

$$a_b = \left(\frac{C}{n_c}\right)^{\frac{1}{3}}$$

$$\alpha_{0,0} = \frac{4\pi\hbar^2\epsilon_r\epsilon_0}{m_\perp e^2} \frac{n_c^{\frac{1}{3}}}{C}$$

(3.68)

The doping concentration of $1.8 \times 10^{20}$cm$^{-3}$ thus gives $\alpha_{0,0} = 0.0708$ to 3 significant figures. Meanwhile a value of $4.3 \times 10^{20}$cm$^{-3}$ gives $\alpha_{0,0} = 0.0946$ to 3 s.f. Both concentrations are sourced from [2], and a value of $C = 0.26$ is taken from [125]. Both scaling parameters are without dimension or units.

### 3.7.2.2. Mott Scaled Ground State Energy

The energy of the Mott scaled $1S(A_1)$ state can be estimated by two methods, by assuming firstly a spherically symmetric wavefunction, and secondly a prolate wavefunction lengthened along the silicon axis of differing effective mass; in both cases the energies calaculated are relative to the conduction band minima in silicon, and $\epsilon_r$ is the relative dielectric permittivity of silicon, 11.7 [80].

Firstly, the naive treatment as a purely hydrogenic energy level results in scaling the energy as in equation 3.70. This equation is assembled from equations 4.23 to 4.25 from [95], shown in appendix B.4. For this perfectly symmetrical treatment the effective mass,$m*$, cannot be degenerate in different directions, and thus the vector average is used as in equation 3.69.

Secondly, by using the EMT energy expression from equation 3.35, two possible energies are obtained. One with the $\beta$ parameter set to 1, and then another by scaling $\beta$ such that it satisfies the minimisation criteria of equation 3.36; because the energy minimisation condition linking the two variational parameters mixes both power and trigonometric functions in such a manner as to be non-trivial to

analytically solve, a numerical routine is used to match $\beta$ to the Mott transition scaled $\alpha_{0,0}$.

$$m^* = m_e \frac{\left(m_\perp + 2m_\parallel\right)}{3} = 0.453 m_e \qquad (3.69)$$

$$E_{1S,hydrogen} = \frac{\alpha_{0,0} m^* e^4}{32\pi^2 \epsilon_r^2 \epsilon_0^2 \hbar^2} \qquad (3.70)$$

The energy equation, 3.70, is then shown in SI unit form.

$$E_{1S} = \frac{m_\perp e^4}{32\pi^2 \hbar^2 (\epsilon_r \epsilon_0)^2} \left\{ \frac{1}{3}\alpha_{0,0}^2 \left(\beta + 2\right) - \frac{2\alpha_{0,0}}{\left(1 - \frac{\gamma}{\beta}\right)^{\frac{1}{2}}} \arcsin\left(\left(1 - \frac{\gamma}{\beta}\right)^{\frac{1}{2}}\right) \right\} \qquad (3.71)$$

These different estimates of the $1S(A_1)$ energy are then compared to those experimentally measured[94], in table 3.8. This is a comparison of the energy that a scaled hydrogenic and an EMT scaled $1S$ ground state would have to give the Mott transition Bohr radii.

As can be seen the estimates do not come remotely close to the experimentally measured values, while at the same time being close to each other; this indicates that the spherical to prolate models are close, which was already known as one is simply the scaling of the other along the silicon $z$ axis. The large experimentally measured ground state binding energy, and the small size of the Mott transition scaled $\alpha_{0,0}$, indicate that the ground state wavefunction is small and closely packed to the nucleus. Thus the estimated energy is grossly incorrect in precisely the

| Estimation Method | $\alpha_{0,0}$ | $\beta$ | Binding Energy meV) |
|---|---|---|---|
| Scaled Hydrogenic | 0.0708 | 1 | 3.19 |
|  | 0.0946 | 1 | 4.26 |
| EMT | 0.0708 | 1 | 3.23 |
|  | 0.0946 | 1 | 4.27 |
|  | 0.0708 | 62.3 | 2.03 |
|  | 0.0946 | 45.9 | 2.70 |

Table 3.8.: Comparison of the calculated energies of the $1S(A_1)$ ground state. For all energies the Bohr radii are obtained from both the upper and lower bounds for Mott transition. *Scaled hydrogenic* are simply uniformly scaled hydrogen energies, with the average effective mass and dielectric permittivity of silicon. The *EMT* values are those calculated by equation 3.71; $\beta$ being set to 1 means that the prolate scaling of the wavefunction is determined purely by the effective masses in each direction, while the other betas are scaled so that the Mott Bohr radius and $\beta$ value obey the minimisation conditions of the EMT 1S energy equation. Experimentally measured energies: selenium [94] 318.32meV and sulphur [94] 306.63meV.

circumstances in which the model is not valid. More specifically this highlights the breakdown of the one over $r$ donor potential at an extreme short distance from the donor nucleus.

There is then an additional factor for double donor systems which must be considered. Firstly, the accuracy of the effective mass model for non-ground states is shown in references [115][8][107][94]. Secondly, the degeneracy of the ground state is two, due to spin, and thus both donor electrons can be in the ground state at the same time. Then one can accept, via the arguments above, or assume, that the ground state electrons are extremely close to the nucleus, and thus any interaction between a ground state and non-ground state electron is minimised due to a small overlap. Thus the higher excited state energies, despite ignoring donor-donor interactions, are reasonably accurately predicted.

## 3.7.3. EMT Transition Rates

With the sets of parameters now obtained, calculations of the $2P_0$ and $2P_{\pm 1}$ to $1S(A_1)$ transition rates for atomic selenium donor complexes can proceed. There are three possible rates, each with different parameters.

Firstly, the simple hydrogen model can be used. This is where the donor states are treated as just being scaled hydrogen wavefunctions. The same EMT dipole matrix elements are used for this, albeit when the $\beta$ and $\gamma$ parameters are set to 1, while the effective mass is treated as being the vector average of the perpendicular and parallel masses in silicon at the conduction band minima.

There is then a second category of possible transition rates. For this the $2P_0$ and $2P_{\pm 1}$ parameters are set to those obtained by EMT energy minimisation calculations.

Thirdly, $1S$ state can be scaled via the Mott semiconductor to metal transition. The $2P_0$ state is then scaled via EMT variational calculations.

It must be noted that for all transition rate calculations the $\beta$ parameter must be the same for the initial and final states. This is because this parameter is part of the EMT hamiltonian, therefore each $\beta$ has a separate set of eigenfunctions.

For all possible transition rates, there are factors other than the dipole matrixes that must be considered. Fermi's golden rule for effective mass state transitions from equation 3.56 is restated below in equation 3.72. Here it can be seen that there is a factor in common for all transition rates, followed by the angular frequency cubed, the symmetry weighting vectors, relative degeneracy factors of the states, and then the final term is the dipole matrix element squared.

$$\Gamma_{i,j} = \frac{e^2 \epsilon_r^{\frac{1}{2}}}{3\epsilon_0 \hbar c^3 \pi} \omega_{i,j}^3 \frac{g_j}{g_i} \left(\vec{C}^{j*} \cdot \vec{C}^i\right)^2 \left( |\langle F_0^j |x| F_0^i \rangle|^2 + |\langle F_0^j |y| F_0^i \rangle|^2 + |\langle F_0^j |z| F_0^i \rangle|^2 \right)$$

$$(3.72)$$

**3.7.3.1.** $2P_0 \to 1S$

For all ways of calculating the $2P_0$ to $1S(A_1)$ transition there are several factors in common that can be calculated before the dipole element is considered.

Firstly, the relative degeneracies of the states are $g_j = 6$ for $2P_0$ and $g_k = 1$ for $1S(A_1)$, this ignores spin degeneracy because it is common to all states and thus cancels out; note that the $1S$ states in total have 6 states, due to the 6 conduction band minima in silicon, but the symmetry splitting forces the ground state to be isolated.

Secondly, using the weighting vectors from equation 3.31, the dot product of the symmetry weighting vectors of the $2P_0$ and $1S(A_1)$ states is:

$$
\begin{aligned}
C^{\vec{2P_0}} \cdot C^{1\vec{S}(A_1)} &= \frac{1}{\sqrt{6}}(1,1,1,1,1,1) \cdot \left[ \frac{1}{\sqrt{6}}(1,1,1,1,1,1) \right. \\
&\quad \left. + \frac{1}{2}(2,2,-1,-1,-1,-1) + \frac{1}{\sqrt{2}}(1,-1,1,-1,1,-1) \right] \\
&= \frac{1}{\sqrt{6}}(1,1,1,1,1,1) \cdot \frac{1}{\sqrt{6}}(1,1,1,1,1,1) \\
&= 1
\end{aligned}
$$

$$(3.73)$$

Thirdly, the experimentally measured energies can be used to obtain $\omega_{1S(A_1),2P_0}$. The values are taken from [94], thus $\omega_{1S(A_1),2P_0}$ is:

$$E_{1S,2P_0} = -11.49 + 306.63 = 295.14 meV$$

$$\omega_{1S,2P_0} = \frac{E_{1S,2P_0}}{\hbar}$$

(3.74)

Fourthly, all other quantities are then physical constants. Assessing the dipole matrix elements is then done using equation 3.57. The dipole elements, parameters, and final transition rates for the different models are collated in table 3.9.

| $2P_0$ | $1S(A_1)$ | $\beta$ | $\alpha_{0,0}$ | $\alpha_{1,0}$ | $\Gamma_{1S(A_1),2P_0}$ $10^4 s^{-1}$ | Lifetime $ns$ |
|---|---|---|---|---|---|---|
| Hydrogenic | Hydrogenic | 1 | 2.61 | 1.01 | 3.600 | 27600 |
| Hydrogenic | Mott 1 | 1 | 0.0708 | 1.01 | 1550 | 64.7 |
| Hydrogenic | Mott 2 | 1 | 0.0946 | 1.01 | 2460 | 40.6 |
| EMT | EMT | 0.61 | 1.35 | 1.76 | 8130 | 12.3 |
| EMT | Mott 1 | 0.61 | 0.0708 | 1.76 | 5900 | 16.9 |
| EMT | Mott 2 | 0.61 | 0.0946 | 1.76 | 11000 | 9.09 |

Table 3.9.: The dipole matrix elements and transition rates for the 3 different methods. All values are only given to 3 significant figure accuracy, except for $\beta$ which is given to only 2 significant figures so as to be in agreement with all variational energy calculations. **Hydrogen:** Using naively scaled hydrogen wavefunctions to match the energy. **EMT:** Effective mass theory variationally scaled prolate ellipsoid hydrogenic wavefunctions. **Mott:** Mott transition scaled $1S(A_1)$ states, with 1 and 2 corresponding to the donor concentrations of 1.8 and $4.3 \times 10^{20} \text{cm}^{-3}$ respectively.

From table 3.9 it can be clearly seen that all rates are of the order of $1 - 100$ ns, except for that of that of the hydrogen to hydrogen scaled states where the large lifetime is entirely due to the larger scaling $\alpha_{0,0}$ in the dipole element. Consequently these are assumed to be of questionable veracity in comparison to the other lifetimes.

**Transition Dipole Matrix Element As $\gamma$ Varies**

It is of interest to calculate what the transition rate is for the $2P_0$ to $1S$ EMT states as a function of $\gamma$, the ratio of the perpendicular to longitudinal effective masses. However, the transition rate depends not only on $\gamma$ but on the specific

effective masses, along with the relative dielectric permittivity of the material. For this reason, the unitless dipole matrix element for the transition is calculated as a function of $\gamma$ instead; here the dipole element is not only unitless as for the EMT states elsewhere in this thesis, but is divided by the additional factor of $e^2$. These calculations are shown in figure 3.5.
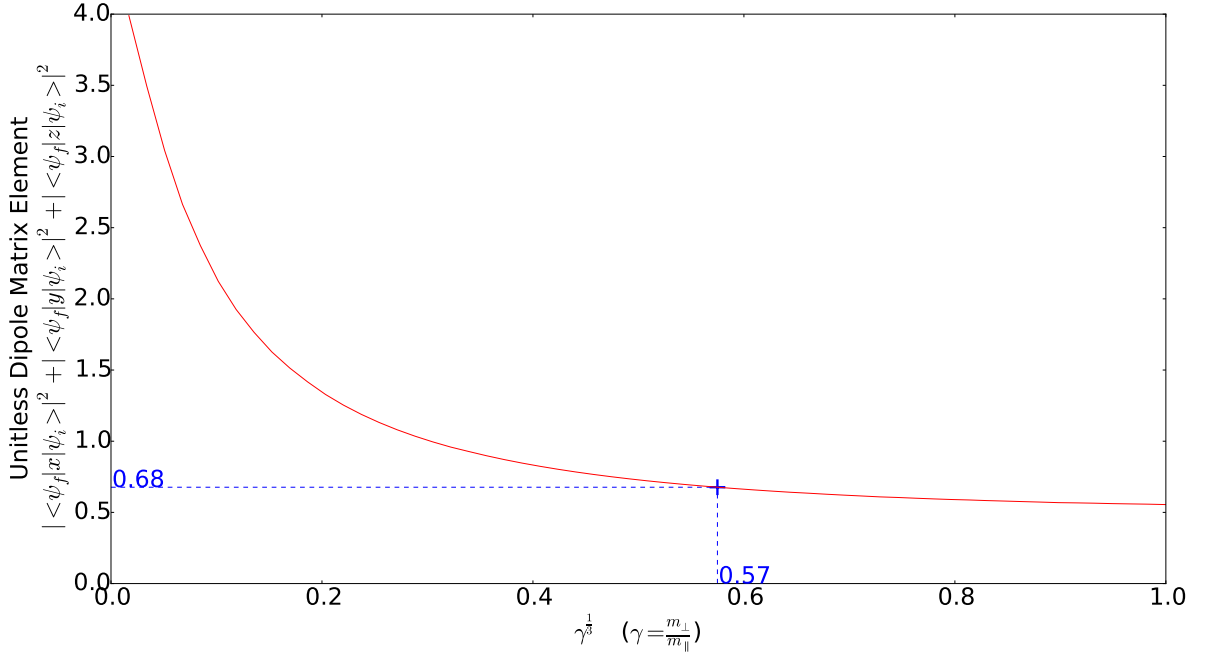


Figure 3.5.: The unitless dipole matrix element for the EMT $2P_0$ to EMT $1S$ transition plotted against $\gamma$, the ratio of perpendicular to parallel effective mass; the $1S$ state is not scaled by the Mott criteria here The values for $\gamma^{\frac{1}{3}}$ and the unitless dipole matrix element in silicon are highlighted by an upright blue cross with dashed blue lines to the two axis; at this point $\gamma = 0.19$ for silicon. The y axis is the unitless dipole matrix element divided by $e^2$, where $\psi_i$ and $\psi_j$ are the initial and final states respectively. The x axis is the $\gamma$ ratio of the effective masses to the third root.

**3.7.3.2.** $2P_{\pm 1} \rightarrow 1S$

Following the same procedure as for the $2P_0$ transition rate calculations, the common factors for $2P_{\pm 1}$ are listed below. Firstly, the relative degeneracies of the states are $g_j = 12$ for $2P_{\pm 1}$ and $g_k = 1$ for $1S(A_1)$, this again ignores spin degeneracy. The $2P_{\pm 1}$ state has twice the number of states as the $2P_0$ due to a set of 6 from the plus

and 6 from the minus $m$ states; this is in effect two separate states with the same energy, wavefunction and thus transition rate.

Secondly, and unfortunately, the $T_2$ representation of the $T_d$ symmetry group using the effective mass states as a basis has not been calculated by the present author. Thus the assumption has been made that, like the $2P_0$ state, the symmetry weighting vectors dot product is 1; $C^{2\vec{P}_{\pm1}}.C^{1\vec{S}(A_1)} = 1$.

Thirdly, and as before, the experimentally measured energies are used to obtain $\omega_{1S(A_1),2P_{\pm1}}$. The values are taken from [94], thus $\omega_{1S(A_1),2P_{\pm1}}$ is given by:

$$E_{1S,2P_{\pm1}} = -6.39 + 306.63 = 300.24 meV$$
$$\omega_{1S(A_1),2P_{\pm1}} = \frac{E_{1S,2P_{\pm1}}}{\hbar}$$

(3.75)

Fourthly, all other quantities are then physical constants,and assessing the dipole matrix elements is done using equation 3.58. The dipole elements, parameters, and final transition rates for the different models are then collated in table 3.10.

| $2P_{\pm1}$ | $1S(A_1)$ | $\beta$ | $\alpha_{0,0}$ | $\alpha_{1,1}$ | $\Gamma_{1S(A_1),2P_{\pm1}}$ $10^4 s^{-1}$ | Lifetime $ns$ |
|---|---|---|---|---|---|---|
| Hydrogenic | Hydrogenic | 1 | 2.61 | 0.753 | 1.34 | 74700 |
| Hydrogenic | Mott 1 | 1 | 0.0708 | 0.753 | 4680 | 21.4 |
| Hydrogenic | Mott 2 | 1 | 0.0946 | 0.753 | 6650 | 15.0 |
| EMT | EMT | 0.61 | 1.35 | 1.18 | 7420000 | 135 |
| EMT | Mott 1 | 0.61 | 0.0708 | 1.18 | 50900000 | 19.6 |
| EMT | Mott 2 | 0.61 | 0.0946 | 1.18 | 85200000 | 11.7 |

Table 3.10.: The dipole matrix elements and transition rates for the 3 different methods. All values are only given to 3 significant figure accuracy, except for $\beta$ which is given to only 2 significant figures so as to be in agreement with all variational energy calculations. **Hydrogenic:** Using naively scaled hydrogen wavefunctions to match the energy. **EMT:** Effective mass theory variationally scaled prolate ellipsoid hydrogenic wavefunctions. **Mott:** Mott transition scaled $1S(A_1)$ states, with 1 and 2 corresponding to the donor concentrations of 1.8 and $4.3 \times 10^{20} cm^{-3}$ respectively.

Table 3.10 shows that all transition rates are between $1 - 135$ ns, except for that of that of the hydrogen to hydrogen scaled states where the large lifetime is entirely due to the larger scaling $\alpha_{0,0}$ in the dipole element. Consequently these are also assumed to be of questionable veracity in comparison to the other lifetimes, as for the $2_0$ transitions.

**Transition Dipole Matrix Element As $\gamma$ Varies**

It is also of interest to calculate what the transition rate is for the $2P_{\pm 1}$ to $1S$ EMT states as a function of $\gamma$. As discussed in the $2P_0$ section, the transition rate depends other factors than $\gamma$: the specific effective masses, the relative dielectric permittivity. Therefore, the unit-less dipole matrix element is calculated as a function of $\gamma$; here the dipole element is unitless as for the EMT states and is divided by $e^2$. The calculations for the $2P_{\pm 1} \rightarrow 1S$ transition is shown in figure 3.6.
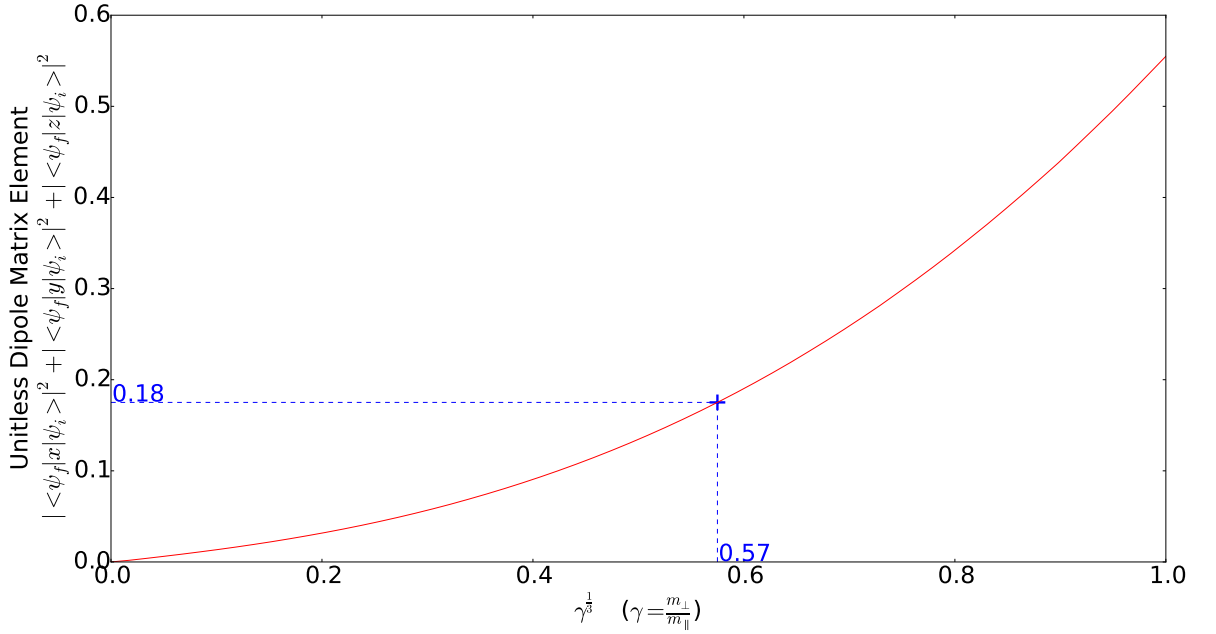
Figure 3.6.: The unitless dipole matrix element for the EMT $2P_{\pm 1}$ to EMT $1S$ transition plotted against $\gamma$, the ratio of perpendicular to parallel effective mass; the 1S state is not scaled by the Mott criteria here. The values for $\gamma^{\frac{1}{3}}$ and the unitless dipole matrix element in silicon are highlighted by an upright blue cross with dashed blue lines to the two axis; at this point $\gamma = 0.19$ for silicon. The y axis is the unitless dipole matrix element divided by $e^2$, where $\psi_i$ and $\psi_j$ are the initial and final states respectively. The x axis is the $\gamma$ ratio of the effective masses to the third root.

# 4. Experimental Methods

## 4.1. Introduction

This chapter contains descriptions of the methods and procedures used for the two forms of experimental measurement performed for this thesis. Firstly, absorbance spectroscopy using a Fourier transform spectrometer is explained. While secondly, and building on the first experiment, step scan Fourier transform spectroscopy is explained; the Si:Se emission measurement is then elaborated in detail. Thirdly, a brief description of the experimental equipment used is given where relevant; for commercially purchasable "off the shelf" components, an extremely brief description, part number, and directions to the manufacturers website are given.

The simplest description of spectroscopy is as the study of the EM spectrum, a measure of intensity as a function of photon energy; spectra are often given in other linearly related quantities, frequency or wavenumber. The choice of scale is usually determined by relation to the measurement technique; for example when wavenumbers $cm^{-1}$ are used to express the spectrum from an FTS measurement, because a physical mirror has moved a distance of some cm.

In order to measure a spectrum one must exploit the fundamental property that is common to all waves, interference. There are then two main spectroscopy techniques, FTS and dispersive spectroscopy; both rely on the property of interference, albeit in

superficially different ways. A dispersive spectrometer requires a diffraction grating with spacings, this must be on order of the wavelength of the light measured in the spectrum. The resulting interference pattern separates the light by wavelength intrinsically creating a spectrum; diffraction gratings for the InfraRed (IR) spectrum are historically difficult to make. However, an FTS does not require a grating, moving a mirror to obtain its interference pattern and has several other advantages other a dispersive system.

In the measurements described here only FTS is used, this involves measuring an interference pattern and taking its FT to obtain the spectrum. For this a vertex 80v spectromter is used, this is allows the measurement of the intensity of a electromagnetic radiation as a function of the photon wavenumber $cm^{-1}$; wavenumbers and the wavelength, in cm, are inversely related. The specific methods of using such a spectrometer, to obtain both time independent and dependent spectra, are briefly discussed here; along with the experiments carried out for this thesis, and how FTS was a vital part of them.

## 4.2. FTIR Rapid Scan Spectroscopy

The FTS rapid scan technique is explained in brief; for more details read appendix C. This is done via reference to a diagram, figure 4.1, in the list below.
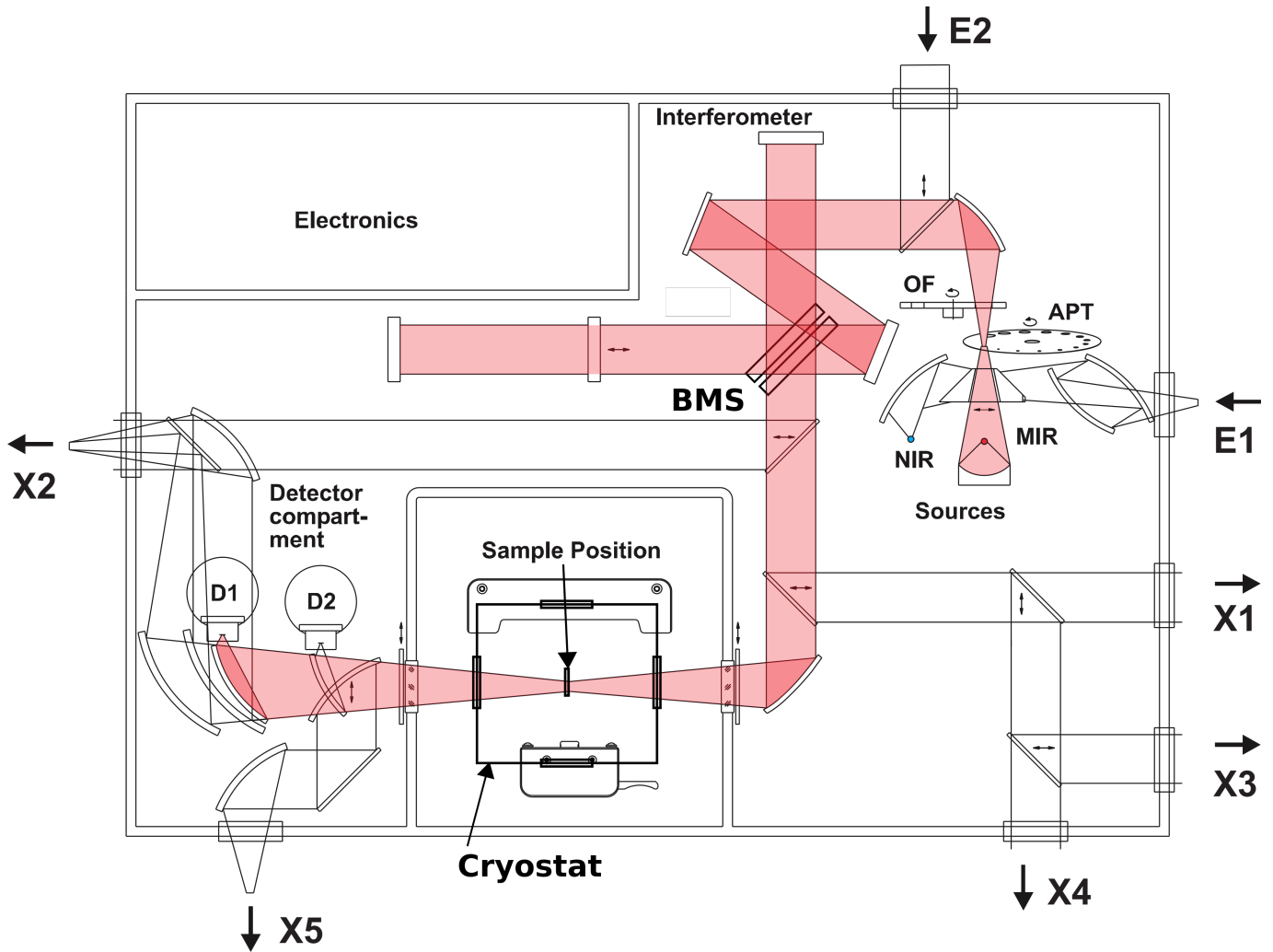
Figure 4.1.: Absorbance Experiment set-up using a Brüker Vertex 80V Fourier Transform spectrometer (for details see [126]). Beam path is highlighted in partially transparent red. **E** labels refer to light input ports. **X** labels then refer to light output ports, where an external detector may be used. Each input or output port can be fitted with a window, this is selected specifically for optical transmission characteristics to fit a particular measurement. **NIR** is a near-infrared lamp. **MIR** is a mid-infrared globar lamp. **BMS** is a beamsplitter, selected for the wavenumber range of what is being measured. **APT** is an optical aperture selector, to control lamp intensity and beam size. **OF** is a optical filter wheel. The spectrometer diagram is based upon that in [127, fig 19].

- Light is emitted by a source, either Near InfraRed (NIR) or Mid InfraRed (MIR), and focused through an aperture and beam offset selector. The default sources for the vertex 80v are a tungsten halogen lamp for visible to NIR, and a globar, a "shaped silicon carbide piece"[127], for MIR.

## 4. Experimental Methods

- The light is collimated by a parabolic mirror and directed into the interferometer section of the spectrometer.

- The interferometer is a Michelson interferometer: aBeam Splitter (BS) directs the input light down two separate and perpendicular beam paths of a similar length, the beam's then recombine again at the BS. The mirror at the end of one of the beams paths moves to change the path length; the other path is of fixed length.

- The recombined beams exits the interferometer and are focused onto the sample position. The Optical Path Difference (OPD) of the separate and perpendicular beam paths determines the wavelength dependent intensity at the sample; this is caused by the interference of the two split beams, as they are out out phase due to their different beam distances.

- Finally, the light exiting the sample is focused onto a detector element. A helium neon guide laser, at $\lambda = 632$nm, runs along the same beam path as the measured light. As the OPDof the two beam paths in the interferometer change, the interference fringes of the HeNe are measured; this allows the OPD to be measured. The intensity as a function of OPD is digitized, and this forms the interferogram.

The key part of the spectrometer is the interferometer, in this the input light is split into two perpendicular beams of equal intensity by the BS. Of these two beams one travels a fixed distance to a mirror, while the distance to the other is variable; this introduces a path length difference between the beams. Once reflected by their respective mirrors, the two beams are recombined at the BS; half of the combined beam intensity is then directed back out in the direction they entered the spectrometer, while the other half continues on in their original direction. Because of the wave nature of light, the combined beam exhibits constructive or destructive

interference; this depends upon the path length difference, and the wavelengths of light present in the beam.

Assuming that the input light is of constant intensity and spectral composition, by scanning the movable mirror and measuring the detector signal as a function of the OPD an interferogram is built up. An example interferogram for an ideal mono-chromatic light source at wavenumber position $\nu$, where $I(\delta x)$ is the interferogram, $\delta x$ is the optical path difference, or twice the mirror position difference, in cm and $A_0$ is the amplitude, is shown below:

$$\nu = \frac{2\pi}{\lambda_{cm}}$$
$$I(\delta x) = \frac{A_0^2}{2}\cos(\nu\delta x)$$

(4.1)

By taking the Fourier transform of the interferogram a spectrum is obtained, where $S(\nu)$ is the spectrum, shown below:

$$S(\nu) = \int_{-\infty}^{\infty} I(\delta x)e^{2\pi i\nu\delta x}d\delta x = \frac{A_0^2}{2}$$

(4.2)

Of course, in reality the mirror cannot be moved from minus to plus infinity to satisfy the Fourier transform; this gives rise to spectral leakage, discussed in appendix C.

## 4.2.1. Absorbance Spectroscopy

Now that the measurement of a spectrum has been outlined, the measurement of an absorbance spectrum can be described. Firstly, a background spectrum is measured using the experiment set-up of figure 4.1; for a background spectrum there is no

sample, only the lamp light spectrum is measured. Secondly, the sample is placed in the sample position, and the spectrum of light that can pass through the sample unabsorbed is measured. The sample temperature is controlled as described in section 4.4.1.2.

The transmittance of the sample is then defined as $T(\nu)$ in equation 4.3; where $S(\nu)_B$ and $S(\nu)$ are the background and sample spectra respectively. Absorbance is then defined as the negative base ten logarithm of the transmittance.

$$T(\nu) = \frac{S(\nu)}{S(\nu)_B} \tag{4.3}$$

$$A(\nu) = -\log_{10}(T) \tag{4.4}$$

## 4.3. Time Resolved Spectroscopic Measurements

Time resolved measurements are a conceptually simple, but practically difficult extension of conventional rapid scan FTS; one example of rapid scan FTS is the absorbance measurement described in 4.2. In order to obtain the time evolution of a spectrum, an interferogram as a function of time must first be measured.

In conventional rapid scan FTS, to obtain an interferogram one mirror is moved continuously; this gives rise to a detector signal that changes as a function of mirror position, and assuming predictable movement speed, of time as well. However, because movement through the full mirror range will not occur instantly, a time changing real spectrum will cause a resulting interferogram that mixes data from

different points along its time evolution. Taking the Fourier transform of this will result in no further spectral information, only if the time evolution of the spectrum is already known can it be reconstructed; this makes rapid scan a useless technique for measuring spectra that change over the measurement time.

Step scan time resolved FTS avoids the problems of rapid scan by making the mirror movement no longer constant. The mirror is instead discretely stepped between points, at each it is kept stationary while the detector signal is measured as a function of time. This is repeated for every discretised data point along the OPD axis in the corresponding rapid scan measurement; this gives a 2D grid of detector signal position, where one axis is time and the other is mirror position (OPD). This is a set of time separated interferograms. Taking the FT of each interferogram then yields a set of time resolved spectra, each one a snapshot of the spectrum at a particular time, in the same manner as for the rapid scan method. This is shown in diagrammatic form in figure 4.2.

A challenge for this type of experiment is that it must be repeated for every point in the interferogram, this can easily amount to thousands of repeats without even considering averaging to reduce random signal noise. A further problem is managing the recording of the detector signal at precise ns intervals, while synchronising this acquisition with the experiment repetition.
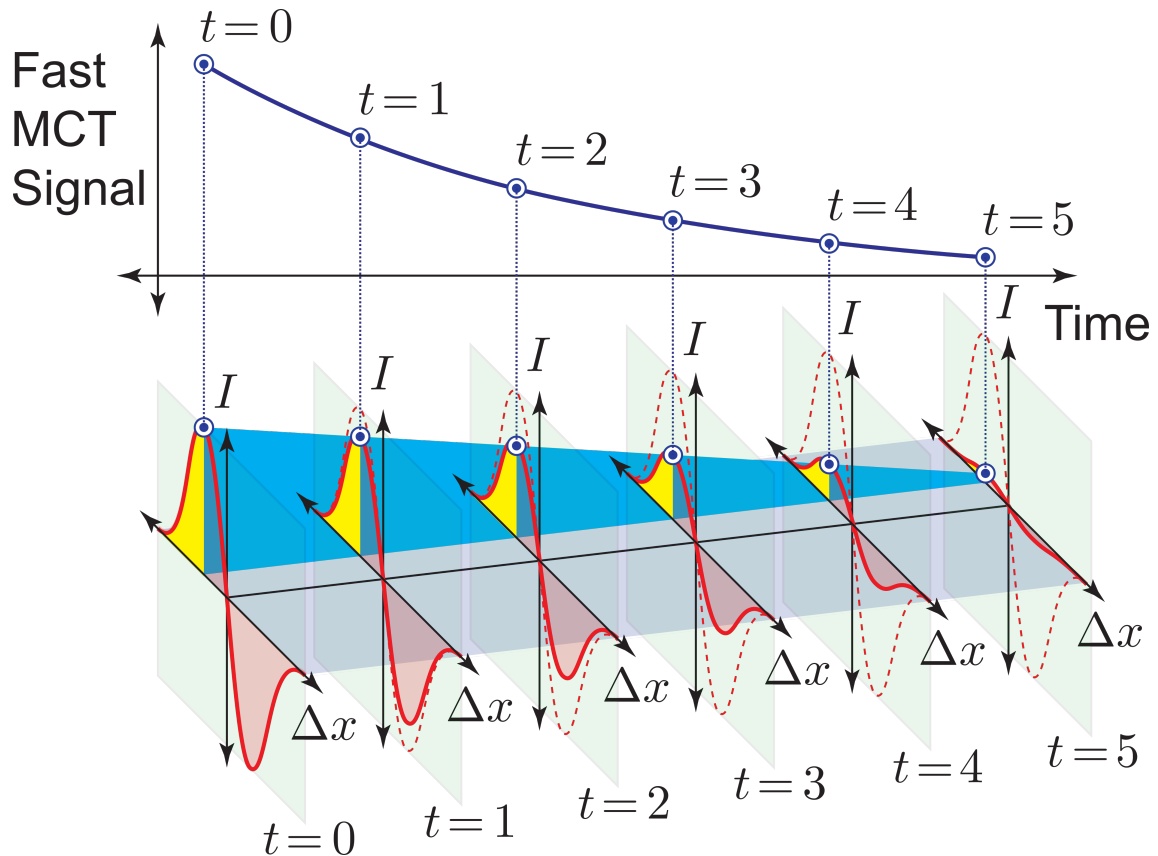
Figure 4.2.: Diagram of step scan operation. **Top:** Detector signal as a function of time. **Bottom:** Time evolution of the reconstructed interferogram; here $I$ is the measured light intensity, and $\Delta x$ the mirror position. This figure was created by S. A. Lynch and is reproduced here with permission.

## 4.4. Time Resolved Si:Se Emission

Now that step scan time resolved FTS has been reviewed, the measurement of emission from a Si:Se sample can be described. This experiment is a time resolved measurement of emission from a Si:Se sample, following optical pumping at 1220nm by a 5ns laser pulse. It is shown diagrammatically in figure 4.3.
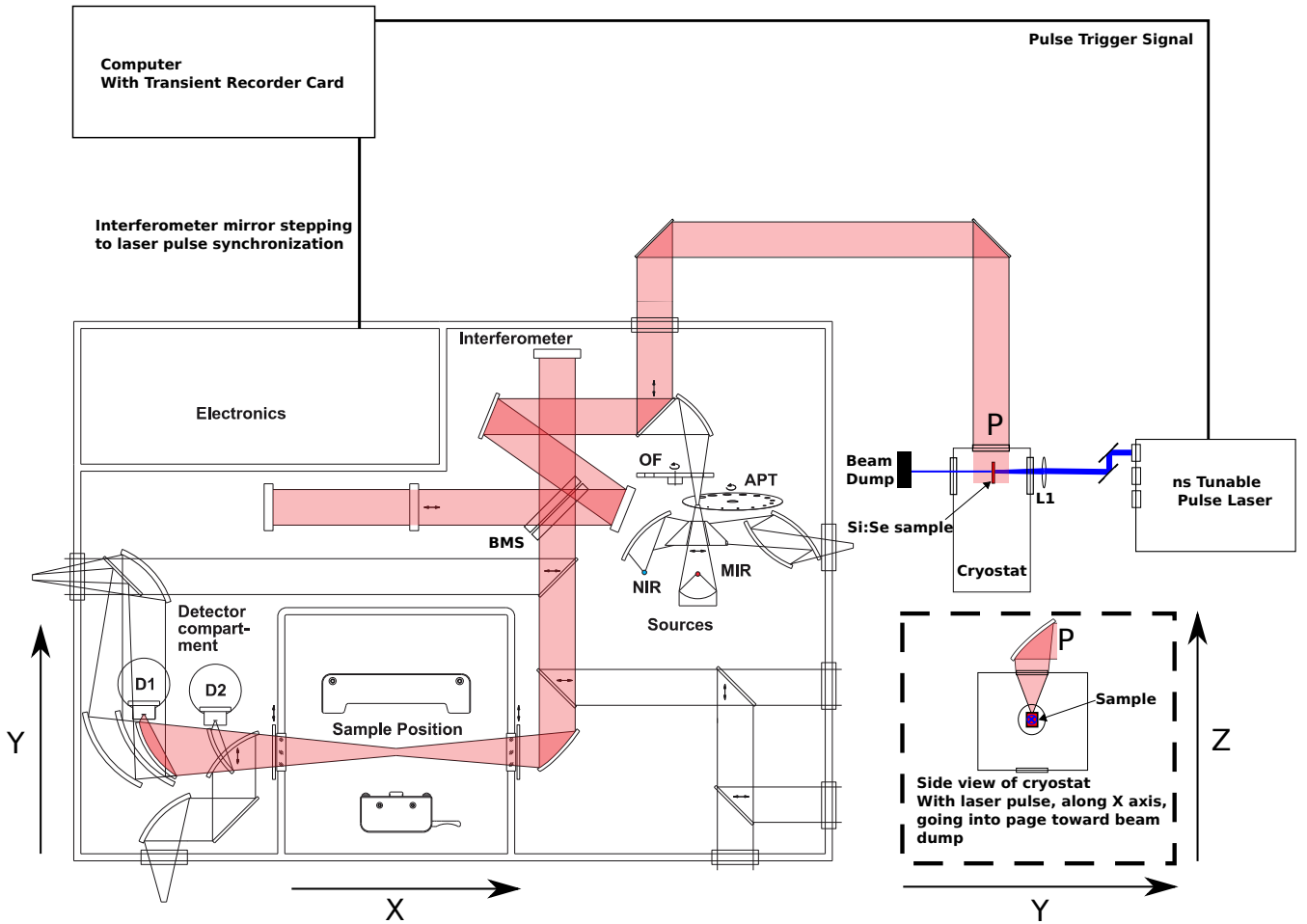
Figure 4.3.: Transient Emission Experiment. The dashed inset shows the cryostat 90 degrees relative to the main figure, the P label marks the same position in both inset and main diagrams, and the X,Y,Z axes are labelled in both. L1 is a $CaF_2$ lens with a focal length of 10cm[128] . Above the cryostat at point P, is an gold off axis parabolic mirror[129].

**Extra Details for Figure 4.3**

From figure 4.3, there are additional details about the specific pieces of equipment used: The ns tunable pulse laser is an Ekspla NT342B-10-DGF-AW [130]. Mirrors used to direct the laser are Thorlabds aluminium mirrors [131]. Thorlabds planar gold mirrors [132] direct the collimated emission from the sample (the gold off axis parabolic mirror mentioned in the figure does the collimating of the isotropic emission from the Si:Se sample). The spectrometer emission input window as well as

the BS are Kbr[133]. The transient recorder card is a Spectrum m3i4142EXP. Finally the signal is measured by a HgCdTe 1mm infra-red photovoltaic detector. The internal spectrometer diagram is based upon that in [127, fig 19].

**Experimental procedure**

The emission experiment proceeds as follows:

- The pump laser emits 1220nm, 8197cm$^{-1}$, pulses at a rate of 10 Hz; each pulse sends a trigger signal to a Spectrum m3i4142EXP transient controller card. Pulses have approximately 7.5 mJ per pulse, lasting for between 3ns and 5ns.

- Planar aluminium mirrors direct the laser pulses to a $CaF_2$ focusing lens with a focal length of 10cm. This is positioned so as to concentrate the laser pulse more strongly upon the sample. However, the laser is not focused upon the sample as this would probably damage it.

- The laser pulse passes through a $CaF_2$ window of the cryostat, and is incident upon the sample.

- Fluorescent emission from the sample spreads out, presumably in all directions, and passes through the $CaF_2$ cryostat windows.

- Emission passing out of the top of the cryostat is then collimated by a gold off axis parabolic mirror.

- The collimated emission beam is directed by gold planar mirrors through a Kbr window at the back of the spectrometer.

- The emission beam passes through the interferometer, and is focused upon the active element of a HgCdTe fast photovoltaic detector; the mirror position remains stationary during this.

- Upon receiving a trigger pulse from the laser the transient recorder card does one of three things: Firstly, it commences recording the detector signal every 2.5ns for 400 data points, this covers 1 $\mu$s. Secondly, the time measurement is repeated, for a total of 32 times, and thus 32 trigger pulses are required. Thirdly, if all 32 time measurements at the current mirror position have occurred, then the mirror is finally stepped to the next position. The mirror is then left to settle for at least 40ms, before the next trigger pulse begins the next measurement; if the next trigger pulse occurs before 40ms then it is the second pulse that begins the measurement.

- Following the mirror stepping, the next trigger pulse causes the first of 32 measurements at the new mirror position. There are then 242880 total pulses, for 7360 interferogram points, and including the mirror stepping time, this gives a total time of six and three quarter hours as an estimate of the measurement time; in reality the measurements took roughly twice this long, it is assumed because the mirror movement and stabilization wait took longer than a single pulse(0.1s), thus doubling the number of trigger pulses required.

A series of the emission experiments described above were performed, each with a different sample temperature. The temperatures used were 10K, 80K, and 300K.

## 4.4.1. Experiment Components

The step scan measurement outlined above is performed with several specific settings, described one by one here.

### 4.4.1.1. Pump Laser

The Ekspla NT342B-10-DGF-AW laser is a tunable wavelength laser. It has three output ports, in total covering the wavelength ranges 410nm to 2600nm; output at

355nm is also possible. A 1064 nm fundamental laser, in conjunction with second and third harmonic generation crystals an optical parametric amplifier and a difference frequency generator, gives the wide wavelength range of the output.

For the time resolved emission experiment the laser pump power output at 1220 nm was measured, this was done by a Coherent Fieldmax 2 laser power meter; 20 repeats were take to give an average of 7.61 mJ per pulse, with a pulse to pulse standard deviation of 0.25 mJ. This measurement of the pulse power was taken immediately before the 10K emission data acquisition began. The duration of the pulse was not measured, as it is below the response time for the fastest detector available in the laboratory at that time; the pulse duration is nominally 3-5 ns [130]. Finally the laser repeats at a rate of 10 Hz, and at each pulse a trigger signal is sent to the transient recorder card.

### 4.4.1.2. Cryostat and Cooling

The cryostat was evacuated to a pressure of approximately $10^{-5}$ mbar, as measured by an Edwards vacuum AIM-X-NW25 gauge [134]. The low pressure was necessary to allow cooling of the samples, as without a vacuum inside the cryostat the ambient heat would leak in and prevent useful cooling. The vacuum was achieved by a combination of an Oerlikon Leybold turbo pump; for low temperatures, 10K, the condensation or adhesion of atmosphere to the cryostat walls may have also contributed to lowering the pressure.

Both absorbance and emission experiments require temperatures in the 4-300 K range. Each sample is held at the end of a cold finger inside a custom flow cryostat; this is similar to those sold by Oxford instruments [135]. An Oxford Instruments iTc Mercury [136] temperature controller and associated sensor is used measure the temperature, while a resistor based heating element again controlled by the Mercury

iTc was used to heat the sample.

To provide the necessary cooling both a constant flow of liquid helium, and a ColdEdge Technologies Stinger pulsed tube cryo-cooler were used. The absorbance data used constant flow, while the Si:Se emission experiment required the cryo-cooler. A recirculation of a fixed amount of helium requiring only constant power to function, helped in enabling the longer step scan emission experiment.

### 4.4.1.3. Spectrometer Settings

The nominal spectral resolution of the emission measurements was $20cm^{-1}$, giving a mirror movement distance of 0.05cm in the interferometer. However, the interferogram was taken as fully double sided, thus the mirror was moved between plus and minus 0.05 cm with respect to the zero path difference position. Because of dispersion, the optical path difference is not constant for all frequencies of light in the spectrum; upon taking the FT of a single sided interferogram with such artefacts an incorrect spectrum results.

By measuring a double sided interferogram a complex spectrum occurs instead of a purely incorrect one, with the error now represented by the angle between the real and imaginary components. Thus these are called phase errors and can be corrected, see appendix C.2.5.3. This means that the true mirror movement distance was 0.1cm. In addition it should be noted that a much higher resolution is possible with the Vertex 80v system, which has a maximum of $0.075cm^{-1}$ for a total possible mirror movement of 13.33cm. However, as the experiment must be repeated 32 times at each mirror position, higher resolutions would cause a prohibitively long measurement time.

A spatial sampling rate of $15798cm^{-1}$ was used; this gives, via the Shannon sampling

theorem D.3.1.1, a possible measurement spectral range of 7899 cm$^{-1}$. This means that the mirror was stepped between 15798 positions per cm, for a total of 1580 interferogram points; the resulting spectrum will also have this many points in total, although this will cover the positive and negative frequency ranges giving only half as many points in the usable spectrum.

A KBr BS was used, with a spectral range of 350cm$^{-1}$ to 8000 cm$^{-1}$ [127]; this is a good fit with the Shannon sampling rate determined possible spectral range of 7899cm$^{-1}$.

### 4.4.1.4. Transient Recorder Card

A key component in the step scan measurement is a Spectrum m3i4142EXP transient recorder card. This allows the measurement of the amplified detector output voltage at 2.5 ns intervals. The input voltage range for the measurements carried out was $\pm$ 500mV, giving a 1V dynamic range. The card has 14 bits to discretise the dynamic range, however, due to random noise, in practice the card had only 12 bits[137]. Thus there are $2^{12} = 4096$ different measurable discrete intensity positions for the detector output. At each trigger pulse from the pump laser this card begins the measurement of the 400, 2.5ns separated, detector voltage values for each interferometer mirror position. This is controlled by a computer running Windows 7 and using the Brüker OPUS spectrometer control software.

### 4.4.1.5. Detector and Amplifier

A Kolmar model MCP0393 photovoltaic detector with a 1mm HgCdTe element was used, its active element requires cooling to liquid nitrogen temperatures to function. The detector is reverse biased by 50mV in order to increase the response speed, this gives an approximate signal rise time of 20ns and a exponential fall lifetime of 40ns. The amplifier and reverse biasing circuit of the Kolmar detector used

are not standard; the standard amplifier was found to be incapable of matching the detector response time of 40ns. Instead a Pasternack PE15A1007 microwave frequency amplifier is connected to the detector SMA output, with a Picosecond Pulse Labs PSPL5575A[138] bias tee to facilitate the 50mV reverse biasing of the detector without affecting the amplifier. A detector and amplifier circuit sketch is shown in figure 4.4.
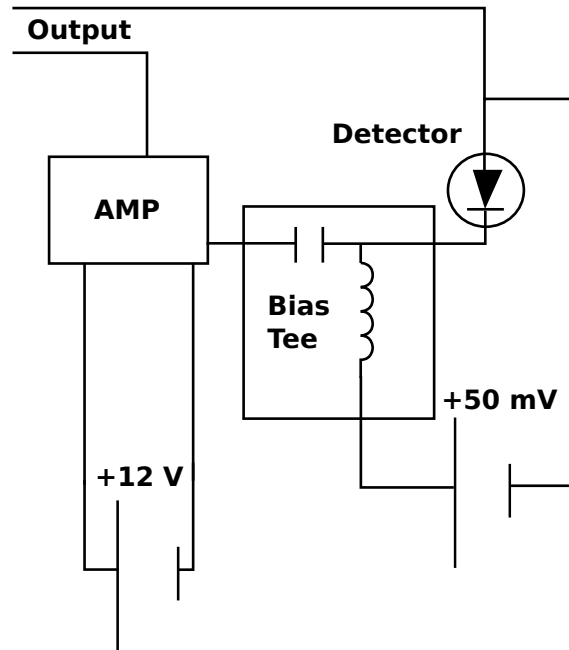


Figure 4.4.: Circuit sketch of the detector amplifier set-up. **Detector:** A Kolmar MCPMCP0393 photovoltaic. **Amplifier:** A Pasternack PE15A1007 microwave frequency amplifier[139]. **Bias Tee:** Picosecond Pulse Labs PSPL5575A[138]. The 12 V line is the power supply for the amplifier, while the 50 mV reverse biases the detector.

## 4.4.2. Summary

The purpose of the experiment outlined above is to measure the fluorescent emission from chalcogen doped silicon samples; this is to investigate whether they can fulfil the DiVincenzo criteria and be used to partly construct a quantum computing architecture. The radiative transition lifetimes can be obtained from fitting to the data obtained. The $2P$ to ground state transitions are the target transitions, due to being the lowest lying optically active transition; however, the full time evolution of

the emission spectrum is of interest as it is unknown.

If the measured lifetimes are longer than those of the corresponding shallow donors, e.g. phosphorus has a lifetime of 200ps [45], then chalcogen donors warrant further work. In addition the measured lifetimes can be compared to the calculated lifetimes from chapter 3, which predict 10–100ns lifetimes. If agreement is found then the EMT description of the wavefunction is approximately correct. This is important as the optical pulse area needed to construct quantum gates, section 1.2.1.2, relies upon the dipole overlap integral which itself requires the wavefunction. Without an ability to accurately predict the system wavefunction, it cannot be used in quantum computing. The extension of the modelled wavefunction in describing not only excited state energies, but transition lifetimes is then a very small step towards this.

The experiment is far from perfect. The primary problem is the slow response of the detector, 20ns rise and 40ns fall, which is just on the threshold of the predicted lifetimes. A major improvement would be moving to a faster detector, although this would require a smaller detector element; with a fixed signal intensity this would make the measurement more sensitive to random noise. Obvious candidates for improvement are then more signal averages, and measurements at a far greater number of temperatures; perhaps 5K increments would be a good place to start. If a wider range of doped samples could be obtained, perhaps with different dopant concentrations, these should also be measured; perhaps the dopant concentration has an effect upon the lifetime.

A major problem with the experiment is that the $2P$ to ground state transitions are the target, and yet non-resonant excitation is used. This was done because resonant excitation laser pulses could not be sufficiently filtered out to prevent detector saturation; even with the perpendicular beam geometry used, the stray scattered laser

light was dominant over the fluorescent emission. This can be fixed by completely changing to a time resolved pump probe experiment, although this then removes the ability to see the whole spectrum evolve in time. The pumping wavelength could also be varied, investigating the effect of pumping to higher up in the conduction band upon the measured lifetime.

# 5. Results

## 5.1. Introduction

This chapter sets out the results of spectroscopic experiments, and details their comparison to the calculations made in chapter 3.7. It is split into three main sections, with the first being a brief discussion of the measured selenium doped silicon sample. This includes sets of absorbance data of several doped silicon samples, in order to explain the selection of the sample which was measured with time resolved spectroscopy. The remaining two sections regard the energy and time axis of emission data from donor electron transitions.

For the energy axis, the transitions in the 71-8 sample are tabulated from absorbance spectra. The absorbance determined, EMT, and literature sourced measured energies are then compared; thus the energy accuracy of EMT, for excited states, is verified, along with some degree of confidence in the wavefunction parameters being established.

For the time axis, the time trace of fluorescent emission from sample 71-8, at appropriate transition energies, is analysed. The analysis is done using relatively simple exponential fitting, and yields average transition lifetimes. This experiment is the time resolved step scan Fourier transform spectroscopy fluorescence experiment, described in detail in chapter 4. The estimated transition rates, calculated by the

union of Fermi's golden rule and the EMT parameters, are then compared with fits to experimental data.

The energy and lifetime data, and the quality of agreement with the EMT model and calculated lifetimes, then allow answers to be formulated to the principal questions of this thesis. Beginning with the zeroth question, or rather the overall meta-motivation for this investigation: are there "deep" donor systems in silicon with radiative lifetimes that are sufficient to be useful qbit candidates? Unfortunately this question is not yet answered, to do so would require additional experimental work such as: demonstrating coherent control of the Rabi cycle of such donor state transitions, determining the phase coherence lifetime of the chalcogen donor systems, demonstrating arbitrary donor electron state initialisation (upon the Bloch sphere map of possible states), along with application of unitary optical quantum gates upon the system.

The zeroth question then leads to the two principal questions answered in this thesis:

- Are there are optical transitions with long radiative lifetimes in chalcogen deep double donor silicon systems?

- Do simple scaled hydrogen wavefunctions from EMT provide a good description of reality for chalcogen deep double donor electrons in silicon?

The first question is motivated by the knowledge that similar pnictogen donor systems in silicon have radiative lifetimes of $\approx$200ps[104][45][105], and a coherence lifetime of $160 \pm 20ps$[101]; for the $2P_0$ state. It is only partly answered in reduced form: Do selenium donors in silicon have longer radiative lifetimes than phosphorus? The answer is yes, and this demonstration of longer times in a selenium system merits further work.

The second question is important because the wavefunction of a system contains all the properties of that system, which can be extracted by the application of the appropriate operator. The demonstration that the EMT model can predict radiative lifetimes allows other information to be predicted, such as Rabi frequency. The answer to this is, yes but only roughly and within an order of magnitude.

There are then, of course, the follow on questions of how different chalcogen donor systems compare. Do some chalcogen donors exhibit longer lifetimes, or better agreement with the EMT model? Perhaps different doping concentrations of the different chalcogens have markedly different properties? Unfortunately these questions remain unanswered, the expansion of these measurements to other chalcogen dopants has been limited by experimental difficulty and time. But importantly some measurements have been made upon a single doped sample, out of the several samples available to the lab at the time the work for this thesis was performed. Before moving on to present and analyse the results, with answers to the two principle questions, it must be explained why the single measured sample was chosen.

It was initially intended to measure all available samples. However, the limitations, and inevitable delays and failures that accompany experimental work, mean that only a single sample has been measured using the time resolved fluorescence technique; reality had some minor disagreements with the plan to measure all.

## 5.2. Sample Selection

The experimental evidence required for this thesis can only be obtained by the analysis of the optical absorbance and fluorescent emission of a Silicon sampled doped with a deep donor chalcogen donor impurity. As is described in more detail in chap-

ter 2, donors of the chalcogen group in silicon form a substitutional double electron donor. The donor may then form one of several complexes at the substitutional site, the most common of these being the atomic and diatomic or molecular. The complexes in silicon have well defined sets of infra-red spectral lines, with a characteristic $\frac{1}{n^2}$ Rydberg like spacing that is familiar to all those who have studied hydrogenic systems. These spectral lines then correspond to transitions of the mid-bandgap, "deep donor", electron states both to each other, and from and to the conduction band of the host silicon lattice.

Absorbance measurements have been performed on many doped samples. However, only one sample has been measured with time resolved spectroscopy. The sample measured, selenium doped silicon labelled sample 71-8, had the strongest absorbance lines measured; these made it the optimal candidate for first measurement. This sample has atomic and diatomic selenium concentrations, along with boron impurity concentrations, of $5.5 \times 10^{15} cm^{-3}$ , $2.8 \times 10^{15} cm^{-3}$ and $2.0 \times 10^{12} cm^{-3}$, respectively. These doping concentrations were obtained by Y Astrov et al [140], by fitting to Hall resistivity data as described in [141] [142].

However, the Mott insulator-metal transition (see section 3.7.2) is used to scale the ground $1S(A_1)$ state in the EMT model; this is then used to estimate radiative transition lifetimes. The data used to perform the scaling is not for selenium, but rather for sulphur impurities. Thus one is faced with the question as to why measure a selenium doped sample instead? The answer is practical, because out of the few samples available the single most promising sample, with the highest doping concentration, was selenium doped. This gives two reasons for the choice of optimal sample, albeit one is rather nebulously defined as "promising", which will be clarified by a brief inspection of absorbance data below.

Firstly, and most importantly, the selenium samples were able to be doped to approximately an order of magnitude higher concentration. This is shown by the possible doping concentrations for sulphur being $\approx 10^{14}\text{cm}^{-3}$ [141][142]. While in contrast the selenium samples are of concentration $\approx 10^{15}\text{cm}^{-3}$ [140]. This higher doping concentration can be expected to give stronger optical fluorescence, at least compared to a sample of the same size under the same conditions; the stronger fluorescence occurs for the simple reason that the presence of more dopant atoms allows more absorbed pumping photons and thus more photons emitted as the donor electron undergoes transitions back to its stable ground state.

The doping concentrations for the different samples, available at the time of work for this thesis, are shown in table 5.1; it clearly shows that sample 71-8 has the highest concentration of both atomic, and diatomic, chalcogen dopants.

| Sample | Atomic Se cm$^{-3}$ | Diatomic Se cm$^{-3}$ | B cm$^{-3}$ |
|--------|---------------------|------------------------|-------------|
| 71-8 | $5.5 \times 10^{15}$ | $2.8 \times 10^{15}$ | $2.0 \times 10^{12}$ |
| 72-7 | $2.6 \times 10^{15}$ | $2.5 \times 10^{14}$ | $2.0 \times 10^{12}$ |
| 73-8 | $1.5 \times 10^{15}$ | $2.0 \times 10^{13}$ | $2.0 \times 10^{12}$ |
| 75-6 | $\approx 10^{15}$ | Not Known | $1.3 \times 10^{15}$ |
| 63-6 | $3.0 \times 10^{14}$ | $7.0 \times 10^{14}$ | $2.7 \times 10^{12}$ |

Table 5.1.: Doping concentrations of atomic and diatomic chalcogen dopants in silicon samples, along with boron impurities. Values are from [140][141][142].

## 5.2.1. Absorbance Spectra of Doped Silicon Samples

The second reason for the choice of sample requires the inspection of the absorbance spectra of the samples available. These are presented below in figure 5.1, for the single temperature 4K. Details of the methods used to obtain absorbance spectra such as these, and all such spectra in this thesis, are shown in section 4.2.
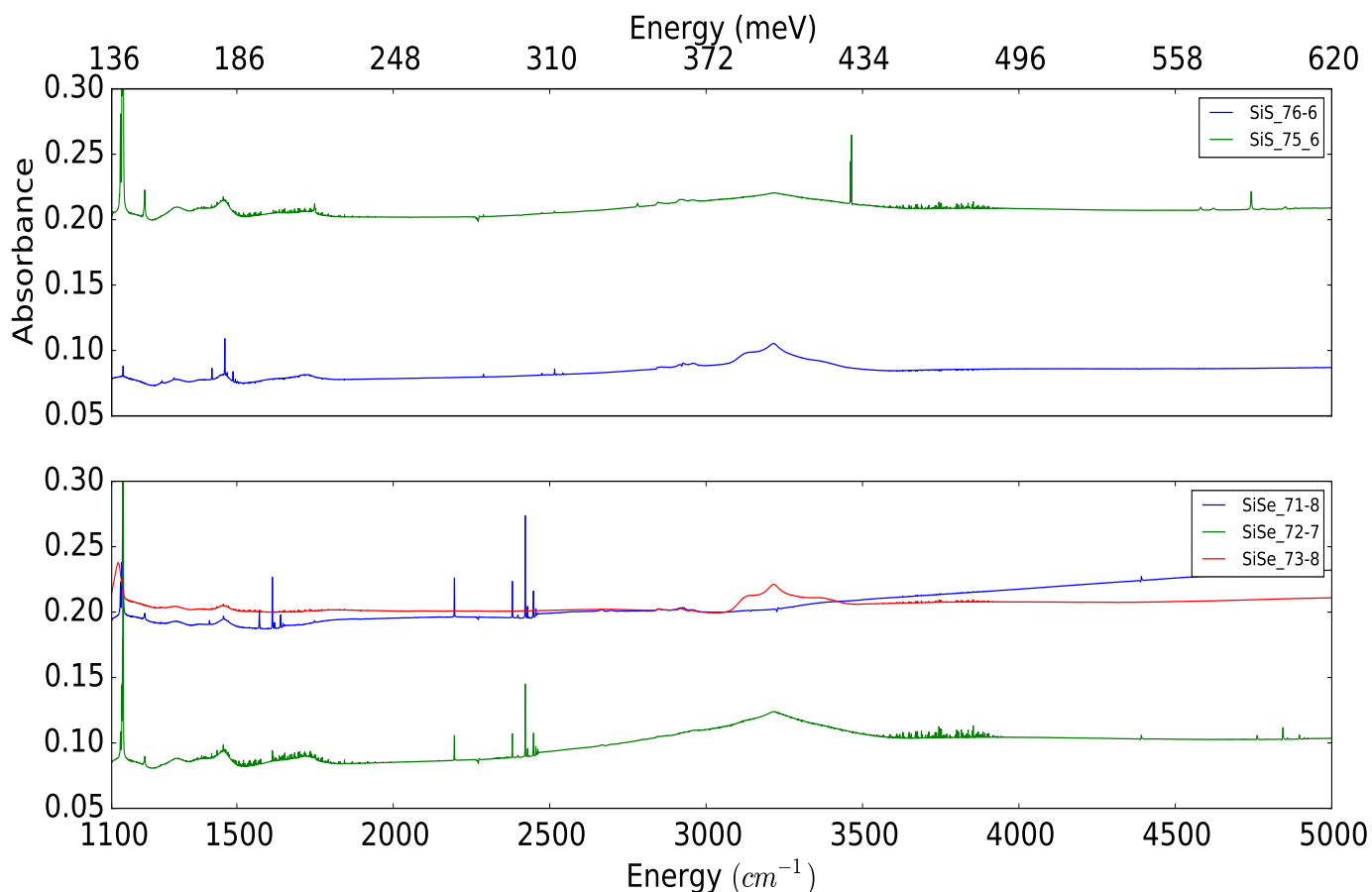
Figure 5.1.: Absorbance data for various doped silicon samples. All data was taken using a vertex 80V Fourier transform spectrometer using the rapid scan FTS technique detailed in appendix C, with the experimental set up described in section 4.2. Samples were cooled to 4K, and the spectral resolution is 0.5 cm$^{-1}$. The doping concentrations are given in the form "sample label: atomic : diatomic : boron impurities"; where the concentration is per cubic cm. **SiS 76-6:** $\approx 10^{15}$ : unknown : $1.3 \times 10^{15}$. **SiS 75-5:** $\approx 10^{15}$ : unknown : $3.0 \times 10^{15}$. **SiSe 72-7:** $2.6 \times 10^{15}$ : $2.4 \times 10^{14}$ : $2.0 \times 10^{12}$. **SiSe 73-8:** $1.5 \times 10^{15}$ : $2.0 \times 10^{13}$ : $2.0 \times 10^{12}$. **SiSe 71-8:** $5.5 \times 10^{15}$ : $2.8 \times 10^{15}$ : $2.0 \times 10^{12}$. It must be noted that this data was measured by S.A. Lynch on 29/11/2012.

Figure 5.1 shows that each of the different samples have different sets of peaks in their spectra. These peaks are, in general, due to electron state transitions of the measured sample. Those that are not are either noise, which is more likely the smaller the size of the peak in both number of points (width) and absolute y axis size compared to the surrounding spectral baseline, or due to contaminants in the

spectrometer.

Water vapour and carbon dioxide are ever present in the atmosphere, and as such are the only contaminants worth being concerned over. It is well known that water vapour has three main absorption bands, corresponding approximately to stretching symmetrically, asymmetrically and rotation; there are then also many additional lines from different isotopes of hydrogen and oxygen. These three bands are located at approximately $3650$cm$^{-1}$, $3750$cm$^{-1}$, and $1590$cm$^{-1}$.[143][144][145][146] While carbon dioxide bands are in the $\approx 600-750$cm$^{-1}$, $2250-2350$cm$^{-1}$, and $3600-3750$cm$^{-1}$ regions [147].

As this absorbance data was taken using a Fourier transform spectrometer, sets of minor peaks in the $1500-1750$cm$^{-1}$ and $3600-3900$cm$^{-1}$ regions can be attributed to water vapour contamination along the interferometer beam path. Thus samples 72-7 and 75-6, which exhibit such sets or bands, should be evaluated with this in mind; that is, the quality of the samples is not affected by water vapour contamination.

Moving on to other features of the absorbance spectra, one comes to the sets of large and small peaks in the approximate region of 1100 cm$^{-1}$. These can be attributed to oxygen contamination in the silicon. Oxygen impurities in the silicon sample are well known to form a molecule like the $Si_2O$ substitutional complexes, these are electrically neutral defect structures [148]. These oxygen structures have an IR vibrational absorption band in the region of 1136.2 $cm^{-1}$ [149], or centred at 1107 $cm^{-1}$ with a FWHM of $\approx 32$ cm$^{-1}$ at room temperature [150]; the oxygen bands are also superimposed upon a silicon transverse optical phonon absorption band, centred at 1118 $cm^{-1}$ with an FWHM of $\approx 50cm^{-1}$. It can be concluded that there are oxygen impurity peaks in the absorbance data. These can be assumed not to affect the quality of the samples, as one is looking for radiative donor transitions

that do not overlap with this spectral region.

This leaves a few remaining clear peaks, which depending upon sample differ in their clarity, and strength; these are attributed to dopant donor electron transitions. The peaks then appear present in several separate and distinct families of a Rydberg like pattern, where each successive peak is at a shorter distance to the last than the prior pair; this is characteristic of $\frac{1}{n^2}$ patterns. These peaks can be assumed to be due to different types of dopant, in this case being atomic, molecular, and ionised donor atom series; this assumption is due to the clear separation of the families of peaks. The ionised family is then unique to the chalcogen double donors, having no correspondent in pnictogen doped silicon due to a lack of sufficient donor electrons.

Thus from inspection of figure 5.1 one can see that the three families of spectral lines are located at $\approx 1500 \mathrm{cm}^{-1}$, $2400 \mathrm{cm}^{-1}$, and $4900 \mathrm{cm}^{-1}$ for selenium doped silicon. Of these only sample 71-8 has all, and with the clearest and strongest sets at all positions. Sample 72-7 has clear sets at $2400 \mathrm{cm}^{-1}$ and $4900 \mathrm{cm}^{-1}$ that are almost as intense as those of 71-8. Sample 73-8 appears to be utterly devoid of any chalcogen dopant.

The sulphur doped samples appear to have slightly shifted families of spectral lines, which is presumably because of the slightly different binding energies for sulphur donor states compared to selenium; however, due to the low quality of the spectral lines it is difficult judge this accurately. Sample 75-6 has a weak family of peaks in the $4700 \mathrm{cm}^{-1}$ region and a single large peak at $3500 \mathrm{cm}^{-1}$; while sample 76-6 has a weak set of peaks in the $1400 \mathrm{cm}^{-1}$ region. Thus the natural conclusion is that the optimal sample for investigation of donor transition lifetimes is 71-8.

# 5.3. Transition Energies: The Spectra

In order to place any time resolved emission into the appropriate context, and also to verify that the measured sample does indeed have optical transitions at the energies shown in the literature, it must first be shown that the sets of spectral lines correspond to the various transitions and different ionisation states or substitutional complexes (atomic or diatomic). The energies of specifically identified states, obtained by the present author's EMT variational calculations, and their comparison with the literature are of importance. Any calculation of a transition rate and thus radiative lifetime depends upon the wavefunction of the state being as accurate as possible, which if given the correct Hamiltonian to describe the system, will result in an energy eigenvalue that is as accurate as possible. The literature values, EMT predicted, and absorbance spectra peaks locations are discussed and compared. This verifies the EMT calculations and the nature of the transitions in the sample.

## 5.3.1. Absorbance Measurements of Selenium Doped Silicon Sample 71-8

Absorbance measurements of the selenium doped silicon sample number 71-8 are shown here in more detail in figure 5.2; the clarity and narrow appearance of these spectral lines, with respect to the transition spacing, indicate the potential for long intrinsic lifetimes (discussed in greater detail in chapter 2).

As can be expected from a simple consideration of coulombic forces, the atomic donor has greater binding energies than the diatomic, due to the repulsive interaction of the two sets of two donor electrons that the diatomic selenium possesses. This then leads to a clear distinction between the sets of spectral lines of neutral and singly ionised selenium donor atoms, thus allowing the groupings of spectral lines in figure 5.2 to be identified; such identification of the families of lines is corroborated by

both data in the literature [94], and by the present author's EMT calculations in section 3.7.1, with the information collated in table 5.3.

The absorbance spectra for each grouping of lines are then shown in more detail, and labelled in accordance with the energies obtained by EMT calculations and the values in the literature [94, table ii], in figure 5.3.

A more detailed comparison with the data from [151, table 1] has allowed the strong absorbance peak at 1136 $cm^{-1}$, and smaller peaks at 1132 $cm^{-1}$, and 1128 $cm^{-1}$ to be correspondingly identified as a set of oxygen-silicon vibrational modes; these are the $^{16}$O, $^{17}$O, and $^{18}$O isotopes of oxygen.
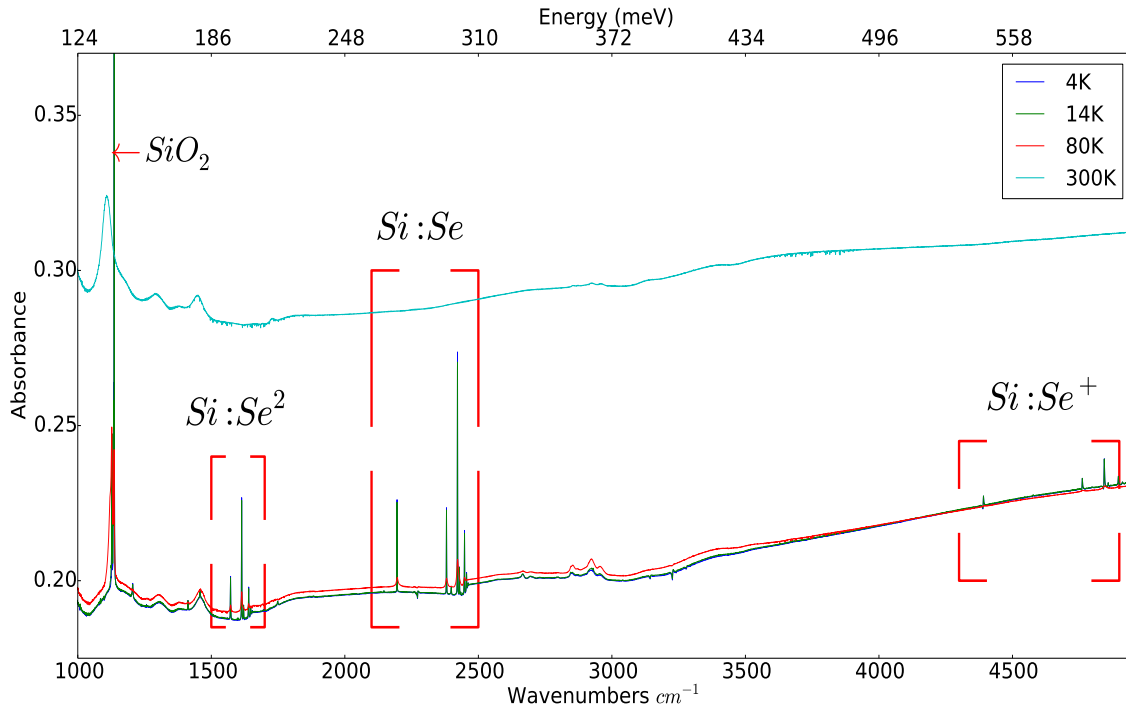


Figure 5.2.: Absorbance spectra of a SiSe sample at 4K,14K,80K and 300K. The measurement was taken at a spectral resolution of 0.5 $cm^{-1}$ , 100 averages, using the 4 term Blackman Harris apodization function, and a spatial sampling rate of 15798 $cm^{-1}$; other conditions and experimental set-up as described in detail in section 4.3. This particular data was measured by my supervisor, S.A. Lynch on 29/11/2012.

From figure 5.2 it is immediately apparent that the distinct families of spectral lines are no longer present at 300K, and the baseline absorbance of the sample has also increased. The 80K data shows a slight rising of the baseline absorbance, but little more detail is visible. It is then necessary to move on to a more zoomed in, spectral grouping specific view, of the data; the specific spectral groupings are shown in more detail in figure 5.3.
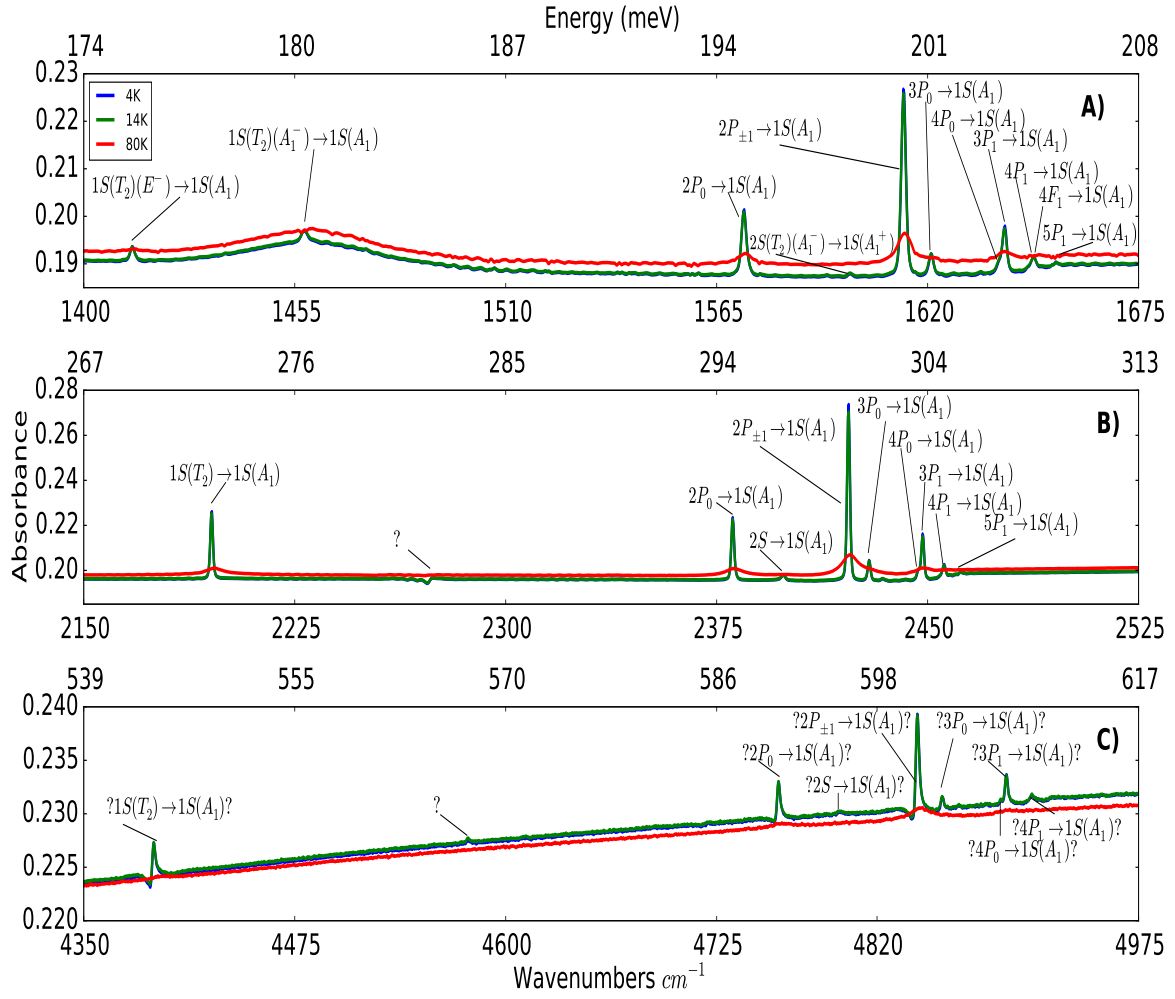
Figure 5.3.: Absorbance spectra of a SiSe sample at 4K,14K,80K. Because at 300K there are no spectral peaks in the absorbance data, it is omitted here. **A)** $Si : Se^2$ - Diatomic substitutional complex. **B)** $Si : Se$ - Atomic substitutional complex. **C)** $Si : Se^+$ - Singly ionised atomic substitutional complex. The top x axis in each sub plot labels the energy in mev, while the bottom is in wavenumbers $(cm^{-1})$. Data is the same as in figure 5.2. Pre-empting the analysis to come in the following section 5.3.2, peaks for sub-plots **A)** and **B)** are labelled by comparison to the energy differences between states in [94]. Peaks in sub-plot **C)** are estimated by comparison to **A)** and **B)**.

Figure 5.3 can clearly be seen to have peaks which are in general weaker and broader, or not visible at all, at 80K compared to 4K and 14K. The various optical transitions in the SiSe sample, and an estimate of their state lifetimes, can then be identified. Central peak positions identify the energy of each transition, while the FWHM of

each peak provides an estimate of the lifetime.

Obtaining this information was done by firstly adjusting the data to remove the baseline upon which the various peaks are superimposed. This analysis was performed by a python 2.7[6] script, making use of the numpy [4], and scipy [5] libraries, with the additional use of the baseline function from the peakutils[152] library. In brief the spectrum baseline, upon which peaks are superimposed, is found by use of an iterative polynomial fitting routine from the peakutils[152] library, which uses a least squares fitting to the data and then reduces the effective weighting of the spectral positions with peaks at each iteration. This continues until only a baseline estimate remains. The spectrum baseline in each region of interest was then subtracted from the spectrum, with the peak positions then identified manually. The FWHM was then estimated by finding the nearest data points at half the local maxima.

In addition to removing the baseline, the $1S(T_2)$ to $1S(A_1)$ transitions on the far left of the spectra in figure 5.3 are not included. This is because this thesis is concerned primarily with the $2P$ to $1S$ transitions and the estimation of the transition rate. This can not be estimated using the same theoretical tools; the $1S(T_2)$ to $1S(A_1)$ transition has a dipole matrix element of zero for parity reasons.

The baseline subtracted data is shown in figure 5.4.
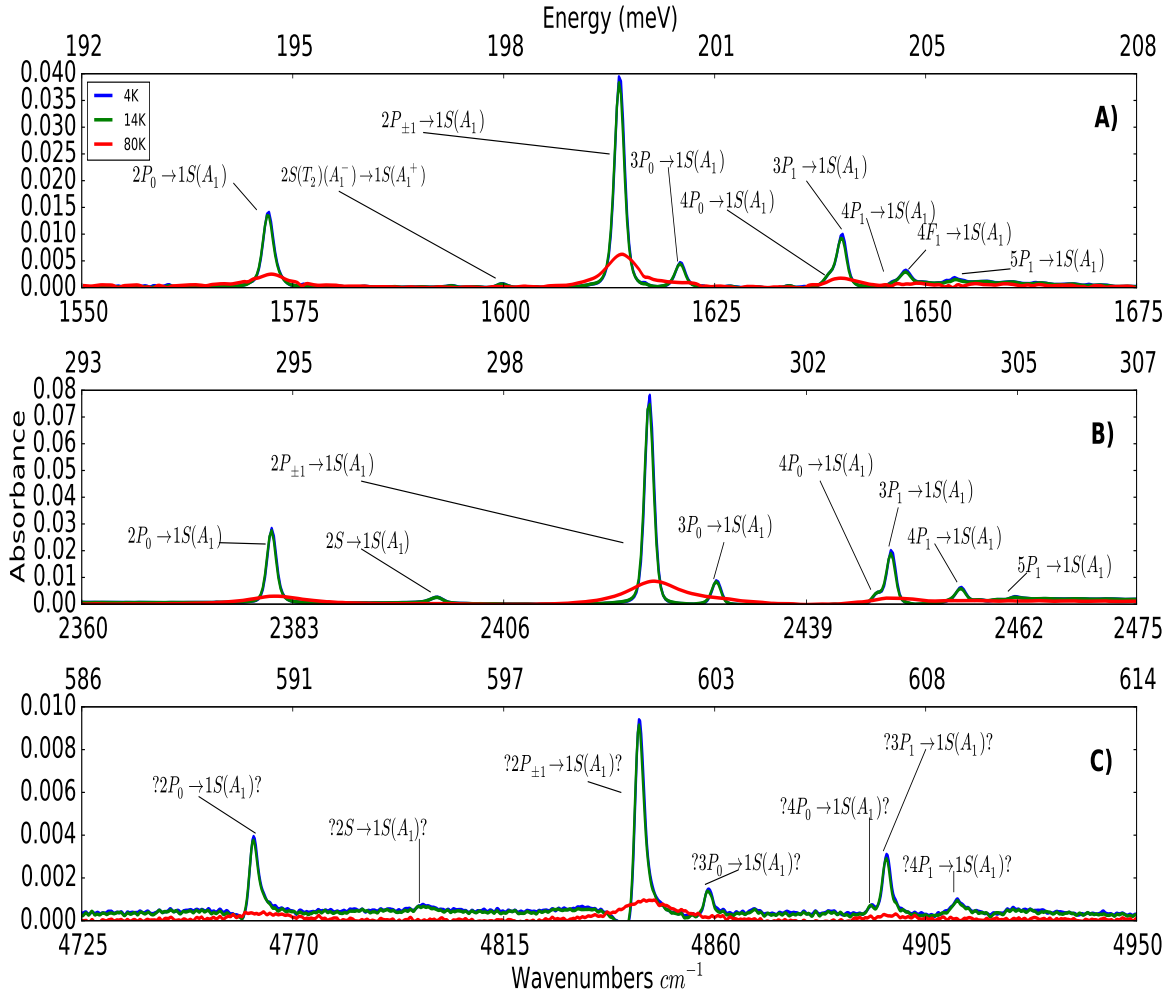
Figure 5.4.: Absorbance spectra of a SiSe sample at 4K,14K,80K. **A)** $Si : Se^2$ - Diatomic substitutional complex. **B)** $Si : Se$ - Atomic substitutional complex. **C)** $Si : Se^+$ - Singly ionised atomic substitutional complex. Data is that of figure 5.4, but with the baseline of each region calculated and subtracted. Pre-empting the analysis to come in the following section 5.3.2, peaks for sub-plots **A)** and **B)** are labelled by comparison to the energy differences between states in [94]. Peaks in sub-plot **C)** are estimated by comparison to **A)** and **B)**.

### 5.3.1.1. Peak Broadening Analysis

The analysis of the peaks in figure 5.4 is presented in this section.

An inspection of the line shape in figures 5.4 and 5.3 shows that, for the ionised selenium complex (section C in both figures), there is a small dip before the $1S(T_2)$, $2P_0$

## 5. Results

and $2P_{\pm 1}$ to $1S(A_1)$ transition peaks. This is characteristic of a Fano resonance[153]. Such a resonance is caused by the coupling of a discrete energy state, in this case the atomic states of selenium donor atoms, to those in a continuum. However, it is not clear what this continuum could be, for the energy range in question is well outside that of silicon phonons. By process of elimination, the only remaining continuum known to the present author are those of the electronic bands of silicon, and the continuum of photon modes in free space. Which of these, if it is indeed them (or even both), that cause the Fano resonance dip before the peak is unclear. It is also unclear why only the $2P$ and $1S(T_2)$ to $1S(A_1)$ transitions exhibit such a feature.

This peak analysis continues with a tabulation of the various peaks, along with their FWHM and estimated lifetime, in table 5.2.

Table 5.2 shows that the FWHM  linewidth estimated lifetime does not significantly change between 4K and 14K. For most peaks they are the same, except for variations of between -9% and -12%, with a single change of -59% for the peak at 1653.34 $cm^{-1}$. Variations between the  FWHM of peaks at 4K and 80K are much larger, ranging from -93 % to -36%.

The exact nature of the change in the peaks is shown in figures  5.5 and 5.6, which show modelled line shape fits to peaks corresponding to $2P_0$ and $2P_{\pm 1}$ to $1S(A_1)$ transitions respectively.  Comparison is made between Gaussian and Lorentzian curves at both 4K and 80K, which then imposes the selection of the two specific transitions because of the weak, or absent, absorption peaks at 80K for any other transitions. The nature of the closet fit to the peak should indicate the dominant mechanism behind the broadening, that is, whether it is caused by: inhomogeneous broadening, associated with a Gaussian peak shape; homogeneous (lifetime) broadening, corresponding to a Lorentzian peak shape.

Figure 5.5 shows the peak believed to correspond to the $2P_0$ to $1S(A_1)$ transition (because of comparison to energy values in the literature, discussed in the following section 5.3.2 ) for the two families of selenium donors, at 4K and 80K. Only the $Si : Se^2$ diatomic and $Si : Se$ atomic families of lines are considered for the $2P_0$ transition, because the absorption peak at 80K is so weak as to render useful fitting to Lorentzian and Gaussian curves difficult, if not outright meaningless. Lorentzian and Gaussian Curves are then fit to the peaks, using a least squares regression routine written in python to find the various parameters. The equations used to fit the Gaussian and Lorentzian curves in figure 5.5 are shown below, where: $\sigma$ is the standard deviation of the Gaussian distribution, and the width of the Lorentzian; $\mu$ is the mean or centre position of each.

$$L(x) = \frac{1}{\pi} \frac{\frac{1}{2}\sigma}{(x - \mu)^2 + \frac{1}{4}\sigma^2} \tag{5.1}$$

$$G(x) = \frac{1}{\sigma\sqrt{2\pi}} e^{-\frac{1}{2}\left(\frac{x-\mu}{\sigma}\right)^2} \tag{5.2}$$

It is clear that at 4K the closest fit is to a Gaussian curve, and at 80K to a Lorentzian. This is true for both families of donor complex, and is both visually clear, and is given by considering the standard errors of the fitting parameters: lesser (or for some, equal to the given number of significant digits) for Gaussian fits at 4K, lesser for the Lorentzian fits at 80K. This indicates that inhomogeneous broadening dominates at 4K, and homogeneous at 80K.
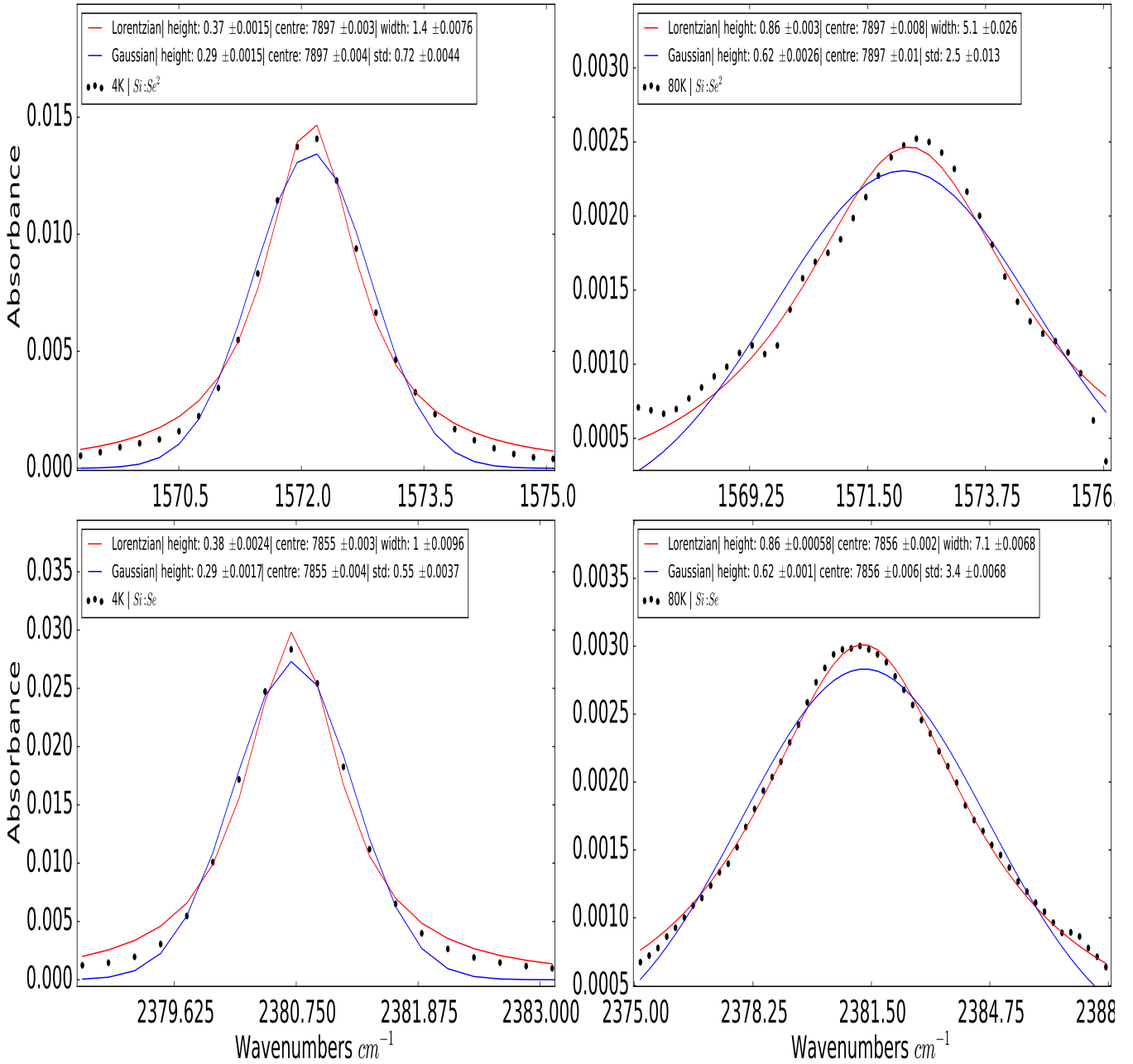
Figure 5.5.: Baseline subtracted absorbance spectra in the region of the $2P_0$ to $1S(A_1)$ transition, of a SiSe sample at 4K(*left*) and 80K(*right*). This is a zoomed in excerpt of the same data as in figure 5.4. Lorentzian (*red*) and Gaussian(*blue*) curves are fit the the experimental data(black points), while the fitting parameters, temperature, and family of lines from which the transition peak is taken from, are shown on each sub-figure with the units in those of the respective axis; fitting parameter errors are to one standard deviation, and the equations used to create the fits are those of equations 5.1 and 5.2.

## 5. Results

Figure 5.6 shows the peak believed to correspond to the $2P_{\pm 1}$ to $1S(A_1)$ transition (because of comparison to energy values in the literature, discussed in the following section 5.3.2 ) for the three families of selenium donors, at 4K and 80K. Lorentzian and Gaussian curves are fit to these peaks, using the same python least squares regression routine to find the various parameters as for the $2P_0$ case, as are the equations used to fit the Gaussian and Lorentzian curves.

It is clear to the eye that in figure 5.5 , for 4K (the left hand side of the figure), the Gaussian fits better than the Lorentzian to the data. This indicates that at 4K the inhomogeneous environments of multiple Si:Se donors is the dominant contribution to the broadening. A more quantitative approach gives the same conclusion, as the one stand deviation error ( standard deviation of the mean value) of the Gaussian fitting parameters is lesser than those of the Lorentzian fits for all of: diatomic($Si : Se^2$), atomic ($Si : Se$), and single ionised ($Si : Se^+$) selenium complexes.

For 80K (the right hand side of the figure) the situation has changed. The Lorentzian curve is now both a visually, and numerically, superior fit to the data; the standard errors of all of the fitting parameters is lower, giving a higher probability that the Lorentzian curve is a better fit to the data. Therefore, homogeneous, such as lifetime limit caused, broadening is now likely to be the dominant mechanism; radiative lifetime decay has a Lorentzian curve shape due to it being the Fourier transform of the exponential decay.

Having considered the two clearest peaks in the spectra, it is clear that in all cases the broadening is likely to be dominantly homogeneous at 80K and inhomogeneous at 4K. A tentative explanation is that at 4K the disorder of the surrounding donor environment has a greater contribution to the broadening than the intrinsic lifetime
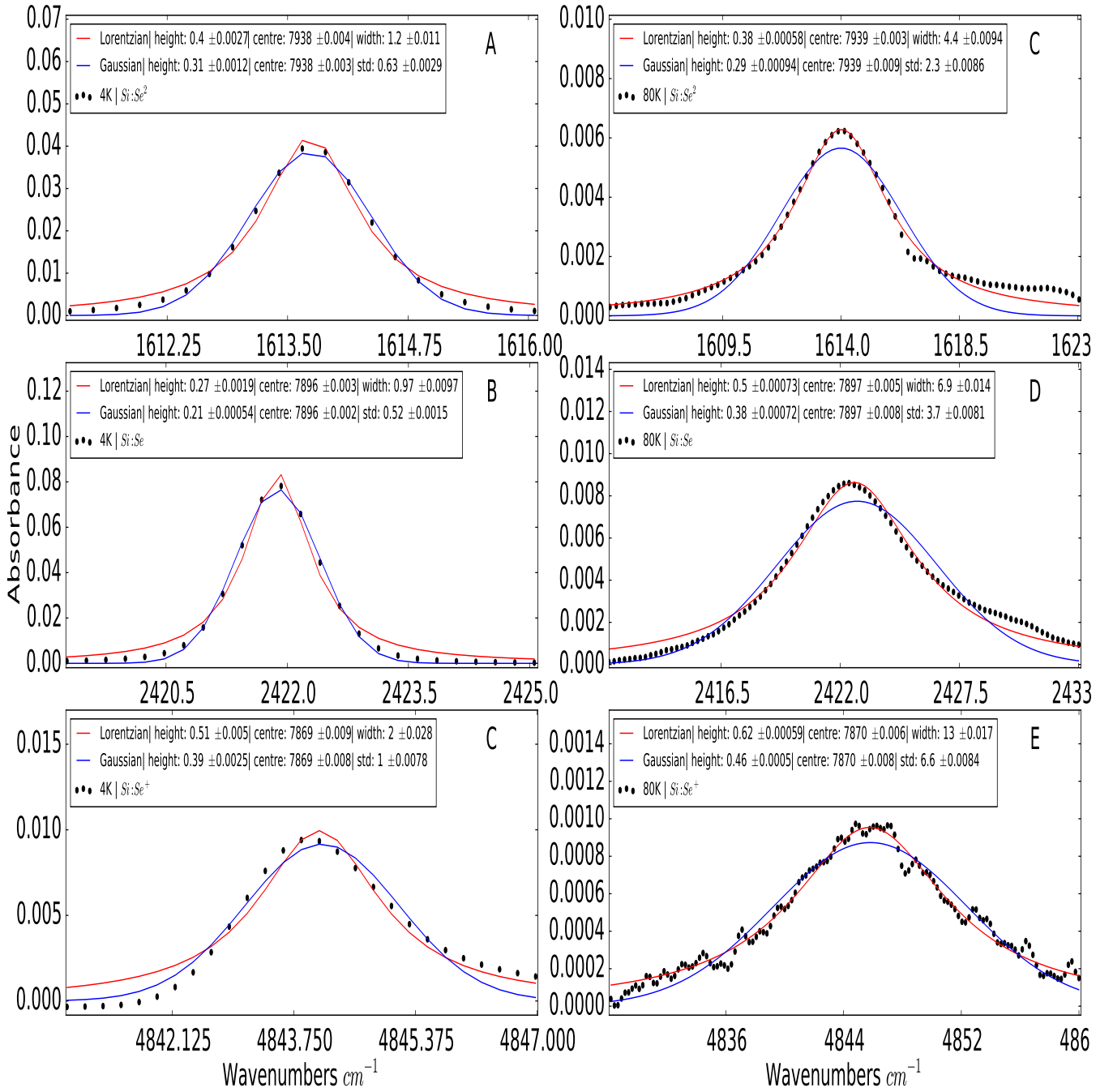
Figure 5.6.: Baseline subtracted absorbance spectra in the region of the $2P_{\pm 1}$ to $1S(A_1)$ transition, of a SiSe sample at 4K(*left*) and 80K(*right*). This is a zoomed in excerpt of the same data as in figure 5.4. Lorentzian (*red*) and Gaussian(*blue*) curves are fit the the experimental data(black points), while the fitting parameters, temperature, and family of lines from which the transition peak is taken from, are shown on each sub-figure with the units in those of the respective axis; fitting parameter errors are to one standard deviation, and the equations used to create the fits are those of equations 5.1 and 5.2.

of the states, recall that (discussed in chapter 3) the $2P$ excited states of donors in silicon extend over a large spatial area, allowing a greater amount of inhomogeneous lattice distortion, defects, other impurities etc to effect each excited electron. However, it is then not clear as to why at 80K the lifetime, or homogeneous, component dominates.

Comparing this to homogeneous and inhomogeneous broadening of donors in silicon in the literature [154], it is found that the presence of silicon phonon modes resonant with a transition can cause additional broadening. However, there are no phonon modes resonant with the $2P$ transitions of selenium donors, due to the deep ground state, removing this as a cause for the homogeneous broadening dominance of higher(80K) temperature transitions; it is plausible, although unlikely, that multiple phonon emission becomes a dominant decay pathway for the 80K excited states, and this may fit with the homogenous broadening mechanisms discussed in[154].

It is reasonable to conclude that temperature does affect the lifetime, with inhomogeneous broadening form the donor environment as the probable dominant cause at 4K, and lifetime caused homogeneous broadening dominating at 80K and, possibly higher, temperatures. The cause of this is change in dominant broadening mechanism is not known or understood by the present author.

### 5.3.1.2. Examination of Possible Water Absorption Lines

To examine the effect of the instrument upon the line shapes, water absorption lines can be investigated. As mentioned elsehwehre in this thesis, there are water absorption bands in the regions of $3650 \text{cm}^{-1}$, $3750 \text{cm}^{-1}$, and $1590 \text{cm}^{-1}$.[143][144][145][146] However, there is at least one set of carbon dioxide bands in the region of $3600 - 3750 \text{cm}^{-1}$ [147]. The 4K absorption spectra shown in figure 5.2 is shown, zoomed in on the region around $3750 cm^{-1}$, in figure5.7. It is not clear whether the three small

peaks in this figure are due to water or $CO_2$ absorption, therefore it is assumed that they are due to water vapour present in the Fourier transform spectrometer. Here the apodization function, used for all Fourier transform spectroscopy in this thesis, the 4 term Blackman Harris function is fit to the three small and narrow peaks that appear. Because water vapour absorption lines are typically extremely narrow, the instrument lineshape should be possible to recover from fitting to them.
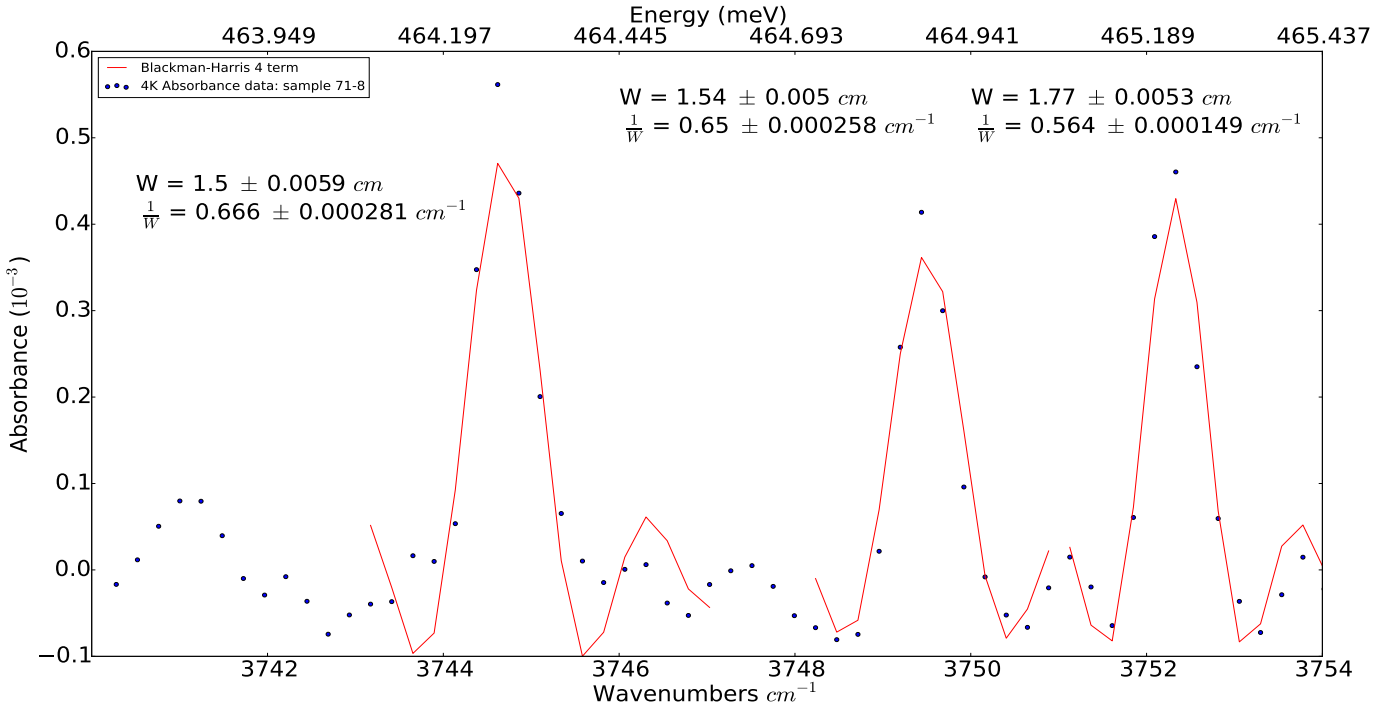


Figure 5.7.: Absorption spectra of a SiSe sample at 4K, zoomed in on the region around $3750cm^{-1}$; this is the same data as in figure 5.2. The measurement was taken at a spectral resolution of 0.5 $cm^{-1}$. The 4 term Blackman Harris apodization function was used (from equation D.39) to fit to the three measured peaks in the spectra; the $W$ parameter is the spatial distance over which the Fourier transform interferogram is measured, thus $\frac{1}{W} = 0.5cm^{-1}$ (if the instrument lineshape is a delta function, otherwise this may be broadened). Fitting parameter information is given for each peak, in text near the corresponding peak, on the figure.

The exact distance of the Fourier transform spectrometer used in the measurement was $\frac{1}{W} = 0.5cm^{-1}$. Comparison to the extracted parameters from the peaks in figure

5.7 shows minor disagreement, as the fit parameters for $\frac{1}{W}$ are 0.564,0.65, and 0.666 $cm^1$ which are not too far from the expected 0.5 $cm^1$. As a result, the instrument line shape is likely to have a small, although it will have some, effect upon any other measured spectral peaks. The final resolution of the spectra can then be taken to be $\approx 0.67cm^{-1}$, which is far more than enough to separate any of the features discussed in any detail in this thesis. The $2P_0$ and $2P_{\pm1}$ to $1S(A_1)$ transitions are of interest, and are at least an order of magnitude, or more, apart from the nearest other peaks in the absorption spectra; the emission spectra, discussed later on in this chapter, is so broad that discernment of individual transitions is impossible, rather, only groupings of transitions can be identified, and these are separated by more than this experimentally found resolution.

The wider consequences of the use of the Blackman Harris 4 term apodization function are the suppression of side lobes near real peaks, and the creation of broad side lobes slightly further away, along with a slightly wider central peak compared to a simple boxcar apodization function. This is, in effect, a trade off for a slightly wider central peak in order to suppress, and push further away, side lobes that would be close to each peak. The effect of this apodization function on a delta function like peak can be seen in the appendix, figure D.2

## 5.3.2. Transition Energy Comparisons

The state energies taken from [94] allow the transition energies to be determined. The transition energies are compared to the measured values of absorbance peaks in table 5.2. This is done to confirm that absorbance peaks really are the transitions they are believed to be. Of course even perfect agreement is not a guarantee, and neither is a minor deviance proof of falsehood, but as long as gross deviances are not found then it is reasonable to assume that the peaks in the Si:Se absorbance spectra are the donor electron states. This comparison is presented in tables 5.3 and 5.4 for

atomic and diatomic selenium donor complexes respectively.

**Atomic Selenium Transitions**

Table 5.3 shows that many of the observed peaks in absorbance spectra (part B figure 5.4, table 5.2) match approximately with transition energies predicted by the literature. The literature transition energies have been matched to the closest observed peak in the measured absorbance spectra. Because the absorbance measurements were taken with a spectral resolution of 0.5 cm$^{-1}$, which is the resolution at which delta function like peaks could be separated, in reality the absorbance peaks are not delta functions and have their own width caused by various factors, such as lifetime or inhomogeneous broadening. Thus any measured absorbance peaks less than 0.5 cm$^{-1}$ from the literature value can be confidently attributed to the literature transition, while other peaks that are further away can also be included in this, as long as the difference is not too large; the exact size of this difference is not trivial to quantise and depends on the intrinsic lifetime of the transition (not always known), the temperature, level of disorder in the material, isotopic composition, etc.

The $5F_0$, $5F_1$, $5P_1$, $6P_1$, and $7P_1$ to $1S(A_1)$ transitions are all extremely close in energy, and appear to be either merged together in a single peak in the absorbance spectra, or many of the transitions are too weak to be observed or absent entirely. There are then three observed absorbance peaks which do not appear to correspond to known possible transitions, at 2195.45, 2273.67, and 2398.73 cm$^{-1}$; the cause of these peaks is not clear.

Of importance are the $2P_0$ and $2P_{\pm 1}$ to $1S(A_1)$ transitions, which agree most accurately with the literature, and have an observed deviance less than the spectral resolution. These two transitions are of importance because they are the deepest energy states which can exhibit optical transitions to the ground state.

**Diatomic Selenium Transitions**

Table 5.4 shows that many of the observed peaks in absorbance spectra (part A of figure 5.4, table 5.2) again match approximately with transition energies predicted by the literature. The literature transition energies have, for precisely the same reasons as for atomic state transitions, been matched to the closest observed peak in the measured absorption spectra. For some sets of literature transitions there is only a single observed peak in the absorbance data, again as for the atomic states this can be for a variety of reasons. Some of the transitions may be too weak to be clearly seen, some may be absent, and some may be merged together in the single observed peak. There is also an observed transition at 1599.88 $cm^{-1}$ that does not appear to match up to any labelled transition from the literature.

Again of importance, for exactly the same reasons as for the atomic states, are the $2P_0$ and $2P_{\pm 1}$ to $1S(A_1)$ transitions, which agree with the literature; there is also, as before, an observed deviance that is less than the spectral resolution.

As a result it is possible to be confident that the key $2P_0$ and $2P_{\pm 1}$ to $1S(A_1)$ transitions for both atomic and diatomic selenium complexes can be clearly identified.

# 5.4. Oscillator Strengths: Linking Absoption Spectra to Dipole Matrix Elements

The absorption spectra presented so far, gives an opportunity to compare the strength of the measured transitions with that predicted by the calculated dipole matrix elements. In order for this comparison to be carried out, the various values are given in the unit-less, normalised, oscillator strength form.

The matrix elements are calculated using several variations of the EMT wavefuncti-

ons, and parameters, calculated in chapter3. These different variations include: EMT wavefunctions from calculations in this thesis, where the parameters are varied to find the minimum energy for both upper and lower states; effective mass states as the upper state, with ground states spatially scaled via Mott semiconductor to conductor transition data[2]; spatially scaled, spherical, hydrogen wavefunctions (that ignore the anisotropic effective mass of silicon), for both upper and lower states; spatially scaled, spherical, hydrogen wavefunctions for the upper state, with Mott transition scaled ground states.

The calculated dipole matrix elements can then be converted into oscillator strengths, for comparison with values in the literature. Finally, both the literature values and the present authors calculations can be compared to oscillator strengths estimated from the absorption spectra shown prior in this chapter.

This forms an intermediate stage between the absorption spectra shown and analysed, section 5.3 , and the dipole matrix element dependant transition rates, calculated in chapter 3. If reasonable agreement is found between the triad of measured absorption spectra estimated oscillator strengths, calculated EMT oscillator strengths, and those found in the literature then the likelihood of the calculated transition rates being true, or at least not wholly inaccurate, is increased (due to them sharing the dipole matrix element with the oscillator strengths). A qualitative more, or less, likely veracity of the dipole matrix elements affects the overall strength of this thesis.

**Oscillator Strength**

The oscillator strength is a unit-less measure of the strength of an absorption/emission transition between two states of a system. In the context of a dipole interaction caused transition, the dipole oscillator strength is defined by:[155]

$$f_{a,b} = \frac{2m^*}{\hbar^2}\left(E_b - E_a\right)|\vec{1}.\vec{r_{b,a}}|^2 \tag{5.3}$$

In equation 5.3 , $f_{a,b}$ is the oscillator strength, $a$ and $b$ the initial and final states of the dipole interaction, $E_a$ and $E_b$ the energies of those states, $\vec{1}$ is a unit polarisation vector, $\vec{r_{b,a}}$ the dipole matrix element, and $m^*$ is the effective mass harmonic mean. The harmonic mean of the effective mass is given by:

$$m^* = \left[\frac{1}{3}\left(\frac{1}{m_{\parallel}^*} + \frac{2}{m_{\perp}^*}\right)\right]^{-1} \tag{5.4}$$

Where, in equation 5.4 , $m_{\parallel}^*$ is the parallel (or longitudinal), and $m_{\perp}^*$ the perpendicular effective mass of silicon, they are weighted differently because two axial direction have the perpendicular effective mass and one the parallel.

The oscillator strength can also be obtained from integrating the area under an absorption curve: [155, eq 2]

$$f_{a,b} = \frac{nm^*c}{2\hbar e^2\pi^2}\int_{band}\sigma(\hbar\omega_{a,b})d(\hbar\omega_{a,b}) \tag{5.5}$$

For equation 5.5 , $\sigma = \frac{\alpha}{N_{imp}}$ is the absorption cross section, $\alpha$ the absorption coefficient (e.g. as for the Beer-Lambert law) and $N_{imp}$ the density of absorbing impurity centres, $n$ is the refractive index, and $\omega_{a,b}$ the angular frequency of the transition between the $a$ and $b$ states.

The unit polarisation vector, $\vec{1}$, introduces an additional piece of complexity into the oscillator strength. Due to the 6 fold degenerate conduction band minima (valleys) in silicon, the dipole matrix element is reduced *relative to that which it would be if the states were built out of states from a single valley*, if the polarisation vector is of magnitude 1. [155].

This reduction does not occur for vacuum electric field perturbation caused dipole transitions, as the field is assumed to be of equal amplitude in all vector directions (discussed in detail in section 3.6.1), giving it a magnitude of $\sqrt{3}$ relative to the unit polariastion used by Claus et al [155]. When squared, as in the dipole matrix element squared, this magnitude difference accounts for the factors of one and two thirds that are the oscillator scaling factors that Claus et al [155] use, although this is covered in more detail in the section discussing the differences in assumptions between the literature oscillator strengths and those from this thesis.

For comparison to the literature, the scaling factors are, in general and unless otherwise explicitly stated, present in the oscillator strengths calculated here by the EMT wavefunctions from this thesis. They are not included in the transition rates of chapter 3.

Before stating the EMT 6 fold conduction band valley introduced scaling factors some terms must be defined: $f_0$ and $f_\pm$ are the oscillator strengths of transitions to the $1S(A_1)$ ground state of a donor in silicon, taking into account silicon's multi conduction band minimum (valley) nature, from $m = 0$ and $m = \pm 1$ states respectively (where $m$ is the magnetic quantum number); $f_\parallel$ and $f_\perp$ are the corresponding (to $m = 0$ and $m = \pm 1$ respectively) oscillator strengths ignoring the multi-valley nature of silicon, i.e as if the states were in free space. For relevance to this thesis,

$2P_0$ transitions correspond to $f_0$, and $2P_{\pm 1}$ to $f_{\pm}$.

$$f_0 = \frac{1}{3} f_{\parallel} \tag{5.6}$$

$$f_{\pm} = \frac{2}{3} f_{\perp} \tag{5.7}$$

## 5.4.1. Expected Causes of Differences Between Oscillator Strengths

There are, of course, likely to be differences in the literature, absorption spectra, and EMTwavefunction from this thesis based oscillator strength calculations. Each of these three are expected to differ to the others due to three primary reasons.

Firstly, the chalcogen selenium is a double donor and is not hydrogen like as in the EMT models in the literature and this thesis, therefore the absorption spectra derived oscillator strengths are likely to differ in some degree to those calculated by such methods. Secondly, as will be explained in more detail below, the Hamiltonian used in the literature to calculate EMT states is different to that used in this thesis, making different wavefunctions and thus oscillator strengths likely. Thirdly, the Mott criteria is not used in the literature to scale the spatial size of ground state. A fourth differences arises, due the choice of polarisation vector of the electric field in the dipole matrix element. These expected differences, and their relations, are sketched in figure 5.8 below.
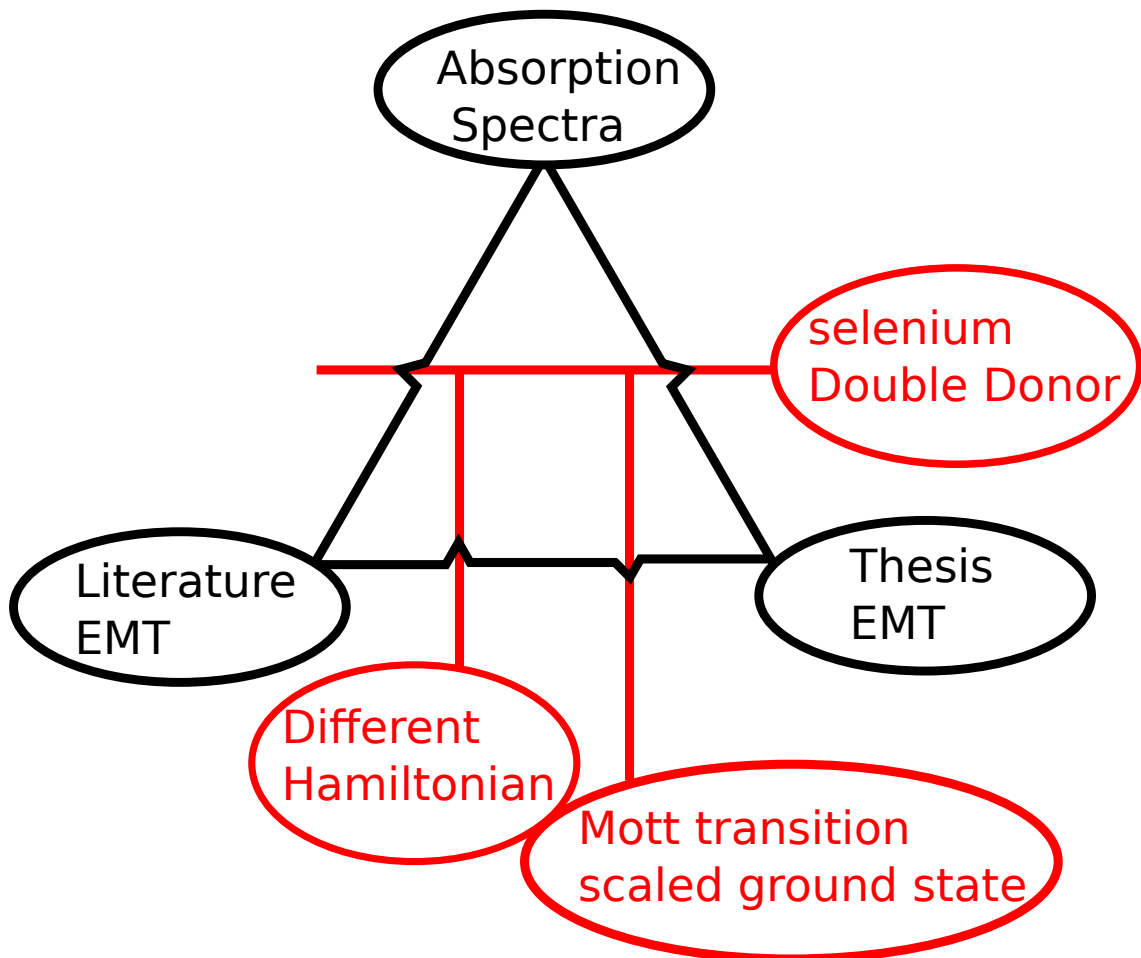
Figure 5.8.: Representative diagram of the likely differences between the three sources of oscillator strengths discussed below, each shown at a vertex of the black triangle. Red lines and labels show the expected causes of discrepancies between each method.

The differences in the assumption between the work in this thesis and the literature are discussed below.

### 5.4.1.1. Selenium Double Donor

The ground state wavefunction in this thesis is spatially scaled, rather than the Hamiltonian being adjusted as above. That is, the wavefunction has a parameter, $\alpha_{0,0}$, which is phenomenologically fit to measured Mott semiconductor to conductor transition data[2] , discussed thoroughly in section 3.7.2 . The result is that the spatial extent of the Mott scaled $1S$ ground state wavefunction is extremely small, while the spatial extent of the Hamiltonain adjusted wavefunction is not known (as this is not published in the literature, only the energy values of the state), but may differ. As the method used to calculate the higher excited states is entirely the same, in this thesis, and the literature, eg. [155], any difference in dipole interaction oscillator strength can be attributed to a difference in the ground state wavefunction.

In contrast to the Mott adjusted ground state, the given sources in the literature adjust the $\alpha'$ parameter of the Hamiltonian to match the measured energy. While the general EMT approach includes a $\beta$ parameter in the Hamiltonian, which is adjusted (in conjunction with $\alpha_{\ell,m}$ to minimise state energy), this does not yield the correct ground state energy. The use of the Mott criteria to scale the ground state then adjusts only the wavefunction, with $\beta$ remaining at the value which gives the incorrect ground state energy. This is because the $\beta$ parameter is shared between the ground, and excited states, while the $\alpha_{\ell,m}$ are not, and therefore $\beta$ is set to that which gives the correct excited, but not ground, state energies.

### 5.4.1.2. Effective Mass Hamiltonian

The calcualted oscillator strengths from the literature [156, section 5.4] [155] differ from those of this thesis, because of a different EMT Hamiltonian. This difference is due to the failure of EMT to accurately predict the ground state energy of donors; the assumptions of EMT break down for the ground state electron, essentially because it is too close to the donor nucleus. The form of the Hamiltonian used in

this thesis, where $r$ is the radial coordinate, is:

$$-\frac{2}{r} \tag{5.8}$$

In order to adjust the ground state energy to match reality, [156, section 5.4] and [155] introduce a phenomenological scaling parameter $\alpha'$ (different to the $\alpha_{\ell,m}$ used elsewhere in this thesis). The adjusted Hamiltonian is then:

$$-\frac{2}{r}\left[1 + (\epsilon_r - 1)e^{-\alpha' r}\right] \tag{5.9}$$

The $\alpha'$ parameter is then adjusted until the EMT energy matches that of the measured ground state.

### 5.4.1.3. Ground State

The ground state wavefunction in this thesis is spatially scaled, rather than the Hamiltonian being adjusted, as above. That is, the $1S$ ground state wavefunction $\alpha_{\ell,m}$ parameter is varied to phenomenologically fit to measured Mott semiconductor to conductor transition data [2] , in contrast to [155] and [156] where the $\alpha'$ parameter of the Hamiltonian is varied so that the state energy matches that which is measured. In the EMT variational method, the excited states are found by minimising the energy of the states by varying $\beta$ and $\alpha_{\ell,m}$ parameters, where $\beta$ is part of the Hamiltonian. This differs from the $\alpha'$ parameter, because $\beta$ is constant for all states, excited and ground, while $\alpha'$ only affects the ground state.

The result is that the spatial extent of the Mott scaled $1S$ ground state wavefunction

is extremely small, while the spatial extent of the Hamiltonian adjusted wavefunction is not known (as this is not published in the literature, only the energy values of the state). However, because the excited states are obtained the same way, via variational minimisation, it is extremely likely that they are the same. If the resulting oscillator strengths are different, then the only possible explanation, besides calculation error, is different ground states, or more precisely, different ground states with different spatial sizes, or scaling.

### 5.4.1.4. Polarisation Magnitude

The dipole matrix elements for the oscillator strengths have a scaling factor, shown in [155] . This scaling factor can arise from two places, and due to the lack of clarity in the explaination of [155], it is not completely clear which is the cause: the effect of the silicon crystals symmetry on the effective mass states, or that there is a polarisation vector of magnitude 1. Therefore, to be certain of which is the cause, the two possible causes are considered in the context of the $2P_0$ to $1S(A_1)$ transition.

Firstly, the $2P_0$ state is split into one $A_1$, two $E$, and three $T_1$ components. The $T_1$ cannot undergo a transition to the $1S(A_1)$ state, because the amplitude components of the 6 different effective mass conduction band valley states cancel each other out. However, the single $A_1$, and each of the $E$ states, in isolation, can be shown to have the appropriate scaling factor. This is shown in section 3.6.1.1 . Summing the states together gives a total factor of 1. Then, of course, it is appropriate to account for the correct degeneracy of the excited state. by dividing by the number of excited states any donor electron may be in, as in the non effective mass case.

Secondly, as the first possible cause gives the total dipole squared factor of 1, and only a third for each one of three parts, all the matrix elements of the $2P_0$ states ($A_1$,

$E, T_1$) summed together can have the factor of one third, but only for a polarisation magnitude of 1. For the uniform in all directions polarisation case, described in section 3.6.1.1 , this can be made clear by considering the polarisation vector used in equations 3.53, and 3.54 .

$$\vec{E} = (1, 1, 1) \tag{5.10}$$

If the polarisation vector is normalised to be of magnitude 1 then it becomes:

$$\vec{E} = \frac{1}{\sqrt{3}}(1, 1, 1) \tag{5.11}$$

The magnitude 1 polarisation vector then modifies the $2P_0(A_1)$ to $1S(A_1)$ matrix element, equation 3.54 , to become:

$$\frac{4}{36}\left( |\langle F^{fi}_{\pm kx}| \frac{1}{\sqrt{3}} z | F^{ex}_{\pm kx} \rangle |^2 + |\langle F^{fi}_{\pm ky}| \frac{1}{\sqrt{3}} x | F^{ex}_{\pm ky} \rangle |^2 + |\langle F^{fi}_{\pm kz}| \frac{1}{\sqrt{3}} y | F^{ex}_{\pm kz} \rangle |^2 \right)$$

$$\tag{5.12}$$

$$= \frac{12}{36} |\langle F^{fi}_{\pm kx}| z | F^{ex}_{\pm kx} \rangle |^2$$

$$= \frac{1}{3}\frac{1}{3} |\langle F^{fi}_{\pm kx}| z | F^{ex}_{\pm kx} \rangle |^2$$

Setting the polarisation to the unit magnitude one makes the two $2P_0(E)$ to $1S(A_1)$ matrix elements, equations **??** and **??** , then become:

$$\frac{1}{6} |\langle F^{fi}_{\pm kx}|z\frac{1}{\sqrt{3}}|F^{ex}_{\pm kx}\rangle|^2 + \frac{1}{6}|\langle F^{fi}_{\pm ky}|x\frac{1}{\sqrt{3}}|F^{ex}_{\pm ky}\rangle|^2$$

$$= \frac{2}{6}\frac{1}{3}|\langle F^{fi}_{\pm kx}|z|F^{ex}_{\pm kx}\rangle|^2 \tag{5.13}$$

$$\frac{1}{6} |\langle F^{fi}_{\pm kx}|z\frac{1}{\sqrt{3}}|F^{ex}_{\pm kx}\rangle|^2 + \frac{1}{6}|\langle F^{fi}_{\pm kz}|y\frac{1}{\sqrt{3}}|F^{ex}_{\pm kz}\rangle|^2$$

$$= \frac{2}{6}\frac{1}{3}|\langle F^{fi}_{\pm kx}|z|F^{ex}_{\pm kx}\rangle|^2 \tag{5.14}$$

Summing the contributions, of the one $2P_0(A_1)$, and two $2P_0(E)$, to $1S(A_1)$ matrix elements ( for the unit magnitude polarisation, gives the total matrix element:

$$\frac{1}{3}\frac{1}{3}|\langle F^{fi}_{\pm kx}|z|F^{ex}_{\pm kx}\rangle|^2 + \frac{2}{6}\frac{1}{3}|\langle F^{fi}_{\pm kx}|z|F^{ex}_{\pm kx}\rangle|^2 + \frac{2}{6}\frac{1}{3}|\langle F^{fi}_{\pm kx}|z|F^{ex}_{\pm kx}\rangle|^2$$

$$= \frac{1}{3}|\langle F^{fi}_{\pm kx}|z|F^{ex}_{\pm kx}\rangle|^2 \tag{5.15}$$

The factor of one third that Clauws et al [155] give is found to be a direct consequence of the polarisation vectors magnitude. Therefore, it does not need to be included in the radiative emission, as it is effectively accounted for by the strength of the electric field amplitude, only the oscillator strength calculations.

## 5.4.2. Comparisons of Oscillator Strengths

The oscillator strengths are presented here, with notable differences summarised in the ending section.

### 5.4.2.1. Oscillator Strengths From This Thesis

Oscillator strengths from this thesis, calculation, and determined from integrating the area under absorption curves.

### From Calculation

The different oscillator strengths from the wavefunctions calculated in this thesis are given here. All include the scaling factors of one, or two, thirds. The different methods of calculating the wavefunctions are the same as those for tables 3.9 and 3.10. As the oscillator strength involves the energy difference between the states, it can be calculated using the energy values from the literature[94]. The oscillator strengths are then given in table 5.5.

The oscillator strengths calculated by hydrogenic, fully spherical, wavefunctions for the excited are approximately the same for both $2P_0$ and $2P_{\pm 1}$ to $1S(A_1)$ transitions, regardless of how the ground state is calculated. However, for the EMT states, there appears to be a factor of 3 difference: for the EMT scaled ground state the $2P_0$ is thrice that of the $2P_{\pm 1}$; for the Mott scaled ground state the $2P_{\pm 1}$ is thrice that of the $2P_0$.

### From Absorption Spectra

The absorption spectra allows the extraction of an oscillator strength, via the use of equation 5.5. The oscillator strength is extracted from the baseline removed spectra of figure 5.4 for 4K. Only 4K is chosen as this should show the most accurate absorption peaks, and allow more accurate oscillator strengths to be determined;

the calculated oscillator strength is temperature independent, and so it is most valid to compare to measured oscillator strengths that exhibit the smallest possible thermal effects. The integral over the absorption band, $\int_{band} \sigma(\hbar\omega_{a,b})d(\hbar\omega_{a,b})$, is obtained by simply calculating the area under the points of the absorption data. Between each 2 successive points a straight line is drawn, and the areas of all such trapezoids summed together is then taken to be the integral, where the boundary of the absorption bands is determined by the authors inspection. The absorption as measured is the absorbance coefficient, $\alpha$, multiplied by the thickness of the sample which is known to be $\approx$ 1mm. The average concentration of donor centres is then needed to obtain the absorption cross section $\sigma$, which can be obtained from table 5.1. The resulting areas under the curve, along with the corresponding oscillator strengths are shown below.
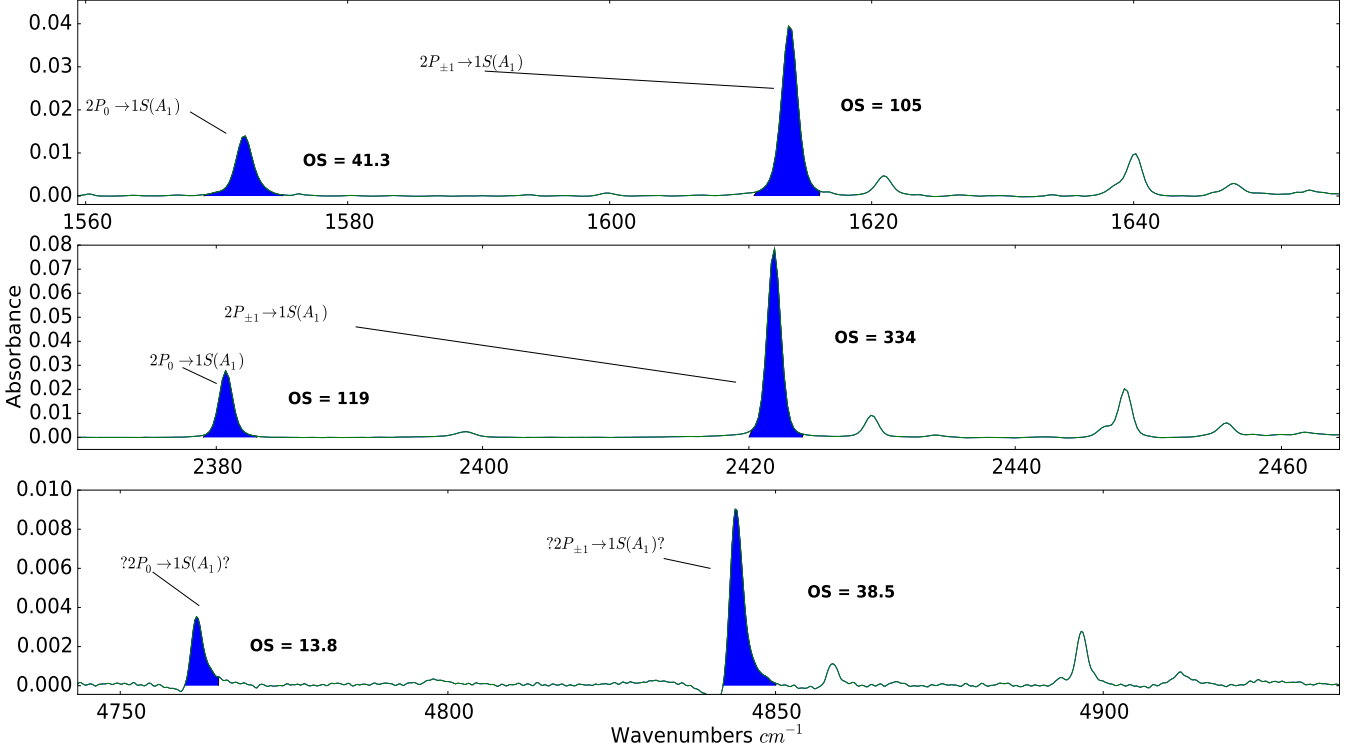
Figure 5.9.: Absorption spectra of a SiSe sample at 4K. **OS:** Oscillator strength. The blue shaded areas indicate the area under the absorption peaks used to calculate the oscillator strengths, which were calculated using equation 5.5; $\sigma = \frac{A}{LN_{imp}}$, where $A$ is the absorbance, $L = 1mm$ the thickness of the silicon sample, and $N_{imp}$ the concentration of donor impurities. **Top:** Atomic selenium donor complex: donor concentration = $5.5 \times 10^{15}\text{cm}^{-1}$. **Middle:** Diatomic selenium donor complex: donor concentration = $2.8 \times 10^{15}\text{cm}^{-1}$. **Bottom:** Ionised atomic selenium donor complex: the donor concentration is not known for this, therefore that of the atomic complex was used. Doping concentrations are from table 5.1. Left and right shaded peaks correspond to the $2P_0$ and $2P_{\pm 1}$ to $1S(A_1)$ transitions respectively.

The oscillator strengths from figure 5.9 are collected into table 5.6.

### 5.4.2.2. Oscillator Strengths From the Literature

Oscillator strengths from [156, section 5.4] , for the $2P_0$ and $2P_{\pm 1}$ to $1S(A_1)$ transitions, are collected into table 5.7. It should be noted that these include those from [155]. The oscillator strengths, in both sources, are calculated by the use of EMT to find hydrogenic wavefunctions for the excited states, for one (source c) this is via

a variational method as in chapter 3. However, source b is originally published in a journal the present author does not have access to and so all that can be said of it is what is reprduced in [156] , that is, it uses the same Hamiltonian as source c, but does not use a variational method. The ground state is found the same way, however there is an additional phenomenological parameter introduced to the Hamiltonian, to adjust the obtained energy to match that measured, as discussed in section 5.4.1.2. This additional Hamiltonian element is likely to change the ground state wavefunctions spatial extent, relative to that obtained by the present author's own calculations.

The literature values approximately agree with each other.

## 5.4.2.3. Concluding Differences

The different calculated, literature sourced, and measurement inferred oscillator strengths are collated here in table 5.8, both $2P_0$ and $2P_{\pm 1}$ to $1S(A_1)$ transition oscillator strengths are shown.

An inspection of table 5.8 shows that there are some similarities between some of the oscillator strengths, and also that some of the methods of calculating the oscillator strength do not appear to match that measured at all.

### Intra-Category Consistency

Firstly, let the self consistency of each of the three overall categories be assessed.

The two literature sources agree very well with each other, for both transitions, which is to be expected given that it is implied that they use the same Hamiltonian (modified coulombic term to account for the screening potential of the donor core).

However, the different methods of the present authors own EMT calculated oscillator strengths do not agree with each other. This is to be expected, as the wavefunctions will differ considerably, as in the hydrogenic and EMT wavefunctions are obtained with different Hamiltonians; EMT refers to wavefunctions found by variationally minimising the energy, using prolate anisotropic hydrogen wavefunctions, and Mott scaled are the same wavefunctions but found by comparison to semiconductor to conduction transition data. In addition, the Mott scaled ground states are, in both hydrogenic and EMT cases, much smaller in spatial extent than those obtained by pure calculation. It is odd that the $2P_0$ and $2P_{\pm 1}$ oscillator strengths differ approximately by a factor of three for the EMT to Mott oscillator strengths, but a factor of one third for the EMT to EMT oscillator strength. The poor agreement of the hydrogenic to hydrogenic oscillator strengths, to the other values calculated by the present author, is likely due to the entirely incorrect scaling of both excited and ground states, the donor electron is not just hydrogen after all. The different groupings of calculated oscillator strengths, hydrogenic to Mott scaled and EMT to Mott scaled, are all within an order of magnitude of each other within their respective subcategories.

The absorption spectra determined oscillator strengths are also all within an order of magnitude of each other, but differ considerably. This is to be expected as there are considerably different situations for atomic, diatomic, and single ionised donor impurities.

**Inter-Category Consistency**

Secondly, the differences and agreements between the three overall categories can be assessed.

**Literature - Calculation**

The literature does not agree with the present authors calculations, there being at

best a factor of $\approx 2$ difference for the hydrogenic to Mott 2 values. This difference may be because of the different methods used to obtain the wavefunctions, i.e different EMT Hamiltonian used, Mott (spatially) scaled ground state, and the assumption that the purely hydrogenic wavefunctions are just scaled fully symmetric scaled hydrogen wavefunctions, which is not true for donors in silicon.

**Literature - Absorption Spectra**

In general the literature does not agree with the oscillator strengths obtained from absorption spectra. The $2P_0$ atomic, and $2P_{\pm 1}$ singly ionised donor centres are the only ones that have oscillator strengths that approximately match those of the literature. As the literature values are calculated with the assumption of having a single, rather than a double, donor it is to be expected that the values agree only for the singly ionised centre.

**Calculation - Absorption Spectra**

In general the calculated oscillator strengths do not agree with those obtained from absorption spectra. This is likely because the spherically symmetric hydrogenic wavefunctions are known to be incorrect, as is that of the EMT ground state. However, the EMT wavefunction is known to be approximately correct, for non ground states in deep donors, and the Mott scaled ground state relies upon experimental evidence [2] , therefore it is expected to be approximately correct for the single donor, or ionised, case, which it appears to be.

Furthermore, the atomic impurities have two donor electrons, and this is likely to complicate the ground state wavefunction (assuming the one is excited and one remains in the ground state when the transition is measured); the diatomic impurity transitions are complicated by the presence of an entire additional impurity atom. Both are likely to render the assumptions of the ground state wavefunction incorrect, along with the assumptions of the Mott transition model. That is, a single donor

with a slowly varying wavefunciton - isolated in a sea of silicon with no nearby impurities to cause rapid spatial changes in the wavefunction. The Mott criteria doping concentration, used to spatially scale the ground state, is given as an upper and lower bound, therefore the finding that one bound gives much closer agreement to measured oscillator strengths can be used to update estimates of which Mott bound is closer to the truth. The Mott scaled 2 ground state gives values that are much closer, almost identical, for both $2P_0$ and $2P_{\pm 1}$ oscillator strengths, making the corresponding doping concentration more likely to be the correct one.

**Summary**

Using simple EMT to obtain the excited state wavefunction, and the Mott semiconductor to conductor transition for the ground state, of a singly ionised double donor predicts the correct oscillator strengths. Atomic double donor oscillator strengths are approximately 2.7 to 2.9 times this, and diatomic donor complexes have those that are a factor of 8.6 greater(than the ionised); the uniformity of the factor between the EMT -Mott prediction and the ionised/atomic/diatomic donors immediately raises the question of whether it holds for higher, i.e. 3P, etc, states as well.

# 5.5. Transition Lifetimes: Time Resolved Spectra

Following the measurement of the peak energies of the Si:Se sample is the measurement of the radiative emission lifetime. This is done by the experimental procedure shown in detail in section 4.3, here it is merely the data and analysis that are presented.

The experiment consists of using step scan time-resolved Fourier transform spectroscopy, to measure the emission from Si:Se sample 71-8 following excitation by a 1220nm, approximately 5ns, laser pulse. The emission is directed into a Vertex 80V Fourier transform spectrometer via a series of aluminium mirrors. The experimental data

consists of an emission spectra extending from 1000 to 5000 cm$^{-1}$, and in time over 1000 ns; as there are no discernible features past 3000 cm$^{-1}$, and 400ns, all displayed graphs are cut off past these points. There are then three datasets, corresponding to the temperatures 10K, 80K, and 300K. The data is presented in three forms.

1. The overall data is displayed as a contour plot of the amplified detector signal over the 1000 to 3000 cm$^{-1}$, and 0ns to 400ns, ranges. This shows the overall evolution of the emission intensity with respect to time, wavenumber, and temperature.

2. For each temperature the emission over the full time range 0ns to 1000ns is averaged, and shown superimposed alongside the corresponding temperatures' absorbance spectra. The donor electron transition peaks in the absorbance spectra become weaker, and broader, as the temperature increases. Because of this, and to facilitate clear identification of the averaged emission peaks with specific transition groupings, a copy of this figure is shown where the absorbance spectra at each temperature is replaced by that at 10K; the 10K absorbance spectra having the clearest, and most sharply defined, transition peaks.

3. The natural log of the time trace, along the wavenumber positions corresponding to the transitions of primary interest $2P_0$ and $2P_{\pm 1} \rightarrow 1S(A_1)$, for both atomic and diatomic substitutional centres is shown; a least squares fitting procedure has been used to generate a straight fit line to this data, thus extracting the estimated emission lifetime.

These figures then allow the examination of: the spectral character, which transitions are likely dominating emission from the sample, the quality of lifetime fits, and a comparison of the fitting to simple scaled hydrogen and EMT transition rate models.

## 5.5.1. Experimental data

The overall data is shown in figure 5.10. It is apparent that there is a rapid increase in the measured optical signal at $\approx$75 ns from the beginning of the measurement, this indicates that the pumping laser pulse begins at this time. The signal intensity is increased from the start of this pulse across the entire measured range; it is assumed that in the vicinity of emission peaks that this results from both the sinc function sidelobes inherent in Fourier transform spectroscopy, and the broadband emission to be expected from the heating of the Si:Se sample following the laser pumping.

At 10K the optical signal is strongest and appears to be split into a set of four distinct emission bands, while intensity is greatest at 2000 cm$^{-1}$ and 105 ns. These bands appear to be in the regions of (1150-1500), (1550-1650), (1700-2300) and (2375 -2700) cm$^{-1}$; these bands are referred to as first, second, and so on in increasing wavenumber order. Each of the emission bands extends in time for $\approx$175 ns.

At 80K the emission for all bands has become far weaker, and now only extends for $\approx$100 ns. The first emission band, at 1550-1650 cm$^{-1}$, is far weaker in proportion to the others and extends over a smaller wavenumber range; it now only covers $\approx 1280 - 1500$cm$^{-1}$.

Finally for 300K the emission appears greatly reduced in both intensity and breadth of spectrum, with the first band being almost invisible; this is largely due to the loss of emission outside a 1300cm$^{-1}$ to 1350 cm$^{-1}$ range for this band. As the first band becomes weaker it becomes ever more indistinguishable from the broadband increase in emission following pumping.
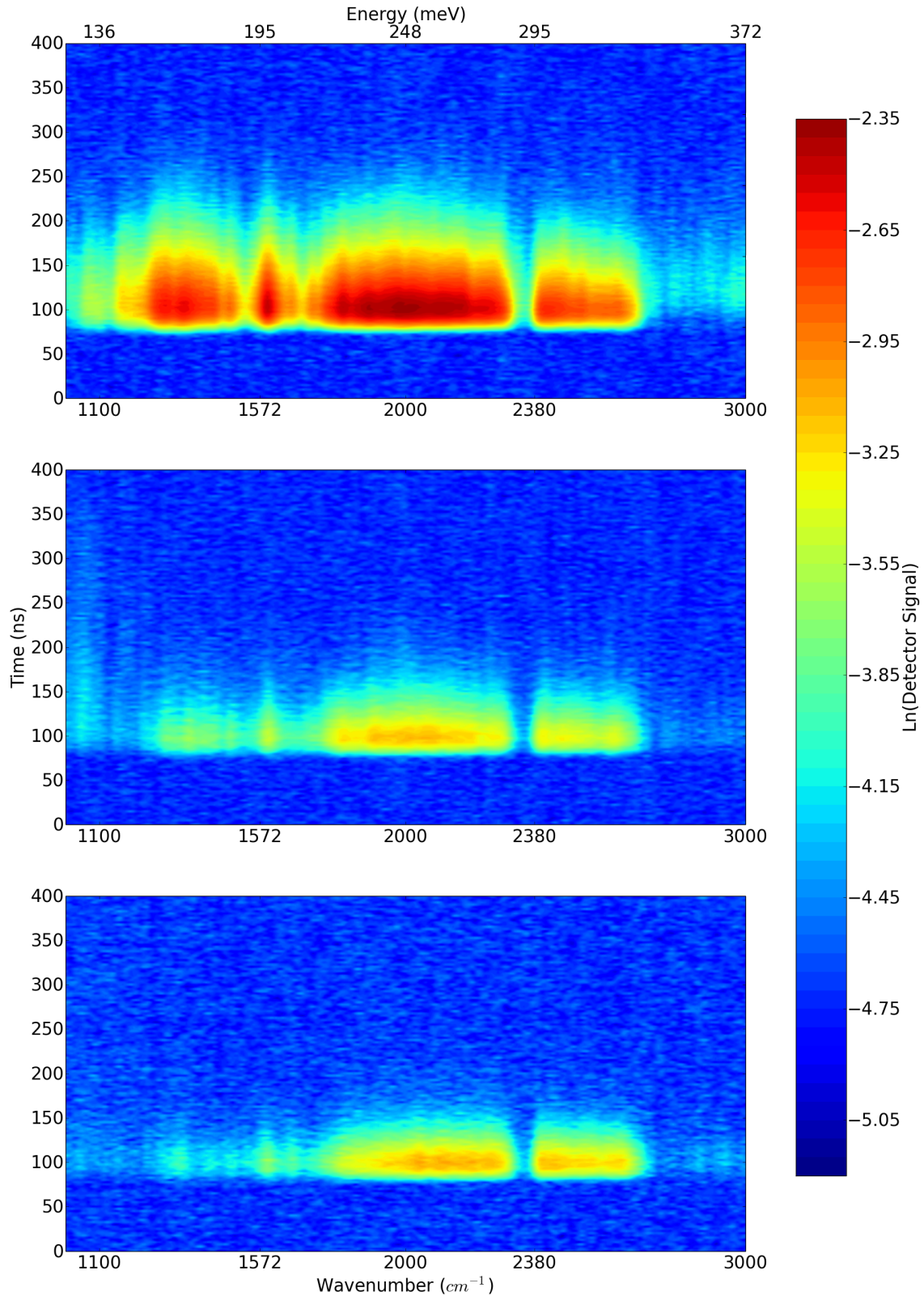
Figure 5.10.: Si:Se emission following 1220 nm $\approx$ 5ns laser pulse. **Top:** 10K. **Middle:** 80K. **Bottom:** 300K. The $2P_0 \rightarrow 1S(A_1)$ transition energies are marked on the x axis at 1572 and 2380 cm$^{-1}$ , or 195 and 295 meV, for atomic and diatomic Si:Se centres respectively.

As it is difficult for the human eye to easily compare the time traces of the emission data in figure 5.10 the same data is shown, but rescaled, in figure 5.11. The rescaling is done to the detector signal data before the natural log is taken, thus this is equivalent to merely shifting the datasets up in the log scale. Rescaling the data in the same way but post logarithm is less clear, as the widespread signal floor (eg. blue region in the 10K data) is greater in value for the 80K and 300K data.
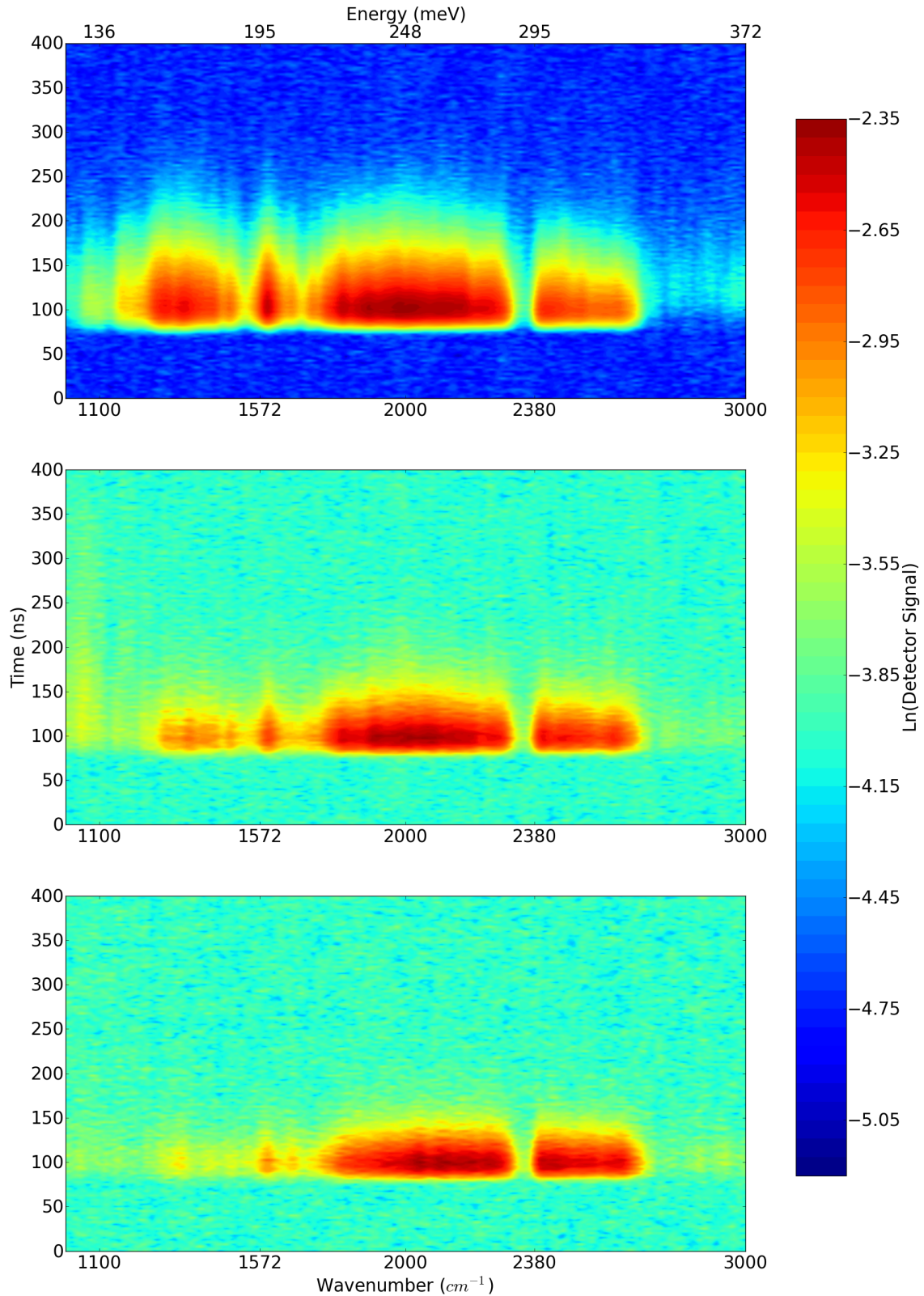
Figure 5.11.: Rescaled version of figure 5.10 The 80K and 300K data sets are rescaled by factors of $\approx 2.1$ and $\approx 2.0$ respectively, so that their peak detector signal is the same as that at 10K; the time trace of the emission can be more easily compared between temperatures. **Top:** 10K. **Middle:** 80K. **Bottom:** 300K. The $2P_0 \rightarrow 1S(A_1)$ transition energies are marked on the x axis at 1572 and 2380 cm$^{-1}$ , or 195 and 295 meV, for atomic and diatomic Si:Se centres respectively.

## 5.5.1.1. Averaged Emission Data with Absorbance Spectra

Figure 5.12 shows that at 4K two of the four emission bands line up roughly with the start of the atomic and diatomic Si:Se complex families of transitions in the absorption spectra. It appears that the set of atomic donor absorption peaks may correspond to the emission band centred at $1572\text{cm}^{-1}$. Similarly, the diatomic peaks correspond to emission that begins at $\approx 2380\text{cm}^{-1}$ and extends broadly until 2700 $\text{cm}^{-1}$; it is not clear why this emission should be so broad compared to that at 1572 $\text{cm}^{-1}$. However, the bands are extremely broad. It may be that phonon absorption contributes to this, as the Debye energy is 64.5 mev which would may explain the broadness of the peak beginning around $2380cm^{-1}$. However, there are two problems with this, firstly any such phonon absorption or emission caused broadening of the emission bands may be expected to not only extend in one direction, i.e. why only phonon absorption and not emission? Secondly, why is the broadness of the emission bands appear to be temperature independent?

Meanwhile the origin of the emission bands centred on 2000 $\text{cm}^{-1}$ and 1300 $\text{cm}^{-1}$ are unaccounted for. As the temperature increases the emission intensity lowers, while emission between 1200 and 1500 $\text{cm}^{-1}$ disappears almost entirely by 300K. The absorbance peaks are broadened at 80K and absent at 300K.

Figure 5.13 shows how the positions of the emission bands remain approximately constant.
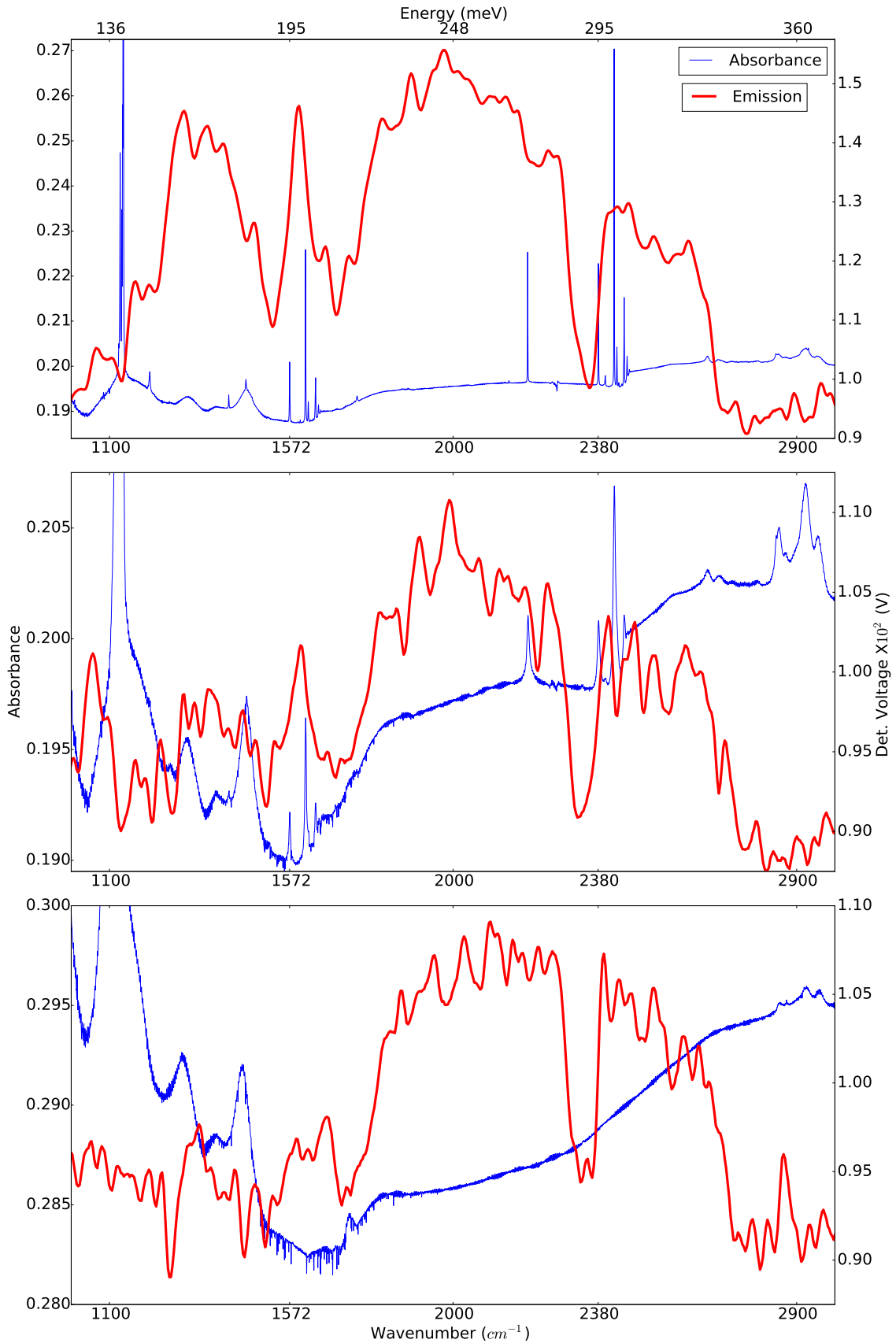
Figure 5.12.: Si:Se emission data averaged over the total time of the measurement, detector voltage shown on the right axis. Absorbance data, shown on the left axis. **Top:** 10K. **Middle:** 80K. **Bottom:** 300K. The emission data is averaged over the total measurement time of one microsecond, with 400 data points each sepatated by 2.5ns.

Figure 5.13 has the same emission data as from figure 5.12, however the absorbance data is now the same 10K data set so as to more clearly show the overlap of the emission and different transition positions.
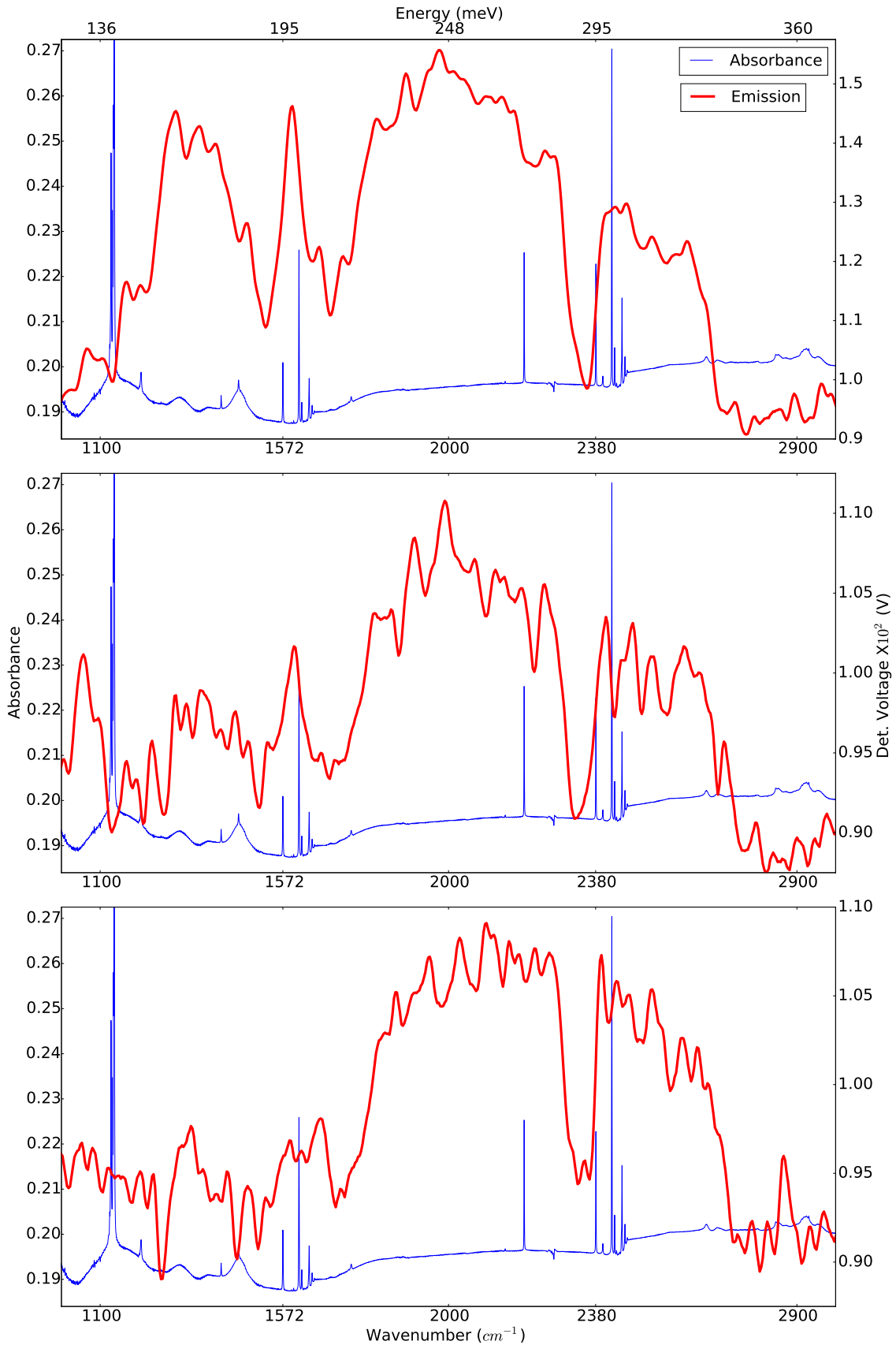
Figure 5.13.: Si:Se emission data averaged over the total time of the measurement, detector voltage shown on the right axis. Absorbance data, shown on the left axis. **Top:** 10K. **Middle:** 80K. **Bottom:** 300K. The emission data is averaged over the total measurement time of one microsecond, with 400 data points each separated by 2.5ns

**5.5.1.2.** $2P_0$ **and** $2P_{\pm 1} \rightarrow 1S(A_1)$ **Time Traces**

The aforementioned radiative transitions are of primary interest. They are also the first and second strongest sets of absorption peaks, and can thus be expected to be strong emitters. Thus traces along the time axis, showing only one set of energy data points, will show the evolution of the measured detector signal at a single wavenumber point, and thus the emission from the Si:Se sample. By fitting to the time trace of emission, and assuming a single exponential decay, the decay time constant can be estimated.

Thus sets of time traces, for both the $2P_0$ and $2P_{\pm 1}$ transitions, at the three measured temperatures 10K, 80K and 300K, are shown for atomic and diatomic selenium donor complexes in figures 5.14 and 5.15 respectively; where fitting lines are included in red and extend past the point that the data is fit to, in order to clearly show where the fit fails. The detector signal measuring emission is shown in blue.

**Fitting Procedure**

Non-coherent radiative emission is proportional to the number of excited atoms, thus an exponential decay of emission will result with the assumed form of equation 5.16; where $A$ is a scaling constant, $Y(t)$ is the intensity as a function of time $t$, and $\tau$ is the radiative emission decay constant. In order to fit to an exponentially decaying optical emission the natural logarithm of the emission intensity is taken, and a linear least squares fitting routine is used; this gives a straight line equation as in 5.17.

This has an advantage over fitting to the exponential decay form of the data. An arbitrary fixed difference between the data and fitting line will give a greater percentage error at the low value exponential tail as compared to that at the peak value; because there are many more low value points than high, an exponential fit

will preferentially fit to the low value points. Fitting to a linear decay, as when the logarithm of the data is taken, also has this problem, but because the data intensity only varies linearly rather than exponentially, the overweighting is lessened, giving a better overall fit between data and model at the decay tail. The fitting is then performed by the python numpy.polyfit function [4], and errors are then obtained from the data to fit covariance matrixes in the usual manner [157]. The time points, over which the lines are fit to the data, were determined manually, by varying the time so as to minimise the statistical error in the fit. In addition to this, a real trend in the data will be fitted to even with a low number of data points, as long as the noise remains constant and random, although the fitting uncertainty will be larger. By reducing the fitting time until the lifetime is approximately invariant (small changes will occur due to the noise in the data), an estimate of the lifetime is obtained and the time range to fit over is then extended until the fit begins to diverge from the data.

$$Y(t) = Ae^{-\frac{t}{\tau}} \tag{5.16}$$

$$ln(Y(t)) = ln(A) - \frac{t}{\tau} \tag{5.17}$$

Figure 5.14 shows the atomic transitions. Fitting errors are small in this, and it is apparent to the eye that the fitting lines agree well with the data for all temperatures, and both transitions. In the 10K and 80K plots, most especially for 80K $2P_{\pm 1}$, there is weak evidence of a second decay process; a second straight line region of the logarithm data indicates that there may be a slower radiative process, with a longer lifetime. Due to time constraints this second potential decay has not been

investigated. However, a proposed explanation is a slower process occurring, with the $2P$ states as the lower level; it is possible that this slow process is filling in the $2P$ states at a much slower rate than they are depopulated, giving rise to a second straight line region in the logarithm data.

For both transitions the lifetime fits show a shortening as the temperature increases. Non-radiative decay processes which reduce the excited state population will manifest as a shortening of the fit lifetime. Because of this the shorter lifetimes at higher temperature are to be expected, due to the increased probability of phonon assisted non-radiative transitions reducing the excited state populations.
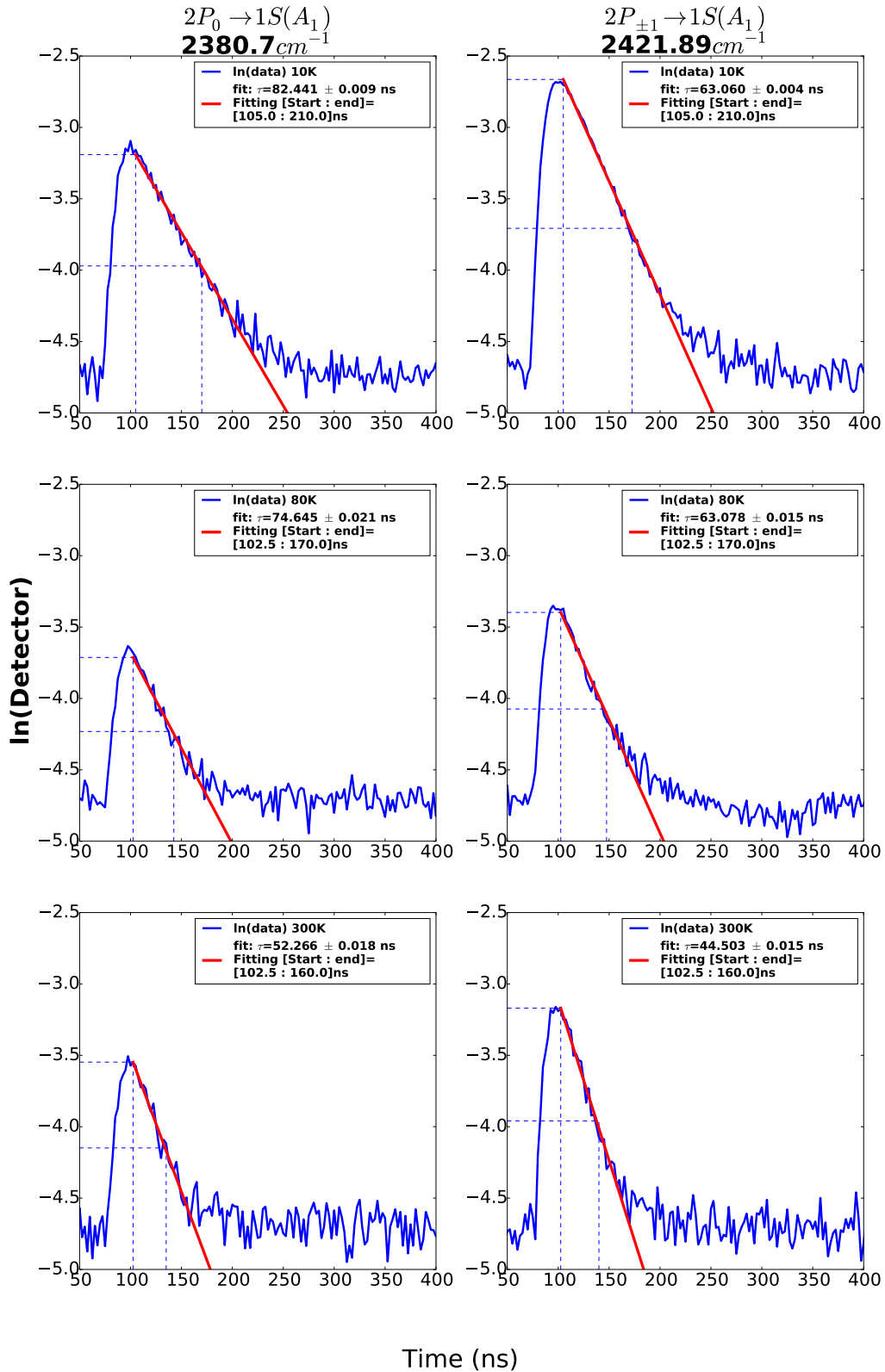
Figure 5.14.: Emission time traces at wavenumbers corresponding to **atomic** $2P_0$ and $2P_{\pm 1}$ to $1S(A_1)$ Si:Se donor electron transitions. **Detector:** detector voltage amplified by the circuit in figure 4.4. **Top:** 10K. **Middle:** 80K. **Bottom:** 300K. Fitting line parameters are given in inset legends; dashed lines show the fit peak and half maximum points, with corresponding times.

Figure 5.15 then shows the diatomic transitions. It can be clearly seen, and fitting errors corroborate this, that the fitting lines agree very well with the data for all temperatures and both transitions. In the 10K and 80K plots, most especially for 80K and $2P_{\pm 1}$, there is weak evidence of a second decay process. This manifests as a second straight line region of the logarithm data, and indicates that there is a slower, longer lived, radiative process occurring. Due to time constraints this second potential decay has not been investigated in details, however a possible explaination is a slower process with the $2P$ states as the lower level; it is thus possible that this slow process is filling in the $2P$ states at a much slower rate than they are depopulated, giving rise to a second straight line region in the logarithm data.
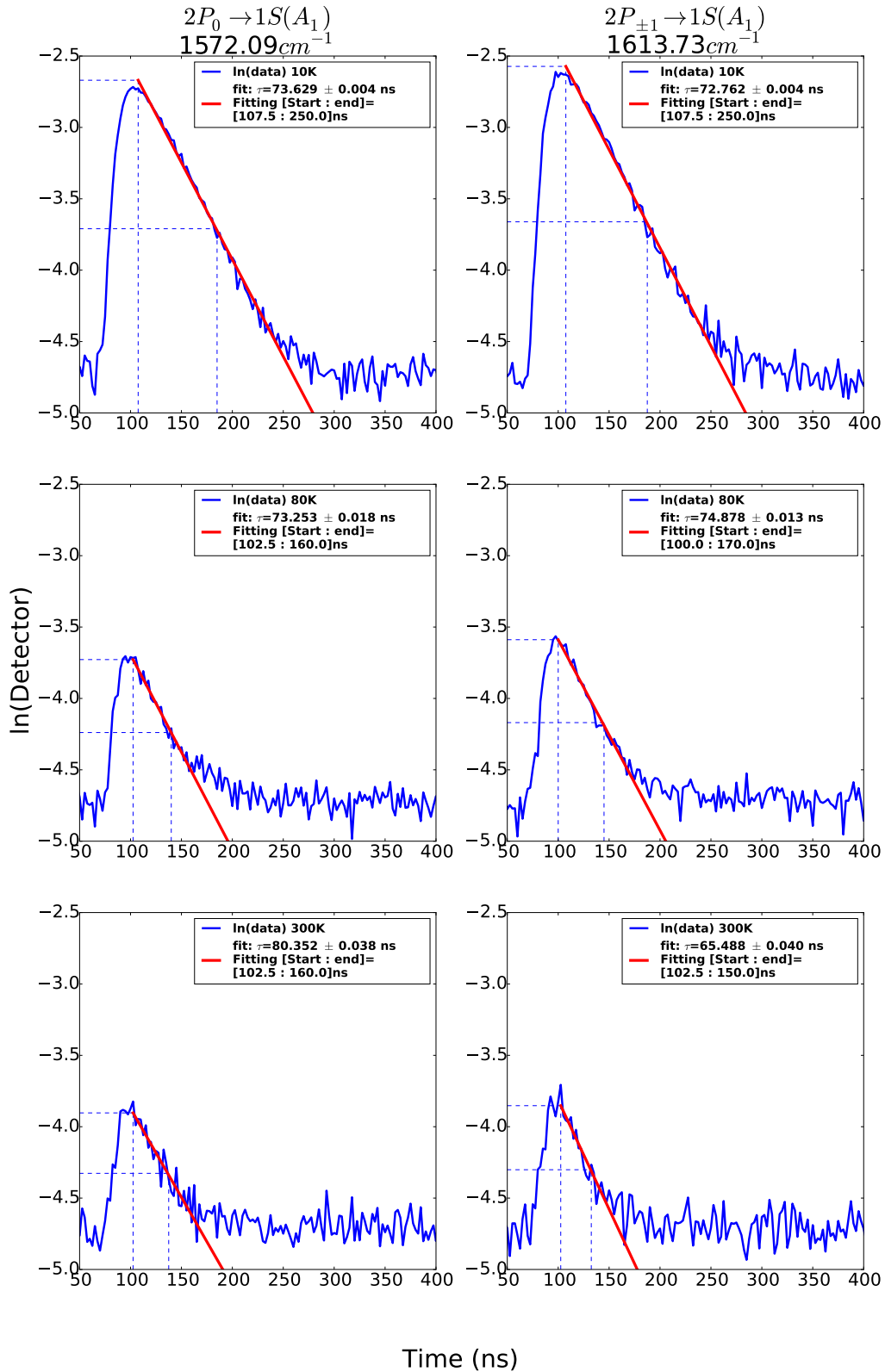
Figure 5.15.: Emission time traces at wavenumber corresponding to **diatomic** $2P_0$ and $2P_{\pm 1}$ to $1S(A_1)$ Si:Se donor electron transitions. **Detector:** detector voltage amplified by the circuit in figure 4.4. **Top:** 10K. **Middle:** 80K. **Bottom:** 300K. Fitting line parameters are given in inset legends; dashed lines show the fit peak and half maximum points, with corresponding times.

A cartoon schematic of the believed donor electron behaviour is shown in figure 5.16. This shows the optical pumping of the donor electrons into the conduction band, their presumed phonon decay to the band bottom, or direct optical transition to ground, followed by a set of transitions from excited donor states; the emission spectrum is then shown at the bottom of the figure.
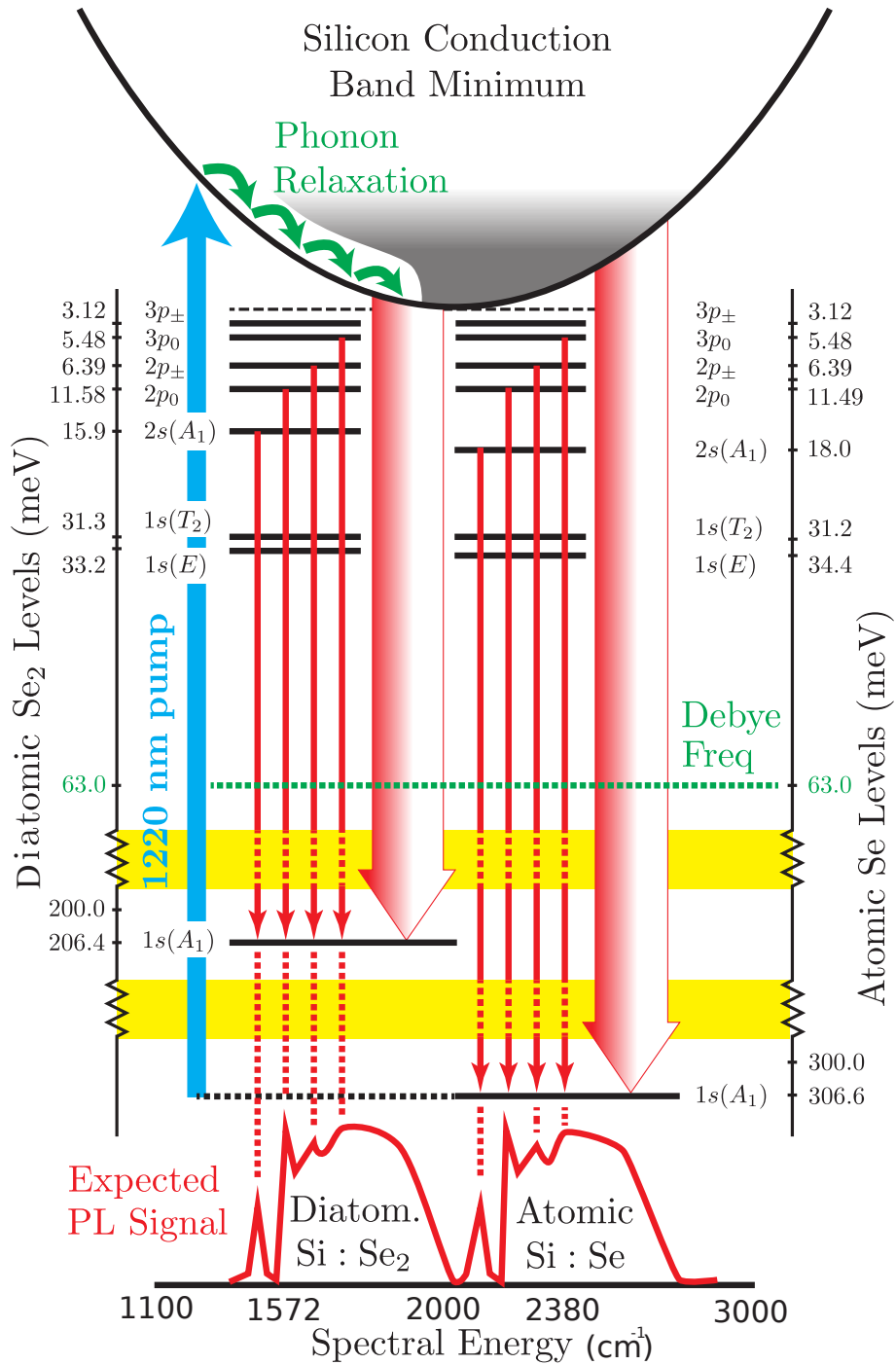
Figure 5.16.: Proposed electron decay pathways, along with a corresponding emission spectra. **y axis:** Energy levels of the atomic and diatomic selenium donor electrons, on the right and left. **x axis:** Photo-luminescence shown in cm$^{-1}$; $2P_0$ transitions for atomic and diatomic donors, marked at 1572cm$^{-1}$ and 2380cm$^{-1}$. The **Blue arrow:** 1220nm pump laser. **Green arrows:** Phonon mediated conduction band relaxation. Debye frequency is shown in green.

## 5.5.2. Experiment to Theory Comparison

The fit lifetimes for both atomic and diatomic selenium donor complexes are collected and compared to those estimated by Fermi's golden rule, in table 5.9; transitions occurring in diatomic complexes could not be predicted as accurately as the atomic transitions. This is because the EMT and simple hydrogen wavefunction modelling completely ignores any effects from a nearby selenium atom, as for the diatomic states.

Comparing the lifetimes values in table 5.9, it can be seen that all the measured lifetimes are longer than the detector response time of 40 ns; this lifetime is defined as that to reach $\frac{1}{e}$ of the peak intensity. Strictly speaking, the total measured signal must be longer than 40ns to be sure of this, and if the rise time of 20ns is also considered then that gives a target of 60ns. Beginning at the start of the signal rise, which occurs at $\approx$75ns, there is between 75 to 100 ns until signals have decayed. A conclusion to be drawn from this is that the measured lifetimes must be due to the radiative emission.

The measured lifetimes for each set of transitions remains roughly constant with selenium complex and temperature categories, for example all atomic $2P_0$ transitions are similar. Weaker agreement is found with the estimated lifetimes. The strongest agreement for the $2P_0$ is the scaled hydrogen, with 101 ns compared to measured values within the 52.3 - 82.4 ns range. This is unexpected because the scaled hydrogen model does not account for the degeneracy of the effective masses of the donor electrons in the silicon.

Meanwhile the best agreement for the $2P_{\pm1}$ is the EMT to EMT scaled transition, with a value of 135 ns to the measured 44.5 - 74.9 ns range. This is also unexpected because the EMT scaled $1S(A_1)$ state is known to be incorrect due to the energy

inaccuracy.

However, there is agreement within an order of magnitude between the experiment and theory. Firstly, this suggests that the Mott transition scaled $1S(A_1)$ state is not wholly accurate. The effects of the second selenium donor electron may not be as small as initially estimated. As they have the weakest absorbance lines, it is not surprising that the ionised transitions do have any measurable emission; any emission from ionised states could be expected to be unaffected by the second donor electron, as it is not localised at that same nucleus. Regardless of the cause, it seems that the ground state wavefunction is only approximately estimated.

An counterintuitive aspect of the lifetimes shown in table 5.9 is that those for the diatomic complexes get longer, rather than shorter, with increasing temperature; this could be similar to that for the phosphorus donor states in [45], where the $2P_{\pm1}$ state exhibits a stronger positive temperature dependence than the $2P_0$, although both do to some extent. This is, however, only measured here for the $2P_0$ state, and could be erroneous.

## 5.6. Alternative Possible Decay Pathways and Complicating Factors

The measured decay lifetimes discussed have so far been assumed to be purely due to radiative emission, however, this is only one of several possible decay pathways for the excited donor electrons; of course, all transition rates calculated via Fermi's golden rule are purely dipole interaction caused radiative emission. Not only are there alternate decay pathways, but it is possible that the effect of things such as the recombination from the conduction band may take longer than believed.

## 5. Results

To see some of the possible alternate decay pathways, along with complications to the simple radiative decay picture, refer to figure 5.16. The possible alternate relaxation pathways are listed, roughly in the order that they can occur in the experiment.

These pathway complications include:

1. Speed of phonon assisted relaxation, or cascade, to conduction band minimum.

2. Recombination speed from the conduction band to excited donor states.

3. Cascades between excited states causing delay.

4. Relaxation to intermediate states, and subsequent re-excitation or decay.

5. Re-ionisation by photon, or phonon, absorption.

6. Trapping of electrons in silicon defects, or other impurities.

7. Multiple donor atom complexes complicating things.

The first issue to consider is the speed of phonon assisted relaxation to the conduction band minima. If the excited donor electrons take a significant amount of time to fall to the conduction band minima, then any capture of those electrons by excited donor states is delayed. This relaxation to the conduction band minima is mediated by phonon emission and interaction. If the excited electrons are near the conduction band minima, then a recent ultrafast carrier relaxation study [158] suggests that the relaxation may be as fast as $\approx$ 240 fs; if the electrons are excited to a different valley in the conduction band, then the relaxation to the conduction band minima may take only an additional $\approx$ 100 fs.

The next issue is the capture rate, or recombination speed, for electrons transitioning from the conduction band minima to excited donor states. This has a markedly

different characteristic shape, reciprocal linear [159, eq 1.20], to the exponential form of radiative decay. The present author could not find any experimental information on the carrier capture rate. On a log intensity scale both an exponential and reciprocal decay will appear linear, however, they will not have the same linear trend. Therefore, the lack of two clear linear trends indicates that the capture rate is not dominant, or significant, on the scale of the total emission decay lifetime.

Cascades and relaxation to intermediate states are similar, and linked together. Cascades between excited states refers to an excited electron decaying through, one by one, a plethora of the excited states (that asymptotically approach the conduction band minima, eg. 3p,3f,4d, 5f etc). If the excited electrons are captured by one of these states, that has greater energy than the $2P$ states, then any additional time taken to decay to the $2P$ state will contribute to the measurement of that specific radiative decay rate. This will have the effect of spreading out the measured $2P$ to $1S(A_1)$ decay lifetime. Assuming that a decay to the $2P$ states is even possible, for example if the excited donor electron cascades to the $3P$ state then any transition to the $2P$ state is incredibly unlikely as the dipole matrix element is zero.

Relaxation to intermediate states refers to states such as the $2S$, $1S(E)$, and $1S(T)$, from which there is no dipole interaction caused transition to the ground state. While there is measured emission corresponding to the energies of these states transitioning to the ground $1S(A_1)$ state, such transitions can be expected to be slow as a direct consequence of their zero strength di-polar interaction. The excited electron is susceptible to re-excitation, presumably by phonon absorption as it is unlikely that there will be a large amount of photons of sufficient energy; at least, those not emitted by other excited donor electrons decaying into such a trapping intermediate state, as these will be the only photons to cause a net removal of a donor electron from the intermediate state. These re-excited electrons will then interfere with the

measurement of the radiative decay lifetime in the same way that cascading electrons captured by higher excited states can. That is, by slowly repopulating the $2P$ states and having the effect of spreading out the measured emission decay.

Any of the electrons that have decayed, whether they are in the ground, or an intermediate, state are then susceptible to re-excitation. For electrons in the ground state, any re-excitation is probably from photon absorption. This is due to the lack of phonons in silicon, of sufficient energy, and the low probability of a multiple phonon absorption. However, for intermediate states the re-excitation could come from either photon or phonon, as no state except the ground is deep enough to require multiple phonons to be excited to a higher energy state. If the electron is excited back to the conduction band then this re-excitation becomes re-ionisation. This can interfere with the measurement of the radiative decay rate for various reasons: the electron is susceptible to the delays of cascading back to the $2P$ states; the absorption of a photon prevents measurement of that photon; any subsequent re-emission of a photon gives the appearance of a long decay time, where there has been a decay, photon absorption, and then a second decay. All of these have the effect of spreading out the measured exponential emission decay.

It is also possible that excited electrons in the conduction band are not recaptured by the donor atoms, but are instead trapped in a defect or other impurity state. This can have an affect on the measured lifetime if the impurity is ionised, such that the electron re-enters the conduction band and then is susceptible to the other problems listed above in addition to the time spent in the impurity, and "wandering" in the conduction band, artificially inflating the measured radiative decay lifetime.

Finally, it is possible for multiple donor substitutional complexes to further interfere. If several Se atoms are in close proximity, not only do they affect each others energy

levels, but they could affect the radiative recombination rates (in addition to all the other listed problems). This is because one atoms excited state wavefunctions may overlap the lower energy wavefunctions of another atom. As an example consider the $2P_0$ to $1S(A_1)$ transition, except where the initial and final states are of separate but close atoms. In this case the dipole matrix element will be much less, due to the presumably smaller total wavefunction overlap (it is plausible that for some states the overlap is greater for certain relative atom positions). Thus altering the decay rate.

Many of the above problems can be overcome by the use of direct, resonant, stimulation of the desired transition. For example, by the use of a pump probe experiment. In this case, the sample would be illuminated by some broad band source, while the transmission through the sample was measured as a function of time and wavelength. At some known duration, and pulse shape, laser pulse, of much greater intensity than the broad band source, would stimulate the transition in question. The transmission through the sample, following the end of the laser pulse, could then be measured at the transition energy, giving the decay lifetime. Of course, this does not solve the donor complex, re-ionisation/excitation, or trapping in another defect, problems. However, it does remove the phonon assisted relaxation, recombination from conduction band to donor, cascades between excited states, and relaxation to intermediate state problems.

## 5.7. Conclusions

In order to appropriately conclude this chapter, the results must be placed back into context. To do so, the questions this thesis seeks to assist in answering are recalled: "Are there are optical transitions with long radiative lifetimes in chalcogen deep double donor silicon systems?", and "Do simple scaled hydrogen wavefunctions

from EMT provide a good description of reality for chalcogen deep double donor electrons in silicon?".

The first question is motivated by the knowledge that similar pnictogen donor systems in silicon have radiative lifetimes of $\approx 200$ps[104][45][105], and a coherence lifetime of $160 \pm 20ps$[101]; for the $2P_0$ state of a phosphorus donor electron. It appears that both $2P$ states of selenium donors in silicon have longer radiative lifetimes than phosphorus; all selenium lifetimes are tens of nanoseconds, by a factor of at least 200 to phosphorus. The 10K $2P_0$ state has approximately 80ns for both atomic and diatomic complex donor electrons; correspondingly, the $2P_{\pm 1}$ state has lifetimes of approximately 60ns and 70ns, for atomic and diatomic complexes respectively.

Selenium donor complexes have a longer $2P$ state radiative lifetimes than phosphorus.

However, there are possible flaws with this experimental data. Firstly, the decay time could be dominated by a recombination time from the conduction band to the excited donor states. This could be an explanation as to why the lifetime appears to be similar across such broad emission bands. However, sources such as [45] propose that recombination from the conduction band should take no more than 16ps from complete ionisation, for phosphorus. This could be similar for chalcogen donors, as it is presumed that recombination occurs with excited donor states, not the ground; the excited states both have a binding energy of 11.49meV for the $2P_0$ state.

A possible experiment to resolve this is a direct pump prove measurement. Instead of pumping non-resonantly into the conduction band, a pump pulse is tuned to a transition energy. This pulse is split by a 50/50 BS, and one half of the pulse is directed down a variable optical delay line or pathway. The non-delayed pulse

then resonantly pumps the sample, electrons are excited to higher states, and then begin to decay. After some time the delayed pulse is directed at the sample; the transmission of the second pulse will depend upon how many electrons have decayed back into their ground state. Thus by repeatedly varying the delay line, the direct transition lifetime can be measured.

A second flaw is that the lifetimes are on the threshold of the detector response time, 40ns, with a 45ns lifetime, for the $2P_{\pm 1}$ diatomic state at 10K, being on this edge. A repeat of the conduction band pumping, time resolved emission, experiment with a faster detector would resolve this problem; although a faster detector would require a smaller element, thus making the collected emission light, and detector signal, weaker. However, a faster detector is not required for a direct pump probe experiment.

If the long lifetime is not due to recombination, then the next logical step is to cause controlled Rabi oscillations between the $2P$ and ground states. This, along with the application of precise $\pi$ pulses and the optical "Hann" echo, could allow the measurement of the $T_2$ coherence lifetime of the states; this would be a selenium copy of the experiments peformed for phosphorus in [101]. Further work on fulfilling the DiVincenzo requirements of quantum computing, using chalcogen donor systems, can only proceed if the recombination lifetime is not found to be dominant over the radiative, and if the coherence lifetime is sufficient.

Now the calculated lifetimes are considered for summary. The second question of the thesis is motivated by the need to understand the donor electron wavefunction, if the system is to be used for quantum technological applications; with the primary envisigened apllication being for Qbitinteraction, as in the Stoneham proposal for a quantum computer [1]. Agreement within an order of magnitude between expe-

riment and calculation is obtained. The method of calculated transition rates expected to be most accurate is that between EMT excited, and Mott transition scaled ground, states. This is because the excited state wavefunctions already give accurate agreement with measured spectra [8][115][107][94]; the wavefunction must be similarly accurate. The Mott transition is also a well known phenomenon[123][124][2]. Such calculated lifetimes are then between 9 and 17 ns for the $2P_0$, and 12 and 20 ns for the $2P_{\pm 1}$, states.

The calculated lifetime values expected to be most accurate only differ by a factor of between 4 to 8 from those experimentally measured. The central cell problem is presumed to be the cause of this discrepancy, with the $1S(A_1)$ ground state the most vulnerable to error. An investigation of the literature surrounding the theoretical correction to the central cell problem may provide additional insight. Combined with more precise Mott transition studies, it may be possible to improve the $1S(A_1)$ ground state accuracy.

In summary, time-resolved emission lifetimes, for the $2P_0$ to $1s(A_1)$ ground state of selenium donor electrons in silicon, have been measured to be as long as $\approx 80$ns for atomic donor complexes at 10K. The $2P_{\pm 1}$ transition has a lifetime as short as $\approx 45$ns at 300K, this is on the edge of the detector decay times, and could merely be an upper bound.

The corresponding diatomic transitions are $\approx 80$ns for the $2P_0$ state, and $\approx 65$ns for the $2P_{\pm 1}$.

EMT, and simply scaling wavefunctions, provide a wide range of lifetime estimates. The Mott transition scaled ground state, along with the $2P$ states, both presumed to be reasonably accurate, give lifetime estimates of $\approx 10$ns. Accuracy between

experiment and calculation is then an order of magnitude. This is not validation of the theory, but neither is it complete dismissal; more work is needed for both experiment and theory.

| Peak $cm^{-1}$(meV) | FWHM $cm^{-1}$(meV) | | | Lifetime ($10^{-12}$s) | | |
|---|---|---|---|---|---|---|
| | **4K** | **14K** | **80K** | **4K** | **14K** | **80K** |
| **Si:Se$^2$ From Part A figure 5.4.** | | | | | | |
| 1572.09 (194.914) | 1.687 (0.209) | 1.687 (0.209) | 5.062 (0.628) | 9.884 | 9.884 | 3.295 |
| 1599.88 (198.360) | 1.687 (0.209) | 1.687 (0.209) | 2.652 (0.329) | 9.884 | 9.884 | 6.290 |
| 1613.73 (200.077) | 1.687 (0.209) | 1.687 (0.209) | 4.580 (0.568) | 9.884 | 9.884 | 3.641 |
| 1620.9 (200.966) | 1.687 (0.209) | 1.687 (0.209) | 15.910 (1.973) | 9.884 | 9.884 | 1.048 |
| 1640.1 (203.346) | 1.687 (0.209) | 1.928 (0.239) | 4.821 (0.598) | 9.884 | 8.648 | 3.459 |
| 1647.67 (204.285) | 1.928 (0.239) | 2.170 (0.269) | 6.026 (0.747) | 8.648 | 7.687 | 2.767 |
| 1653.34 (204.988) | 6.509 (0.807) | 15.669 (1.943) | 15.910 (1.973) | 2.562 | 1.064 | 1.048 |
| **Si:Se From Part B figure 5.4.** | | | | | | |
| 2380.7 (295.169) | 1.446 (0.179) | 1.446 (0.179) | 7.473 (0.927) | 11.531 | 11.531 | 2.232 |
| 2398.73 (297.405) | 2.170 (0.269) | 2.411 (0.299) | 33.266 (4.124) | 7.687 | 6.919 | 0.501 |
| 2421.89 (300.276) | 1.446 (0.179) | 1.446 (0.179) | 7.232 (0.897) | 11.531 | 11.531 | 2.306 |
| 2429.25 (301.189) | 1.446 (0.179) | 1.446 (0.179) | 16.633 (2.062) | 11.531 | 11.531 | 1.003 |
| 2448.23 (303.542) | 1.446 (0.179) | 1.446 (0.179) | 7.714 (0.956) | 11.531 | 11.531 | 2.162 |
| 2455.87 (304.489) | 1.687 (0.209) | 1.687 (0.209) | 50.622 (6.276) | 9.884 | 9.884 | 0.329 |
| 2461.71 (305.213) | 28.445 (3.527) | 36.641 (4.543) | 53.274 (6.605) | 0.586 | 0.455 | 0.313 |
| **Si:Se$^+$ From Part C figure 5.4.** | | | | | | |
| 4761.65 (590.369) | 2.411 (0.299) | 2.652 (0.329) | 12.053 (1.494) | 6.919 | 6.290 | 1.384 |
| 4844.02 (600.582) | 2.411 (0.299) | 2.652 (0.329) | 15.187 (1.883) | 6.919 | 6.290 | 1.098 |
| 4858.69 (602.401) | 2.411 (0.299) | 2.652 (0.329) | 33.266 (4.124) | 6.919 | 6.290 | 0.501 |
| 4896.83 (607.130) | 2.411 (0.299) | 2.411 (0.299) | 9.401 (1.166) | 6.919 | 6.919 | 1.774 |
| 4911.5 (608.948) | 5.062 (0.628) | 5.062 (0.628) | 2.411 (0.299) | 3.295 | 3.295 | 6.919 |

Table 5.2.: The peak position, FWHM, and lower bound of the associated lifetime of peaks from figures 5.4 and 5.3; see table 5.3 for comparisons with literature sources. The peak position and FWHM are given in wavenumbers, with the meV value in square brackets alongside. The lifetimes are calculated by using the FWHM linewidth to estimate the uncertainty in the energy and then using Heisenburgs uncertainty principle to estimate the corresponding lifetime.

| Transition[94] | Energy $(cm^{-1})$[mev] [94] | Absorbance Peak$(cm^{-1})$[mev] | $\Delta E$ $(cm^{-1})$[mev] |
|---|---|---|---|
| Conduc. $\rightarrow$ 1S($A_1$) | 2473.1 [306.63] | na | na |
| $2P_0 \rightarrow$ 1S($A_1$) | 2380.5 [295.14] | 2380.7 (295.169) | 0.2 [0.029] |
| $2P_1 \rightarrow$ 1S($A_1$) | 2421.6 [300.24] | 2421.89 (300.276) | 0.29 [0.036] |
| $3P_0 \rightarrow$ 1S($A_1$) | 2428.9 [301.15] | 2429.25 (301.189) | 0.35 [0.039] |
| $3P_1 \rightarrow$ 1S($A_1$) | 2448 [303.51] | 2448.23 (303.542) | 0.23 [0.032] |
| $4P_0 \rightarrow$ 1S($A_1$) | 2446.6 [303.34] | 2448.23 (303.542) | 1.63 [0.208] |
| $4P_1 \rightarrow$ 1S($A_1$) | 2455.4 [304.43] | 2455.87 (304.489) | 0.47 [0.208] |
| $4F_1 \rightarrow$ 1S($A_1$) | 2457.8 [304.73] | 2455.87 (304.489) | 2.07 [0.241] |
| $5F_0 \rightarrow$ 1S($A_1$) | 2460 [305.00] | 2461.71 (305.213) | 1.71 [0.213] |
| $5F_1 \rightarrow$ 1S($A_1$) | 2463 [305.37] | 2461.71 (305.213) | 1.29 [0.157] |
| $5P_1 \rightarrow$ 1S($A_1$) | 2461.4 [305.17] | 2461.71 (305.213) | 0.31 [0.043] |
| $6P_1 \rightarrow$ 1S($A_1$) | 2464.4 [305.55] | 2461.71 (305.213) | 2.69 [0.337] |
| $7P_1 \rightarrow$ 1S($A_1$) | 2466.3 [305.78] | 2461.71 (305.213) | 4.39 [0.567] |

Table 5.3.: Comparison of transition energies of atomic selenium states in silicon from [94], with measured peaks in the absorbance spectra. **Conduc.** : Conduction band.

| Transition[94] | Energy $(cm^{-1})$[mev][94] | Absorbance Peak $(cm^{-1})$[mev] | $\Delta E$ |
|---|---|---|---|
| CdBnd $\rightarrow$ 1S($A_1$) | 1665.1 [206.44] | na | na |
| $2P_0 \rightarrow$ 1S($A_1$) | 1571.7 [194.86] | 1572.09 (194.914) | 0.39 [0.054] |
| $2P_1 \rightarrow$ 1S($A_1$) | 1613.5 [200.05] | 1613.73 (200.077) | 0.39 [0.054] |
| $3P_0 \rightarrow$ 1S($A_1$) | 1620.6 [200.93] | 1620.9 (200.966) | 0.3 [0.036] |
| $3P_1 \rightarrow$ 1S($A_1$) | 1639.9 [203.32] | 1640.1 (203.346) | 0.02 [0.026] |
| $4P_0 \rightarrow$ 1S($A_1$) | 1638.4 [203.13] | 1640.1 (203.346) | 1.7 [0.216] |
| $4P_1 \rightarrow$ 1S($A_1$) | 1647.4 [204.25] | 1647.67 (204.285) | 0.27 [0.035] |
| $4F_1 \rightarrow$ 1S($A_1$) | 1649.8 [204.55] | 1647.67 (204.285) | 2.13 [0.27] |
| $5F_0 \rightarrow$ 1S($A_1$) | 1651.8 [204.8] | 1653.34 (204.988) | 1.54 [0.1882] |
| $5F_1 \rightarrow$ 1S($A_1$) | 1654.8 [205.17] | 1653.34 (204.988) | 1.46 [0.029] |
| $5P_1 \rightarrow$ 1S($A_1$) | 1653.3 [204.98] | 1653.34 (204.988) | 0.04 [0.008] |
| $6P_1 \rightarrow$ 1S($A_1$) | 1656.3 [205.36] | 1653.34 (204.988) | 3.04 [0.372] |
| $7P_1 \rightarrow$ 1S($A_1$) | 1658.4 [205.62] | 1653.34 (204.988) | 5.06 [0.74] |

Table 5.4.: Comparison of transition energies of diatomic selenium states in silicon from [94] with measured peaks in the absorbance spectra.

| Upper Method | $1S(A_1)$ Method | OS $2P_0$ | OS $2P_{\pm 1}$ |
|:---:|:---:|:---:|:---:|
| Hydrogenic | Hydrogenic | 0.254 | 0.0352 |
| Hydrogenic | Mott 1 | 109 | 124 |
| Hydrogenic | Mott 2 | 174 | 176 |
| EMT | EMT | 9.76 | 3.44 |
| EMT | Mott 1 | 7.09 | 23.6 |
| EMT | Mott 2 | 13.2 | 39.6 |

Table 5.5.: Different methods of calculating wavefunctions and their associated oscillator strengths for both $2P_0$ and $2P_{\pm 1}$ to $1S(A_1)$ dipole interaction transitions, given to 3sf. **OS:** Oscillator Strengths. **Hydrogen:** Using fully spherical scaled hydrogen wavefunctions to match the energy. **EMT:** Effective mass theory variationally scaled prolate ellipsoid hydrogenic wavefunctions. **Mott:** Mott transition scaled $1S(A_1)$ states, with 1 and 2 corresponding to the donor concentrations of 1.8 and $4.3 \times 10^{20} \text{cm}^{-3}$ respectively.

| Donor Complex | OS $2P_0$ | OS $2P_{\pm 1}$ |
|:---:|:---:|:---:|
| Atomic | 41.3 | 105 |
| Diatomic | 119 | 334 |
| Singly Ionised | 13.8 | 38.5 |

Table 5.6.: Oscillator strengths obtained from integrating the area under absorption curves in figure 5.9, donor impurity concentration data from table 5.1, and calculated using equation 5.5. **OS:** Oscillator Strengths

| Lit Source | OS $2P_0$ | OS $2P_{\pm 1}$ |
|:---:|:---:|:---:|
| c | 58.6 | 28.8 |
| b | 57.9 | 28.7 |

Table 5.7.: Oscillator strengths for both $2P_0$ and $2P_{\pm 1}$ to $1S(A_1)$ dipole interaction transitions, given to 3sf. **OS:** Oscillator Strengths **Lit Source:** Literature source, from [156, table 5.20]with the same labels; c refers to those from [155] (these values are quoted in the other, more recent, source [156, table 5.20]).

| Source | OS $2P_0$ | OS $2P_{\pm1}$ |
|---|---|---|
| Literature | | |
| c | 58.6 | 28.8 |
| b | 57.9 | 28.7 |
| EMT Calculation | | |
| Hydro - Hydro | 0.254 | 0.0352 |
| Hydro - Mott 1 | 109 | 124 |
| Hydro - Mott 2 | 174 | 176 |
| EMT - EMT | 9.76 | 3.44 |
| EMT - Mott 1 | 7.09 | 23.6 |
| EMT - Mott 2 | 13.2 | 39.6 |
| Absorption Spectra | | |
| Atomic | 41.3 | 105 |
| Diatomic | 119 | 334 |
| Singly Ionised | 13.8 | 38.5 |

Table 5.8.: Collation of the different oscillator strengths from different sources. Only the $2P_0$ and $2P_{\pm1}$ to $1S(A_1)$ dipole interaction strengths, from the area under measured absorption spectra, literature values, and EMT based calculations of the author are shown here. **OS:** Oscillator Strengths, given to 3sf. **Source:** Labels correspond to the source of the OS. **Literature:** OS's from literature sources, [156, table 5.20]with the same labels as given there; c refers to those from [155] (these values are quoted in the other, more recent, source [156, table 5.20]). **EMT Calculation:** Calculated OS's for different methods of estimating the wavefunctions of the states, given as: excited state-ground state calculation method. The different methods are: *Hydro*- Using fully spherical scaled hydrogen wavefunctions to match the energy; *EMT*- Effective mass theory variationally scaled prolate ellipsoid hydrogenic wavefunctions; *Mott*- Mott transition scaled $1S(A_1)$ states, with 1 and 2 corresponding to the donor impurity concentrations of 1.8 and $4.3 \times 10^{20}$cm$^{-3}$ respectively. **Absorption Spectra:** OS obtained from integrating the area under absorption curves in figure 5.9, donor impurity concentration data from table 5.1, and calculated using equation 5.5. *Atomic*, *diatomic*, and *ionised* refers to a single, pair of, or singly ionised impurity atom or atoms.

| Method | $\tau_{1S(A_1),2P_0}$ ( ns ) | $\tau_{1S(A_1),2P_{\pm 1}}$ ( ns ) |
|---|---|---|
| Expt Atomic 10 K | 82.4 | 63.1 |
| Expt Atomic 80 K | 74.6 | 63.1 |
| Expt Atomic 300 K | 52.3 | 44.5 |
| Expt Diatomic 10 K | 73.7 | 72.8 |
| Expt Diatomic 80 K | 73.3 | 74.9 |
| Expt Diatomic 300 K | 80.4 | 65.5 |
| Hydrogen $\rightarrow$ Hydrogen | 2680 | 74700 |
| Hydrogen $\rightarrow$ Mott 1 | 6.27 | 21.4 |
| Hydrogen $\rightarrow$ Mott 2 | 3.94 | 15.0 |
| EMT $\rightarrow$ EMT | 12.3 | 135 |
| EMT $\rightarrow$ Mott 1 | 16.9 | 19.6 |
| EMT $\rightarrow$ Mott 2 | 9.09 | 11.7 |

Table 5.9.: Comparison of the experimentally measured, and estimated lifetimes of the $2P_0$ and $2P_{\pm 1} \rightarrow 1S(A_1)$ radiative transitions in selenium doped silicon. The estimated values are for the wavefunctions most closely matching the atomic state energies, while those scaled by the Mott transition are atomic or diatomic independent. **Expt:** Fits to the experimentally measured emission data. **Hydrogen:** Scaled hydrogen. **EMT:** Effective mass theory variationally scaled prolate wavefunctions. **Mott:** Mott transition Bohr radii scaled $1S(A_1)$ states; **1** and **2** corresponding to donor concentrations of $1.8\text{cm}^{-3}$ to $4.3 \times 10^{20}\text{cm}^{-3}$ respectively.

# 6. Conclusions

Firstly, a summary of the work in this thesis. The importance of quantum computing is reviewed, with emphasis on donor impurity systems in silicon. Donors are discussed, with the potential benefits of chalcogens highlighted.

Effective mass theory is reviewed, and it's applicability to chalcogen donors in silicon discussed. Using effective mass theory, prolate spheroid wavefunctions of the $1S$, $2P_0$, and $2P_{\pm 1}$ states are found using a variational method. Simple, uniformly spatially scaled hydrogen like wavefunctions are also calculated. Effective mass theory gives good energy agreement to absorbance data and the literature for the $2P$ states, but not for the $1S(A_1)$ ground state; the hydrogen scaled wavefunctions are scaled by the energy and therefore always fit it well. Mott semiconductor to conductor transition data from the literature is then used to scale the ground state. Fermi's golden rule is, with the previously calculated wavefunctions, used to estimate dipole radiative transition lifetimes. Estimates are between $\approx 10$ns and 20ns for effective mass theory prolate spheroid $2P$ to Mott scaled $1S(A_1)$ wavefunctions.

A time resolved Fourier transform spectroscopy experiment is described, where a 1220 nm laser pulse excites selenium donor electrons, present in a sample cooled to 10k, 80k and 300k, into the conduction band of silicon, and the resulting emission from the electrons cascade back to the ground state is measured as a function of energy and time. Absorption spectra are used to match selenium donor in silicon

## 6. Conclusions

sample features to the literature and the prior effective mass calculations. Oscillator strengths for these features are compared to those obtained by the dipole matrix elements of the effective mass theory calculated, and Mott scaled ground state, wavefunctions and those of effective mass theory oscillator strengths in the literature. Phenomenological fits are carried out to the selenium sample emission data, modelling it as an exponential decay in radiative intensity. Lifetimes of between $\approx 60\text{ns}$ and 80ns are found.

The primary finding of this thesis are then:

- Oscillator strengths determined from absorption spectra of singly ionised selenium donors in silicon, determined from integrating the area under absorption curves, are 13.8 and 38.5 for $2P_0$ and $2P_{\pm 1}$ to $1S(A_1)$ states. Calculated dipole oscillator strengths, using effective mass $2P$, and Mott transition data scaled $1S(A_1)$, states estimates oscillator strengths of 13.2 and 39.6 for the same transitions.

- The radiative emission of a selenium doped silicon sample, with the properties given for sample 71-8 in table 5.1 cooled to 10K and following pumping by an approximately 7.5mJ laser pulse at 1220nm, can be fit to an exponential decay. For atomic selenium complexes, this gives characteristic lifetimes of 63.1ns and 82.4ns for the $2P_{\pm 1}$ and $2P_0$ to $1S(A_1)$ transitions, while the effective mass theory scaled excited, and Mott transition scaled $1S(A_1)$, states predict lifetimes of 11.7ns and 9.09ns. For diatomic complexes, 72.8ns and 73.7ns are measured for the $2P_{\pm 1}$ and $2P_0$ to $1S(A_1)$ transitions, while the effective mass predictions are lifetimes of 19.6ns and 16.9 ns. Emission from singly ionised selenium complexes is too weak to be detected.

Based on this, using Mott transition data to scale the $1S(A_1)$ ground state is more

accurate than effective mass theory in predicting the correct dipole matrix elements. Singly ionised donors in selenium are likely to be the closest fit to effective mass theory predictions. There is long lived emission from selenium donors in silicon, of which the intrinsic radiative lifetime may be a significant component.

It was expected that the effective mass and Mott scaled ground state lifetime predictions would be most accurate for singly ionised selenium as shown by oscillator strength comparisons, rather than atomic or diatomic, complexes. However, within order of magnitude agreement is found for atomic and diatomic complexes at 10K, indicated by radiative emission data. Much further work remains to: improve modelling of the donor wavefunctions to predict matrix elements and radiative transition rates; clarify whether selenium, or other chalcogen, donor impurities in silicon are suitable for quantum information purposes.

# A. Review of Quantum Mechanics

This appendix contains the minimum necessary quantum mechanics background to understand and interpret both the measured phenomenon in this thesis, and the suitability of the physical system for quantum computing.

## A.1. Postulates of Quantum Mechanics

Quantum mechanics is based upon a set of axioms, or postulates. These postulates form a probabilistic framework, where the main unintuitive consequence is negative and positive probability interference in a vector space describing all possible states of a system. The postulates were historically proposed intermittently, one by one throughout the 20th century, and have proven to be experimentally verified so far. Below the postulates are listed, roughly following [23, p10-12].

The postulates are:

1. Every system can be represented by a probability vector with a phase; this is also a wavefunction $\Psi(x, y, z, t)$, or in Dirac notation $|\Psi\rangle$, which exhibits amplitude interference. This wavefunction is then a ray that comprises all possible directions of the probability vector.

2. All physically observable quantities of the system are fully described by hermitian linear operators that act upon the wavefunction of the system. The measured value is then an eigenvalue of the operator, and the wavefunction is

an eigenvector; only the eigenvalues corresponding to the basis vectors of the space can be observed, superpositions are lost to any individual observer.

3. The probability of measuring a specific eigenvalue is the integration over all space of the dot product of the complex conjugate of the wavefunction before the measurement, with the result of applying the measurement operator to the pre-measurement wavefunction; the probability magnitude is normalised to 1.

4. The wavefunction of a non-relativistic physical system evolves as prescribed by the time dependent Schrödinger equation.

## A.1.1. Expanding the Postulates

A physical system is described by a ray in a vector space of all possible states of the system. A Vector corresponding to a wavefunction of the system is such a ray, and the Hilbert space is the vector space. Measured quantities are the eigenvalues of operators that act upon the wavefunction, which is itself an eigenfunction of the operator. The operator corresponding to the energy of the physical system is known as the Hamiltonian $H$, and describes the time evolution of the system with the time dependent Schrödinger equation; the time independent Schrödinger equation is then simply the eigenvalue equation of the energy operator.

### A.1.1.1. The Hilbert Space and Wavefunction

The Hilbert space is a vector space over the set of complex numbers $\mathbb{C}$, i.e. this is a set of vectors in which each magnitude along a specific basis direction is, in general, a complex number. The Hilbert space has a defined dot product, and all the properties associated with vector spaces such as commutativity, associativity, the existence of the inverse, etc, of the vectors.[160][161]

As a Hilbert space is the vector space of the possible states of the Hamiltonian, this

includes not only the basis states but all their possible linear combinations. For the purposes of quantum mechanics, a complete Hilbert space is then one where it is possible to construct a pair of state vectors, out of some linear combination of basis states, with an energy difference between them that is convergent upon an arbitrarily small value as more terms are added to the linear combinations. This also applies to other measurable operators and their eigenvalues.

Each dimension, or basis vector in the Hilbert space, corresponds to a possible state, although not all possible states are basis vectors. The Hilbert space is a vector space, and any addition of two vectors results in another vector within the space, therefore any linear combination or superposition of the basis vectors is itself then a possible state of the system. The basis vectors in the Hilbert space are commonly chosen to be orthogonal; there must be some set of basis vectors that are orthogonal although it is possible to arbitrarily construct a basis that doesn't follow this pattern. The linear superposition or combination of states forming another valid state, or the wavefunction of the system that is in general a linear combination of states is written as:

$$|\psi_j\rangle = \sum_i C_i |\phi_i\rangle \tag{A.1}$$

The weighting coefficients of the different basis states is then:

$$C_i = \langle \psi_j | \phi_i \rangle \tag{A.2}$$

The orthogonality of the wavefunction basis states, where $\phi_i$ is the basis state in the

*i*th direction and is the same as the basis vector $e_i$ but with undefined magnitude, is then:

$$\sum_{i,j} \langle \phi_i | \phi_j \rangle = \delta_{i,j} \tag{A.3}$$

The wavefunction $|\Psi\rangle$ is a vector in the space of possible states, this can be written, where $N$ the number of dimensions of the space, $e_i$ the *i*th basis vector, and $a_i$ is the complex amplitude coefficient in the *i*th direction, as:

$$|\Psi\rangle = \sum_{i}^{N} a_i |e_i\rangle \tag{A.4}$$

However, the wavefunction is actually a ray, because the result of any operator acting upon the wavefunction multiplied by a scalar constant is the same regardless of the scalar constant. A ray is the same as a vector but with an undefined magnitude, a ray can be seen to be the set of all possible magnitudes for the same direction. The amplitude coefficients are any complex number, or $a_i \in \mathbb{C}$, this complex number factor gives rise to the quantum phase of the wavefunction, and allows interference to occur. This is also the reason why the Hilbert space is over the set of complex number $\mathbb{C}$, and not just the real numbers $\mathbb{R}$.

The inner product of two wavefunctions involves the complex conjugate of the first ray, and the non-conjugated second ray, and it must be noted that this complex conjugate then also involves the coefficients in each basis direction, $a_i$, because these are, in general, complex quantities. This results in the dot product always giving a real number. The inner product of the wavefunction with itself can then be

*A. Review of Quantum Mechanics*

interpreted as the probability of finding the physical system in the state specified by the wavefunction. As the coefficients are in general complex quantities, this forces the wavefunction coefficients to be normalised in such a way that the sum of their squared magnitudes always equals 1 for any system.[23]. The normalisation condition of the wavefunctions, where $a_i$ are the coefficients of the wavefunction for the $i$th basis vector, is written as:

$$\sum_i^N a_i^* a_i = X$$
$$\frac{1}{X} \sum_i^N a_i^* a_i = 1 \tag{A.5}$$

As the normalised coefficients are still complex quantities, they can be represented, where $\omega_k$ is the complex phase angle of the $k$th coefficient, according to:

$$a_k = \frac{e^{i\omega_k}}{X} \tag{A.6}$$

The dot product of the wavefunctions is defined, where $\Psi_i$ is a wavefunction or vector, as:

$$\langle \Psi_1(x,y,z) \, | \, \Psi_2(x,y,z) \rangle = \int_\infty^\infty \int_\infty^\infty \int_\infty^\infty \phi_1^*(x,y,z)\phi_2(x,y,z)dxdydz \tag{A.7}$$

**Multiple particle state spaces**

When considering multiple particles, with their possible states all being vectors in the Hilbert state space, the resulting Hilbert space of possible states of the composite system is the tensor product of the two individual Hilbert spaces of the individual

particles. Writing $H_1$ and $H_2$ as the Hilbert spaces of the first and second particles repetitively, and $H$ as the total Hilbert space of the composite system, with $\otimes$ denotes the tensor product, the new space becomes:

$$H = H_1 \otimes H_2 \tag{A.8}$$

If each of the individual particles has $N$ dimensions, corresponding to discrete states, in their Hilbert space, then the number of possible states in the composite system becomes $N^2$; particle 1 in state 1 now becomes particle 1 in state 1 while particle 2 is in states $1, 2, 3, ....N$. An individual state in the new composite state space, with particle 1 in state $a$ and particle 2 in $b$ is $a \otimes b$.

## A.1.1.2. Linear Hermitian Operators and Measurement

All measurable, observable quantities are represented by linear hermitian operators. These operators map the initial state vector of the system to another such state vector multiplied by a scalar constant, just as an eigenvalue equation.

$$O\phi_k = \lambda_k \phi_k \tag{A.9}$$

Where in equation A.9 $O$ is the operator, $\phi_k$ the wavefunction comprising of the the $k$th basis state out of a set of orthonormal basis states $\{\phi\}$, and $\lambda_k$ is the $k$th eigenvalue. The operators are linear because $O$ acting on $2\phi$ maps to $2\lambda\phi$; linear mapping preserves addition and multiplication. The operator must also be hermitian so that the measured eigenvalues are real, hermitian operators also always have a set of basis vectors $e_i$ that are orthonormal. Because the convention is to choose the

basis states of the Hilbert space to be orthogonal, there is a 1 to 1 correspondence between the eigenvectors and eigenvalues.

When a physical system is measured, and because of the interpretation of the wavefunction as a probability wave forcing normalisation, the average or expected value measured is given by the integral over all space of the operator applied to the wavefunction multiplied by the complex conjugate of the wavefunction. The measurement, where $\lambda_{avg}$ is the averages expected value, and $\Psi(x, y, z)$ is the linear superposition of the basis states of $O$, similarly to equation A.4, is written as:

$$
\begin{aligned}
|\Psi\rangle &= \sum_k^N a_k |\phi_k\rangle \\
\lambda_{avg} &= \int_\infty^\infty \int_\infty^\infty \int_\infty^\infty \Psi^*(x, y, z) O \Psi(x, y, z) dx dy dz \\
&= \langle \Psi | O | \Psi \rangle \\
&= \sum_n^N a_n^* \langle \phi_n | O \sum_k^N a_k |\phi_k\rangle \\
&= \sum_n^N \left( \sum_k^N \left\{ a_k a_n^* \langle \phi_n | O | \phi_k \rangle \right) \right\} \\
O |\phi_k\rangle &= \lambda_k |\phi_k\rangle \\
\langle \Psi | O | \Psi \rangle &= \sum_n^N \left( \sum_k^N \left\{ a_k a_n^* \lambda_k \langle \phi_n | \phi_k \rangle \right\} \right) \\
&= \sum_n^N \left( \sum_k^N \left\{ a_k a_n^* \lambda_k \delta_{k,n} \right\} \right) \\
&= \sum_n^N a_n a_n^* \lambda_n
\end{aligned}
\tag{A.10}
$$

However, equation A.10 only gives the average value, any actual single measured value must be a single $\lambda_k$. Therefore, measurement not only involves the operator acting on the wavefunction, which results in a scalar multiplied by the original

wavefunction, but a second projection operator. In the case of a wavefunction comprising multiple basis states, the result of the first operator is a summation of eigenvalues each multiplied by the relevant eigenvalue. The second measurement operator projects the wavefunction into the eigenspace of the measured eigenvalue.[23]

The eigenspace is the the section of the Hilbert space that contains all the eigenvectors that have the same eigenvalue as that measured. The projection operator then projects the pre-measurement wavefunction onto the linear combination of the vectors in the eigenspace. If the eigenspaces each contain only the one state, corresponding to an orthogonal basis in the original full Hilbert space, then the measurement and projection operator act as:

$$|\Psi\rangle = \sum_k^N a_k |\phi_k\rangle$$
$$O|\Psi\rangle = \sum_k^N a_k \lambda_k |\phi_k\rangle$$
$$M\big(O|\Psi\rangle\big) = \lambda_r |\phi_r\rangle \tag{A.11}$$
$$\sum_k^N a_k^* a_k = 1$$
$$F(r) = P(r = x) \, for \, x \in [N]$$
$$F(r) = a_r^* a_r$$

Where in equation A.11 $\Psi$ is the full wavefunction before measurement, $\phi_k$ the $k$th basis state, $N$ the total number of basis states, $O$ the measurement operator, $\lambda_k$ the $k$th eigenvalue, $M$ the projection operator, and $F(r)$ the discrete probability density function for the probability of the index $r$ to be a value in the set of integer values up to $N$. The operators, corresponding to any measurement, can be represented as a matrix acting on a column vector that represents the wavefunction. This is simply

writing a system of independent linear equations as a matrix. The operator $O$, in the orthonormal basis $\{\phi_i\}$ corresponding to normalised orthogonal basis vectors $e_i$ for $i \in [N]$, acting on the wavefunction $|\Psi\rangle$ , is written as:

$$
\begin{aligned}
\langle\Psi|\,O\,|\Psi\rangle &= \sum_n^N \left( \sum_k^N \langle\phi_n|\,a_n^* O a_k\,|\phi_k\rangle \right) \\
&= \sum_n^N \left( \sum_k^N O_{n,k} \right)
\end{aligned}
\tag{A.12}
$$

The operator matrix elements, from equation A.12, are defined by:

$$
O_{n,k} = \langle\phi_n\,|\,O\,|\,\phi_k\rangle
\tag{A.13}
$$

## A.1.2. The Time Dependent Schrödinger Equation

The universal wave nature of reality has its expression in the Schrödinger equation, a time dependent wave equation, with the original equation obtained from [162], and the modern form, where $\nabla^2 = \frac{\partial^2}{\partial x^2} + \frac{\partial^2}{\partial y^2} + \frac{\partial^2}{\partial z^2}$ is the Laplacian operator, $\hbar$ is the reduced Planck constant, $m$ is the mass of the thing with the wavefunction $\Psi(x,y,z,t)$, and $V(x,y,z,t)$ is the potential energy operator, shown below:

$$
\left( -\frac{\hbar^2}{2m}\nabla^2 + V(x,y,z,t) \right)\Psi(x,y,z,t) = i\hbar\frac{\partial}{\partial t}\Psi(x,y,z,t)
\tag{A.14}
$$

Taking the postulate that any observable has a corresponding hermitian operator, the energy operator or Hamiltonian can be written as $H$.

$$H = -\frac{\hbar^2}{2m}\nabla^2 + V(x, y, z, t) \tag{A.15}$$

The Schrödinger equation is then given in its most widely recognised form.

$$H\Psi(x, y, z, t) = i\hbar\frac{\partial}{\partial t}\Psi(x, y, z, t) \tag{A.16}$$

### A.1.2.1. Time Independent Schrödinger Equation

The time dependent Schrödinger equation is by its own definition time dependent, but for steady states that are not changing with respect to time, a time independent version of the equation can be found. The time independent form of the Schrödinger equation can be obtained by following the procedure outlined by Eisberg and Resnick in [163, p151]. This is shown below:

$$H\psi = E\psi \tag{A.17}$$

This highlights the vector like nature of the wavefunction, The time independent and dependant wavefunctions are related by:

$$\psi(x, y, z, t) = \psi(x, y, z)e^{-\frac{iEt}{\hbar}} \tag{A.18}$$

This shows the time independent wavefunction vector processing about the complex plane, perpendicular to that vector (to all possible vectors in x, y, z). It is this

which gives rise to interference, explicitly stating the amplitude interference that is fundamental to quantum phenomenon.

## A.2. Describing a Quantum system

To describe a non relativistic time independent physical system using quantum mechanics the time independent Schröedinger equation A.17 must be used. This describes the eigenfunctions and eigenstates, or wavefunctions and energies, of the quantum system with the Hamiltonian operator $H$.

**Dirac Notation**

The properties of the Dirac wavefunction notation that is used throughout are stated here. The wavefunction has the properties and can be written as shown in equation A.19; where * denotes the complex conjugate, and $O$ is an arbitrary operator.

$$\Psi(x, y, z) = |\Psi\rangle$$
$$\left( |\Psi\rangle \right)^* = \langle\Psi| = \Psi^*(x, y, z, t) \tag{A.19}$$
$$\langle\Psi|O|\Psi\rangle = \int_{-\infty}^{\infty} \int_{-\infty}^{\infty} \int_{-\infty}^{\infty} \Psi^*(x, y, z)O\Psi(x, y, z)dxdydz$$

**Describing the System**

An arbitrary system can be described by a Hamiltonian $H$, and it is possible to find a set of orthonormal basis eigenfunctions $\{\phi\}$, where each index $i$ corresponds to a separate orthogonal dimension.

$$H\phi_i = E_i\phi_i \tag{A.20}$$

as in equation A.20; In general the states of such a system would be linear superpositions of the basis states, with the $j$th such state given in equation A.21. Some

of the properties of the eigenstates are shown in equation A.22.

$$|\psi\rangle = \sum_i a_i |\phi_i\rangle \tag{A.21}$$

$$\sum_{i,j} \langle\phi_i|\phi_j\rangle = \delta_{i,j}$$

$$a_i = \langle\psi|\phi_i\rangle \tag{A.22}$$

$$\sum_i |a_i|^2 = 1$$

The energy of the system is then given by equation A.23. Where the braket $\langle x|y|z\rangle$ represents the integration over all space of the complex conjugate of $x$ multiplied by $y$ applied to $z$, $*$ represents the complex conjugate.

$$\langle\phi_i|H|\phi_i\rangle = \langle\phi_i|E_i|\phi_i\rangle = \int \phi_i^* H \phi_i dV$$

$$= E_i| \langle\phi_i|\phi_i\rangle \tag{A.23}$$

$$\langle\phi_i|H|\phi_i\rangle = E_i$$

## A.2.1. Hamiltonian Matrices

If a physical system is described by the Hamiltonian operator $H$, then the energies of single basis states are the Schrödinger equation, equation A.20. A matrix equation can then be assembled that describes an arbitrary number of the eigenstates of the Hamiltonian.

Equations A.12 and A.13 are used to assemble the Hamiltonian matrix. The basis states of this Hamiltonian matrix are the same as its right eigenvectors, thus if we have the correct orthogonal basis states the Hamiltonian matrix is diagonal. Consequentially, each eigenvalue will be correspond to only a single basis state, and

only the correct eigenvalues need be found to fully specify the system.

Taking an arbitrary number of the $N$ basis states of $H$, we can lay out the information to be assembled into our matrix A.24; using the states $\{\phi\}$ as the eigenfunctions of the the hamiltonian operator $H$. This uses unmixed eigenvectors, in that the resulting eigenvectors of the hamiltonian matrix comprise a single, unmixed, eigenvector from the basis set $\{\phi\}$.

$$\langle\phi_0|H|\phi_0\rangle = E_0$$
$$\langle\phi_1|H|\phi_1\rangle = E_1$$
$$...$$
$$\langle\phi_n|H|\phi_n\rangle = E_n$$

(A.24)

In the Hamiltonian matrix, column corresponds to the first state's index $x$ and row to the second state's index $y$, this is shown in equation A.25. Because the set of basis states $\{\phi\}$ are orthonormal, the non-diagonal elements,$(x \neq y)$, of equation A.25 are zero. The full Hamiltonian matrix is then shown in equation A.26.

$$\langle\phi_x|H|\phi_y\rangle$$

(A.25)

$$H = \begin{bmatrix} \langle\phi_0|H|\phi_0\rangle & \langle\phi_1|H|\phi_0\rangle & ... & \langle\phi_n|H|\phi_0\rangle \\ \langle\phi_0|H|\phi_1\rangle & \langle\phi_1|H|\phi_1\rangle & ... & ... \\ ... & ... & \langle\phi_2|H|\phi_2\rangle & ... \\ \langle\phi_0|H|\phi_n\rangle & ... & ... & \langle\phi_n|H|\phi_n\rangle \end{bmatrix}$$

(A.26)

The eigenfunctions of the Hamiltonian matrix are given by equation A.27 for the

first and second states and so on. This results in an eigenvector matrix $V$ as in equation A.28. It can be seen that for this case, for an orthonormal basis, the eigenvector matrix is the unit identity matrix $I$.

$$
\begin{bmatrix} 1 \\ 0 \\ ... \\ ... \\ 0 \end{bmatrix}
\begin{bmatrix} 0 \\ 1 \\ ... \\ ... \\ 0 \end{bmatrix}
\tag{A.27}
$$

$$
V = \begin{bmatrix}
1 & 0 & ... & ... \\
0 & 1 & 0 & ... \\
... & 0 & 1 & 0 \\
... & ... & 0 & 1
\end{bmatrix} = I
\tag{A.28}
$$

The energy eigenvalue matrix $E$ is then given by equation A.29.

$$
E = \begin{bmatrix}
E_0 & 0 & ... & ... \\
0 & E_1 & 0 & ... \\
... & 0 & E_2 & 0 \\
... & ... & 0 & E_n
\end{bmatrix}
\tag{A.29}
$$

The Schrödinger equation gives us the Hamiltonian matrix multiplied by the eigenvector matrix equal to the energy eigenvalue matrix multiplied by the eigenvector matrix, shown in equation A.30. Condensed into matrix equation form this becomes equation A.31. Given the basis functions, this then allows the calculation of an arbitrary number of states in matrix form. However, representing the states as a matrix does not give any benefit over individual consideration in this case.

$$
\begin{bmatrix}
\langle\phi_0|H|\phi_0\rangle & ... & ... & \langle\phi_n|H|\phi_0\rangle \\
... & \langle\phi_1|H|\phi_1\rangle & ... & ... \\
... & ... & \langle\phi_2|H|\phi_2\rangle & ... \\
\langle\phi_0|H|\phi_n\rangle & ... & ... & \langle\phi_n|H|\phi_n\rangle
\end{bmatrix}
\begin{bmatrix}
1 & 0 & ... & ... \\
0 & 1 & 0 & ... \\
... & 0 & 1 & 0 \\
... & ... & 0 & 1
\end{bmatrix} =
$$

$$
\begin{bmatrix}
E_0 & 0 & ... & ... \\
0 & E_1 & 0 & ... \\
... & 0 & E_2 & 0 \\
... & ... & 0 & E_n
\end{bmatrix}
\begin{bmatrix}
1 & 0 & ... & ... \\
0 & 1 & 0 & ... \\
... & 0 & 1 & 0 \\
... & ... & 0 & 1
\end{bmatrix}
\tag{A.30}
$$

$$
HV = EV \tag{A.31}
$$

## A.2.2. Unknown Wavefunctions

Despite the representation of a physical system as a set of matrix equations via the Schrödinger equation, if the exact set of basis functions is not known, then the H matrix cannot be exactly calculated, nor can the eigenvalues of the system be found. It is, however, in general, possible to experimentally measure the eigenvalues of the system, perhaps optically using spectroscopy, or with other means.

There are several possible reasons for not knowing the basis functions of the system. For any multi-body situation, for example atomic systems more complex than hydrogen, exact closed form analytical basis functions are not known; they may even not exist at all. The hamiltonian itself may also be an approximation, causing the basis states themselves to only be an approximation to the true states of the system, even if the eigenvalues are experimentally measured. Regardless of the reason, if unknown, the true eigenfunctions of the system may be guessed. A set of trial functions is used for the basis states, these functions then, in general, depend upon

some variational parameters. These parameters scale the basis states, and allow the calculated eigenvalues to be tuned until they match those measured.

This variational tuning of a set of trial basis functions can be done for unmixed or mixed eigenvectors. For the unmixed case this means that a single trial basis state corresponds to each measured eigenvalue; the trial H matrix calculated will be diagonal, the set of trial basis functions selected must then form an orthogonal basis. This will look exactly as outlined above in the hamiltonian matrixes section A.2.1.

## A.2.2.1. Mixed Eigenvectors: The Variational Rayleigh-Ritz Method

The Rayleigh-Ritz method is simply assembling a trial wavefunction out of another set of trial basis functions. The idea being that an ever closer approximation to reality can be obtained by both adding more trial basis function terms to the trial wavefunction, and by fine tuning some set of variational parameters that the set of trial basis functions depends upon.

The physical system has the wavefunction $|\Psi\rangle$, which is a linear superposition of $|\Phi\rangle$ states, and by extension of $|\phi\rangle$ states. However, any interaction with the system will cause the wavefunction to be projected onto one of the $|\Phi\rangle$ states.

$$|\Phi_j\rangle = \sum_i C_i |\phi_i\rangle$$

$$|\Psi_k\rangle = \sum_j a_j |\Phi_j\rangle \quad \text{(A.32)}$$

$$|\Psi_k\rangle = \sum_j \sum_i a_j C_i |\phi_i\rangle$$

For the variational method, each $|\phi\rangle$ state function has one or more parameters $\{\alpha\}$

that can be varied to obtain the desired eigenvalues of the H matrix. Varying these parameters changes the orthogonality of the $\{\phi\}$ functions, and thus also changes the orthogonality of the new set of basis states $\{\Phi\}$. Thus when calculating the H matrix elements $\langle\phi_x|H|\phi_y\rangle$ for each set of values for the variational parameters, the resulting matrix can, and most probably will, be non-diagonal. By diagonalising the H matrix the eigenfunctions, $\{\Phi\}$, which are linear superpositions of the $\{\phi\}$ basis states with the current values of the variational parameters $\{\alpha\}$, are weighted in such a manner that the new eigenfunctions are orthogonal.

This new orthogonal basis may then be used to find the eigenvalues of the corresponding diagonalised H matrix. If the eigenvalues are known, perhaps due to experiment, then the variational parameters can be tuned and the H matrix rediagonalised until the calculated eigenvalues are as close as possible to those measured. However, this is a complex multi-dimensional global optimization problem, and it is not, in general, possible to be certain if the optimal set of variational parameters has been found. This is a variational form of the Rayleigh-Ritz method, first developed independently by both Rayleigh [121, Lord Rayleigh was J.W. Strutt before the title] and Ritz[120]; as a historical note Rayleigh used this to construct basis states for the resonance of an open ended church organ.

**Representation of the Variational Rayleigh-Ritz Method**

To show the Rayleigh-Ritz method, the matrix Schrödinger equation is used. Let us consider the Schröedinger equation for states $\Phi_i$, assembled from the variationally dependent basis described earlier $\{\phi\}$:

$$H\,|\Phi_i\rangle = E_i\,|\Phi_i\rangle \tag{A.33}$$

A new matrix equation for the trial wavefunction $\Phi_k$ must be constructed:

$$H \left| \Phi_k \right\rangle = E_k \left| \Phi_k \right\rangle$$

$$H \sum_i C_{i,k} \left| \phi_i \right\rangle = E_k \sum_i C_{i,k} \left| \phi_i \right\rangle$$

$$\left\langle \phi_j |H| \sum_i C_{i,k} \phi_i \right\rangle = \left\langle \phi_j |E_k \sum_i C_{i,k} \phi_i \right\rangle \tag{A.34}$$

$$\sum_i C_{i,k} \left\langle \phi_j |H| \phi_i \right\rangle = E_k \sum_i C_{i,k} \left\langle \phi_j | \phi_i \right\rangle$$

$$\sum_i C_{i,k} \left\langle \phi_j |H| \phi_i \right\rangle = E_k \sum_i C_{i,k} \delta_{i,j}$$

$$\sum_i C_{i,k} \left\langle \phi_j |H| \phi_i \right\rangle = E_k C_{j,k}$$

The Hamiltonian elements are defined as:

$$h_{j,i} = \left\langle \phi_j |H| \phi_i \right\rangle \tag{A.35}$$

Using the Hamiltonian elements definition from equation A.35, the result of equation A.34 becomes:

$$\sum_i C_{i,k} h_{j,i} = E_k C_{j,k} \tag{A.36}$$

Equation A.36 can be written with $n$ basis states representing the single $\Phi_k$ state. Here the trial wavefunctions have multiple components, and as such their eigenvectors are no longer simple $(1, 0, 0, ..., 0)$ vectors but instead, for the $k$th state, become:

$$
\begin{bmatrix}
C_{1,k} \\
C_{2,k} \\
... \\
C_{n,k}
\end{bmatrix}
\tag{A.37}
$$

The matrix equation version of equation A.36 is then:

$$
\begin{bmatrix}
h_{11} & h_{12} & ... & h_{1n} \\
h_{21} & h_{22} & ... & ... \\
... & ... & h_{33} & ... \\
h_{n1} & ... & ... & h_{nn}
\end{bmatrix}
\begin{bmatrix}
C_{1,k} \\
C_{2,k} \\
... \\
C_{n,k}
\end{bmatrix}
= E_k
\begin{bmatrix}
C_{1,k} \\
C_{2,k} \\
... \\
C_{n,k}
\end{bmatrix}
\tag{A.38}
$$

The H matrix from equation A.38 describes a single eigenfunction in the new linear superposition of variational parameter basis states, when diagonalised. This can be expanded to multiple $\Phi_k$ states by expanding the eigenvector matrix to include up to $n$ eigenvectors, corresponding to the same number of energy eigenvalues;

$$
\begin{bmatrix}
h_{11} & h_{12} & ... & h_{1n} \\
h_{21} & h_{22} & ... & ... \\
... & ... & h_{33} & ... \\
h_{n1} & ... & ... & h_{nn}
\end{bmatrix}
\begin{bmatrix}
C_{1,1} & ... & ... & C_{1,n} \\
C_{2,1} & C_{2,2} & ... & ... \\
... & ... & C_{3,3} & C_{n-1,n} \\
C_{n,1} & ... & ... & C_{n,n}
\end{bmatrix}
$$
$$
=
\begin{bmatrix}
C_{1,1} & ... & ... & C_{1,n} \\
C_{2,1} & C_{2,2} & ... & ... \\
... & ... & C_{3,3} & C_{n-1,n} \\
C_{n,1} & ... & ... & C_{n,n}
\end{bmatrix}
\begin{bmatrix}
E_1 & 0 & ... & 0 \\
0 & E_2 & 0 & ... \\
... & 0 & E_3 & 0 \\
0 & ... & 0 & E_n
\end{bmatrix}
\tag{A.39}
$$

254

Matrixes are defined as:

$$H = \begin{bmatrix} h_{11} & h_{12} & ... & h_{1n} \\ h_{21} & h_{22} & ... & ... \\ ... & ... & h_{33} & ... \\ h_{n1} & ... & ... & h_{nn} \end{bmatrix}$$

$$V = \begin{bmatrix} C_{1,1} & ... & ... & C_{1,n} \\ C_{2,1} & C_{2,2} & ... & ... \\ ... & ... & C_{3,3} & C_{n-1,n} \\ C_{n,1} & ... & ... & C_{n,n} \end{bmatrix} \quad (A.40)$$

$$E = \begin{bmatrix} E_1 & 0 & ... & 0 \\ 0 & E_2 & 0 & ... \\ ... & 0 & E_3 & 0 \\ 0 & ... & 0 & E_n \end{bmatrix}$$

Then equation A.39 can be written in matrix shorthand as:

$$HV = VE \quad (A.41)$$

Then all that is required is to calculate the Hamiltonian matrix $H$, then use linear algebra techniques to find the right eigenvectors $V$ and their associated eigenvalues $E$. This then changes the problem from one of finding eigenvalues to finding eigenvectors. While each of the basis states used is itself an eigenstate of the Hamiltonian operator, any possible linear combination of such states is also a valid eigenstate of the operator, they are then not necessarily orthogonal due to the variational parameters.

There are two additional points that must be considered. Firstly, only in the combinations of the eigenstates that give the same energy as measured are of interest; some sets of basis functions will of course be a closer approximation to reality than others. Secondly, the Hamiltonian operator is often itself an approximation, and as such any eigenstates and energies are also approximations.

## A.2.2.2. Considering the Ground State

To justify finding the variational parameters by matching the calculated energy eigenvalues to those experimentally measured, the following argument is used.

Consider the wavefunction of the ground state of the Hamiltonian $|\Psi_g\rangle$. This wavefunction is a linear superposition of the trial basis $\{\phi\}$, and of the calculated orthogonal basis $\{\Phi\}$. If the ground state has been calculated correctly it will be entirely made up of the $|\Phi_g\rangle$ state, and if incorrectly then there will be other components. If the wavefunction is assumed to comprise arbitrary components.

$$|\Psi_g\rangle = \sum_{j}^{n} a_j |\Phi_j\rangle \tag{A.42}$$

Because the energy eigenvalue $E_g$ is by definition the lowest energy value, and as the sum of the $a_j^* a_j$ coefficients must be 1 due to normalisation conditions, the energy of the wavefunction must then be equal to or greater than that of the true ground wavefunction of the Hamiltonian. This is shown explicitly below

$$\langle \Psi_g | H | \Psi_g \rangle = \sum_{x,y} \langle \psi_g | \Phi_x \rangle \langle \Phi_x | H | \Phi_y \rangle \langle \Phi_y | \psi_g \rangle$$

$$= \sum_{x,y} \langle \psi_g | \Phi_x \rangle \, \delta_{x,y} E_y \, \langle \Phi_y | \psi_g \rangle$$

$$= \sum_{y} E_y \langle \psi_g | \Phi_y \rangle \langle \Phi_y | \psi_g \rangle$$

$$= \sum_{y} E_y |\langle \Phi_y | \psi_g \rangle|^2$$

$$|\Psi_g\rangle = \sum_{j}^{n} a_j \, |\Phi_j\rangle \tag{A.43}$$

$$\langle \psi_g | H | \psi_g \rangle = \sum_{y} E_y | \sum_{i} a_i \langle \Phi_y | \Phi_i \rangle |^2$$

$$\langle \psi_g | H | \psi_g \rangle = \sum_{y} E_y | \sum_{i} a_i \delta_{i,y} |^2$$

$$\langle \psi_g | H | \psi_g \rangle = \sum_{y} E_y |a_y|^2$$

Thus by minimising the ground state energy, the closest approximation to the true ground state wavefunction in the variational trial basis $\{\phi\}$ is found. This ground state wavefunction is then the same as the new ground state basis function calculated by diagonalising the Hamiltonian matrix, $|\Psi_g\rangle = |\Phi_g\rangle$. The same result can be obtained by subtracting the measured energy ground state from that calculated, then the difference is variationally minimised. Minimising the variationally calculated ground state energy forces the weighting of the lowest energy new basis state term to be dominant, ideally 1.

The rest of the $\Phi$ state energies will then be the ground energy plus some additional energy; by minimising this additional energy, the closest approximation to the second lowest energy state using the same trial basis is found. It must be noted that this energy is minimised by varying the variational parameters and that the resulting state functions are orthogonal due to being found by the diagonalisation of the H

matrix, thus each state function is found simultaneously to the others.

**Non Ground states**

The conclusion of this section is also applicable when only using a single variational state to approximate the ground, or any other, state. That is, the variationally found parameters of a single trial wavefunction that minimises the energy are the parameters that most closely match the true ground state. This can then be extended to the non-ground states, although depending on the parity of the Hamiltonian the variationally found minimum energy wavefunction of these non ground states will not in general just be the closest to the correct "true" state, but mixed with states of the same parity (i.e. finding the 2S state will be mixed with the 1S, 3S, 3D, etc). If the variational basis has been appropriately chosen, such that the wavefunction is a realistic approximation of the "true" wavefunction, then this mixing should be reduced; the further away the chosen wavefunction is from reality, the less this is so.

Mathematically, this is choosing the variational wavefunction so that one of the $a_j$ weighting terms is dominant, from equation A.42. The variational function with respect to the measured energy of the state in question can also be minimised, this reduces the effective weighting of the ground $\Phi$ state in the calculation.

## A.3. Fermi's Golden Rule

Fermi's golden rule, so named after the famous Italian physicist Enrico Fermi, is an equation for calculating the transition rate between two states of a system. It is only necessary to know both the wavefunctions of the initial and final states, and the density of the final state at the energy of the energy difference between the two states. Fermi's golden rule is shown in equation A.44 [164, p552][31, p51]; where $i$ and $f$ index the initial and final states respectively, and $H_p$ is the Hamiltonian

of the perturbation to the system that can cause the system to transition between states.

$$\Gamma_{i,f} = \frac{2\pi}{\hbar} |\langle f|H_p|i \rangle|^2 \rho(E_f) \tag{A.44}$$

### A.3.0.1. Derivation

Fermi's golden rule is calculated by considering a small perturbation to the Hamiltonian of the system. The derivation of Fermi's golden rule that is given here follows that given in [164, p552], and is the present authors preferred derivation; this derivation does not require the consideration of absorption stimulated by a driving wave, the subsequent application of the rotating wave approximation and then the use of Einstein rate equations and thermodynamic equilibrium arguments to relate the stimulated absorption rate to the spontaneous emission rate. The interested reader may look at the many available texts with such derivations, e.g. chapters four and nine of [31], or chapter two of [165].

Consider a system described by the time dependent Schrödinger equation, with Hamiltonian $H_0$, with a wavefunction that is in general a linear superposition of possible eigenstates of that Hamiltonian. Such a system has the properties outlined in equation A.45, these are also outlined in section A.1, but are repeated here to clarify the derivation to follow.

$$H_0 |\Psi^0(x,y,z,t)\rangle = i\hbar \frac{\partial}{\partial t} |\Psi^0(x,y,z,t)\rangle$$

$$|\Psi^0(x,y,z,t)\rangle = \sum_n C_n^0 |\phi_n^0(x,y,z)\rangle e^{-\frac{itE_n^0}{\hbar}}$$

$$H_0 |\phi_n^0(x,y,z)\rangle = E_n^0 |\phi_n^0(x,y,z)\rangle$$

$$\langle \phi_n^0(x,y,z)|\phi_k^0(x,y,z)\rangle = \delta_{n,k}$$

$$\tag{A.45}$$

## A. Review of Quantum Mechanics

A small, time dependant, perturbation is then introduced to the system, described by Hamiltonian $H_p(t)$. The Schrödinger equation and the wavefunctions of the system, now with time dependent amplitude coefficients $C_n^0(t)$ due to the perturbation to the system, becomes :

$$\left(H_0 + H_p(t)\right) |\Psi(x,y,z,t)\rangle = i\hbar \frac{\partial}{\partial t} |\Psi(x,y,z,t)\rangle$$

$$|\Psi(x,y,z,t)\rangle = \sum_n C_n^0(t) |\phi_n^0(x,y,z)\rangle \, e^{-\frac{itE_n^0}{\hbar}} \tag{A.46}$$

The wavefunction $\Psi(x,y,z,t)$ is then inserted into the Schrödinger equation $\left(H_0 + H_p(t)\right)\Psi(x,y,z,t) = i\hbar\frac{\partial}{\partial t}\Psi(x,y,z,t)$. The left side of the Schrödinger equation is:

$$
\begin{aligned}
\left(H_0 + H_p(t)\right) |\Psi(t)\rangle &= \left(H_0 + H_p(t)\right) \sum_n C_n^0(t) |\phi_n^0\rangle \, e^{-\frac{itE_n^0}{\hbar}} \\
&= \sum_n \left(H_0 + H_p(t)\right) C_n^0(t) |\phi_n^0\rangle \, e^{-\frac{itE_n^0}{\hbar}} \\
&= \sum_n \left(E_n^0 + H_p(t)\right) C_n^0(t) |\phi_n^0\rangle \, e^{-\frac{itE_n^0}{\hbar}}
\end{aligned}
\tag{A.47}
$$

The right hand side is:

$$
\begin{aligned}
i\hbar \frac{\partial}{\partial t} |\Psi(t)\rangle &= i\hbar \frac{\partial}{\partial t} \sum_n C_n^0(t) |\phi_n^0\rangle \, e^{-\frac{itE_n^0}{\hbar}} \\
&= i\hbar \left( \sum_n \frac{\partial C_n^0(t)}{\partial t} |\phi_n^0\rangle \, e^{-\frac{itE_n^0}{\hbar}} - \frac{i}{\hbar} \sum_n E_n^0 C_n^0(t) |\phi_n^0\rangle \, e^{-\frac{itE_n^0}{\hbar}} \right) \\
&= i\hbar \sum_n \frac{\partial C_n^0(t)}{\partial t} |\phi_n^0\rangle \, e^{-\frac{itE_n^0}{\hbar}} + \sum_n E_n^0 C_n^0(t) |\phi_n^0\rangle \, e^{-\frac{itE_n^0}{\hbar}}
\end{aligned}
\tag{A.48}
$$

## A. Review of Quantum Mechanics

To calculate the transition rate between two states it must first be assumed that, before the perturbation, the system is in one state $j$ and the final state to be considered is $k$. Both sides of the Schrödinger equation are then multiplied by $\langle \phi_k^0 |$. Left.

$$\langle \phi_k^0 | \sum_n \left( E_n^0 + H_p(t) \right) C_n^0(t) \, |\phi_n^0\rangle \, e^{-\frac{it E_n^0}{\hbar}}$$
$$= \sum_n \left( E_n^0 \langle \phi_k^0 | \phi_n^0 \rangle + \langle \phi_k^0 | H_p(t) | \phi_n^0 \rangle \right) C_n^0(t) e^{-\frac{it E_n^0}{\hbar}} \tag{A.49}$$
$$= E_k^0 C_k^0(t) e^{-\frac{it E_k^0}{\hbar}} + \sum_n \langle \phi_k^0 | H_p(t) | \phi_n^0 \rangle \, C_n^0(t) e^{-\frac{it E_n^0}{\hbar}}$$

And right.

$$\langle \phi_k^0 | \left( i\hbar \sum_n \frac{\partial C_n^0(t)}{\partial t} \, |\phi_n^0\rangle \, e^{-\frac{it E_n^0}{\hbar}} + \sum_n E_n^0 C_n^0(t) \, |\phi_n^0\rangle \, e^{-\frac{it E_n^0}{\hbar}} \right)$$
$$= i\hbar \sum_n \frac{\partial C_n^0(t)}{\partial t} \, \langle \phi_k^0 | \phi_n^0 \rangle \, e^{-\frac{it E_n^0}{\hbar}} + \sum_n E_n^0 C_n^0(t) \, \langle \phi_k^0 | \phi_n^0 \rangle \, e^{-\frac{it E_n^0}{\hbar}} \tag{A.50}$$
$$= i\hbar \frac{\partial C_k^0(t)}{\partial t} e^{-\frac{it E_k^0}{\hbar}} + E_k^0 C_k^0(t) e^{-\frac{it E_k^0}{\hbar}}$$

Equating the left, equation A.49, and right, equation A.50, sides of the Schrödinger equation is written below. This shows the rate of change of the final states probability $C_k^0(t)$ as a function of time, and the perturbation $H_p(t)$.

$$E_k^0 C_k^0(t) e^{-\frac{itE_k^0}{\hbar}} + \sum_n \langle \phi_k^0 | H_p(t) | \phi_n^0 \rangle \, C_n^0(t) e^{-\frac{itE_n^0}{\hbar}} = i\hbar \frac{\partial C_k^0(t)}{\partial t} e^{-\frac{itE_k^0}{\hbar}} + E_k^0 C_k^0(t) e^{-\frac{itE_k^0}{\hbar}}$$

$$\sum_n \langle \phi_k^0 | H_p(t) | \phi_n^0 \rangle \, C_n^0(t) e^{-\frac{itE_n^0}{\hbar}} = i\hbar \frac{\partial C_k^0(t)}{\partial t} e^{-\frac{itE_k^0}{\hbar}}$$

$$-\frac{i}{\hbar} \sum_n \langle \phi_k^0 | H_p(t) | \phi_n^0 \rangle \, C_n^0(t) e^{-\frac{it\left[E_n^0 - E_k^0\right]}{\hbar}} = \frac{\partial C_k^0(t)}{\partial t}$$

$$(A.51)$$

A set of assumptions and operations are then applied to equation A.51. Firstly, because the transition rate is the rate of change of the probability, i.e. the magnitude of the $C_n^0(t)$ coefficients squared, and not the amplitude or the coefficients themselves, the coefficients must first be found. To do this equation A.52 is integrated with respect to time, between the start of the perturbation at $t = 0$ and some arbitrary time later $t = T$.

$$-\frac{i}{\hbar} \sum_n \int_0^T \langle \phi_k^0 | H_p(t) | \phi_n^0 \rangle \, C_n^0(t) e^{-\frac{it\left[E_n^0 - E_k^0\right]}{\hbar}} dt = \int_0^T \frac{\partial C_k^0(t)}{\partial t} dt$$

$$-\frac{i}{\hbar} \sum_n \int_0^T \langle \phi_k^0 | H_p(t) | \phi_n^0 \rangle \, C_n^0(t) e^{-\frac{it\left[E_n^0 - E_k^0\right]}{\hbar}} dt = C_k^0(T) - C_k^0(0)$$

$$(A.52)$$

The assumption is then made that the system is initially in a single state $j$, with $C_j^0(0) = 1$, and all other coefficients at $t = 0$ being zero. Applying this to equation A.52 results in :

$$-\frac{i}{\hbar} \int_0^T \langle \phi_k^0 | H_p(t) | \phi_j^0 \rangle \, C_j^0(t) e^{-\frac{it\left[E_j^0 - E_k^0\right]}{\hbar}} dt = C_k^0(T) \qquad (A.53)$$

It is then assumed over the time period $t = 0$ to $t = T$ that the perturbation is approximately constant, $H_p(0 \leq t \leq T) \approx H_p$, and the system is slow to respond to the perturbation such that $C_j^0(0 \leq t \leq T) \approx 1$. Applied to equation A.53, this results in:

$$-\frac{i}{\hbar} \langle \phi_k^0 | H_p | \phi_j^0 \rangle \int_0^T e^{-\frac{it\left[E_j^0 - E_k^0\right]}{\hbar}} dt = C_k^0(T) \tag{A.54}$$

Relabelling the energy difference between the initial and final states, $\frac{E_k^0 - E_j^0}{\hbar} = \omega_{j,k}$, and solving the time integral gives:

$$\begin{aligned} C_k^0(T) &= -\frac{i}{\hbar} \langle \phi_k^0 | H_p | \phi_j^0 \rangle \int_0^T e^{it\omega_{j,k}} dt \\ &= -\langle \phi_k^0 | H_p | \phi_j^0 \rangle \frac{\left(e^{iT\omega_{j,k}} - 1\right)}{\hbar\omega_{j,k}} \\ &= -\langle \phi_k^0 | H_p | \phi_j^0 \rangle e^{\frac{iT\omega_{j,k}}{2}} \frac{\left(e^{\frac{iT\omega_{j,k}}{2}} - e^{-\frac{iT\omega_{j,k}}{2}}\right)}{\hbar\omega_{j,k}} \\ &= -2i \langle \phi_k^0 | H_p | \phi_j^0 \rangle e^{\frac{iT\omega_{j,k}}{2}} \frac{\left(e^{\frac{iT\omega_{j,k}}{2}} - e^{-\frac{iT\omega_{j,k}}{2}}\right)}{2i\hbar\omega_{j,k}} \\ &= -2i \langle \phi_k^0 | H_p | \phi_j^0 \rangle e^{\frac{iT\omega_{j,k}}{2}} \frac{\sin(\frac{T\omega_{j,k}}{2})}{\hbar\omega_{j,k}} \end{aligned} \tag{A.55}$$

Squaring the amplitude coefficient of the final state, $C_k^0(T)$, of equation A.55 then gives:

$$|C_k^0(T)|^2 = 4| \langle \phi_k^0 | H_p | \phi_j^0 \rangle |^2 \frac{\sin^2(\frac{T\omega_{j,k}}{2})}{\hbar^2\omega_{j,k}^2} \tag{A.56}$$

# A. Review of Quantum Mechanics

In the limit of large $T$ the $sin^2$ term becomes a delta function.

$$\lim_{\alpha \to \infty} \frac{\sin^2(\alpha x)}{\alpha x^2} = \pi \delta(x)$$

$$\delta(\beta x) = \frac{1}{|\beta|} \delta(x)$$

(A.57)

Incorporating the large $T$ limit of equation A.57 into equation A.56 results in:

$$
\begin{aligned}
\lim_{T \to \infty} \left( |C_k^0(T)|^2 \right) &= |\langle \phi_k^0| H_p |\phi_j^0 \rangle|^2 \frac{T}{\hbar^2} \lim_{T \to \infty} \left( \frac{\sin^2(\frac{T\omega_{j,k}}{2})}{T\left(\frac{\omega_{j,k}}{2}\right)^2} \right) \\
&= |\langle \phi_k^0| H_p |\phi_j^0 \rangle|^2 \frac{T\pi}{\hbar^2} \delta(\frac{\omega_{j,k}}{2}) \\
&= \frac{2\pi T}{\hbar^2} |\langle \phi_k^0| H_p |\phi_j^0 \rangle|^2 \delta(\omega_{j,k})
\end{aligned}
$$

(A.58)

The delta function in equation A.54 does not refer to the energy of any photon emission, but to the energy difference between final and initial states. That is, if considering an atomic electron transition with corresponding photon emission it is the total energy of the final electron energy, and photon states, minus the initial that is considered. Therefore, it can be seen as no more than a statement of the uncertainty principle, e.g. as the time tends to infinity the total energy difference of the transitions initial and final states must be zero. At any single non-infinite time point the delta function is actually a sinc function, with a central peak and series of smaller side-lobes in energy, that is, a transition occurring has a non zero probability for energies of initial and final states that do not sum to zero.

As the squared magnitude of the probability coefficient $C$ is the probability of the system being in the final state $k$, the rate of transition to that state is given by the derivative with respect to the time $T$.

$$\frac{\partial\left(|C_k^0(T)|^2\right)}{\partial T} = \frac{\partial}{\partial T} \frac{2\pi T}{\hbar^2} |\langle\phi_k^0| H_p |\phi_j^0\rangle|^2 \delta(\omega_{j,k})$$

$$= \frac{2\pi}{\hbar^2} |\langle\phi_k^0| H_p |\phi_j^0\rangle|^2 \delta(\omega_{j,k}) \qquad \text{(A.59)}$$

The $\omega_{j,k}$ term is then converted back into the energy of the initial and final states.

$$\frac{\partial\left(|C_k^0(T)|^2\right)}{\partial T} = \frac{2\pi}{\hbar^2} |\langle\phi_k^0| H_p |\phi_j^0\rangle|^2 \delta\left(\frac{E_k^0 - E_j^0}{\hbar}\right)$$

$$= \frac{2\pi}{\hbar} |\langle\phi_k^0| H_p |\phi_j^0\rangle|^2 \delta(E_k^0 - E_j^0) \qquad \text{(A.60)}$$

Equation A.60 shows the transition rate for a single state $|\phi_j^0\rangle$ transitioning to another single state $|\phi_k^0\rangle$. To obtain the total transition rate $\Gamma_{j,k}$ between all states of the same initial, $E_j^0$, and final, $E_k^0$, energies requires inclusion of their degeneracies into equation A.56. Each part of the multiply degenerate final state $|\phi_k^0\rangle$ has an equal chance of being transitioned to from the initial state $|\phi_j^0\rangle$; the total probability of a transition is the sum of the transition probabilities for each final state. Therefore, the transition rate must be multiplied by the degeneracy of the final states $g_k$.

If the initial state of the system, $|\phi_j^0\rangle$ has a degeneracy of $g_j$, then there is an equal probability of it being in each of the identical degenerate initial states, that is, there is a probability of $\frac{1}{g_j}$ for each.

This can be verified by considering a number of systems, equal to the degeneracy of the initial state $g_j$, that do not interact with each other. Because they do not interact, the total transition rate must only be $g_j$ times that of each individual system. Therefore, the total transition rate must be the same as that of a single system; if

$A$ is the modification to the transition rate due to the initial state degeneracy, then $g_j A = 1$ and it is then clear that $A = \frac{1}{g_j}$.

Including both the probability of the system being in each degenerate initial state, and that of the degenerate final states, gives Fermi's golden rule, where $\Gamma_{j,k}$ is the total transition rate between the initial, $|\phi_j^0\rangle$, and final, $|\phi_k^0\rangle$, states with degeneracies $g_j$ and $g_k$.

$$\Gamma_{j,k} = \frac{2\pi}{\hbar} \frac{g_k}{g_j} |\langle \phi_k^0| H_p |\phi_j^0\rangle|^2 \delta(E_k^0 - E_j^0) \tag{A.61}$$

## A.3.1. Obtaining the Spontaneous Emission Rate from Fermi's Golden Rule

Fermi's golden rule, equation A.61, can then be used to obtain the spontaneous emission rate for a two level atom emitting photons as an electron decays from an excited to ground energy state. This is now explicitly considered to be the interaction of the electric field of a free space vacuum with an atom-electron system with two levels of separate degeneracies.

For Fermi's golden rule to be applicable the wavefunctions in the matrix element, $|\langle \phi_k^0| H_p |\phi_j^0\rangle|^2$, must also include the wavefunctions of a quantised EM field. This can be explicitly seen in the delta function that arises in Fermi's golden rule, equation A.61, where the transition rate is non zero only when the energy of the initial and final states are the same. The initial and final state energies then include that of the EM field and the electron, such that the final energy of the EM field is plus one photon for the final state energy.

This leaves a few points that must be considered before the transition rate calculation

can proceed:

- Firstly, for spontaneous emission and assuming that the perturbation that causes this is an electric field, what that electric field is, and where it comes from.

- Secondly, what the states are for the atom and electromagnetic field system, and how they affect the Fermi's golden rule transition rate derived so far.

- Thirdly, what the perturbing Hamiltonian for the electric field interacting with the atom-electron system is.

- Fourthly, when using the wavefunctions, electric field, and correct Hamiltonian approximations obtained so far, what the appropriate degeneracies for the system are.

### A.3.1.1. Vacuum Field

For spontaneous emission, the perturbation to the 2 level atomic system is assumed to be the electric field present in a vacuum with no photons. This is the vacuum field.

The quantised radiation field can be treated as a quantum harmonic oscillator [165]. For $N$ photons, at frequency $\omega$, the energy of the quantised radiation field is given below [31, eq 7.31][165, eq 4.3.26]:

$$E_\omega = \hbar\omega\left(N + \frac{1}{2}\right) \tag{A.62}$$

The vacuum field has the energy of zero photons, that is, $\frac{\hbar\omega}{2}$. To find the electric field strength, $E_0$, for the perturbing dipole moment, in terms of a classical field, the

energy of the quantised radiation field and a classical field can be equated. Because the zero photon energy has no preferential direction, this energy is assumed to be equally divided amongst the three Cartesian axis. Conveniently, it is the magnitude that is found by the comparison between the $N = 0$ quantum harmonic oscillator and energy in a classical electromagnetic field.

Thus the state of the vacuum EM field is approximated in a semi-classical fashion, being found from comparison to the zeroth energy level of a quantised harmonic oscillator. The energy of the classical EM wave is evaluated over a finite volume $V$, because in the final Fermi's golden rule calculation a compensating factor of $\frac{1}{V}$ cancels it out. This compensating factor comes from the density of states of photon modes at the frequency corresponding to the energy of the transition of the two level atom-electron system.

The initial and final state energies of the electron are $E_j^a$ and $E_k^a$ respectively, with the frequency corresponding to this transition taken to be $\omega_{j,k}$.

$$\omega_{j,k} = \frac{E_j^a - E_k^a}{\hbar} \tag{A.63}$$

From equation A.62 the energy of the quantised radiation field, at angular frequency $\omega_{j,k}$ with zero photons is then:

$$\frac{\hbar \omega_{j,k}}{2} \tag{A.64}$$

The energy density in an oscillating, classical, electromagnetic field is the sum of the

energy density in both an electric, $\vec{E}$, and magnetic, $\vec{B}$, field, both fields are time and space dependant, with the energy evenly divided amongst them. If the dielectric permittivity and magnetic susceptibilies of free space are $\epsilon_0$ and $\mu_0$ respectively, then adjusting [166, eq 6.86, p191] from Gaussian to SI units gives the average spatial energy density of an electromagnetic field in a volume $V$ as:

$$\frac{1}{2}\int_V \left(\epsilon_0 \vec{E}^2 + \frac{\vec{B}^2}{\mu_0}\right)dV \tag{A.65}$$

Because the randomly fluctuating electric field is not a spatially propagating transverse wave, the energy is assumed to only be in the electric field. As the energy density in an EM wave is evenly divided amongst the electric and magnetic fields, the prior assumption introduces a factor of two, the energy in the electric field is given as:

$$\int_V \epsilon_0 \vec{E}^2 dV = \epsilon_0 \vec{E}^2 V \tag{A.66}$$

Equating the energy in a classical electromagnetic field and a quantised radiation field at frequency $\omega_{j,k}$ allows the electric field strength to be found.

$$\begin{aligned}\epsilon_0 \vec{E}^2 V &= \frac{\hbar \omega_{j,k}}{2} \\ |\vec{E}| &= \sqrt{\frac{\hbar \omega_{j,k}}{2\epsilon_0 V}}\end{aligned} \tag{A.67}$$

However, equation A.67 only finds the magnitude of the vacuum electric field, while

the dipole matrix element for Fermi's golden rule requires the field amplitude.

Because the vacuum field is randomly fluctuating the average field amplitude must be used. That is, the magnitude found by considering the energy is the average and so the amplitude obtained must also be an average. The average electric field vector is then $\vec{E_0} = (a, b, c)$, where the magnitude is fixed and is $|\vec{E}|^2 = a^2 + b^2 + c^2$. There are then three methods to find the average field amplitude in each direction, based on knowing the magnitude. While the average amplitude may be positive or negative, because the magnitude requires the square of the amplitude this is used, and the sign of the amplitude does not matter as it may be positive or negative (in equal measure over a sufficiently long time).

Firstly, it can be assumed that the average amplitude in each spatial direction is the same, as there is no preferred direction, therefore choosing the x, y, z spatial basis the average amplitude in each direction will be the same. The average electric field vector is then $\vec{E_0}$, with the average amplitude in each direction being $E_0$ as they are each the same. Therefore the average electric field vector can be written where each spatial component is the average amplitude in that direction.

$$\vec{E_0} = E_0(\vec{i} + \vec{j} + \vec{k}) \tag{A.68}$$

The magnitude of the electric field vector from equation A.68 is then:

$$|\vec{E_0}| = |E_0\vec{i} + E_0\vec{j} + E_0\vec{k}|$$

$$= (E_0^2 + E_0^2 + E_0^2)^{\frac{1}{2}} = (3E_0^2)^{\frac{1}{2}} \tag{A.69}$$

$$= \sqrt{3}E_0$$

The average electric field vector, in terms of the magnitude, is then given by:

$$\vec{E_0} = \frac{|\vec{E_0}|}{\sqrt{3}}(1,1,1) \tag{A.70}$$

Secondly, the average amplitude squared in each direction can be considered. Each of the $a$, $b$, $c$ parts can vary from 0 to $|\vec{E_0}|$, and so these can be averaged. However, it is the squared value that must be averaged, as the amplitude average will be zero, while the intensity average will not be zero. Each spatial part will have the same average, with that of the x component $a^2$ considered below, where $\bar{a}^2$ denotes the average.

$$\bar{a}^2 = \int_0^{|\vec{E_0}|} \frac{a^2}{|\vec{E_0}|^2} da$$

$$= [\frac{a^3}{3|\vec{E_0}|^2}]_0^{|\vec{E_0}|} = \frac{|\vec{E_0}|^2}{3} \tag{A.71}$$

$$\bar{a} = \frac{|\vec{E_0}|}{\sqrt{3}}$$

The exact same integral can be carried out for the y and z components, giving the average field in terms of the magnitude of the vector as:

$$\vec{E_0} = \frac{|\vec{E_0}|}{\sqrt{3}}(1, 1, 1) \tag{A.72}$$

Thirdly, the x, y, and z components of the field vector can be considered in polar coordinates and averaged over all possible orientations. Again, because the average is zero, the average of the components squared must be considered. The average x component squared, $\bar{a}^2$, is given by:

$$
\begin{aligned}
a &= |\vec{E_0}| \cos(\phi) \sin(\theta) \\
\bar{a}^2 &= \int_0^{2\pi} \int_0^{\pi} \frac{a^2}{4\pi} \sin(\theta) d\theta d\phi \\
&= |\vec{E_0}|^2 \int_0^{2\pi} \int_0^{\pi} \frac{\cos^2(\phi) \sin^3(\theta)}{4\pi} d\theta d\phi \\
&= |\vec{E_0}|^2 \frac{4}{3} \int_0^{2\pi} \frac{\cos^2(\phi)}{4\pi} d\phi = |\vec{E_0}|^2 \frac{4}{3} \frac{\pi}{4\pi} \\
&= \frac{|\vec{E_0}|^2}{3} \\
\bar{a} &= \frac{|\vec{E_0}|}{\sqrt{3}}
\end{aligned}
\tag{A.73}
$$

The average y component squared, $\bar{b}^2$, is given by:

$$b = |\vec{E_0}| \sin(\phi) \sin(\theta)$$

$$\bar{b}^2 = \int_0^{2\pi} \int_0^\pi \frac{b^2}{4\pi} \sin(\theta) d\theta d\phi$$

$$= |\vec{E_0}|^2 \int_0^{2\pi} \int_0^\pi \frac{\sin^2(\phi) \sin^3(\theta)}{4\pi} d\theta d\phi$$

$$= |\vec{E_0}|^2 \frac{4}{3} \int_0^{2\pi} \frac{\sin^2(\phi)}{4\pi} d\phi = |\vec{E_0}|^2 \frac{4}{3} \frac{\pi}{4\pi} \qquad\text{(A.74)}$$

$$= \frac{|\vec{E_0}|^2}{3}$$

$$\bar{b} = \frac{|\vec{E_0}|}{\sqrt{3}}$$

The average y component squared, $\bar{b}^2$, is given by:

$$c = |\vec{E_0}| \cos(\theta)$$

$$\bar{c}^2 = \int_0^{2\pi} \int_0^\pi \frac{c^2}{4\pi} \sin(\theta) d\theta d\phi$$

$$= |\vec{E_0}|^2 \int_0^{2\pi} \int_0^\pi \frac{\cos^2(\theta) \sin(\theta)}{4\pi} d\theta d\phi$$

$$= |\vec{E_0}|^2 2\pi \int_0^\pi \frac{\cos^2(\theta) \sin(\theta)}{4\pi} d\theta = |\vec{E_0}|^2 \frac{2\pi}{4\pi} \frac{2}{3} \qquad\text{(A.75)}$$

$$= \frac{|\vec{E_0}|^2}{3}$$

$$\bar{c} = \frac{|\vec{E_0}|}{\sqrt{3}}$$

Therefore, the average field vector in terms of the magnitude of the vector is given by:

$$\vec{E_0} = (\bar{a}, \bar{b}\bar{c})$$

$$= \frac{|\vec{E_0}|}{\sqrt{3}}(1, 1, 1) \qquad\text{(A.76)}$$

Each of equations A.70, A.72, and A.76 give the same average electric field vector. The methods used to obtain them are directly equivalent.

Equating the magnitude of the electric field vector from equation A.67 with the magnitude obtained by summing the squared of the amplitudes from equations A.70, A.72, and A.76, gives the electric field amplitude in terms of the frequency $\omega_{j,k}$, and the volume of the space is considered to be $V$ (which will be cancelled out later on by a compensating factor in the free space density of states for the electric field). The expression of the magnitude in terms of equal amplitudes is given in equation A.69. The equating of this with the energy obtained magnitude is shown below.

$$
\begin{aligned}
\sqrt{3}E_0 &= \sqrt{\frac{\hbar\omega_{j,k}}{2\epsilon_0 V}} \\
E_0 &= \frac{1}{\sqrt{3}}\sqrt{\frac{\hbar\omega_{j,k}}{2\epsilon_0 V}}
\end{aligned}
\tag{A.77}
$$

**Final Vacuum Electric Field**

There are then two final additions before the final electric field is obtained.

Firstly, the electric field must be oscillatory, otherwise no transition can be stimulated (even for the zero photon spontaneous emission), this introduces a factor of $e^{i\omega_{j,k}t}$ to each polarisation direction.

Secondly, as the electric field is that of the zero photon vacuum it is assumed to be randomly varying. Therefore a time varying random phase term, dependant upon spatial polarisation, is added to the oscillatory term, i.e $e^{i\phi_{x,y,z}(t)}$. The final electric field perturbation to the donor electron is then:

$$\vec{E_0}(t) = \frac{1}{\sqrt{3}}\sqrt{\frac{\hbar\omega_{j,k}}{2\epsilon_0 V}}\left(\vec{i}e^{i\phi_x(t)} + \vec{j}e^{i\phi_x(t)} + \vec{k}e^{i\phi_x(t)}\right)e^{i\omega_{j,k}t} \qquad (A.78)$$

It should be noted that while the above, equation A.78 electric field amplitudes are averages, the electric field will still be oscillating at the frequency of the transition, $\omega_{j,k}$, in order to stimulate the "spontaneous" emission. Also, while the field is the average of the randomly varying vacuum field, the phases of the x, y, and z parts are different and incoherent with respect to each other and therefore do not exhibit amplitude interference.

### A.3.1.2. Note on Wavefunctions

Pre-empting the form of the perturbation Hamiltonian being an electric dipole, the initial and final radiation field must be part of the initial and final wavefunctions in the dipole matrix element. Because the energy is conserved if the emitted photons are included in the final and initial states - a quantised dipole Hamiltonian is also necessary. This can be done as is shown in [165, chapter 4]. This includes 0 and 1 photon states in the wavefunctions, and writes the interaction of light and matter in terms of the EMvector potential, which itself is written in terms of photon creation and annihilation operators. The result of this is that only the atomic wavefunctions need be considered in Fermi's golden rule, and this is all that is considered in the following treatment of spontaneous emission.

### A.3.1.3. The Interaction Hamiltonian: Obtaining the Dipole

Following [167, appendix B.2], in order to obtain the interaction Hamiltonian coupling an electromagnetic field to an electron, the Hamiltonian can be written as:

$$H = \frac{1}{2m}\left(\vec{p} + e\vec{A}\right)^2 + V(\vec{r}) \tag{A.79}$$

Where $m$ is the mass of the electron being interacted with, $e$ is the electron charge, $\vec{A}$ is the electromagnetic vector potential. The vector potential, along with the scalar electric potential (or voltage) $\phi$, specifies the EMfield; $\vec{B}$ is the magnetic field vector, and $E$ the electric, both are in general space and time dependant, but this is dropped here for convenience.

$$\vec{B} = \nabla \times \vec{A}$$
$$\vec{E} = -\nabla\phi - \frac{\partial \vec{A}}{\partial t} \tag{A.80}$$

It should be noted that all following is chosen to be in such a gauge that there is no divergence of the electric vector potential, i.e the coulomb gauge, where:

$$\nabla.\vec{A} = 0 \tag{A.81}$$

By writing the non interacting part of the hamiltonian as $H_0$, equation A.79 then becomes:

$$H = \frac{1}{2m}\left(\vec{p}^2 + e^2\vec{A}^2 + e\vec{p}.\vec{A} + e\vec{A}.\vec{p}\right) + V(\vec{r})$$

$$= H_0 + \frac{e}{2m}\left(\vec{p}.\vec{A} + \vec{A}.\vec{p}\right) + \frac{e^2\vec{A}^2}{2m} \qquad \text{(A.82)}$$

$$= H_0 + H_p$$

Because $e$ is a small value, the $e^2A^2$ term is much smaller than the $eA$ terms. Additionally, due to the selection of the coulomb gauge the $\vec{p}$ and $\vec{A}$ vector commute, because they are part of an operator which must be applied to something else (some wavefunction of a state), which is not immediately obvious. To show this, firstly recall $\vec{p} = -i\hbar\nabla$. It must then be kept in mind that the parts of the Hamiltonian are operators. That is, they must be considered applied to something else:

$$\vec{p}.\vec{A}\,|\psi\rangle = -i\hbar\nabla.\vec{A}\,|\psi\rangle$$

$$= -i\hbar\left[\left(\nabla.\vec{A}\right)|\psi\rangle + \vec{A}.\left(\nabla\,|\psi\rangle\right)\right] \qquad \text{(A.83)}$$

$$= -i\hbar\left[\nabla.\vec{A} + \vec{A}.\nabla\right]|\psi\rangle$$

As $\vec{A}$ has been chosen to be in the coulomb gauge, equation A.81 gives $\nabla.\vec{A} = 0$. Therefore the first term on the right of equation A.83 is zero:

$$\vec{p}.\vec{A}\,|\psi\rangle = -i\hbar\left[\nabla.\vec{A} + \vec{A}.\nabla\right]|\psi\rangle$$

$$= -i\hbar\left[0 + \vec{A}.\nabla\right]|\psi\rangle \qquad \text{(A.84)}$$

$$= -i\hbar\vec{A}.\nabla\,|\psi\rangle$$

Considering only the operators, and not the state they are to be applied to, from equation A.84 ,and rearranging, gives the commutation of $\vec{p}$ and $\vec{A}$:

$$\vec{p}.\vec{A} = -i\hbar\vec{A}.\nabla$$

$$\vec{p}.\vec{A} = \vec{A}.\vec{p} \qquad\qquad (A.85)$$

$$\vec{p}.\vec{A} - \vec{A}.\vec{p} = [\vec{p}, \vec{A}] = 0$$

This then accounts for the factor of two in the Hamiltonian.

$$H_p \approx \frac{e}{m}\vec{p}.\vec{A} \qquad\qquad (A.86)$$

It can then be assumed that the vector potential is some travelling wave solution of Maxwell's equations.

$$\vec{A} \approx \vec{A}_0 e^{i[\vec{k}.\vec{r}-\omega t]} \qquad\qquad (A.87)$$

If the Taylor expansion of equation A.87 is taken it yields:

$$\vec{A} \approx \vec{A}_0 e^{-i\omega t}\left(1 + i\vec{k}.\vec{r} + \frac{i}{2}[\vec{k}.\vec{r}]^2 + ...\right) \qquad\qquad (A.88)$$

Taking equation A.88 to the first order term only gives an interaction Hamiltonian.

$$H_p \approx \frac{e^- e^{-i\omega t}}{m}\vec{p}.\vec{A}_0 \qquad\qquad (A.89)$$

For equation A.89, $e^-$ denotes the charge of a single electron. The ultimate purpose of this is to obtain the interaction Hamiltonian and use that the evaluate the dipole element squared. Because of this the explicit time dependence $e^{-i\omega t}$ becomes irrelevant, as in the final dipole element squared this becomes $e^{i\omega t}e^{-i\omega t} = 1$. Therefore the time dependence part of the electromagnetic vector potential is dropped for convenience and clarity in all following steps. The commutation relation of $H_0$ and the position operator $\vec{r}$ is then:

$$[\vec{r}, H_0] = \frac{i\hbar}{m}\vec{p} \tag{A.90}$$

Equation A.90, can then be exploited to rearrange the interaction Hamiltonian:

$$\begin{aligned}H_p &\approx \frac{e}{m}\vec{p}.\vec{A_0} \\ &= \frac{e}{i\hbar}[\vec{r}, H_0].\vec{A_0}\end{aligned} \tag{A.91}$$

Taking the matrix element from the Fermi's golden rule transition rate in equation A.61, but now because of the point in section A.3.1.2the states $\phi_k^0$ are no longer those of the whole system including the radiation field, but only of the electron-atom system and are relabelled $\phi_k^a$. As a result of this, and incorporating the perturbation Hamiltonian from equation A.91, the Fermi's golden rule transition rate becomes:

$$
\begin{aligned}
\langle \phi_k^a | \, H_p \, | \phi_j^a \rangle &= \frac{e}{i\hbar} \langle \phi_k^a | \, [\vec{r}, H_0].\vec{A}_0 \, | \phi_j^a \rangle \\
&= \frac{e}{i\hbar} \langle \phi_k^a | \, \vec{r}.\vec{A}_0 H_0 - H_0 \vec{r}.vecA_0 \, | \phi_j^a \rangle \\
&= \frac{e}{i\hbar} \left[ \langle \phi_k^a | \, \vec{r}.\vec{A}_0 H_0 \, | \phi_j^a \rangle - \langle \phi_k^a | \, H_0 \vec{r}.\vec{A}_0 \, | \phi_j^a \rangle \right] \\
&= \frac{e}{i\hbar} \left[ \langle \phi_k^a | \, \vec{r}.\vec{A}_0 E_j^a \, | \phi_j^a \rangle - \langle \phi_k^a | \, E_k^a \vec{r}.vecA_0 \, | \phi_j^a \rangle \right] \\
&= \frac{e}{i\hbar} \left( E_j^a - E_k^a \right) \langle \phi_k^0 | \, \vec{r}.\vec{A}_0 \, | \phi_j^0 \rangle
\end{aligned}
\tag{A.92}
$$

The relation of the electric field and magnetic vector potential then allows the matrix element to be rewritten.

$$
\vec{E}_0 = \frac{(E_j - E_k)}{i\hbar} \vec{A}_0
$$
$$
\frac{e}{i\hbar} \left( E_j - E_k \right) \langle \phi_k^0 | \, \vec{r}.\vec{A}_0 \, | \phi_j^0 \rangle = \langle \phi_k^0 | \, e\vec{r}.\vec{E}_0 \, | \phi_j^0 \rangle
\tag{A.93}
$$

$\vec{E}_0$ is the electric field vector. As a final result, the interaction Hamiltonian is then:

$$
H_p \approx e\vec{r}.\vec{E}_0
\tag{A.94}
$$

Where $\vec{r} = x\vec{i} + y\vec{j} + z\vec{k}$ is a radial vector, $\vec{E}_0 = E_{x0}\vec{i} + E_{y0}\vec{j} + E_{z0}\vec{k}$, $e$ is the electric charge of a single electron, and $\vec{i}, \vec{j}, \vec{k}$ are unit vectors in each spatial direction.

### A.3.1.4. Degeneracies

For transition rates calculated by Fermi's golden rule in equation A.61 the degeneracies of the states must be included. Despite it being possible to only have to consider the electron wavefunctions ( section A.3.1.2) the degeneracies include both those of

the electron and the electric field(photon state). Taking $a$ t index the electron-atom system and $p$ for the photons then gives the degeneracies.

$$g_j = g_j^a g_j^p$$
$$g_k = g_k^a g_k^p \tag{A.95}$$

The electron degeneracies, $a$, are then just those the electron states. Conveniently, there is then only a single way for the number of photons to be zero.

$$g_j^p = 1 \tag{A.96}$$

However, because the photon states are in a continuum with respect to energy, because $\omega$ can vary continuously, $g_k^p$ must be replaced with the density of states at the corresponding energy. That is, we must consider the total number of final states in the infinitesimal interval $E_k^0$ to $E_k^0 + dE_k^0$. The density of final states for the whole system is $\rho(E_k^0)$. Taking the transition rate from equation A.61, and accounting for the density of states results in:

$$\begin{aligned}
\Gamma_{j,k} &= \int_{-\infty}^{\infty} \frac{2\pi}{\hbar} \frac{1}{g_j^a} | \langle \phi_k^0 | H_p | \phi_j^0 \rangle |^2 \delta(E_k^0 - E_j^0) \rho(E_k^0) dE_k^0 \\
&= \frac{2\pi}{\hbar} \frac{1}{g_j^a} | \langle \phi_k^0 | H_p | \phi_j^0 \rangle |^2 \rho(E_j^0)
\end{aligned} \tag{A.97}$$

Because the initial and final state energies are the same, the initial state energy can be replaced with that of the final energy, i.e $E_k^0 = E_j^0$, this is no more than a labelling convenience, as the density of states is the density of final states irrespective of the

energy it is at.

$$\Gamma_{j,k} = \frac{2\pi}{\hbar} \frac{1}{g_j^a} |\langle \phi_k^0| H_p |\phi_j^0 \rangle|^2 \rho(E_k^0) \tag{A.98}$$

The relationship between the density of total final states and the density of photon states and degeneracy of final electron states is given by:

$$\rho(E_k^0) = g_k^a \rho(\hbar\omega_{j,k}) \tag{A.99}$$

Where $\rho(\hbar\omega_{j,k})$ is the density of states for photons at the frequency $\omega_{j,k}$, that corresponding to the energy of the electron state transition. Taking into account that only the electron wavefunctions are necessary for the matrix element (section A.3.1.2), along with equation A.99, results in the transition rate.

$$\Gamma_{j,k} = \frac{2\pi}{\hbar} \frac{g_k^a}{g_j^a} |\langle \phi_k^a| H_p |\phi_j^a \rangle|^2 \rho(\hbar\omega_{j,k}) \tag{A.100}$$

### A.3.1.5. Photon Density of States

Equation A.100 requires that the density of final photon states be known. The density of photon states in a vacuum is reproduced here following [31, Appendix C]hl. The general form of the electromagnetic wave is taken to be:

$$\vec{E}(\vec{r}, t) = \sum_{\vec{k}} E_{\vec{k}} e^{i(\vec{k}.\vec{r} - \omega t)} \tag{A.101}$$

Maxwell's equations in free space specify:

$$\nabla.E = 0 \qquad\qquad (A.102)$$

This is fulfilled if:

$$\vec{k}.\vec{E}(\vec{r},t) = 0 \qquad\qquad (A.103)$$

Thus the electric field wave must be transverse. This gives a factor of two that must be considered in the density of states, the two different polarisations. If, for a vacuum, we consider the light to be in an arbitrarily large cubed space of volume $V$, of side length $L$, the electric field must be zero at the boundaries. Where $n_{x,y,z} \in \mathbb{Z}$, this gives the conditions:

$$
\begin{aligned}
k_x &= \frac{2\pi n_x}{L} \\
k_y &= \frac{2\pi n_y}{L} \\
k_z &= \frac{2\pi n_z}{L}
\end{aligned}
\qquad\qquad (A.104)
$$

It is clear that each state occupies a volume in momentium space of $\left(\frac{2\pi}{L}\right)^3$. The number of states, $\rho(k)dk$, in the space $k \to k + dk$ is then the volume of a spherical shell of thickness $dk$ divided by the volume per unit state and then multiplied by two to account for the different polarisations. If $\rho(k)$ is the density of states this

can be shown by:

$$\begin{aligned}
\rho(k)dk &= 2\frac{4\pi k^2}{\left(\frac{2\pi}{L}\right)^3}dk \\
&= \frac{L^3 k^2}{\pi^2}
\end{aligned} \tag{A.105}$$

Therefore the density of states is:

$$\rho(k) = \frac{Vk^2}{\pi^2} \tag{A.106}$$

The density of states in frequency is then related to that in wavevector by:

$$\begin{aligned}
\rho(\omega)d\omega &= \rho(k)dk \\
\rho(\omega)d\omega &= \frac{Vk^2}{\pi^2}\frac{d\omega}{dk} \\
\omega &= ck \\
\frac{d\omega}{dk} &= c \\
\rho(\omega)d\omega &= \frac{V\omega^2}{c^3\pi^2}
\end{aligned} \tag{A.107}$$

And then the relation of the density of states in frequency becomes that in energy:

$$\rho(\omega)d\omega = g(E)dE$$

$$\rho(\omega) = g(E)\frac{dE}{d\omega}$$

$$E = \hbar\omega \tag{A.108}$$

$$\frac{dE}{d\omega} = \hbar$$

$$\rho(E) = \frac{V\omega^2}{\hbar c^3 \pi^2}$$

### A.3.1.6. Final Dipole Interaction Emission Rate

The final transition rate is then obtained from the arguments outlined above. Firstly the transition rate from equation A.100 is:

$$\Gamma_{j,k} = \frac{2\pi}{\hbar}\frac{g_k^a}{g_j^a}| \langle\phi_k^0| H_p |\phi_j^0\rangle |^2\rho(\hbar\omega_{j,k}) \tag{A.109}$$

The density of photon states at the appropriate frequency from equation A.107 make the transition rate:

$$\Gamma_{j,k} = \frac{2\pi}{\hbar}\frac{g_k^a}{g_j^a}| \langle\phi_k^0| H_p |\phi_j^0\rangle |^2\frac{V\omega_{j,k}^2}{\hbar c^3 \pi^2} \tag{A.110}$$

Taking the perturbation Hamiltonian to be the dipole from equation A.94 then gives:

$$\Gamma_{j,k} = \frac{2\pi}{\hbar}\frac{g_k^a}{g_j^a}| \langle\phi_k^0| e\vec{r}.\vec{E_0} |\phi_j^0\rangle |^2\frac{V\omega_{j,k}^2}{\hbar c^3 \pi^2} \tag{A.111}$$

## A. Review of Quantum Mechanics

Setting the electric field to that of the vacuum electric field from equation A.78 and using the identity $\vec{r} = x\vec{i} + y\vec{j} + z\vec{k}$ results in:

$$
\begin{aligned}
\Gamma_{j,k} &= \frac{2\pi}{\hbar} \frac{g_k^a}{g_j^a} |\langle\phi_k^a| e\left(x\vec{i} + y\vec{j} + z\vec{k}\right) \cdot \frac{1}{\sqrt{3}} \sqrt{\frac{\hbar\omega_{j,k}}{2\epsilon_0 V}} \left(e^{i\phi_x(t)}\vec{i} + e^{i\phi_y(t)}\vec{j} + e^{i\phi_z(t)}\vec{k}\right) e^{i\omega_{j,k}t} |\phi_j^a\rangle|^2 \frac{V\omega_{j,k}^2}{\hbar c^3 \pi^2} \\
&= \frac{2\pi}{\hbar} \frac{1}{3} \frac{\hbar\omega_{j,k}}{2\epsilon_0 V} \frac{V\omega_{j,k}^2}{\hbar c^3 \pi^2} \frac{g_k^a}{g_j^a} |\langle\phi_k^a| e\left(x\vec{i} + y\vec{j} + z\vec{k}\right) \cdot \left(e^{i\phi_x(t)}\vec{i} + e^{i\phi_y(t)}\vec{j} + e^{i\phi_z(t)}\vec{k}\right) |\phi_j^a\rangle|^2 \\
&= \frac{e^2 \omega_{j,k}^3}{3\hbar\epsilon_0 c^3 \pi} \frac{g_k^a}{g_j^a} |\langle\phi_k^a| \left(x\vec{i} + y\vec{j} + z\vec{k}\right) \cdot \left(e^{i\phi_x(t)}\vec{i} + e^{i\phi_y(t)}\vec{j} + e^{i\phi_z(t)}\vec{k}\right) |\phi_j^a\rangle|^2
\end{aligned}
\tag{A.112}
$$

Because of the randomly varying phases $e^{i\phi_{x,y,z}(t)}$, each component must be squared and summed, rather than summed and squared. That is, for the spontaneous emission case the components must be summed as intensities rather than amplitudes. This is in contrast to the result for a coherent electric field where the different components are to be summed as amplitudes, rather than intensities. Therefore, the individual matrix element components in equation A.112 , when the magnitude squared is taken, becomes:

$$
\begin{aligned}
|\langle\phi_k^a| x e^{i\phi_x(t)} |\phi_j^a\rangle|^2 &= e^{i\phi_x(t)} \langle\phi_k^a| x |\phi_j^a\rangle e^{-i\phi_x(t)} \langle\phi_k^a| x |\phi_j^a\rangle \\
&= |\langle\phi_k^a| x |\phi_j^a\rangle|^2
\end{aligned}
\tag{A.113}
$$

Therefore, using equation A.113 , equation A.112 becomes:

$$
\Gamma_{j,k} = \frac{e^2 \omega_{j,k}^3}{3\hbar\epsilon_0 c^3 \pi} \frac{g_k^a}{g_j^a} \left(|\langle\phi_k^a| x |\phi_j^a\rangle|^2 + |\langle\phi_k^a| y |\phi_j^a\rangle|^2 + |\langle\phi_k^a| z |\phi_j^a\rangle|^2\right)
\tag{A.114}
$$

286

Equation A.114 gives the final transition rate. where $\phi^a_{kORj}$ is the electron state wavefunction, $k$ indexes the final state, $j$ the initial, $g^a$ is the electron state degeneracy, $\omega_{j,k}$ the angular frequency of the electron transition, $\epsilon_0$ the dielectric constant in free space, $\hbar$ Planck's constant, $c$ the speed of light in a vacuum, and x, y, and z are then the coordinates for the three spatial axes. This result is identical to that obtained if considering the stimulated absorption rate of a two level system, relating that to the spontaneous emission rate via Einstein's rate equations, and applying a thermodynamic equilibrium condition.

# B. Derivations of Effective Mass Theory Wavefunction Equations

Following are the various derivations of the equations presented in chapter 3, the introduction to effective mass theory. These are the derivations and necessary working that is either not given in the literature, or in the case of the dipole elements has not been obtained before.

## B.1. The Unitless Effective Mass Hamiltonian

Begin with the effective mass Hamiltonian, equation B.1.

$$H_1 = -\frac{\hbar^2}{2m_\perp}\left(\frac{\partial^2}{\partial x_i^2} + \frac{\partial^2}{\partial y_i^2}\right) - \frac{\hbar^2}{2m_\parallel}\frac{\partial^2}{\partial z_i^2} - \frac{e^2}{4\pi\epsilon_r\epsilon_0 r} \tag{B.1}$$

Take the units of length and energy to be $a_B$ and $E_0$ respectively, while setting $\gamma$ to be the ratio of perpendicular to longitudinal effective masses, defined in equation B.2; where $\epsilon_r$ is the relative dielectric permittivity and $\epsilon_0$ is that in vacuum.

## B. Derivations of Effective Mass Theory Wavefunction Equations

$$\gamma = \frac{m_\perp}{m_\parallel}$$

$$a_B = \frac{4\pi\hbar^2 \epsilon_r \epsilon_0}{m_\perp e^2} \tag{B.2}$$

$$E_0 = \frac{m_\perp e^4}{32\hbar^2(\pi\epsilon_r\epsilon_0)^2}$$

As the Hamiltonian $H_1$ has units of energy, divide $H_1$ from equation B.1 by $E_0$ from equation B.2, resulting in equation B.3.

$$H_1 = -\frac{\hbar^2}{2m_\perp}\left(\frac{\partial^2}{\partial x^2} + \frac{\partial^2}{\partial y^2}\right) - \frac{\hbar^2}{2m_\parallel}\frac{\partial^2}{\partial z^2} - \frac{e^2}{4\pi\epsilon_r\epsilon_0 r}$$

$$\frac{H_1}{E_0} = -\frac{\hbar^2}{2m_\perp}\frac{2\hbar^2(4\pi\epsilon_r\epsilon_0)^2}{m_\perp e^4}\left(\frac{\partial^2}{\partial x^2} + \frac{\partial^2}{\partial y^2}\right) - \frac{\hbar^2}{2m_\parallel}\frac{2\hbar^2(4\pi\epsilon_r\epsilon_0)^2}{m_\perp e^4}\frac{\partial^2}{\partial z^2} - \frac{2\hbar^2(4\pi\epsilon_r\epsilon_0)^2}{m_\perp e^4}\frac{e^2}{4\pi\epsilon_r\epsilon_0 r}$$

$$\frac{H_1}{E_0} = -\frac{2\hbar^4(4\pi\epsilon_r\epsilon_0)^2}{2m_\perp^2 e^4}\left(\frac{\partial^2}{\partial x^2} + \frac{\partial^2}{\partial y^2}\right) - \frac{2\hbar^4(4\pi\epsilon_r\epsilon_0)^2}{2m_\parallel m_\perp e^4}\frac{\partial^2}{\partial z^2} - \frac{2\hbar^2(4\pi\epsilon_r\epsilon_0)}{m_\perp e^2 r}$$

$$\tag{B.3}$$

Then consider the second order differentials with respect to distance units. If capitalised coordinates,X,Y,Z are now the unit-less coordinates then their relation to the non unit-less x, y, and z is given below:

*B. Derivations of Effective Mass Theory Wavefunction Equations*

$$\{X, Y, Z\} = \{\frac{x}{a_B}, \frac{y}{a_B}, \frac{z}{a_B}\}$$

$$R = (X^2 + Y^2 + Z^2)^{\frac{1}{2}} = \frac{1}{a_B}(x^2 + y^2 + z^2)^{\frac{1}{2}} = \frac{r}{a_B} \tag{B.4}$$

$$\frac{\partial^2}{\partial\{x, y, z\}^2} = \left(\frac{\partial\{X, Y, Z\}}{\partial\{x, y, z\}}\right)^2 \frac{\partial^2}{\partial\{X, Y, Z\}^2} = \left(\frac{1}{a_B}\right)^2 \frac{\partial^2}{\partial\{X, Y, Z\}^2}$$

Therefore equation B.4 shows that to convert into unit-less form, the second order differential terms must be preceded by a factor of $\left(\frac{1}{a_B}\right)^2$. Now taking the unit-less coordinates to be written as x,y,z for the sake of convenience, and dividing the second order differential terms from equation B.3 by the relevant factors from equation B.4, results in the dimensionless effective mass Hamiltonian:

$$H_1 = -\frac{2\hbar^4(4\pi\epsilon_r\epsilon_0)^2}{2m_\perp^2 e^4}\left(\frac{1}{a_B}\right)^2\left(\frac{\partial^2}{\partial x^2} + \frac{\partial^2}{\partial y^2}\right) - \frac{2\hbar^4(4\pi\epsilon_r\epsilon_0)^2}{2m_\parallel m_\perp e^4}\left(\frac{1}{a_B}\right)^2\frac{\partial^2}{\partial z^2} - \left(\frac{1}{a_B}\right)\frac{2\hbar^2(4\pi\epsilon_r\epsilon_0)}{m_\perp e^2 r}$$

$$H_1 = -\frac{2\hbar^4(4\pi\epsilon_r\epsilon_0)^2}{2m_\perp^2 e^4}\frac{m_\perp^2 e^4}{\hbar^4(4\pi\epsilon_r\epsilon_0)^2}\left(\frac{\partial^2}{\partial x^2} + \frac{\partial^2}{\partial y^2}\right) - \frac{2\hbar^4(4\pi\epsilon_r\epsilon_0)^2}{2m_\parallel m_\perp e^4}\frac{m_\perp^2 e^4}{\hbar^4(4\pi\epsilon_r\epsilon_0)^2}\frac{\partial^2}{\partial z^2}$$
$$- \frac{m_\perp e^2}{\hbar^2(4\pi\epsilon_r\epsilon_0)}\frac{2\hbar^2(4\pi\epsilon_r\epsilon_0)}{m_\perp e^2 r}$$

$$H_1 = -\left(\frac{\partial^2}{\partial x^2} + \frac{\partial^2}{\partial y^2}\right) - \frac{m_\perp}{m_\parallel}\frac{\partial^2}{\partial z^2} - \frac{2}{r}$$

$$H_1 = -\left(\frac{\partial^2}{\partial x^2} + \frac{\partial^2}{\partial y^2}\right) - \gamma\frac{\partial^2}{\partial z^2} - \frac{2}{r}$$

$$(\text{B.5})$$

It must be noted that the x, y, and z in equation B.5 are unit-less, despite the same coordinate labels as for the non unit-less form in the preceding equations.

## B.2. Scaled Cartesian Coordinates for the Effective Mass Hamiltonian

The Hamiltonian can be rescaled into a transformed Cartesian coordinate system, $(x, y, z) \rightarrow (x, y, g)$. This is primarily for our convenience, as it allows the use of scaled hydrogenic wavefunctions that appear as hydrogen wavefunctions in the new coordinates.

Begin by choosing a new coordinate system $(x, y, g)$, with $g$ scaled to $z$. The relationship between the two sets of coordinates is then:

## B. Derivations of Effective Mass Theory Wavefunction Equations

$$g = (\frac{\beta}{\gamma})^{\frac{1}{2}} z$$

$$z = (\frac{\gamma}{\beta})^{\frac{1}{2}} g \qquad \text{(B.6)}$$

$$z^2 = (\frac{\gamma}{\beta}) g^2$$

The partial differentials of the two coordinate systems from equation B.6 are then:

$$\partial z = (\frac{\gamma}{\beta})^{\frac{1}{2}} \partial g$$

$$\frac{\partial g}{\partial z} = \left(\frac{\beta}{\gamma}\right)^{\frac{1}{2}} \qquad \text{(B.7)}$$

$$\left(\frac{\partial g}{\partial z}\right)^2 = \frac{\beta}{\gamma}$$

The first and second order differential operators are written as:

$$\frac{\partial}{\partial z} = \frac{\partial g}{\partial z}\frac{\partial}{\partial g}$$

$$\frac{\partial^2}{\partial z^2} = \left(\frac{\partial g}{\partial z}\right)^2 \frac{\partial^2}{\partial g^2} \qquad \text{(B.8)}$$

$$= \frac{\beta}{\gamma}\frac{\partial^2}{\partial g^2}$$

Inserting the operators from equation B.8 into equation B.5 then changes the effective mass Hamiltonian.

## B. Derivations of Effective Mass Theory Wavefunction Equations

$$
\begin{aligned}
H_1 &= -\left(\frac{\partial^2}{\partial x^2} + \frac{\partial^2}{\partial y^2}\right) - \gamma\frac{\partial^2}{\partial z^2} - \frac{2}{r} \\
&= -\left(\frac{\partial^2}{\partial x^2} + \frac{\partial^2}{\partial y^2}\right) - \gamma\frac{\beta}{\gamma}\frac{\partial^2}{\partial g^2} - \frac{2}{r} \\
&= -\left(\frac{\partial^2}{\partial x^2} + \frac{\partial^2}{\partial y^2}\right) - \beta\frac{\partial^2}{\partial g^2} - \frac{2}{r}
\end{aligned}
\tag{B.9}
$$

The Laplacian operator is well known, and can be written as:

$$
\nabla_g^2 = \frac{\partial^2}{\partial x^2} + \frac{\partial^2}{\partial y^2} + \frac{\partial^2}{\partial g^2}
\tag{B.10}
$$

The Hamiltonian from equation B.9 can then be reorganized.

$$
\begin{aligned}
H_1 &= -\left(\frac{\partial^2}{\partial x^2} + \frac{\partial^2}{\partial y^2}\right) - \beta\frac{\partial^2}{\partial g^2} - \frac{2}{r} \\
&= -\left(\frac{\partial^2}{\partial x^2} + \frac{\partial^2}{\partial y^2}\right) - \frac{\partial^2}{\partial g^2} + \frac{\partial^2}{\partial g^2} - \beta\frac{\partial^2}{\partial g^2} - \frac{2}{r} \\
&= -\left(\frac{\partial^2}{\partial x^2} + \frac{\partial^2}{\partial y^2} + \frac{\partial^2}{\partial g^2}\right) + \left(1 - \beta\right)\frac{\partial^2}{\partial g^2} - \frac{2}{r} \\
&= -\nabla_g^2 + \left(1 - \beta\right)\frac{\partial^2}{\partial g^2} - \frac{2}{r}
\end{aligned}
\tag{B.11}
$$

The final stage is to find the new radial coordinate $r_g$ for the spherical coordinate system.

$$
\begin{aligned}
r &= (x^2 + y^2 + z^2)^{\frac{1}{2}} \\
&= (x^2 + y^2 + (\frac{\gamma}{\beta})g^2)^{\frac{1}{2}}
\end{aligned}
\tag{B.12}
$$

The Hamiltonian from equation B.11 is then fully transformed to the $(x, y, g)$ coordinates by substitution from equation B.12.

$$H_1 = -\nabla_g^2 + \left(1 - \beta\right)\frac{\partial^2}{\partial g^2} - \frac{2}{r_g(x^2 + y^2 + (\frac{\gamma}{\beta})g^2)^{\frac{1}{2}}} \tag{B.13}$$

## B.2.1. Spherical Coordinates

The $(x, y, g)$ Hamiltonian can be easily transformed into a spherical coordinate system. The spherical coordinates are $\{r_g, \theta_g, \phi_g\}$.

The spherical and Cartesian coordinates are related, where subscript $g$ indicates the new scaled coordinates.

$$
\begin{aligned}
x &= r_g \sin(\theta_g) \cos(\phi) \\
y &= r_g \sin(\theta_g) \sin(\phi) \\
g &= r_g \cos(\theta_g) \\
r_g &= (x^2 + y^2 + g^2)^{\frac{1}{2}} \\
r &= (x^2 + y^2 + z^2)^{\frac{1}{2}} \\
&= (x^2 + y^2 + (\frac{\gamma}{\beta})g^2)^{\frac{1}{2}} \\
&= r_g\left(1 - (1 - \frac{\gamma}{\beta})\cos^2(\theta)\right)^{\frac{1}{2}} \\
\theta_g &= \arccos(\frac{g}{r_g}) \\
\theta &= \arccos(\frac{z}{r}) \\
\phi &= \phi_g = \arctan(\frac{y}{x})
\end{aligned}
\tag{B.14}
$$

## B. Derivations of Effective Mass Theory Wavefunction Equations

For completeness, the Laplacian operator is written here in spherical coordinates as:
[168].

$$\nabla_g^2 = \frac{1}{r_g^2} \frac{\partial}{\partial r_g}(r_g^2 \frac{\partial}{\partial r_g}) + \frac{1}{r_g^2 \sin(\theta_g)} \frac{\partial}{\partial \theta_g}(\sin(\theta_g) \frac{\partial}{\partial \theta_g}) + \frac{1}{r_g^2 \sin^2(\theta_g)} \frac{\partial^2}{\partial \phi_g^2} \qquad (B.15)$$

The second order differential operator, with respect to $g$, in the Hamiltonian must then be considered.

### B.2.1.1. Changing a Second Order Differential Operator to Spherical Coordinates

By application of the chain rule the second order $g$ differential can be expanded in terms of spherical coordinates.

$$\frac{\partial}{\partial g} = \frac{\partial \theta_g}{\partial g} \frac{\partial}{\partial \theta_g} + \frac{\partial r_g}{\partial g} \frac{\partial}{\partial r_g}$$

$$\frac{\partial^2}{\partial g^2} = \frac{\partial}{\partial g} \left( \frac{\partial \theta_g}{\partial g} \frac{\partial}{\partial \theta_g} + \frac{\partial r_g}{\partial g} \frac{\partial}{\partial r_g} \right)$$

$$\frac{\partial^2}{\partial g^2} = \frac{\partial^2 \theta_g}{\partial g^2} \frac{\partial}{\partial \theta_g} + \frac{\partial \theta_g}{\partial g} \frac{\partial}{\partial g} \frac{\partial}{\partial \theta_g} + \frac{\partial^2 r_g}{\partial g^2} \frac{\partial}{\partial r_g} + \frac{\partial r_g}{\partial g} \frac{\partial}{\partial g} \frac{\partial}{\partial r_g}$$

$$= \frac{\partial^2 \theta_g}{\partial g^2} \frac{\partial}{\partial \theta_g} + \frac{\partial \theta_g}{\partial g} \left[ \frac{\partial \theta_g}{\partial g} \frac{\partial}{\partial \theta_g} + \frac{\partial r_g}{\partial g} \frac{\partial}{\partial r_g} \right] \frac{\partial}{\partial \theta_g} + \frac{\partial^2 r_g}{\partial g^2} \frac{\partial}{\partial r_g} + \frac{\partial r_g}{\partial g} \left[ \frac{\partial \theta_g}{\partial g} \frac{\partial}{\partial \theta_g} + \frac{\partial r_g}{\partial g} \frac{\partial}{\partial r_g} \right] \frac{\partial}{\partial r_g}$$

$$= \frac{\partial^2 \theta_g}{\partial g^2} \frac{\partial}{\partial \theta_g} + \left( \frac{\partial \theta_g}{\partial g} \right)^2 \frac{\partial^2}{\partial \theta_g^2} + \frac{\partial \theta_g}{\partial g} \frac{\partial r_g}{\partial g} \frac{\partial}{\partial r_g} \frac{\partial}{\partial \theta_g} + \frac{\partial^2 r_g}{\partial g^2} \frac{\partial}{\partial r_g} + \frac{\partial r_g}{\partial g} \frac{\partial \theta_g}{\partial g} \frac{\partial}{\partial \theta_g} \frac{\partial}{\partial r_g} + \left( \frac{\partial r_g}{\partial g} \right)^2 \frac{\partial^2}{\partial r_g^2}$$

$$= \frac{\partial^2 \theta_g}{\partial g^2} \frac{\partial}{\partial \theta_g} + \frac{\partial^2 r_g}{\partial g^2} \frac{\partial}{\partial r_g} + \left( \frac{\partial \theta_g}{\partial g} \right)^2 \frac{\partial^2}{\partial \theta_g^2} + \left( \frac{\partial r_g}{\partial g} \right)^2 \frac{\partial^2}{\partial r_g^2} + 2 \frac{\partial \theta_g}{\partial g} \frac{\partial r_g}{\partial g} \frac{\partial}{\partial r_g} \frac{\partial}{\partial \theta_g}$$

$$\qquad (B.16)$$

## B. Derivations of Effective Mass Theory Wavefunction Equations

The 5 different terms can then be addressed. Firstly, the first order differentials of $\theta_g$ with respect to $g$ are shown below.

$$
\begin{aligned}
\theta_g &= \arccos(\frac{g}{r_g}) = \arccos(\frac{g}{(x^2 + y^2 + g^2)^{\frac{1}{2}}}) \\
\frac{\partial \theta_g}{\partial g} &= \left( \frac{1}{\left(x^2 + y^2 + g^2\right)^{\frac{1}{2}}} + \frac{-1}{2} \frac{2g^2}{\left(x^2 + y^2 + g^2\right)^{\frac{3}{2}}} \right) \frac{-1}{\sqrt{1 - \frac{g^2}{(x^2+y^2+g^2)}}} \\
&= \left( \frac{1}{r_g} - \frac{g^2}{r_g^3} \right) \frac{-1}{\sqrt{1 - \frac{g^2}{r_g^2}}} \\
&= \frac{-1}{r_g} \left( 1 - \frac{g^2}{r_g^2} \right) \frac{1}{\sqrt{1 - \frac{g^2}{r_g^2}}} \\
&= \frac{-1}{r_g} \sqrt{1 - \frac{g^2}{r_g^2}} \\
&= \frac{-1}{r_g} \sqrt{1 - \frac{r_g^2 \cos(\theta_g)^2}{r_g^2}} \\
&= \frac{-1}{r_g} \sqrt{1 - \cos(\theta_g)^2} \\
&= \frac{-1}{r_g} \sqrt{\sin^2(\theta_g) + \cos^2(\theta_g) - \cos^2(\theta_g)} \\
&= \frac{-1}{r_g} \sqrt{\sin^2(\theta_g)} \\
&= -\frac{\sin(\theta_g)}{r_g} \\
\left( \frac{\partial \theta_g}{\partial g} \right)^2 &= \frac{\sin^2(\theta_g)}{r_g^2}
\end{aligned}
\tag{B.17}
$$

Secondly, the second order differentials of $\theta_g$ with respect to $g$ are:

## B. Derivations of Effective Mass Theory Wavefunction Equations

$$
\begin{aligned}
\frac{\partial^2 \theta_g}{\partial g^2} &= \frac{\partial}{\partial g}\left(\frac{\partial \theta_g}{\partial g}\right) \\
&= \frac{\partial}{\partial \theta_g}\frac{\partial \theta_g}{\partial g}\left(\frac{\partial \theta_g}{\partial g}\right) \\
&= \left(\frac{\partial}{\partial \theta_g}\frac{\partial \theta_g}{\partial g}\right)\left(\frac{\partial \theta_g}{\partial g}\right) + \left(\frac{\partial \theta_g}{\partial g}\right)\left(\frac{\partial}{\partial \theta_g}\frac{\partial \theta_g}{\partial g}\right) \\
&= 2\frac{\partial \theta_g}{\partial g}\frac{\partial}{\partial \theta_g}\left(\frac{\partial \theta_g}{\partial g}\right) \\
&= -2\frac{\sin(\theta_g)}{r_g}\frac{\partial}{\partial \theta_g}\left(-\frac{\sin(\theta_g)}{r_g}\right) \\
&= \left(-2\frac{\sin(\theta_g)}{r_g}\right)\left(-\frac{\cos(\theta_g)}{r_g}\right) \\
&= 2\frac{\sin(\theta_g)\cos(\theta_g)}{r_g^2}
\end{aligned}
\tag{B.18}
$$

Thirdly, the first order derivative of $r_g$ with respect to $g$ is:

$$
\begin{aligned}
r_g &= \left(x^2 + y^2 + g^2\right)^{\frac{1}{2}} \\
\frac{\partial r_g}{\partial g} &= \frac{g}{\left(x^2 + y^2 + g^2\right)^{\frac{1}{2}}} \\
&= \frac{g}{r_g} \\
&= \frac{r_g \cos(\theta_g)}{r_g} \\
&= \cos(\theta_g) \\
\left(\frac{\partial r_g}{\partial g}\right)^2 &= \cos^2(\theta_g)
\end{aligned}
\tag{B.19}
$$

Fourthly, the second order derivative of $r_g$ with respect to $g$ is:

297

$$\frac{\partial^2 r_g}{\partial g^2} = \frac{\partial}{\partial g}\left(\frac{g}{\left(x^2+y^2+g^2\right)^{\frac{1}{2}}}\right)$$

$$= \frac{1}{\left(x^2+y^2+g^2\right)^{\frac{1}{2}}} - \frac{g^2}{\left(x^2+y^2+g^2\right)^{\frac{3}{2}}}$$

$$= \frac{1}{r_g} - \frac{g^2}{r_g^3}$$

$$= \frac{1}{r_g}\left(1 - \frac{r_g^2\cos^2(\theta_g)}{r_g^2}\right)$$

$$= \frac{1}{r_g}\left(1 - \cos^2(\theta_g)\right)$$

$$= \frac{1}{r_g}\left(\sin^2(\theta_g) + \cos^2(\theta_g) - \cos^2(\theta_g)\right)$$

$$= \frac{\sin^2(\theta_g)}{r_g}$$

(B.20)

The differential operator has then been converted into spherical coordinates. Collecting the five expressions from equations B.17, B.18, B.19, and B.20 results in the full expression.

$$\frac{\partial^2}{\partial g^2} = \frac{\partial^2\theta_g}{\partial g^2}\frac{\partial}{\partial\theta_g} + \frac{\partial^2 r_g}{\partial g^2}\frac{\partial}{\partial r_g} + \left(\frac{\partial\theta_g}{\partial g}\right)^2\frac{\partial^2}{\partial\theta_g^2} + \left(\frac{\partial r_g}{\partial g}\right)^2\frac{\partial^2}{\partial r_g^2} + 2\frac{\partial\theta_g}{\partial g}\frac{\partial r_g}{\partial g}\frac{\partial}{\partial r_g}\frac{\partial}{\partial\theta_g}$$

$$= 2\frac{\sin(\theta_g)\cos(\theta_g)}{r_g^2}\frac{\partial}{\partial\theta_g}$$

$$+ \frac{\sin^2(\theta_g)}{r_g}\frac{\partial}{\partial r_g} + \frac{\sin^2(\theta_g)}{r_g^2}\frac{\partial^2}{\partial\theta_g^2}$$

$$+ \cos^2(\theta_g)\frac{\partial^2}{\partial r_g^2} - 2\frac{\sin(\theta_g)}{r_g}\cos(\theta_g)\frac{\partial}{\partial r_g}\frac{\partial}{\partial\theta_g}$$

(B.21)

Incorporating the terms from equation B.21 into the effective mass Hamiltonian from equation B.11, results gives:

$$H_1 = -\nabla_g^2 + \left(1 - \beta\right) \left[ 2\frac{\sin(\theta_g)\cos(\theta_g)}{r_g^2}\frac{\partial}{\partial \theta_g} \right.$$
$$+ \frac{\sin^2(\theta_g)}{r_g}\frac{\partial}{\partial r_g} + \frac{\sin^2(\theta_g)}{r_g^2}\frac{\partial^2}{\partial \theta_g^2} + \cos^2(\theta_g)\frac{\partial^2}{\partial r_g^2}$$
$$\left. - 2\frac{\sin(\theta_g)}{r_g}\cos(\theta_g)\frac{\partial}{\partial r_g}\frac{\partial}{\partial \theta_g} \right]$$
$$- \frac{2}{r_g\left(1 - (1 - \frac{\gamma}{\beta})\cos^2(\theta)\right)^{\frac{1}{2}}}$$

(B.22)

## B.3. Applying the Effective Mass Hamiltonian to Single Hydrogenic Basis States

The application of the unitless effective mass Hamiltonian to single hydrogenic basis state wavefunctions, followed by multiplication by the complex conjugate of the wavefunction and integration over all space.

The energy expectation integrals are of the form specified below.

$$E_j = \langle F_j | H_1 | F_j \rangle$$
$$= \int_{-\infty}^{\infty}\int_{-\infty}^{\infty}\int_{-\infty}^{\infty} F_j^*(x, y, (\frac{\beta}{\gamma})^{\frac{1}{2}}z) H_1 F_j(x, y, (\frac{\beta}{\gamma})^{\frac{1}{2}}z) dx\,dy\,dz$$

(B.23)

Taking into account the change of the integration from $(x, y, z)$ to $(x, y, g)$ coordinates, defined above in equation B.6 and the partial differentials in equation B.7, changes equation B.23 to become:

$$E_j = \int_{-\infty}^{\infty}\int_{-\infty}^{\infty}\int_{-\infty}^{\infty} F_j^*(x, y, g) H_1 F_j(x, y, g) dx\,dy\left(\frac{\gamma}{\beta}\right)^{\frac{1}{2}}dg$$

(B.24)

Changing to spherical coordinates, equation B.24 becomes the same as equation 3.33 of the main body text.

$$E_j = \left(\frac{\gamma}{\beta}\right)^{\frac{1}{2}} \int_0^\infty \int_0^\pi \int_0^{2\pi} r_g^2 \sin(\theta_g) F_j^*(r_g, \theta_g, \phi_g) H_1 F_j(r_g, \theta_g, \phi_g) dr_g d\theta_g d\phi_g \quad \text{(B.25)}$$

## B.3.1. $1S$

The $1S$ wavefunction is taken to be as in equation 3.34. This is the hydrogen wavefunction, but in unitless form, where $a_b$ the Bohr radius has been replaced by $\frac{1}{\alpha_{0,0}}$, and is now in the spherical $g$ coordinate system rather than $z$.

$$F_{1S(A_1)}(r_g) = \left(\frac{\beta}{\gamma}\right)^{\frac{1}{4}} \frac{\alpha_{0,0}^{\frac{3}{2}}}{\sqrt{\pi}} e^{-\alpha_{0,0} r_g} \quad \text{(B.26)}$$

To evaluate the energy expectation overlap integral the Hamiltonian operator, equation B.22, must be applied to the wavefunction, equation B.26. Because the $1S$ wavefunction has no dependence upon $\theta_g$, all such terms in the Hamiltonian will be zero, the Hamiltonian then becomes:

$$\begin{aligned} H_1 = -\nabla_g^2 + \left(1 - \beta\right) &\left[\frac{\sin^2(\theta_g)}{r_g} \frac{\partial}{\partial r_g} + \cos^2(\theta_g) \frac{\partial^2}{\partial r_g^2}\right] \\ &- \frac{2}{r_g \left(1 - (1 - \frac{\gamma}{\beta}) \cos^2(\theta)\right)^{\frac{1}{2}}} \end{aligned} \quad \text{(B.27)}$$

Calculating the energy of the $1S$ state in terms of the variational parameters $\alpha$ and $\beta$ gives equation B.28, which can then be split into three terms and evaluated

separately.

$$
\begin{aligned}
E_j = \left(\frac{\gamma}{\beta}\right)^{\frac{1}{2}} \int_0^\infty \int_0^\pi \int_0^{2\pi} & r_g^2 \sin(\theta_g) \left(\frac{\beta}{\gamma}\right)^{\frac{1}{4}} \frac{\alpha_{0,0}^{\frac{3}{2}}}{\sqrt{\pi}} e^{-\alpha_{0,0}r_g} \left( -\nabla_g^2 \right. \\
& + \left(1-\beta\right) \left[ \frac{\sin^2(\theta_g)}{r_g} \frac{\partial}{\partial r_g} + \cos^2(\theta_g) \frac{\partial^2}{\partial r_g^2} \right] \\
& \left. - \frac{2}{r_g \left(1-(1-\frac{\gamma}{\beta})\cos^2(\theta)\right)^{\frac{1}{2}}} \right) \left(\frac{\beta}{\gamma}\right)^{\frac{1}{4}} \frac{\alpha_{0,0}^{\frac{3}{2}}}{\sqrt{\pi}} e^{-\alpha_{0,0}r_g} \, dr_g d\theta_g d\phi_g
\end{aligned}
$$

(B.28)

$$
\begin{aligned}
= \frac{\alpha_{0,0}^3}{\pi} \int_0^\infty \int_0^\pi \int_0^{2\pi} & r_g^2 \sin(\theta_g) e^{-\alpha_{0,0}r_g} \left( -\nabla_g^2 \right. \\
& + \left(1-\beta\right) \left[ \frac{\sin^2(\theta_g)}{r_g} \frac{\partial}{\partial r_g} + \cos^2(\theta_g) \frac{\partial^2}{\partial r_g^2} \right] \\
& \left. - \frac{2}{r_g \left(1-(1-\frac{\gamma}{\beta})\cos^2(\theta)\right)^{\frac{1}{2}}} \right) e^{-\alpha_{0,0}r_g} \, dr_g d\theta_g d\phi_g
\end{aligned}
$$

**First term for $1S$ energy**

The first part of the $1S$ energy expression from equation B.28 is then evaluated for the $\phi_g$ integral.

$$
\begin{aligned}
& \frac{-\alpha_{0,0}^3}{\pi} \int_0^\infty \int_0^\pi \int_0^{2\pi} \left( r_g^2 \sin(\theta_g) e^{-\alpha_{0,0}r_g} \nabla_g^2 e^{-\alpha_{0,0}r_g} \right) dr_g d\theta_g d\phi_g \\
& = -2\alpha_{0,0}^3 \int_0^\infty \int_0^\pi \left( r_g^2 \sin(\theta_g) e^{-\alpha_{0,0}r_g} \nabla_g^2 e^{-\alpha_{0,0}r_g} \right) dr_g d\theta_g
\end{aligned}
$$

(B.29)

The application of the Laplacian operator, equation B.15, to the exponential term in equation B.29, is:

$$\nabla_g^2 e^{-\alpha_{0,0}r_g} = -\left(\frac{1}{r_g^2}\frac{\partial}{\partial r_g}(r_g^2\frac{\partial}{\partial r_g}) + \frac{1}{r_g^2\sin(\theta_g)}\frac{\partial}{\partial\theta_g}(\sin(\theta_g)\frac{\partial}{\partial\theta_g}) + \frac{1}{r_g^2\sin^2(\theta_g)}\frac{\partial^2}{\partial\phi_g^2}\right)e^{-\alpha_{0,0}r_g}$$

$$= \left(\frac{1}{r_g^2}\frac{\partial}{\partial r_g}(r_g^2\frac{\partial}{\partial r_g})\right)e^{-\alpha_{0,0}r_g}$$

$$= \frac{1}{r_g^2}\frac{\partial}{\partial r_g}(-\alpha_{0,0}r_g^2 e^{-\alpha_{0,0}r_g})$$

$$= \frac{1}{r_g^2}\left(-2\alpha_{0,0}r_g + \alpha_{0,0}^2 r_g^2\right)e^{-\alpha_{0,0}r_g}$$

$$= \left(-2\frac{\alpha_{0,0}}{r_g} + \alpha_{0,0}^2\right)e^{-\alpha_{0,0}r_g}$$

$$\text{(B.30)}$$

Substituting the result from equation B.30 back into equation B.29, and making use of the integration identity shown in equation B.31 yields:

$$\int_0^\infty r^X e^{-rY}\,dr$$

$$\int u\,dv = uv - \int v\,du$$

$$u = r^X | du = Xr^{X-1}$$

$$dv = e^{-rY} | v = -\frac{e^{-rY}}{Y}$$

$$= \left[-\frac{r^X}{Y}e^{-rY}\right]_0^\infty + \int_0^\infty \frac{X}{Y}r^{X-1}e^{-rY}\,dr \qquad \text{(B.31)}$$

$$= \int_0^\infty \frac{X!}{Y^X}e^{-rY}\,dr$$

$$\int_0^\infty r^X e^{-rY}\,dr = \frac{X!}{Y^{X+1}}$$

$$- 2\alpha_{0,0}^3 \int_0^\infty \int_0^\pi \left( r_g^2 \sin(\theta_g) e^{-\alpha_{0,0} r_g} \nabla_g^2 e^{-\alpha_{0,0} r_g} \right) dr_g d\theta_g$$

$$= -2\alpha_{0,0}^3 \int_0^\infty \int_0^\pi \left( r_g^2 \sin(\theta_g) e^{-\alpha_{0,0} r_g} \left( -2\frac{\alpha_{0,0}}{r_g} + \alpha_{0,0}^2 \right) e^{-\alpha_{0,0} r_g} \right) dr_g d\theta_g$$

$$= -2\alpha_{0,0}^4 \int_0^\infty \int_0^\pi \left( \sin(\theta_g) \left( -2r_g + \alpha_{0,0} r_g^2 \right) e^{-2\alpha_{0,0} r_g} \right) dr_g d\theta_g$$

$$= -2\alpha_{0,0}^4 [-\cos(\theta_g)]_0^\pi \int_0^\infty \left( \left( -2r_g + \alpha_{0,0} r_g^2 \right) e^{-2\alpha_{0,0} r_g} \right) dr_g$$

$$= -4\alpha_{0,0}^4 \int_0^\infty \left( \left( -2r_g + \alpha_{0,0} r_g^2 \right) e^{-2\alpha_{0,0} r_g} \right) dr_g \tag{B.32}$$

$$= -4\alpha_{0,0}^4 \left( \frac{-2}{4\alpha_{0,0}^2} + \frac{2\alpha_{0,0}}{8\alpha_{0,0}^3} \right)$$

$$= 2\alpha_{0,0}^2 - \alpha_{0,0}^2$$

$$= \alpha_{0,0}^2$$

**Second term for $1S$ energy**

The second term of the $1S$ energy expression from equation B.28 is then evaluated.

$$\frac{\alpha_{0,0}^3}{\pi} \int_0^\infty \int_0^\pi \int_0^{2\pi} r_g^2 \sin(\theta_g) \left( e^{-\alpha_{0,0} r_g} (1 - \beta) \left[ \frac{\sin^2(\theta_g)}{r_g} \frac{\partial}{\partial r_g} \right. \right.$$

$$\left. + \cos^2(\theta_g) \frac{\partial^2}{\partial r_g^2} \right] e^{-\alpha_{0,0} r_g} dr_g d\theta_g d\phi_g$$

$$= 2\alpha_{0,0}^3 \int_0^\infty \int_0^\pi r_g^2 \sin(\theta_g) \left( e^{-\alpha_{0,0} r_g} (1 - \beta) \left[ \frac{\sin^2(\theta_g)}{r_g} \frac{\partial}{\partial r_g} \right. \right. \tag{B.33}$$

$$\left. + \cos^2(\theta_g) \frac{\partial^2}{\partial r_g^2} \right] e^{-\alpha_{0,0} r_g} dr_g d\theta_g$$

The application of the differential with respect to $r_g$ operators from equation B.33 is then evaluated.

$$\frac{\partial}{\partial r_g} e^{-\alpha_{0,0} r_g} = -\alpha_{0,0} e^{-\alpha_{0,0} r_g}$$

$$\frac{\partial^2}{\partial r_g^2} e^{-\alpha_{0,0} r_g} = \alpha_{0,0}^2 e^{-\alpha_{0,0} r_g}$$

(B.34)

Substituting the expression from equation B.34 back into equation B.33 then gives:

$$
2\alpha_{0,0}^3 \int_0^\infty \int_0^\pi r_g^2 \sin(\theta_g) \left( e^{-\alpha_{0,0} r_g} \left(1 - \beta\right) \left[ \frac{-\alpha_{0,0} \sin^2(\theta_g)}{r_g} \right. \right.
$$

$$
\left. + \cos^2(\theta_g) \alpha_{0,0}^2 \right] e^{-\alpha_{0,0} r_g} dr_g d\theta_g
$$

$$
= 2\alpha_{0,0}^3 \left(1 - \beta\right) \int_0^\infty \int_0^\pi r_g^2 \sin(\theta_g) \left[ \frac{-\alpha_{0,0} \sin^2(\theta_g)}{r_g} \right.
$$

$$
\left. + \cos^2(\theta_g) \alpha_{0,0}^2 \right] e^{-2\alpha_{0,0} r_g} dr_g d\theta_g
$$

$$
= 2\alpha_{0,0}^4 \left(1 - \beta\right) \int_0^\infty \int_0^{2\pi} \left[ - r_g \sin^3(\theta_g) \right.
$$

$$
\left. + r_g^2 \cos^2(\theta_g) \sin(\theta_g) \alpha_{0,0} \right] e^{-2\alpha_{0,0} r_g} dr_g d\theta_g
$$

(B.35)

Again making use of the integral identity from equation B.31, equation B.35 then becomes:

$$
2\alpha_{0,0}^4 \left(1 - \beta\right) \int_0^\pi \left[ - \frac{1}{4\alpha_{0,0}^2} \sin^3(\theta_g) \right.
$$

$$
\left. + \frac{1}{4\alpha_{0,0}^3} \cos^2(\theta_g) \sin(\theta_g) \alpha_{0,0} \right] d\theta_g
$$

$$
= \frac{\alpha_{0,0}^2}{2} \left(1 - \beta\right) \int_0^\pi \left[ - \sin^3(\theta_g) + \cos^2(\theta_g) \sin(\theta_g) \right] d\theta_g
$$

(B.36)

## B. Derivations of Effective Mass Theory Wavefunction Equations

The angular integrals from equation B.36 are evaluated:

$$\int_0^\pi \cos^2(\theta_g)\sin(\theta_g)d\theta_g = \left[-\frac{1}{3}\cos^3(\theta_g)\right]_0^\pi = -\left(\frac{-1-1}{3}\right) = \frac{2}{3}$$

$$\int_0^\pi \sin^3(\theta_g)d\theta_g = \int_0^\pi \sin(\theta_g)\sin^2(\theta_g)d\theta_g$$

$$= \int_0^\pi \sin(\theta_g)\Big(1 - \cos^2(\theta_g)\Big)d\theta_g \qquad\qquad (B.37)$$

$$= \int_0^\pi \Big(\sin(\theta_g) - \cos^2(\theta_g)\sin(\theta_g)\Big)d\theta_g$$

$$\int_0^\pi \sin(\theta_g)d\theta_g = \left[-\cos(\theta_g)\right]_0^\pi = -(-1-1) = 2$$

The angular integrals from equation B.37 are put together, as in equation B.36, to give:

$$\int_0^\pi \left[-\sin^3(\theta_g) + \cos^2(\theta_g)\sin(\theta_g)\right]d\theta_g = -\int_0^\pi \sin(\theta_g)d\theta_g + 2\int_0^\pi \cos^2(\theta_g)\sin(\theta_g)d\theta_g$$

$$= -2 + 2(\frac{2}{3}) = -2 + \frac{4}{3}$$

$$= -\frac{2}{3}$$

$$(B.38)$$

Substituting equation B.38 back into equation B.36 yields the second $1S$ energy term.

$$\frac{\alpha_{0,0}^2}{2}\Big(1 - \beta\Big)\left[-\frac{2}{3}\right]$$

$$= -\frac{1}{3}\alpha_{0,0}^2\Big(1 - \beta\Big)$$

$$(B.39)$$

305

**Third term for $1S$ energy**

The third term of the $1S$ energy expression from equation B.28 is then evaluated.

$$\frac{\alpha_{0,0}^3}{\pi} \int_0^\infty \int_0^\pi \int_0^{2\pi} \left( r_g^2 \sin(\theta_g) \left( e^{-\alpha_{0,0}r_g} \left[ -\frac{2}{r_g \left( 1 - (1 - \frac{\gamma}{\beta}) \cos^2(\theta) \right)^{\frac{1}{2}}} \right] e^{-\alpha_{0,0}r_g} \right) \right)$$

$$dr_g d\theta_g d\phi_g$$

$$= \frac{-2\alpha_{0,0}^3}{\pi} \int_0^\infty \int_0^\pi \int_0^{2\pi} \left( r_g^2 \sin(\theta_g) \left( \left[ \frac{e^{-2\alpha_{0,0}r_g}}{r_g \left( 1 - (1 - \frac{\gamma}{\beta}) \cos^2(\theta) \right)^{\frac{1}{2}}} \right] \right) \right) dr_g d\theta_g d\phi_g$$

$$= -4\alpha_{0,0}^3 \int_0^\infty \int_0^\pi \left( r_g \sin(\theta_g) \frac{e^{-2\alpha_{0,0}r_g}}{\left( 1 - (1 - \frac{\gamma}{\beta}) \cos^2(\theta) \right)^{\frac{1}{2}}} \right) dr_g d\theta_g$$

$$= -4\alpha_{0,0}^3 \int_0^\infty \left( r_g e^{-2\alpha_{0,0}r_g} \right) dr_g \int_0^\pi \frac{\sin(\theta_g)}{\left( 1 - (1 - \frac{\gamma}{\beta}) \cos^2(\theta) \right)^{\frac{1}{2}}} d\theta_g$$

$$= -4\alpha_{0,0}^3 \frac{1}{4\alpha_{0,0}^2} \int_0^\pi \frac{\sin(\theta_g)}{\left( 1 - (1 - \frac{\gamma}{\beta}) \cos^2(\theta) \right)^{\frac{1}{2}}} d\theta_g$$

$$= -\alpha_{0,0} \int_0^\pi \frac{\sin(\theta_g)}{\left( 1 - (1 - \frac{\gamma}{\beta}) \cos^2(\theta) \right)^{\frac{1}{2}}} d\theta_g$$

$$(B.40)$$

The $\theta_g$ angular integral from equation B.40 can then be simplified with the substitution in equation B.41.

$$u = \left( 1 - \frac{\gamma}{\beta} \right)^{\frac{1}{2}} \cos(\theta_g)$$

$$du = -\left( 1 - \frac{\gamma}{\beta} \right)^{\frac{1}{2}} \sin(\theta_g) d\theta_g$$

$$\theta_g = 0, u = \left( 1 - \frac{\gamma}{\beta} \right)^{\frac{1}{2}}$$

$$\theta_g = \pi, u = -\left( 1 - \frac{\gamma}{\beta} \right)^{\frac{1}{2}}$$

$$(B.41)$$

## B. Derivations of Effective Mass Theory Wavefunction Equations

The angular integral is then shown as:

$$-\frac{1}{\left(1-\frac{\gamma}{\beta}\right)^{\frac{1}{2}}}\int_{\left(1-\frac{\gamma}{\beta}\right)^{\frac{1}{2}}}^{-\left(1-\frac{\gamma}{\beta}\right)^{\frac{1}{2}}}\frac{1}{\left(1-u^2\right)^{\frac{1}{2}}}du \tag{B.42}$$

The integral in equation B.42 can then be compared with the well known integral shown in equation B.43.

$$\int\frac{1}{\left(1-u^2\right)^{\frac{1}{2}}}du = \arcsin(u) \tag{B.43}$$

$$-\frac{1}{\left(1-\frac{\gamma}{\beta}\right)^{\frac{1}{2}}}\int_{\left(1-\frac{\gamma}{\beta}\right)^{\frac{1}{2}}}^{-\left(1-\frac{\gamma}{\beta}\right)^{\frac{1}{2}}}\frac{1}{\left(1-u^2\right)^{\frac{1}{2}}}du$$

$$=-\frac{1}{\left(1-\frac{\gamma}{\beta}\right)^{\frac{1}{2}}}\left[\arcsin(-\left(1-\frac{\gamma}{\beta}\right)^{\frac{1}{2}})-\arcsin(\left(1-\frac{\gamma}{\beta}\right)^{\frac{1}{2}})\right]$$

$$=-\frac{1}{\left(1-\frac{\gamma}{\beta}\right)^{\frac{1}{2}}}\left[-2\arcsin(\left(1-\frac{\gamma}{\beta}\right)^{\frac{1}{2}})\right]$$

$$=\frac{2}{\left(1-\frac{\gamma}{\beta}\right)^{\frac{1}{2}}}\arcsin(\left(1-\frac{\gamma}{\beta}\right)^{\frac{1}{2}}) \tag{B.44}$$

Reinserting the angular expression from equation B.44, back into equation B.40 gives the third term.

$$-\frac{2\alpha_{0,0}}{\left(1-\frac{\gamma}{\beta}\right)^{\frac{1}{2}}}\arcsin(\left(1-\frac{\gamma}{\beta}\right)^{\frac{1}{2}}) \tag{B.45}$$

### $1S$ complete energy function

The three $1S$ energy terms from equations B.32, B.39, and B.45 can be assembled together to give the final energy expression.

$$
\begin{aligned}
E_{1S}(\alpha_{0,0}, \beta, \gamma) &= \left( \alpha_{0,0}^2 - \frac{1}{3}\alpha_{0,0}^2 \left( 1 - \beta \right) - \frac{2\alpha_{0,0}}{\left( 1 - \frac{\gamma}{\beta} \right)^{\frac{1}{2}}} \arcsin\!\left( \left( 1 - \frac{\gamma}{\beta} \right)^{\frac{1}{2}} \right) \right) \\
&= \frac{1}{3}\alpha_{0,0}^2 \left( \beta + 2 \right) - \frac{2\alpha_{0,0}}{\left( 1 - \frac{\gamma}{\beta} \right)^{\frac{1}{2}}} \arcsin\!\left( \left( 1 - \frac{\gamma}{\beta} \right)^{\frac{1}{2}} \right)
\end{aligned}
\tag{B.46}
$$

## B.3.2. $2P_0$

The $2p_0$ wavefunction is taken to be as in equation B.47. This is the hydrogen wavefunction, but in unitless form, where $a_b$ the Bohr radius has been replaced by $\frac{1}{\alpha_{1,0}}$, and is now in the spherical $g$ rather then the $z$ coordinate system.

$$
F_{2p_0}(r_g) = \left( \frac{\beta}{\gamma} \right)^{\frac{1}{4}} \frac{\alpha_{1,0}^{\frac{5}{2}}}{4\sqrt{2\pi}} r_g \cos(\theta_g) e^{-\frac{\alpha_{1,0} r_g}{2}}
\tag{B.47}
$$

Evaluating the energy expectation value, with Hamiltonian operator from equation B.27, and the $2p_0$ wavefunction from equation B.47, results in:

$$E_j = \left(\frac{\gamma}{\beta}\right)^{\frac{1}{2}} \int_0^\infty \int_0^\pi \int_0^{2\pi} r_g^2 \sin(\theta_g) \left(\frac{\beta}{\gamma}\right)^{\frac{1}{4}} \frac{\alpha_{1,0}^{\frac{5}{2}}}{4\sqrt{2\pi}} r_g \cos(\theta_g) e^{-\frac{\alpha_{1,0}r_g}{2}} \Bigg( -\nabla_g^2$$

$$+ \left(1 - \beta\right) \Bigg[ 2\frac{\sin(\theta_g)\cos(\theta_g)}{r_g^2} \frac{\partial}{\partial\theta_g}$$

$$+ \frac{\sin^2(\theta_g)}{r_g}\frac{\partial}{\partial r_g} + \frac{\sin^2(\theta_g)}{r_g^2}\frac{\partial^2}{\partial\theta_g^2} + \cos^2(\theta_g)\frac{\partial^2}{\partial r_g^2}$$

$$- 2\frac{\sin(\theta_g)}{r_g}\cos(\theta_g)\frac{\partial}{\partial r_g}\frac{\partial}{\partial\theta_g} \Bigg]$$

$$- \frac{2}{r_g\left(1 - (1 - \frac{\gamma}{\beta})\cos^2(\theta)\right)^{\frac{1}{2}}} \Bigg) \left(\frac{\beta}{\gamma}\right)^{\frac{1}{4}} \frac{\alpha_{1,0}^{\frac{5}{2}}}{4\sqrt{2\pi}} r_g \cos(\theta_g) e^{-\frac{\alpha_{1,0}r_g}{2}} dr_g d\theta_g d\phi_g$$

$$\text{(B.48)}$$

$$= \frac{\alpha_{1,0}^5}{32\pi} \int_0^\infty \int_0^\pi \int_0^{2\pi} r_g^2 \sin(\theta_g) r_g \cos(\theta_g) e^{-\frac{\alpha_{1,0}r_g}{2}} \Bigg( -\nabla_g^2$$

$$+ \left(1 - \beta\right) \Bigg[ 2\frac{\sin(\theta_g)\cos(\theta_g)}{r_g^2} \frac{\partial}{\partial\theta_g}$$

$$+ \frac{\sin^2(\theta_g)}{r_g}\frac{\partial}{\partial r_g} + \frac{\sin^2(\theta_g)}{r_g^2}\frac{\partial^2}{\partial\theta_g^2} + \cos^2(\theta_g)\frac{\partial^2}{\partial r_g^2}$$

$$- 2\frac{\sin(\theta_g)}{r_g}\cos(\theta_g)\frac{\partial}{\partial r_g}\frac{\partial}{\partial\theta_g} \Bigg]$$

$$- \frac{2}{r_g\left(1 - (1 - \frac{\gamma}{\beta})\cos^2(\theta)\right)^{\frac{1}{2}}} \Bigg) r_g \cos(\theta_g) e^{-\frac{\alpha_{1,0}r_g}{2}} dr_g d\theta_g d\phi_g$$

Equation B.48 can then, as for the $1S$ wavefunction, be split into three parts.

**First term for $2p_0$ energy expression**

The first $2P_0$ energy term from equation B.48 is evaluated by the application of the Laplacian operator to the $2P_0$ wavefunction.

## B. Derivations of Effective Mass Theory Wavefunction Equations

$$\frac{\alpha_{1,0}^5}{32\pi} \int_0^\infty \int_0^\pi \int_0^{2\pi} \left( r_g^2 \sin(\theta_g) r_g \cos(\theta_g) e^{-\frac{\alpha_{1,0} r_g}{2}} \right.$$
$$\left. \times \left( -\nabla_g^2 \right) r_g \cos(\theta_g) e^{-\frac{\alpha_{1,0} r_g}{2}} dr_g d\theta_g d\phi_g \right)$$

(B.49)

The $\nabla^2$ operator is applied to the $2p_0$ wavefunction.

$$\nabla_g^2 \left( r_g \cos(\theta_g) e^{-\frac{\alpha_{1,0} r_g}{2}} \right) = \left( \frac{1}{r_g^2} \frac{\partial}{\partial r_g} \left( r_g^2 \frac{\partial}{\partial r_g} \right) \right.$$
$$\left. + \frac{1}{r_g^2 \sin(\theta_g)} \frac{\partial}{\partial \theta_g} \left( \sin(\theta_g) \frac{\partial}{\partial \theta_g} \right) + \frac{1}{r_g^2 \sin^2(\theta_g)} \frac{\partial^2}{\partial \phi_g^2} \right) \left( r_g \cos(\theta_g) e^{-\frac{\alpha_{1,0} r_g}{2}} \right)$$

$$= \left( \frac{1}{r_g^2} \frac{\partial}{\partial r_g} \left( r_g^2 \frac{\partial}{\partial r_g} \right) \right.$$
$$\left. + \frac{1}{r_g^2 \sin(\theta_g)} \frac{\partial}{\partial \theta_g} \left( \sin(\theta_g) \frac{\partial}{\partial \theta_g} \right) \right) \left( r_g \cos(\theta_g) e^{-\frac{\alpha_{1,0} r_g}{2}} \right)$$

(B.50)

The first part of the Laplacian operator applied to the $2P_0$ wavefunction, equation B.50, is then:

$$\left(\frac{1}{r_g^2}\frac{\partial}{\partial r_g}\left(r_g^2\frac{\partial}{\partial r_g}\right)\right)r_g\cos(\theta_g)e^{-\frac{\alpha_{1,0}r_g}{2}}$$

$$= \cos(\theta_g)\frac{1}{r_g^2}\frac{\partial}{\partial r_g}\left(r_g^2\left[e^{-\frac{\alpha_{1,0}r_g}{2}} - \frac{\alpha_{1,0}r_g}{2}e^{-\frac{\alpha_{1,0}r_g}{2}}\right]\right)$$

$$= \cos(\theta_g)\frac{1}{r_g^2}\frac{\partial}{\partial r_g}\left(r_g^2 e^{-\frac{\alpha_{1,0}r_g}{2}} - \frac{\alpha_{1,0}r_g^3}{2}e^{-\frac{\alpha_{1,0}r_g}{2}}\right)$$

$$= \cos(\theta_g)\frac{1}{r_g^2}\left(2r_g e^{-\frac{\alpha_{1,0}r_g}{2}} - \frac{\alpha_{1,0}r_g^2}{2}e^{-\frac{\alpha_{1,0}r_g}{2}} - \frac{3\alpha_{1,0}r_g^2}{2}e^{-\frac{\alpha_{1,0}r_g}{2}} + \frac{\alpha_{1,0}^2 r_g^3}{4}e^{-\frac{\alpha_{1,0}r_g}{2}}\right)$$

$$= \cos(\theta_g)e^{-\frac{\alpha_{1,0}r_g}{2}}\frac{1}{r_g^2}\left(2r_g - \frac{\alpha_{1,0}r_g^2}{2} - \frac{3\alpha_{1,0}r_g^2}{2} + \frac{\alpha_{1,0}^2 r_g^3}{4}\right)$$

$$= \cos(\theta_g)e^{-\frac{\alpha_{1,0}r_g}{2}}\left(\frac{2}{r_g} - \frac{\alpha_{1,0}}{2} - \frac{3\alpha_{1,0}}{2} + \frac{\alpha_{1,0}^2 r_g}{4}\right)$$

$$= \cos(\theta_g)e^{-\frac{\alpha_{1,0}r_g}{2}}\left(\frac{2}{r_g} - 2\alpha_{1,0} + \frac{\alpha_{1,0}^2 r_g}{4}\right)$$

$$\text{(B.51)}$$

The second part of the Laplacian operator applied to the $2P_0$ wavefunction, equation B.50, is then:

$$\frac{1}{r_g^2\sin(\theta_g)}\frac{\partial}{\partial\theta_g}\left(\sin(\theta_g)\frac{\partial}{\partial\theta_g}\right)r_g\cos(\theta_g)e^{-\frac{\alpha_{1,0}r_g}{2}}$$

$$= -\frac{1}{r_g^2\sin(\theta_g)}\frac{\partial}{\partial\theta_g}\left(\sin(\theta_g)r_g\sin(\theta_g)e^{-\frac{\alpha_{1,0}r_g}{2}}\right)$$

$$= -\frac{1}{r_g\sin(\theta_g)}\frac{\partial}{\partial\theta_g}\left(\sin^2(\theta_g)e^{-\frac{\alpha_{1,0}r_g}{2}}\right) \qquad \text{(B.52)}$$

$$= -\frac{1}{r_g\sin(\theta_g)}\left(2\sin(\theta_g)\cos(\theta_g)e^{-\frac{\alpha_{1,0}r_g}{2}}\right)$$

$$= -\frac{2\cos(\theta_g)}{r_g}e^{-\frac{\alpha_{1,0}r_g}{2}}$$

Assembling the results from equations B.51 and B.52 gives the result of the Laplacian in total.

$$\nabla_g^2\left(r_g\cos(\theta_g)e^{-\frac{\alpha_{1,0}r_g}{2}}\right) = \cos(\theta_g)e^{-\frac{\alpha_{1,0}r_g}{2}}\left(\frac{2}{r_g} - 2\alpha_{1,0} + \frac{\alpha_{1,0}^2 r_g}{4}\right) - \frac{2\cos(\theta_g)}{r_g}e^{-\frac{\alpha_{1,0}r_g}{2}}$$

$$= \cos(\theta_g)e^{-\frac{\alpha_{1,0}r_g}{2}}\left(\frac{2}{r_g} - 2\alpha_{1,0} + \frac{\alpha_{1,0}^2 r_g}{4} - \frac{2}{r_g}\right)$$

$$= \cos(\theta_g)e^{-\frac{\alpha_{1,0}r_g}{2}}\left(- 2\alpha_{1,0} + \frac{\alpha_{1,0}^2 r_g}{4}\right)$$

$$(B.53)$$

The result from equation B.53 is then substituted into equation B.49 to then give the first energy term.

$$-\frac{\alpha_{1,0}^5}{32\pi}\int_0^\infty\int_0^\pi\int_0^{2\pi} r_g^2\sin(\theta_g)r_g\cos(\theta_g)e^{-\frac{\alpha_{1,0}r_g}{2}}\left(-\nabla_g^2\right.$$

$$\left.\right)r_g\cos(\theta_g)e^{-\frac{\alpha_{1,0}r_g}{2}}dr_g d\theta_g d\phi_g$$

$$= -\frac{\alpha_{1,0}^5}{32\pi}\int_0^\infty\int_0^\pi\int_0^{2\pi} r_g^2\sin(\theta_g)r_g\cos(\theta_g)e^{-\frac{\alpha_{1,0}r_g}{2}}\cos(\theta_g)e^{-\frac{\alpha_{1,0}r_g}{2}}$$

$$\left(- 2\alpha_{1,0} + \frac{\alpha_{1,0}^2 r_g}{4}\right)dr_g d\theta_g d\phi_g$$

$$= -\frac{\alpha_{1,0}^5}{32\pi}\int_0^\infty\int_0^\pi\int_0^{2\pi} r_g^2\sin(\theta_g)r_g\cos^2(\theta_g)e^{-\alpha_{1,0}r_g}$$

$$\left(- 2\alpha_{1,0} + \frac{\alpha_{1,0}^2 r_g}{4}\right)dr_g d\theta_g d\phi_g \qquad (B.54)$$

$$= -\frac{\alpha_{1,0}^5}{32\pi}\int_0^\infty\int_0^\pi\int_0^{2\pi} \sin(\theta_g)r_g\cos^2(\theta_g)e^{-\alpha_{1,0}r_g}$$

$$\left(- 2\alpha_{1,0}r_g^2 + \frac{\alpha_{1,0}^2 r_g^3}{4}\right)dr_g d\theta_g d\phi_g$$

$$= -\frac{\alpha_{1,0}^5}{16}\int_0^\infty\int_0^\pi \sin(\theta_g)\cos^2(\theta_g)e^{-\alpha_{1,0}r_g}$$

$$\left(- 2\alpha_{1,0}r_g^3 + \frac{\alpha_{1,0}^2 r_g^4}{4}\right)dr_g d\theta_g$$

$$= -\frac{\alpha_{1,0}^5}{16}\int_0^\infty e^{-\alpha_{1,0}r_g}\left(- 2\alpha_{1,0}r_g^3 + \frac{\alpha_{1,0}^2 r_g^4}{4}\right)dr_g\int_0^\pi \sin(\theta_g)\cos^2(\theta_g)d\theta_g$$

The integrals from equation B.54 are then evaluated, with the radial integral yet again solved with the use of the identity in equation B.31, below:

$$
\begin{aligned}
&-\frac{\alpha_{1,0}^5}{16}\int_0^\infty e^{-\alpha_{1,0}r_g}\left(-2\alpha_{1,0}r_g^3+\frac{\alpha_{1,0}^2 r_g^4}{4}\right)dr_g\int_0^\pi \sin(\theta_g)\cos^2(\theta_g)d\theta_g\\
&=-\frac{\alpha_{1,0}^5}{16}\left(-2\frac{6\alpha_{1,0}}{\alpha_{1,0}^4}+\frac{24\alpha_{1,0}^2}{4\alpha_{1,0}^5}\right)\left[-\frac{1}{3}\cos(\theta_g)^3\right]_0^\pi\\
&=-\frac{\alpha_{1,0}^5}{16}\left(-\frac{12}{\alpha^3(1,0)}+\frac{6}{\alpha^3(1,0)}\right)\frac{2}{3}\\
&=-\frac{1}{24}\left(-12\alpha_{1,0}^2+6\alpha_{1,0}^2\right)\\
&=\frac{\alpha_{1,0}^2}{4}
\end{aligned}
\tag{B.55}
$$

**Second term for $2P_0$ energy expression**

The second $2p_0$ energy term from equation B.48, where the $(1-\beta)$ set of terms is applied to the $2P_0$ wavefunction, is evaluated as:

$$
\begin{aligned}
&\frac{\alpha_{1,0}^5}{32\pi}\int_0^\infty\int_0^\pi\int_0^{2\pi}r_g^2\sin(\theta_g)r_g\cos(\theta_g)e^{-\frac{\alpha_{1,0}r_g}{2}}\\
&\times\left(1-\beta\right)\Bigg[2\frac{\sin(\theta_g)\cos(\theta_g)}{r_g^2}\frac{\partial}{\partial\theta_g}\\
&+\frac{\sin^2(\theta_g)}{r_g}\frac{\partial}{\partial r_g}+\frac{\sin^2(\theta_g)}{r_g^2}\frac{\partial^2}{\partial\theta_g^2}+\cos^2(\theta_g)\frac{\partial^2}{\partial r_g^2}\\
&-2\frac{\sin(\theta_g)}{r_g}\cos(\theta_g)\frac{\partial}{\partial r_g}\frac{\partial}{\partial\theta_g}\Bigg]r_g\cos(\theta_g)e^{-\frac{\alpha_{1,0}r_g}{2}}dr_g d\theta_g d\phi_g
\end{aligned}
\tag{B.56}
$$

The first, and second, order differentials of the $2P_0$ wavefunction, from equation B.56, are then evaluated:

$$\frac{\partial}{\partial r_g} r_g \cos(\theta_g) e^{-\frac{\alpha_{1,0} r_g}{2}} = \cos(\theta_g) e^{-\frac{\alpha_{1,0} r_g}{2}} - \frac{\alpha_{1,0}}{2} r_g \cos(\theta_g) e^{-\frac{\alpha_{1,0} r_g}{2}}$$

$$= \left[1 - \frac{\alpha_{1,0}}{2} r_g\right] \cos(\theta_g) e^{-\frac{\alpha_{1,0} r_g}{2}}$$

$$\frac{\partial^2}{\partial r_g^2} r_g \cos(\theta_g) e^{-\frac{\alpha_{1,0} r_g}{2}} = \left[-\frac{\alpha_{1,0}}{2} - \frac{\alpha_{1,0}}{2} + \frac{\alpha_{1,0}^2 r_g}{4}\right] \cos(\theta_g) e^{-\frac{\alpha_{1,0} r_g}{2}}$$

$$= \left[-\alpha_{1,0} + \frac{\alpha_{1,0}^2 r_g}{4}\right] \cos(\theta_g) e^{-\frac{\alpha_{1,0} r_g}{2}} \tag{B.57}$$

$$\frac{\partial}{\partial \theta_g} r_g \cos(\theta_g) e^{-\frac{\alpha_{1,0} r_g}{2}} = -r_g \sin(\theta_g) e^{-\frac{\alpha_{1,0} r_g}{2}}$$

$$\frac{\partial^2}{\partial \theta_g^2} r_g \cos(\theta_g) e^{-\frac{\alpha_{1,0} r_g}{2}} = -r_g \cos(\theta_g) e^{-\frac{\alpha_{1,0} r_g}{2}}$$

The values from equation B.57 are then substituted into the parts of equation B.56.

$$2\frac{\sin(\theta_g)\cos(\theta_g)}{r_g^2} \frac{\partial}{\partial \theta_g} r_g \cos(\theta_g) e^{-\frac{\alpha_{1,0} r_g}{2}} = -2\frac{\sin(\theta_g)\cos(\theta_g)}{r_g^2} r_g \sin(\theta_g) e^{-\frac{\alpha_{1,0} r_g}{2}}$$

$$= -2\frac{\sin^2(\theta_g)\cos(\theta_g)}{r_g} e^{-\frac{\alpha_{1,0} r_g}{2}} \tag{B.58}$$

$$\frac{\sin^2(\theta_g)}{r_g} \frac{\partial}{\partial r_g} r_g \cos(\theta_g) e^{-\frac{\alpha_{1,0} r_g}{2}} = \frac{\sin^2(\theta_g)}{r_g}\left[1 - \frac{\alpha_{1,0}}{2} r_g\right] \cos(\theta_g) e^{-\frac{\alpha_{1,0} r_g}{2}}$$

$$= \frac{\sin^2(\theta_g)\cos(\theta_g)}{r_g}\left[1 - \frac{\alpha_{1,0}}{2} r_g\right] e^{-\frac{\alpha_{1,0} r_g}{2}} \tag{B.59}$$

$$\frac{\sin^2(\theta_g)}{r_g^2}\frac{\partial^2}{\partial\theta_g^2}r_g\cos(\theta_g)e^{-\frac{\alpha_{1,0}r_g}{2}} = -\frac{\sin^2(\theta_g)}{r_g^2}r_g\cos(\theta_g)e^{-\frac{\alpha_{1,0}r_g}{2}}$$
$$= -\frac{\sin^2(\theta_g)\cos(\theta_g)}{r_g}e^{-\frac{\alpha_{1,0}r_g}{2}} \tag{B.60}$$

$$\cos^2(\theta_g)\frac{\partial^2}{\partial r_g^2}r_g\cos(\theta_g)e^{-\frac{\alpha_{1,0}r_g}{2}} = \cos^2(\theta_g)\left[-\alpha_{1,0}+\frac{\alpha_{1,0}^2 r_g}{4}\right]\cos(\theta_g)e^{-\frac{\alpha_{1,0}r_g}{2}}$$
$$= \cos^3(\theta_g)\left[-\alpha_{1,0}+\frac{\alpha_{1,0}^2 r_g}{4}\right]e^{-\frac{\alpha_{1,0}r_g}{2}} \tag{B.61}$$

$$-2\frac{\sin(\theta_g)}{r_g}\cos(\theta_g)\frac{\partial}{\partial r_g}\frac{\partial}{\partial\theta_g}r_g\cos(\theta_g)e^{-\frac{\alpha_{1,0}r_g}{2}} = 2\frac{\sin(\theta_g)}{r_g}\cos(\theta_g)\left[1-\frac{\alpha_{1,0}}{2}r_g\right]\sin(\theta_g)e^{-\frac{\alpha_{1,0}r_g}{2}}$$
$$= 2\frac{\sin^2(\theta_g)\cos(\theta_g)}{r_g}\left[1-\frac{\alpha_{1,0}}{2}r_g\right]e^{-\frac{\alpha_{1,0}r_g}{2}}$$

$$\tag{B.62}$$

The set of terms from equations B.58, B.59, B.60, B.61, and B.62 are then collected together:

$$-2\frac{\sin^2(\theta_g)\cos(\theta_g)}{r_g}e^{-\frac{\alpha_{1,0}r_g}{2}} + \frac{\sin^2(\theta_g)\cos(\theta_g)}{r_g}\left[1-\frac{\alpha_{1,0}}{2}r_g\right]e^{-\frac{\alpha_{1,0}r_g}{2}}$$
$$-\frac{\sin^2(\theta_g)\cos(\theta_g)}{r_g}e^{-\frac{\alpha_{1,0}r_g}{2}} + \cos^3(\theta_g)\left[-\alpha_{1,0}+\frac{\alpha_{1,0}^2 r_g}{4}\right]e^{-\frac{\alpha_{1,0}r_g}{2}}$$
$$+2\frac{\sin^2(\theta_g)\cos(\theta_g)}{r_g}\left[1-\frac{\alpha_{1,0}}{2}r_g\right]e^{-\frac{\alpha_{1,0}r_g}{2}}$$
$$= \left\{\frac{\sin^2(\theta_g)\cos(\theta_g)}{r_g}\left[1-\frac{\alpha_{1,0}}{2}r_g\right]\right. \tag{B.63}$$
$$-\frac{\sin^2(\theta_g)\cos(\theta_g)}{r_g} + \cos^3(\theta_g)\left[-\alpha_{1,0}+\frac{\alpha_{1,0}^2 r_g}{4}\right]$$
$$+2\frac{\sin^2(\theta_g)\cos(\theta_g)}{r_g}\left[1-\frac{\alpha_{1,0}}{2}r_g\right] \left. -2\frac{\sin^2(\theta_g)\cos(\theta_g)}{r_g}\right\}e^{-\frac{\alpha_{1,0}r_g}{2}}$$
$$= \left\{-\frac{3\alpha_{1,0}}{2}r_g\frac{\sin^2(\theta_g)\cos(\theta_g)}{r_g} + \cos^3(\theta_g)\left[-\alpha_{1,0}+\frac{\alpha_{1,0}^2 r_g}{4}\right]\right\}e^{-\frac{\alpha_{1,0}r_g}{2}}$$

## B. Derivations of Effective Mass Theory Wavefunction Equations

Substituting the result from equation B.63 back into the energy integral from equation B.56 then gives:

$$
\frac{\alpha_{1,0}^5}{32\pi} \int_0^\infty \int_0^\pi \int_0^{2\pi} r_g^2 \sin(\theta_g) r_g \cos(\theta_g) e^{-\frac{\alpha_{1,0} r_g}{2}}
$$
$$
\times \left(1 - \beta\right) \left\{ -\frac{3\alpha_{1,0}}{2} r_g \frac{\sin^2(\theta_g)\cos(\theta_g)}{r_g} \right.
$$
$$
\left. + \cos^3(\theta_g)\left[ -\alpha_{1,0} + \frac{\alpha_{1,0}^2 r_g}{4} \right] \right\} e^{-\frac{\alpha_{1,0} r_g}{2}} dr_g d\theta_g d\phi_g
$$

(B.64)

$$
= \left(1 - \beta\right) \frac{\alpha_{1,0}^5}{16} \int_0^\infty \int_0^\pi \left\{ -\frac{3\alpha_{1,0}}{2} r_g \sin^3(\theta_g) \cos^2(\theta_g) r_g^2 \right.
$$
$$
\left. + r_g^3 \sin(\theta_g) \cos^4(\theta_g)\left[ -\alpha_{1,0} + \frac{\alpha_{1,0}^2 r_g}{4} \right] \right\} e^{-\alpha_{1,0} r_g} dr_g d\theta_g
$$

The evaluation of the angular expressions from equation B.64 are then:

$$
\int_0^\pi \sin^3(\theta_g) \cos^2(\theta_g) d\theta_g = \int_0^\pi \sin(\theta_g)\left(1 - \cos^2(\theta_g)\right) \cos^2(\theta_g) d\theta_g
$$
$$
= \int_0^\pi \left( \sin(\theta_g) \cos^2(\theta_g) - \sin(\theta_g) \cos^4(\theta_g) \right) d\theta_g
$$
$$
= \left[ -\frac{1}{3} \cos^3(\theta_g) \right]_0^\pi - \left[ -\frac{1}{5} \cos^5(\theta_g) \right]_0^\pi
$$
$$
= -\frac{1}{3}\left[ -1 - 1 \right]_0^\pi + \frac{1}{5}\left[ -1 - 1 \right]_0^\pi \qquad \text{(B.65)}
$$
$$
= \frac{2}{3} - \frac{2}{5} = \frac{4}{15}
$$
$$
\int_0^\pi \sin(\theta_g) \cos^4(\theta_g) d\theta_g = \left[ -\frac{1}{5} \cos^5(\theta_g) \right]_0^\pi
$$
$$
= -\frac{1}{5}\left[ -1 - 1 \right]_0^\pi = \frac{2}{5}
$$

Substituting the results from the angular integral, equation B.65, into the energy

316

expression in equation B.64, making use of the identity from equation B.31 to allow the evaluation of the radial integral, this then gives us:

$$
\left(1-\beta\right)\frac{\alpha_{1,0}^5}{16}\int_0^\infty\int_0^\pi\left\{-\frac{3\alpha_{1,0}}{2}r_g\sin^3(\theta_g)\cos^2(\theta_g)r_g^2\right.
$$
$$
\left.+r_g^3\sin(\theta_g)\cos^4(\theta_g)\left[-\alpha_{1,0}+\frac{\alpha_{1,0}^2 r_g}{4}\right]\right\}e^{-\alpha_{1,0}r_g}dr_g d\theta_g
$$

$$
=\left(1-\beta\right)\frac{\alpha_{1,0}^5}{16}\int_0^\infty\left\{-\frac{3\alpha_{1,0}}{2}r_g\frac{4}{15}r_g^2\right.
$$
$$
\left.+\frac{2}{5}r_g^3\left[-\alpha_{1,0}+\frac{\alpha_{1,0}^2 r_g}{4}\right]\right\}e^{-\alpha_{1,0}r_g}dr_g
$$

$$
=\left(1-\beta\right)\frac{\alpha_{1,0}^5}{16}\int_0^\infty\left\{-\frac{2\alpha_{1,0}r_g^3}{5}+\left[-\frac{2}{5}\alpha_{1,0}r_g^3+\frac{\alpha_{1,0}^2 r_g^4}{10}\right]\right\}e^{-\alpha_{1,0}r_g}dr_g
$$

$$
=\left(1-\beta\right)\frac{\alpha_{1,0}^5}{16}\left\{-\frac{12\alpha_{1,0}}{5\alpha_{1,0}^4}+\left[-\frac{12}{5\alpha_{1,0}^4}\alpha_{1,0}+\frac{24\alpha_{1,0}^2}{10\alpha_{1,0}^5}\right]\right\} \tag{B.66}
$$

$$
=\left(1-\beta\right)\frac{\alpha_{1,0}^5}{16}\left\{-\frac{12}{5\alpha^3(1,0)}+\left[-\frac{12}{5\alpha^3(1,0)}+\frac{24}{10\alpha^3(1,0)}\right]\right\}
$$

$$
=\left(1-\beta\right)\frac{1}{16}\left\{-\frac{12\alpha_{1,0}^2}{5}+\left[-\frac{12\alpha_{1,0}^2}{5}+\frac{24\alpha_{1,0}^2}{10}\right]\right\}
$$

$$
=\left(1-\beta\right)\alpha_{1,0}^2\left\{-\frac{3}{20}-\frac{3}{20}+\frac{3}{20}\right\}
$$

$$
=-\frac{3}{20}\left(1-\beta\right)\alpha_{1,0}^2
$$

**Third term for $2P_0$ energy expression**

The third $2p_0$ energy term from equation B.48 is then evaluated:

$$
= \frac{\alpha_{1,0}^5}{32\pi} \int_0^\infty \int_0^\pi \int_0^{2\pi} r_g^2 \sin(\theta_g) r_g \cos(\theta_g) e^{-\frac{\alpha_{1,0} r_g}{2}}
$$

$$
\times \left( -\frac{2}{r_g \left( 1 - (1 - \frac{\gamma}{\beta}) \cos^2(\theta) \right)^{\frac{1}{2}}} \right) r_g \cos(\theta_g) e^{-\frac{\alpha_{1,0} r_g}{2}} dr_g d\theta_g d\phi_g
$$

$$
= -2 \frac{\alpha_{1,0}^5}{16} \int_0^\infty \int_0^\pi \frac{r_g^3 \sin(\theta_g) \cos^2(\theta_g) e^{-\alpha_{1,0} r_g}}{\left( 1 - (1 - \frac{\gamma}{\beta}) \cos^2(\theta) \right)^{\frac{1}{2}}} dr_g d\theta_g
$$

$$
= -\frac{\alpha_{1,0}^5}{8} \int_0^\infty r_g^3 e^{-\alpha_{1,0} r_g} dr_g \int_0^\pi \frac{\sin(\theta_g) \cos^2(\theta_g)}{\left( 1 - (1 - \frac{\gamma}{\beta}) \cos^2(\theta) \right)^{\frac{1}{2}}} d\theta_g \tag{B.67}
$$

$$
= -\frac{\alpha_{1,0}^5}{8} \frac{6}{\alpha_{1,0}^4} \int_0^\pi \frac{\sin(\theta_g) \cos^2(\theta_g)}{\left( 1 - (1 - \frac{\gamma}{\beta}) \cos^2(\theta) \right)^{\frac{1}{2}}} d\theta_g
$$

$$
= -\frac{3\alpha_{1,0}}{4} \int_0^\pi \frac{\sin(\theta_g) \cos^2(\theta_g)}{\left( 1 - (1 - \frac{\gamma}{\beta}) \cos^2(\theta) \right)^{\frac{1}{2}}} d\theta_g
$$

The integral from equation B.67 can be solved by the use of the following substitutions:

$$
\cos(\theta_g) = \frac{\sin(y)}{(1 - \frac{\gamma}{\beta})^{\frac{1}{2}}}
$$

$$
(1 - \frac{\gamma}{\beta}) \cos^2(\theta_g) = \sin^2(y)
$$

$$
y = \arcsin \left( (1 - \frac{\gamma}{\beta}) \cos(\theta_g) \right)
$$

$$
-\sin(\theta_g) d\theta_g = \frac{\cos(y) dy}{(1 - \frac{\gamma}{\beta})^{\frac{1}{2}}} \tag{B.68}
$$

$$
y_0 = \arcsin \left( (1 - \frac{\gamma}{\beta})^{\frac{1}{2}} \right)
$$

$$
y_1 = -y_0 = \arcsin \left( -(1 - \frac{\gamma}{\beta}) \right)
$$

The angular integral from equation B.67 can then be evaluated by the use of the substitutions in equation B.68.

$$\int_0^\pi \frac{\sin(\theta_g)\cos^2(\theta_g)}{\left(1-(1-\frac{\gamma}{\beta})\cos^2(\theta)\right)^{\frac{1}{2}}}d\theta_g$$

$$= \int_{y_0}^{-y_0} \frac{\cos^2(\theta_g)\sin(\theta_g)}{\left(1-\sin^2(y)\right)^{\frac{1}{2}}}\left(-\frac{\cos(y)}{(1-\frac{\gamma}{\beta})^{\frac{1}{2}}\sin(\theta_g)}\right)dy$$

$$= \frac{-1}{(1-\frac{\gamma}{\beta})^{\frac{1}{2}}}\int_{y_0}^{-y_0} \cos^2(\theta_g)dy$$

$$= \frac{-1}{(1-\frac{\gamma}{\beta})^{\frac{1}{2}}}\int_{y_0}^{-y_0} \frac{\sin^2(y)}{(1-\frac{\gamma}{\beta})}dy$$

$$= \frac{-1}{(1-\frac{\gamma}{\beta})^{\frac{3}{2}}}\int_{y_0}^{-y_0} \frac{\left(1-\cos(2y)\right)}{2}dy$$

$$= \frac{1}{2(1-\frac{\gamma}{\beta})^{\frac{3}{2}}}\left[\frac{\sin(2y)}{2}-y\right]_{y_0}^{-y_0} \tag{B.69}$$

$$= \frac{1}{2(1-\frac{\gamma}{\beta})^{\frac{3}{2}}}\left[\frac{\sin(-2y_0)-\sin(2y_0)}{2}-(-y_0-y_0)\right]$$

$$= \frac{1}{2(1-\frac{\gamma}{\beta})^{\frac{3}{2}}}\left[2y_0-\sin(2y_0)\right]$$

$$= \frac{1}{2(1-\frac{\gamma}{\beta})^{\frac{3}{2}}}\left[2\arcsin\left((1-\frac{\gamma}{\beta})^{\frac{1}{2}}\right)-\sin(2\arcsin\left((1-\frac{\gamma}{\beta})^{\frac{1}{2}}\right))\right]$$

$$= \frac{1}{2(1-\frac{\gamma}{\beta})^{\frac{3}{2}}}\left[2\arcsin\left((1-\frac{\gamma}{\beta})^{\frac{1}{2}}\right)-2(1-\frac{\gamma}{\beta})^{\frac{1}{2}}\sqrt{1-(1-\frac{\gamma}{\beta})}\right]$$

$$= \frac{1}{(1-\frac{\gamma}{\beta})^{\frac{3}{2}}}\left[\arcsin\left((1-\frac{\gamma}{\beta})^{\frac{1}{2}}\right)-(1-\frac{\gamma}{\beta})^{\frac{1}{2}}\left(\frac{\gamma}{\beta}\right)^{\frac{1}{2}}\right]$$

Putting the angular integral result from equation B.69 back into equation B.67 then gives the final third term:

$$-\frac{3\alpha_{1,0}}{4(1-\frac{\gamma}{\beta})^{\frac{3}{2}}}\left[\arcsin\left((1-\frac{\gamma}{\beta})^{\frac{1}{2}}\right)-(1-\frac{\gamma}{\beta})^{\frac{1}{2}}\left(\frac{\gamma}{\beta}\right)^{\frac{1}{2}}\right] \tag{B.70}$$

### $2P_0$ complete energy function

Assembling the three $2P_0$ energy terms from equations B.55, B.66, and B.70 gives

the final energy expression:

$$
\begin{aligned}
E_{2P_0}(\alpha_{1,0}, \beta, \gamma) &= \frac{\alpha_{1,0}^2}{4} - \frac{3}{20}\Big(1 - \beta\Big)\alpha_{1,0}^2 \\
&\quad - \frac{3\alpha_{1,0}}{4(1 - \frac{\gamma}{\beta})^{\frac{3}{2}}}\Big[\arcsin\big((1 - \frac{\gamma}{\beta})^{\frac{1}{2}}\big) - (1 - \frac{\gamma}{\beta})^{\frac{1}{2}}\big(\frac{\gamma}{\beta}\big)^{\frac{1}{2}}\big)\Big]
\end{aligned}
$$

(B.71)

$$
= \frac{1}{20}\Big(3\beta + 2\Big)\alpha_{1,0}^2 - \frac{3\alpha_{1,0}}{4(1 - \frac{\gamma}{\beta})^{\frac{3}{2}}}\Big[\arcsin\big((1 - \frac{\gamma}{\beta})^{\frac{1}{2}}\big) - (1 - \frac{\gamma}{\beta})^{\frac{1}{2}}\big(\frac{\gamma}{\beta}\big)^{\frac{1}{2}}\big)\Big]
$$

## B.3.3. Sufficient Brute Force Application of the EMT Hamiltonian

The EMT Hamiltonian, in spherical coordinates, includes terms with each coordinate. Consequently, the application of this to $1S$ and $2P_0$ states must include energy expectation terms corresponding to both the radial $r_g$ and polar angle $\theta_g$ coordinates. The $2P_{\pm 1}$ state is then the only additional state beyond $1S$ and $2P_0$ that is of any interest. The azimuthal ($\phi_g$) component of $2P_{\pm 1}$ is acted upon by the relevant part of the Laplacian operator, which then evaluates to zero in the energy expectation integral. Thus it can be concluded that the above "brute force" evaluation of the effective mass energy functions for the $1S$ and $2P_0$ states includes terms for all coordinate components; at least all those states relevant to the emitting of radiation via transitions to the ground state in chalcogen doped silicon, as experimentally measured in this thesis (see chapter 5).

As will be discussed below in further detail, Faulkner [107] determined a formula for energy expectation functions. Armed with energy functions for all coordinate components of the Hamiltonian, a comparison between them and those resulting from the Faulkner equation [107, eq 2.19] is possible. Good (in this case identical) agreement is found, justifying confidence in the accuracy of both, and also that the

further state energy functions($2P_{\pm 1}$) can be found by the Faulkner equations.

## B.3.4. Faulkner Hamiltonian Matrix Elements

Faulkner [107] determined the elements of a multi-basis state representation Hamiltonian matrix; this is in effect the Rayleigh-Ritz approach. However, Faulkner does not show the derivations of his matrix elements, which for the diagonal elements also give the functions that Kohn [8] must have found, despite this a derivation does not appear in the literature. A prudent approach is to use the Faulkner matrix elements as a check, to compare to the energy expression obtained for the $1S$ and $2P_0$ states.

The Faulkner [107, eq 2.19] diagonal matrix elements are reproduced below:

$$
\begin{aligned}
\langle n, \ell | H_1 | n', \ell \rangle = H(n, \ell, n', \ell) &= -2I(\ell, \ell, m)J^1(n', \ell, n, \ell) \\
&+ \left\{ 1 - (1 - \beta)\frac{1}{3}\left[ 1 + \frac{2\ell(\ell + 1) - 6m^2}{(2\ell - 1)(2\ell + 3)} \right] \right\} \\
&\times \left[ -\delta_{n,n'}\frac{\alpha_{\ell,m}^2}{n^2} + 2\alpha_{\ell,m}J^1(n', \ell, n, \ell) \right]
\end{aligned}
\tag{B.72}
$$

For the sake of convenience, Faulkner writes his matrix elements in terms of additional basis functions $I$ and $J^0, J^1...$, such basis functions from equation B.3.4 are then defined:

$$
I(\ell', \ell, m) = \int_0^\pi \int_0^{2\pi} Y_{\ell',m}^*(\theta_g, \phi_g)Y_{\ell,m}(\theta_g, \phi_g)\frac{\sin(\theta_g)d\theta_g d\phi_g}{[1 - (1 - \frac{\gamma}{\beta})\cos(\theta_g)^2]^{\frac{1}{2}}}
\tag{B.73}
$$

$$
J^1(n', \ell', n, \ell) = \int_0^\infty rR_{n',\ell'}(\alpha_{\ell',m}, r)R_{n,\ell}(\alpha_{\ell,m}, r)dr
\tag{B.74}
$$

### B.3.4.1. Faulkner Matrix Element for the $1S$ State

Evaluating the $\langle 1S|H_1|1S \rangle$ Faulkner matrix element then gives equation B.75.

$$
\begin{aligned}
\langle 1S|H_1|1S \rangle = \langle 1,0|H_1|1,0 \rangle &= -2I(1,0,0)J^1(1,0,1,0) + \left\{ 1 - (1-\beta)\frac{1}{3} \right\} \\
&\times \left[ -\frac{\alpha_{0,0}^2}{1^2} + 2\alpha_{0,0}J^1(1,0,1,0) \right] \\
&= -2I(1,0,0)J^1(1,0,1,0) + \frac{(2+\beta)}{3}\left[ -\frac{\alpha_{0,0}^2}{1^2} + 2\alpha_{0,0}J^1(1,0,1,0) \right]
\end{aligned}
\tag{B.75}
$$

These matrix elements are also valid for some non-diagonal elements with the same $\ell$ angular momentium quantum number but differing $n$ numbers, while the two states must have the same $m$ due to the non mixing of the angular momentium projection by the effective mass Hamiltonian operator.

All values are unitless, as per the unitless effective mass Hamiltonian, and $\ell$, $m$,$n$ are the well known quantum numbers for the hydrogenic wavefunctions.

It should be noted that evaluating the Faulkner Matrix elements allows the multiple basis state expression of the effective mass hydrogenic representation, and involves more basis functions ($J^{(}0)$, $J^{(}2)$...) that are not given here for off diagonal elements( see [107] for the full matrix).

The $1S$ wavefunction is given by:

## B. Derivations of Effective Mass Theory Wavefunction Equations

$$R_{1,0}(\alpha_{1,0}, r_g) = 2\alpha_{0,0}^{\frac{3}{2}} e^{-\alpha_{0,0} r_g}$$

$$Y_{0,0}(\theta_g, \phi_g) = \frac{1}{2\sqrt{\pi}}$$

(B.76)

The $J^1$ function is then evaluated:

$$
\begin{aligned}
J^1(1,0,1,0) &= \int_0^\infty r_g R_{n',\ell'}(\alpha(\ell'), r_g) R_{n,\ell}(\alpha_{\ell,m}, r_g) dr_g \\
&= 4\alpha_{0,0}^3 \int_0^\infty r_g e^{-2\alpha_{0,0} r_g} dr_g \\
&= 4\alpha_{0,0}^3 \frac{1}{(2\alpha_{0,0})^2} \\
&= \alpha_{0,0}
\end{aligned}
$$

(B.77)

Finally the $I$ function is then evaluated:

$$
\begin{aligned}
I(0,0,0) &= \int_0^\pi \int_0^{2\pi} Y_{\ell',m}^*(\theta_g, \phi_g) Y_{\ell,m}(\theta_g, \phi_g) \frac{\sin(\theta_g) d\phi_g d\theta_g}{[1 - (1 - \frac{\gamma}{\beta}) \cos(\theta_g)^2]^{\frac{1}{2}}} \\
&= \int_0^\pi \int_0^{2\pi} \frac{1}{4\pi} \frac{\sin(\theta_g) d\phi_g d\theta_g}{[1 - (1 - \frac{\gamma}{\beta}) \cos(\theta_g)^2]^{\frac{1}{2}}} \\
&= \frac{1}{2} \int_0^\pi frac\sin(\theta_g) d\theta_g [1 - (1 - \frac{\gamma}{\beta}) \cos(\theta_g)^2]^{\frac{1}{2}}
\end{aligned}
$$

(B.78)

By using the result of equation B.44, the angular integral in equation B.78 is determined to be:

$$I(0,0,0) = \frac{1}{2} \int_0^\pi \frac{\sin(\theta_g)d\theta_g}{[1 - (1 - \frac{\gamma}{\beta})\cos(\theta_g)^2]^{\frac{1}{2}}}$$

$$= \frac{1}{\left(1 - \frac{\gamma}{\beta}\right)^{\frac{1}{2}}} \arcsin\left(\left(1 - \frac{\gamma}{\beta}\right)^{\frac{1}{2}}\right) \tag{B.79}$$

Thus the final $1S$ energy function is:

$$\langle 1S|H_1|1S\rangle = -2I(1,0,0)J^1(1,0,1,0) + \frac{(2+\beta)}{3}\left[-\frac{\alpha_{0,0}^2}{1^2} + 2\alpha_{0,0}J^1(1,0,1,0)\right]$$

$$= -2I(1,0,0)\alpha_{0,0} + \frac{(2+\beta)}{3}\left[-\alpha_{0,0}^2 + 2\alpha_{0,0}\alpha_{0,0}\right]$$

$$= -2\alpha_{0,0}I(1,0,0) + \frac{(2+\beta)}{3}\alpha_{0,0}^2$$

$$= -\frac{2\alpha_{0,0}}{\left(1 - \frac{\gamma}{\beta}\right)^{\frac{1}{2}}} \arcsin\left(\left(1 - \frac{\gamma}{\beta}\right)^{\frac{1}{2}}\right) + \frac{(2+\beta)}{3}\alpha_{0,0}^2$$

$$\tag{B.80}$$

## B.3.4.2. Minimisation Condition for $\alpha_{0,0}$ for $1S$

The $\alpha$ and $\beta$ parameters can be related by taking the differential of the $1S$ energy expression.

$$0 = \frac{\partial}{\partial \alpha_{0,0}}\left(-2\alpha_{0,0}I(1,0,0) + \frac{(2+\beta)}{3}\alpha_{0,0}^2\right)$$

$$= -2I(1,0,0) + \frac{2(2+\beta)}{3}\alpha_{0,0}$$

$$I(1,0,0) = \frac{(2+\beta)}{3}\alpha_{0,0} \tag{B.81}$$

$$I(1,0,0)\frac{3}{(2+\beta)} = \alpha_{0,0}$$

This finds the values of $\alpha$ and $\beta$ that give the minimum energy.

## B. Derivations of Effective Mass Theory Wavefunction Equations

### B.3.4.3. Faulkner Matrix Element for the $2P_0$ State

Evaluating the $\langle 2P_0|H_1|2P_0\rangle$ Faulkner matrix element then gives:

$$
\begin{aligned}
\langle 2P_0|H_1|2P_0\rangle &= \langle 2,1|H_1|2,1\rangle = -2I(1,1,0)J^1(2,1,2,1) \\
&+ \left\{ 1 - (1-\beta)\frac{1}{3}\left[ 1 + \frac{2(1+1)-6(0)^2}{(2-1)(2+3)} \right] \right\} \\
&\times \left[ -\frac{\alpha_{1,0}^2}{2^2} + 2\alpha_{1,0}J^1(2,1,2,1) \right] \\
&= -2I(1,1,0)J^1(2,1,2,1) + \left\{ 1 - (1-\beta)\frac{1}{3}\left[ 1 + \frac{4}{(1)(5)} \right] \right\} \\
&\times \left[ -\frac{\alpha_{1,0}^2}{4} + 2\alpha_{1,0}J^1(2,1,2,1) \right] \\
&= -2I(1,1,0)J^1(2,1,2,1) + \left\{ 1 - (1-\beta)\frac{3}{5} \right\} \\
&\times \left[ -\frac{\alpha_{1,0}^2}{4} + 2\alpha_{1,0}J^1(2,1,2,1) \right] \\
\\
&= -2I(1,1,0)J^1(2,1,2,1) + \frac{(2+3\beta)}{5} \\
&\times \left[ -\frac{\alpha_{1,0}^2}{4} + 2\alpha_{1,0}J^1(2,1,2,1) \right]
\end{aligned}
\tag{B.82}
$$

The $2P_0$ radial and spherical components are then given by:

$$
R_{2,1}(\alpha_{1,0}, r_g) = \frac{\alpha_{1,0}^{\frac{5}{2}}}{2\sqrt{6}} r_g e^{-\frac{\alpha_{1,0}r_g}{2}}
$$

$$
Y_{1,0}(\theta_g, \phi_g) = \frac{\sqrt{3}}{2\sqrt{\pi}} \cos(\theta_g)
\tag{B.83}
$$

The $I$ function for the $2P_0$ energy is then given by:

## B. Derivations of Effective Mass Theory Wavefunction Equations

$$
\begin{aligned}
I(1,1,0) &= \int_0^\pi \int_0^{2\pi} Y_{\ell',m}^*(\theta_g, \phi_g) Y_{\ell,m}(\theta_g, \phi_g) \frac{\sin(\theta_g) d\phi_g d\theta_g}{[1 - (1 - \frac{\gamma}{\beta}) \cos(\theta_g)^2]^{\frac{1}{2}}} \\
&= \int_0^\pi \int_0^{2\pi} \frac{\sqrt{3}}{2\sqrt{\pi}} \cos(\theta_g) \frac{\sqrt{3}}{2\sqrt{\pi}} \cos(\theta_g) \frac{\sin(\theta_g) d\phi_g d\theta_g}{[1 - (1 - \frac{\gamma}{\beta}) \cos(\theta_g)^2]^{\frac{1}{2}}} \\
&= \frac{3}{4\pi} \int_0^\pi \int_0^{2\pi} \frac{\cos^2(\theta_g) \sin(\theta_g) d\phi_g d\theta_g}{[1 - (1 - \frac{\gamma}{\beta}) cos(\theta_g)^2]^{\frac{1}{2}}} \\
&= \frac{3}{2} \int_0^\pi \frac{\cos^2(\theta_g) \sin(\theta_g) d\theta_g}{[1 - (1 - \frac{\gamma}{\beta}) \cos(\theta_g)^2]^{\frac{1}{2}}}
\end{aligned} \tag{B.84}
$$

The result from equation B.69 is used to evaluate equation B.84 , thus resulting in the $I$ function integral of:

$$
\begin{aligned}
&\frac{3}{2} \int_0^\pi \frac{\cos^2(\theta_g) \sin(\theta_g) d\theta_g}{[1 - (1 - \frac{\gamma}{\beta}) \cos(\theta_g)^2]^{\frac{1}{2}}} \\
&= \frac{3}{2(1 - \frac{\gamma}{\beta})^{\frac{3}{2}}} \left[ \arcsin \left((1 - \frac{\gamma}{\beta})^{\frac{1}{2}}\right) - (1 - \frac{\gamma}{\beta})^{\frac{1}{2}} (\frac{\gamma}{\beta})^{\frac{1}{2}} \right]
\end{aligned} \tag{B.85}
$$

The $J$ functions for the $2P_0$ energy are then evaluated to be:

$$
\begin{aligned}
J^1(2,1,2,1) &= \int_0^\infty r_g R_{n',\ell'}(\alpha_{\ell',m}, r_g) R_{n,\ell}(\alpha_{\ell,m}, r_g) dr_g \\
&= \int_0^\infty r_g \frac{\alpha_{1,0}^{\frac{5}{2}}}{2\sqrt{6}} r_g e^{-\frac{\alpha_{1,0} r_g}{2}} \frac{\alpha_{1,0}^{\frac{5}{2}}}{2\sqrt{6}} r_g e^{-\frac{\alpha_{1,0} r_g}{2}} dr_g \\
&= \frac{\alpha_{1,0}^5}{24} \int_0^\infty r_g^3 e^{-\alpha_{1,0} r_g} dr_g \\
&= \frac{\alpha_{1,0}^5}{24} \left( \frac{3!}{\alpha_{1,0}^4} \right) \\
&= \frac{\alpha_{1,0}}{4}
\end{aligned} \tag{B.86}
$$

The $I$ and $J$ functions for the $2P_0$ state, equations B.85 and B.86 respectively, are substituted into the matrix element from equation B.82 below:

$$\langle 2P_0|H_1|2P_0\rangle = -2I(1,1,0)J^1(2,1,2,1) + \frac{(2+3\beta)}{5}$$

$$\times \left[ -\frac{\alpha_{1,0}^2}{4} + 2\alpha_{1,0}J^1(2,1,2,1) \right]$$

$$= -2I(1,1,0)\frac{\alpha_{1,0}}{4} + \frac{(2+3\beta)}{5}$$

$$\times \left[ -\frac{\alpha_{1,0}^2}{4} + 2\alpha_{1,0}\frac{\alpha_{1,0}}{4} \right] \tag{B.87}$$

$$= -I(1,1,0)\frac{\alpha_{1,0}}{2} + \frac{\alpha_{1,0}^2(2+3\beta)}{20}$$

$$= \frac{\alpha_{1,0}^2(2+3\beta)}{20} - \frac{3\alpha_{1,0}}{4(1-\frac{\gamma}{\beta})^{\frac{3}{2}}} \left[ \arcsin\left((1-\frac{\gamma}{\beta})^{\frac{1}{2}}\right) - (1-\frac{\gamma}{\beta})^{\frac{1}{2}}\left(\frac{\gamma}{\beta}\right)^{\frac{1}{2}} \right]$$

Thus the Faulkner Hamiltonian matrix energy function, equation B.71, is the same as that obtained by brute force application of the Hamiltonian to the $2P_0$ wavefunction, equation B.87.

### B.3.4.4. Minimisation Condition for $\alpha_{1,0}$ for $2P_0$

The $\alpha$ and $\beta$ parameters can be related by taking the differential of the $2P_0$ energy expression:

$$0 = \frac{\partial}{\partial\alpha_{0,0}}\left( -I(1,1,0)\frac{\alpha_{1,0}}{2} + \frac{\alpha_{1,0}^2(2+3\beta)}{20} \right)$$

$$= -\frac{I(1,1,0)}{2} + \frac{\alpha_{1,0}(2+3\beta)}{10} \tag{B.88}$$

$$\frac{I(1,1,0)}{2} = \frac{\alpha_{1,0}(2+3\beta)}{10}$$

$$\frac{5I(1,1,0)}{(2+3\beta)} = \alpha_{1,0}$$

This finds the values of $\alpha$ and $\beta$ that give the minimum energy.

### B.3.4.5. Faulkner Matrix Element for the $2p_{\pm 1}$ State

Evaluating the $\langle 2P_{\pm 1}|H_1|2P_{\pm 1}\rangle$ Faulkner matrix element then results in:

$$\langle 2P_{\pm 1}|H_1|2P_{\pm 1}\rangle = \langle 2,1|H_1|2,1\rangle = -2I(1,1,1)J^1(2,1,2,1)$$
$$\left\{ 1 - (1-\beta)\frac{1}{3}\left[ 1 + \frac{2(1+1)-6(1)^2}{(2-1)(2+3)} \right] \right\}$$
$$\times \left[ -\frac{\alpha_{1,1}^2}{2^2} + 2\alpha_{1,1}J^1(2,1,2,1) \right]$$

$$= -2I(1,1,1)J^1(2,1,2,1) + \left\{ 1 - (1-\beta)\frac{1}{3}\left[ 1 - \frac{2}{5} \right] \right\}$$
$$\times \left[ -\frac{\alpha_{1,0}^2}{2^2} + 2\alpha_{1,1}J^1(2,1,2,1) \right] \tag{B.89}$$

$$= -2I(1,1,1)J^1(2,1,2,1) + \left\{ 1 - \frac{3}{5}(1-\beta)\frac{1}{3} \right\}$$
$$\times \left[ -\frac{\alpha_{1,1}^2}{2^2} + 2\alpha_{1,1}J^1(2,1,2,1) \right]$$

$$= -2I(1,1,1)J^1(2,1,2,1) + \frac{1}{5}(4+\beta)\left[ -\frac{\alpha_{1,1}^2}{2^2} + 2\alpha_{1,1}J^1(2,1,2,1) \right]$$

The $2P_{\pm 1}$ radial and spherical components are given by:

$$R_{2,1}(\alpha_{1,1}, r_g) = \frac{\alpha_{1,0}^{\frac{5}{2}}}{2\sqrt{6}} r_g e^{-\frac{\alpha_{1,1}r_g}{2}}$$

$$\tag{B.90}$$

$$Y_{1,1}(\theta_g, \phi_g) = \frac{\sqrt{3}}{2\sqrt{2\pi}} \sin(\theta_g)e^{\pm i\phi_g}$$

## B. Derivations of Effective Mass Theory Wavefunction Equations

The radial components of the $2P_{\pm 1}$ and $2P_0$ states are the same and are not evaluated again here. This leaves only the evaluation of the $I$ integral, shown below:

$$
\begin{aligned}
I(1,1,1) &= \int_0^\pi \int_0^{2\pi} \frac{\sqrt{3}}{2\sqrt{2\pi}} \sin(\theta_g) e^{\mp i\phi_g} \frac{\sqrt{3}}{2\sqrt{2\pi}} \sin(\theta_g) e^{\pm i\phi_g} \frac{\sin(\theta_g) d\phi_g d\theta_g}{[1-(1-\frac{\gamma}{\beta})\cos(\theta_g)^2]^{\frac{1}{2}}} \\
&= \frac{3}{8\pi} \int_0^\pi \int_0^{2\pi} \sin(\theta_g) \sin(\theta_g) \frac{\sin(\theta_g) d\phi_g d\theta_g}{[1-(1-\frac{\gamma}{\beta})\cos(\theta_g)^2]^{\frac{1}{2}}} \\
&= \frac{3}{4} \int_0^\pi \frac{\sin^3(\theta_g) d\theta_g}{[1-(1-\frac{\gamma}{\beta})\cos(\theta_g)^2]^{\frac{1}{2}}}
\end{aligned}
$$

(B.91)

The substitution below can then be made:

$$
\cos(\theta_g) = \frac{\sin(y)}{(1-\frac{\gamma}{\beta})^{\frac{1}{2}}}
$$

$$
-\sin(\theta_g) d\theta_g = \frac{\cos(y)}{(1-\frac{\gamma}{\beta})^{\frac{1}{2}}}
$$

$$
\sin^2(\theta_g) = 1 - \cos^2(\theta_g) = 1 - \frac{\sin^2(y)}{1-\frac{\gamma}{\beta}}
$$

(B.92)

$$
y_0 = \arcsin((1-\frac{\gamma}{\beta})^{\frac{1}{2}})
$$

$$
y_1 = \arcsin(-(1-\frac{\gamma}{\beta})^{\frac{1}{2}}) = -y_0
$$

The angular integral from equation B.91 is then evaluated using the substitutions from equation B.93 below:

$$\frac{3}{4}\int_0^\pi \frac{\sin^3(\theta_g)d\theta_g}{[1-(1-\frac{\gamma}{\beta})\cos(\theta_g)^2]^{\frac{1}{2}}}$$

$$=-\frac{3}{4}\int_0^\pi \frac{\sin^3(\theta_g)\cos(y)}{\sin(\theta_g)(1-\frac{\gamma}{\beta})^{\frac{1}{2}}}\frac{dy}{[1-\sin^2(y)]^{\frac{1}{2}}}$$

$$=-\frac{3}{4}\int_0^\pi \frac{\sin^2(\theta_g)}{(1-\frac{\gamma}{\beta})^{\frac{1}{2}}}dy$$

$$=-\frac{3}{4(1-\frac{\gamma}{\beta})^{\frac{1}{2}}}\int_0^\pi \left(1-\frac{\sin^2(y)}{(1-\frac{\gamma}{\beta})}\right)dy$$

$$=-\frac{3}{4(1-\frac{\gamma}{\beta})^{\frac{1}{2}}}\int_0^\pi \left(1-\frac{[1-\cos(2y)]}{2(1-\frac{\gamma}{\beta})}\right)dy$$

$$=-\frac{3}{4(1-\frac{\gamma}{\beta})^{\frac{1}{2}}}\int_0^\pi \left(1-\frac{1}{2(1-\frac{\gamma}{\beta})}+\frac{\cos(2y)}{2(1-\frac{\gamma}{\beta})}\right)dy$$

$$=-\frac{3}{4(1-\frac{\gamma}{\beta})^{\frac{1}{2}}}\left[y\left(1-\frac{1}{2(1-\frac{\gamma}{\beta})}\right)+\frac{\sin(2y)}{4(1-\frac{\gamma}{\beta})}\right]_{y_0}^{-y_0}$$

$$=-\frac{3}{4(1-\frac{\gamma}{\beta})^{\frac{1}{2}}}\left[-2y_0\left(1-\frac{1}{2(1-\frac{\gamma}{\beta})}\right)-\frac{\sin(2y_0)}{2(1-\frac{\gamma}{\beta})}\right]$$

$$=-\frac{3}{4(1-\frac{\gamma}{\beta})^{\frac{1}{2}}}\left[-2\arcsin((1-\frac{\gamma}{\beta})^{\frac{1}{2}})\left(1-\frac{1}{2(1-\frac{\gamma}{\beta})}\right)-\frac{\sin(2\arcsin((1-\frac{\gamma}{\beta})^{\frac{1}{2}}))}{2(1-\frac{\gamma}{\beta})}\right]$$

$$=-\frac{3}{4(1-\frac{\gamma}{\beta})^{\frac{1}{2}}}\left[-2\arcsin((1-\frac{\gamma}{\beta})^{\frac{1}{2}})\left(1-\frac{1}{2(1-\frac{\gamma}{\beta})}\right)-\frac{(1-\frac{\gamma}{\beta})^{\frac{1}{2}}\sqrt{1-(1-\frac{\gamma}{\beta})}}{(1-\frac{\gamma}{\beta})}\right]$$

$$=\frac{3}{4(1-\frac{\gamma}{\beta})^{\frac{1}{2}}}\left[2\arcsin((1-\frac{\gamma}{\beta})^{\frac{1}{2}})\left(1-\frac{1}{2(1-\frac{\gamma}{\beta})}\right)+\frac{\sqrt{\frac{\gamma}{\beta}}}{(1-\frac{\gamma}{\beta})^{\frac{1}{2}}}\right]$$

$$\text{(B.93)}$$

Putting the result from the angular integral, equation B.91, and the radial function $J^1$, equation B.86 but with $\alpha_{1,0}$ replaced with $\alpha_{1,1}$, back into the energy expression, equation B.89 then yields the final energy function for the $2P_{\pm1}$ state, shown below:

$$-2I(1,1,1)J^1(2,1,2,1) + \frac{1}{5}(4+\beta)\left[-\frac{\alpha_{1,0}^2}{2^2} + 2\alpha_{1,1}J^1(2,1,2,1)\right]$$

$$= -2I(1,1,1)\frac{\alpha_{1,1}}{4} + \frac{1}{5}(4+\beta)\left[-\frac{\alpha_{1,0}^2}{4} + 2\alpha_{1,1}\frac{\alpha_{1,1}}{4}\right]$$

$$= -\frac{\alpha_{1,1}}{2}I(1,1,1) + \frac{1}{20}(4+\beta)\alpha_{1,1}^2$$

$$= -\frac{3\alpha_{1,1}}{8(1-\frac{\gamma}{\beta})^{\frac{1}{2}}}\left[2\arcsin((1-\frac{\gamma}{\beta})^{\frac{1}{2}})\left(1-\frac{1}{2(1-\frac{\gamma}{\beta})}\right) + \frac{\sqrt{\frac{\gamma}{\beta}})}{(1-\frac{\gamma}{\beta})^{\frac{1}{2}}}\right] + \frac{1}{20}(4+\beta)\alpha_{1,1}^2$$

$$(B.94)$$

### B.3.4.6. Minimisation Condition for $\alpha_{1,1}$ for $2P_{\pm 1}$

The $\alpha$ and $\beta$ parameters can be related by taking the differential of the $2P_{\pm 1}$ energy expression, finding the values of that give the minimum energy, shown below:

$$
\begin{aligned}
0 &= \frac{\partial}{\partial \alpha_{1,1}}\left(-\frac{\alpha_{1,1}}{2}I(1,1,1) + \frac{1}{20}(4+\beta)\alpha_{1,1}^2\right) \\
&= -\frac{I(1,1,1)}{2} + \frac{1}{10}(4+\beta)\alpha_{1,1} \\
5I(1,1,1) &= (4+\beta)\alpha_{1,1} \\
\frac{5I(1,1,1)}{(4+\beta)} &= \alpha_{1,1}
\end{aligned}
$$

$$(B.95)$$

## B.3.5. Verifying the State Energies in the Free Space Hydrogen Limit

### B.3.5.1. The $1S$ State

When all parameters, $\alpha_{0,0}, \beta, \gamma$ are equal to 1 the energy of the EMT1 state should reduce to giving the energy of the $1S$ state of a hydrogen atom in free space. The energy of the $1S$ state is that of equation B.46 or B.80, from the direct application of the effective mass Hamiltonian to the hydrogenic basis state or From Faulkners matrix elements, it is regardless which one is taken as they are both the same. As the equation breaks down at the exact point all parameters are equal to 1, the energy can be checked by taking the limit as the parameters tend towards 1.

$$
\lim_{\alpha_{0,0},\beta,\gamma \to 1} \left( E_{1S}(\alpha_{0,0}, \beta, \gamma) \right)
$$
$$
= \lim_{\alpha_{0,0},\beta,\gamma \to 1} \left( \frac{1}{3}\alpha_{0,0}^2 \left( \beta + 2 \right) - \frac{2\alpha_{0,0}}{\left( 1 - \frac{\gamma}{\beta} \right)^{\frac{1}{2}}} \arcsin \left( \left( 1 - \frac{\gamma}{\beta} \right)^{\frac{1}{2}} \right) \right)
\tag{B.96}
$$

Due to the additive properties of limits, equation B.96 can be evaluated as:

$$
\lim_{\alpha_{0,0},\beta \to 1} \left( \frac{1}{3}\alpha_{0,0}^2 \left( \beta + 2 \right) \right)
$$
$$
- \lim_{\alpha_{0,0},\beta,\gamma \to 1} \left( \frac{2\alpha_{0,0}}{\left( 1 - \frac{\gamma}{\beta} \right)^{\frac{1}{2}}} \arcsin \left( \left( 1 - \frac{\gamma}{\beta} \right)^{\frac{1}{2}} \right) \right)
\tag{B.97}
$$

The first limit term from equation B.97 for the energy of the $1S$ state can then be evaluated as below.

## B. Derivations of Effective Mass Theory Wavefunction Equations

$$\lim_{\alpha_{0,0},\beta \to 1} \left( \frac{1}{3} \alpha_{0,0}^2 (\beta + 2) \right) = \frac{1}{3} (1)^2 (1 + 2)$$

$$= 1 \tag{B.98}$$

The multiplicative properties of limits then allows the second part of equation B.97 to itself be split into two parts, with the final limit being the product of the two multiplied together. This is shown below:

$$\lim_{\alpha_{0,0},\beta,\gamma \to 1} \left( - \frac{2\alpha_{0,0}}{\left(1 - \frac{\gamma}{\beta}\right)^{\frac{1}{2}}} \arcsin \left( \left(1 - \frac{\gamma}{\beta}\right)^{\frac{1}{2}} \right) \right)$$

$$= \lim_{\alpha_{0,0} \to 1} \left( - 2\alpha_{0,0} \right) \lim_{\beta,\gamma \to 1} \left( \frac{\arcsin \left( \left(1 - \frac{\gamma}{\beta}\right)^{\frac{1}{2}} \right)}{\left(1 - \frac{\gamma}{\beta}\right)^{\frac{1}{2}}} \right) \tag{B.99}$$

The first limit, from equation B.99 is then:

$$\lim_{\alpha_{0,0} \to 1} \left( 2\alpha_{0,0} \right) = 2 \tag{B.100}$$

The second limit, from equation B.99 is then evaluated by making the substitution:

$$u = \left(1 - \frac{\gamma}{\beta}\right)^{\frac{1}{2}}$$

$$\gamma, \beta = 1 \tag{B.101}$$

$$u = 0$$

The substitution from equation B.101 can be applied to the second limit from

equation B.99 . Applying L'Hospitals rule then allows the limit to be found.

$$\lim_{\beta,\gamma \to 1} \left( \frac{\arcsin\left( \left(1 - \frac{\gamma}{\beta}\right)^{\frac{1}{2}} \right)}{\left(1 - \frac{\gamma}{\beta}\right)^{\frac{1}{2}}} \right)$$
$$= \lim_{u \to 0} \left( \frac{\arcsin\left( u \right)}{u} \right) = \lim_{u \to 0} \left( \frac{\frac{\partial}{\partial u} \arcsin\left( u \right)}{\frac{\partial}{\partial u} u} \right) \qquad (B.102)$$
$$= \lim_{u \to 0} \left( \frac{\frac{1}{(1-u^2)^{\frac{1}{2}}}}{1} \right) = \frac{1}{1} = 1$$

Bringing the results of the limits from equations B.98, B.100, and B.102 and combining them into the total limit of the $1S$ energy function, equation 3.35, results in the final limit:

$$\lim_{\alpha_{0,0},\beta,\gamma \to 1} \left( E_{1S}(\alpha_{0,0}, \beta, \gamma) \right) = 1 - 2(1) = -1 \qquad (B.103)$$

This is in unitless form, where the unit of energy is that of the $1S$ state of a hydrogen atom in free space therefore the original energy equation B.46 is deemed to give the correct value in the hydrogen limit. The value is negative because it is the energy of a bound state.

## B.3.5.2. The $2P_0$ State

When all parameters,$\alpha_{1,0}, \beta, \gamma$ are equal to 1 the energy of the $2P_0$ state should reduce to giving the energy of the $2P$ state of a hydrogen atom in free space. The energy of the $2P_0$ state is that of equation B.71 or B.87, again, as for the $1S$ state, these are from the direct application of the effective mass hamiltonian to the hydrogenic basis state or From Faulkners matrix elements respectively; it is irrelevant

which energy function is taken as they are both the same. As the $2P_0$ state energy equation breaks down at the exact point all parameters are equal to 1 the limit must be taken.

$$\lim_{\alpha_{1,0},\beta,\gamma\to1}\left(E_{2P_0}(\alpha_{1,0},\beta,\gamma)\right)$$

$$=\lim_{\alpha_{1,0},\beta,\gamma\to1}\left(\frac{1}{20}\left(3\beta+2\right)\alpha_{1,0}^2-\frac{3\alpha_{1,0}}{4(1-\frac{\gamma}{\beta})^{\frac{3}{2}}}\left[\arcsin\left((1-\frac{\gamma}{\beta})^{\frac{1}{2}}\right)-(1-\frac{\gamma}{\beta})^{\frac{1}{2}}(\frac{\gamma}{\beta})^{\frac{1}{2}}\right]\right)$$

$$\text{(B.104)}$$

Exploiting the additive properties of limits again, equation B.104 becomes:

$$\lim_{\alpha_{1,0},\beta\to1}\left(\frac{1}{20}\left(3\beta+2\right)\alpha_{1,0}^2\right)$$

$$-\lim_{\alpha_{1,0},\beta,\gamma\to1}\left(\frac{3\alpha_{1,0}}{4(1-\frac{\gamma}{\beta})^{\frac{3}{2}}}\left[\arcsin\left((1-\frac{\gamma}{\beta})^{\frac{1}{2}}\right)-(1-\frac{\gamma}{\beta})^{\frac{1}{2}}(\frac{\gamma}{\beta})^{\frac{1}{2}}\right]\right)$$

$$\text{(B.105)}$$

The first limit from equation B.105, is:

$$\lim_{\alpha_{1,0},\beta\to1}\left(\frac{1}{20}\left(3\beta+2\right)\alpha_{1,0}^2\right)=\frac{1}{20}\left(3+2\right)$$

$$=\frac{5}{20}=\frac{1}{4}$$

$$\text{(B.106)}$$

The second limit from equation B.105 can then be further broken down:

$$- \lim_{\alpha_{1,0},\beta,\gamma\to 1} \left( \frac{3\alpha_{1,0}}{4(1-\frac{\gamma}{\beta})^{\frac{3}{2}}} \left[ \arcsin\left((1-\frac{\gamma}{\beta})^{\frac{1}{2}}\right) - (1-\frac{\gamma}{\beta})^{\frac{1}{2}}\left(\frac{\gamma}{\beta}\right)^{\frac{1}{2}} \right] \right)$$

$$= - \lim_{\alpha_{1,0}\to 1} \left( \frac{3\alpha_{1,0}}{4} \right) \left[ \lim_{\beta,\gamma\to 1} \left( \frac{\arcsin\left((1-\frac{\gamma}{\beta})^{\frac{1}{2}}\right)}{(1-\frac{\gamma}{\beta})^{\frac{3}{2}}} \right) \right.$$

$$\left. - \lim_{\beta,\gamma\to 1} \left( \frac{(\frac{\gamma}{\beta})^{\frac{1}{2}}}{(1-\frac{\gamma}{\beta})} \right) \right] \tag{B.107}$$

The limit outside the square brackets in equation B.107 is then:

$$- \lim_{\alpha_{1,0}\to 1} \left( \frac{3\alpha_{1,0}}{4} \right) = \frac{3}{4} \tag{B.108}$$

The first term within the square brackets of equation B.107 can be evaluated with the substitution below:

$$(1-\frac{\gamma}{\beta})^{\frac{1}{2}} = Z$$

$$\gamma, \beta \to 1 \tag{B.109}$$

$$Z \to 0$$

The evaluation of the first limit in the square brackets of equation B.107 with the substitution of equation B.109 is shown below.

$$\lim_{\beta,\gamma\to 1} \left( \frac{\arcsin\left((1-\frac{\gamma}{\beta})^{\frac{1}{2}}\right)}{(1-\frac{\gamma}{\beta})^{\frac{3}{2}}} \right)$$

$$= \lim_{Z\to 0} \left( \frac{\arcsin\left(Z\right)}{Z^3} \right) \tag{B.110}$$

L'Hospitals rule is then applied to equation B.110:

$$\lim_{Z \to 0} \left( \frac{\frac{\partial}{\partial Z} \arcsin\left(Z\right)}{\frac{\partial}{\partial Z} Z^3} \right) = \lim_{Z \to 0} \left( \frac{\frac{1}{(1-Z^2)^{\frac{1}{2}}}}{3Z^2} \right) \tag{B.111}$$

The limit from equation B.111 can then be found by the use of the further substitution:

$$Z^2 = X$$
$$Z \to 0 \tag{B.112}$$
$$X \to 0$$

The substitution from equation B.112 can be applied to equation B.111:

$$\lim_{Z \to 0} \left( \frac{\frac{1}{(1-Z^2)^{\frac{1}{2}}}}{3Z^2} \right) = \lim_{X \to 0} \left( \frac{\frac{1}{(1-X)^{\frac{1}{2}}}}{3X} \right) \tag{B.113}$$

Again applying L'Hospitals rule allows the limit from equation B.113 to finally be evaluated.

$$\lim_{X \to 0} \left( \frac{\frac{\partial}{\partial X} \frac{1}{(1-X)^{\frac{1}{2}}}}{\frac{\partial}{\partial X} 3X} \right)$$

$$= \lim_{X \to 0} \left( \frac{(-\frac{1}{2})(-1)\frac{1}{(1-X)^{\frac{3}{2}}}}{3} \right) \tag{B.114}$$

$$= \lim_{X \to 0} \left( \frac{\frac{1}{2(1-X)^{\frac{3}{2}}}}{3} \right) = \frac{\frac{1}{2}}{3}$$

$$= \frac{1}{6}$$

The second limit from within the square brackets of equation B.107 must then be evaluated. This can be done via the use of the substitution:

$$U = \frac{\gamma}{\beta}$$

$$\gamma, \beta \to 1 \tag{B.115}$$

$$U \to 1$$

Using the substitution from equation B.115 on the second limit in equation B.107 is shown below:

$$\lim_{\beta,\gamma \to 1} \left( \frac{\left(\frac{\gamma}{\beta}\right)^{\frac{1}{2}}}{\left(1 - \frac{\gamma}{\beta}\right)} \right) = \lim_{U \to 1} \left( \frac{U^{\frac{1}{2}}}{(1-U)} \right) \tag{B.116}$$

Applying L'Hospitals rule to the limit in equation B.116 gives:

## B. Derivations of Effective Mass Theory Wavefunction Equations

$$\lim_{U \to 1} \left( \frac{\frac{\partial}{\partial U} U^{\frac{1}{2}}}{\frac{\partial}{\partial U}(1-U)} \right) = \lim_{U \to 1} \left( \frac{\frac{1}{2} U^{\frac{-1}{2}}}{-1} \right)$$
$$= -\frac{1}{2}$$

(B.117)

Finally brining in the limits from equations B.106, B.108, B.114 and B.117 and putting them back into equation B.105 gives:

$$\lim_{\alpha_{1,0},\beta \to 1} \left( \frac{1}{20} \left( 3\beta + 2 \right) \alpha_{1,0}^2 \right)$$
$$- \lim_{\alpha_{1,0},\beta,\gamma \to 1} \left( \frac{3\alpha_{1,0}}{4(1-\frac{\gamma}{\beta})^{\frac{3}{2}}} \left[ \arcsin \left( (1-\frac{\gamma}{\beta})^{\frac{1}{2}} \right) - (1-\frac{\gamma}{\beta})^{\frac{1}{2}} (\frac{\gamma}{\beta})^{\frac{1}{2}} \right] \right)$$
$$= \frac{1}{4} - \frac{3}{4} \left[ \frac{1}{6} - \frac{-1}{2} \right] = \frac{1}{4} - \frac{3}{4} \left[ \frac{1}{6} + \frac{1}{2} \right]$$
$$= -\frac{1}{4}$$

(B.118)

As this final energy is again unitless, and the unit of energy is the $1S$ ground state energy of hydrogen, it is clear that the energy equation B.71 gives the correct energy. This is because of the $\frac{E_{1S}}{n^2}$ energy of the hydrogen atom, and for the $2P_0$ state $n = 2$, thus a unitless energy of one quarter is to be expected in in the limit of $\alpha_{1,0}, \beta, \gamma$ all tending towards 1. Again the energy is negative because it is that of a bound state.

### B.3.5.3. The $2P_{\pm 1}$ State

As for the $1S$ and $2P_0$ states before, when all parameters $\alpha_{1,1}, \beta, \gamma$ are equal to 1 the effective mass energy of the $2P_{\pm 1}$ state should reduce to that of a hydrogen atom in free space. This $2P_{\pm 1}$ state energy is given by the Faulkner matrix element in equation B.94. However, again as for the $1S$ and $2P_0$ states, the energy equation breaks down at the exact point all parameters are equal to 1. Therefore the limit is taken as all parameters tend towards 1.

## B. Derivations of Effective Mass Theory Wavefunction Equations

Conveniently all the required limits have been calculated for the $1S$ and $2P_0$ states. The limit of equation B.94, as all parameters tend towards 1, is:

$$
\lim_{\alpha_{1,1},\beta,\gamma\to 1}\left(E_{2P_{\pm 1}}(\alpha_{1,1},\beta,\gamma)\right)
$$

$$
= \lim_{\alpha_{1,1},\beta,\gamma\to 1}\left(-\frac{3\alpha_{1,1}}{8(1-\frac{\gamma}{\beta})^{\frac{1}{2}}}\left[2\arcsin\left((1-\frac{\gamma}{\beta})^{\frac{1}{2}}\right)\left(1-\frac{1}{2(1-\frac{\gamma}{\beta})}\right)+\frac{\sqrt{\frac{\gamma}{\beta}})}{(1-\frac{\gamma}{\beta})^{\frac{1}{2}}}\right]\right.
$$

$$
\left.+\frac{1}{20}(4+\beta)\alpha_{1,1}^2\right)
$$

$$(B.119)$$

Exploiting the additive and multiplicative properties of limits allows equation B.119 to be broken down into:

$$
\lim_{\alpha_{1,1},\beta\to 1}\left(\frac{1}{20}(4+\beta)\alpha_{1,1}^2\right)-\lim_{\alpha_{1,1}\to 1}\left(\frac{3\alpha_{1,1}}{8}\right)\left[2\lim_{\beta,\gamma\to 1}\left(\frac{\arcsin\left((1-\frac{\gamma}{\beta})^{\frac{1}{2}}\right)}{(1-\frac{\gamma}{\beta})^{\frac{1}{2}}}\right)\right.
$$

$$
-\lim_{\beta,\gamma\to 1}\left(\frac{\arcsin\left((1-\frac{\gamma}{\beta})^{\frac{1}{2}}\right)}{(1-\frac{\gamma}{\beta})^{\frac{3}{2}}}\right)
$$

$$
\left.+\lim_{\beta,\gamma\to 1}\left(\frac{\sqrt{\frac{\gamma}{\beta}})}{(1-\frac{\gamma}{\beta})}\right)\right]
$$

$$(B.120)$$

The first limit from equation B.120 is then:

$$
\lim_{\alpha_{1,1},\beta\to 1}\left(\frac{1}{20}(4+\beta)\alpha_{1,1}^2\right)=\frac{5}{20}
$$

$$
=\frac{1}{4}
$$

$$(B.121)$$

The second limit from equation B.120 is then:

$$\lim_{\alpha_{1,1} \to 1} \left( \frac{3\alpha_{1,1}}{8} \right) = \frac{3}{8} \tag{B.122}$$

The third limit from equation B.120 is the same as that in equation B.102, this is:

$$\lim_{\beta,\gamma \to 1} \left( \frac{\arcsin\left( (1 - \frac{\gamma}{\beta})^{\frac{1}{2}} \right)}{(1 - \frac{\gamma}{\beta})^{\frac{1}{2}}} \right) = 1 \tag{B.123}$$

The fourth limit from equation B.120 has also already been evaluated earlier, and is the same as that in equation B.110.

$$\lim_{\beta,\gamma \to 1} \left( \frac{\arcsin\left( (1 - \frac{\gamma}{\beta})^{\frac{1}{2}} \right)}{(1 - \frac{\gamma}{\beta})^{\frac{3}{2}}} \right) = \frac{1}{6} \tag{B.124}$$

The fifth, and final, limit from equation B.120 has also already been evaluated earlier, and is the same as that in equation B.116.

$$\lim_{\beta,\gamma \to 1} \left( \frac{\sqrt{\frac{\gamma}{\beta}})}{(1 - \frac{\gamma}{\beta})} \right) = \frac{-1}{2} \tag{B.125}$$

Assembling the limits from equations B.121 B.122 B.123 B.124 B.125, and putting them back into equation B.120, yields:

$$\frac{1}{4} - \frac{3}{8}\left[2(1) - \frac{1}{6} + \left(\frac{-1}{2}\right)\right]$$

$$= \frac{1}{4} - \frac{3}{8}\left[2 - \frac{4}{6}\right] = \frac{1}{4} - \frac{3}{8}\left[\frac{8}{6}\right] \tag{B.126}$$

$$= -\frac{1}{4}$$

As this final energy is again unitless, and the unit of energy is the $1S$ ground state energy of hydrogen, it is clear that the energy equation B.126gives the correct energy, $\frac{-1}{n^2}$; where $n = 2$ for the $2P_{\pm 1}$ state. This is the same as that for the $2P_0$ state, and the energy is again negative because it is that of a bound state.

## B.4. Uniformly Scaled Hydrogen Model

The energy of a hydrogen atom $E_h$, and the Bohr radius $a_{b,h}$ modified to account for the effective mass, $m^*$, and relative dielectric permittivity, $\epsilon_r$, are given by: [95]

$$E = -\frac{e^4 m^*}{32\pi^2 \epsilon_0^2 \epsilon_r^2 \hbar^2 n^2}$$

$$a_b = \frac{4\pi \epsilon_0 \epsilon_r \hbar^2}{m^* e^2} \tag{B.127}$$

$$E = \frac{\hbar^2}{2m^* a_b^2 n^2}$$

In the same manner as for the scaled hydrogenic EMT basis states an $\alpha_{\ell,m}$ scaling factor for the Bohr Radius can be introduced.

$$a_b \rightarrow \frac{a_b}{\alpha_{\ell,m}}$$

$$E = \frac{\alpha_{\ell,m}^2 \hbar^2}{2m^* a_b^2 n^2}$$

$$E = \frac{\alpha_{\ell,m}^2 m^* e^4}{32\pi^2 \hbar^2 \epsilon_0^2 \epsilon_r^2 n^2}$$  (B.128)

$$\alpha_{0,0} = \sqrt{\frac{32 E \pi^2 \hbar^2 \epsilon_0^2 \epsilon_r^2 n^2}{m^* e^4}} = \frac{4\pi \hbar \epsilon_0 \epsilon_r n}{e^2}\sqrt{\frac{2E}{m^*}}$$

## B.5. Dipole Element Derivations

Transition rates are calculated by the use of Fermi's golden rule require dipole matrix elements. The derivations of these for both the $2P_0$ and $2P_{\pm 1}$ to $1S$ elements are presented here. Using the result of equation 3.53, only the donor envelope functions and the symmetry determined weighting coefficients of the six effective mass basis states are required. In the absence of the weighting factors, the state can be assumed to be weighted to a value of 1. For all but the ground state, where the states of differing symmetry are not degenerate, both weighted and un-weighted states should be treated as having a degeneracy factor of six; this degeneracy is due to the six effective mass basis states, themselves due to the six conduction band minima in Silicon.

$$\vec{C^{k*}}.\vec{C^k} \, \langle F_0^k | (xe^{i\phi_x(t)} + ye^{i\phi_y(t)} + ze^{i\phi_z(t)}) | F_0^j \rangle$$  (B.129)

In each of the dipole elements it should be noted that the $\left(\frac{\beta}{\gamma}\right)^{\frac{1}{4}}$ factors present in each of the wavefunctions are cancelled out by an inverse factor due to the change from $(x, y, z)$ to $(x, y, g)$, and then to $(r_g, \theta_g, \phi_g)$ coordinates.

## B. Derivations of Effective Mass Theory Wavefunction Equations

For the sake of convenience the randomly varying phase factors of $e^{i\phi_{x,y,z}(t)}$ are omitted in the derivations below, as they disappear in the final summing of intensities.

**B.5.0.1.** $2p_0$ **to** $1S(A_1)$ **Dipole Element**

The $2p_0$ to $1S$ dipole matrix element is derived. The wavefunctions used are those given in equations B.76 and B.83 above.

$$\langle F_{1S}|(xe^{i\phi_x(t)} + ye^{i\phi_y(t)} + ze^{i\phi_z(t)})|F_{2P_0}\rangle = \int_0^\infty \int_0^{2\pi} \int_0^\pi r_g^2 \sin(\theta_g)F_{1S}^*(r_g, \theta_g, \phi_g)(xe^{i\phi_x(t)}$$

$$+ ye^{i\phi_y(t)} + ze^{i\phi_z(t)}) \times F_{2P_0}(r_g, \theta_g, \phi_g)dr_g d\theta_g d\phi_g$$

$$= \int_0^\infty \int_0^{2\pi} \int_0^\pi r_g^2 \sin(\theta_g)\frac{1}{\sqrt{\pi}}\alpha_{0,0}^{\frac{3}{2}}e^{-\alpha_{0,0}r_g}(x + y + z)$$

$$\times \frac{\alpha_{1,0}^{\frac{5}{2}}}{4\sqrt{2\pi}}r_g \cos(\theta_g)e^{-\frac{\alpha_{1,0}r_g}{2}}dr_g d\theta_g d\phi_g$$

$$= \frac{\alpha_{1,0}^{\frac{5}{2}}}{4\pi\sqrt{2}}\alpha_{0,0}^{\frac{3}{2}} \int_0^\infty \int_0^{2\pi} \int_0^\pi e^{-\left[\alpha_{0,0}+\frac{\alpha_{1,0}}{2}\right]r_g} \cos(\theta_g) \sin(\theta_g)r_g^3(xe^{i\phi_x(t)} + ye^{i\phi_y(t)} + ze^{i\phi_z(t)})dr_g d\theta_g d\phi_g$$

$$\text{(B.130)}$$

The x, y, and z coordinate parts of the dipole are given by:

$$z = \left(\frac{\beta}{\gamma}\right)^{\frac{1}{2}}r_g \cos(\theta_g)$$

$$x = r_g \sin(\theta_g) \cos(\phi_g) \qquad \text{(B.131)}$$

$$y = r_g \sin(\theta_g) \sin(\phi_g)$$

From this it can be seen that each part of the dipole element will have the same radial $r_g$ component, makings use of equation B.31, this is given by:

$$\int_0^\infty r_g^4 e^{-\left[\alpha_{0,0}+\frac{\alpha_{1,0}}{2}\right]r_g} dr_g$$

$$= \frac{4!}{\left[\alpha_{0,0}+\frac{\alpha_{1,0}}{2}\right]^5} \tag{B.132}$$

The angular parts for both x, and y, are then zero.

$$\int_0^{2\pi} \int_0^\pi \sin(\theta_g)\cos(\phi_g)\cos(\theta_g)\sin(\theta_g) d\theta_g d\phi_g$$

$$= \int_0^{2\pi} \int_0^\pi \sin^2(\theta_g)\cos(\phi_g)\cos(\theta_g) d\theta_g d\phi_g$$

$$= \int_0^\pi \sin^2(\theta_g)\cos(\theta_g) d\theta_g \int_0^{2\pi} \cos(\phi_g) d\phi_g \tag{B.133}$$

$$= \int_0^\pi \sin^2(\theta_g)\cos(\theta_g) d\theta_g \left[-\sin(\phi_g)\right]_0^{2\pi}$$

$$= \int_0^\pi \sin^2(\theta_g)\cos(\theta_g) d\theta_g \left[0-0\right]_0^{2\pi}$$

$$= 0$$

$$\int_0^{2\pi} \int_0^\pi \sin(\theta_g)\sin(\phi_g)\cos(\theta_g)\sin(\theta_g) d\theta_g d\phi_g$$

$$= \int_0^{2\pi} \int_0^\pi \sin^2(\theta_g)\cos(\theta_g)\sin(\phi_g) d\theta_g d\phi_g$$

$$= \int_0^\pi \sin^2(\theta_g)\cos(\theta_g) d\theta_g \int_0^{2\pi} \sin(\phi_g) d\phi_g \tag{B.134}$$

$$= \int_0^\pi \sin^2(\theta_g)\cos(\theta_g) d\theta_g \left[-\cos(\theta_g)\right]_0^{2\pi}$$

$$= \int_0^\pi \sin^2(\theta_g)\cos(\theta_g) d\theta_g \left[-1+1\right]_0^{2\pi}$$

$$= 0$$

The z, and only, component is then given by:

$$\int_0^{2\pi} \int_0^{\pi} \cos(\theta_g) \sin(\theta_g) \left(\frac{\beta}{\gamma}\right)^{\frac{1}{2}} \cos(\theta_g) d\theta_g d\phi_g$$

$$= \left(\frac{\beta}{\gamma}\right)^{\frac{1}{2}} \int_0^{2\pi} \int_0^{\pi} \cos^2(\theta_g) \sin(\theta_g) d\theta_g d\phi_g$$

$$= 2\pi \left(\frac{\beta}{\gamma}\right)^{\frac{1}{2}} \int_0^{\pi} \cos^2(\theta_g) \sin(\theta_g) d\theta_g$$

$$= 2\pi \left(\frac{\beta}{\gamma}\right)^{\frac{1}{2}} \left[ -\frac{1}{3} \cos^3(\theta_g) \right]_0^{\pi} \qquad (\text{B.135})$$

$$= 2\pi \left(\frac{\beta}{\gamma}\right)^{\frac{1}{2}} \left[ \frac{1}{3} + \frac{1}{3} \right]$$

$$= \frac{4}{3} \pi \left(\frac{\beta}{\gamma}\right)^{\frac{1}{2}}$$

Assembling the radial and angular integral results from equations B.132 and B.135 back into equation B.130 then gives the total dipole element.

$$e^{i\phi_z(t)} \frac{\alpha_{1,0}^{\frac{5}{2}}}{4\pi\sqrt{2}} \alpha_{0,0}^{\frac{3}{2}} \frac{4!}{\left[ \alpha_{0,0} + \frac{\alpha_{1,0}}{2} \right]^5} \frac{4}{3} \pi \left(\frac{\beta}{\gamma}\right)^{\frac{1}{2}}$$

$$= e^{i\phi_z(t)} \frac{24}{3\sqrt{2}} \left(\frac{\beta}{\gamma}\right)^{\frac{1}{2}} \frac{\alpha_{0,0}^{\frac{3}{2}} \alpha_{1,0}^{\frac{5}{2}}}{\left[ \alpha_{0,0} + \frac{\alpha_{1,0}}{2} \right]^5}$$

$$= e^{i\phi_z(t)} \frac{8}{\sqrt{2}} \left(\frac{\beta}{\gamma}\right)^{\frac{1}{2}} \frac{\alpha_{0,0}^{\frac{3}{2}} \alpha_{1,0}^{\frac{5}{2}}}{\left[ \frac{2\alpha_{0,0}}{2} + \frac{\alpha_{1,0}}{2} \right]^5} \qquad (\text{B.136})$$

$$= e^{i\phi_z(t)} \frac{8(2^5)}{\sqrt{2}} \left(\frac{\beta}{\gamma}\right)^{\frac{1}{2}} \frac{\alpha_{0,0}^{\frac{3}{2}} \alpha_{1,0}^{\frac{5}{2}}}{\left[ 2\alpha_{0,0} + \alpha_{1,0} \right]^5}$$

$$= e^{i\phi_z(t)} \frac{2^8}{\sqrt{2}} \left(\frac{\beta}{\gamma}\right)^{\frac{1}{2}} \frac{\alpha_{0,0}^{\frac{3}{2}} \alpha_{1,0}^{\frac{5}{2}}}{\left[ 2\alpha_{0,0} + \alpha_{1,0} \right]^5}$$

The dipole element squared, the actual factor of importance in the Fermi's golden rule transition rate, is given by:

$$2^{15}\left(\frac{\beta}{\gamma}\right)\frac{\alpha_{0,0}^3\alpha_{1,0}^5}{\left[2\alpha_{0,0}+\alpha_{1,0}\right]^{10}} \tag{B.137}$$

Reintroducing the appropriate factor, $a_B$, to make the dipole matrix elements no longer unitless.

$$2^{15}\left(\frac{\beta}{\gamma}\right)\frac{\frac{\alpha_{0,0}^3}{a_B^3}\frac{\alpha_{1,0}^5}{a_B^5}}{\left[2\frac{\alpha_{0,0}}{a_B}+\frac{\alpha_{1,0}}{a_B}\right]^{10}}$$
$$= 2^{15}\frac{a_B^{10}}{a_B^8}\left(\frac{\beta}{\gamma}\right)\frac{\alpha_{0,0}^3\alpha_{1,0}^5}{\left[2\alpha_{0,0}+\alpha_{1,0}\right]^{10}} \tag{B.138}$$
$$= 2^{15}a_B^2\left(\frac{\beta}{\gamma}\right)\frac{\alpha_{0,0}^3\alpha_{1,0}^5}{\left[2\alpha_{0,0}+\alpha_{1,0}\right]^{10}}$$

To obtain equation B.138 $\alpha_{\ell,m}$ is simply replaced with $\frac{\alpha_{\ell,m}}{a_B}$, where $a_B$ is defined in equation B.2.

The Bohr radius is:

$$a_B = \frac{4\pi\hbar^2\epsilon_r\epsilon_0}{m_\perp e^2} \tag{B.139}$$

Using the Bohr radius from equation B.139, the final dipole element becomes:

$$2^{19}\frac{\pi^2\hbar^4\epsilon_r^2\epsilon_0^2}{m_\perp^2 e^4}\left(\frac{\beta}{\gamma}\right)\frac{\alpha_{0,0}^3\alpha_{1,0}^5}{\left[2\alpha_{0,0}+\alpha_{1,0}\right]^{10}} \tag{B.140}$$

## B. Derivations of Effective Mass Theory Wavefunction Equations

### B.5.1. $2p_{\pm 1}$ to $1S(A_1)$ Dipole Element

Using the wavefunctions given above in equations B.76, and B.90, the $2p_{\pm 1}$ to $1S$ dipole matrix element is derived.

$$
\langle F_{1S}|(xe^{i\phi_x(t)} + ye^{i\phi_y(t)} + ze^{i\phi_z(t)})|F_{2P_{\pm 1}}\rangle = \int_0^\infty \int_0^{2\pi} \int_0^\pi r_g^2 \sin(\theta_g) F_{1S}^*(r_g, \theta_g, \phi_g)(xe^{i\phi_x(t)}
$$

$$
+ ye^{i\phi_y(t)} + ze^{i\phi_z(t)}) \times F_{2P_{\pm 1}}(r_g, \theta_g, \phi_g) dr_g d\theta_g d\phi_g
$$

$$
= \int_0^\infty \int_0^{2\pi} \int_0^\pi r_g^2 \sin(\theta_g) \frac{1}{\sqrt{\pi}} \alpha_{0,0}^{\frac{3}{2}} e^{-\alpha_{0,0} r_g} (xe^{i\phi_x(t)} + ye^{i\phi_y(t)} + ze^{i\phi_z(t)})
$$

$$
\times \frac{\alpha_{1,1}^{\frac{5}{2}}}{8\sqrt{\pi}} r_g \sin(\theta_g) e^{-\frac{\alpha_{1,1}}{2} r_g} e^{\pm i\phi_g} dr_g d\theta_g d\phi_g
$$

$$
= \frac{\alpha_{0,0}^{\frac{3}{2}} \alpha_{1,1}^{\frac{5}{2}}}{8\pi} \int_0^\infty \int_0^{2\pi} \int_0^\pi r_g^3 \sin^2(\theta_g) e^{-\left[\frac{\alpha_{1,1}}{2} + \alpha_{0,0}\right] r_g} (xe^{i\phi_x(t)} + ye^{i\phi_y(t)} + ze^{i\phi_z(t)}) e^{\pm i\phi_g} dr_g d\theta_g d\phi_g
$$

$$
\text{(B.141)}
$$

The radial component of the integral is then the same as for the $2P_0$ to $1S$ dipole, except with $\alpha_{1,0}$ replaced with $\alpha_{1,1}$. Using the same x, y, and z as in equation B.131, the angular parts of the integral are evaluated below.

## B. Derivations of Effective Mass Theory Wavefunction Equations

$$\int_0^{2\pi} \int_0^{\pi} \sin^2(\theta_g) \sin(\theta_g) \cos(\phi_g) e^{\pm i\phi_g} d\theta_g d\phi_g$$

$$= \int_0^{\pi} \sin^3(\theta_g) d\theta_g \int_0^{2\pi} \cos(\phi_g) e^{\pm i\phi_g} d\phi_g$$

$$= \frac{4}{3} \int_0^{2\pi} \cos(\phi_g) e^{\pm i\phi_g} d\phi_g$$

$$= \frac{4}{3} \int_0^{2\pi} \cos(\phi_g) \left( \cos(\phi_g) \pm i \sin(\phi_g) \right) d\phi_g \qquad \text{(B.142)}$$

$$= \frac{4}{3} \int_0^{2\pi} \cos^2(\phi_g) d\phi_g$$

$$= \frac{4}{3} \int_0^{2\pi} \frac{1}{2} \{ 1 + \cos(2\phi_g) \} d\phi_g$$

$$= \frac{2}{3} \left[ \phi_g + \frac{\sin(2\phi_g)}{2} \right]_0^{2\pi}$$

$$= \frac{4\pi}{3}$$

$$\int_0^{\pi} \sin^3(\theta_g) d\theta_g = \int_0^{\pi} \sin(\theta_g) \left( 1 - \cos^2(\theta_g) \right) d\theta_g$$

$$= \left[ \frac{\cos^3(\theta_g)}{3} - \cos(\theta_g) \right]_0^{\pi}$$

$$= \left[ \frac{-1 - 1}{3} - (-1 - 1) \right] = \left[ \frac{-2}{3} + (2) \right] \qquad \text{(B.143)}$$

$$= \frac{4}{3}$$

$$\int_0^{2\pi} \int_0^{\pi} \sin^2(\theta_g) \sin(\theta_g) \sin(\phi_g) e^{\pm i\phi_g} d\theta_g d\phi_g$$

$$= \int_0^{2\pi} \int_0^{\pi} \sin^3(\theta_g) \sin(\phi_g) e^{\pm i\phi_g} d\theta_g d\phi_g$$

$$= \frac{4}{3} \int_0^{2\pi} \sin(\phi_g) e^{\pm i\phi_g} d\phi_g$$

$$= \frac{4}{3} \int_0^{2\pi} \sin(\phi_g) \big( \cos(\phi_g) \mp i\sin(\phi_g) \big) d\phi_g$$

$$= \frac{4}{3} \int_0^{2\pi} \sin(\phi_g) \big( \mp i\sin(\phi_g) \big) d\phi_g \qquad \text{(B.144)}$$

$$= \mp i\frac{4}{3} \int_0^{2\pi} \sin^2(\phi_g) d\phi_g$$

$$= \mp i\frac{4}{3} \int_0^{2\pi} \frac{1}{2} \big( 1 - \cos(2\phi_g) \big) d\phi_g$$

$$= \mp i\frac{2}{3} \big[ 1 - \frac{\sin(2\phi_g)}{2} \big]_0^{2\pi}$$

$$= \mp i\frac{4\pi}{3}$$

$$\left(\frac{\beta}{\gamma}\right)^{\frac{1}{2}} \int_0^{2\pi} \int_0^{\pi} \sin^2(\theta_g) \cos(\theta_g) e^{\pm i\phi_g} d\theta_g d\phi_g$$

$$= \left(\frac{\beta}{\gamma}\right)^{\frac{1}{2}} \int_0^{\pi} \sin^2(\theta_g) \cos(\theta_g) d\theta_g \int_0^{2\pi} e^{\pm i\phi_g} d\phi_g$$

$$= \left(\frac{\beta}{\gamma}\right)^{\frac{1}{2}} \int_0^{\pi} \sin^2(\theta_g) \cos(\theta_g) d\theta_g \left[ \frac{e^{\pm i\phi_g}}{\pm i} \right]_0^{2\pi} \qquad \text{(B.145)}$$

$$= 0$$

Assembling the angular parts from equations B.142 and B.144, along with the suitable $\alpha$ altered radial part from equation B.132, into equation B.141, then yields the final dipole moment.

$$\frac{\alpha_{0,0}^{\frac{3}{2}}\alpha_{1,1}^{\frac{5}{2}}}{8\pi}\frac{4!}{\left[\alpha_{0,0}+\frac{\alpha_{1,1}}{2}\right]^5}\left(\frac{4\pi}{3}e^{i\phi_x(t)}\mp i\frac{4\pi}{3}e^{i\phi_y(t)}\right)$$
$$=\frac{\alpha_{0,0}^{\frac{3}{2}}\alpha_{1,1}^{\frac{5}{2}}}{\left[\alpha_{0,0}+\frac{\alpha_{1,1}}{2}\right]^5}\left(4e^{i\phi_x(t)}\mp i4e^{i\phi_y(t)}\right)$$

(B.146)

The dipole element (magnitude) squared is given by:

$$\frac{\alpha_{0,0}^3\alpha_{1,1}^5}{\left[\alpha_{0,0}+\frac{\alpha_{1,1}}{2}\right]^{10}}\left(4^2\mp\pm i^24^2\right)\left(4\pm i4\right)$$
$$=\frac{\alpha_{0,0}^3\alpha_{1,1}^5}{\left[\alpha_{0,0}+\frac{\alpha_{1,1}}{2}\right]^{10}}\left(16-i^216\right)$$
$$=2^5\frac{\alpha_{0,0}^3\alpha_{1,1}^5}{\left[\alpha_{0,0}+\frac{\alpha_{1,1}}{2}\right]^{10}}$$
$$=2^5\frac{\alpha_{0,0}^3\alpha_{1,1}^5}{\left[\frac{2\alpha_{0,0}}{2}+\frac{\alpha_{1,1}}{2}\right]^{10}}$$
$$=2^{15}\frac{\alpha_{0,0}^3\alpha_{1,1}^5}{\left[2\alpha_{0,0}+\alpha_{1,1}\right]^{10}}$$

(B.147)

Taking into account the reintroduction of the $a_B$ factor, as for the $1S$ dipole element, gives the non unitless $2P_{\pm1}$ dipole element squared.

$$2^{15}a_B^2\frac{\alpha_{0,0}^3\alpha_{1,1}^5}{\left[2\alpha_{0,0}+\alpha_{1,1}\right]^{10}}$$

(B.148)

Thus again using the Bohr radius defined in equation B.139, the final dipole element is:

$$2^{19} \frac{\pi^2 \hbar^4 \epsilon_r^2 \epsilon_0^2}{m_\perp^2 e^4} \frac{\alpha_{0,0}^3 \alpha_{1,1}^5}{\left[2\alpha_{0,0} + \alpha_{1,1}\right]^{10}} \tag{B.149}$$

Of course, this is for a single one of the two degenerate $m = \pm 1$ $2P$ states, so the complete transition rate will be twice that given by this dipole element.

## B.5.2. Derivation of the Effective Mass Dipole Matrix Elements in the Isotropic Hydrogen Limit

To check the veracity of the EMT dipole transition matrix elements, their values in the limit of all parameters tending towards those of an isolated hydrogen atom in free space are taken. The EMT wavefunction scaling parameters $\alpha_{0,0}$, $\alpha_{1,0}$, $\alpha_{1,1}$, the hamiltonian $z$ axis scaling factor $\beta$, the ratio of the perpendicular and parallel (to the $z$ axis) effective masses $\gamma$, and the relative dielectric permittivity $\epsilon_r$ all tend towards their isotropic free space values of 1; the effective mass of the electron $m_\perp$ tends towards the mass of an electron in free space $m_e$.

### B.5.2.1. $2P_0$ to $1S$

The transition rate matrix element squared is taken from equation B.138, and it's isotropic free space limit is given below; here and for the $2P_{\pm 1}$ case the 0 subscript on the EMT envelope functions $F$ is dropped, as it is unnecessary here, and replaced with $EMT$ for clarity.

$$\lim_{\substack{\alpha_{0,0},\alpha_{1,0},\beta,\gamma,\epsilon_r \to 1 \\ m_\perp \to m_e}} \left( |\langle F_{EMT}^{1S}|x|F_{EMT}^{2P_0}\rangle|^2 + |\langle F_{EMT}^{1S}|y|F_{EMT}^{2P_0}\rangle|^2 + |\langle F_{EMT}^{1S}|z|F_{EMT}^{2P_0}\rangle|^2 \right)$$

$$= \lim_{\beta,\gamma,\alpha_{0,0},\alpha_{1,0} \to 1} \left( 2^{15}(\frac{\beta}{\gamma}) \frac{\alpha_{0,0}^3 \alpha_{1,0}^5}{[2\alpha_{0,0} + \alpha_{1,0}]^{10}} \right) \lim_{\substack{m_\perp \to m_e \\ \epsilon_r \to 1}} \left( a_B^2 \right)$$

$$= \frac{2^{15}}{3^{10}} \lim_{\substack{m_\perp \to m_e \\ \epsilon_r \to 1}} \left( a_B^2 \right)$$

$$(\text{B.150})$$

The scaled Bohr radius, $a_B$, in equation B.151 , and the unscaled Bohr radius, $a_0$, are given by:

$$a_B = \frac{4\pi\hbar^2 \epsilon_0 \epsilon_r}{m_\perp e^2}$$
$$a_0 = \frac{4\pi\hbar^2 \epsilon_0}{m_e e^2}$$

$$(\text{B.151})$$

The scaled Bohr radius in the isotropic free space limit is:

$$\lim_{\substack{m_\perp \to m_e \\ \epsilon_r \to 1}} \left( a_B \right) = \lim_{\substack{m_\perp \to m_e \\ \epsilon_r \to 1}} \left( \frac{4\pi\hbar^2 \epsilon_0 \epsilon_r}{m_\perp e^2} \right)$$
$$= \frac{4\pi\hbar^2 \epsilon_0}{m_e e^2} = a_0$$

$$(\text{B.152})$$

Therefore using the Bohr radius limit of equation B.152 , the EMT limit from equation B.150 becomes:

$$\frac{2^{15}}{3^{10}} a_0^2$$

$$(\text{B.153})$$

**B.5.2.2.** $2P_{\pm1}$ **to** $1S$

The free space isotropic limit of the EMT$2P_{pm1} \to 1S$ transition rate, from equation 3.58 is taken below; the Bohr radius limits from equation B.152 are used along with the same limits (except that now $\alpha_{1,0}$ is replaced by $\alpha_{1,1}$).

$$
\begin{aligned}
&\lim_{\substack{\alpha_{1,0},\alpha_{1,1},\beta,\gamma,\epsilon_r \to 1 \\ m_\perp \to m_e}} \left( |\langle F_{EMT}^{1S}|x|F_{EMT}^{2P_{\pm1}}\rangle|^2 + |\langle F_{EMT}^{1S}|y|F_{EMT}^{2P_{\pm1}}\rangle|^2 + |\langle F_{EMT}^{1S}|z|F_{EMT}^{2P_{\pm1}}\rangle|^2 \right) \\
&= \lim_{\beta,\gamma,\alpha_{0,0},\alpha_{1,1} \to 1} \left( 2^{15} \frac{\alpha^3(0,0)\alpha^5(1,1)}{\left[2\alpha_{0,0} + \alpha_{1,1}\right]^{10}} \right) \lim_{\substack{m_\perp \to m_e \\ \epsilon_r \to 1}} \left( a_B^2 \right) \\
&= \frac{2^{15}}{3^{10}} a_0^2
\end{aligned}
$$

$$(\text{B.154})$$

## B.5.3. Derivation of the Free Space Hydrogen Dipole Matrix Elements

The dipole matrix elements for the $2P_0$ and $2P_{\pm1}$ to $1S$ transitions of a hydrogen atom in a vacuum, or free space, must be derived for comparison to those of EMT donor states. For this, where the Bohr radius $a_0$ is defined in equation B.151 the hydrogen wavefunctions are:

$$
\begin{aligned}
\psi_{1S} &= \frac{e^{\frac{-r}{a_0}}}{\sqrt{\pi}a_0^{\frac{3}{2}}} \\
\psi_{2P_0} &= \frac{r\cos(\theta)e^{\frac{-r}{2a_0}}}{4\sqrt{2\pi}a_0^{\frac{5}{2}}} \\
\psi_{2P_1} &= \frac{r\sin(\theta)e^{\frac{-r}{2a_0}}}{8\sqrt{\pi}a_0^{\frac{5}{2}}} e^{\pm i\phi}
\end{aligned}
$$

$$(\text{B.155})$$

**B.5.3.1.** $2P_0$ **to** $1S$

The total dipole matrix element can be split into x,y, and z polarisation parts; each

is converted into spherical coordinates so as to fit with the same coordinates that the hydrogen wavefunctions are in.

### $x$ **Polarisation**

The $x = r\sin(\theta)\cos(\phi)$ polarisation dipole matrix element is given by:

$$\int_0^\infty \int_0^\pi \int_0^{2\pi} \frac{e^{\frac{-r}{a_0}}}{\sqrt{\pi}a_0^{\frac{3}{2}}} r\sin(\theta)\cos(\phi)\frac{r\cos(\theta)e^{\frac{-r}{2a_0}}}{4\sqrt{2\pi}a_0^{\frac{5}{2}}}r^2\sin(\theta)drd\theta d\phi \qquad (\text{B.156})$$

The $\phi$ angular term of equation B.156 is:

$$\int_0^{2\pi}\cos(\phi)d\phi = 0 \qquad (\text{B.157})$$

Therefore the entire $x$ polarisation term is zero.

### $y$ **Polarisation**

The $y = r\sin(\theta)\sin(\phi)$ polarisation dipole matrix element is given by:

$$\int_0^\infty \int_0^\pi \int_0^{2\pi} \frac{e^{\frac{-r}{a_0}}}{\sqrt{\pi}a_0^{\frac{3}{2}}} r\sin(\theta)\sin(\phi)\frac{r\cos(\theta)e^{\frac{-r}{2a_0}}}{4\sqrt{2\pi}a_0^{\frac{5}{2}}}r^2\sin(\theta)drd\theta d\phi \qquad (\text{B.158})$$

Just as for the $x$ polarisation, the $\phi$ angular term of equation B.158 is zero:

$$\int_0^{2\pi}\sin(\phi)d\phi = 0 \qquad (\text{B.159})$$

As the $x$, the entire $y$ polarisation term is zero.

### $z$ Polarisation

The $z = r\cos(\theta)$ polarisation dipole matrix element is given by:

$$
\int_0^\infty \int_0^\pi \int_0^{2\pi} \frac{e^{\frac{-r}{a_0}}}{\sqrt{\pi}a_0^{\frac{3}{2}}} r\cos(\theta) \frac{r\cos(\theta)e^{\frac{-r}{2a_0}}}{4\sqrt{2\pi}a_0^{\frac{5}{2}}} r^2 \sin(\theta) dr d\theta d\phi
$$

$$
= \frac{1}{4\pi\sqrt{2}a_0^{\frac{8}{2}}} \int_0^\infty r^4 e^{-\frac{3r}{2a_0}} dr \int_0^\pi \cos^2(\theta)\sin(\theta)d\theta \int_0^{2\pi} 1 d\phi
$$

$$(B.160)$$

The radial component of equation B.160 can be evaluated with the assistance of equation B.31. Meanwhile, the $\theta$ angular term can be evaluated by the result of equation B.38 ; the $\phi$ angular term is then trivial. This results in:

$$
\frac{1}{4\pi\sqrt{2}a_0^{\frac{8}{2}}} \int_0^\infty r^4 e^{-\frac{3r}{2a_0}} dr \int_0^\pi \cos^2(\theta)\sin(\theta)d\theta \int_0^{2\pi} 1 d\phi
$$

$$
= \frac{1}{4\pi\sqrt{2}a_0^{\frac{8}{2}}} \left( \frac{24}{(\frac{3}{2a_0})^5} \right) \left( \frac{2}{3} \right) \left( 2\pi \right)
$$

$$
= \sqrt{2}\frac{2^7}{3^5}a_0
$$

$$(B.161)$$

### Total Matrix Element

Therefore the total dipole matrix element, for the $2P_0$ to $1S$ transition, squared is:

$$
|\langle\psi_{hydrogen}^{1S}|x|\psi_{hydrogen}^{2P_0}\rangle|^2 + |\langle\psi_{hydrogen}^{1S}|y|\psi_{hydrogen}^{2P_0}\rangle|^2 + |\langle\psi_{hydrogen}^{1S}|z|\psi_{hydrogen}^{2P_0}\rangle|^2 = |0|^2
$$

$$
+ |0|^2 + |\sqrt{2}\frac{2^7}{3^5}a_0|^2
$$

$$
= \frac{2^{15}}{3^{10}}a_0^2
$$

$$(B.162)$$

## B. Derivations of Effective Mass Theory Wavefunction Equations

### B.5.3.2. $2P_{\pm 1}$ to $1S$

Following the same procedure as for the $2P_0$ state, the dipole matrix elements are evaluated for each of the x, y, and z polarisation independently, summed, and then squared.

### $x$ Polarisation

The $x = r\sin(\theta)\cos(\phi)$ polarisation dipole matrix element is given by:

$$
\int_0^\infty \int_0^\pi \int_0^{2\pi} \frac{e^{\frac{-r}{a_0}}}{\sqrt{\pi}a_0^{\frac{3}{2}}} r\sin(\theta)\cos(\phi)\frac{r\sin(\theta)e^{\frac{-r}{2a_0}}}{8\sqrt{\pi}a_0^{\frac{5}{2}}}e^{\pm i\phi}r^2\sin(\theta)drd\theta d\phi
$$
$$
= \frac{1}{8\pi a_0^{\frac{8}{2}}}\int_0^\infty r^4 e^{-\frac{3r}{2a_0}}dr \int_0^\pi \sin^3(\theta)d\theta \int_0^{2\pi}\cos(\phi)e^{\pm i\phi}d\phi
$$

(B.163)

The radial component of equation B.163 can be evaluated with the assistance of equation B.31, and the $\theta$ and $\phi$ angular terms can be evaluated by the result of equation B.142 . This results in:

$$
\frac{1}{8\pi a_0^4}\left(\frac{24}{(\frac{3}{2a_0})^5}\right)\left(\frac{4}{3}\right)\left(\pi\right)
$$
$$
= \frac{2^7}{3^5}a_0
$$

(B.164)

### $y$ Polarisation

The $y = r\sin(\theta)\sin(\phi)$ polarisation dipole matrix element is:

$$
\int_0^\infty \int_0^\pi \int_0^{2\pi} \frac{e^{\frac{-r}{a_0}}}{\sqrt{\pi}a_0^{\frac{3}{2}}} r\sin(\theta)\sin(\phi)\frac{r\sin(\theta)e^{\frac{-r}{2a_0}}}{8\sqrt{\pi}a_0^{\frac{5}{2}}}e^{\pm i\phi}r^2\sin(\theta)drd\theta d\phi
$$
$$
= \frac{1}{8\pi a_0^{\frac{8}{2}}}\int_0^\infty r^4 e^{-\frac{3r}{2a_0}}dr \int_0^\pi \sin^3(\theta)d\theta \int_0^{2\pi}\sin(\phi)e^{\pm i\phi}d\phi
$$

(B.165)

The radial component of equation B.165 can be evaluated with the assistance of equation B.31, the $\theta$ and $\phi$ angular terms can be evaluated by the result of equation B.144 .

$$\frac{1}{8\pi a_0^{\frac{8}{2}}}\left(\frac{24}{(\frac{3}{2a_0})^5}\right)\left(\frac{4}{3}\right)\left(\mp i\pi\right)$$
$$= \mp i\frac{2^7}{3^5}a_0 \tag{B.166}$$

### $z$ Polarisation

The $z = r\cos(\theta)$ polarisation dipole matrix element is given by:

$$\int_0^\infty \int_0^\pi \int_0^{2\pi} \frac{e^{\frac{-r}{a_0}}}{\sqrt{\pi}a_0^{\frac{3}{2}}} r\cos(\theta)\frac{r\sin(\theta)e^{\frac{-r}{2a_0}}}{8\sqrt{\pi}a_0^{\frac{5}{2}}}e^{\pm i\phi}r^2\sin(\theta)drd\theta d\phi \tag{B.167}$$

The *phi* angular component of equation B.167 can then be trivially found to be zero:

$$\int_0^{2\pi} e^{\pm i\phi}d\phi = 0 \tag{B.168}$$

### Total Matrix Element

Therefore, the total dipole matrix element for the $2P_{\pm 1}$ to $1S$ transition squared is:

$$| \langle \psi_{hydrogen}^{1S} | x | \psi_{hydrogen}^{2P_{\pm 1}} \rangle |^2 + | \langle \psi_{hydrogen}^{1S} | y | \psi_{hydrogen}^{2P_{\pm 1}} \rangle |^2 + | \langle \psi_{hydrogen}^{1S} | z | \psi_{hydrogen}^{2P_{\pm 1}} \rangle |^2 = | \frac{2^7}{3^5} a_0 |^2$$

$$+ | \mp i \frac{2^7}{3^5} a_0 |^2 + |0|^2$$

$$= \left( \frac{2^7}{3^5} a_0 \right)^2 + \mp \pm i^2 \left( \frac{2^7}{3^5} a_0 \right)$$

$$= \frac{2^{15}}{3^{10}} a_0^2$$

$$(B.169)$$

# C. Spectroscopy Methods

The goal of this appendix is to describe the time resolved FTS technique used in the acquisition of the data presented in the main thesis (chapter 5). To that end an illustrative structure is adopted, to fully justify the choice of spectroscopy method.

Firstly, DS is introduced, as this is the most experimentally simple and historically the earliest form of spectroscopy, this provides the necessary contrast with the later and more complete description of FTS; without knowledge of DS the advantages of FTS do not fully reveal themselves.

Secondly, FTS is then described in detail, about both the general method and the specific technique used to obtain time resolution. The rapid scan and step scan FTS techniques are described, and the limitations imposed by the methods upon practical experiment are either explored or stated.

Third and finally, the specific hardware limitations as present for the capture of the data in this thesis are given, with reference to the theoretical limitations discussed previously.

## C.1. Dispersive Spectroscopy

While there are multiple methods of DS, a monochromator is a typical DS instrument. This is ideal for comparison with an FT spectrometer. Irrespective of the exact implementation, monochromators exploit interference or dispersion to separate light of differing wavelengths. This is achieved by the use of either a dispersive element such as a prism, or by a diffraction grating. In both cases light is separated in intensity as a function of wavelength by wave interactions.

For example purposes a common monochromator design is the Czerny Turner design, shown in figure C.1.

The light that leaves the dispersive or diffractive element $d$, in figure C.1, is spatially separated as a function of wavelength, once focused upon the exit aperture f the light is then angularly separated. The monochromator then functions by moving the exit aperture $f$ between different horizontal positions. These positions then correspond to the first order diffraction maxima for the different wavelengths; of course moving the exit aperture far enough will cause it to encounter second, and third maxima and so on until either the light intensity is too weak to detect or the aperture cannot be moved any further due to physical limitations of the monochromator. The exact distance moved then depends on the diffraction grating or dispersive element used, the wavelengths of the light, and the distance between the focusing mirror and the exit aperture. This is as given by the well known diffraction equation, where $d$ is the distance from point $d$ to $e$ and then to the exit aperture $f$ in figure C.1.

$$d\sin(\theta) = m\lambda \qquad (C.1)$$

## C.1.1. Limitations of DS

The main limitation of DS is the reduced SNR, compared to FTS, from only measuring one wavelength at a time. There is also the practical limitation of obtaining diffraction gratings of the appropriate size. To obtain high spectral resolutions a large number of gratings is required, this means that the size of the grating must also be larger.

# C.2. FTS

While dispersive spectroscopy can rely on interference phenomena and a FT of the light intensity performed by the geometry of far field diffraction to function, FTS has by convention a different meaning. Some form of FT is necessary to obtain the light spectrum from a measured function of light intensity. However, the key difference is that in FTS the FT is mathematically applied by the spectroscopist to the measured data. This is in contrast to DS, where the FT is performed physically.

The FT relates functions dependent upon conjugate variable pairs, and the aim of spectroscopy is to distinguish light photons of different energy, light intensity must be measured as a function of a variable that is conjugate to an energy scale parameter. The energy of light photons is given by the famous relation:

$$
\begin{aligned}
E &= hf \\
&= \frac{hc}{\lambda} \\
&\propto \frac{1}{\lambda} \\
&\propto \nu
\end{aligned}
\tag{C.2}
$$

Equation C.2 allows us to know that we must measure the conjugate variable to

either frequency, wavelength $\lambda$, or one over the wavelength which is the wavenumber $\nu$.

As the units of wavelength are those of distance, it can be seen that measuring light intensity is a way that the intensity is a function of distance. Then taking the FT will yield a function of a parameter linearly proportional to energy. Measuring as a function of time is the same as a function of distance, that is the two are related linearly. If a detector responded to all wavelengths equally, could not be saturated, and had a set of digitization electronics that were able to measure the light intensity at an arbitrarily large rate, then there would be no interferometry.

However, to fulfil the Shannon-Nyquist sampling criteria, the light intensity must be measured twice each full wavelength. For an example IR wave take a wavelength of 1000nm, which gives a sample rate of $\approx 1.5 \times 10^{15}$ measurements per second. Modern electronics cannot operate at this speed.

Instead interference can be exploited to measure a standing wave, thus removing the ridiculous time sampling rates required and instead imposing spatial sampling rate requirements. If there is an optical cavity with size 1000nm then the light intensity must be measured at two or more points to be certain that it is the 1000nm standing wave and not one of its harmonics; a measurement of the light intensity must occur every 500nm. This is an $\approx 2 \times 10^{6}$ spatial sample rate, or $3 \times 10^{9}$ less than what is required in time. Thus with a sufficiently large set of optical cavities, and a reproducible optical signal, it can be seen with a measurement of any optical spectrum; of course this is with no components of shorter wavelength than 1000nm, but even gross changes in the wavelength require 9 orders of magnitude before this is comparable with the time sample rate.

This brings us immediately to the use of an interferometer. Interfering two light beams that have a phase difference is the same as measuring the light intensity at different spatial points in an optical resonant cavity. The phase difference is then related to the difference in physical distance that the two light beams have travelled. Extending the physical distance the light travels is then the same as changing the size of the resonant optical cavity. This leads to the simplest form of interferometer, the Michelson interferometer.

## C.2.1. The Michelson Interferometer

The Michelson interferometer is so named because the same design was used in the work by Albert A. Michelson and Edward W. Morley to measure the velocity of the earth in the "luminiferous ether" in 1887. While the "luminiferous ether" was disproved, the wave nature of light means that the design is valid for spectroscopy.

It is vital to state the assumptions essential to the operation of the interferometer. That is, the light being measured must have a coherence length equal to or greater than the physical distance travelled by the light. The intensity, phase evolution, and frequency make up must be constant over a minimum distance or time range. Waves with random phases do no exhibit interference. This fundamental assumption is even more so for transient time resolved spectroscopy, as discussed in section C.4.1.1.

The Michelson interferometer design is shown in fig C.2, reproduced from [170, fig 1, p335]. The operation of the interferometer is explained below with reference to this figure.

- Light enters the interferometer at point $A$.

- Beamsplitter $B$ directs half of the incident light to mirrors $M_1$ and $M_2$, via reflection and transmission respectively.

- The now separate light beams are reflected by mirrors $M_1$ and $M_2$.

- Beamsplitter $B$ directs half of each reflected beam towards detector $D$. The other half is directed back out towards the source $A$ and is not used in this interferometer geometry.

- The two light beams propagating towards '$D$' will then interfere with each other. The light is the same except for a phase factor $\phi$, which dependent upon the different optical path length between the beamsplitter '$B$' and the mirrors '$M_1$' and '$M_2$'.

- The intensity, as measured at $D$, then depends upon $\phi$.
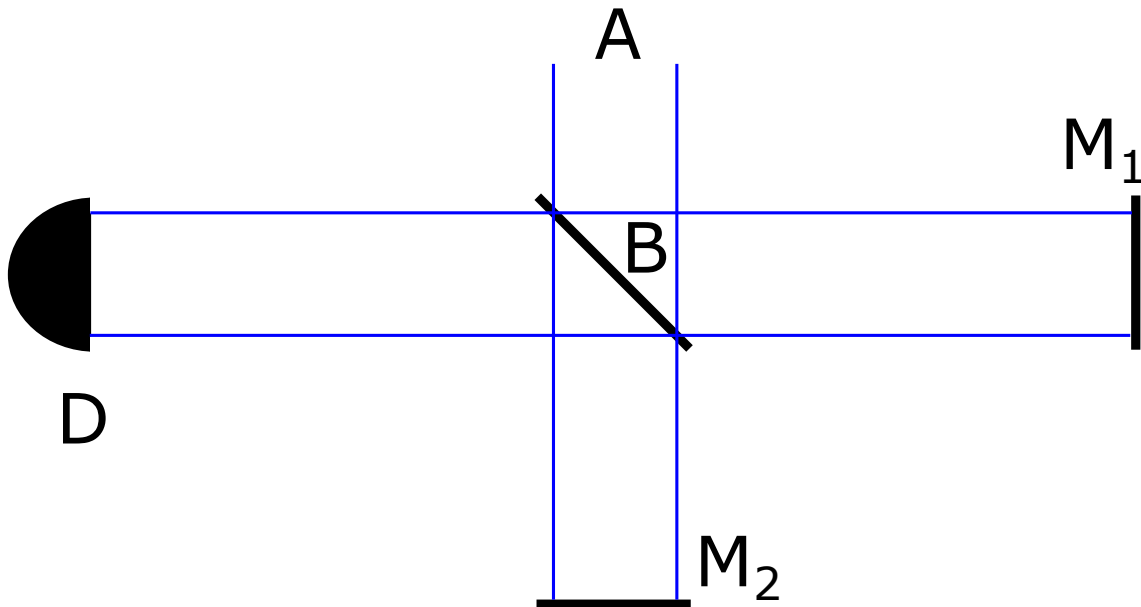


Figure C.2.: Simplified schematic of Michelson interferometer. Black lines are interferometer components, blue are light paths. A) Light input B) Beamsplitter $M_1$) Mirror 1 $M_2$) Mirror 2 D) Detector.

### C.2.1.1. Analysis of the Light Amplitude

It is illustrative to consider the amplitude of a monochromatic light wave at the detector point in a Michelson interferometer. Zero transmission and reflection losses, and a perfectly coherent and collimated input beam are assumed here. The two beams interfering at the detector are then described as the cosine waves, where $A_0$ and

$\omega$ are the amplitude and angular frequency of the light entering the interferometer, $t$ is time, $E_1(t)$ and $E_2(t)$ are the two beams at the detector, and $\phi$ is the phase difference caused by the two beams' unequal optical paths.

$$
\begin{aligned}
E_1(t) &= \frac{A_0}{\sqrt{2}} \cos(\omega t) \\
E_2(t) &= \frac{A_0}{\sqrt{2}} \cos(\omega t + \phi)
\end{aligned}
\tag{C.3}
$$

The intensity of of the light at the detector, $I(t, \phi)$, is then:

$$
\begin{aligned}
I(t, \phi) &= E_1 + E_2 \\
&= \left( \frac{A_0}{\sqrt{2}} \cos(\omega t + \phi) + \frac{A_0}{\sqrt{2}} \cos(\omega t) \right)^2 \\
&= \frac{A_0^2}{2} \left( \cos(\omega t + \phi)^2 + \cos(\omega t)^2 + 2\cos(\omega t + \phi)\cos(\omega t) \right) \\
\cos(\omega t + \phi)\cos(\omega t) &= \frac{\cos(2\omega t + \phi) + \cos(\phi)}{2} \\
I(t, \phi) &= \frac{A_0^2}{2} \left( \cos(\omega t + \phi)^2 + \cos(\omega t)^2 + \cos(2\omega t + \phi) + \cos(\phi) \right)
\end{aligned}
\tag{C.4}
$$

Of course, the detector will not instantaneously respond to the light, but rather integrate and average. Factors affecting this include the responsivity of the detector and related detection electronics to that particular frequency, quantum efficiency of the detector, and also the response time of the detector.

The integration of the detector signal, $D(\Delta t, \phi)$, is then the averaging of the light intensity over many optical oscillations. Here the time over which this integration occurs, $\Delta t$, is assumed to be at least one period of oscillation if not much longer. The phase difference, and OPD between the two beam paths are then $\phi$ and $2\Delta x$,

where the difference in mirror to BS distances is $\Delta x$. These quantities are related, where $c$ is the speed of light, $k = \frac{2\pi}{\lambda}$ is then the wavevector, and $n$ is the refractive index of the interferometer interior.

$$\phi = \frac{2\omega\delta x}{nc} = k\delta x \tag{C.5}$$

The consideration of the detector signal, integrated and averaged over the minimum time $\Delta t$, is shown below.

$$D(\Delta t, \phi) \propto \frac{A_0^2}{2} \int_0^{\Delta t} \left( \cos(\omega t + \phi)^2 + \cos(\omega t)^2 + \cos(2\omega t + \phi) + \cos(\phi) \right) dt$$

$$cos(\omega t)^2 = \frac{1 + \cos(2\omega t)}{2}$$

$$D(\Delta t, \phi) \propto \frac{A_0^2}{2} \int_0^{\Delta t} \left( \frac{1 + \cos(2\omega t + 2\phi)}{2} + \frac{1 + \cos(2\omega t)}{2} + \cos(2\omega t + \phi) + \cos(\phi) \right) dt$$

$$\propto \frac{A_0^2}{2} \int_0^{\Delta t} \left( 1 + \frac{\cos(2\omega t + 2\phi)}{2} + \frac{\cos(2\omega t)}{2} + \cos(2\omega t + \phi) + \cos(\phi) \right) dt$$

$$\propto \frac{A_0^2}{2} \left\{ \left( 1 + \cos(\phi) \right) \Delta t + \left[ -\frac{\sin(2\omega t + 2\phi)}{4\omega} - \frac{\sin(2\omega t)}{4\omega} - \frac{\sin(2\omega t + \phi)}{2\omega} \right]_0^{\Delta t} \right\}$$

$\Delta t$ corresponds to much longer than full oscillation period,

thus oscillating terms are averaged zero.

$$\propto \frac{A_0^2}{2} \left( 1 + \cos(\phi) \right) \Delta t$$

$$D(\delta t, \phi) \propto \frac{A_0^2}{2} \left( 1 + \cos(\frac{2\omega \Delta x}{cn}) \right) \Delta t \tag{C.6}$$

The result from equation C.6 can be followed with two further points. Firstly, that $\frac{2\omega}{cn} = k$, where $k$ is the wavevector. Secondly, that the time $\Delta t$ is the integration, or signal averaging time of the detector used, is constant and thus it can be ignored

as the detector signal will still be proportional to the other factors. The detector signal is then:

$$D(\delta t, \phi) \propto \left(1 + \cos(k\delta x)\right) \tag{C.7}$$

Equation C.7 then tells us what the intensity of light, or ideal detector signal, is at the detector point of the Michelson interferometer as a function of $\delta x$ for a monochromatic wave. Thus it is seen that the detector signal has a constant component, and a cosine component dependent upon the OPD $\delta x$ added. As this has a constant component and a varying component, an interferogram is built up out of the varying component by changing $\delta x$. This interferogram result is:

$$I(\delta x) = \frac{A_0^2}{2} \cos(k\delta x) \tag{C.8}$$

Based upon equation C.8 it is possible to determine the frequency, $\omega$, of the light input to the interferometer.

The above section arrives at the same result as an FT. The cosine FT and the result from equation C.6 are compared.

$$I(\Delta x) = \frac{A_0^2}{2}\cos(2\pi\nu_0\Delta x)$$

$$I_{\mathrm{FT}}(\Delta x) = \int_{-\infty}^{\infty} S(\nu)cos(2\pi\nu\Delta x)d\nu$$

$$I_{\mathrm{FT}}(\Delta x) = S(\nu_0)cos(2\pi\nu_0\Delta x)$$

$$I_{\mathrm{FT}}(\Delta x) = I(\Delta x)$$

(C.9)

Because the FT integral over frequency space is zero, apart from a single frequency for a monochromatic wave, it can be seen that the cosine FT is then the same as the result from equation C.6. If the initial waves are considered as complex waves of form $Ae^{i\omega t}$, the final result would be the same as the complex FT.

The light intensity as a function of OPD in an interferometer is an interferogram. It can be seen that the FT of the interferogram is the same as the spectrum.

## C.2.2. The Spectrum

The total intensity of the interferogram is then just the FT of the spectrum and vice versa. Equation C.10 makes this explicit.

$$I(\delta x) = \int_{-\infty}^{\infty} S(\nu)e^{2\pi i\nu\delta x}d\nu$$

$$S(\nu) = \int_{-\infty}^{\infty} I(\delta x)e^{2\pi i\nu\delta x}d\delta x$$

(C.10)

A measured interferogram contains all the information that is in a spectrum. To measure the spectrum fully the interferogram must be measured over an infinite range of OPD between the two interferometer mirror paths. However, this is impossible, imposing limits on the measurement and resulting spectrum. Conveniently

the limits imposed by finite mirror movements are easily dealt with by basic FT theory. Details on FTs are shown in appendix D. The effect of the FT limits upon the real spectrum are then discussed in section C.2.3.3 as one of the fundamental limitations of FTS.

## C.2.3. Fundamental Limitations of FTS

Once it has been established that a spectrum is obtainable by taking the FT of an interferogram, the limitations of such a method must be considered. While they are many, several are not only present in FTS. The limits of optical components and beam divergence, ect as discussed below are not limited to FTS and themselves directly, or in a slightly altered form, present in any conceivable form of spectroscopy. Here limits that are impossible to avoid, and are significant for FTS, are discussed.

One of the minor disadvantages is that unlike DS, where a single wavelength may be measured in isolation, because the spectrum in FTS is obtained via a Fourier transform the entire spectrum must be measured. By itself this can increase the necessary measurement time.

### C.2.3.1. Optical Components and Environment

The quality and type of optical components used in FTS can affect the performance in both relative spectral sensitivity, and the time necessary to obtain sufficient SNR.

To show how the selection of these optical components can affect a spectrum, consider the simplest case of the Michelson interferometer. Measurements made using a Michelson interferometer will be forced to include at least two mirrors and a BS, along with the atmosphere that the light beam must travel through. Write the power reflectivity and transmittance as $R_m(\nu)$ and $T_{BS}(\nu)$ for the mirrors and the beam splitter respectively. Assuming that the two mirrors are identical and in a perfect

vacuum, then the final light at the detector from mirror one is $R_{m1}(\nu)T_{BS}(\nu)R_{BS}(\nu)$, and mirror two $R_{m2}(\nu)R_{BS}(\nu)R_{BS}(\nu)$ Moving from a vacuum to an atmosphere, it can be assumed that the power losses of the light due to travelling through the atmosphere can be treated by the Lambert part of the well known Beer-Lambert law [171]. This results in an additional factor of $e^{-\mu(\nu)L}$, where $L$ is the optical path distance and $\mu(\nu)$ is the absorption coefficient at wavenumber $\nu$. Ignoring phase factors by assuming that OPD between the two mirrors is zero, the total intensity is:

$$I(\nu) \propto 2R_m(\nu)T_{BS}(\nu)R_{BS}(\nu)e^{-\mu(\nu)L} \tag{C.11}$$

Thus it is made clear that deviances in the reflectivity or transmission of the components with respect to $\nu$, differences between the two mirrors, or deviations from a 50:50 BS can all affect the relative spectral sensitivity. The intensity at specific $\nu$ is affected, and thus the SNR is also.

### C.2.3.2. Beam Divergence, Vibrations, and Mirror Misalignment

All interferometors rely on interference between two light beams to determine spectra, and in order for two light beams to interfere they must overlap spatially. This allows two practical problems to arise, the divergence of the light beam entering the interferometer, and misalignment of the mirrors. There is also a third problem that arises due to the need to move the interferometer mirrors, vibration of those mirrors.

**Beam Divergence**

Firstly, for an ideal measurement only perfectly collimated light enters the interferometer. This can only occur for light emitted from an infinitesimal point, whereas the light in the interferometer must enter by passing through an aperture of finite

size. It is observed that any light will not be perfectly collimated and thus will diverge while travelling through the interferometer. For these diverging light beams the extreme divergent light paths will have different OPDs to the central, and these differences only increase as the two mirror distances do.

Figure C.3 shows an example of beam divergence. Using trigonometry it can be seen that at the point that the two beams coincide the additional optical path length past M1 of the beam that is reflected from M1 is $2\Delta X \tan(\theta) \sin(\theta) = 2\Delta X \frac{\sin^2(\theta)}{\cos(\theta)}$. The additional optical path length of the beam that is reflected from M2 is then $\frac{2\Delta X}{\cos(\theta)}$. The total OPD is given by:

$$
\begin{aligned}
OPD &= \frac{2\Delta X}{\cos(\theta)} - 2\Delta X \frac{\sin^2(\theta)}{\cos(\theta)} \\
&= 2\Delta X \left( \frac{1 - \sin^2(\theta)}{\cos(\theta)} \right) \\
&= 2\Delta X \left( \frac{\cos^2(\theta)}{\cos(\theta)} \right) \\
&= 2\Delta X \cos(\theta)
\end{aligned}
\tag{C.12}
$$

It can thus be seen that for ever increasing mirror movement, $\Delta X$, the phase difference between the divergent beams will increase. The phase of the divergent beams will also differ from the central beams, leading to a loss of coherence. This argument is paraphrased from [172, p42-43].
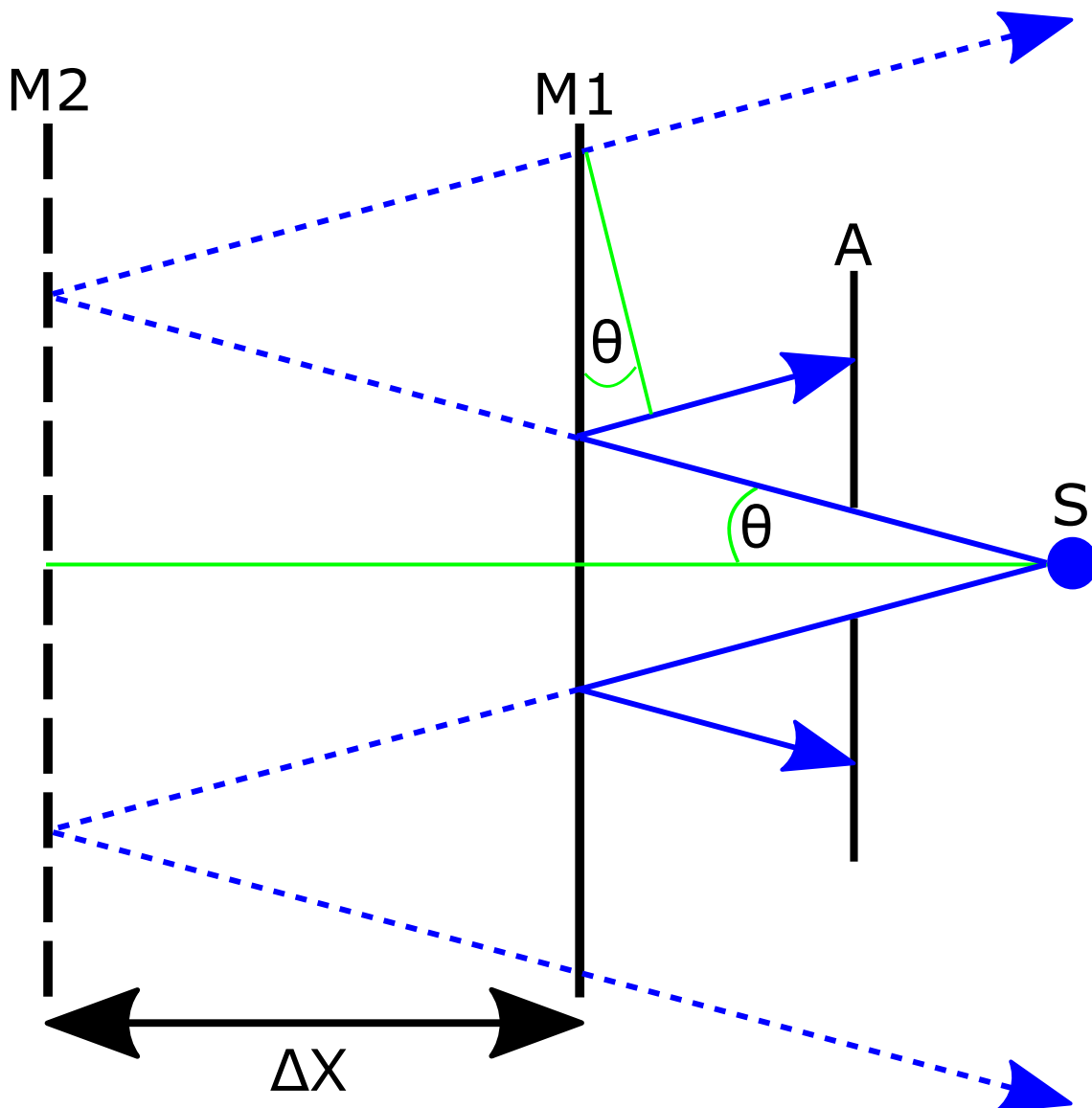
Figure C.3.: Illustration of the effect of beam divergence on a Michelson type interferometer. M1 is the fixed mirror, M2 the moving mirror at position $\Delta X$ relative to M1. A is an aperture for light source S. The light divergence angle $\theta$ causes the light reflected from M1 and M2 to have different optical path lengths. This figure is a reproduction of figure 2.14 in [172, p42]

**Mirror Misalignment**

Secondly, the mirrors used to reflect the two light beams may not be aligned correctly. For a misaligned mirror the OPD is no longer linearly related to the mirror position, instead including trigonometric terms. If the mirror is sufficiently misaligned then interference is prevented from occurring. Even more problematic is the

possibility of the reflected misaligned light interfering with different parts of the beam from the other mirror; at sufficient levels this has the effect of rendering the light incoherent as the phase relationship to OPD is no longer predictable.

The deviance due to mirror misalignment is even greater than that of beam divergence. Figure C.4 shows an example of a misaligned mirror. Using trigonometry it can be seen that the OPD of the beam reflected from M1 is $\frac{\Delta XX}{\cos(2\theta)}$. The total OPD between the central beam reflected from M2 and the beam reflected by $M1$ is then as in equation C.13. Note that it is the electric and magnetic fields which interfere, it is then the projection of the beam along the central path that interferes with the undeviating beam. The projection of the deviating beam along the central path is then $\cos(2\theta)$, and assumes linear polarisation; for rotating polarisation this interference becomes more complex. The conclusion is that any mirror misalignment greatly reduces both the strength and coherence of the measurement.

$$
\begin{aligned}
OPD &= \Delta XX + 2\Delta X - \frac{\Delta XX}{\cos(2\theta)} \\
&= 2\Delta X + \Delta XX \left( 1 - \frac{1}{\cos(2\theta)} \right)
\end{aligned}
\tag{C.13}
$$
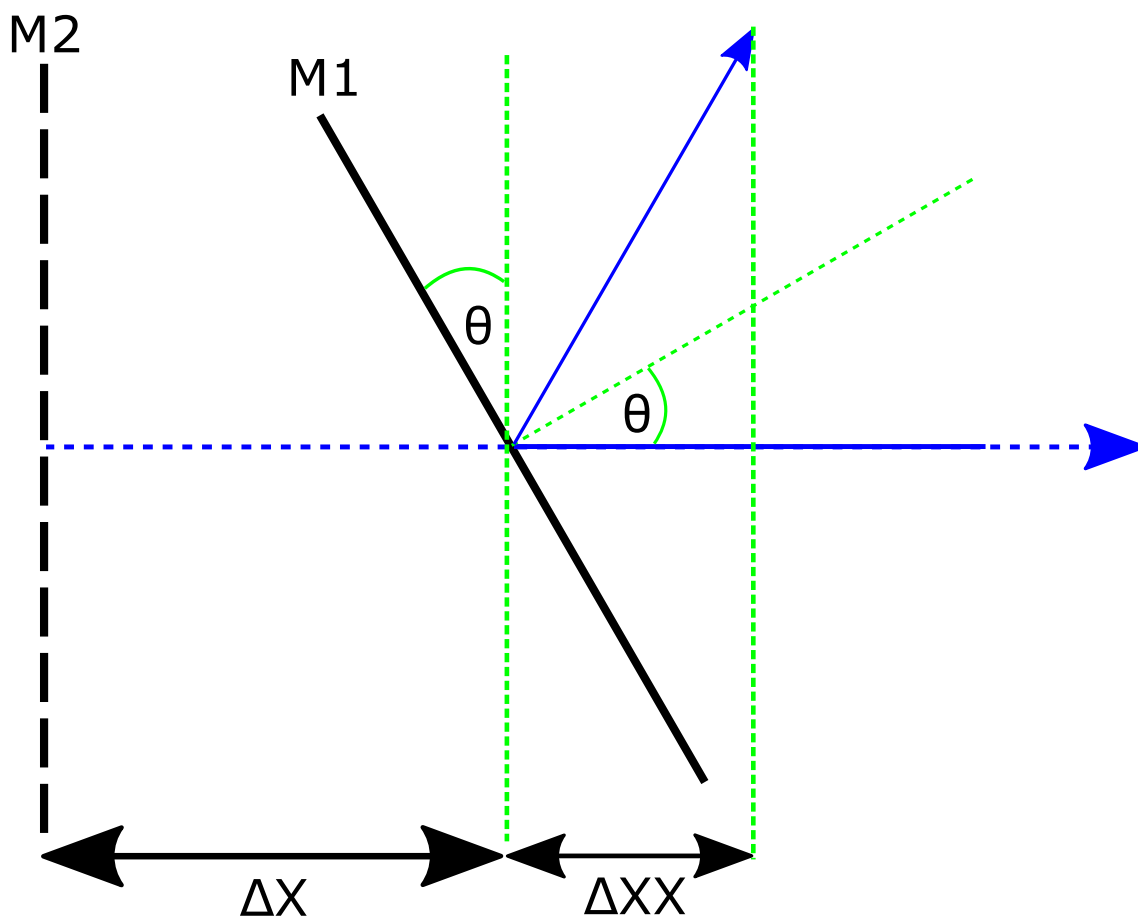
Figure C.4.: Illustration of the effect of beam misalignment on a Michelson type interferometer. M1 is the misaligned mirror, M2 the other moved mirror. $\Delta X$ is the extra mirror movement distance, $\Delta XX$ the distance that the interference of the beams is considered at, and $\theta$ is the angle of misalignment.

**Vibrations**

Vibrations of the mirrors in the interferometer can cause the same negative effects that are associated with mirror misalignment. Figure C.5 shows an example of the effect of vibrations upon the light beam. To mitigate vibrations it is typical for the moving mirror to be "floating' on an air bed of compressed gas. Nitrogen is commonly used as it is found in diatomic $N_2$ molecular form, and in such a state has no asymmetry and thus no molecular dipole element, and thus should not strongly interact with light. This is ideally suited to IR spectroscopy as the energy range of such light is usually similar to the molecular vibration energies; of course, higher energy light can interact, via electronic transitions, with the molecular nitrogen.
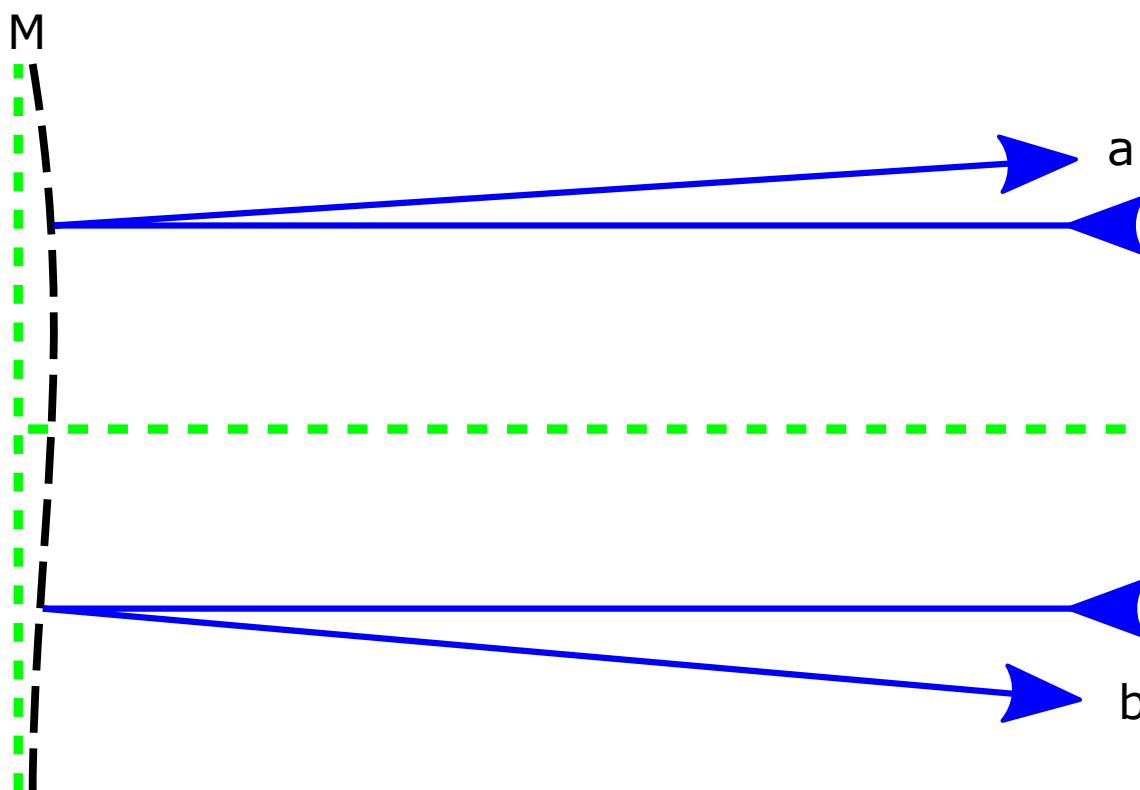
Figure C.5.: Illustration of the effect of vibrations upon the interferometer mirror. M is the mirror, a and b show the diverging effect upon the collimated incident light.

**Conclusions**

These three problems all disrupt the coherent interference of the light, which in turn causes two problems. The SNR of the measurement is reduced because of lower light intensity, either because the two beams are not parallel and thus it is only a projection of their magnitude that can interfere, or because the angular deviation is so great that the light hits the walls of the interferometer. Then the OPD of some of the light is changed; if this changed and unknown OPD, or incoherent light is then the greater part of the light, the entire measurement is invalid.

The mirrors may also be rough or dirty, enough to cause diffuse rather than specular reflection; this will always be true on some scale, but for IR spectroscopy the wavelength is large enough to minimise this problem.

## C.2.3.3. Mirror Movement Distance: Spectrum Resolution

In any spectrum how close can two peaks be before they cannot be distinguished is a vitally important metric. This is the spectral resolution. For FTS the resolution limit arises due to the restriction of the mirror movement, and thus the OPD of the interferogram. This is mathematically equivalent to imposing a boxcar apodization function upon the FT of the interferogram. As a direct consequence this introduces what is known as spectral leakage. The FT, spectral leakage and apodization functions are discussed in more detail in appendix D.

The mirror movement distance affects the spectral resolution in the same way that the size of a diffraction grating does for a dispersive spectroscopy system.

The effect of the apodization is given by equation C.14, where $S(\nu)$ is the spectrum, $A(\Delta x)$ is the apodization function, and $I(\Delta x)$ is the interferogram. Note that $\mathcal{F}\{A(t)\}$ indicates the FT of the function $A(t)$ while $*$ denotes convolution. Observe that the resulting spectrum, $S(\nu)$, is a smeared out version of the "true" spectrum $\mathcal{F}\{I(\Delta x)\}$.

$$S(\nu) = \mathcal{F}\{A(\Delta x)\} * \mathcal{F}\{I(\Delta x)\} \qquad \text{(C.14)}$$

The restriction of the mirror movement is the same as applying a boxcar apodization to the interferogram, and the FT of a boxcar function is a sinc function (section D.3.3.2). The sinc function here is as given in equation C.15, this is different by $2\pi$ to that in section D.3.3.2 due to simple variable change of $x = 2\pi\nu$.

A monochromatic light wave, represented by a delta function like spike in the spectrum, will be manifest in the apodized spectrum as a sinc function. If a measu-

rement is taken of a pair of monochromatic waves at wavenumbers $\nu_1$ and $\nu_2$ then their resulting spectrum will consist of a pair of sinc functions, as shown in equation C.16; where $2W$ is the spectrometer mirror movement distance, from $-$ to $+$ $W$ about the zero OPD point.

$$\text{sinc}(2\pi\nu W) = \frac{\sin(2\pi\nu W)}{2\pi\nu W} \tag{C.15}$$

$$I(\Delta x) = \cos(2\pi\nu_1\Delta x) + \cos(2\pi\nu_2\Delta x)$$
$$S(\nu) = \text{sinc}(2\pi[\nu - \nu_1]W) + \text{sinc}(2\pi[\nu - \nu_2]W) \tag{C.16}$$

The assessment of the possible resolution then depends upon arbitrary criteria, and in reality the noise level. At what point are the two sinc functions too close to separate? There are several commonly used criteria for this, including the Rayleigh criteria, the FWHM point and the first zero crossing of the sinc functions.[172]

**First Zero Crossing**

Griffiths and de Haseth consider the theoretical minimum resolution to be determined by the coincidence of the first zero crossings of the two sinc functions[172].

$$\text{sinc}(2\pi\nu W) = \frac{\sin(2\pi\nu W)}{2\pi\nu W} = 0$$
$$\sin(2\pi\nu W) = 0$$
$$2\pi\nu W = n\pi(n \in \mathbb{Z}) \tag{C.17}$$
$$\nu = \frac{1}{2W}$$

Thus for two sinc functions to have their first zero crossing points at the same point,

their centre point separation must be twice this, giving a spectral resolution of $\frac{1}{W}$.

**Rayleigh Criterion**

The Rayleigh criterion is another possible resolution benchmark, and indicates an increase in the effective resolution of the system. It is named after John William Strutt (1842-1919), the 3rd Baron Rayleigh, and was originally used to specify diffraction limits of resolution in circular apertured telescopes [173]. Because of its origin in light intensity diffraction pattern which cannot be below zero, the Rayleigh criterion is applicable to sinc squared functions. When the first zero point of a sinc squared function coincides with the central peak position of the other, and vice versa, the Rayleigh criterion has been met[173]. Lord Rayleigh's resolution criterion appears to double the effective resolution over the theoretical minimum of the first zero crossing, giving a spectral resolution of $\frac{1}{2W}$. However, it is not possible to resolve the separate peaks of the two sinc functions because the negative lobes in each sinc function obscure the peak of the other.

For a pair of $\text{sinc}^2$ functions the composite curve drops by $\approx 19\%$ in-between them, seen in section $b$ of figure C.6. Instead, taking approximately this percentage drop as the Rayleigh criterion, a peak center separation of $\approx \frac{0.736}{W}$ is obtained for a 19% percentage drop relative to each sinc functions peak. This is then resolvable.

**FWHM**

The FWHM resolution is defined where the central peak positions of the two sinc functions are at each other's FWHM point. A closed form analytical solution does not exist, essentially because of the mixing of polynomial and trigonometric functions. Iterative numerical methods must be used to find the FWHM of the sinc function, which is approximately $\frac{3.79}{2\pi W} = \frac{0.605}{W}$ .

$$\text{sinc}(2\pi\nu W) = \frac{1}{2}$$
$$\frac{\sin(2\pi\nu W)}{2\pi\nu W} = \frac{1}{2} \qquad \text{(C.18)}$$
$$\sin(2\pi\nu W) = \pi\nu W$$

**Summary of Resolution Criteria**

The three resolution criteria and their effective resolutions are collected in table C.1, and shown in figure C.6. It should be noted that the various resolution criteria are for the ideal zero noise case, and that the ultimate resolvability limits of two frequencies depends upon many other factors; relative signal strengths, SNR in each signal, absolute noise in each signal, and the baseline and its noise level that the two signals are superimposed upon.

| Criteria | Resolution |
|---|---|
| Zero crossing | $\frac{1}{W}$ |
| Rayleigh $sinc^2$ | $\left(\frac{0.5}{W}\right)$ |
| Rayleigh $sinc$ | $\left(\frac{0.736}{W}\right)$ |
| FWHM | $\frac{0.605}{W}$ |

Table C.1.: Different Resolution limits in terms of $W$, half the total mirror movement distance.
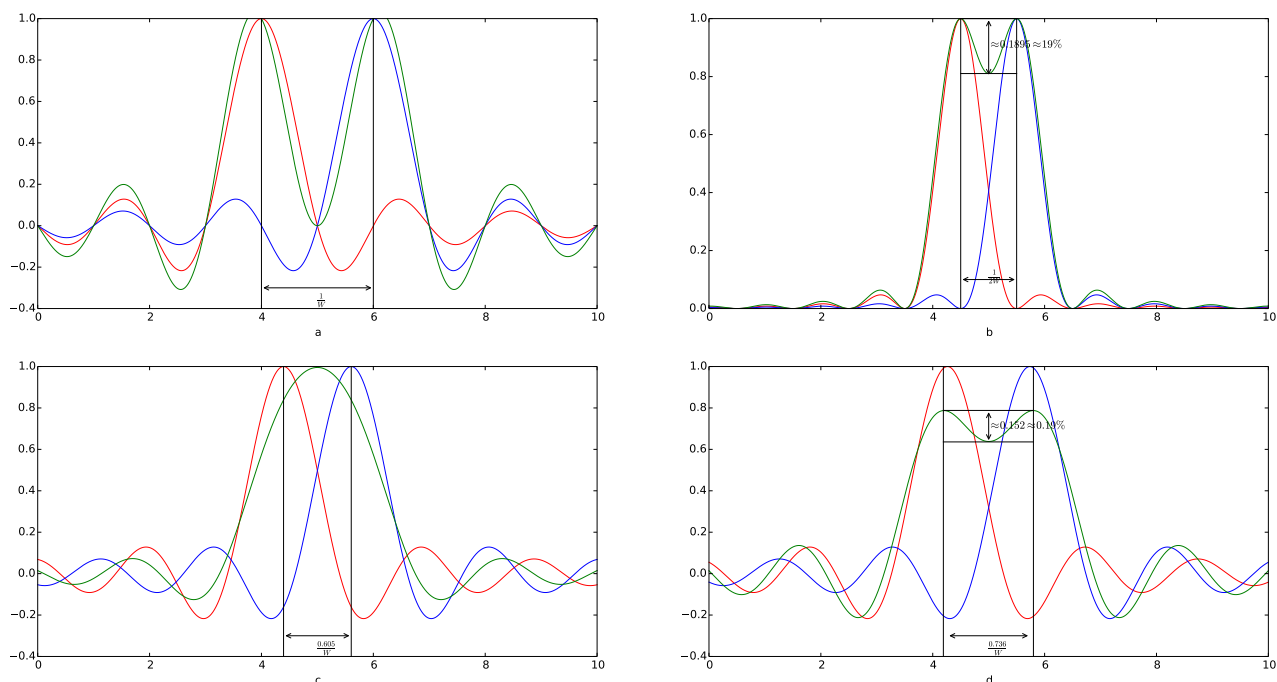
Figure C.6.: Different resolution criteria. ***a*** First zero crossing. ***b*** Rayleigh criteria for $sinc^2$. ***c*** FWHM. ***d*** Rayleigh criteria for *sinc*. The relative drop in magnitude from the peaks is highlighted for *b* and *d* to show the Rayleigh criteria.

Different resolution regimes show that features at less than the minimum resolution can be resolved by a human observer, but there are limits to this that will ultimately depend on relative signal strengths. Imagine two sinc functions of wildly differing amplitude that cannot be resolved at the supposed minimum resolution, where the larger dominates and the weaker appears as a small addition to the larger sidelobes, so to be pedantic resolution limits cannot be set without knowing the minimum and maximum possible signal strengths and the noise levels.

## C.2.4. Fundamental Advantages of FTS

There are several well known fundamental advantages to FTS, all of which increase the SNR of the measurement compared to an equivalent dispersive measurement. [172] These are all historically named after the early pioneers of FTS, who were

381

either members of the Jacquinot research group at the Aimé -Cotton Laboratory or Peter Fellgett who independantly developed many of the same techniques.[174]

### C.2.4.1. Throughput or Jacquinot advantage

The throughput, or "Jacquinot" advantage, is named after Piere Jacquinot (1910-2002), who in the 1960's was one of the independent driving forces behind the development of FTS.[174]

The Jacquinot advantage arises from having a signal beam of greater size, assuming uniform intensity then the total light is thus greater, causing a greater SNR than that of a dispersive measurement. This occurs because DS requires the use of collimated light, or as close to this as can be obtained in practice. To obtain perfectly collimated light it must be emitted from an infinitesimally small point source, which cannot be achieved in reality. As a compromise a small aperture is placed at the entrance, which is known as a Jacquinot stop, another aperture is then placed at the exit of the dispersive spectrometer for wavelength selection (section C.1). In principle the aperture size used in FTS is restricted, this is due to a larger aperture allowing greater angular beam divergence than a smaller one, and the effect of beam divergence in the interferometer as the mirror is moved can adversely affect the measured spectrum (section C.2.3.2). However, this restriction is typically less than that of the entrance slit of a dispersive spectrometer. Additionally there is no need for an exit slit in FTS. For both noise sources that are and are not dependent upon signal magnitude, a larger aperture will give a greater signal and thus a greater SNR.

### C.2.4.2. Multiplexing or Fellgett advantage

The multiplex, or "Fellgett" advantage, is named after Peter Fellgett (1922-2008), who was one of the early pioneers of FTS.[175] The advantage only arises when

compared to a dispersive spectrometer measuring at a fixed resolution for a fixed time, with the same optical throughput and detector responsivity. Because the interferometer measures the entire spectrum at once, in the time taken to measure the full spectrum with the dispersive spectrometer, the interferometer would have taken $n$ measurements; the number of spectral elements $n$, resolution $\Delta\nu$, maximum and minimum spectrum points $\nu_{min}$ $\nu_{max}$ are related by equation C.19. Thus by co-adding the spectra the SNR is increased.

$$n\Delta\nu = \nu_{max} - \nu_{min} \tag{C.19}$$

**Limits of Fellgett's Advantage**   There are limits to Fellgetts advantage. Spectra cannot be co-added to average away a non-random noise source, such as a detector dark current. Additionally the SNR can be affected by the shape of the spectrum and the apodization function used.

As is shown in section C.2.5.1, the SNR is improved relative to a dispersive measurement from co-adding multiple spectra. This co-addition SNR increase is proportional to $\sqrt{n}$, where $n$ is the number of spectra. However, a second effect is present, originating from the variance in the photon flux affecting the interferogram intensity; the variance in intensity at each point then propagates into the final spectrum.[172] This extra noise ultimately depends upon the apodization function selected, and the incident spectral shape. This gives two conflicting mechanisms for effecting the SNR. Thus the multiplexing advantage is limited by the dominant noise source, if Poissonian photon flux variations dominate and a boxcar apodization is used then [172] claim the advantage is completely removed.

## C.2.4.3. Accuracy and Averaging or Connes advantage

The accuracy, or Connes advantage, is named after Janine Connes (1932-), who was initially involved with the Jacquinot group in the 1950s and created some of the mathmatical foundations of early FTS theory in her thesis. [174][176] This advantage is not necessarily inherent to interferomic FTS, but to the typical way the OPD is measured when measuring an interferogram.

Measurement depends upon accurately knowing the OPD of the two interfering light beams at the point the interferogram is sampled. A common method of determining the mirror position is by having a reference laser beam through the interferometer. This reference beam passes through the interferometer, and is incident upon a separate detector than the measured spectrum. As the reference laser is very close to a monochromatic source, its intensity as a function of mirror movement is cosinusoidal. Counting the times that this reference signal peaks, or how many interference fringes have been passed through, allows the distance moved to be known in terms of the reference beam wavelength. This is limited by a few factors, the intensity and frequency stability of the reference beam, and the divergence of the beam which imposes limits on the maximum mirror movement (see section C.2.3.2).

A typical reference beam used is a Helium Neon laser, with red light of wavelength 632.8 nm. There are typically four steps of discrimination in the reference beam intensity; fully in phase where OPD is an integer multiple of the wavelength with maximum signal, fully out of phase where OPD is an integer multiple plus one half of the wavelength with minimum signal, and one or three quarters out of phase where OPD is an integer multiple plus one or three quarters of the wavelength with half of the maximum signal. This imposes limits on the maximum sampling rate and thus the bandwidth that can be measured. For quarter reference beam wavelength discrimination this gives a maximum measurable bandwidth of zero to the frequency

corresponding to half the wavelength.

The greater accuracy in the OPD corresponds to greater wavenumber accuracy in the spectrum. This also facilitates the co-addition of interferograms, or spectra, thus allowing an increase in SNR.

## C.2.5. Obtaining the Real Final Spectrum

Once an interferogram has been measured, yet before the application of the FT, there are several necessary and some unnecessary but useful procedures that can be performed in order to improve the quality of the final FT spectrum.

Apodization must be applied to the interferogram, because even if no additional apodization is applied the finite nature of the real interferogram is itself an apodization. Co-addition can be applied to either the interferogram or spectrum to increase SNR, while phase correction can only be applied to a spectrum; if the interferogram is double sided and symmetric then phase correction is not necessary. The necessity of zero filling depends upon the sample rate and size of the interferogram; Fast Fourier Transform (FFT) algorithms require a power of two number of data points to function and thus if this condition is not met then zero filling is required. Zero filling may also be a purely cosmetic procedure, one that makes the final spectrum look clearer to a human observer, and adds no information to the spectrum.

Once zero filling, and or co-addition of interferograms, has been carried out the FT is applied. Finally any spectrum co-addition can be carried out, and phase correction is applied to the spectrum, thus the final spectrum is obtained. The spectrum from FTS typically uses wavenumbers $S(\nu)$ as the energy scale, with units of $cm^{-1}$; where the interferometer mirror movement in specified in cm.

## C.2.5.1. Co-addition of Spectra

Multiple interferograms can be co-added together in order to increase the SNR and average away random noise fluctuations. This is made possible because of the Connes advantage (section C.2.4.3), which states that the OPD $2\Delta x$ is known to a high degree of accuracy. It should be noted that co-addition of interferograms or spectra is identical, the same SNR improvement will occur in either domain assuming that the OPD positions have no error. Co-addition is not necessary to obtain a spectrum, but does increase the SNR of the final spectrum.

The co-addition increase in the SNR can be shown by considering a measurement with signal strength $S$ and variance $\sigma_S^2$, with noise then equal to the standard deviation $\sigma_S$ and $\overline{S}$ being the mean average $S$ value. We must also assume that the noise in each measurement is the same, and that each measurement is uncorrelated. If we take $n$ measurements then the total signal and total variance is as shown in equation C.20.

$$
\begin{aligned}
S_{total} &= n\overline{S} \\
\sigma_{total}^2 &= n\sigma^2 \\
\sigma_{total} &= \sqrt{n}\sigma \\
SNR_n &= \frac{n\overline{S}}{\sqrt{n}\sigma} \\
&= \frac{\sqrt{n}\overline{S}}{\sigma} \\
&= \sqrt{n}SNR_1
\end{aligned}
\tag{C.20}
$$

The result from equation C.20 gives the same increase in SNR as considering the SNR of the mean average of the signal.

$$\overline{S} = \frac{1}{n} \sum_{i=1}^{N} S_i$$

$$\sigma_{mean}^2 = Var[\overline{S}]$$

$$Var[\overline{S}] = Var[\frac{1}{n} \sum_{i=1}^{n} S_i] = \frac{1}{n^2} Var[\sum_{i=1}^{n} S_i]$$

$$= \frac{1}{n^2} \sum_{i=1}^{n} var[S_i]$$

$$= \frac{1}{n^2} n var[S] \qquad (C.21)$$

$$\sigma_{mean}^2 = \frac{var[S]}{n}$$

$$\sigma_{mean} = \frac{\sigma_S}{\sqrt{n}}$$

$$SNR_{mean} = \frac{\overline{S}}{\sigma_{mean}} = \overline{S} \frac{\sqrt{n}}{\sigma_S}$$

$$SNR_{mean} = \sqrt{n} \frac{\overline{S}}{\sigma_S}$$

## C.2.5.2. Zero Filling

In any real measurement the interferogram is discrete, thus the FT becomes the DFT (section D.3.2). While the discrete spectrum contains all of the information that is present in the interferogram, it can often appear to be a poor spectrum due to jagged jumps and single point peaks that may appear to be noise. There is also the issue with the DFT being computed with FFT algorithms, these are faster and in the case of the Cooley-Turkey algorithm only function on interferogram arrays that have a power of 2 number of points.[177] To overcome a lack of data points for the FFT, interpolation can find the values of extra points in-between currently existing ones; however, this interpolation can be time consuming and lead to errors in the resulting spectrum. A common and simple interpolation method that avoids costly computation, and that is used in the interferogram domain, is known as zero filling. [172, p227]

To zero fill an interferogram merely append extra data points to the end of the interferogram. This appending should result in the same final spectrum regardless of which end or ends the zero points are appended to. The lack of effect upon the final spectrum is illustrated by considering the DFT. If a discrete interferogram is measured, $I_n = I(n\Delta X)$, of $N$ discrete uniformly spaced points with spacing $\Delta X$ or sampling rate $\frac{1}{\Delta X}$, this gives the discrete spectrum $S_k = S(k\Delta\nu)$, again of $N$ discrete uniformly spaced points with spacing $\Delta\nu = \frac{1}{N\Delta X}$, or sample rate $N\Delta X$.

$$S_k = \sum_{n=0}^{N-1} I_n e^{i2\pi k \frac{n}{N}}$$

$$I_n = \frac{1}{N} \sum_{k=0}^{N-1} S_k e^{-i2\pi k \frac{n}{N}}$$

(C.22)

In order to smooth the spectrum by adding data points, data points containing zero can be added to the end of the interferogram. As an example double the size of the interferogram by adding $N$ additional data points, so that the prior interferogram data is contained in the first $N$ points. Now the interferogram $I_n^0$, has $2N$ uniformly spaced points, with the same spacing and sampling rate as the non-zero-filled interferogram; the sampling rate of the measured interferogram cannot be changed by data manipulations. However, the new spectrum ,$S_k^0$, will have a new spacing $\Delta\nu^0 = \frac{1}{2N\Delta X}$ and sample rate $2N\Delta X$, thus doubling the amount of data points in the spectrum. This occurs because the number of points in the spectrum has to double, yet the maximum frequency in the spectrum cannot increase because the interferogram sample rate has not increased and thus the spectral sampling rate must then double. As the physical measurement is unaffected, this additional spectral sample rate does not give any increased spectral accuracy, as the Shannon-Nyquist criterion may indicate (section D.3.1.1), nor does it represent a real increase

in resolution. The zero filled interferogram and spectrum are shown in equation C.23.

$$I_n^0 = \frac{1}{2N} \sum_{k=0}^{2N-1} S_k^0 e^{-i\pi k \frac{n}{N}}$$

$$S_k^0 = \sum_{n=0}^{2N-1} I_n^0 e^{i\pi k \frac{n}{N}}$$

$$= \sum_{n=0}^{N-1} I_n^0 e^{i\pi k \frac{n}{N}} + 0 \qquad \text{(C.23)}$$

$$= \sum_{n=0}^{N-1} I_n e^{i\pi k \frac{n}{N}}$$

$$= \sum_{n=0}^{N-1} I_n e^{i2\pi k \frac{n}{N}} e^{-i\pi k \frac{n}{N}}$$

To mathematically explain the DFT result in equation C.23, consider the convolution theorem which is as valid for the DFT as it is for the FT. The full DFT of the interferogram is shown as $S_k^c$ while the measured spectrum is $S_k^m$; $g_n$ is then the discrete apodization function of the measurement, with FT $G_k$.

$$S_k^c = \sum_{n=-\infty}^{\infty} I_n e^{i\pi kn}$$

$$S_k^m = \sum_{n=-\infty}^{\infty} g_n I_n e^{i\pi kn}$$

$$S_k^m = \sum_{p=-\infty}^{\infty} G_p S_{p-k}^c \qquad \text{(C.24)}$$

$$S_k^m = S_p^c * G_p$$

It can be seen that the point limited DFT from equation C.23 is the convolution of the DFT of the $e^{-i\pi k \frac{n}{N}}$ factor with the prior spectrum. This is convenient, as it is widely known that the FT of an exponential of this form is a Dirac delta

function, thus the DFT of the exponential factor is a discrete Dirac delta function. The additional discrete spectrum points are just the sampled values of the spectrum without additional distortion; the spectrum is not affected by the zero filling.

$$S_k^0 = \left( \sum_{n=0}^{N-1} I_n e^{i2\pi k \frac{n}{N}} \right) * \left( \sum_{n=-\infty}^{\infty} e^{-i\pi k \frac{n}{N}} e^{i\pi kn} \right)$$

$$\sum_{p=-\infty}^{\infty} e^{-i\pi k \frac{n}{N}} e^{i\pi kp} = \delta(k - \frac{2}{N}) \qquad\qquad\text{(C.25)}$$

$$S_k^0 = S_p * \delta(p - \frac{2}{N})$$

The interpolated spectrum resulting from the zero filling can then be seen as the same as fitting a sinc function to each point in the non-zero-filled spectrum, so that the sum of all the fitted sinc functions gives the same values as all the discrete points sampled. The sum of these fitted sinc functions is then sampled when adding data points to the spectrum by zero filling. It should be noted that the sinc function is only valid for boxcar apodization, it is in general the FT of whatever apodization function is used on the interferogram.

### C.2.5.3. Phase Correction

The intensity of light is always a real value, however, the result of a complex FT is in general complex. This complex spectrum results from measuring a spectrum with an interferometer because it is possible for phase errors to occur. These errors, which have a multitude of causes, can be corrected in either the spectral or inteferogram domains.

Phase errors manifest in the spectrum and inteferogram, where $S_{pe}(\nu)$ is the spectrum with the phase error, $S(\nu)$ that without, and $\phi(\nu)$ the phase error, are shown as:

$$S_{pe}(\nu) = S(\nu)e^{i\phi(\nu)}$$

$$I_{pe}(\Delta x) = \int_{-\infty}^{\infty} S_{pe}(\nu)e^{2\pi i\nu\delta x}d\nu \tag{C.26}$$

The phase error spectrum contains complex modulations with respect to $\nu$. The convolution theorem can be used to express this differently, so that the interferogram with phase errors present is the convolution of the interferogram, with the FT of the phase error function $g(\nu) = e^{i\phi(\nu)}$. This is then shown in equation C.27; where $I_{pe}(\Delta x)$ is the interferogram with the phase error, $I(\Delta x)$ that without, and $G(\nu)$ the FT of $g(\nu)$.

$$
\begin{aligned}
I_{pe}(\Delta x) &= \int_{-\infty}^{\infty} S_{pe}(\nu)e^{2\pi i\nu\delta x}d\nu \\
&= \int_{-\infty}^{\infty} S(\nu)e^{i\phi(\nu)}e^{2\pi i\nu\delta x}d\nu \\
I(\Delta x) &= \int_{-\infty}^{\infty} S(\nu)e^{2\pi i\nu\delta x}d\nu \\
G(\Delta x) &= \int_{-\infty}^{\infty} e^{i\phi(\nu)}e^{2\pi i\nu\delta x}d\nu \\
I_{pe}(\Delta x) &= I(\Delta x) * G(\Delta x) \\
&= \int_{-\infty}^{\infty} I(\Delta x - \omega)G(\omega)d\omega
\end{aligned}
\tag{C.27}
$$

It should be noted that the phase error can arise due to discrete sampling problems, but the same final problem can arise due to other causes. The mathematical correction to both the spectrum and interferogram is discrete blind, that is the equations shown here all use the integral form of the FT but the conclusions reached are identical if the DFT is used. As a second note all quantities in this phase correction section, such as $S(\nu)$, are actually the average expected values $\overline{S(\nu)}$.

**Causes of Phase Errors**

There are various root causes of phase errors, however, there is only one fundamental reason, a lack of symmetry. Phase errors are caused by a lack of symmetry about the zero OPD point of the interferogram. This can be seen by inspection of the complex FT, equation C.28; where the $e^{2i\pi\nu\Delta x}$ factor is split into symmetric and non-symmetric cos and sin components respectively. The symmetric components of $F(\Delta x)$ will be non-zero in the cosine term, and the non-symmetric components in the sine term.

$$
\begin{aligned}
f(\nu) &= \int_{-\infty}^{\infty} F(\Delta x)e^{2i\pi\Delta x\nu}d\Delta x \\
f(\nu) &= \int_{-\infty}^{\infty} F(\Delta x)\cos(2\pi\Delta x\nu)d\Delta x + \int_{-\infty}^{\infty} F(\Delta x)\sin(2\pi\Delta x\nu)d\Delta x
\end{aligned}
\tag{C.28}
$$

The first cause is mis-attributing the zero OPD point in the interferogram when taking the FT, this causes an offset in the $\Delta x$ position and immediately makes the interferogram non-symmetric. If the zero OPD position is offset by $-Y$ from the true position, the spectrum becomes as shown in equation C.29; this phase error is then constant for all $\nu$. In any real measurement the interferogram is discretely sampled, the same phase shift occurs if the zero OPD point is missed due to finite sampling error.

$$S(\nu) = \int_{-\infty}^{\infty} I(\Delta x)e^{2i\pi\Delta x\nu}d\Delta x$$

$$\Delta x \to \Delta X + Y$$

$$d\Delta x = d\Delta X$$

$$S_{OPDerror}(\nu) = \int_{-\infty}^{\infty} I(\Delta X + Y)e^{2i\pi(\Delta X + Y)\nu}d\Delta X$$

$$S_{OPDerror}(\nu) = e^{2i\pi Y\nu} \int_{-\infty}^{\infty} I(\Delta X + Y)e^{2i\pi\Delta X\nu}d\Delta X$$

$$S_{OPDerror}(\nu) = e^{2i\pi Y\nu}S(\nu)$$

(C.29)

The second cause of phase errors is dispersion of light as it passes through a medium. As most spectra are not taken in a perfect vacuum, and indeed often FTS is used to measure the transmission of light through some material sample, the light in the interferometer must travel through some medium. The frequency dependent refractive index of the medium, and the air itself in the interferometer, causes the OPD that each wavelength travels through to differ.

In any normal measurement the primary cause of dispersive phase errors is the different optical distance travelled through the beam splitter. One of the two optical pathways must pass completely through twice, and the other only once. As the dispersion and thickness of the beam splitter is known, in order to be designed in the first place, a compensating optical plate can be placed into the single pass through spectrometer arm. This compensating plate will then have the same optical distances as that of theBS; a different compensator plate is then likely to be required for each different BS.

The differing, wavelength dependant, optical distances cause the $\Delta x$ factor to also include a wavenumber dependant term, $\theta(\nu)$,.

$$\Delta x \rightarrow \Delta x + \theta(\nu)$$

$$S_{Dispersionerror}(\nu) = \int_{-\infty}^{\infty} I(\Delta x) e^{2i\pi(\Delta x + \theta(\nu))\nu} d\Delta x$$

$$S_{Dispersionerror}(\nu) = e^{2i\pi\nu\theta(\nu)} \int_{-\infty}^{\infty} I(\Delta x) e^{2i\pi\Delta x\nu} d\Delta x \qquad \text{(C.30)}$$

$$S_{Dispersionerror}(\nu) = e^{2i\pi\nu\theta(\nu)} S(\nu)$$

It is not immediately obvious how dispersion caused phase errors make the interferogram non-symmetric, but by considering the $e^{2i\pi\nu\theta(\nu)}$ factor in equation C.30 it becomes clear. As the FT of a symmetric function is symmetric and vice versa for non-symmetric functions, if $e^{2i\pi\nu\theta(\nu)}$ is symmetric then there will be no phase error as the spectra will be purely real and vice versa. This highlights a problem that would be extremely worrying if it were not so easily solvable, that is, the dispersion phase error is symmetric then no phase error is detectable. The spectrum that resulted from a symmetric phase error would be incorrectly scaled along the wavenumber scale. However, this can be completely avoided by the inclusion of a known reference light beam, which is typically present and used to determine the mirror position in an interferometer as per the Connes advantage, as described in section C.2.4.3. It is also very unlikely that a symmetric phase error spectrum would occur, the first two causes listed here cannot cause this.

A third cause of phase errors is due to mirror misalignment and optical beam divergence within the interferometer. As the OPD between the mirrors is increased, the mirror position increases, and thus the deviation of the light path increases. In the case of beam divergence it is only the extreme light paths that are affected; the central light path can be assumed to remain unaffected. This is not as simple to show as the prior two causes of phase error, as it depends on the mirror angle, beam divergence and mirror distance. This clearly affects the symmetry of the interferogram,

as the OPD deviance increases with mirror movement and thus is non-symmetric.

A fourth cause is the phase shift caused by the detection electronics, which regardless of design (e.g. parasitic capacitance, inductance will always occur to some extent), will act to shift the phase of different frequency signals a differing amount. Electrical caused phase shift imposes a lack of symmetry in the same way that dispersion does.

A fifth cause is the selection of a non-symmetric apodization function, which by definition imposes a lack of symmetry upon the interferogram.

All the induced phase shifts can be corrected by the same techniques.

**Non-Symmetric Interferograms**

It can sometimes be assumed that phase errors vary slowly, allowing a deliberate measurement of non-symmetric interferograms[178] The key reason for this is that the resolution in the spectral domain is inversely proportional to the length of the interferogram. If there is a practical limitation for the distance that the mirror can move, a lopsided interferogram can be measured, which can then be used to compute a low resolution phase spectrum and this can be used to correct the higher resolution spectrum. Using a non-symmetric interferogram requires the use of targeted apodization functions, as the additional signal components from the extra length of interferogram on one side, will be disproportionately weighted in the final spectrum compared to those only present in the symmetric part. Thus the apodization function must weight the symmetric part of the interferogram so that the average weighting factor is one half. As discontinuities are to be avoided in apodization functions, the most simple example of this is shown by using a trapezoid connecting to a rectangle, where the trapezoid slope passes through half at the zero OPD point.

**Correcting the Spectrum Phase: The Mertz Method**

To correct the phase error in the spectrum there is a very simple and effective method, developed by Mertz [179]. Calculate the phase of the complex number at each point in the spectrum $S_{pe}(\nu)$ , and then multiply the spectrum by the inverse phase at that point. This is multiplicative phase correction.

$$
\begin{aligned}
S_{pe}(\nu) &= S(\nu)e^{i\phi(\nu)} \\
S_{pe}(\nu) &= S(\nu)\Big( \cos(\phi(\nu)) + i\sin(\phi(\nu)) \Big) \\
\phi(\nu) &= \arctan(\frac{\Re(S_{pe}(\nu))}{\Im(S_{pe}(\nu))}) \\
S_{Mertz}(\nu) &= S(\nu) = S_{pe}(\nu)e^{-i\phi(\nu)}
\end{aligned}
\tag{C.31}
$$

For comparison purposes with the power spectrum, the propagation of variance in the Mertz phase corrected spectrum must be considered. For this purpose only Poissonian intensity noise is considered. It can be shown how the variance in the light intensity should propagate into the complex phase error spectrum $S_{pe}(\nu)$, assuming that $\Delta x$, $\nu$, and $\phi(\nu)$ are all ideal and have no error or variance associated with them. If there is no variance associated with the phase angle $\phi$, then the variance of the phase error spectrum $S_{pe}(\nu)$ is the same as that of the power spectrum, thus I split the real and imaginary parts and consider their variance individually.

$$S_{pe}(\nu) = e^{i\phi(\nu)} \int_{-\infty}^{\infty} I(\Delta x)e^{i2\pi\nu\Delta x}d\Delta x$$

$$S_{pe}(\nu) = e^{i\phi(\nu)}S(\nu)$$

$$\Re\{S_{pe}(\nu)\} = \cos\big(\phi(\nu)\big)S(\nu)$$

$$\Im\{S_{pe}(\nu)\} = \sin\big(\phi(\nu)\big)S(\nu) \tag{C.32}$$

$$Var[\Re\{S_{pe}(\nu)\}] = \cos^2\big(\phi(\nu)\big)Var[S(\nu)]$$

$$Var[\Im\{S_{pe}(\nu)\}] = \sin^2\big(\phi(\nu)\big)Var[S(\nu)]$$

The Mertz phase corrected spectrum is expressed:

$$
\begin{aligned}
S_{Mertz}(\nu) &= \Big(\Re\{S_{pe}(\nu)\} + i\Im\{S_{pe}(\nu)\}\Big)e^{-i\phi(\nu)}\\
&= \Big(\Re\{S_{pe}(\nu)\} + i\Im\{S_{pe}(\nu)\}\Big)\Big(\cos\big(-\phi(\nu)\big) + i\sin\big(-\phi(\nu)\big)\Big)\\
&= \Big(\Re\{S_{pe}(\nu)\} + i\Im\{S_{pe}(\nu)\}\Big)\Big(\cos\big(\phi(\nu)\big) - i\sin\big(\phi(\nu)\big)\Big)\\
&= \Re\{S_{pe}(\nu)\}\cos\big(\phi(\nu)\big) + i\Im\{S_{pe}(\nu)\}\cos\big(\phi(\nu)\big)\\
&\quad - \Re\{S_{pe}(\nu)\}i\sin\big(\phi(\nu)\big) - i\Im\{S_{pe}(\nu)\}i\sin\big(\phi(\nu)\big)\\
&= \Re\{S_{pe}(\nu)\}\cos\big(\phi(\nu)\big) + \Im\{S_{pe}(\nu)\}\sin\big(\phi(\nu)\big)\\
&\quad - i\Re\{S_{pe}(\nu)\}\sin\big(\phi(\nu)\big) + i\Im\{S_{pe}(\nu)\}\cos\big(\phi(\nu)\big)
\end{aligned}
\tag{C.33}
$$

As the Mertz corrected phase spectrum must be purely real, the complex components must cancel.

$$\Re\{S_{pe}(\nu)\}\sin\big(\phi(\nu)\big) = \Im\{S_{pe}(\nu)\}\cos\big(\phi(\nu)\big)$$

$$S_{Mertz}(\nu) = \Re\{S_{pe}(\nu)\}\cos\big(\phi(\nu)\big) + \Im\{S_{pe}(\nu)\}\sin\big(\phi(\nu)\big) \tag{C.34}$$

The variance in the Mertz phase corrected spectrum is then the sum of the square of the coefficients times the variances of the real and imaginary components, plus a covariance term, because the real and imaginary components are not independent. Evaluating this and neglecting the covariance term gives equations C.35 and C.36. The covariance term is neglected here because this is only used to compare to the same result for the power spectrum method. While both have covariance terms the ultimate point is that the power spectrum results in a nosier spectrum, not to specify the exact noise which has multiple other contributing factors that have been neglected here.

$$
\begin{aligned}
Var[S_{Mertz}(\nu)] &= Var[\Re\{S_{pe}(\nu)\}]\cos^2\big(\phi(\nu)\big) + Var[\Im\{S_{pe}(\nu)\}]\sin^2\big(\phi(\nu)\big) \\
&= \cos^2\big(\phi(\nu)\big)Var[S(\nu)]\cos^2\big(\phi(\nu)\big) + \sin^2\big(\phi(\nu)\big)Var[S(\nu)]\sin^2\big(\phi(\nu)\big) \\
&= Var[S(\nu)]\cos^4\big(\phi(\nu)\big) + Var[S(\nu)]\sin^4\big(\phi(\nu)\big) \\
&= Var[S(\nu)]\bigg(\cos^4\big(\phi(\nu)\big) + \sin^4\big(\phi(\nu)\big)\bigg)
\end{aligned}
$$

(C.35)

$$
Var[S_{Mertz}(\nu)] = Var[S(\nu)]\bigg(\cos^4\big(\phi(\nu)\big) + \sin^4\big(\phi(\nu)\big)\bigg)
$$

(C.36)

Mertz phase correction results in a spectrum with greater noise than one without phase correction.

### Correcting the Interferogram Phase: the Forman Method

Just as multiplication and convolution are linked via the convolution theorem, phase correction can be applied by a convolution method rather than the multiplicative Mertz method. Forman is widely credited with creating this method.[180] This is

achieved by taking the FT of the Mertz phase spectrum $e^{i\phi(\nu)}$, and then convolving this with the interferogram, and is mathematically identical to the Mertz method, and yet also more computationally demanding.

$$S_{pe}(\nu) = \int_{-\infty}^{\infty} I_{pe}(\Delta x)e^{2i\pi\Delta x\nu}d\Delta x$$

$$S_{pe}(\nu) = \int_{-\infty}^{\infty} I(\Delta x)e^{i\phi(\nu)}e^{2i\pi\Delta x\nu}d\Delta x$$

$$G(\Delta x) = \int_{-\infty}^{\infty} e^{-i\phi(\nu)}e^{2i\pi\Delta x\nu}d\nu \qquad (C.37)$$

$$S(\nu) = S_{pe}(\nu) * G(\Delta x)$$

$$S(\nu) = \int_{-\infty}^{\infty} S_{pe}(\nu - \tau)G(\tau)d\tau$$

**Power Spectrum**

The simplest method for correcting phase errors is by calculating the power spectrum. This is achieved by squaring the magnitude of both the real and imaginary components of the FT spectrum, adding them, and then taking the square root. The final spectrum must then be real, and this is shown in equation C.38.

$$S_{power}(\nu) = S(\nu) = |S_{pe}(\nu)e^{-i\phi(\nu)}| = \sqrt{|\Re(S_{pe}(\nu))|^2 + |\Im(S_{pe}(\nu))|^2} \qquad (C.38)$$

However, it is widely claimed that the power spectrum increases noise in a non-linear manner compared to the other methods. [178] To attempt to show this in comparison to Mertz phase correction, the first order expansion of the variance using the delta method can be taken:

$$S_{power}(\nu) = \sqrt{|\Re(S_{pe}(\nu))|^2 + |\Im(S_{pe}(\nu))|^2}$$

$$Var[S_{power}(\nu)] \approx \left(\frac{|\Re(S_{pe}(\nu))|}{S_{power}(\nu)}\right)^2 Var[|\Re(S_{pe}(\nu))|] + \left(\frac{|\Im(S_{pe}(\nu))|}{S_{power}(\nu)}\right)^2 Var[|\Im(S_{pe}(\nu))|]$$

$$\approx \left(\frac{|\cos\left(\phi(\nu)\right)S(\nu)|}{S_{power}(\nu)}\right)^2 \cos^2\left(\phi(\nu)\right)Var[S(\nu)]$$

$$+ \left(\frac{|\sin\left(\phi(\nu)\right)S(\nu)|}{S_{power}(\nu)}\right)^2 \sin^2\left(\phi(\nu)\right)Var[S(\nu)]$$

$$\approx \left(\frac{|\cos\left(\phi(\nu)\right)S(\nu)|}{S(\nu)}\right)^2 \cos^2\left(\phi(\nu)\right)Var[S(\nu)]$$

$$+ \left(\frac{|\sin\left(\phi(\nu)\right)S(\nu)|}{S(\nu)}\right)^2 \sin^2\left(\phi(\nu)\right)Var[S(\nu)]$$

$$\approx \left(\cos\left(\phi(\nu)\right)\right)^2 \cos^2\left(\phi(\nu)\right)Var[S(\nu)]$$

$$+ \left(\sin\left(\phi(\nu)\right)\right)^2 \sin^2\left(\phi(\nu)\right)Var[S(\nu)]$$

$$\approx \left(\cos^4\left(\phi(\nu)\right) + \sin^4\left(\phi(\nu)\right)\right)Var[S(\nu)]$$

$$(C.39)$$

This shows that the first order approximation to the variance in the power spectrum is the same as the variance in the Mertz corrected spectrum. In addition to the first order terms, the power spectrum has second, third, etc terms; each of the additional terms must be positive and real, thus the total variance in the power spectrum is greater than that of the Mertz. A similar comparison can be made for the covariance term that has been neglected in both the Mertz and power spectrum variance analyses.

## C.3. Rapid Scan Fourier Transform Spectroscopy

Rapid scan FTS is the most widely used form of FTS. In Rapid Scan Fourier Transform Spectroscopy (RSFTS), the OPD between the two split light beams is

varied by scanning one of the mirrors through a set of positions at ideally constant speed. Hence the name rapid scan, as the mirror rapidly moves through the OPD positions.

If the speed of the mirror movement is $V$ then the OPD, $\delta x$, varies as $2Vt$. This gives the measured interferogram, $I(\delta x)$. The interferogram is:

$$I(t) = \frac{A_0^2}{2}\cos(k2Vt) \tag{C.40}$$

There are several points that must be considered when performing a rapid scan measurement, which are described in the following sections.

## C.3.1. Electronic Coupling: AC for Rapid Scan

Alternating Current (AC) coupling allows changes in the measured intensity to be recorded, removing any baseline offset in the measurement and increasing the effective signal discrimination for the same number of bits in the Analogue to Digital Converter (ADC). This occurs because the mirror is rapidly scanned and thus the measured intensity at the detector rapidly changes. This change in the interferogram intensity is about a non-zero point, as there is a non-zero baseline in a interferomic measurement as shown earlier in equation C.7.

The detector in the interferometer is typically connected to an amplification and digitization electronic circuit comprised of amplifiers, filters and an ADC, with AC coupling . That circuit will have an inductance, and a capacitance, which gives the electronic component of the detector a characteristic frequency dependent response time. The effect of OPD differences on the signal measured is relative to the wave-

length and the mirror movement speed, the electronic response time must be fast enough that the measured signal has reached approximately the correct value before the mirror has moved too far.

The detector will also be sensitive to light of a specific wavenumber range, $k_{lower} < k < k_{upper}$ , with mirror movements also having a set of rapid scanning speeds. This allows the tuning of the detection electronic circuits to have a capacitive low frequency cut-off point below or near $k2V$ (from equation C.40). As a result of this, non interferogram related signals can be attenuated out, increasing SNR. As a contrast, Direct Current (DC) coupled connections allow all frequency components detected to pass, and include the constant offset that AC coupling avoids.

The measured signal is digitized by an ADC with a certain number of bits to a signal range, consequently there is a minimum signal discrimination. Using DC coupling for rapid scan measurements includes the constant offset and thus reduces the dynamic range or signal discrimination precision of the ADC. In turn the SNR is also reduced.

## C.3.2. Fundamental Advantages of Rapid Scan FTS

### C.3.2.1. Mirror Movement Speed: Greater SNR

The primary advantage of rapid scan spectroscopy is the measurement speed, typically allowing a greater SNR in the same time as could result from any other measurement in the same time under the same conditions.

Interferogram intensity depends upon OPD alone in the simple wave picture, but when viewed as photon states we obtain Poissonian noise in the measured interferogram intensity at any OPD point. However, as the OPD is constantly varied, repeated measurements can quickly be obtained. Without considering digitization

electronics, and assuming that the measurement is taken in a gas or vacuum not optically active in the spectral range measured, the interferogram is symmetrical with respect to mirror movement direction.

The moving mirror can move from $-W$ to $+W$ and then back to $-W$, with data having been collected continuously, resulting in two sets of data in a short time. Adding multiple interferograms or spectra together, the noise in the interferogram is reduced by $\sqrt{N}$; where $N$ is the number of full interferograms measured. This leads to a noise reduction of $\sqrt{2}$ relative to one measurement just to reposition the interferometer mirror in its original starting position. They key of this advantage is that rapid scan spectroscopy allows for many interferogram measurements in a set time.

The faster the scanning speed the more interferograms that can be obtained, however, other factors then become important. Detector and digitzation electronics response times, wavelength of the interferometer position reference beam, physically moving the mirror at high speed, obtaining a significant amount of light on the detector to average, and having the light from one OPD point averaged on the detector long enough that the oscillations at the lights frequency are averaged over, are all important effects limiting the possible rapid scan speeds.

## C.3.3. Fundamental Limitations of Rapid Scan FTS

There are several limitations imposed by the rapid mirror movement in RSFTS. Indeed these faults are present to some extent no matter what the mirror speed, as long as the mirror is moving while the interferogram is being measured they can only be reduced and not removed.

## C.3.3.1. Mirror Movement: Vibrations

Rapid scan spectroscopy requires that the orientation of the mirrors in the interferometer does not change. As discussed in section C.2.3.2, a misaligned mirror or divergent light beam restricts the resolution and efficacy of an interferometer. At any instant in time a mirror that is vibrating is essentially a deformed surface, thus the different regions of the mirror are misaligned. This will change the interference conditions at the detection point, and reduce the effective signal, or render the measurement useless. These effects will depend upon the size of the vibration relative to the wavelength of the light measured, the distance of the mirror movement, and the angular divergence of the light beam.

## C.3.3.2. Mirror Movement: Speed

In what may initially appear to contradict section C.3.2.1, the rapid movement of the scanning mirror may cause a low SNR. In an ideal detector system this disadvantage would never become apparent. Any detector will integrate or average the light signal over time, rather than responding instantaneously to the electric field. The detector and related electronics will also have a certain amount of noise, both from acting as antennae, the Poissonian shot noise of electrical current variations and thermally generated noise (dark current). As the mirror scanning velocity $V$ is increased, it is clear that the averaging time at each OPD point will decrease. If the averaging time is too low then certain optical frequencies will not be averaged and the measured signal will not be representative of the true spectrum.

## C.3.3.3. Time Evolving Spectrum

The final limitation of the rapid scan technique arises if a spectrum that is changing in time must be measured. Taking the mirror movement speed to be $V$ the interferogram is then $I(Vt)$, which upon FT is only going to lead to a valid spectrum if the measured light is not changing significantly in the time scale of the measurement.

The distortion of a time changing spectrum by a rapid scan measurement can be seen by a simple thought experiment, consider a perfectly flat incident spectrum of intensity $A_0$ that is decaying exponentially with form $e^{-\frac{t}{\tau_0}}$. The interferogram and the spectrum would then evolve in time.

$$I(Vt) = A_0 e^{-\frac{t}{\tau_1}}$$
$$S(\nu) = \int_{-\infty}^{\infty} A_0 e^{-\frac{t}{\tau_0}} e^{2i\pi\nu\Delta x} d\Delta x \qquad \text{(C.41)}$$

Substituting $t$ as:

$$\Delta x = Vt$$
$$t = \frac{\Delta x}{V} \qquad \text{(C.42)}$$

It is recognised that the FT of an exponential is a Dirac delta function.

$$\int_{-\infty}^{\infty} \delta(\nu - p)e^{-2i\pi\nu\Delta x} d\nu = e^{-2i\pi p\Delta x} \qquad \text{(C.43)}$$

The final spectrum is then:

$$e^{-\frac{\Delta x}{V\tau_0}} = e^{-2i\pi p\Delta x}$$

$$-\frac{\Delta x}{V\tau_0} = -2i\pi p\Delta x$$

$$-\frac{i}{2\pi V\tau_0} = p$$

$$S(\nu) = \int_{-\infty}^{\infty} e^{-\frac{t}{\tau_0}} e^{2i\pi\nu\Delta x} d\Delta x$$

$$= A_0 \int_{-\infty}^{\infty} e^{-\frac{\Delta x}{V\tau_0}} e^{2i\pi\nu\Delta x} d\Delta x$$

$$S(\nu) = A_0\delta(\nu + -\frac{i}{2\pi V\tau_0})$$

(C.44)

There are two key points here; attempting to measure a significantly time evolving spectrum with the rapid scan technique leads to the distortion of the spectrum, and the resulting spectrum is complex, not in intensity as in phase errors, but in frequency (wavenumber or energy scale). The time change of the spectrum results in a phase offset in frequency.

If the light is changing significantly during the whole rapid scan measurement, the resulting measurements are not correct.

## C.4. Time Resolved Step Scan FTS

While rapid scan spectroscopy allows the fast acquisition of high SNR spectra, it is not the optimum technique for measuring a time evolving spectrum. The simplest FT based technique for measuring time evolving spectra is know as the step scan technique. SSFTS modifies the rapid scan technique to allow for the measurement of transient spectra, however, there are some limitations to the time resolution possible. The key factor in determining whether the step scan method can be used at all, is whether the spectrum in energy and temporal dimensions is repeatable on

demand. The time evolution of the spectrum must be able to be triggered to begin on demand, for as many times as the interferogram intensity would be measured to obtain a non time evolving spectrum.

Firstly, the modification to go from rapid scan to step scan is simple. Recall the key detail of the FTS interferometer as used for rapid scan, a Michelson interferometer with two optical paths, one of variable length, and each ending in a mirror. For step scan instead of the interferometer mirror constantly moving and the interferogram intensity being measured discretely during that movement, the mirror is moved between discrete positions, and then stopped, the measurement is then triggered and then the interferogram intensity at that OPD position is measured every $\Delta t$ for total $T_{max}$ time. The mirror is then moved, or "stepped", to the next discrete position and the time evolution of the interferogram at this OPD is then measured as before. This allows the building up of a 2D grid of interferogram data points, $I(n_x \Delta x, n_t \Delta t)$; where $n_x$ and $n_t$ are the OPD and time indexes. The 2D grid of data is then a set of $\Delta t$ time separated interferograms, shown in figure C.7 which when Fourier transformed will be a set of $\Delta t$ time separated spectra.
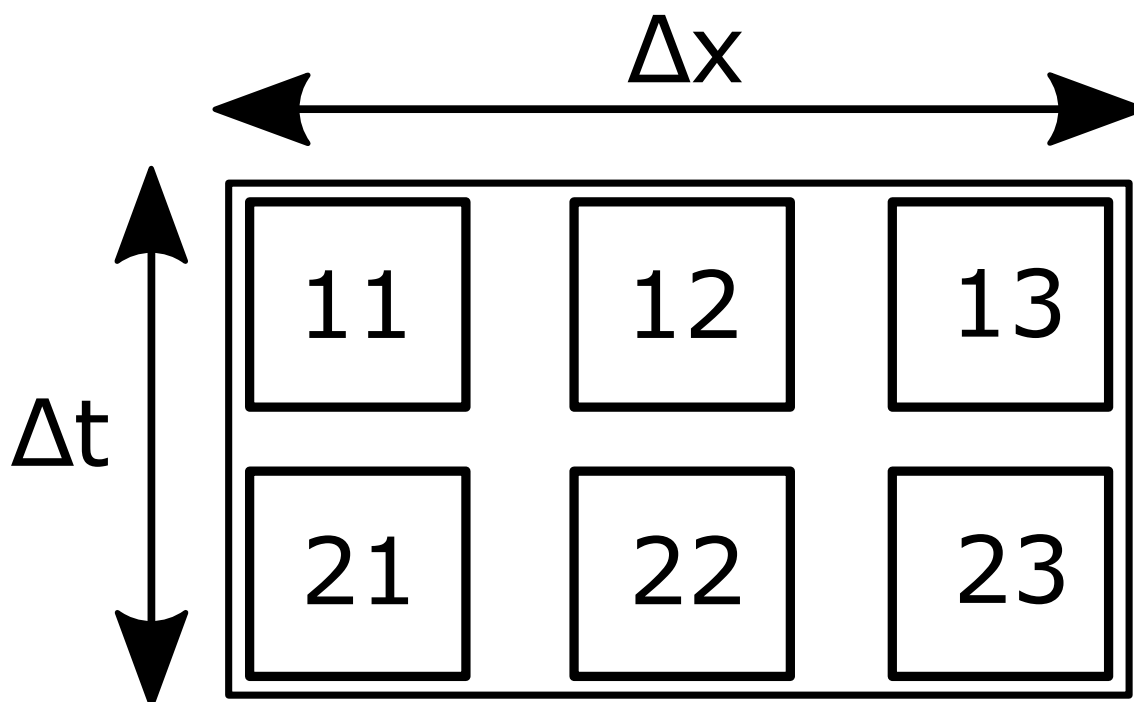
Figure C.7.: 2D grid showing the data capture of a step scan measurement. Each block represents the intensity of the light as measured by a detector at one $n_x \Delta x$ and $n_t \Delta t$ position. For a sample step scan measurement; the interferometer mirror is in position 1, the experiment or other cause of the spectrum to be measured is triggered and the signal intensity is measured and stored in as block 11, then $\Delta t$ time elapses the signal is measured again and this time stored as block 12, the mirror is then "stepped" to position 2 and the spectrum is triggered again, the signal is measured and stored as block 21, $\Delta t$ time elapses and the signal is measured and stored as block 22, and so on until the grid is fully filled. In this representation each row is a time separated interferogram.

The relationship between the interferograms and spectra, and how the time change of the spectra is measured, shown in figure C.8.
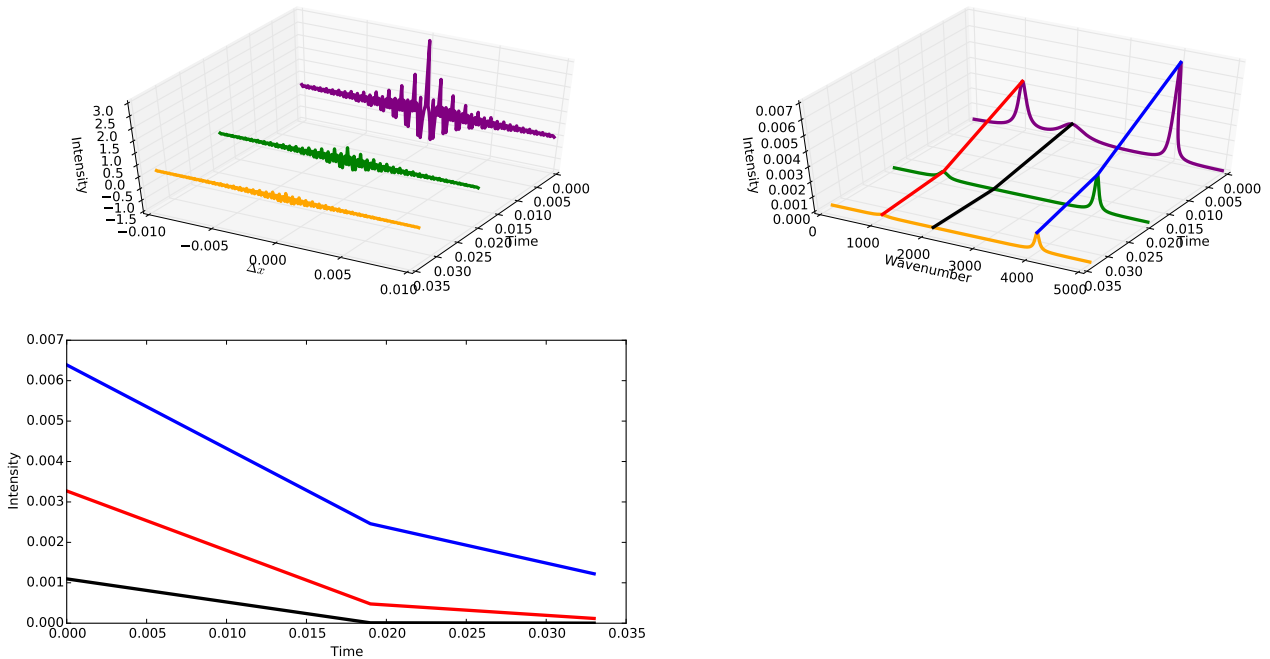
Figure C.8.: Plotted here are the interferograms and resulting FT spectra of a time decaying optical signal at several times. The purple, green, and yellow curves correspond to each other and are the first second and third measurements respectively. The time decay of the various peak intensities is also plotted. **Top Left)** Interferograms **Top Right)** Spectra **Bottom Left)** Spectrum peak Intensities as a function of time.

The separation of the discrete mirror positions is, of course, determined by the Shannon-Nyquist criteria, section D.3.1.1, thus the points are separated by at most half the wavelength of the shortest wavelength expected to be measured. It is typical to allow for some settling time after the mirror has moved, this is because vibrations will be caused by the mirror movement which may reduce the coherence of the light being measured (see section C.2.3.2); depending on the optical intensity and shape of the spectrum and apodization function used, a reduction in optical coherence or a coherence loss caused reduction in intensity may adversely affect the SNR of the measurement.

Thus using the step scan technique with appropriate detectors, digitization electronics, sufficient mirror stabilization time and mirror movement length, and an experiment of sufficient repeatability, leads to a measured spectrum with time evolution information.

## C.4.1. Fundamental Limitations of SSFTS

The limits of the step scan technique are exactly the same as for rapid scan, or any other form of FTS, in the spectral or energy domain. The SNR improvements of rapid scan over dispersive spectroscopy, however, are also lessened. Finally, time resolution of any step scan measurement, or any other time resolved spectroscopic measurement, is limited by two factors.

Step scan measurements take longer to complete than rapid scan measurements. The causes for this are multiple, firstly the extra time required to step and stop the mirror along with any stabilization waiting time rather than the continous mirror movement as in rapid scan. Secondly, while at each mirror position the full time $T_{max}$ of the time measurement must pass before the mirror can be stepped. These two factors greatly extend the measurement time, although compared to a dispersive measurement that also had time resolution the FTS advantages remain. Thus the SNR improvement over a comparable DS measurement remains.

### C.4.1.1. Optical Time Limits

The step scan technique is physically limited in its time resolution. This originates from the fundamental interference between the two light beams in an interferometer, and the assumption in FTS that any detector is integrating or averaging over at least one full period of the longest wavelength light measured. Focusing on this fundamental optical interference limit, a simple consideration of the limit of time resolution in an interferometric spectrometer is shown here.

## C. Spectroscopy Methods

To begin, consider a two mirror interferometer, with one fixed and one moving mirror. Some light of arbitrary frequency distribution is emitted into the entrance aperture of the interferometer; this light then follows the same path as is standard, resulting in interference at a detector of light with some phase difference $\phi$. If the time $t$ refers to the time of the signal from the stationary mirror, then $t + \delta t$ is the time of the signal from the moving mirror. These quantities, where $c$ is the speed of light in a vacuum, $n$ the refractive index of the interferometer interior, $\omega$ is the angular frequency, and $\delta x$ the moving mirror displacement from the zero point, are related below.

$$
\begin{aligned}
\Delta t &= 2\delta x \frac{n}{c} \\
\phi &= 2\delta x \frac{2\pi}{\lambda} \\
&= 2\delta x \frac{n\omega}{c}
\end{aligned}
\qquad\qquad \text{(C.45)}
$$

Taking the maximum mirror displacement to be $\Delta L$, then the spectrometer will interfere light emitted at the times $t$ and $t + 2\frac{\Delta L n}{c}$. If the time resolution is then $\Delta t$ then light from between $t - \frac{\Delta t}{2}$ to $t + \frac{\Delta t}{2}$ cannot be distinguished. Therefore it might naively be expected that any light emitted at time $t > 2\frac{\Delta L n}{c}$ is just barely distinguishable from that emitted at time t. However, the light interfered is averaged over one full wavelength, thus the light must be incident upon the detector for the time $\frac{\lambda}{\frac{c}{n}} = \frac{n\lambda}{c} = \frac{1}{f}$ to be averaged. Combining these factors, it is found that the time resolution $\Delta t$ must be as:

$$\Delta t \geq 2\frac{\Delta L n}{c} + \frac{1}{f}$$
$$\geq 2\frac{\Delta L n}{c} + \frac{n\lambda}{c} \tag{C.46}$$
$$\geq \frac{n}{c}\left(2\Delta L + \lambda\right)$$

Using the first zero crossing minimum resolution criteria for spectral resolution.

$$\Delta L = \frac{1}{\Delta\nu}$$
$$\Delta t \geq \frac{n}{c}\left(\frac{2}{\Delta\nu} + \lambda\right) \tag{C.47}$$

Thus for any desired spectral resolution the corresponding best time resolution possible can be found. In reality this gives approximately ns resolution limits. If the spectral resolution is 0.075 $cm^{-1}$, and the longest wavelength measured is 1mm (the limits of IR), then the best time resolution possible is $4.7 \times 10^{-10}$s.
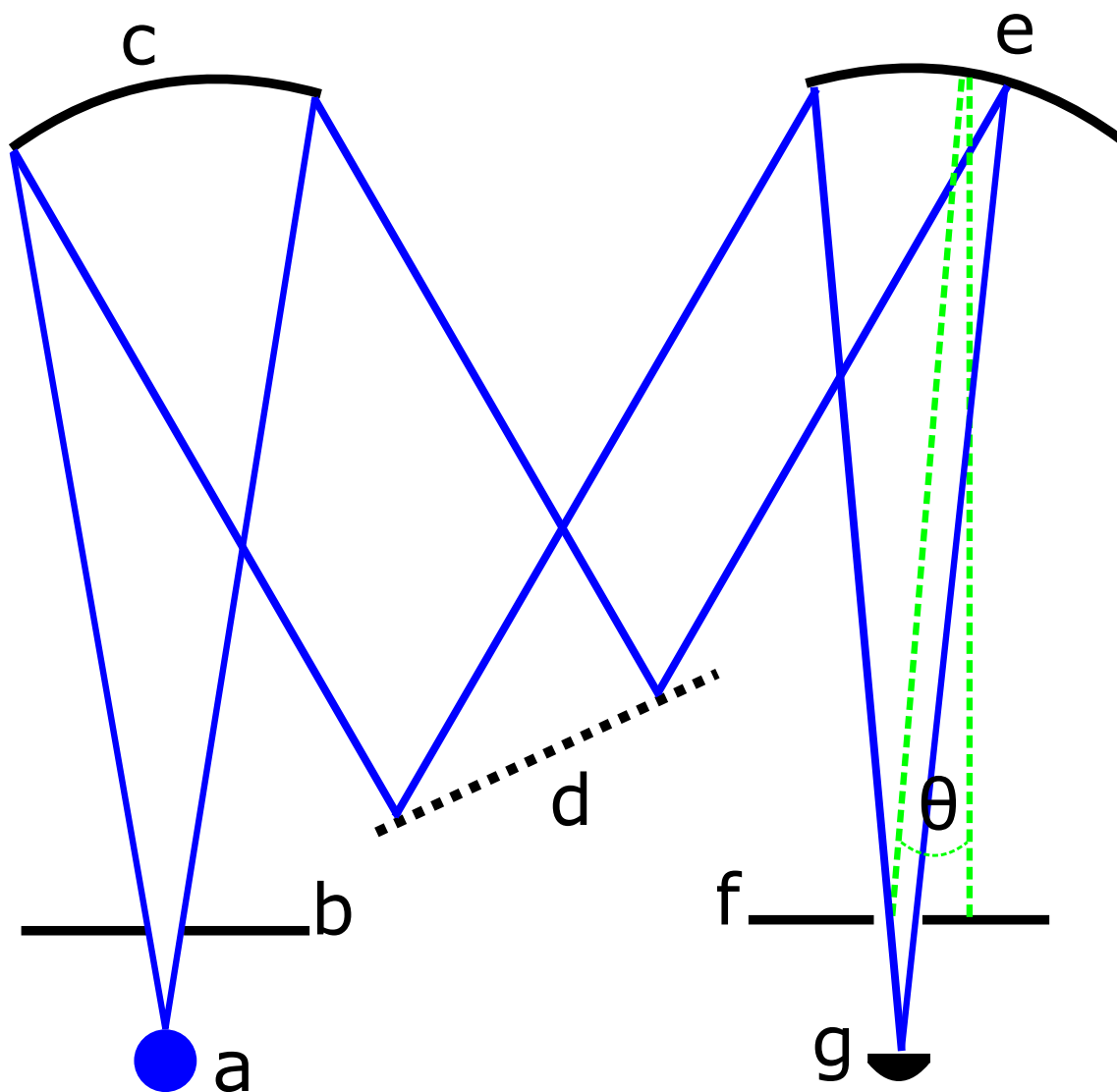
Figure C.1.: Generalisation of the Czerny-Turner monochromator design. **a)**Light Source **b)** Entrance Aperture **c)** Collimating Mirror **d)** Diffraction Grating OR Dispersive Element (prism) **e)** Focusing Mirror **f)** Exit Aperture **g)** Detection Point. $\theta$) The angle of each wavelength at the exit aperture, with respect to the line of normal incidence. This is a modified reproduction from [169, p 793, figure 2]

# D. The Fourier Transform

## D.1. Introduction

Fourier analysis is a method of expressing a function in terms of sine and cosine basis functions. This chapter contains a discussion of the FT, FS and the various limiting factors which are applicable to practical use. Beginning with the FS, I then proceed onto the FT as the generalised limiting case of an FS of a function with indefinite period. The discrete FT is then discussed, along with the limitations of popular methods to compute this quickly. Common artefacts in the FT are discussed, including aliasing, convolution, apodization and the behaviour of Dirac delta functions. This provides a solid foundation upon which to base later discussions of FTS in other chapters of this thesis.

## D.2. The Fourier Series

Named after Joseph Fourier (1768-1830), the FS is a method of expressing any periodic function as a discrete sum of sine and cosine functions, each with differing amplitude and frequency. If we have an abstract function $f(x)$, with a finite period such that it has frequency $\frac{1}{T}$, where T is the period, $A_0$ is the average value of the periodic function $f(x)$, while $A_n$ and $B_n$ are the amplitudes of the cosine and sine basis functions with frequency index $n$ respectively, then it can be represented by:

## D. The Fourier Transform

$$f(x) = \frac{1}{2}A_0 + \sum_{n=1}^{\infty} A_n \cos(nx) + \sum_{n=1}^{\infty} B_n \sin(nx) \qquad \text{(D.1)}$$

The amplitudes of the , $A_n$ and $B_n$, can be found by consideration of the orthogonality properties of sine and cosine functions.

$$\delta_{i,j} = \begin{cases} 0, & i \neq j \\ 1, & i = j \end{cases}$$

$$\int_{-\pi}^{\pi} \cos(ix)\cos(jx)dx = \pi\delta_{ij}$$

$$\int_{-\pi}^{\pi} \sin(ix)\sin(jx)dx = \pi\delta_{ij} \qquad \text{(D.2)}$$

$$\int_{-\pi}^{\pi} \cos(ix)\sin(jx)dx = 0$$

$$\int_{-\pi}^{\pi} \cos(ix)dx = 0$$

$$\int_{-\pi}^{\pi} \sin(ix)dx = 0$$

From the orthogonality relations of sine and cosine we can see that for $x \in [-\pi, \pi]$, only the integration of a sine or cosine multiplied by a sine or cosine of the same frequency results in a non-zero value; sine and cosine functions are not only orthogonal to each other, but to all other sine and cosine functions of differing frequency. The nth amplitude of the Fourier components are given by:

$$A_0 = \frac{1}{\pi} \int_{-\pi}^{\pi} f(x)dx$$

$$A_n = \frac{1}{\pi} \int_{-\pi}^{\pi} f(x)\cos(nx)dx \qquad \text{(D.3)}$$

$$B_n = \frac{1}{\pi} \int_{-\pi}^{\pi} f(x)\sin(nx)dx$$

This is only valid for the interval $[-\pi, \pi]$. To apply the Fourier series to the interval $[-S, S]$, where $S$ is an arbitrary limit, requires a change of variable.

$$
\begin{aligned}
x &= \frac{\pi y}{S} \\
dx &= \frac{\pi dy}{S}
\end{aligned}
\tag{D.4}
$$

The Fourier series can then be written as:

$$
\begin{aligned}
f(y) &= \frac{A_0}{2} + \sum_{n=1}^{\infty} A_n \cos(\frac{n\pi y}{S}) + \sum_{n=1}^{\infty} B_n \sin(\frac{n\pi y}{S}) \\
A_0 &= \frac{1}{S} \int_{-S}^{S} f(y) dy \\
A_n &= \frac{1}{S} \int_{-S}^{S} f(y) \cos(\frac{n\pi y}{S}) dy \\
B_n &= \frac{1}{S} \int_{-S}^{S} f(y) \sin(\frac{n\pi y}{S}) dy
\end{aligned}
\tag{D.5}
$$

While implied by the above, $[-S, S]$, any interval $[z_0, z_0 + 2S]$ for the function $f(z)$ with frequency $\frac{1}{S}$, is valid. All the information about the periodic function $f(x)$ is contained within one period of that function. Introducing Euler's formula for complex numbers allows the above to be written as:

$$
\begin{aligned}
e^{ix} &= \cos(x) + i\sin(x) \\
f(x) &= \sum_{n=-\infty}^{\infty} C_n e^{i2\pi n \frac{x}{2S}} \\
C_n &= \frac{1}{2S} \int_{-S}^{S} f(x) e^{2i\pi n \frac{x}{2S}} dx
\end{aligned}
\tag{D.6}
$$

## D.2.1. FS to Transform

The FS and FT are applicable to functions comprised of discretely spaced harmonics and a continuum of all frequencies respectively. Starting with:

$$f(x) = \sum_{-\infty}^{\infty} C_n e^{i2\pi n \frac{x}{2S}} \tag{D.7}$$

The FS can only be applied to periodic functions, but if we have a function that has no defined period or has a period extending into infinity then we can take the limit as $S \to \infty$.

$$L = \pi \frac{n}{S}$$
$$f(x) = \sum_{n=-\infty}^{\infty} C_n e^{ixL}$$
$$C_n \to C_n dn \tag{D.8}$$
$$f(x) \to \sum_{n=-\infty}^{\infty} C_n dn e^{ixL}$$

The interval between the harmonics in the FSbecomes an infinitesimal interval $dL$.

$$dn = dL\frac{S}{\pi} \tag{D.9}$$

Using equation D.9 the FS becomes:

$$f(x) = \sum_{n=-\infty}^{\infty} C_n dL \frac{S}{\pi} e^{ixL} \tag{D.10}$$

Taking the limit as S tends to infinity. As $S \to \infty$ , $L \to infintisimal$. Thus the

FS becomes the FT

$$f(x) = \int_{n=-\infty}^{\infty} C_n \frac{S}{\pi} e^{ixL} dL \tag{D.11}$$

To reach the conventional form of theFT, the coefficients $C_n$ must be changed to $C_L$. Rearranging and substituting equation D.8 into, $C_n \frac{S}{\pi}$, gives:

$$C_L = C_n \frac{S}{\pi} = \frac{S}{\pi} \frac{1}{2S} \int_{-S}^{S} f(x) e^{-ixL} dx \tag{D.12}$$

But in equation D.12 we must also take into account that, $S \to \infty$.

$$C_L = \frac{1}{2\pi} \int_{-\infty}^{\infty} f(x) e^{-ixL} dx$$
$$f(x) = \int_{-\infty}^{\infty} C_L e^{ixL} dL \tag{D.13}$$

Thus we obtain the FT.

## D.3. The Fourier Transform

The minimum necessary information to understand the FT. Replace $C_L$ from above with the continuous function $F(L)$. Thus we obtain the familiar FT; alternatively the FT can be expressed with a variable has been changed , $L = 2\pi X$.

$$f(x) = \int_{-\infty}^{\infty} F(L)e^{ixL}dL$$

$$f(x) = \int_{-\infty}^{\infty} F(X)e^{2\pi ixX}dX$$

$$F(L) = \frac{1}{2\pi}\int_{-\infty}^{\infty} f(x)e^{-ixL}dx \qquad \text{(D.14)}$$

$$F(L) = \int_{-\infty}^{\infty} f(x)e^{-2\pi ixX}dx$$

The FT is a transformation that expresses an abstract function dependant on variable $x$, $f(x)$, as a function of the variable conjugate to $x$; for example both energy and time, and position and momentium are pairs of conjugate variables. The FT does this by integrating over the overlap of the function multiplied a set of sine and cosine basis functions; i.e. projecting the function onto the set of basis functions.

## D.3.1. FT Theorems

In order to fully understand the limits of the FT, the origins of areftects and how to overcome them, two theorems are necessary. The Shannon sampling, and the convolution theorems.

### D.3.1.1. The Shannon sampling theorem

The Shannon sampling theorem, also called the Nyquist-Shannon theorem, tells us exactly what sampling rate to use. Sampling a function at this rate allows perfect reconstruction of the function, as long as it is a band-limited function. A band-limited function is a function, $f(t)$ with FT $F(\omega)$, such that it has no $\omega$ components past a certain cut off value $\omega_{max}$. $\omega$ is used instead of frequency $f$ to avoid confusion with function $f(t)$.

$$\omega = 2\pi f \qquad \text{(D.15)}$$

Shannon's original phrasing of the theorem is presented below.

*'THEOREM 1: If a function f(t) contains no frequencies higher than W cps, it is completely determined by giving its ordinates at a series of points spaced 1/2W seconds apart.'*[181]

I follow the derivation of Shannon [181] below. Firstly, let $F(\omega)$ be the FT of $f(t)$;

$$f(t) = \frac{1}{2\pi} \int_{-\infty}^{\infty} F(\omega)e^{i\omega t} d\omega \qquad (\text{D.16})$$

If the signal $F(\omega)$ does not contain any frequencies above $W$, and thus no angular frequencies $\omega$ above $2\pi W$, then the FT becomes:

$$f(t) = \frac{1}{2\pi} \int_{-2\pi W}^{2\pi W} F(\omega)e^{i\omega t} d\omega \qquad (\text{D.17})$$

Because there are assumed to be no frequencies above $W$, then the smallest time period of any frequency in the signal is $\frac{1}{W}$. It might be intuitively expected that to be able to tell the signal with period $\frac{1}{W}$ apart from its harmonics, $\frac{1}{2W}, \frac{1}{3W}...$, the signal must be measured at frequency $\frac{2}{W}$, that is double the frequency of the desired signal. If the time dependant function $f(t)$, with period $\frac{1}{W}$, is measured at the frequency $2W$, we sample the function at the intervals given by:

$$t_n = \frac{n}{2W}$$
$$n \in \mathbb{Z} \qquad (\text{D.18})$$

We can then express the bandwidth limited FT from equation D.17 as:

$$f(\frac{n}{2W}) = \frac{1}{2\pi} \int_{-2\pi W}^{2\pi W} F(\omega) e^{i\omega \frac{n}{2W}} \, d\omega \qquad (D.19)$$

*'The integral on the right will be recognized as essentially the nth coefficient in a Fourier-series expansion of the function F(w), taking the interval $-$ W to $+$ W as a fundamental period.'*[181]

Thus we can conclude that the sampling of the function $f(t)$, at rate $\frac{1}{2W}$, gives all the information required to determine the spectrum. As long at the function is perfectly band-limited. This vital to the later understanding of the phenomenon know as "aliasing", discussed in section D.3.3.1.

### D.3.1.2. The Convolution Theorem

The convolution theorem is vital to understanding the "spectral leakage" artefact of the FT, discussed in section D.3.3.2.

The convolution theorem is simply a relation between the FT of a pair of functions, and their overlap integral. Firstly, we must define a pair of functions, $f(t)$ and $g(x)$, and their Fourier transforms $F(\omega)$ and $G(\omega)$. The point-wise multiplication of $F(\omega)$ by $G(\omega)$ is the same as the Fourier transform of the convolution of their Fourier transforms, $f(t)$ and $g(x)$. Convolution is the shifting or "running" overlap integral; an overlap integral where one function is fixed in place while the other is run across the integration domain, thus the integration sums each point of each function with each point of the other. The convolution theorem, where $*$ is the convolution symbol and $\mathcal{F}\{d\}$ is shorthand for the FT of $d$, can be expressed as:

$$f(t) * g(t) = \int_{\infty}^{\infty} f(\tau)g(t - \tau)d\tau$$

$$\mathcal{F}(\omega)G(\omega) = \int_{-\infty}^{\infty} \left( \int_{\infty}^{\infty} f(\tau)g(t - \tau)d\tau \right) e^{i\omega t}dt$$

$$= \int_{-\infty}^{\infty} f(t) * g(t)e^{i\omega t}dt$$

$$\mathcal{F}(\omega)G(\omega) = F\{f(t) * g(t)\}$$

(D.20)

## D.3.2. The DFT

An inspection of the FT, equations D.14 and D.8, will reveal that to determine the arbitrarily long $f(x)$ the continuous function $F(L)$ is needed at all $L$ from $-\infty$ to $+\infty$. There are two problems with this. Firstly, the measured function $F(L)$ will never be measured continuously over an infinite set of data-points infinitesimally separated. Secondly, such a function, $f(x)$, will also not extend infinitely stretching from $-\infty to + \infty$. For any function $f(x)$ that is sampled in reality, we must determine at what rate to sample the function $\Delta x$ , and over what range of $L$, if we are to correctly reconstruct $f(x)$ from our measurement. The DFT is a way of expressing the FT in a discrete way, such that we can overcome the first of these problems. The DFT is closely related to the FS. Discretisingthe FT requires the several substitutions, along with the replacement of the integral with a finite sum over $L$. The sampling rate must be defined, thus we measure $f(x)$ for total $x_T$ with $N$ sampled data points. The Shannon sampling theorem gives the minimum sampling rate, $2L_{max}$, with point separation $\frac{1}{2L_{max}}$, for the band-limited function $F(L)$ with bandwidth $L_{max}$. Then the sampling rate becomes:

$$\Delta x = \frac{x_T}{N} = \frac{1}{2L_{max}}$$

$$\Delta L = \frac{2L_{max}}{N} = \frac{1}{\Delta x}$$

(D.21)

The discretisation changes are then:

$$
\begin{aligned}
&\textit{Continuous} \qquad \textit{Discrete} \\
&\qquad L \to n\Delta L \\
&\qquad x \to k\Delta x \\
&\qquad F(L) \to F_n \\
&\qquad f(x) \to f_k \\
&\qquad \int_{-\infty}^{\infty} \to \sum_{n=0}^{N-1}
\end{aligned}
\tag{D.22}
$$

The DFT, and its inverse, become:

$$
\begin{aligned}
f_k &= \sum_{n=0}^{N-1} F_n e^{ik\frac{n}{N}} \\
F_n &= \frac{1}{2\pi N} \sum_{n=0}^{N-1} f_x e^{-ik\frac{n}{N}}
\end{aligned}
\tag{D.23}
$$

## D.3.3. FT Artefacts

There is one artefact that plagues the FT with two separate causes, aliasing and spectral leakage. The artefact is obtaining the incorrect component or components at $F(f)$ from the FT of $f(t)$. In the subsequent sections, D.3.3.1 and D.3.3.2, I briefly present the cause of these artefacts along with a discussion of their effects and how we can correct or avoid them.

### D.3.3.1. Aliasing

Aliasing arises because of overstepping the limits imposed by the Shannon sampling theorem, section D.3.1.1. Vital to the understanding of aliasing is the convolution

theorem, discussed previously in section D.3.1.2. To illustrate the origin of alia-sing, we begin by considering the discrete sampling of the function, $f(x)$, to be a multiplication with a Dirac comb. The FT of this is then:

$$\int_{\infty}^{\infty} \delta(a-x)f(a)da = f(x) \tag{D.24}$$

The Dirac delta function, $\delta(x)$, is defined by its action upon another, as in eq D.24,while the Dirac comb is then defined as:

$$\text{III}(x,\Delta x) = \sum_{n=-\infty}^{\infty} \delta(x-n\Delta x)$$
$$F(L) = \frac{1}{2\pi}\int_{-\infty}^{\infty} \text{III}(x,\Delta x)f(x)e^{-ixL}dx \tag{D.25}$$

From the convolution theorem we know that a multiplication in one domain, $x$, is the same as convolution in the other, $L$.

$$F(L) = \int_{-\infty}^{\infty} \text{III}(x,\Delta x)e^{-ixL}dx * \frac{1}{2\pi}\int_{-\infty}^{\infty} f(x)e^{-2\pi ixL}dx \tag{D.26}$$

We can then evaluate the FT of $\text{III}(x,\Delta x)$, $\mathcal{F}\{\text{III}(x,\Delta x)\}$.

$$\int_{-\infty}^{\infty} \text{Ш}(x, \Delta x)e^{2\pi i x L}dx$$

$$= \int_{-\infty}^{\infty} \Delta x \sum_{n=-\infty}^{\infty} \delta(x - n\Delta x)e^{2\pi i x L}dx$$

$$= \sum_{n=-\infty}^{\infty} \int_{-\infty}^{\infty} \delta(x - n\Delta x)e^{2\pi i x L}dx \tag{D.27}$$

$$= \sum_{n=-\infty}^{\infty} e^{2\pi i n \Delta x L}$$

We find that the FT of a Dirac comb is another Dirac comb with its $\Delta x$ inverted to $\frac{1}{\Delta x}$.

$$\text{Ш}(x, \Delta x) = \sum_{k=-\infty}^{\infty} \delta(x - k\Delta x) = \sum_{n=-\infty}^{\infty} C_n e^{i2\pi n \frac{x}{\Delta x}}$$

$$C_n = \frac{1}{\Delta x} \int_0^{\Delta x} \text{Ш}(x, \Delta x)e^{2i\pi n \frac{x}{\Delta x}}dx$$

$$= \frac{1}{\Delta x} \int_0^{\Delta x} \sum_{k=-\infty}^{\infty} \delta(x - k\Delta x)e^{2i\pi n \frac{x}{\Delta x}}dx$$

$$= \frac{1}{\Delta x} \sum_{k=1}^{1} \int_0^{\Delta x} \delta(x - k\Delta x)e^{2i\pi n \frac{x}{\Delta x}}dx \tag{D.28}$$

$$= \frac{1}{\Delta x} e^{2i\pi n \frac{\Delta x}{\Delta x}}$$

$$C_n = \frac{1}{\Delta x} e^{2i\pi n} = \frac{1}{\Delta x}$$

$$\text{Ш}(x, \Delta x) = \frac{1}{\Delta x} \sum_{n=-\infty}^{\infty} e^{i2\pi n \frac{x}{\Delta x}}$$

The FT of the Dirac comb $\text{Ш}(x, \Delta x)$ is the same as another scaled Dirac comb $\Delta x \text{Ш}(L, \frac{1}{\Delta x})$.

$$\text{III}(x, \Delta x) = \frac{1}{\Delta x} \sum_{n=-\infty}^{\infty} e^{i2\pi n \frac{x}{\Delta x}}$$

$$\mathcal{F}\{\text{III}(x, \Delta x)\} = \sum_{n=-\infty}^{\infty} e^{2\pi i n \Delta x L}$$

$$\text{III}(L, \frac{1}{\Delta x}) = \frac{1}{\Delta x} \sum_{n=-\infty}^{\infty} e^{i2\pi n L \Delta x}$$

$$\mathcal{F}\{\text{III}(x, \Delta x)\} = \Delta x \text{III}(L, \Delta x)$$

(D.29)

The Dirac comb $\text{III}(x, \Delta x)$ is shown below as a figure.
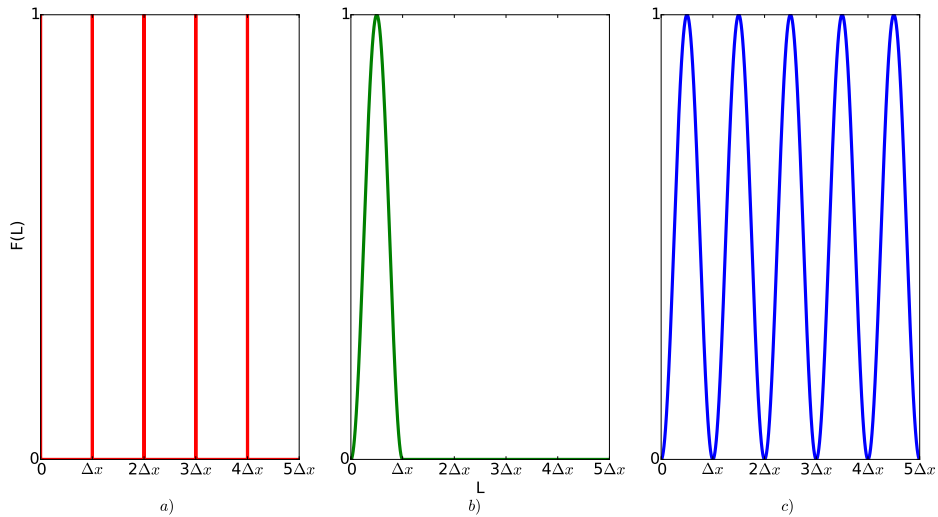


Figure D.1.: a) The Dirac comb $\text{III}(x, \Delta x)$. b) An example function $F(L) = \sin(\frac{2\pi L}{\Delta x})^2$ c) Convolution of $a$ and $b$. It is then clear how discrete sampling in one Fourier domain leads to copying, or aliasing, the spectrum in the other domain.

However, aliasing is not only the copying of the function $F(L)$, but also the mirror inversion about each copying point. This can been seen explicitly, where for the DFT $n, k$ are discrete point indexes of the conjugate variable pair, $N$ is the total number of points of $f_k$ sampled, in the DFT.

426

$$F(L) = \int_{-W}^{W} f(x)e^{-2\pi i x X} dx$$

$$F_n = \frac{1}{N} \sum_{n=0}^{N-1} f_x e^{-i2\pi k \frac{n}{N}}$$

(D.30)

Replacing the DFT index $n$ with $N - n$ gives:

$$F_n = \frac{1}{N} \sum_{n=0}^{N-1} f_x e^{-i2\pi n k \frac{1}{N}}$$

$$k \to N - k | F_{N-n} = \frac{1}{N} \sum_{n=0}^{N-1} f_x e^{-i2\pi [N-n] k \frac{1}{N}}$$

$$= \frac{1}{N} \sum_{n=0}^{N-1} f_x e^{-i2\pi k} e^{i2\pi n k \frac{1}{N}}$$

(D.31)

$$= \frac{1}{N} \sum_{n=0}^{N-1} f_x e^{-i2\pi(-n)k \frac{1}{N}}$$

$$F_{N-n} = \frac{1}{N} \sum_{n=0}^{N-1} f_x e^{i2\pi n k \frac{1}{N}}$$

Thus is can be seen that $F_{N-n}$ is the same as $F_{-n}$. This mirror symmetry confirms the Shannon sampling theorem, section D.3.1.1, as we must measure at rate equal to twice the desired minimum $n$. The mirror reflection of the repeated spectrum is then made clear , where the spectrum at position $N - n$ is the same as at $-n$, which is mirror reflection about zero and then $\frac{N}{2}$. This then shows that there is folding about $0, \frac{N}{2}, \frac{3N}{2}$,ect.

$$F_{N-n} = F_{-n} = F_n$$

(D.32)

## D.3.3.2. Spectral Leakage

Spectral leakage is a direct consequence of the finite duration of any FT and the convolution theorem. This can be easily seen from inspection of the FT, equation D.14. The FT depends on the measured function, $F(L)$, being defined from minus to plus infinity. No real measurement can occur infinitely, thus we must replace equation D.14, where $2W$ is the total $L$ that $F(L)$ is measured for.

$$f(x) = \int_{-W}^{W} F(L)e^{ixL}dL \tag{D.33}$$

Equation D.33 can be re-written as:

$$f(x) = \int_{-\infty}^{\infty} A(L)F(L)e^{ixL}dL \tag{D.34}$$

The FT of $A(L)$, equation D.36, is convolved with the FT of $F(L)$. The window function $A(L)$, is a boxcar function.

$$A(L) = \begin{cases} 1, & \text{if } -W \geq L \leq W. \\ 0, & \text{otherwise.} \end{cases} \tag{D.35}$$

$$
\begin{aligned}
\mathcal{F}\{A(L)\} &= \int_{-\infty}^{\infty} A(L)e^{ixL}dL \\
&= \int_{-W}^{W} e^{ixL}dL \\
&= \left[\frac{1}{ix}e^{ixL}\right]_{-W}^{W} \\
&= \frac{1}{ix}\left[e^{ixW} - e^{-ixW}\right] \\
&= \frac{1}{x}\left[\frac{e^{ixW} - e^{-ixW}}{i}\right] \\
&= \frac{1}{x}2\sin(xW) \\
&= 2W\frac{\sin(xW)}{xW} \\
&= 2W\,\mathrm{sinc}(xW)
\end{aligned}
\tag{D.36}
$$

It can be seen that each component of $F(L)$ is spread out over a central peak, and some "spectral leakage" occurs due to the side-lobes of the central peak. The raw sinc function results from a boxcar $A(L)$ function. By changing the exact nature of the $A(L)$ function, the width of the central peak, and size of the side-lobes relative to the central peak,can be changed. In general, the more suppressed the side-lobes, the wider the central peak and vice-versa. This is called apodization, from the Greek root for "removing the foot", where the foot removed is the interferogram altered by the application of the apodization function.

Spectral leakage is caused by the discontinuity in the FT function $A(L)F(L)$. By minimising this discontinuity, we can reduce the spectral leakage. The boxcar apodization function has a large discontinuity, jumping from finite values to zero instantly, thus also possessing an infinite second order derivative. By using a function that minimises these, we can minimise the spectral leakage.

The Blackman-Harris functions are such a group of multiple term functions, with varying coefficients for each term. Adjusting the coefficients, and the number of terms, allows fine tuning of the desired central peak width and sidelobe leakage.[182]

The Blackman-Harris 4 term function is:

$$
B(L) = \begin{cases} \left( \begin{aligned} & a_0 - a_1 \cos(\tfrac{2\pi[L+W]}{2W}) + a_2 \cos(\tfrac{4\pi[L+W]}{2W}) - a_3 \cos(\tfrac{6\pi[L+W]}{2W}) \\ & = a_0 - a_1 \cos(\tfrac{\pi[L+W]}{W}) + a_2 \cos(\tfrac{2\pi[L+W]}{W}) - a_3 \cos(\tfrac{3\pi[L+W]}{W}) \end{aligned} \right), & \text{if } -W \geq L \leq W. \\[2ex] 0, & \text{otherwise.} \end{cases}
$$

$$a_0 = 0.35875$$

$$a_1 = 0.48829$$

$$a_2 = 0.14128$$

$$a_3 = 0.01168$$

$$\text{(D.37)}$$

## D. The Fourier Transform

The Blackman-Harris 4 term function FT is:

$$\int_{-W}^{W} \cos(\frac{n\pi[L+W]}{W})e^{ixL}dL = \int_{-W}^{W} \left( \frac{e^{i\frac{n\pi[L+W]}{W}} + e^{-i\frac{n\pi[L+W]}{W}}}{2} \right)e^{ixL}dL$$

$$= \int_{-W}^{W} \left( \frac{e^{iL[\frac{n\pi}{W}+x]+in\pi} + e^{-iL[\frac{n\pi}{W}-x]-in\pi}}{2} \right)dL$$

$$= \left[ \frac{e^{iL[\frac{n\pi}{W}+x]+in\pi}}{2i[\frac{n\pi}{W}+x]} - \frac{e^{-iL[\frac{n\pi}{W}-x]-in\pi}}{2i[\frac{n\pi}{W}-x]} \right]_{-W}^{W}$$

$$= \frac{\left(e^{iW[\frac{n\pi}{W}+x]+in\pi} - e^{-iW[\frac{n\pi}{W}+x]+in\pi}\right)}{2i[\frac{n\pi}{W}+x]} + \frac{\left(e^{iW[\frac{n\pi}{W}-x]-in\pi} - e^{-iW[\frac{n\pi}{W}-x]-in\pi}\right)}{2i[\frac{n\pi}{W}-x]}$$

$$= \frac{\left(e^{i[2n\pi+Wx]} - e^{-iWx}\right)}{2i[\frac{n\pi}{W}+x]} + \frac{\left(e^{-iWx} - e^{-i[2n\pi-xW]}\right)}{2i[\frac{n\pi}{W}-x]}$$

$$= \frac{\left(e^{iWx} - e^{-iWx}\right)}{2i[\frac{n\pi}{W}+x]} + \frac{\left(e^{-iWx} - e^{ixW}\right)}{2i[\frac{n\pi}{W}-x]}$$

$$= \frac{\sin(Wx)}{[\frac{n\pi}{W}+x]} - \frac{\sin(Wx)}{[\frac{n\pi}{W}-x]}$$

$$= \frac{W\sin(Wx)}{[n\pi+Wx]} - \frac{W\sin(Wx)}{[n\pi-Wx]}$$

(D.38)

The cosine term arguments in the Blackman-Harris function are offset by $W$, this exploits their periodicity to bring the function and it's derivatives, with respect to the position at $-W, W$, close to zero; omission of the offset would bring the function to zero at $0, 2W$, etc. The Blackman-Harris function is a highly effective apodisation function for the suppression of sidelobes.[182] The convolution of both a sinc and the FT of the 4 term Blacman-Harris function with a Dirac delta function is shown as an example in figure D.2.

$$\mathcal{F}\{B(L)\} = \int_{-\infty}^{\infty} B(L)e^{ixL}dL = \int_{-W}^{W} B(L)e^{ixL}dL$$

$$= \int_{-W}^{W} \left( a_0 - a_1 \cos(\frac{\pi[L+W]}{W}) + a_2 \cos(\frac{2\pi[L+W]}{W}) - a_3 \cos(\frac{3\pi[L+W]}{W}) \right) e^{ixL}dL$$

$$= a_0 W \mathrm{sinc}(xW)$$

$$- a_1 W \left( \frac{\sin(Wx)}{[\pi + Wx]} - \frac{\sin(Wx)}{[\pi - Wx]} \right)$$

$$+ a_2 W \left( \frac{\sin(Wx)}{[2\pi + Wx]} - \frac{\sin(Wx)}{[2\pi - Wx]} \right)$$

$$- a_3 W \left( \frac{\sin(Wx)}{[3\pi + Wx]} - \frac{\sin(Wx)}{[3\pi - Wx]} \right)$$

(D.39)
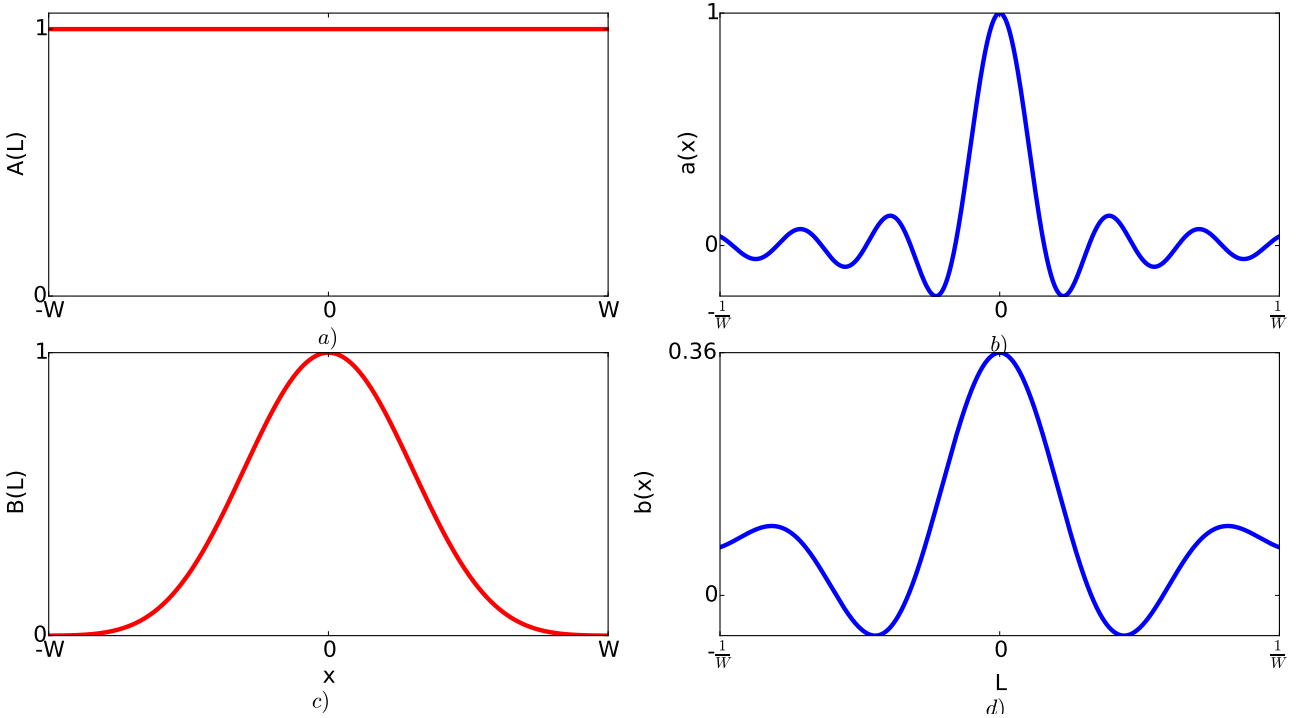


Figure D.2.: a)Boxcar function $A(L)$ b)$a(x) = \mathcal{F}\{A(L)\}$ c)Blackman-Harris function $B(L)$ d)$b(x) = \mathcal{F}\{B(L)\}$. Examples of two different apodization functions and their respective FTs. The boxcar is zero outside of the $[-W, W]$ domain shown, and has the narrowest central peak of all apodization functions. The Blackman-Harris 4 term function has suppressed sidelobes, at the cost of a greatly widened central peak.

# Bibliography

[1] A. M. Stoneham, A. J. Fisher, and P. T. Greenland, "Optically driven silicon-based quantum gates with potential for high-temperature operation," *Journal Of Physics: Condensed Matter*, vol. 15, no. 27, pp. L447–L451, 2003.

[2] M. T. Winkler, D. Recht, M.-J. Sher, A. J. Said, E. Mazur, and M. J. Aziz, "Insulator-to-metal transition in sulfur-doped silicon," *Phys. Rev. Lett.*, vol. 106, p. 178701, Apr 2011.

[3] J. D. Hunter, "Matplotlib: A 2d graphics environment," *Computing In Science & Engineering*, vol. 9, no. 3, pp. 90–95, 2007.

[4] S. van der Walt, S. C. Colbert, G. Varoquaux, *et al.*, "Numpy: "the fundamental package for scientific computing with python"," 2005–. [`www.numpy.org/`; accessed 12/07/2017].

[5] E. Jones, T. Oliphant, P. Peterson, *et al.*, "SciPy: Open source scientific tools for Python," 2001–. [`http://www.scipy.org/`; accessed 12/07/2017].

[6] G. van Rossum, "Python 2.7." http://www.python.org, 1995. [`http://www.python.org`: accessed 12/07/2017.

[7] B. E. Kane, "Silicon based quantum computing," *Fortschritte der Physik*, vol. 48, pp. 1023–1041, Oct 2000.

[8] W. Kohn and J. M. Luttinger, "Theory of donor states in silicon," *Physical Review*, vol. 98, no. 4, p. 915, 1955.

[9] D. P. DiVincenzo, "Topics in quantum computers," *eprint arXiv:cond-mat/9612126*, December 1996.

[10] D. P. DiVincenzo, "The physcial implementation of quantum computation," *Fortschritte der Physik*, vol. 48, no. 9-11, pp. 771–183, 2000.

[11] B. E. Kane, "A silicon-based nuclear spin quantum computer," *Nature*, vol. 393, pp. 133–137, may 1998.

# BIBLIOGRAPHY

[12] R. P. Feynman, "Simulating physics with computers," *International Journal of Theoretical Physics*, vol. 21, no. 6/7, 1982.

[13] H. Wang, S. Kais, A. Aspuru-Guzik, and M. R. Hoffmann, "Quantum algorithm for obtaining the energy spectrum of molecular systems," *Phys. Chem. Chem. Phys.*, vol. 10, pp. 5388–5393, 2008.

[14] P. W. Shor, "Algorithms for quantum computation: Discrete logarithms and factoring," *Proceeds of the 35th Annual Symposium on Foundations of Computer Science*, pp. 124–134, 1994.

[15] P. W. Shor, "Polynomial-time algorithms for prime factorization and discrete logarithms on a quantum computer," *SIAM Journal on Computing*, vol. 26, no. 5, pp. 1484–1509, 1997.

[16] E. L. et al, "Computing prime factors with a josephson phase qubit quantum processor," *Nature Physics*, vol. 8, pp. 719–723, 2012.

[17] L. M. K. V. et al, "Experimental realization of shor's quantum factoring algorithm using nuclear magnetic resonance," *Nature*, vol. 414, pp. 883–887, 2001.

[18] C.-Y. Lu, D. E. Browne, T. Yang, and J.-W. Pan, "Demonstration of a compiled version of shor's quantum factoring algorithm using photonic qubits," *Phys. Rev. Lett.*, vol. 99, p. 250504, Dec 2007.

[19] B. P. Lanyon, T. J. Weinhold, N. K. Langford, M. Barbieri, D. F. V. James, A. Gilchrist, and A. G. White, "Experimental demonstration of a compiled version of shor's algorithm with quantum entanglement," *Phys. Rev. Lett.*, vol. 99, p. 250505, Dec 2007.

[20] L. K. Grover, "A fast quantum mechanical algorithm for database search," *eprint arXiv:quant-ph/9605043*, may 1996.

[21] C. H. Bennett, "Quantum information and computation," *Physics Today*, vol. 48, p. 24, oct 1995.

[22] D. P. DiVincenzo, "Quantum computation," *Science*, vol. 270, pp. 255–261, oct 1995.

[23] J.-M. Schwindt, *Conceptual Basis of Quantum Mechanics*. Springer International Publishing, 2016.

[24] M. A. Nielsen and I. L. Chuang, *Quantum Computation and Quantum Information*. Cambridge University Press, 2013.

[25] R. Blatt and C. F. Roos, "Quantum simulations with trapped ions," *Nature Physics*, vol. 8, pp. 277–284, 2012.

[26] J. M. Gambetta, J. M. Chow, and M. Steffen, "Building logical qubits in a superconducting quantum computing system," *npj Quantum Information*, vol. 3, 2017.

[27] J. J. P. et al, "A single-atom electron spin qubit in silicon," *Nature*, vol. 489, pp. 541 – 545, September 2012.

[28] L. Allen and J. H. Eberly, *Optical Resonance and Two-Level Atoms.* Dover, 1987.

[29] M. Steger, K. Saeedi, M. L. W. Thewalt, J. J. L. Morton, H. Riemann, N. V. Abrosimov, P. Becker, and H.-J. Pohl, "Quantum information storage for over 180 s using donor spins in a 28si "semiconductor vacuum"," *Science*, vol. 336, no. 6086, pp. 1280–1283, 2012.

[30] P. T. G. et a, "Coherent control of rydberg states in silicon," *Nature*, vol. 465, pp. 1057–1061, June 2010.

[31] M. Fox, *Quantum Optics, An Introduction.* Oxford University Press, 2006.

[32] W. K. Wootters and W. H. Zurek, "A single quantum cannot be cloned," *Letters To Nature*, vol. 299, pp. 802–803, 1982.

[33] A. G. et al, "Observation of collective excitation of two individual atoms in the rydberg blockade regime," *Nature Physics*, vol. 5, pp. 115–118, 2009.

[34] B. Andreas, Y. Azuma, G. Bartl, P. Becker, H. Bettin, M. Borys, I. Busch, M. Gray, P. Fuchs, K. Fujii, H. Fujimoto, E. Kessler, M. Krumrey, U. Kuetgens, N. Kuramoto, G. Mana, P. Manson, E. Massa, S. Mizushima, A. Nicolaus, A. Picard, A. Pramann, O. Rienitz, D. Schiel, S. Valkiers, and A. Waseda, "Determination of the avogadro constant by counting the atoms in a $^{28}$Si crystal," *Phys. Rev. Lett.*, vol. 106, p. 030801, Jan 2011.

[35] R. H. Dicke, "Coherence in spontaneous radiation processes," *Physical Review*, vol. 93, no. 1, pp. 99–109, 1953.

[36] A. M. Steane, "Error correcting codes in quantum theory," *Phys. Rev. Lett.*, vol. 77, pp. 793–797, Jul 1996.

[37] G. W. et al., "Error correcting codes in quantum theory," *Physical Review Letters*, vol. 506, p. 204–207, february 2014.

[38] A. Barenco, C. H. Bennett, R. Cleve, D. P. DiVincenzo, N. Margolus, P. Shor, T. Sleator, J. A. Smolin, and H. Weinfurter, "Elementary gates for quantum computation," *Phys. Rev. A*, vol. 52, pp. 3457–3467, Nov 1995.

[39] D. P. DiVincenzo, "Two-bit gates are universal for quantum computation," *Phys. Rev. A*, vol. 51, pp. 1015–1022, Feb 1995.

[40] W. G. Unruh, "Maintaining coherence in quantum computers," *Phys. Rev. A*, vol. 51, pp. 992–997, Feb 1995.

[41] G. P. Berman, G. D. Doolen, P. C. Hammel, and V. I. Tsifrinovich, "Magnetic resonance force microscopy quantum computer with tellurium donors in silicon," *Phys. Rev. Lett.*, vol. 86, pp. 2894–2896, Mar 2001.

[42] S. Lloyd, "A potentially realizable quantum computer," *Science*, vol. 261, no. 5128, pp. 1569–1571, 1993.

[43] J. M. et al., "Solid state quantum memory using the 31p nuclear spin," *Nature*, vol. 455, October 2008.

[44] G. Wolfowicz, P.-A. Mortemousque, R. Guichard, S. Simmons, M. L. W. Thewalt, K. M. Itoh, and J. J. L. Morton, "29 si nuclear spins as a resource for donor spin qubits in silicon," *New Journal of Physics*, vol. 18, no. 2, p. 023021, 2016.

[45] N. Q. Vinh, P. T. Greenland, K. Litvinenko, B. Redlich, A. F. G. van der Meer, S. A. Lynch, M. Warner, A. M. Stoneham, G. Aeppli, D. J. Paul, C. R. Pidgeon, and B. N. Murdin, "Silicon as a model ion trap: Time domain measurements of donor rydberg states," *Proceedings of the National Academy of Sciences*, vol. 105, no. 31, pp. 10649–10653, 2008.

[46] M. Veldhorst, J. C. C. Hwang, C. H. Yang, A. W. Leenstra, B. de Ronde, J. P. Dehollain, J. T. Muhonen, F. E. Hudson, K. M. Itoh, A. Morello, and A. S. Dzurak, "An addressable quantum dot qubit with fault-tolerant control-fidelity," *Nature Nanotechnology*, vol. 9, pp. 981–985, 2014.

[47] D. Loss and D. P. DiVincenzo, "Quantum computation with quantum dots," *Phys. Rev. A*, vol. 57, pp. 120–126, Jan 1998.

[48] J. M. Elzerman, R. Hanson, L. H. W. van Beveren, B. Witkamp, L. M. K. Vandersypen, and L. P. Kouwenhoven, "Single-shot read-out of an individual electron spin in a quantum dot," *Nature*, vol. 430, pp. 431–435, 2004.

[49] C. H. Yang, R. R. A. Rossi, N. S. Lai, F. A. Mohiyaddin, S. Lee, C. Tahan, G. Klimeck, A. Morello, and A. S. Dzurak, "Spin-valley lifetimes in a silicon quantum dot with tunable valley splitting," *Nature Communications*, vol. 4, no. 2069, 2013.

[50] T. Ferrus, A. Rossi, M. Tanner, G. Podd, P. Chapman, and D. A. Williams, "Detection of charge motion in a non-metallic silicon isolated double quantum dot," *New Journal of Physics*, vol. 13, no. 10, p. 103012, 2011.

[51] C. H. Yang, A. Rossi, N. S. Lai, R. Leon, W. H. Lim, and A. S. Dzurak, "Charge state hysteresis in semiconductor quantum dots," *Applied Physics Letters*, vol. 105, no. 18, p. 183505, 2014.

[52] T. Ferrus, A. Rossi, A. Andreev, T. Kodera, T. Kambara, W. Lin, S. Oda, and D. A. Williams, "Ghz photon-activated hopping between localized states in a silicon quantum dot," *New Journal of Physics*, vol. 16, no. 1, p. 013016, 2014.

[53] K. J. Morse, R. J. S. Abraham, A. DeAbreu, C. Bowness, T. S. Richards, H. Riemann, N. V. Abrosimov, P. Becker, H.-J. Pohl, M. L. W. Thewalt, and S. Simmons, "A photonic platform for donor spin qubits in silicon," *Science Advances*, vol. 3, no. 7, 2017.

[54] M. F. Crommie, C. P. Lutz, and D. M. Eigler, "Confinement of electrons to quantum corrals on a metal surface," *Science*, vol. 262, no. 5131, pp. 218–220, 1993.

[55] J. L. O'Brien, S. R. Schofield, M. Y. Simmons, R. G. Clark, A. S. Dzurak, N. J. Curson, B. E. Kane, N. S. McAlpine, M. E. Hawley, and G. W. Brown, "Towards the fabrication of phosphorus qubits for a silicon quantum computer," *Phys. Rev. B*, vol. 64, p. 161401, Sep 2001.

[56] T. Reusch, N. Curson, S. Schofield, T. Hallam, and M. Simmons, "Phosphorus and hydrogen atoms on the (001) surface of silicon: A comparative scanning tunnelling microscopy study of surface species with a single dangling bond," *Surface Science*, vol. 600, pp. 318–324, jan 2006.

[57] D. R. Bowler, J. H. G. Owen, C. M. Goringe, K. Miki, and G. A. D. Briggs, "An experimental-theoretical study of the behaviour of hydrogen on the si(001) surface," *Journal of Physics: Condensed Matter*, vol. 12, no. 35, p. 7655, 2000.

[58] S. Schofield, P. Studer, C. Hirjibehedin, N. Curson, G. Aeppli1, and D. Bowler, "Quantum engineering at the silicon surface using dangling bonds," *Nature Communications*, vol. 4, no. 1649, 2013.

[59] M. Møller, S. P. Jarvis, L. Guérinet, P. Sharp, R. Woolley, P. Rahe, and P. Moriarty, "Automated extraction of single h atoms with stm: tip state dependency," *Nanotechnology*, vol. 28, no. 7, p. 075302, 2017.

[60] J. B. Ballard, T. W. Sisson, J. H. G. Owen, W. R. Owen, E. Fuchs, J. Alexander, J. N. Randall, and J. R. V. Ehr, "Multimode hydrogen depassivation lithography: A method for optimizing atomically precise write times," *Journal of Vacuum Science & Technology B,*

*Nanotechnology and Microelectronics: Materials, Processing, Measurement, and Phenomena*, vol. 31, no. 6, p. 06FC01, 2013.

[61] T. Hallam, F. J. Rueß, N. J. Curson, K. E. J. Goh, L. Oberbeck, M. Y. Simmons, and R. G. Clark, "Effective removal of hydrogen resists used to pattern devices in silicon using scanning tunneling microscopy," *Applied Physics Letters*, vol. 86, no. 14, p. 143116, 2005.

[62] M. Fuechsle, J. A. Miwa1, S. Mahapatra, H. Ryu, S. Lee, O. Warschkow, L. C. L. Hollenberg, G. Klimeck, and M. Y. Simmons, "A single-atom transistor," *Nature Nanotechnology*, vol. 7, pp. 242–246, 2012.

[63] M. A. Broome, S. K. Gorman, M. G. House, S. J. Hile, J. G. Keizer, D. Keith, C. D. Hill, T. F. Watson, W. J. Baker, L. C. L. Hollenberg, and M. Y. Simmons, "Two-electron spin correlations in precision placed donors in silicon," *Nature Communications*, vol. 9, no. 980, 2018.

[64] J. Clarke and F. K. Wilhelm, "Superconducting quantum bits," *Nature*, vol. 453, pp. 1031–1042, 2008.

[65] J. R. Friedman, V. Patel, W. Chen, S. K. Tolpygo, and J. E. Lukens, "Quantum superposition of distinct macroscopic states," *Nature*, vol. 406, pp. 43–46, 2000.

[66] C. H. van der Wal, A. C. J. ter Haar, F. K. Wilhelm, R. N. Schouten, C. J. P. M. Harmans, T. P. Orlando, S. Lloyd, and J. E. Mooij, "Quantum superposition of macroscopic persistent-current states," *Science*, vol. 290, no. 5492, pp. 773–777, 2000.

[67] Y. Nakamura, C. D. Chen, and J. S. Tsai, "Spectroscopy of energy-level splitting between two macroscopic quantum states of charge coherently superposed by josephson coupling," *Phys. Rev. Lett.*, vol. 79, pp. 2328–2331, Sep 1997.

[68] Y. Nakamura, Y. A. Pashkin, and J. S. Tsai, "Coherent control of macroscopic quantum states in a single-cooper-pair box," *Nature*, vol. 398, p. 786, 1999.

[69] V. Bouchiat, D. Vion, P. Joyez, D. Esteve, and M. H. Devoret, "Quantum coherence with a single cooper pair," *Physica Scripta*, vol. T76, 1998.

[70] K. Bladh, T. Duty, D. Gunnarsson, and P. Delsing, "The single cooper-pair box as a charge qubit," *New Journal of Physics*, vol. 7, no. 1, p. 180, 2005.

[71] J. M. Martinis, S. Nam, J. Aumentado, and C. Urbina, "Rabi oscillations in a large josephson-junction qubit," *Phys. Rev. Lett.*, vol. 89, p. 117901, Aug 2002.

[72] K. B. Cooper, M. Steffen, R. McDermott, R. W. Simmonds, S. Oh, D. A. Hite, D. P. Pappas, and J. M. Martinis, "Observation of quantum oscillations between a josephson phase qubit and a microscopic resonator using fast readout," *Phys. Rev. Lett.*, vol. 93, p. 180401, Oct 2004.

[73] K. R. Brown, J. Kim, and C. Monroe, "Co-designing a scalable quantum computer with trapped atomic ions," *Npj Quantum Information*, vol. 2, no. 16034, 2016.

[74] D. Yu, L. C. Kwek, L. Amico, and R. Dumke, "Superconducting qubit-resonator-atom hybrid system," *Quantum Science and Technology*, vol. 2, no. 3, p. 035005, 2017.

[75] R. Blatt and D. Wineland, "Entangled states of trapped atomic ions," *Nature*, vol. 453, pp. 1008–1015, 2008.

[76] C. Monroe and J. Kim, "Scaling the ion trap quantum processor," *Science*, vol. 339, no. 6124, pp. 1164–1169, 2013.

[77] T. Monz, P. Schindler, J. T. Barreiro, M. Chwalla, D. Nigg, W. A. Coish, M. Harlander, W. Hänsel, M. Hennrich, and R. Blatt, "14-qubit entanglement: Creation and coherence," *Phys. Rev. Lett.*, vol. 106, p. 130506, Mar 2011.

[78] C. Monroe, R. Raussendorf, A. Ruthven, K. R. Brown, P. Maunz, L.-M. Duan, and J. Kim, "Large-scale modular quantum-computer architecture with atomic memory and photonic interconnects," *Phys. Rev. A*, vol. 89, p. 022317, Feb 2014.

[79] A. R. S. et al, "Electrical detection of coherent $^{31}$p spin quantum states," *Nature Physics*, vol. 2, pp. 835–838, 2006.

[80] Unknown, "Ioffe semiconductor parameters repository." `http://www.ioffe.ru/SVA/NSM/Semicond/Si/basic.html`. Accessed: 21-03-2017.

[81] C. Kittel, *Introduction to Solid State Physics*. Wiley, 8th edition ed., 2005.

[82] L. A. N. L. USA, "Periodic table." `http://periodic.lanl.gov/images/periodictable.pdf`. Accessed: 10-04-2017.

[83] C. Flensburg and R. F. Stewart, "Lattice dynamical debye-waller factor for silicon," *Phys. Rev. B*, vol. 60, pp. 284–291, Jul 1999.

[84] J. H. Parker, D. W. Feldman, and M. Ashkin, "Raman scattering by silicon and germanium," *Phys. Rev.*, vol. 155, pp. 712–714, Mar 1967.

[85] F. Shimura, *Semiconductor Silicon Crystal Technology*. Elsevier, first ed., 2012.

[86] Intel, "Making of a chip." `http://download.intel.com/pressroom/kits/chipmaking/` `Making_of_a_Chip.pdf`. Accessed: 26-04-2017.

[87] M. Tilli, T. Motooka, V.-M. Airaksinen, S. Franssila, M. Paulasto-Krockel, and V. Lindroos, *Handbook of Silicon Based MEMS Materials and Technologies*. Elsevier, second ed., 2015.

[88] P. Becker, D. Schiel, H.-J. Pohl, A. K. Kaliteevski, O. N. Godisov, M. F. Churbanov, G. G. Devyatykh, A. V. Gusev, A. D. Bulanov, S. A. Adamchik, V. A. Gavva, I. D. Kovalev, N. V. Abrosimov, B. Hallmann-Seiffert, H. Riemann, S. Valkiers, P. Taylor, P. D. Bièvre, and E. M. Dianov, "Large-scale production of highly enriched 28 si for the precise determination of the avogadro constant," *Measurement Science and Technology*, vol. 17, no. 7, p. 1854, 2006.

[89] B. Andreas, Y. Azuma, G. Bartl, P. Becker, H. Bettin, M. Borys, I. Busch, P. Fuchs, K. Fujii, H. Fujimoto, E. Kessler, M. Krumrey, U. Kuetgens, N. Kuramoto, G. Mana, E. Massa, S. Mizushima, A. Nicolaus, A. Picard, A. Pramann, O. Rienitz, D. Schiel, S. Valkiers, A. Waseda, and S. Zakel, "Counting the atoms in a 28 si crystal for a new kilogram definition," *Metrologia*, vol. 48, no. 2, p. S1, 2011.

[90] A. Picard, P. Barat, M. Borys, M. Firlus, and S. Mizushima, "State-of-the-art mass determination of 28 si spheres for the avogadro project," *Metrologia*, vol. 48, no. 2, p. S112, 2011.

[91] P. Becker, H. Friedrich, K. Fujii, W. Giardini, G. Mana, A. Picard, H.-J. Pohl, H. Riemann, and S. Valkiers, "The avogadro constant determination via enriched silicon-28," *Measurement Science and Technology*, vol. 20, no. 9, p. 092002, 2009.

[92] Y. Azuma, P. Barat, G. Bartl, H. Bettin, M. Borys, I. Busch, L. Cibik, G. D'Agostino, K. Fujii, H. Fujimoto, A. Hioki, M. Krumrey, U. Kuetgens, N. Kuramoto, G. Mana, E. Massa, R. Meeß, S. Mizushima, T. Narukawa, A. Nicolaus, A. Pramann, S. A. Rabb, O. Rienitz, C. Sasso, M. Stock, R. D. V. Jr, A. Waseda, S. Wundrack, and S. Zakel, "Improved measurement results for the avogadro constant using a 28 si-enriched crystal," *Metrologia*, vol. 52, no. 2, p. 360, 2015.

[93] A. Giesekus and L. M. Falicov, "Ground-state configuration of double acceptors in silicon and germanium," *Phys. Rev. B*, vol. 42, pp. 8975–8981, Nov 1990.

[94] E. Janzén, R. Stedman, G. Grossmann, and H. G. Grimmeiss, "High-resolution studies of sulfur- and selenium-related donor centers in silicon," *Phys. Rev. B*, vol. 29, pp. 1907–1918, Feb 1984.

# BIBLIOGRAPHY

[95] P. Y. Yu and M. Cardona, *Fundamentals of Semiconductors: Physics and Materials Properties*. Graduate Texts in Physics, Springer Berlin Heidelberg, 1 ed., 2010.

[96] J. Salfi, M. Tong, S. Rogge, and D. Culcer, "Quantum computing with acceptor spins in silicon," *Nanotechnology*, vol. 27, no. 24, p. 244001, 2016.

[97] V. D. Tkachev, A. V. Mudryi, and N. S. Minaev, "Noble gas atoms as chemical impurities in silicon," *physica status solidi (a)*, vol. 81, no. 1, pp. 313–321, 1984.

[98] C. L. Claeys, P. Rai-Choudhury, M. Watanabe, and P. Stallhofer, *High Purity Silicon VI: Proceedings of the sixth international symposium*. The Electrochemical Society, in cooperation with SPIE, 2000-2017 ed., 2000.

[99] D. P. DiVincenzo, "Two-bit gates are universal for quantum computation," *Physical Review A*, vol. 51, no. 2, pp. 1015–1022, 1995.

[100] H. G. Grimmeiss, "Deep level impurities in semiconductors," *Annual Review of Material Sciences*, vol. 7, no. 1, pp. 341–376, 1977.

[101] P. T. Greenland and S. A. L. et al, "Coherent control of rydberg states in silicon," *Nature*, vol. 465, pp. 1057–1061, June 2010.

[102] D. Karaiskaj, J. A. H. Stotz, T. Meyer, M. L. W. Thewalt, and M. Cardona, "Impurity absorption spectroscopy in $^{28}$si the importance of inhomogeneous broadening," *Physical Review Letters*, vol. 90, no. 18, pp. 186402–1 – 186402–4, 2003.

[103] M. Steger, A. Yang, D. Karaiskaj, M. L. W. Thewalt, E. E. Haller, J. W. Ager, M. Cardona, H. Riemann, N. V. Abrosimov, A. V. Gusev, A. D. Bulanov, A. K. Kaliteevskii, O. N. Godisov, P. Becker, and H.-J. Pohl, "Shallow impurity absorption spectroscopy in isotopically enriched silicon," *Phys. Rev. B*, vol. 79, p. 205210, May 2009.

[104] S. A. L. et al, "Inhomogeneous broadening of phosphorus donor lines in the far-infrared spectra of single-crystalline sige," *Physical Review B*, vol. 82, 2010.

[105] H.-W. Hübers, S. G. Pavlov, S. A. Lynch, T. Greenland, K. L. Litvinenko, B. Murdin, B. Redlich, A. F. G. van der Meer, H. Riemann, N. V. Abrosimov, P. Becker, H.-J. Pohl, R. K. Zhukavin, and V. N. Shastin, "Isotope effect on the lifetime of the $2p_0$ state in phosphorus-doped silicon," *Phys. Rev. B*, vol. 88, p. 035201, Jul 2013.

[106] W. Kohn and J. M. Luttinger, "Motion of electrons and holes in perturbed periodic fields," *Physical Review*, vol. 97, no. 4, pp. 869–883, 1955.

[107] R. A. Faulkner, "Higher donor excited states for prolate-spheroid conduction bands: A reevaluation of silicon and germanium," *Phys. Rev.*, vol. 184, pp. 713–721, Aug 1969.

[108] B. Pajot and A. M. Stoneham, "A spectroscopic investigation of the lattice distortion at substitutional sites for groups v and vi donors in silicon," *Journal of Physics C: Solid State Physics*, vol. 20, no. 32, p. 5241, 1987.

[109] A. Yang, M. Steger, H. J. Lian, M. L. W. Thewalt, M. Uemura, A. Sagara, K. M. Itoh, E. E. Haller, J. W. Ager, S. A. Lyon, M. Konuma, and M. Cardona, "High-resolution photoluminescence measurement of the isotopic-mass dependence of the lattice parameter of silicon," *Phys. Rev. B*, vol. 77, p. 113203, Mar 2008.

[110] H. G. Grimmeiss, E. Janzén, H. Ennen, O. Schirmer, J. Schneider, R. Wörner, C. Holm, E. Sirtl, and P. Wagner, "Tellurium donors in silicon," *Phys. Rev. B*, vol. 24, pp. 4571–4586, Oct 1981.

[111] M. S. et al, "Impurity absorption spectroscopy of the deep double donor sulfur in isotopically enriched silicon," *Physica B: Condensed Matter*, vol. 401-402, pp. 600–603, December 2007.

[112] M. S. et al, "High resolution absorption spectroscopy of the deep impurities s and se in 28si revealing the 77se hyperfine splitting," *Physical Review B*, vol. 80, 2009.

[113] M. L. W. T. et al, "Can highly enriched $^{28}$si reveal new things about old defects?," *Physica B: Condensed Matter*, vol. 401-402, pp. 587–592, december 2007.

[114] R. Carlson, R. Hall, and E. Pell, "Sulfur in silicon," *Journal of Physics and Chemistry of Solids*, vol. 8, pp. 81 – 83, 1959.

[115] W. Kohn, "Shallow impurity states in silicon and germanium," in *Solid State Physics Volume 5* (F. Seitz and D. Turnbull, eds.), ch. 4, pp. 257–320, Academic Press, 1957.

[116] A. L. Saraiva, A. Baena, M. J. Calderón, and B. Koiller, "Theory of one and two donors in silicon," *Journal of Physics: Condensed Matter*, vol. 27, no. 15, p. 154208, 2015.

[117] E. W. Weisstein, "L'hospital's rule.," *MathWorld–A Wolfram Web Resource*, 2017.

[118] E. W. Weisstein, "Associated laguerre polynomial.," *MathWorld–A Wolfram Web Resource*, 2017.

[119] E. W. Weisstein, "Associated legendre polynomial.," *MathWorld–A Wolfram Web Resource*, 2017.

## BIBLIOGRAPHY

[120] W. Ritz, "Über eine neue methode zur lösung gewisser variationsprobleme der mathematischen physik," *Journal für die reine und angewandte Mathematik (Crelle's Journal)*, vol. 1909, no. 135, pp. 1–61, 1909.

[121] J. W. Strutt, "On the theory of resonance," *Philisophical transactions*, vol. 161, pp. 77–118, 1870.

[122] A. D. Boardman, D. E. O'Connor, and P. A. Young, *Symmetry and its Applications in Science.* McGraw-Hill, 1973.

[123] N. F. Mott, "On the transition to metallic conduction in semiconductors," *Canadian Journal of Physics*, vol. 34, no. 12A, pp. 1356–1368, 1956.

[124] M. N. Alexander and D. F. Holcomb, "Semiconductor-to-metal transition in $n$-type group iv semiconductors," *Rev. Mod. Phys.*, vol. 40, pp. 815–829, Oct 1968.

[125] P. P. Edwards and M. J. Sienko, "Universality aspects of the metal-nonmetal transition in condensed media," *Phys. Rev. B*, vol. 17, pp. 2575–2581, Mar 1978.

[126] Brüker, "Brüker 80v overview." [`https://www.bruker.com/products/infrared-near-infrared-and-raman-spectroscopy/ft-ir-research-spectrometers/vertex-series/vertex-8080v/overview.html`; accessed 05/09/2017].

[127] Brüker, "Vertex 80v user manual," 2006.

[128] Thorlabs, "Plano-convex round cylindrical lenses, caf2, mounted," 2017. [`https://www.thorlabs.com/newgrouppage9.cfm?objectgroup_id=7654`; accessed 19/09/2017].

[129] E. Optics, "Off-axis parabolic metal mirrors," 2017. [`https://www.edmundoptics.com/optics/optical-mirrors/off-axis-parabolic-mirrors/Off-Axis-Parabolic-Metal-Mirrors/`; accessed 19/09/2017].

[130] Ekspla, "Nt342 series high energy broadly tunable lasers," 2017. [`http://ekspla.com/product/nt300-series-tunable-lasers/`; accessed 19/09/2017].

[131] Thorlabs, "Uv enhanced and protected aluminum mirrors," 2017. [`https://www.thorlabs.com/newgrouppage9.cfm?objectgroup_id=264`; accessed 19/09/2017].

[132] Thorlabs, "Protected gold mirrors," 2017. [`https://www.thorlabs.com/newgrouppage9.cfm?objectgroup_id=744`; accessed 19/09/2017].

[133] E. optics, "Potassium bromide (kbr) windows," 2017. [`https://www.edmundoptics.com/optics/windows-diffusers/ultraviolet-uv-infrared-ir-windows/potassium-bromide-kbr-windows/`; accessed 19/09/2017].

[134] Edwards, "Aim-s-nw25 magentron gauge," 2017. [`https://shop.edwardsvacuum.com/products/d14641000/view.aspx`; accessed 19/09/2017].

[135] O. Instruments, "Helium cryostats 4 k." [`https://www.oxford-instruments.com/products/cryogenic-environments/optical-cryostats-for-spectroscopy/liquid-helium-cryostats-(4k)`; accessed 19/09/2017].

[136] O. Instruments, "Programmable temperature controller, multi-channel - mercury itc." [`https://www.oxford-instruments.com/products/cryogenic-environments/measurement-mercury-electronics/programmable-temperature-controller-multi-channel`; accessed 19/09/2017].

[137] Spectrum, "High speed 14 bit transient recorder a/d converter board hardware manual," 2011.

[138] P. Labs, "Pspl5575a - picosecond pulse labs, bias tee, 12ghz, 50v, sma," 2017. [`http://onecall.farnell.com/tektronix/pspl5575a/bias-tee-12ghz-50v-sma-jack-jack/dp/2432815`; accessed 19/09/2017].

[139] Pasternack, "29 dbm ip3, 2.5 db nf, 16 dbm p1db, 0.009 mhz to 3 ghz, low noise amplifier, 32 db gain, sma," 2017. [`https://www.pasternack.com/2.5-db-3-ghz-low-noise-amplifier-32-db-gain-sma-pe15a1007-p.aspx`; accessed 19/09/2017].

[140] Y. A. Astrov, V. B. Shuman, L. M. Portsel, and A. N. Lodygin, "Doping of silicon with selenium by diffusion from the gas phase," *Semiconductors*, vol. 48, pp. 413–416, Mar 2014.

[141] Y. A. Astrov, L. M. Portsel, A. N. Lodygin, and V. B. Shuman, "Gas-phase doping of silicon with sulfur," *Semiconductor Science and Technology*, vol. 26, no. 5, p. 055021, 2011.

[142] Y. A. Astrova, S. A. Lynch, V. B. Shumana, L. M. Portsela, A. A. Makhovaa, and A. N. Lodygina, "Silicon with an increased content of monoatomic sulfur centers: Sample fabrication and optical spectroscopy," *Semiconductors*, vol. 47, p. 247–251, 2013.

[143] J. T. et all, "Iupac critical evaluation of the rotational-vibrational spectra of water vapor. part i. energy levels and transition wavenumbers for $h_2^{17}o$, and $h_2^{18}o$.," *Journal of Quantitative Spectroscopy and Radiative Transfer*, vol. 110, pp. 573–596, 2009.

[144] J. T. et all, "Iupac critical evaluation of the rotational-vibrational spectra of water vapor. part ii. energy levels and transition wavenumbers for $hd^{16}o$, $hd^{17}o$, and $hd^{18}o$.," *Journal of Quantitative Spectroscopy and Radiative Transfer*, vol. 111, pp. 2160–2184, 2010.

# BIBLIOGRAPHY

[145] J. T. et all, "Iupac critical evaluation of the rotational–vibrational spectra of water vapor, part iii: Energy levels and transition wavenumbers for $h_2^{16}o$.," *Journal of Quantitative Spectroscopy and Radiative Transfer*, vol. 117, pp. 29–58, 2013.

[146] J. T. et all, "Iupac critical evaluation of the rotational–vibrational spectra of water vapor. part iv. energy levels and transition wavenumbers for $d_2^{16}o$, $d_2^{17}o$, and $d_2^{18}o$," *Journal of Quantitative Spectroscopy and Radiative Transfer*, vol. 142, pp. 93–108, 2014.

[147] NIST, "Carbon dioxide ir spectrum," 2017. [`http://webbook.nist.gov/cgi/cbook.cgi?ID=C124389&Type=IR-SPEC&Index=1#IR-SPEC`; accessed 19/09/2017].

[148] R. C. Newman, "Defects in silicon," *Reports On Progress In Physics*, vol. 45, pp. 1163–1210, 1982.

[149] P. G. S. et al, "Spectroscopic parameters of lvm absorption bands of carbon and oxygen impurities in isotopic enriched silicon $^{28}$si, $^{29}$si and $^{30}$si," *Physics and Technology of Semiconductors*, vol. 39, no. 3, pp. 320–326, 2005.

[150] A. Sassella, "Measurement of interstitial oxygen concentration in silicon below $10^{15}$ atoms/$cm^3$," *Applied Physics Letters*, vol. 79, pp. 4339–4341, 2001.

[151] S. Zakel, S. Wundrack, H. Niemannand, O. Rienitz, and D. Schiel, "Infrared spectrometric measurement of impurities in highly enriched 'si28'," *Metrologia*, vol. 48, no. 2, pp. S14–S19, 2011.

[152] L. H. Negri, "Peakutils: ""." "https://pypi.python.org/pypi/PeakUtils", 2017. [`http://pythonhosted.org/PeakUtils/`; accessed 12/07/2017].

[153] U. Fano, "Effects of configuration interaction on intensities and phase shifts," *Phys. Rev.*, vol. 124, pp. 1866–1878, Dec 1961.

[154] N. Stavrias, K. Saeedi, B. Redlich, P. T. Greenland, H. Riemann, N. V. Abrosimov, M. L. W. Thewalt, C. R. Pidgeon, and B. N. Murdin, "Competition between homogeneous and inhomogeneous broadening of orbital transitions in si:bi," *Phys. Rev. B*, vol. 96, p. 155204, Oct 2017.

[155] P. Clauws, J. Broeckx, E. Rotsaert, and J. Vennik, "Oscillator strengths of shallow impurity spectra in germanium and silicon," *Phys. Rev. B*, vol. 38, pp. 12377–12382, Dec 1988.

[156] B. Pajot and B. Clerjaud, *Optical Absorption of Impurities and Defects in Semiconducting Crystals: Electronic Absorption of Deep Centres and Vibrational Spectra.* Springer-Verlag Berlin Heidelberg, 2013.

[157] E. W. Weisstein, "Least squares fitting," *MathWorld–A Wolfram Web Resource*, 2017.

[158] T. Ichibayashi and K. Tanimura, "Ultrafast carrier relaxation in si studied by time-resolved two-photon photoemission spectroscopy: Intravalley scattering and energy relaxation of hot electrons," *Phys. Rev. Lett.*, vol. 102, p. 087403, Feb 2009.

[159] V. N. Abakumov, V. I. Perel, and I. N. Yassievich, *Nonradiative Recombination In Semiconductors*, vol. 33 of *Modern Problems In Condensed Matter Sciences*. North-Holland, 1991.

[160] E. W. Weisstein, "Hilbert space," *MathWorld–A Wolfram Web Resource*, 2017.

[161] E. W. Weisstein, "Vector space," *MathWorld–A Wolfram Web Resource*, 2017.

[162] E. Schrödinger, "Quantisierumg als eigenwertblem," *Annalen der Physik*, vol. 384, no. 4, pp. 361–376, 1926.

[163] R. Eisberg and R. Resnick, *Quantum Physics of Atoms, Molecules, Solids, Nuclei and Particles*. John Wiley & Sons, 1985.

[164] L. J. Brillson, *Surfaces and Interfaces of Electronic Materials*. Wiley-VCH, first ed., 2010.

[165] R. Loudon, *The Quantum Theory of Light*. Oxford Science Publications, Oxford University Press, third ed., 200.

[166] J. D. Jackson, *Classical Electrodynamics*. Wiley, 1962.

[167] M. Fox, *Optical Properties of Solids*. Oxford University Press, 2010.

[168] E. W. Weisstein, "Laplacian," *MathWorld–A Wolfram Web Resource*, 2017.

[169] M. Czerny and A. F. Turner, "Über den astrigmatismus bei spiegelspektrometern," *Zeitschrift für Physik*, vol. 61, no. 11-12, pp. 792–797, 1930.

[170] A. A. Michelson and E. W. Morley, "On the relative motion of the earth and the luminiferous ether," *The American Journal of Science - Third Series*, vol. 34, no. 203, 1887.

[171] T. G. Mayerhöfer, H. Mutschke, and J. Popp, "Employing theories far beyond their limits—the case of the (boguer-) beer–lambert law," *ChemPhysChem*, vol. 17, no. 13, pp. 1948–1955, 2016.

[172] P. R. Griffiths and J. A. de Haseth, *Fourier Transform Infrared Spectroscopy*. John Wiley and Sons, second edition ed., 2007.

[173] L. R. F.R.S., "Xxxi. investigations in optics, with special reference to the spectroscope," *Philosophical Magazine Series 5*, vol. 8, no. 49, pp. 261–274, 1879.

[174] P. Connes, "Pierre jacquinot and the beginnings of fourier transform spectrometry," *Journal de Physique II*, vol. 2, no. 4, pp. 565–571., 1992.

[175] R. Mitchell, "Obituary of peter berners fellgett." `https://www.rse.org.uk/cms/files/fellows/obits_alpha/fellgett_p_b.pdf`. Accessed: 15-01-2017.

[176] J. Connes, "Domaine d'utilisation de la méthode par transformée de fourier," *J. Phys. Radium*, vol. 19, no. 3, pp. 197 – 208, 1958.

[177] J. W. Cooley and J. W. Tukey, "An algorithm for the machine calculation of complex fourier series," *Mathematics of Computation*, vol. 19, no. 90, pp. 297–301, 1965.

[178] C. D. Porter and D. B. Tanner, "Correction of phase errors in fourier spectroscopy," *International Journal of Infrared and Millimeter Waves*, vol. 4, no. 2, 1983.

[179] L. Mertz, "Correction of phase errors in interferograms," *Applied Optics*, vol. 2, no. 12, pp. 1332–1332, 1963.

[180] M. L. Forman, W. H. Steel, , and G. A. Vanasse, "Correction of asymmetric interferograms obtained in fourier spectroscopy," *Journal of the Optical Society of America*, vol. 56, no. 1, pp. 59–63, 1966.

[181] C. E. Shannon, "Communication in the presence of noise," *Proceedings of the IEEE*, vol. 37, no. 1, pp. 10–21, 1949.

[182] F. J. Harris, "On the use of windows for harmonic analysis with the discrete fourier transform," *Proceedings of the IEEE*, vol. 66, pp. 51–83, January 1978.